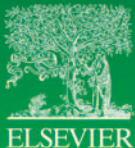# FUNDAMENTALS AND PROPERTIES OF MULTIFUNCTIONAL NANOMATERIALS

Edited by
Sabu Thomas, Nandakumar Kalarikkal, and Ann Rose Abraham

ELSEVIER

Fundamentals and Properties of Multifunctional Nanomaterials

Micro and Nano Technologies

Fundamentals and Properties of Multifunctional Nanomaterials

Edited by

Sabu Thomas

Nandakumar Kalarikkal

Ann Rose Abraham

For information on all Elsevier publications visit our website at
https://www.elsevier.com/books-and-journals

Working together
to grow libraries in
developing countries

www.elsevier.com • www.bookaid.org

Contents

Transport properties of nanoscopic solids as probed by spectroscopic techniques

Dejan M. Djokić[1], Novica Paunović[1], Bojan Stojadinović[1], Dimitrije Stepanenko[1], Saša Lazović[2], Zorana Dohčević-Mitrović[1]

[1]*Nanostructured Matter Laboratory, Institute of Physics Belgrade, University of Belgrade, Belgrade, Serbia;* [2]*Biomimetics Laboratory, Institute of Physics Belgrade, University of Belgrade, Belgrade, Serbia*

1. Introduction

Nanoscale world is at the border between the quantum realm at the smaller dimensions and the classical one at larger. At the quantum side of this divide, systems under consideration consist of few particles and the properties of the sample often do not average into well-behaved quantities with deviations from the mean value much smaller than the mean value itself. So standard assumptions of both the classical physics and the standard statistics can break down within the nanoscale domain. This occurrence impacts the methods for probing the transport at the nanoscale.

Noncontact measurements of transport can offer distinct advantages. Macroscopic contacts necessary for the standard transport measurements often disturb the system since they are immensely larger than it. The structure of the contacts needs to impact the system as little as possible, requiring cooling to very low temperatures. Thermal noise introduced by contacts is hard to distinguish from the quantum noise that is an interesting property of the probed system.

Experiment is always performed on an object composed of nonidentical units and averaging of the properties does not automatically occur within the measurement apparatus. Moreover, the most interesting properties are often encoded into distribution of the results of measurements, and not exclusively in their mean values. Quantum side of the breakdown is somewhat different. The quantum transport theory deals with universality of the transport. In the quantum limit, as most transparently seen in the Landauer formula for conductivity, the whole variety of the transport behavior boils down to the number and transmitivities of transport channels. The variety of quantum behavior in transport appears due to macroscopic quantum phenomena or lies hidden in the variability of nominally identical nanoscale systems.

To probe the rich variety of transport phenomena at the nanoscale, it is preferable to look at the properties of conducting quasiparticles than to look at the integral characteristics of a collection of them. Quasiparticles are most easily accessed through spectroscopic techniques, like Raman spectroscopy, electron spin resonance (ESR), and infrared reflection (IRR) spectroscopy. Resonant nature of excitations and response detection in spectroscopy offer us a way to discriminate between constituents of the nanoscale system and look exclusively at the processes that are in resonance with the appropriate driving. Therefore the noncontact spectroscopic measurements give us an opportunity to see the nanoscale world in more detail.

This chapter is partitioned in three sections which are organized as follows. In the first section, we provide a short introduction to the Raman scattering technique followed with a review on an indirect finding of the two different variable range hopping (VRH) transport mechanisms based on the analysis of the temperature dependent electronic Raman background of nanocrystalline $BiFeO_3$ [1]. The subsequent section tackles a summary on how both particle size decreased and Nd doping influence the Plasmon−phonon interaction and optical conductivity in CeO_{2-y} nanocrystals investigated by IRR spectroscopy [2]. Finally, in the third section, the main aspects of conduction ESR have been briefly introduced in which terms the temperature evolution and character of transport properties of single-walled carbon nanotubes have been elaborated [3].

2. Raman scattering

2.1 Short introduction to Raman scattering technique

In solid state spectroscopy, the inelastic scattering of photons by lattice vibrations (LVs) is known as Raman effect. The photon energy can be lost or gained in such processes, which

is accomplished by the phonon creation or annihilation, and termed in literature as Stokes or anti-Stokes Raman excitation, respectively. Brillouin Raman scattering (RS), however, stands for a particular case of RS that concerns the scattering by acoustic phonons of very low frequencies, unlike common Raman which involves optical phonons. The theory of Raman spectroscopy can be found elsewhere. Nevertheless, for a rather comprehensive elaboration the reader is further referred to seminal Mitra's work [4], some of which fragments we will rely on in what follows.

Following the first principles of electromagnetism, the incident electromagnetic field of the photons is coupled with the phonons via dipole moments that are induced by the phonon field. The electronic 3×3 polarizability tensor α_{mn} is modulated by the variation of the lattice due to the normal vibration of frequency ω_p and can be expanded in terms of the time dependent atomic displacement components $u_p = u_p(0)e^{i\omega_p t}$ as

$$\alpha_{mn} = \alpha_{mn}^{(0)} + \sum_p \alpha_{mn,p}^{(1)} u_p + \frac{1}{2}\sum_p \sum_q \alpha_{mn,pq}^{(2)} u_p u_q + \dots \tag{2.1}$$

where

$$\alpha_{mn,p}^{(1)} = \left(\frac{\partial \alpha_{mn}}{\partial u_p}\right)_{u_p=0}, \quad \alpha_{mn,pq}^{(2)} = \left(\frac{\partial^2 \alpha_{mn}}{\partial u_p \partial u_q}\right)_{u_p=0,\ u_q=0} \dots \tag{2.2}$$

If $\overrightarrow{E}$ denotes the electric field of incident electromagnetic radiation with frequency ω,

$$\overrightarrow{E} = \overrightarrow{E}(0)e^{i\omega t}, \tag{2.3}$$

then the induced dipole moment can be written as

$$\overrightarrow{M} = \widehat{\alpha}\,\overrightarrow{E}, \tag{2.4}$$

which ultimately yields induced dipole moment along p mode

$$\overrightarrow{M}_p = \widehat{\alpha}^{(0)}\overrightarrow{E}_0 e^{i\omega t} + \widehat{\alpha}^{(1)}\overrightarrow{E}_0 e^{i(\omega \pm \omega_p)t}u_p(0) + \widehat{\alpha}^{(2)}\overrightarrow{E}_0 e^{i(\omega \pm 2\omega_p)t}u_p^2(0) + \dots \tag{2.5}$$

First term in Eq. (2.5) represents nothing but elastic Raleigh scattering process. The energy of the electromagnetic radiation remains unchanged in this case. The derivative of the electronic polarizability in the second term in Eq. (2.5) gives rise to the first-order RS processes when incident photon $\left(\hbar \overrightarrow{k}_1, \hbar\omega_1\right)$ is absorbed or created to create or destroy a phonon $\left(\hbar \overrightarrow{k}, \hbar\omega\right)$. The final photon, with both different wave vector and frequency $\left(\hbar \overrightarrow{k}_2, \hbar\omega_2\right)$ from the incident one, gets emitted in such a way that the energy and the momentum are totally conserved. Reduced Planck's constant is denoted as $\hbar$.

In doped semiconductors and disordered metals, spectral recoil of light in RS consistently comprises a number of distinctive peaks generated by optically active phonons, as well as, an extended frequency continuum which is in direct relationship with electronic response [6]. This continuous spectral background originates from low-energy electronic excitations, which reflects the charge carrier scattering rate, and is familiarly known in literature as the Raman electronic background [1,7−11]. Falkovsky [7] was first to provide a theoretical foundation for the spectral profiles of Raman electronic background in "dirty" metals. The effects of electronic excitations in Raman are usually observed at low-energy scales and are attributed to scattering by phonons or impurities involving finite momentum transfers ($k \neq 0$) as a result of the finite penetration depth of light in materials. Later on, Zawadowski and Cardona [8] proposed a Feynman diagrammatic approach to estimating the Kubo spectral response function within the scope of ladder approximation [12] at $q \approx 0$. Most importantly, these authors were first to recognize an intimately related link between the nonresonant electronic excitations seen in Raman with the carrier transport.

As with nonresonant RS electronic response, the related Feynman diagrams (see Fig. 2.1) are composed of wavy lines denoting photon propagators. Their initial and final (momentum, energy) are respectively $\left(\hbar \vec{k}_1, \hbar\omega_1 \right)$ and $\left(\hbar \vec{k}_2, \hbar\omega_2 \right)$. An electron-hole pair of (momentum: $\vec{k} = \vec{k}_1 - \vec{k}_2$, energy: $\omega = \omega_1 - \omega_2$), scattered by phonons and/or impurities, become generated by the incoming photon propagator. Phonon propagator, given in dashed line (Fig. 2.1), can be excited by the electron/hole inside a pair and is further captured by its counterpart (hole/electron), as is enforced by the ladder approximation. At last, upon summing up all the dominating ladder-like diagrams, Raman differential cross section due to the purely electronic response [9,11], reads as

$$\frac{\mathrm{d}^2\sigma}{\mathrm{d}\omega\mathrm{d}\Omega} \propto \frac{1}{1 - \exp(-\hbar\omega/k_B T)} \times \frac{\omega\tau}{1 + (\omega\tau)^2}. \tag{2.6}$$
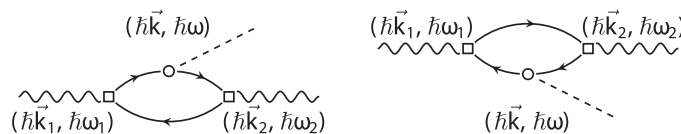
Figure 2.1
Raman scattering of light (*wavy lines*) due to phonons (*dashed lines*). Electron-hole formations (*solid lines*) represented via loops in the Feynman diagrams of third order (first order Raman scattering). Processes involving electron and hole contributions are given in left and right diagrams, respectively. Vertex □ represents electron-photon interaction, while vertex represents electron-phonon interaction as is given in Ref. [5]. *The drawing is adapted from D.M. Djokić, B. Stojadinović, D. Stepanenko, Z. Dohčević-Mitrović, Probing charge carrier transport regimes in BiFeO₃ nanoparticles by Raman spectroscopy, Scr. Mater. 181 (2020) 6−9.* https://doi.org/10.1016/j.scriptamat.2020.02.008.

At a particular value of the effective scattering rate, $1/\tau$, the proportionality factor in Eq. (2.6) is a function of different variables depending on the type of the experimental setup [10]. The temperature-dependent Bose-Einstein factor and expression resembling Drude function are respectively given as the second and third term in the product of Eq. (2.6), while $1/\tau$ involves two terms in the sum as follows

$$1/\tau = 1/\tau_0 + Dq^2. \tag{2.7}$$

$1/\tau_0$ stands for the charge carrier scattering rate due to phonons/impurities in $q \to 0$ limit, which is concerned with nothing but bulk channels. The second term (Dq^2), however, gives rise to the effects of processes nonconserving momenta, very often pronounced in nanocrystals [1]. It is safe to neglect the bulk term $(1/\tau_0)$ if there is no experimental evidence for the electronic Raman background in the case of bulk materials. D is the diffusion constant which is, based on the Einstein relation, related to electric conductivity σ in the following manner

$$D = \sigma/\left(g(\varepsilon_F)e^2\right), \tag{2.8}$$

where $e = 1.6 \times 10^{-19}$ C. The average value of the electronic density states close to the Fermi level [9] is denoted with $g(\varepsilon_F)$.

2.2 Multiferroic $BiFeO_3$ nanoparticles

Crystalline bismuth ferrite stands for a multiferroic material increasingly attracting the attention among the researchers and is also one of few materials to provide both ferroelectric ($T_C \approx 1100$ K) and antiferromagnetic ($T_N \approx 643$ K) properties at room temperature [13] and even higher. It is important to know that $BiFeO_3$ has proven undemanding to obtain in ambient conditions. $BiFeO_3$ is classed as rhombohedrally distorted ABO_3 perovskite structure (space group $R3c$) with lattice parameter $a_{rh} = 3.965$ Å, a rhombohedral angle α_{rh} of 89.30−89.48°, and ferroelectric polarization along $[111]_{pseudocubic}$ direction at room temperature [14]. Primitive unit cell consists of two unit formulas and contains 10 atoms. This structure can be represented as two distorted perovskite unit cells, connected along the main pseudocubic diagonal [111] to form a rhombohedral unit cell, as is given in Fig. 2.2A. Bi^{3+} ions are situated at A lattice sites and are surrounded by 12 oxygen atoms. On the other hand side, Fe^{3+} ions are located at B lattice sites, and they are surrounded by six oxygen atoms with which it forms a FeO_6 octahedron. In this configuration, Bi^{3+} and Fe^{3+} ions are shifted along [111] direction, and two oxygen octahedrons are rotated around [111] direction in the opposite directions by 14° that can be seen from the position of the green octahedrons in Fig. 2.2B. This means that the Fe-O-Fe angle deviates from 180° to amount nearly 154−156° [16,17]. The unit cell can also be described in a hexagonal frame of reference, where the hexagonal
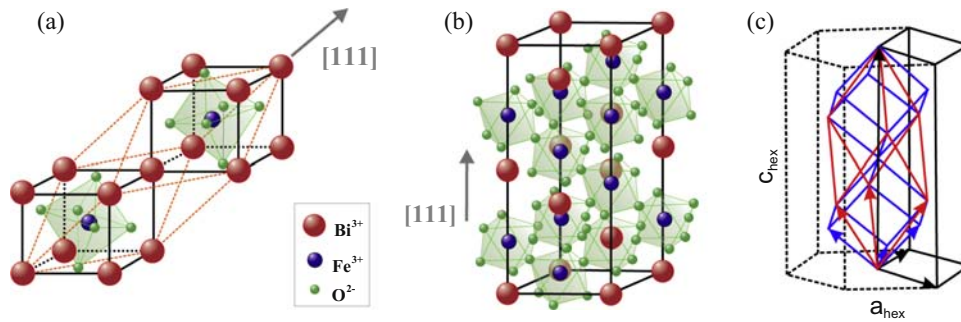
Figure 2.2
Schematic representation of (A) rhombohedral structure framed by orange dashed lines, (B) hexagonal perovskite structure of $BiFeO_3$ with [111] ferroelectric polarization direction given in gray arrow, and (C) hexagonal cell (black), rhombohedral (red), and pseudocubic (blue) unit cell with corresponding unit vectors drawn in *arrows. The figure is to a rather large extent reworked from J.-G. Park, M.D. Le, J. Jeong, S. Lee, Structure and spin dynamics of multiferroic BiFeO₃, J. Phys. Condens. Mat. 26 (2014) 433202. https://doi.org/10.1088/0953-8984/26/43/433202.*

c-axis is aligned parallel to the diagonals of the perovskite cube. In other terms, $[001]_{hexagonal} \parallel [111]_{pseudocubic}$. The corresponding hexagonal lattice parameters (Fig. 2.2C) are $a_{hex} = 5.579$ Å and $c_{hex} = 13.869$ Å [14,18].

Bulk $BiFeO_3$ is a semiconductor with literature values of the bandgap determined by optical measurements at room temperature in the range from 2.1 to 2.8 eV. Several authors claim that $BiFeO_3$ has a direct bandgap transition at about 2.1−2.8 eV [19−22]. There are, however, published studies in which it has been shown that $BiFeO_3$ has an indirect bandgap transition of about 0.4−1.0 eV, quite smaller as compared to the values obtained for the direct transition [23]. Density functional theory calculations [24,25] have corroborated an indirect energy transition of about 2.1 eV, while in the room temperature absorption spectra recorded on $BiFeO_3$ thin film, the transition at approximately 2.17 eV has been observed [26].

Finally, according to Catalan and some of the references therein [16], based on two-probe DC resistivity measurements carried out on high-quality bulk samples of $BiFeO_3$, the log resistivity value undergoes two slopes in Arrhenius law with increasing temperature. Actually, it has been found that the activation energy of the charge carriers decreases from nearly 1.3 down to nearly 0.6 eV as the material is heated above T_N with the anomaly around it. However, one does not expect such type of conducting behavior when the scale of the crystal moves down to several nanometers. Indeed, in the case of defective nanoparticles with a core/shell structure [1], the nanoparticle shell may have metallic and/ or semiconducting features, while the nanoparticle core prominently features insulating properties. This casts a shadow over models that are commonly applied in pristine bulk materials to fit the resistivity data in systems with disorder and/or decreased dimensions.

At a scale ranging down to nanometers, $BiFeO_3$ has proven very prospective for a potential use in satellite communications, electrically accessed magnetic memory, commercial applications for photovoltaics and alternative sensors [16]. Most essentially, the electric resistance of $BiFeO_3$ is found to be a key parameter that should comply with the prime industrial requirements. Accomplishing high-electric conductivity value in this nanoscopic compound from its powders is one of the major assets and is perceived as a very promising in development of the novelty. Moreover, it proves quite demanding to identify the charge carrier transport, as well as, to distill electric conductivity value using the contact probes themselves invasively [27,28]. On the other hand, RS tool is widely known as a local and highly informative experimental probe capable of assessing the origin and dynamics of charge carriers in conducting materials. This makes Raman technique a reliable, yet noninvasive, means for investigating the transport properties of materials that are treated with utmost delicacy.

Fairly recent temperature-dependent RS study, carried out on the multiferroic $BiFeO_3$ nanoparticles of high purity and relied on the temperature evolution electronic Raman background [1], has explored an exciting prospect of extracting the relevant piece of information about the electric transport in this nanoscopic compound. μ-RS measurements were recorded over the temperature range of 80−723 K, while the related spectra were gathered at the backscattering arrangement with solid state 532 nm Nd:YAG laser as excitation at sub-mW laser powers on the sample itself. There were more than 13 optical phonon modes (symmetry: A_1 and E) detected in the experiment, while the spectra were decomposed with Lorentzian lineshape profiles, as is presented in Fig. 2.3 at four different temperatures. The entire number, together with frequency positions, of the optically active phonon modes of $BiFeO_3$ nanoparticles detected with Raman were found exactly the same with those observed in temperature-dependent RS spectra undertaken for bulk crystalline $BiFeO_3$ [29]. However, the authors [1] properly commented on the emerged splittings of a number of few polar LO+TO phonon modes, which naturally appear in the case of $BiFeO_3$ nanoparticles [30,31]. As with bulk, the prediction based on the factor group analysis turns out to be in accordance with the experiment implying 13 ($4A_1 + 9E$) optically active modes in phonon Raman spectra [32].

In contrast to Raman spectra recorded for on bulk $BiFeO_3$, Raman active optical modes pertinent to $BiFeO_3$ nanoparticles were evidenced to seat on quite a broad spectroscopic profile (Fig. 2.3 shaded in light gray). Such a spectroscopic feature has a pronounced temperature dependence and is familiarly known as Raman electronic background. In literature, indeed there are spectroscopic backgrounds akin to one studied in Ref. [1] such as nonresonant Raman continuous profile observed in metal-oxide thin films [33]. However, the related profile is quite shapeless, moreover with strong intensity, and is ascribed to entirely electronic RS recoil independent of bands due to the phonons. This Raman electronic background emerges as a result of the surface roughness at atomic scale.
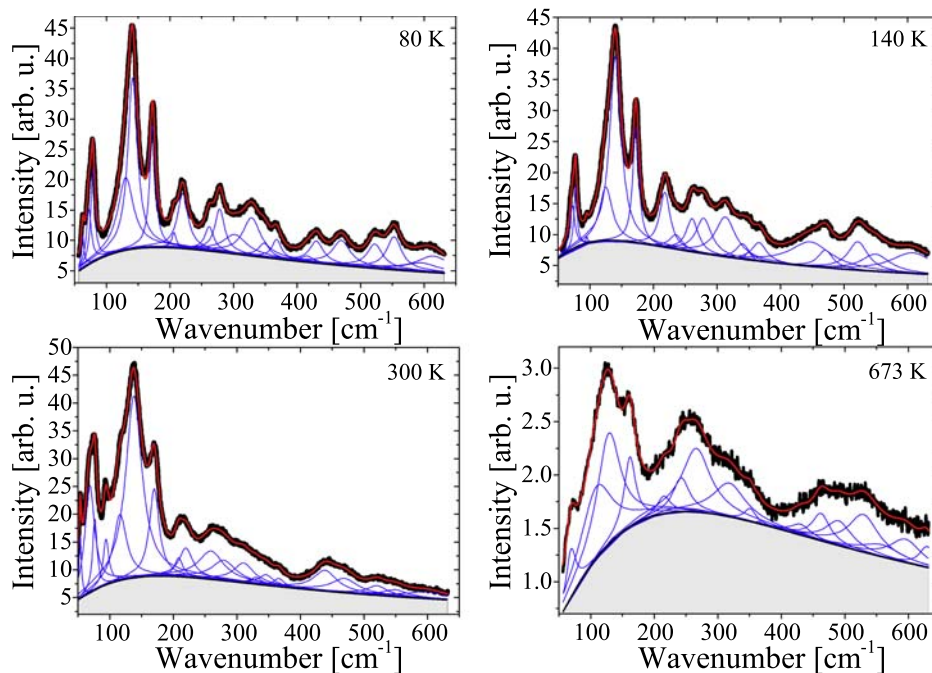
Figure 2.3

Raman scattering spectra given for four representative temperatures (data points presented in black). The spectra are composed of a continuous electronic background (shaded in light gray) and Lorentzian phonon peaks (*lines* in blue). The overall *fitting line* is drawn with *red line*. *The figure is adopted from the published work D.M. Djokić, B. Stojadinović, D. Stepanenko, Z. Dohčević-Mitrović, Probing charge carrier transport regimes in BiFeO₃ nanoparticles by Raman spectroscopy, Scr. Mater. 181 (2020) 6—9.* https://doi.org/10.1016/j.scriptamat.2020.02.008.

In addition, it has been reported that, in extremely small metallic particles [34] and metallic thin film islands with adsorbents [35], RS due to the particle-hole pair excitations brings about the emergence of the phononless continuous electronic background. This can be explained in terms of the momentum conservation violation generated in the presence of the electronic states at surface. Furthermore, even in the bulk hole-doped manganese perovskites, the broad electronic Raman response associated with the scattering by conduction electrons has been determined to cause a drastic change at the phase transition, as shown by Liu et al. [36]. The evolution of the effects of electron correlations in this compound could be assessed computably with temperature.

The authors of Ref. [1] have fittingly cast the surface states situated at particle boundaries in the role of localization centers via which the conduction can run efficiently. In terms of energy, these states are located near the vicinity of the Fermi level and they are, in general, unequally distributed to evolve with both spatial and energy gap between them. Therefore, the charge carrier conduction mechanism in which the hopping energy varies

with the hopping range can be safely modeled for description of the transport over an extended temperature range in disordered semiconductors and/or amorphous solids, such as nanoscaled materials. Commonly, exceptionally high-electric resistivity values are observed in such systems. As such, these values serve as a definite fingerprint to rule out any conventional metallic/semiconducting type of conductivity mechanism intrinsic to (semi)conductors. VRH mechanism, nonetheless [37], stands for a rather viable transport mechanism in nanoparticles with no other alternative acceptable, as was reported in Ref. [1] for $BiFeO_3$ nanoparticles. Two different types of VRH charge carrier transport mechanisms in $3D$ have been probed in a contactless way using temperature-dependent Raman spectroscopy, and it has been evidenced that these two are affected by different degrees of the electron correlation strengths on the opposite sides of the antiferromagnetic phase transition. Below the transition temperature, the transport undergoes the mechanism explained by Efros and Shklovskii [38], whereas at high temperatures, the charge carrier transport adheres to the traditional Mott VRH theory [37].

Here we provide a brief account of the Mott and Efros–Shklovskii laws based on a concise analysis from a seminal paper by Arginskaya and Kozub [39]. The central focus of this study was on a considerable diversity of theoretical results emerging from calculations for the exponential prefactors in various VRH expressions, as well as, the crossover from VRH conductivity of Mott type in which the density of electronic states at Fermi level is $g(\varepsilon \approx \varepsilon_F) = const$ toward VRH conductivity running via states separated by a Coulomb gap when $g(\varepsilon \approx \varepsilon_F) \propto \varepsilon^2$. Aharony et al. [40] have made an attempt to obtain the universal analytic expression for the temperature dependence of conductivity, $\sigma(T)$, in the crossover region from Mott to Efros–Shklovskii law. In general terms, temperature dependence of the VRH conductivity $\sigma(T)$ can be written down as

$$\sigma(T) = \sigma_n \exp\left(-\frac{T_n}{T}\right)^n, \tag{2.9}$$

where n might take on $1/4$ or $1/2$ in $3D$ with respect to the law chosen, Mott's or Efros–Shklovskii's. Constant factors σ_n and T_n depend on the preferred of the two models. However, the common feature of most of the relevant studies in the field of VRH boils down to simplistic approaches in estimating the exponential prefactor σ_n. As a traditional rule, σ_n is generally assumed to have no temperature dependence.

Factors σ_n and T_n, which are given in Eq. (2.9), can be computed straightforwardly by optimizing the correlation linking the energy and spatial separation between the lattice sites. Once an electric field is applied, hopping in the direction of the field is rather preferred at different probabilities with respect to both distance and energy separation. As with the $3D$ free electron case, in original Mott paper [37], it was in a simplified way presented that the hopping energy is inversely proportional to the cube of the hopping distance, while the hopping frequency ν for a given temperature T was found to depend on

two following parameters: r as the spatial distance between the sites in units of localization length ξ and W as their typical hopping energy separation. Namely,

$$\nu = \nu_0 \exp\left(-\frac{2r}{\xi} - \frac{W}{k_B T}\right), \tag{2.10}$$

where $\nu \equiv \nu_0$ for both $r = 0$ and $W = 0$, whereas $k_B = 1.38 \times 10^{-23}$ J/K stands for Boltzmann constant. The hopping frequency characterizes the relative number of directed charge carrier hops due to the electric field. Indeed, in noncrystalline systems, the variables r and W are not randomly independent so that one can be combined into a single parameter by minimizing the total exponent in (Eq. 2.10). In the actual fact, the hopping from one site to another with a lower energy/distance occurs at high rate. However, reaching both low energy/distance sites at the same time remains utterly impossible. The same reasoning applies for the large energy/distance sites that altogether justifies the application of variation method and thence the term "variable" in VRH.

Variable hopping processes translate a charge carrier by a range r within a time $\sim 1/\nu$, but at a preferred W value that maximizes the electric current via hopping. This proportionality squarely leads to the VRH expression for conductivity which is given in (Eq. 2.9). Yet, to relate r with W or vice versa, one has to further assume that most of the mobile carriers come from a narrow energy window near the Fermi level of width $\sim k_B T$. In such a way, the carrier density n_c of spin $S = 1/2$ which as the other factor prominently figures in the expression for the conductivity and can be computed by integration as

$$n_c = 2 \int_{\varepsilon_F}^{\varepsilon_F + k_B T} g(\varepsilon) d\varepsilon, \tag{2.11}$$

where $g(\varepsilon)$ measures the total number of states (dN) per both energy (dE) and volume unit (V), each of which is double degenerated ($2S + 1 = 2$).

One must emphasize that the wise choice of $g(\varepsilon)$ leads to the correct expression for the exponent T_n, which differs by switching from 3D Mott ($n = 1/4$) to Efros−Shklovskii regime ($n = 1/2$). Experimental measurements in disordered systems do reveal that the electron density of states (DOSs) may strongly vary in the vicinity of Fermi level, and it seems reasonable to suggest that the theoretical concept of uniform DOSs near the Fermi level is certainly insufficient to describe conduction mechanisms which account for the Coulomb gap, as there is a jump in the electron DOSs due to Coulomb interactions between localized states. In general, one can write down

$$k_B T_n = \begin{cases} c_p/\left(g(\varepsilon_F)\xi^3\right), & \text{for } n = 1/4 \\ e^2/(4\pi\varepsilon_0\varepsilon_r\xi), & \text{for } n = 1/2 \end{cases} \tag{2.12}$$

where $k_B = 1.38 \times 10^{-23}$ J/K and $\varepsilon_0 = 8.85 \times 10^{-12}$ F/m, while ξ stands for the localization length of electron wave function of the surface states. c_p represents the percolation constant varying from 5 to 20. ε_r corresponds to the relative permittivity constant. Nevertheless, even when the DOSs is not constant, the $3D$ Mott VRH conductivity pattern is fully recovered if presented like Eq. (2.9), but is rather referred to as the $3D$ Efros–Shklovskii VRH [38] when n is, in particular, equal to $1/2$. In Ref. [41], a few temperature dependencies of the hopping conductivity, which come under exponent $1/4$ or $1/2$, are presented and the reader is further redirected to this reference to properly infer the validity of use of VRH at high temperatures in disordered materials.

Nanoscaled $BiFeO_3$ puts itself forward as a suitable candidate for exploring the crossover from $1/2$ to $1/4$ exponent VRH conductivity as demonstrated in Ref. [1] based on the Raman spectra. More interesting is the fact that crystalline $BiFeO_3$ nanoparticles do not only undergo a crossover but even a pronounced phase transition at ~ 640 K below which Coulomb correlations take place to form the antiferromagnetic ordering. Above the transition temperature, however, these correlations become overwhelmed by the temperature fluctuations through the concrete manifestation of the metallic-like paramagnetic state.

There is a presence of localized surface states occupying the energies near the Fermi level in the $BiFeO_3$ nanomaterial. These states through a mediation back the VRH transport even over a broad range of temperature. Temperature variations of $\ln(1/\tau)$, which is proportional to $\ln(\sigma)$ based on the Einstein relation from Eq. (2.8) are linearized against T^{-n} in Fig. 2.4A with $n = 1/2$ and Fig. 2.4B with $n = 1/4$, in the strongly correlated ($T < T_N$) and paramagnetic phase ($T > T_N$), respectively. Relying on the calculation for $\varepsilon_r \approx 28$ from the impedance dielectric spectroscopy of $BiFeO_3$ nanoparticles [42] and following (12) one can find that $\xi \approx 7$ nm, while the DOSs $g(\varepsilon_F)$ in the high-temperature phase nearly amounts 2.1×10^{18} localized states per (eV $\times$ cm^3). The result $\xi \approx 7$ nm is physically meaningful since $\xi < \langle \ell \rangle$, where the average particle size $\langle \ell \rangle \approx 66$ nm has been computed from the Gauβian particle size distribution recorded by Scanning Electron Microscopy at room temperature on $BiFeO_3$ (Fig. 2.4C and D). Finally, $\rho = 1/\sigma \approx 4\pi^2 \tau / \left(\langle \ell \rangle^2 e^2 g(\varepsilon_F) \right) \approx 350$ mΩcm, which stands for an extraordinarily high value that is not commonly encountered in conventional metals. This value goes beyond the maximum resistivity value (~ 1 mΩcm) limited by the Mott-Ioffe-Regel criterion [43,44], which categorizes crystalline $BiFeO_3$ nanoparticles into a family of bad conductors and ultimately suggests that the conduction bands are vanishing. This eliminates any possibility for the fixed thermally activated transport generic to intrinsic semiconductors to dominate over $3D$ VRH.
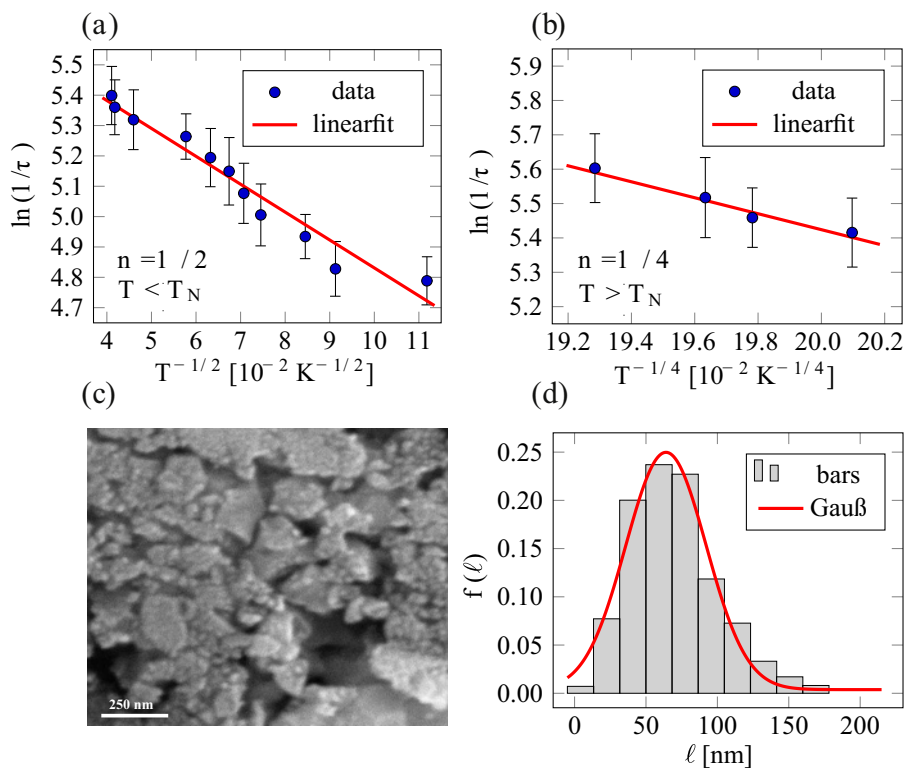
Figure 2.4
The dependence (T^{-n}) versus ($\ln(1/\tau)$) in both paramagnetic phase (subfigure (A), $n = 1/2$) and antiferromagnetic phase (subfigure (B), $n = 1/4$) with the linear fitting curves given in red. The surface morphology of the nanocrystalline $BiFeO_3$ particles made with TESCAN SM-300 (subfigure (C)) and the corresponding histogram of the distribution of the particle size given in gray, fitted by the Gauß distribution (red line), where (64 ± 2) nm is mean value and (28 ± 2)nm is standard deviation (subfigure (D)). The frequency of occurrence is labeled as $f(\ell)$. *The entire figure is taken from D.M. Djokić, B. Stojadinović, D. Stepanenko, Z. Dohčević-Mitrović, Probing charge carrier transport regimes in BiFeO₃ nanoparticles by Raman spectroscopy, Scr. Mater. 181 (2020) 6–9.* https://doi.org/10.1016/j.scriptamat.2020.02.008.

In certain disordered semiconductors, Ioffe and Regel [45], as well as Mott [46], have altogether realized that conduction states pertinent to such systems fail to survive due to the indefinite reduction in free mean path of carriers that scatters by. The key argument is that it can never become shorter than the typical interatomic spacing. In this case, the concept of carrier velocity cannot be properly formulated, and the entire coherent quasiparticle motion is lost. The notion of a minimum metallic conductivity is actually in accordance with a minimum mean free path.

Generally, the choice of $3D$ VRH ought to be provisionally accepted as an assumption. In the case of $BiFeO_3$ nanoparticles, the existence of the Mott VRH mechanism has already been deduced from the DC/AC measurements. These results are presented in Ref. [27]. Furthermore, the assumption about the validity of VRH is substantiated by the fact that the estimated resistivity value ultimately exceeds the Mott-Ioffe-Regel maximum ($350\,m\Omega cm \gg 1\,m\Omega cm$). This implies that the conduction band energy sector tends to fade away leaving no room for the fixed thermally activated transport to prevail, which typically requires a markedly high density of conduction band states. Therefore, the $BiFeO_3$ nanoparticles are safe to be termed as bad conductors that retain metallic behavior, through qualitative features such as temperature evolution. Quantitatively, however, the bad conductors very much resemble the electric insulators as was observed in Ref. [1]. Specifically, the $BiFeO_3$ nanoparticle shell exhibits metallic behavior whereas the core insulator one, which is a case in defective nanoparticles with a core/shell structure.

3. Infrared reflection

3.1 Short introduction to infrared reflection technique

Infrared solid state spectroscopy stands for one of the most powerful and versatile techniques meant for optically probing a diverse family of materials in a contactless manner. The IRR response can assume either a purely electronic or a purely LV character. The two cases have distinctly different approaches to the quantitative treatment of the interaction processes between the radiation field and matter. The latter has conclusively proven powerful for analyzing propagating vibrations with which crystal structures can be revealed in ionic crystals and polar semiconductors. This analytical probe is highly useful even for systems poor in the degree of crystallinity, which is oftentimes encountered in nanoscopic matter.

In the long-wave limit ($q \approx 0$), optically active vibrations of an ionic bipartite lattice encapsulate the motion of one type of atoms relative to that of the other sublattice, yet both in spatial phase. The natural concomitants of such motions comprise strong electric dipoles of the material that can, accordingly, be directly coupled with the external electric field at a given polarization angle of the incident electromagnetic radiation. The theory of the IRR response originating form the interaction between the radiation field and the matter is purely phenomenological and can be found elsewhere [4,47,48], based on Maxwell's and the macroscopic equations describing the vibrations in a polar material. The reflective IRR spectroscopic recoil begins with a singularity in the dielectric function observed at the transverse optical (TO) frequency of the polar phonon mode. The singularity occurs as the radiation field of the incident electromagnetic wave couples with the TO phonon mode. Coulombic force effects in the polar crystal shift the LO mode to higher energies in contrast to the TO mode. The TO mode has a complex pole of the

complex dielectric response function $\widetilde{\varepsilon}(\omega)$, whereas the LO mode is associated with a complex zero of $\widetilde{\varepsilon}(\omega)$. Consequently, the incident infrared electromagnetic waves at frequencies over the so-called *reststrahlen* TO-LO window are dispersed in such a way that they fail to propagate through the condensed medium, but undergo reflection. In an ideal polar crystal with undamped oscillators, the frequency selective reflectivity amounts exactly 100%, but the reality is rather followed with the oscillator damping. Formally, the reflectivity is given by the Fresnel formula

$$R(\omega) = \left| \frac{\widetilde{n}(\omega) - 1}{\widetilde{n}(\omega) + 1} \right|^2 = \frac{(n(\omega) - 1)^2 + \kappa^2(\omega)}{(n(\omega) + 1)^2 + \kappa^2(\omega)}, \tag{2.13}$$

where $R(\omega)$ is the frequency-dependent fraction of light intensity reflected. Complex frequency dependent index of refraction, $\widetilde{n}(\omega)$, is related to the complex dielectric response as

$$\widetilde{n}(\omega) = n(\omega) - i\kappa(\omega) = \sqrt{\widetilde{\varepsilon}(\omega)}. \tag{2.14}$$

The frequency dependent real part, $n(\omega)$, and imaginary part, $\kappa(\omega)$ as the extinction coefficient, of the complex refractive index $\widetilde{n}(\omega)$ satisfy the following relationships

$$\varepsilon_1(\omega) = n(\omega)^2 - \kappa(\omega)^2 \quad \text{and} \quad \varepsilon_2(\omega) = 2n(\omega)\kappa(\omega), \tag{2.15}$$

where finally

$$\widetilde{\varepsilon}(\omega) \equiv \varepsilon_1(\omega) + i\varepsilon_2(\omega). \tag{2.16}$$

For this reason, it is of uppermost importance to model, as well as, parametrize $\widetilde{n\varepsilon}(\omega)$ that properly describe the system probed by the IRR technique.

IRR signal of poorly conductive ionic crystals with large splitting between TO and LO frequencies is commonly fitted with a complex dielectric function given by the following expression

$$\widetilde{\varepsilon}(\omega) = \varepsilon_\infty \prod_j \frac{\omega_{\text{LO}j}^2 - \omega^2 + i\omega\gamma_{\text{LO}j}}{\omega_{\text{TO}j}^2 - \omega^2 + i\omega\gamma_{\text{TO}j}}, \tag{2.17}$$

where $\omega_{\text{LO}j}$ and $\omega_{\text{TO}j}$ are longitudinal and transverse frequencies of the j-th oscillator, respectively, while $\gamma_{\text{TO}j}$ and $\gamma_{\text{LO}j}$ are their energy dampings, and ε_∞ corresponds to the high-frequency dielectric constant ($\omega \to \infty$). This model presents four tunable parameters for each TO/LO mode and is employed for description of purely phononic spectra. The model is familiarly known as the LV model, or habitually, four-parameter factorized form of the dielectric function. Its major disadvantage consists in the fact that it considers no contribution from the itinerant electronic excitations, neither single particle nor collective [49].

However, a great deal of semiconductors has a sizable portion of itinerant charge carriers. Accordingly, the full description of the infrared optical reflectivity data of such materials has to allow for both phonon and electronically collective (plasmon) excitations. The cohabitation between the phonons and plasmons brings inexorably about a somewhat pronounced interaction between the plasmons and LO phonons. This effect becomes the most striking if the plasma frequency ω_P lies situated close to the LO phonon energy. In this case, the complex dielectric function [50] can be factorized to read as follows

$$\widetilde{\varepsilon}(\omega) = \varepsilon_\infty \frac{\prod_{j=1}^{m+n}\left(\omega^2 + i\omega\gamma_{\mathrm{LO}j} - \omega_{\mathrm{LO}j}^2\right)}{\omega^m \prod_{j=1}^{m}\left(\omega + i\gamma_{P_j}\right)\prod_{j=1}^{n}\left(\omega^2 + i\omega\gamma_{\mathrm{TO}j} - \omega_{\mathrm{TO}j}^2\right)}, \tag{2.18}$$

where $\omega_{\mathrm{TO}j}$ and $\gamma_{\mathrm{TO}j}$ are frequencies and damping of the TO modes, respectively. γ_P represents the plasma damping rate. The equation directly expresses the coupled plasmon-LO phonon frequencies $\omega_{\mathrm{LO}j}$ and damping rates $\gamma_{\mathrm{LO}j}$. This model is in literature termed as the coupled plasmon-phonon (CPP) model.

In conducting oxides [48], on the other hand side, the Drude model can be employed with no coupling for fitting the infrared reflectivity spectra. The plasmon contribution to the complex dielectric function is expressed through the Drude term so that $\widetilde{\varepsilon}(\omega)$ is composed of two additive terms in the following manner

$$\widetilde{\varepsilon}(\omega) = \varepsilon_\infty \left(\prod_j \frac{\omega_{\mathrm{LO}j}^2 - \omega^2 + i\omega\gamma_{\mathrm{LO}j}}{\omega_{\mathrm{TO}j}^2 - \omega^2 + i\omega\gamma_{\mathrm{TO}j}} - \frac{\omega_P^2}{\omega(\omega - i\gamma_P)}\right). \tag{2.19}$$

The first product term is concerned with the pure phonon contribution, while the second term represents the contributions originating from the collective electronic excitations—plasmons. The $\omega_{(\mathrm{TO/LO})j}$ and $\gamma_{(\mathrm{TO/LO})j}$ are (TO/LO) frequencies and the related damping rates of the decoupled phonon modes. The ω_P and γ_P are the plasma frequency and its daping rate. This model brings us a material advantage in decoupling the phonon from the plasmon contributions, and is called the decoupled plasmon-phonon (DPP) model. Besides the aforementioned "classical" Drude term, sometimes the so-called Double-damped Drude term is used, as is given in

$$\widetilde{\varepsilon}(\omega) = \varepsilon_\infty \left(\prod_j \frac{\omega_{\mathrm{LO}j}^2 - \omega^2 + i\omega\gamma_{\mathrm{LO}j}}{\omega_{\mathrm{TO}j}^2 - \omega^2 + i\omega\gamma_{\mathrm{TO}j}} - \frac{\omega_P^2 + i(\gamma_P - \gamma_0)\omega}{\omega(\omega - i\gamma_0)}\right). \tag{2.20}$$

The difference between the dynamic damping (γ_P) at plasma frequency and the static damping (γ_0) at zero frequency represents particular distinctiveness of this model. The second term in the additive form of $\widetilde{\varepsilon}(\omega)$ turns into the classical Drude term once

$\gamma_P = \gamma_0$. The use of this model, which is also called DPP, provides more flexibility. In fact, a rather precise description of the parametrized complex dielectric function is offered by the model in numerical fittings based on it.

As with nanomaterials, the related IRR spectra can be properly analyzed using the Bruggeman effective medium approximation [51]. The basic Bruggeman model includes the influence of porosity as

$$\left(\frac{\tilde{\varepsilon}(\omega) - \tilde{\varepsilon}_{\text{eff}}(\omega)}{\tilde{\varepsilon}(\omega) + 2\tilde{\varepsilon}_{\text{eff}}(\omega)}\right)\tilde{f} + \left(\frac{1 - \tilde{\varepsilon}_{\text{eff}}(\omega)}{1 + 2\tilde{\varepsilon}_{\text{eff}}(\omega)}\right)\left(1 - \hat{f}\right) = 0. \tag{2.21}$$

A decrease of the powder volume fraction as compared to the ambient air leads to a decrease in the reflectivity values, and thence the IRR features may become significantly broadened if there is a greater air fraction in the powder. For the binary material with a great degree of inhomogeneity, constituted of the material $\tilde{\varepsilon}(\omega)$ and air ($\varepsilon_{\text{air}} = 1$) with the volume fractions $\tilde{f}$ and $1 - \tilde{f}$, respectively, the empirical relation for the complex effective dielectric function $\tilde{\varepsilon}_{\text{eff}}(\omega)$ must obey the above-written equation.

3.2 Doped nanocrystalline CeO$_2$

As one of the most stable oxide of cerium, cerium dioxide CeO$_2$ is considered to be highly important functional material with outstanding applications in many various fields. It crystallizes into a fluorite face centered cubic structure with space group F_{m3m} (No. 225) to form a simple cubic oxygen suba lattice where the cerium ions occupy alternate cube centers (see Fig. 2.5A) [52]. In terms of Wyckoff positions, Ce atoms are located at the centers of the tetrahedrons (4a) (0,0,0) of which corners are populated with
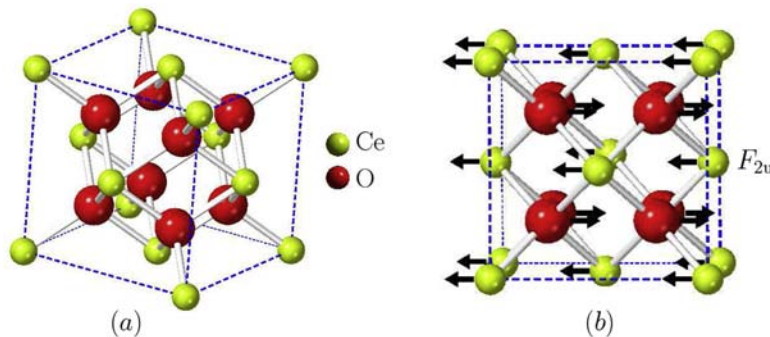
Figure 2.5
The fluorite face centered cubic crystal structure of CeO$_2$ (A) and its normal mode of the infrared active lattice vibrations of (B). Ce ions are denoted in green, while O ions are denoted in red.

oxygen ions (8c) (1/4, 1/4, 1/4). Observing the existence of the center of inversion, the structure has exactly one IRR (F_{2u}) and one Raman (F_{2g}) active mode [32], both of which are triple degenerated. As is shown in Fig. 2.5B, the normal mode of the infrared optically active vibrations consist of motions of both Ce and O atoms, but in the opposite directions.

Nanocrystalline CeO_2 is distinguished by its enhanced electric conductivity, size lattice relaxation, as well as, many other advantages to bulk CeO_2. As to what has been reviewed in Ref. [53], decreasing particle size of crystalline CeO_2 particles down to nanoceria dioxide crystals results in the formation of oxygen vacancies which can be further employed as descriptors for determining the valence state of Ce in the nanoparticles. Actually, the large surface to volume ratio, then the inclination toward the oxygen consumption, and basically, freeing Ce because of the reversible transition between Ce^{3+} and Ce^{4+} ions altogether lead to enormous catalytic capacity of this material. Nanoscaled CeO_2 is furthermore found applicable to the active area of research for renewable energy, solid oxide fuel cells, water and air purification, optical glass polishing and decolorizing, UV ray filters, and many others [53].

Doped nanocrystalline CeO_2, however, deserves a special attention as the optimal doping with Cu or Nd has proven efficient in inducing the semiconductor-to-metallic state crossover [2,52] in nanoceria dioxide. Moreover, electrons localized at the vacancies may behave like free charge carriers to contribute drastically to the electrical conductivity [54]. This originates from the presence of free charge carriers, which are numbered in the nanoceria lattice, as the number of oxygen vacancies becomes increased by Nd content [55].

Following Ref. [2], the IRR spectroscopy has been applied to nondestructively investigate the mechanism of the influence of the plasmon due to the enhanced conductivity upon the phonon spectra with increasing Nd content in nanocrystalline CeO_2 This material is a polar semiconductor so that both phonon and plasmon excitations can be registered in the IRR spectra, whereby the plasmon-phonon coupling mechanism can be explored, while the extent to which the system acquires metallicity can be assessed. Radović et al. [2] have recorded the infrared reflectivity spectra on pure and Nd-doped CeO_{2-y} nanopowders at ambient temperature in far-infrared region from 100 up to 700 cm^{-1}.

Fig. 2.6 shows the IRR spectra of undoped and Nd-doped CeO_{2-y} nanopowders fitted with the two models: coupled plasmon-phonon and decoupled plasmon-phonon with double-damped Drude term. The concentration of the dopant is increased from 0% to 25%. The IRR spectra markedly differ from those done on bulk CeO_2, as the bulk reststrahlen region is split into two extended TO-LO modes over 200−550 cm^{-1} range with decreasing crystallite size. The splitting is more pronounced in samples with rather small crystallite sizes and is accompanied with the redshift of the two LO modes, as well. Also, one can
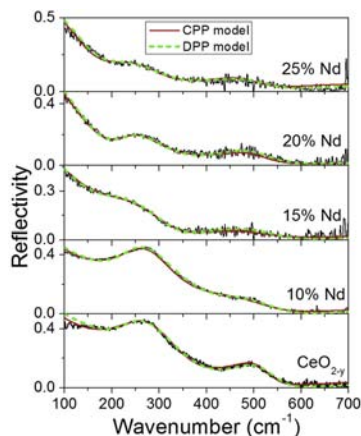
Figure 2.6

Infrared reflectivity spectra of undoped and Nd-doped CeO_{2-y} nanopowders involving the two theoretical fits based on coupled plasmon-phonon and decoupled plasmon-phonon model. *The credits for the figure are given to M. Radović, Z. Dohčević-Mitrović, N. Paunović, S. Bošković, N. Tomić, N. Tadić, I. Belča, Infrared study of plasmon-phonon coupling in pure and Nd-doped CeO_{2-y} nanocrystals, J. Phys. D Appl. Phys. 48 (2015) 065301–065306.* https://doi.org/10.1088/0022-3727/48/6/065301.

notice that with the raise of the dopant concentration, the low energy Drude tail and the screening of the phonon modes became more and more prominent, due to the strong presence of the free charge carriers. In the actual fact, increasing Nd content in the nanoceria dioxide lattice can generate a huge number of oxygen vacancies [2], while the plasmon-phonon interaction in the Nd-doped samples gets stronger.

Following the fits based upon both models applied (Fig. 2.6), all the plasmon modes registered in all nanoceria dioxide samples exhibit a frequency decrease with Nd doping, as can be seen from Fig. 2.7. The shift in the plasma frequency toward lower energies with increasing Nd concentration occurs owing to the weighted effective charge carrier mass, as there is no dopant impact on the free carrier concentration [2]. In fact, the plasma frequency is inversely proportional to the effective electron mass. This feature, together with the enhanced plasmon-phonon coupling with Nd doping, affords us a better insight into the transport properties of crystalline nanoceria based on the infrared-derived optical conductivity [48].

4. Electron spin resonance

4.1 Short introduction to electron spin resonance technique

ESR exemplifies a very sensitive and informative experimental technique, based on the use of magnetic field, which continues to find countless applications not only in solid state and
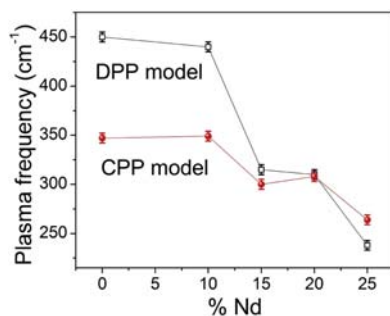
Figure 2.7

Evolution of the plasma frequency with the increased Nd dopant concentration as inferred from the two models: coupled plasmon-phonon and decoupled plasmon-phonon. *The credits for the figure are given to M. Radović, Z. Dohčević-Mitrović, N. Paunović, S. Bošković, N. Tomić, N. Tadić, I. Belča, Infrared study of plasmon-phonon coupling in pure and Nd-doped CeO$_{2-y}$ nanocrystals, J. Phys. D Appl. Phys. 48 (2015) 065301−065306.* https://doi.org/10.1088/0022-3727/48/6/065301.

nano, but also in biomedical and environmental sciences. By means of ESR spectroscopy, one is able to directly probe electron spin response at resonance that certainly makes ESR as one of the most powerful probe to investigate magnetic properties in various compounds. More interestingly, ESR stands for both noninvasive and contactless tool with ability to analyze accurately the nature and dynamics of charge carriers in conductive systems no matter how their geometry welcomes electrical leads and contacts in an electrical circuit.

Familiarly known as CESR in abbreviated term, conduction electron spin resonance has captivated much scientific attention for its capacity to measure the electrical conductivity of systems from bulk over microsized down to nanoscopic conducting materials. In the actual fact, in the conducting systems, the free electron motion exerting eddy current leaves an impact upon the recorded signal at resonance through asymmetry as the definite signature. This was originally recognized by Feher and Kip [56], Dyson [57] who put forward that asymmetric CESR lineshapes originate as linear combinations due to the two facts: (1) the attenuation of the AC field through the skin depth and (2) the capability of itinerant electrons to diffuse backward and forward through the skin depth region in many instances between consecutive spin flips that is only critical to transmission-based CESR techniques. In the case of transmissive CESR, magnetization can penetrate far deeply into metals unlike the AC magnetic field. This gives an extra contribution to enhancing the asymmetry of the signals at resonance [58,59].

Dating back to the 1950's, Freeman John Dyson is the first in the field to be credited with fully deriving the asymmetric CESR profiles. For the obvious reasons, such CESR lines are referred in literature to as Dysonians of which asymmetry extent is oftentimes quantified using A/B ratio (see the inset in Fig. 2.8), as common signature of metallicity in CESR experiments.

As with CESR operating in the reflection mode, Chapman et al. [61] developed an approach based on Dyson's theory to grasp both on- and off-resonance signal for the various crystal shapes, such as flat plates, long cylinders, and spheres. This allows the prediction of the asymmetric nature of CESR absorption profiles depending on geometry of the conducting samples with different size. Furthermore, Platzman and Wolf [62] examined spin waves excitations at resonance in paramagnetic metals that are described within the frame of Fermi-liquid theory. Their extended theory boils down to Dyson's in the limit of short momentum relaxation times. Dyson's theory was additionally generalized to involve various shapes of conducting crystals at desirable resonant magnetic field directions [63−65]. Later on, Kaplan pointed out that there is a substantial discrepancy between Dyson's theory and experimental results recorded in CESR based on the reflection mode [66]. Actually, CESR becomes recoiled rather with electric than magnetic component of the frequency-dependent electromagnetic field. The component of electric field is known to get easily coupled with the free electron momentum across the surface via relativistic spin-orbit interaction. This fact finds its application in the quantum mechanical density matrix method, which ultimately brings about the rather general form of CESR signal as [67]:

$$\chi''(\omega)\cos\phi + \chi'(\omega)\sin\phi. \tag{2.22}$$

Terms χ'' and χ' represent the absorptive and dispersive parts of the CESR signal. The magnitudes of their contributions are measured with $\cos\phi$ and $\sin\phi$, respectively, both of which disappear in the limit of highly conductive samples, where ϕ is the signal phase. Eq. (2.22) does represent a particular manifestation of Dysonian, which falls into the range of the so-called "NMR limit" [68,69]. In that case, the electron diffusion rate is considerably slower as compared to the spin relaxation rate, and there is no need to consider other limits so as to reasonably infer CESR spectra of usual metallic samples. Spin dynamics itself as regards this case can lead to nothing but Lorentzian-profiled absorptions (χ''), unlike the situations with reduced dimensionality or motionally narrowed signals [70,71].

In a recent CESR study [60], the authors have favored Kaplan's approach, made for analyzing the CESR lineshape, to impart a valuable piece of information on the conductivity of samples with different geometries. Key lengths and points of CESR lines, necessary for simplification of a fitting procedure of CESR lineshape, have been established in this account to analytically derive, as well as, grasp the geometry independent asymmetry ratio limit $A/B \rightarrow (5+3\sqrt{3})/4$, encountered in literature as universal 2.55 limit, when the CESR is carried out on extremely conducting samples. A/B ratio value markedly evolves once nano- or microsized metallic samples start to agglomerate into larger ones that makes the CESR technique especially helpful in

monitoring the extent to which the clustering takes place [72,73]. Moreover, in Ref. [60], the phase dependence of the asymmetry ratio A/B is given as

$$A/B = \frac{\left(1 + 2\cos\dfrac{2\phi}{3}\right)\left(3\cos\left(\dfrac{\pi}{6} - \dfrac{\phi}{3}\right) + \sin\phi\right)}{4\cos\left(\dfrac{\pi}{6} - \dfrac{\phi}{3}\right)\left(1 + \sin\left(\dfrac{\pi}{6} - \dfrac{2\phi}{3}\right)\right)^2}, \tag{2.23}$$

which can be further employed to relate A/B with the conductivity. Namely, Chapman et al. [61] introduced the parameter $\eta \equiv d/\delta$, where d represents the characteristic length od the sample (thickness or diameter), while δ is the skin depth at given resonant frequency. It is exactly this quantity that is in correlation with the sample conductivity. The absorptive and dispersive parts of the CESR signal in Ref. [61] are respectively $x(\eta)$ and $y(\eta)$ so that $y(\eta)/x(\eta)$ exactly corresponds to $\tan\phi$ in Ref. [60]. According to Ref. [61], $x(\eta)$ and $y(\eta)$ for the three relevant geometries look like

$$\text{Plate} \Rightarrow \begin{cases} x(\eta) = \dfrac{\sinh(\eta) + \sin(\eta)}{2\eta(\cosh(\eta) + \cos(\eta))} + \dfrac{1 + \cosh(\eta)\cos(\eta)}{(\cosh(\eta) + \cos(\eta))^2}, \\[4mm] y(\eta) = \dfrac{\sinh(\eta) - \sin(\eta)}{2\eta(\cosh(\eta) + \cos(\eta))} + \dfrac{\sinh(\eta)\sin(\eta)}{(\cosh(\eta) + \cos(\eta))^2}. \end{cases} \tag{2.24}$$

$$\text{Cylinder} \Rightarrow \begin{cases} x(\eta) = 1 - \dfrac{2(\text{Ber}(\vartheta)\text{Ber}'(\vartheta) + \text{Bei}(\vartheta)\text{Bei}'(\vartheta))(\text{Ber}(\vartheta)\text{Bei}'(\vartheta) - \text{Ber}'(\vartheta)\text{Bei}(\vartheta))}{\left(\text{Ber}^2(\vartheta) + \text{Bei}^2(\vartheta)\right)^2}, \\[4mm] y(\eta) = \dfrac{\left(\text{Ber}^2(\vartheta) - \text{Bei}^2(\vartheta)\right)\left(\text{Bei}'^2(\vartheta) - \text{Ber}'^2(\vartheta)\right) - 4\text{Ber}(\vartheta)\text{Bei}(\vartheta)\text{Ber}'(\vartheta)\text{Bei}'(\vartheta)}{\left(\text{Ber}^2(\vartheta) + \text{Bei}^2(\vartheta)\right)^2}, \\[4mm] \text{where } \vartheta \equiv \eta/\sqrt{2}. \end{cases} \tag{2.25}$$

$$\text{Sphere} \Rightarrow \begin{cases} \dfrac{4}{9}x(\eta) = \dfrac{8 + \eta^4}{\eta^4} - \\[4mm] \dfrac{8(\sinh(\eta) + \sin(\eta))}{\eta^3(\cosh(\eta) - \cos(\eta))} + \dfrac{8\sinh(\eta)\sin(\eta)}{\eta^2(\cosh(\eta) - \cos(\eta))^2} + \dfrac{\sinh(\eta) - \sin(\eta)}{\eta(\cosh(\eta) - \cos(\eta))} - \dfrac{\sinh^2(\eta) - \sin^2(\eta)}{(\cosh(\eta) - \cos(\eta))^2}, \\[4mm] \dfrac{4}{9}y(\eta) = \\[4mm] \dfrac{8(\sinh(\eta) - \sin(\eta))}{\eta^3(\cosh(\eta) - \cos(\eta))} - \dfrac{4\left(\sinh^2(\eta) - \sin^2(\eta)\right)}{\eta^2(\cosh(\eta) - \cos(\eta))^2} + \dfrac{\sinh(\eta) + \sin(\eta)}{\eta(\cosh(\eta) - \cos(\eta))} - \dfrac{2\sinh(\eta)\sin(\eta)}{(\cosh(\eta) - \cos(\eta))^2}. \end{cases} \tag{2.26}$$

This set of the three dependencies allows us to compute A/B versus $\log\eta$ as is presented in Fig. 2.8. Oftentimes, A/B can be expended in the form of the linear approximation with respect to either η or is proportional to the conductivity of the probed spins. The latter approximation works well in the case of the carbon nanotubes [3] of which CESR-based charge carrier transport is going to be discussed in detail throughout the upcoming section.

4.2 Carbon nanotubes

As a building brick that takes fascinating variety of forms such as diamond, fossil fuels, and graphite, together with innumerable compounds derived from it, carbon stands for one of the most impressive elements in the periodic table. Increased focus of renewed scientific interest in carbon has stepped into the realm of novel carbon-based materials, specifically known as the carbon allotropes at nanoscopic level, such as carbon nanotubes. These were first discovered as multiwalled forms by Iijima in 1991 [74] initiating the golden era of the physics and chemistry of carbon nanostructures. Carbon nanotubes are distinguished by their outstanding electronic, mechanical, and transport properties revealing uncorrelated (semi)conducting nature of the tubes in relation to the curvature and chirality. They also prove suitable for various applications which spam from the use as light and electron emitters [75] up to optical biosensors for life sciences and biomedicine [76].
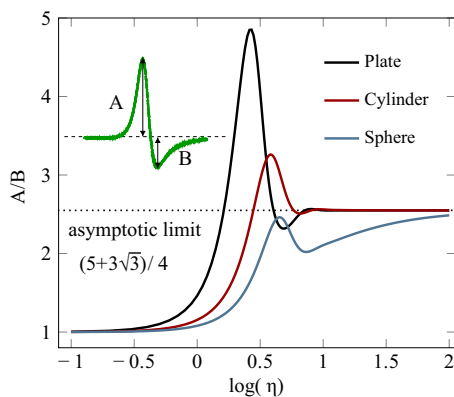
Figure 2.8

Asymmetry ratio A/B dependence on $\log(\eta)$ regarding the three relevant geometries: infinite plate (black), long cylinder (dark red), and sphere (dark blue). All the three curves converge to the asymptotic A/B ratio of $(5+3\sqrt{3})/4$ at $\eta \to \infty$. The inset represents graphically the A/B ratio in an arbitrarily selected CESR line. *The figure is adopted from D.M. Djokić, D. Stepanenko, Z. Dohčević-Mitrović, Extreme conduction electron spin resonance: A/B→(5+3√3)/4, the universal limit of lineshape asymmetry ratio, J. Magn. Magn. Mater. 491 (2019) 165616. https://doi.org/10.1016/j.jmmm.2019.165616.*

Even with the aid of nanoscaled technologies, making ideal electric contacts to adequately probe nanotube conductivity remains a perplexing puzzle. Electron backscattering, imbalanced injection of incident electron modes, and high-ohmic contact resistance are identified as the chief culprits at minuscule dimensions. However, nanotubes with large diameters have the added advantage of favoring low-ohmic contact resistance in a four-probe electric measurement [77]. This made them perfectly suited for the investigation of quantum interference caused by the Aharonov—Bohm effect specific by the pronounced magneto-resistance oscillations as a function of magnetic flux [78].

Despite their short diameters, transport electric properties of multiwalled nanotubes oftentimes remain consistent with theoretical models used to describe disordered conductors in 2D. This might be explained by the fact that the electron wavelength is quite smaller than the nanotube diameter [79]. On the other hand side, one-dimensional essence of carbon nanotubes becomes already evident through specific heat and thermal lattice conductivity measurements since the phonon wavelength exceeds typical nanotube diameters [80], unlike the before-mentioned electron wavelength. Moreover, according to Ref. [81], it has been demonstrated that the electric transport in single walled carbon nanotubes exhibit a dependence in agreement with Luttinger liquid models.

Temperature and power-dependent CESR on an ensemble of metallic SWCNTs have been performed to infer their transport properties based on the insights into the spin dynamics [3]. The powder-form samples comprised acid-purified laser-oven SWCNTs which were prepared using the standardized annealing procedure, while the related CESR spectra were recorded as a function of temperature from 3.4 K to the ambient temperature at the X-band spectrometer. To yield a rather detailed insight into the transport mechanism, the authors of Ref. [3] studied the temperature evolution of the asymmetry Dysonian line shape parameter, $\alpha \equiv A/B$, which is to the first order approximation proportional to the conductance of the probed electron spins. These can relax by interaction with itinerant electrons that are present in metallic SWCNTs. In addition, the spin dephasing rate at resonance narrows with increasing temperature, which is a signature of the motional narrowing, a phenomenon that is particular to metallic systems.

Temperature dependence of the natural logarithm of conductivity, $\ln(\sigma)$ which in this case boils down to $\ln(\alpha)$, is oftentimes plotted versus n-th root of inverse temperature [41]. Exponent n provides information on the charge carrier transport mechanism and when n approaches 1/4, it leaves a hallmark of 3D Mott VRH transport mechanism [37].

As shown in Fig. 2.9, the Dysonian asymmetry parameter tends to follow a three-dimensional variable-range hopping behavior at low T. From the scaling relationships in Eq. (2.12), the localization length of the electronic wave function, ξ, is roughly estimated to be ~ 100 nm, whereas the DOSs $g(\varepsilon_F)$ amounts $\sim 10^{19}$ localized states per (eV $\times$ cm^3)
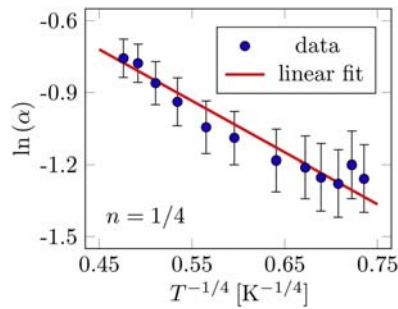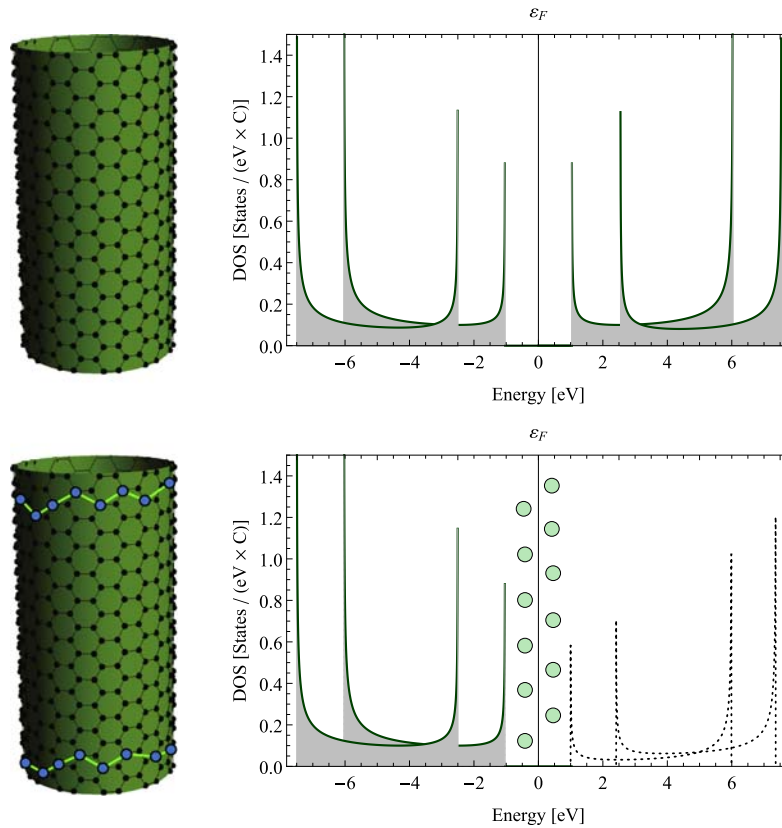
Figure 2.9

Natural logarithm of the asymmetry parameter, $\alpha \equiv A/B$, graphed versus the fourth root of inverse temperature. The logarithm is found to undergo the 3D VRH mechanism. *The data are taken from W.D. Rice, R.T. Weber, P. Nikolaev, S. Arepalli, V. Berka, A.L. Tsai, J. Kono, Spin relaxation times of single-wall carbon nanotubes, Phys. Rev. B 88 (2013) 041401—041405.* https://doi.org/10.1103/PhysRevB.88.041401.

around the Fermi energy. The traditional four-point probe transport measurements on the similarly prepared SWCNT samples [3] have, to some extent, corroborated the present picture of the CESR observed 3D VRH at low *T*.

As with nanoscopic systems such as SWCNTs, one can even venture to state that the VRH conduction mechanism, owing to the localized edge/surface states positioned around Fermi level, may extend even over a wide range of temperatures [1]. At high temperatures, the conduction mechanism in bulk systems commonly runs intrinsically via thermal activation through conduction bands. On the other hand side, there are, as a rule, defect states across the nanotube surface, effectively making its pristine length quite short and comparable to nanoscaled dimensions (Fig. 2.10). In this case, the overlaps between the orbitals decrease to cause the bands to become less dense. This leads to the band splittings to eventually open up wide gaps at rather high energies. Bands that are high in energy have, therefore, tendency to fade away so does the conduction band, as contrary to an ideally pristine SWCNT. It is thus reasonable to adopt that VRH mechanisms may apply up to somewhat higher temperatures in defected nanotubes. Certainly, the intrinsic thermally activated transport via conduction band can be ignored comparing to the VRH due to the evanescent DOSs, as is given in Fig. 2.10.

5. Concluding remarks

In summary, noncontact measurements of transport have been evidenced to offer various advantages to studying novel nanoscopic materials such as: multiferroic crystalline $BiFeO_3$ nanoparticles, doped nanocrystalline CeO_2 used for fuel cell applications, as well as,

Figure 2.10

Plots of the electronic density of states versus energy for an ideally pristine (upper part) and a defected semiconducting SWCNT (lower part), computed using the tight-binding model. The electronic states of the defects forming the effective SWCNT edges are given in *green circles*. They are distributed around Fermi level at zero energy above which the DOS perishes gradually as the energy goes higher.

single walled carbon nanotubes exploited for molecular electronics and spintronics. The transport properties of these novel multifunctional materials have been reviewed in this chapter in the light of noninvasive spectroscopic techniques which involve: RS, IRR, and ESR. Through brief introductions made at the beginning of each section, these three contactless spectroscopic tools have been described in detail.

Acknowledgments

References

[1] D.M. Djokić, B. Stojadinović, D. Stepanenko, Z. Dohčević-Mitrović, Probing charge carrier transport regimes in BiFeO^3 nanoparticles by Raman spectroscopy, Scripta Mater. 181 (2020) 6−9, https://doi.org/10.1016/j.scriptamat.2020.02.008.

[2] M. Radović, Z. Dohčević-Mitrović, N. Paunović, S. Bošković, N. Tomić, N. Tadić, I. Belča, Infrared study of plasmon-phonon coupling in pure and Nd-doped CeO^{2-y} nanocrystals, J. Phys. D Appl. Phys. 48 (2015) 065301−065306, https://doi.org/10.1088/0022-3727/48/6/065301.

[3] W.D. Rice, R.T. Weber, P. Nikolaev, S. Arepalli, V. Berka, A.L. Tsai, J. Kono, Spin relaxation times of single-wall carbon nanotubes, Phys. Rev. B 88 (2013) 041401−041405, https://doi.org/10.1103/PhysRevB.88.041401.

[4] S.S. Mitra, Infrared and Raman Spectra Due to Lattice Vibrations, Springer US, 1969, pp. 333−451, https://doi.org/10.1007/978-1-4757-1123-3_14.

[5] M. Cardona, Light Scattering in Solids I - Introductory Concepts, Springer-Verlag, Berlin), 1983.

[6] L.A. Falkovsky, Investigation of semiconductors with defects using Raman scattering, Phys. Usp. 47 (2004) 249−272, https://doi.org/10.1070/pu2004v047n03abeh001735.

[7] L.A. Falkovsky, Raman scattering of light by electrons in a metal with impurities, Sov. Phys. JETP 68 (1989) 661−663.

[8] A. Zawadowski, M. Cardona, Theory of Raman scattering on normal metals with impurities, Phys. Rev. B 42 (1990) 10732−10734, https://doi.org/10.1103/PhysRevB.42.10732.

[9] T.P. Devereaux, Theory for the effects of impurities on the Raman spectra of superconductors, Phys. Rev. B 45 (1992) 12965−12975, https://doi.org/10.1103/PhysRevB.45.12965.

[10] E.Y. Sherman, O.V. Misochko, Raman scattering in metals with disorder: beyond the zero-momentum approximation, J. Phys. Condens. Matter 15 (2003) 3751−3758, https://doi.org/10.1088/0953-8984/15/22/309.

[11] T.P. Devereaux, R. Hackl, Inelastic light scattering from correlated electrons, Rev. Mod. Phys. 79 (2007) 175−233, https://doi.org/10.1103/RevModPhys.79.175.

[12] A.A. Abrikosov, L.P. Gorkov, I.E. Dzyaloshinsky, Quantum Field Theoretical Methods in Statistical Physics, Pergamon Press, Oxford), 1965.

[13] H. Zhang, K. Kajiyoshi, Hydrothermal synthesis and size-dependent properties of multiferroic bismuth ferrite crystallites, J. Am. Ceram. Soc. 93 (2010) 3842, https://doi.org/10.1111/j.1551-2916.2010.03953.x.

[14] F. Kubel, H. Schmid, Structure of a ferroelectric and ferroelastic monodomain crystal of the perovskite BiFeO$_3$, Acta Crystallogr. B 46 (1990) 698, https://doi.org/10.1107/S0108768190006887.

[15] J.-G. Park, M.D. Le, J. Jeong, S. Lee, Structure and spin dynamics of multiferroic BiFeO^3, J. Phys. Condens. Mat. 26 (2014) 433202, https://doi.org/10.1088/0953-8984/26/43/433202.

[16] G. Catalan, J.F. Scott, Physics and applications of bismuth ferrite, Adv. Mater. 21 (2009) 2463−2485, https://doi.org/10.1002/adma.200802849.

[17] C.-H. Yang, D. Kan, I. Takeuchi, V. Nagarajan, J. Seidel, Doping BiFeO^3: approaches and enhanced functionality, Phys. Chem. Chem. Phys. 14 (2012) 15953, https://doi.org/10.1039/C2CP43082G.

[18] J.D. Bucci, B.K. Robertson, W.J. James, The precision determination of the lattice parameters and the coefficients of thermal expansion of BiFeO$_3$, J. Appl. Cryst. 5 (1972) 187−191, https://doi.org/10.1107/S0021889872009173.

[19] J.F. Ihlefeld, N.J. Podraza, Z.K. Liu, R.C. Rai, X. Xu, T. Heeg, Y.B. Chen, J. Li, R.W. Collins, J.L. Musfeldt, X.Q. Pan, J. Schubert, R. Ramesh, D.G. Schlom, Optical band gap of BiFeO^3 grown by molecular-beam epitaxy, Appl. Phys. Lett. 92 (2008) 142908, https://doi.org/10.1063/1.2901160.

[20] Y. Xu, M. Shen, Structure and optical properties of nanocrystalline BiFeO^3 films prepared by chemical solution deposition, Mater. Lett. 62 (2008) 3600, https://doi.org/10.1016/j.matlet.2008.04.006.

[21] A. Kumar, R.C. Rai, N.J. Podraza, S. Denev, M. Ramirez, Y.-H. Chu, L.W. Martin, J. Ihlefeld, T. Heeg, J. Schubert, D.G. Schlom, J. Orenstein, R. Ramesh, R.W. Collins, J.L. Musfeldt, V. Gopalan, Linear and nonlinear optical properties of $BiFeO_3$, Appl. Phys. Lett. 92 (2008) 121915, https://doi.org/10.1063/1.2901168.

[22] J. Allibe, K. Bougot-Robin, E. Jacquet, I.C. Infante, S. Fusil, C. Carrétéro, J.-L. Reverchon, B. Marcilhac, D. Creté, J.-C. Mage, A. Barthélémy, M. Bibes, Optical properties of integrated multiferroic $BiFeO^3$ thin films for microwave applications, Appl. Phys. Lett. 96 (2010) 182902, https://doi.org/10.1063/1.3402763.

[23] M. Shariq, D. Kaur, V.S. Chandel, M.A. Siddiqui, Investigation on multiferroic properties of $BiFeO^3$ ceramics, Mater. Sci. Poland 31 (2013) 471, https://doi.org/10.2478/s13536-013-0128-2.

[24] S.J. Clark, J. Robertson, Band gap and Schottky barrier heights of multiferroic $BiFeO_3$, Appl. Phys. Lett. 90 (2007) 132903, https://doi.org/10.1063/1.2716868.

[25] H. Wang, Y. Zheng, M.-Q. Cai, H. Huang, H.L. Chan, First-principles study on the electronic and optical properties of $BiFeO_3$, Solid State Commun. 149 (2009) 641, https://doi.org/10.1016/j.ssc.2009.01.023.

[26] S.R. Basu, L.W. Martin, Y.H. Chu, M. Gajek, R. Ramesh, R.C. Rai, X. Xu, J.L. Musfeldt, Photoconductivity in $BiFeO^3$ thin films, Appl. Phys. Lett. 92 (2008) 091905, https://doi.org/10.1063/1.2887908.

[27] A. Mukherjee, M. Banerjee, S. Basu, N.T.K. Thanh, L.A.W. Green, M. Pal, Enhanced magnetic and electrical properties of Y and Mn co-doped $BiFeO^3$ nanoparticles, Physica B: Cond. Matt. 448 (2014) 199−203, https://doi.org/10.1016/j.physb.2014.03.082.

[28] S. Ruby, S.S.R. Inbanathan, Structural properties and electrical conduction mechanisms of $Bi^{0.9}Sm^{0.05}Tb^{0.05}FeO^3$ thin film, Appl. Surf. Sci. 449 (2018) 10−14, https://doi.org/10.1016/j.apsusc.2017.11.231.

[29] H. Fukumura, H. Harima, K. Kisoda, M. Tamada, Y. Noguchi, M. Miyayama, Raman scattering study of multiferroic $BiFeO^3$ single crystal, J. Magn. Magn. Mat. 310 (2007) e367−e369, https://doi.org/10.1016/j.jmmm.2006.10.282.

[30] J. Hlinka, J. Pokorny, S. Karimi, I.M. Reaney, Angular dispersion of oblique phonon modes in $BiFeO^3$ from micro-Raman scattering, Phys. Rev. B 83 (2011) 020101−020104, https://doi.org/10.1103/PhysRevB.83.020101.

[31] J. Bielecki, P. Svedlindh, D.T. Tibebu, S. Cai, S.-G. Eriksson, L. Börjesson, C.S. Knee, Structural and magnetic properties of isovalently substituted multiferroic $BiFeO^3$: insights from Raman spectroscopy, Phys. Rev. B 86 (2012) 184422−184437, https://doi.org/10.1103/PhysRevB.86.184422.

[32] D.L. Rousseau, R.P. Bauman, S.P.S. Porto, Normal mode determination in crystals, J. Raman Spectrosc. 10 (1981) 253−290, https://doi.org/10.1002/jrs.1250100152.

[33] A. Otto, J. Timper, J. Billmann, G. Kovacs, I. Pockrand, Surface roughness induced electronic Raman scattering, Surf. Sci. 92 (1980) L55−L57, https://doi.org/10.1016/0039-6028(80)90237-X.

[34] R. Monreal, F. Flores, Y. Gao, T. López-Ríos, Raman scattering by electron-hole pairs at metal surfaces, Europhys. Lett. 4 (1987) 115−120, https://doi.org/10.1209/0295-5075/4/1/019.

[35] C.Y. Chen, E. Burstein, S. Lundquist, Giant Raman scattering by pyridine and cn adsorbed on silver, Solid State Commun. 32 (1979) 63−66, https://doi.org/10.1016/0038-1098(79)90998-0.

[36] H.L. Liu, S. Yoon, S.L. Cooper, S.-W. Cheong, P.D. Han, D.A. Payne, Probing anisotropic magnetotransport in manganese perovskites using Raman spectroscopy, Phys. Rev. B 58 (1998) R10115−R10118, https://doi.org/10.1103/PhysRevB.58.R10115.

[37] N.F. Mott, E.A. Davis, Electronic Processes in Non-crystalline Materials, Oxford University Press, 1979.

[38] A.L. Efros, B.I. Shklovskii, Coulomb gap and low temperature conductivity of disordered systems, J. Phys. C Solid State Phys. 8 (1975) L49−L51, https://doi.org/10.1088/0022-3719/8/4/003.

[39] N.V. Arginskaya, V.I. Kozub, Potential influence of pre-exponential factors on the temperature dependence of variable-range hopping conductivity, Soviet JETP 79 (1994) 466−472.

[40] A. Aharony, Y. Zhang, M.P. Sarachik, Universal crossover in variable range hopping with Coulomb interactions, Phys. Rev. Lett. 68 (1992) 3900−3903, https://doi.org/10.1103/PhysRevLett.68.3900.

[41] L. Zuppiroli, L. Forró, Hopping conductivity in polaronic situations, Phys. Lett. A 141 (1989) 181−185, https://doi.org/10.1016/0375-9601(89)90785-8.

[42] B. Stojadinović, Faculty of Physics, University of Belgrade, 2018 (Ph.D. thesis).

[43] O. Gunnarsson, M. Calandra, J.E. Han, *Colloquium*: saturation of electrical resistivity, Rev. Mod. Phys. 75 (2003) 1085−1099, https://doi.org/10.1103/RevModPhys.75.1085.

[44] N.E. Hussey, K. Takenaka, H. Takagi, Universality of the Mott-Ioffe-Regel limit in metals, Philos. Mag. A 84 (2004) 2847−2864, https://doi.org/10.1080/14786430410001716944.

[45] A. Ioffe, A. Regel, Non-crystalline, amorphous and liquid electronic semiconductors, Prog. Semicond. 4 (1960) 237−291.

[46] N.F. Mott, Conduction in non-crystalline systems IX. The minimum metallic conductivity, Philos. Mag. J. Theor. Exp. Appl. Phys 26 (4) (1972) 1015−1026, https://doi.org/10.1080/14786437208226973.

[47] F. Gervais, Infrared dispersion in several polar-mode crystals, Opt. Commun. 22 (1977) 116−118, https://doi.org/10.1016/0030-4018(77)90260-7.

[48] F. Gervais, Optical conductivity of oxides, Mater. Sci. Eng. R Rep. 39 (2002) 29−92, https://doi.org/10.1016/S0927-796X(02)00073-6.

[49] R.F. Wallis, M. Balkanski, Many-body Aspects of Solid State Spectroscopy, Elsevier Science Ltd, Amsterdam, the Netherlands, 1986.

[50] A.A. Kukharskii, Plasmon-phonon coupling in GaAs, Solid State Commun. 13 (1973) 1761−1765, https://doi.org/10.1016/0038-1098(73)90724-2.

[51] D.A.G. Bruggeman, Berechnung verschiedener physikalischer Konstanten von heterogenen substanzen. I. Dielektrizitatskonstanten und Leitfahigkeiten der Mischkorper aus isotropen Substanzen, Ann. Phys. 416 (7) (1935) 636−664, https://doi.org/10.1002/andp.19354160705.

[52] Z.V. Popović, M. Grujić-Brojčin, N. Paunović, M.M. Radonjić, V.D. Araújo, M.I.B. Bernardi, M.M. de Lima, A. Cantarero, Far-infrared spectroscopic study of CeO_2 nanocrystals, J. Nanopart. Res. 17 (2015) 23−30, https://doi.org/10.1007/s11051-015-2859-y.

[53] A. Younis, D. Chu, S. Li, Cerium oxide nanostructures and their applications, in: Functionalized Nanomaterials, 2016, pp. 52−68, https://doi.org/10.5772/65937. Ch. 3.

[54] P. Jasinski, T. Suzuki, H.U. Anderson, Nanocrystalline undoped ceria oxygen sensor, Sensor. Actuator. B Chem. 95 (2003) 73−77, https://doi.org/10.1016/S0925-4005(03)00407-6.

[55] X. Han, J. Lee, H.-I. Yoo, Oxygen-vacancy-induced ferromagnetism in CeO_2 from first principles, Phys. Rev. B 79 (2009) 100403−100406, https://doi.org/10.1103/PhysRevB.79.100403.

[56] G. Feher, A.F. Kip, Electron spin resonance absorption in metals. I Experimental, Phys. Rev. 98 (1955) 337−348, https://doi.org/10.1103/PhysRev.98.337.

[57] F.J. Dyson, Electron spin resonance absorption in metals. II. Theory of electron diffusion and the skin effect, Phys. Rev. 98 (1955) 349−359, https://doi.org/10.1103/PhysRev.98.349.

[58] M.I. Azbel, V.I. Gerasimenko, I.M. Lifshitz, Paramagnetic resonance and polarization of nuclei in metals, Sov. Phys. JETP 5 (1957) 986−996.

[59] M.I. Azbel, V.I. Gerasimenko, I.M. Lifshitz, On the theory of paramagnetic resonance in metals, Sov. Phys. JETP 8 (1959) 480−487.

[60] D.M. Djokić, D. Stepanenko, Z. Dohčević-Mitrović, Extreme conduction electron spin resonance: $A/B \to (5+3\sqrt{3})/4$, the universal limit of lineshape asymmetry ratio, J. Magn. Magn. Mater. 491 (2019) 165616, https://doi.org/10.1016/j.jmmm.2019.165616.

[61] A.C. Chapman, P. Rhodes, E.F.W. Seymour, The effect of eddy currents on nuclear magnetic resonance in metals, Proc. Phys. Soc. B 70 (1957) 345−360, https://doi.org/10.1088/0370-1301/70/4/301.

[62] P.M. Platzman, P.A. Wolff, Spin-wave excitation in nonferromagnetic metals, Phys. Rev. Lett. 18 (1967) 280−283, https://doi.org/10.1103/PhysRevLett.18.280.

[63] H.R. Webb, Electron-spin-resonance line shape in spherical metal particles, Phys. Rev. 158 (1967) 225−233, https://doi.org/10.1103/PhysRev.158.225.

[64] J.H. Pifer, R. Magno, Conduction-electron spin resonance in a lithium film, Phys. Rev. B 3 (1971) 663−673, https://doi.org/10.1103/PhysRevB.3.663.

[65] A.H. Kahn, Theory of microwave eddy currents and paramagnetic resonance in materials of intermediate conductivity, Phys. Rev. B 16 (1977) 64−72, https://doi.org/10.1103/PhysRevB.16.64.

[66] J.I. Kaplan, J. Reuben, Electron spin resonance line shapes of paramagnetic species on surfaces, J. Phys. Chem. 86 (1982) 4465−4466, https://doi.org/10.1021/j100220a001.

[67] A.G. Marshall, D.C. Roe, Dispersion versus absorption: spectral line shape analysis for radiofrequency and microwave spectrometry, Analyt. Chem. 50 (1978) 756−763, https://doi.org/10.1021/ac50027a023.

[68] L. Walmsley, G. Ceotto, J.H. Castilho, C. Rettori, Magnetic field modulation frequency, sample size and electromagnetic configuration effects on the spin resonance spectra of graphite intercalation compounds, Synth. Met. 30 (1989) 97−107, https://doi.org/10.1016/0379-6779(89)90645-0.

[69] L. Walmsley, Translating conduction-electron spin-resonance lines into lorentzian lines, J. Magn. Reson. A 122 (1996) 209−213, https://doi.org/10.1006/jmra.1996.0196.

[70] M. Oshikawa, I. Affleck, Electron spin resonance in S=½ antiferromagnetic chains, Phys. Rev. B 65 (2002) 134410−134437, https://doi.org/10.1103/PhysRevB.65.134410.

[71] J.P. Joshi, S.V. Bhat, On the analysis of broad Dysonian electron paramagnetic resonance spectra, J. Magn. Res. 168 (2004) 284−287, https://doi.org/10.1016/j.jmr.2004.03.018.

[72] K.W. Blazey, K.A. Müller, F. Blatter, E. Schumacher, Conduction electron spin resonance of Caesium metallic clusters in zeolite X, Europhys. Lett. 4 (1987) 857−861, https://doi.org/10.1209/0295-5075/4/7/017.

[73] J.J. van der Klink, H.B. Brom, NMR in metals, metal particles and metal cluster compounds, Prog. Nucl. Magn. Reson. Spectr. 36 (2) (2000) 89−201, https://doi.org/10.1016/S0079-6565(99)00020-5.

[74] S. Iijima, Helical microtubules of graphitic carbon, Nature 354 (1991) 56−58, https://doi.org/10.1038/354056a0.

[75] L. Forró, C. Schönenberger, Physical Properties of Multi-Wall Nanotubes, Springer Berlin Heidelberg, Berlin, Heidelberg, 2001, pp. 329−391, https://doi.org/10.1007/3-540-39947-X_13.

[76] D.M. Djokić, A. Goswami, Quantum yield in polymer wrapped single walled carbon nanotubes: a computational model, Nanotechnology 28 (2017) 465204, https://doi.org/10.1088/1361-6528/aa8f38.

[77] A. Bachtold, M. Henny, C. Terrier, C. Strunk, C. Schönenberger, J.-P. Salvetat, J.-M. Bonard, L. Forró, Contacting carbon nanotubes selectively with low-ohmic contacts for four-probe electric measurements, Appl. Phys. Lett. 73 (1998) 274−276, https://doi.org/10.1063/1.121778.

[78] A. Bachtold, C. Strunk, J.-P. Salvetat, J.-M. Bonard, L. Forró, T. Nussbaumer, C. Schönenberger, Aharonov-Bohm oscillations in carbon nanotubes, Nature 397 (1999) 673−675, https://doi.org/10.1038/17755.

[79] L. Langer, V. Bayot, E. Grivei, J.-P. Issi, J.P. Heremans, C.H. Olk, L. Stockman, C. Van Haesendonck, Y. Bruynseraede, Quantum transport in a multiwalled carbon nanotube, Phys. Rev. Lett. 76 (1996) 479−482, https://doi.org/10.1103/PhysRevLett.76.479.

[80] W. Yi, L. Lu, Z. Dian-lin, Z.W. Pan, S.S. Xie, Linear specific heat of carbon nanotubes, Phys. Rev. B 59 (1999) R9015−R9018, https://doi.org/10.1103/PhysRevB.59.R9015.

[81] M. Bockrath, D.H. Cobden, J. Lu, A.G. Rinzler, R.E. Smalley, L. Balents, P.L. McEuen, Luttinger-liquid behaviour in carbon nanotubes, Nature 998 (1999) 598−601, https://doi.org/10.1038/17569.

Comparative study of structural and electrical properties of Pr and Ce doped BiFeO₃ ceramics synthesized by auto-combustion method

B. Stojadinović [a], Z. Dohčević-Mitrović [a, *], N. Paunović [a], N. Ilić [b], N. Tasić [b], I. Petronijević [c], D. Popović [c], B. Stojanović [a]

[a] Center for Solid State Physics and New Materials, Institute of Physics Belgrade, University of Belgrade, Pregrevica 118, 11080 Belgrade, Serbia
[b] Institute for Multidisciplinary Research, University of Belgrade, Kneza Višeslava 1, 11000 Belgrade, Serbia
[c] Faculty of Physics, University of Belgrade, Studentski trg 12-16, 11000 Belgrade, Serbia

ABSTRACT

Polycrystalline $Bi_{1-x}Pr(Ce)_xFeO_3$ ceramics ($x = 0$, 0.03, 0.05 and 0.10) were prepared by auto-combustion method using urea as a fuel. The influence of Pr(Ce) doping on structural, vibrational, morphological, dielectric and ferroelectric properties of BiFeO₃ polycrystalline ceramics was investigated. From X-ray diffraction (XRD) and scanning electron microscopy measurements it was observed that Pr(Ce) doping generated a reduction of the crystallite (grain) size of BiFeO₃ and contraction of the rhombohedral cell due to the increased compressive strain. The changes seen in the XRD and Raman spectra of 10% Pr(Ce)-doped samples, pointed to a probable appearance of orthorhombic (pseudotetragonal) crystal structure. The pristine BiFeO₃ exhibited rounded shape, non-saturated ferroelectric hysteresis loop. The dielectric constant and dielectric loss have shown strong dispersion at lower frequencies, typical for conductive BiFeO₃. Dielectric and ferroelectric properties at room temperature were improved with Pr doping. Concerning the Ce-doped samples, only the 3% Ce-doped sample exhibited a better shaped hysteresis loop and improved dielectric properties compared to the pristine BiFeO₃. With further increase of Ce content the ferroelectric properties degraded.

© 2015 Elsevier B.V. All rights reserved.

1. Introduction

Materials which exhibit multiferroic behavior are very rare, and usually have low magnetic ordering temperature which constrains their application [1]. Among multiferroic materials, BiFeO₃ with a rhombohedrally distorted perovskite structure of space group R3c, belongs to a very few known magnetoelectric materials which exhibits both ferroelectricity and magnetic ordering at and above room temperature (ferroelectric Curie temperature $T_C \sim 1100$ K and Neel temperature $T_N \sim 640$ K) [2,3]. These features make BiFeO₃ particularly applicable in the fields of microelectronics, digital recording or magnetoelectric sensors [4,5]. BiFeO₃ can be potentially used in ferroelectric random access memory (FeRAM) applications [6] due to large spontaneous polarization [7–9], but of particular interest is to investigate the possible existence of magnetoelectric coupling in BiFeO₃ and its potential application in magnetic random access memories (MRAM) [10]. However, main disadvantages for the application of BiFeO₃ in devices is low resistivity (i.e. high leakage current) which causes large dielectric loss, poor ferroelectric loop at room temperature and small remnant polarization due to the presence of oxygen vacancies and secondary phases.

Doping of BiFeO₃ with rare earth ions at A-site [11–15], as well as doping with alkaline earth divalent ions such as Ca^{2+}, Ba^{2+} and Sr^{2+} [16] proved to be an effective way to improve its ferroelectric properties. In fact, A-site doping with ions of smaller radius influences the Fe–O–Fe bond angle, giving a more insulating character to BiFeO₃ [17]. The codoping with 4f elements at A-site and 3d elements at B-site is another effective way to reduce the leakage current in BiFeO₃ and to improve its multiferroic properties [18–21]. In the majority of previous reports referring the rare earth ions doping of BiFeO₃, only a few studies have been devoted to the investigation of ferroelectric properties of Pr(Ce)-doped BiFeO₃ ceramics [22–26] or thin films [27–29]. It can be expected that Bi substitution with $Pr^{3+/4+}(Ce^{3+/4+})$ ions will prevent Bi volatilization and reduce the oxygen vacancy concentration, enhancing at the

same time the insulating properties of $BiFeO_3$. Furthermore, Pr(Ce) doping can induce larger structural distortion and, even a structural transformation in $BiFeO_3$, which can have strong influence on ferroelectric properties of these materials [29,30].

In this paper, Pr(Ce)-doped $BiFeO_3$ ceramics were synthesized by auto-combustion method which represents a very facile, fast and low-cost method. A systematic study of the effect of Pr(Ce) doping on the structural, vibrational, ferroelectric, and dielectric properties of $BiFeO_3$ ceramics has been reported.

2. Experimental details

Pristine and Pr(Ce)-doped $BiFeO_3$ ($Bi_{1-x}Pr(Ce)_xFeO_3$, $x = 0.03$, 0.05 and 0.1) polycrystalline samples were synthesized by auto-combustion method using urea as a fuel. The fuel, besides providing the energy for the reaction, acts as a complexant and prevents the precipitation of metal ions in the form of hydroxides [31]. The $Bi_{1-x}Pr(Ce)_xFeO_3$ precursor solutions were prepared using $Bi(NO_3)_3 \cdot 6H_2O$ (Alfa Aesar, 98.0%), $Ce(NO_3)_3 \cdot 6H_2O$ (Acros Organics, 99.5%), $Pr(NO_3)_3 \cdot 6H_2O$ (Sigma–Aldrich, 99.9%), $Fe(NO_3)_3 \cdot 9H_2O$ (Alfa Aesar, 98.0–101.0%), HNO_3 (65%) and urea (Riedel-de Haen, 99.0–100.5%) as starting materials. The iron(III), cerium and praseodymium nitrates were dissolved in a minimal amount of distilled water, whereas bismuth nitrate was dissolved in a minimal amount of diluted nitric acid. The solutions were mixed and stirred for 15 min, after which the solution of urea was added. The molar ratio of urea to nitrates was 5:1. The obtained suspension was stirred and heated at 80–90 °C. During the heating a small amount of the precipitate, formed after urea addition, was dissolved and the clear solution was obtained. After a partial water evaporation, a yellow-white precipitate was formed and the solution was turned into gel. At the same time the self-ignition started. The reaction was fast and had finished in a few minutes. Large amount of gasses was released, without a flame. A black resin, remained after the auto-combustion reaction, was dried at 150–200 °C for one hour. The dried product was then grinded in a mortar and the obtained reddish powder was annealed at 600 °C for two hours with a heating rate of 10 °C/min. The powders were pressed into disks under the pressure of 300 MPa and sintered at 800 °C for 1 h in a closed dish, together with a small amount of Bi_2O_3 added in order to compensate the Bi loss during the heat treatment.

The structure and crystallinity of the $Bi_{1-x}Pr(Ce)_xFeO_3$ polycrystalline ceramics were investigated by X-ray diffraction (XRD) method, using Phillips PW1710 diffractometer with Cu Kα radiation. The surface morphology was studied by scanning electron microscopy (SEM, TESCAN SM-300). SEM micrographs were recorded on gold sputtered non-treated surfaces of ceramic samples.

Raman spectra were recorded in backscattering configuration using Tri Vista 557 Raman system equipped with a nitrogen-cooled CCD detector. The $\lambda = 514.5$ nm line of Ar^+/Kr^+ mixed laser was used as an excitation source with an incident laser power less than 60 mW in order to minimize the heating effects. The ferroelectric hysteresis loops were acquired at 1 kHz using a Radiant Precision Multiferroic Analyzer. The dielectric properties of the samples were examined in the frequency range from 80 Hz to 120 kHz using a Digital Programmable LCR Bridge HM8118 (Hameg). Each sample was placed in a closed capacitor cell housed in a Faraday cage with an AC signal of 1.5 V applied across the cell. The disk-shaped samples had a diameter close to the diameter of cell electrodes (8 mm). The same capacitor cell and Digital LCR Meter 4285A (HP/Agilent) were also used for the measurement of the dielectric properties at frequencies from 80 kHz to 8 MHz. All measurements were performed at room temperature.

3. Results and discussion

3.1. Structural and morphological properties

Fig. 1a shows XRD patterns of pristine $BiFeO_3$ and $Bi_{1-x}Pr_xFeO_3$ ceramics. All diffraction peaks of the pristine $BiFeO_3$ sample match with the rhombohedral structure (R3c) without the presence of a secondary phase. Polycrystalline $Bi_{1-x}Pr_xFeO_3$ samples crystallize in a slightly distorted R3c structure. The slight lattice distortion is manifested by a gradual shift of XRD peaks to higher 2θ values with Pr doping. The shift of XRD peaks to higher 2θ values can be ascribed to the unit cell contraction i.e. the decrease in lattice parameters due to the substitution of Bi^{3+} ions with smaller Pr dopant. The unit cell parameters of pristine $BiFeO_3$ and
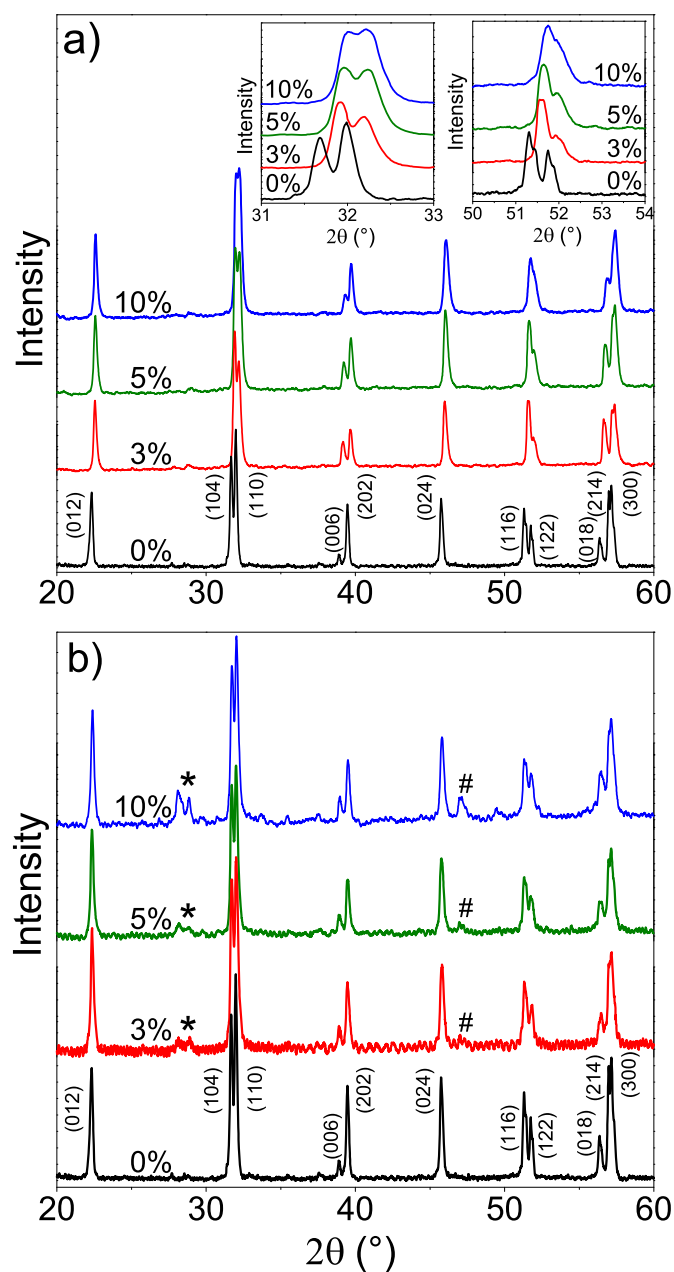

Fig. 1. X-ray diffraction patterns of the a) $Bi_{1-x}Pr_xFeO_3$ and b) $Bi_{1-x}Ce_xFeO_3$ samples ($0 \le x \le 0.1$). The (*) and (#) designate the appearance of additional phases discussed in the text.

$Bi_{1-x}Pr_xFeO_3$ samples are listed in Table 1. As can be seen from Table 1, with increasing Pr content, a reduction of both a and c lattice parameters, i.e. a contraction of the $BiFeO_3$ lattice, was observed.

The doublet peaks corresponding to the (104) and (110) planes around $2\theta \sim 32°$, and (116) and (122) planes around $2\theta \sim 52°$, with doping were shifted to higher 2θ values and almost merged into a single peak for the 10% Pr-doped sample. According to the literature data [32–34], these changes point to the beginning of partial phase transition from a rhombohedral (R3c) to an orthorhombic (Pbnm) structure. The enlarged 2θ regions where these peaks appear are presented in the insets of Fig. 1a. The partial structural transition can produce a distortion of the FeO_6 octahedron due to the changes in Fe–O bond length and O–Fe–O bond angles, affecting the electrical properties of $BiFeO_3$ [33,35]. Moreover, no additional peaks related to a secondary phase or other impurity phases have been observed in the sintered samples, implying a good solubility of Pr dopant in the $BiFeO_3$ lattice.

The XRD patterns of $Bi_{1-x}Ce_xFeO_3$ samples are presented in Fig. 1b and indexed to the rhombohedral $BiFeO_3$ structure. However, some weak diffraction peaks (marked with an asterisk) which correspond to a mullite ($Bi_2Fe_4O_9$) phase [36] appeared and became more pronounced with increased content of Ce dopant. As in the case of $Bi_{1-x}Pr_xFeO_3$ samples, lattice parameters (a and c) slightly decreased (see Table 1) implying that Ce substitution leads to the contraction of the unit cell and distortion of R3c structure. In addition, with increasing Ce content the peak at $2\theta \sim 46°$ (marked with #) splits into two peaks. This is particularly noticeable for the 10% Ce-doped sample. According to Liu et al. [29], these peaks can be indexed as (200) and (002) peaks of pseudotetragonal structure. Such a behavior suggests that in 10% Ce-doped sample partial structural transformation from a rhombohedral to the pseudotetragonal phase started.

The crystallite size and strain in the $Bi_{1-x}Pr(Ce)_xFeO_3$ polycrystalline samples were calculated using the Williamson-Hall (W–H) plots [37] and are presented in Table 1. The example of W–H plots for pure and 3% Pr(Ce)-doped $BiFeO_3$ samples are given in Fig. S1. From Table 1, it can be seen that the average crystallite size was reduced with doping, whereas the strain values increased and reached the highest value for the 10% Pr(Ce)-doped samples. It can be concluded that Pr(Ce) doping induces increased compressive strain responsible for the $BiFeO_3$ lattice contraction. The similar contraction of the $BiFeO_3$ lattice due to the compressive strain (stress) has been seen in Sm-doped $BiFeO_3$ thin films [38]. Furthermore, the increased strain in $Bi_{1-x}Pr(Ce)_xFeO_3$ samples can produce a distortion of rhomohedral structure, which can induce gradual structural phase transformation as in a case of Y-doped $BiFeO_3$ nanopowders [39].

The surface morphology of $BiFeO_3$ and $Bi_{1-x}Pr(Ce)_xFeO_3$ ($x = 0.05, 0.1$) samples is shown in Fig. 2. The undoped (Fig. 2a) and Pr-doped $BiFeO_3$ samples (Fig. 2b and c) exhibit rather dense microstructure (82 and 78% of the theoretical density for undoped $BiFeO_3$ and 10% Pr-doped samples) with a clearly visible grains and
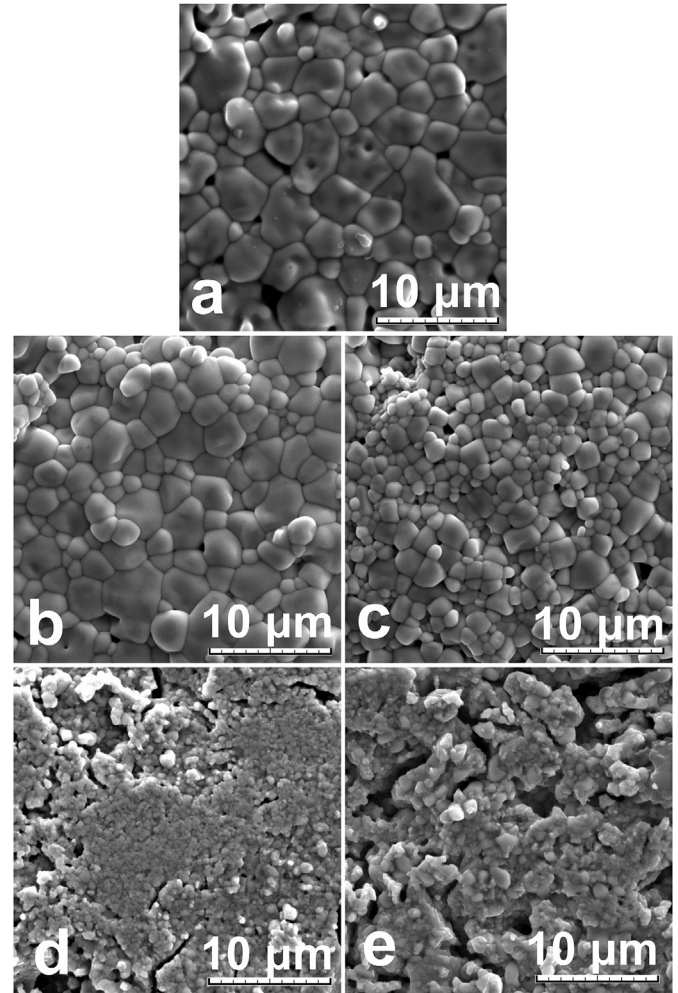

Fig. 2. SEM images of the surface morphology of a) $BiFeO_3$, b) $Bi_{0.95}Pr_{0.05}FeO_3$, c) $Bi_{0.90}Pr_{0.10}FeO_3$, d) $Bi_{0.95}Ce_{0.05}FeO_3$, and e) $Bi_{0.90}Ce_{0.10}FeO_3$ samples.

grain boundary. The morphology of Ce-doped samples (Fig. 2d and e) is different from that of pure and Pr-doped samples. These samples exhibit less pronounced grain boundary microstructure with increased intergranular porosity and lower sample density (65% of the theoretical density for 10% Ce-doped sample). SEM images showed that in Pr(Ce)-doped samples the grain size decreased. The grain size decrease in Pr(Ce)-doped samples can be explained by inhibiting effect of increased Pr(Ce) dopant content on grain growth or can be attributed to the suppressed oxygen vacancy formation in these samples, as oxygen vacancies favorize the grain growth during the sintering process [33]. In addition, if there is a decrease of oxygen vacancy concentration, the reaction rate in the solid phase is slowed down, grains remain smaller and the

Table 1
The lattice parameters, average crystallite size and strain values for $Bi_{1-x}Pr(Ce)_xFeO_3$ samples.

Samples	Lattice parameter a (Å)	Lattice parameter c (Å)	Strain (%)	Crystalite size (nm)
$BiFeO_3$	5.617 ± 0.004	13.760 ± 0.010	0.10 ± 0.02	28.9 ± 2.2
$Bi_{0.97}Pr_{0.03}FeO_3$	5.587 ± 0.005	13.686 ± 0.012	0.16 ± 0.03	22.2 ± 1.6
$Bi_{0.95}Pr_{0.05}FeO_3$	5.582 ± 0.003	13.672 ± 0.007	0.18 ± 0.04	21.9 ± 1.9
$Bi_{0.90}Pr_{0.10}FeO_3$	5.576 ± 0.004	13.657 ± 0.009	0.36 ± 0.05	19.3 ± 1.9
$Bi_{0.97}Ce_{0.03}FeO_3$	5.597 ± 0.004	13.735 ± 0.013	0.20 ± 0.01	25.2 ± 0.9
$Bi_{0.95}Ce_{0.05}FeO_3$	5.598 ± 0.005	13.736 ± 0.010	0.24 ± 0.01	24.0 ± 1.6
$Bi_{0.90}Ce_{0.10}FeO_3$	5.595 ± 0.003	13.730 ± 0.011	0.32 ± 0.04	22.9 ± 2.6

densification is weaker.

3.2. Raman analysis

The structural evolution of $BiFeO_3$ structure with Pr(Ce) ion substitution can be reflected through the Raman spectra as well. For R3c rhombohedral structure, the group theory analysis predicts 13 Raman active modes (4 A_1 and 9 doubly degenerate E modes) [40–45], but the number of clearly seen Raman modes at room temperature is much less than predicted [43]. The room

temperature Raman spectra of $BiFeO_3$ and $Bi_{1−x}Pr(Ce)_xFeO_3$ samples are presented in Fig. 3.

In the Raman spectrum of $BiFeO_3$ sample (Fig. 3a), two A_1 modes at 171 and around 218 cm^{-1} [39] and two E modes at 75 and 265 cm^{-1} [43] can be clearly seen. The strong and wide Raman peak at 136 cm^{-1} is composed of two modes, E mode at 132 cm^{-1} and A_1 mode at around 140 cm^{-1}, which can be resolved by parallel polarization measurements at low temperatures [43]. The other E phonon modes at around 330, 368, 428, 475, 520 and 599 cm^{-1} are barely visible. In the Raman spectra of $Bi_{1−x}Pr_xFeO_3$ samples, the E mode at 75 cm^{-1} and A_1 mode at around 218 cm^{-1} exhibit shift to higher frequencies. The Raman peak at 136 cm^{-1} is also shifted to higher frequencies. After deconvolution of the 136 cm^{-1} peak using Lorentzian profiles, the position of the E mode remained unchanged, whereas the A_1 mode was shifted to higher frequencies (see dashed line in Fig. 3a). The other E modes (around 475, 520 and 599 cm^{-1}) become more prominent with increasing Pr content. In the Raman spectra of $Bi_{1−x}Ce_xFeO_3$ samples, more pronounced changes in the Raman modes position and intensity are observed in the case of 10% Ce-doped sample.

The exact positions of the Raman modes in the 10% Pr(Ce)-doped samples, for which the possible structural phase transformation was observed, were determined using the Lorentzian fit. In Fig. 3c are shown the deconvoluted Raman spectra of $BiFeO_3$, $Bi_{0.90}Pr_{0.10}FeO_3$ and $Bi_{0.90}Ce_{0.10}FeO_3$ samples. The obtained mode positions are summarized in Table 2.

As can be seen from Table 2, the E and A_1 modes (75, 140 cm^{-1}) which are related to Bi−O bonds, as well as the E modes (428, 520 and 599 cm^{-1}) which are characteristic for the Fe−O bonds [44,46], are shifted to higher frequencies for both $Bi_{0.90}Pr_{0.10}FeO_3$ and $Bi_{0.90}Ce_{0.10}FeO_3$ samples. The A_1 mode at around 218 cm^{-1}, which is characteristic for Bi−O bonds is shifted to higher frequencies in $Bi_{0.90}Pr_{0.10}FeO_3$ sample. The blueshift of the E and A_1 modes, for which the contribution of Bi−O bonds dominates, is expected when the substitution with smaller atomic mass Pr(Ce) ions at Bi-site happens, because the Raman mode frequency is dependent on the atomic mass (M) of the substituent according to the relation $\omega \sim (k/M)^{1/2}$ [22,26]. The appearance of the increased compressive strain in $BiFeO_3$ lattice with increased amount of Pr(Ce) dopant is also responsible for the blueshift of the frequency of the Raman A_1 and E modes, characteristic for both Bi−O and Fe−O bonds.

The E mode at 599 cm^{-1}, which is of low intensity in the pristine $BiFeO_3$ and almost invisible in $Bi_{0.90}Ce_{0.10}FeO_3$, becomes very prominent in $Bi_{0.90}Pr_{0.10}FeO_3$ sample. Compared to the pristine $BiFeO_3$, the relative intensity ratio of A_1 modes at about 140 and 171 cm^{-1} (I_{140}/I_{171}) is increased in 10% Pr(Ce)-doped samples ($I_{140}/I_{171} = 0.69$, 1.1, and 2.1 for $BiFeO_3$, 10% Ce and 10% Pr-doped samples, respectively). The change of the relative intensity of these two A_1
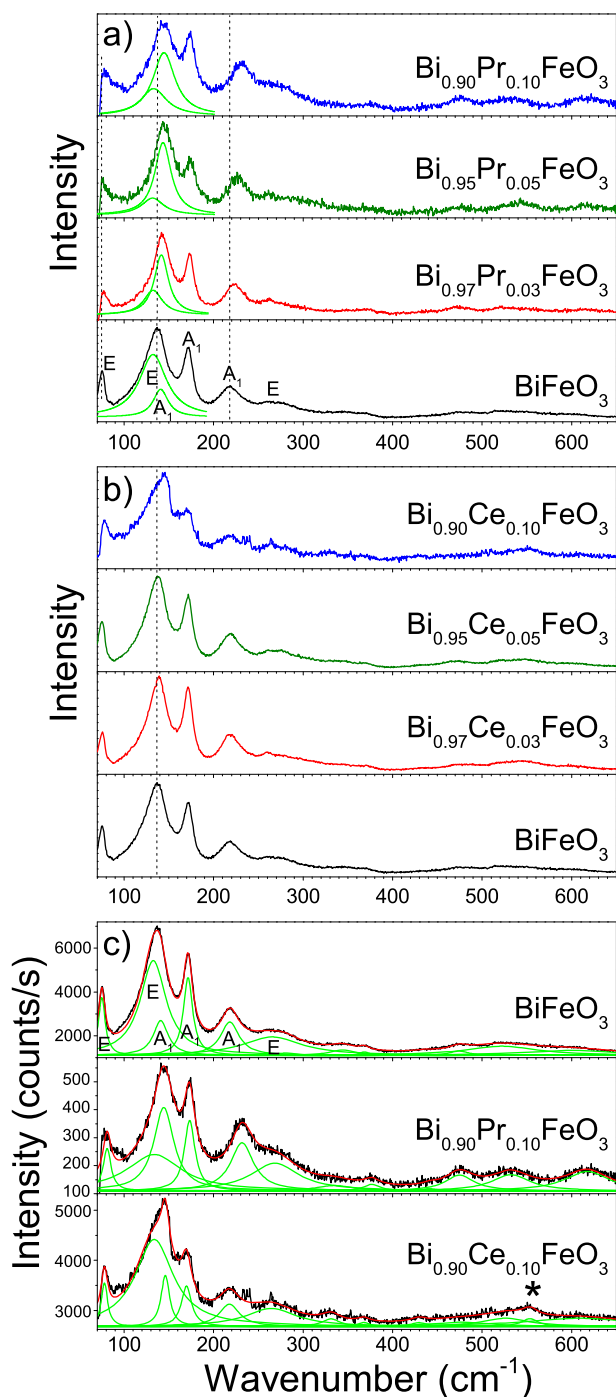
Fig. 3. Room-temperature Raman spectra of (a) $Bi_{1−x}Pr_xFeO_3$ and (b) $Bi_{1−x}Ce_xFeO_3$ samples ($0 \le x \le 0.1$), together with (c) deconvoluted Raman spectra of $BiFeO_3$, $Bi_{0.90}Pr_{0.10}FeO_3$ and $Bi_{0.90}Ce_{0.10}FeO_3$ samples.

Table 2
Positions of the Raman modes for $BiFeO_3$, $Bi_{0.90}Pr_{0.10}FeO_3$, and $Bi_{0.90}Ce_{0.10}FeO_3$ samples.

Raman modes (in cm^{-1})	$BiFeO_3$	$Bi_{0.90}Pr_{0.10}FeO_3$	$Bi_{0.90}Ce_{0.10}FeO_3$
E	75.4	81.2	77.4
E	132.3	132.9	132.7
A_1	140.8	144.5	145.0
A_1	171.2	172.7	169.6
A_1	218.7	231.6	217.5
E	265.2	269.0	265.1
E	330.6	333.3	331.3
E	368.6	376.0	367.1
E	428.4	440.6	429.2
E	475.8	475.0	476.8
E	520.4	532.8	526.9
E	599.2	617.7	611.7

modes reflects the change in Bi–O bonds and the stereochemical activity of Bi lone electron pair with Pr(Ce) doping [23]. Furthermore, any changes in the position or intensity of the 140, 171 and 599 cm^{-1} modes are related to the changes in the ferroelectric properties of BiFeO$_3$ as well [22,45]. In the Raman spectrum of Bi$_{0.90}$Ce$_{0.10}$FeO$_3$ appears an additional mode (marked with an asterisk in Fig. 3c) at around 553 cm^{-1}. This mode can be ascribed to the mode of Bi$_2$Fe$_4$O$_9$ phase [47]. The appearance of this mode is in accordance with the XRD pattern of Bi$_{0.90}$Ce$_{0.10}$FeO$_3$ in which the presence of a mullite phase has been seen. The changes observed in the Raman spectra of doped samples gave a clear evidence about the lattice distortion induced by Pr(Ce) doping.

3.3. Dielectric properties

The frequency dependence of the dielectric constant (ε') and loss tangent (tan δ) of Bi$_{1-x}$Pr(Ce)$_x$FeO$_3$ samples are shown in Fig. 4. It can be observed from Fig. 4a that the dielectric constant of the pristine BiFeO$_3$ at low frequencies has the highest value ($\varepsilon' = 159$) and shows a strong dispersion in the low-frequency region. Such a behavior is characteristic for the presence of oxygen or bismuth vacancies, which are responsible for the appearance of charge carriers at grain boundaries or interfaces (i.e. the local space charge), and an increased conductivity in BiFeO$_3$ [48]. The contribution of the local space charge to the dielectric constant usually manifests as a strong dispersion at low frequencies. The presence of oxygen vacancies also increases the probability of a hopping conduction mechanism between Fe^{2+} and Fe^{3+} ions, which can be reflected through an increased value of the dielectric constant [48].

The dielectric constant of Pr(Ce)-doped samples significantly decreases and exhibits much smaller dispersion at low frequencies (Fig. 4a). The overall decrease of the dielectric constant can be attributed to a reduced conductivity and a decreased space charge relaxation at the interface [49], but can also originate from the contraction of the unit cell volume when Bi ions are substituted with smaller Pr(Ce) ions. The unit cell contraction can result in a decreased polarization because of less free volume for the displacement of Fe^{3+} ions in FeO$_6$ octahedra. The dielectric constant of Bi$_{1-x}$Pr$_x$FeO$_3$ samples exhibits relatively small ($x = 0.03$, 0.05) or almost no dielectric dispersion ($x = 0.1$). Such a behavior can be explained by the fact that the incorporation of Pr$^{3+/4+}$ ions into the BiFeO$_3$ lattice reduces the oxygen vacancy concentration and conductivity of BiFeO$_3$ [49, 29]. Ce-doped samples ($x = 0.03$, 0.05) have lower value of dielectric constant

than Pr-doped ones and show almost no frequency dispersion. The value of dielectric constant and its dispersion increases for the Bi$_{0.90}$Ce$_{0.10}$FeO$_3$ sample. The increase of dielectric constant can originate from the increased oxygen vacancy concentration and the appearance of local space charges at the grain boundaries or interfaces [48,49]. The change of the dielectric constant with frequency in BiFeO$_3$ and Bi$_{1-x}$Pr(Ce)$_x$FeO$_3$ samples can be well explained by the Maxwell–Wagner relaxation effect which refers to the interfacial polarization [48,49].

The loss tangent (tan δ) shows a similar variation with frequency as the dielectric constant. At low frequencies, the loss tangent of the undoped BiFeO$_3$ sample shows a higher value, due to the increased defect concentration and conductivity and shows a broad relaxation peak in the intermediate frequency range (10 kHz–1 MHz). The broad relaxation peaks are usually caused by inhomogenous grain conductivity [49]. The tan δ curves show dispersive characteristics in the low-frequency region for Pr-doped samples, with much less pronounced relaxation peaks. At frequencies higher than 10 kHz, the value of tan δ is reduced and is significantly lower than in the pristine BiFeO$_3$, due to reduced oxygen vacancy concentration and conductivity. The Ce-doped samples with lower content of Ce ($x = 0.03$, 0.05) have low value of tan δ over the whole frequency range. The tan δ becomes much higher in the case of Bi$_{0.90}$Ce$_{0.10}$FeO$_3$ sample, pointing to increased conductivity of Bi$_{0.90}$Ce$_{0.10}$FeO$_3$ sample.

3.4. Ferroelectric properties

The ferroelectric hysteresis (P–E) loops for Bi$_{1-x}$Pr(Ce)$_x$FeO$_3$ samples are presented in Fig. 5. In the inset of Fig. 5b is given P–E loop of the pristine BiFeO$_3$.

The BiFeO$_3$ exhibited a rounded shape i.e. a non-saturated (lossy) P–E loop, and was not able to withstand applied electric field stronger than 2 kV, which is typical for a conductive BiFeO$_3$ material. The ferroelectric performances of pristine BiFeO$_3$ are consistent with the dielectric measurements. The ferroelectric loops of the Pr(Ce)-doped samples (Fig. 5a and b), exhibited less pronounced leakage effect than for the pristine BiFeO$_3$, but were still non-saturated. This is an expected behavior, since the incorporation of Pr$^{3+/4+}$(Ce$^{3+/4+}$) ions in the BiFeO$_3$ lattice should suppress the formation of bismuth and oxygen vacancies. With increasing Pr content, the maximal polarization (P$_M$) and the remnant polarization (P$_R$) have increased and reached the values of 0.4 and 0.35 μC/cm^2 for Bi$_{0.90}$Pr$_{0.10}$FeO$_3$. The P$_M$ and P$_R$ values are comparable with the previously reported data on BiFeO$_3$ ceramics
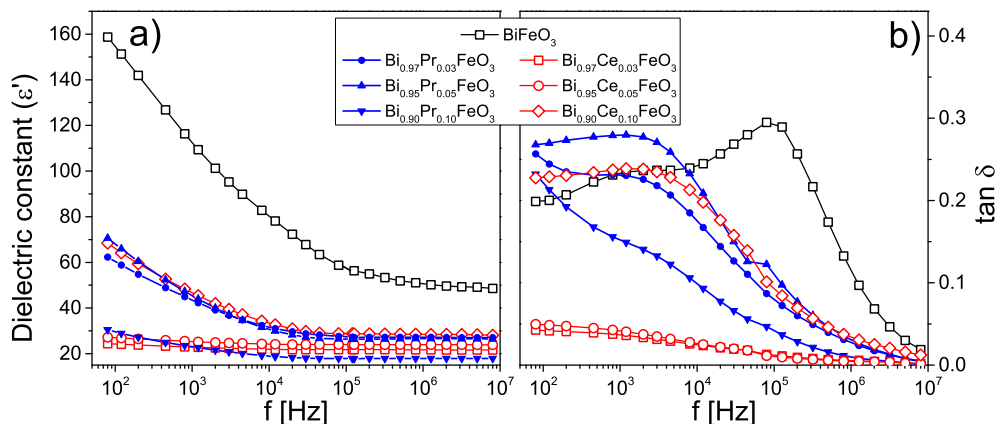
Fig. 4. Room temperature (a) dielectric constant (ε') and (b) loss tangent (tan δ) of Bi$_{1-x}$Pr(Ce)$_x$FeO$_3$ samples ($0 \le x \le 0.1$) as a function of frequency.
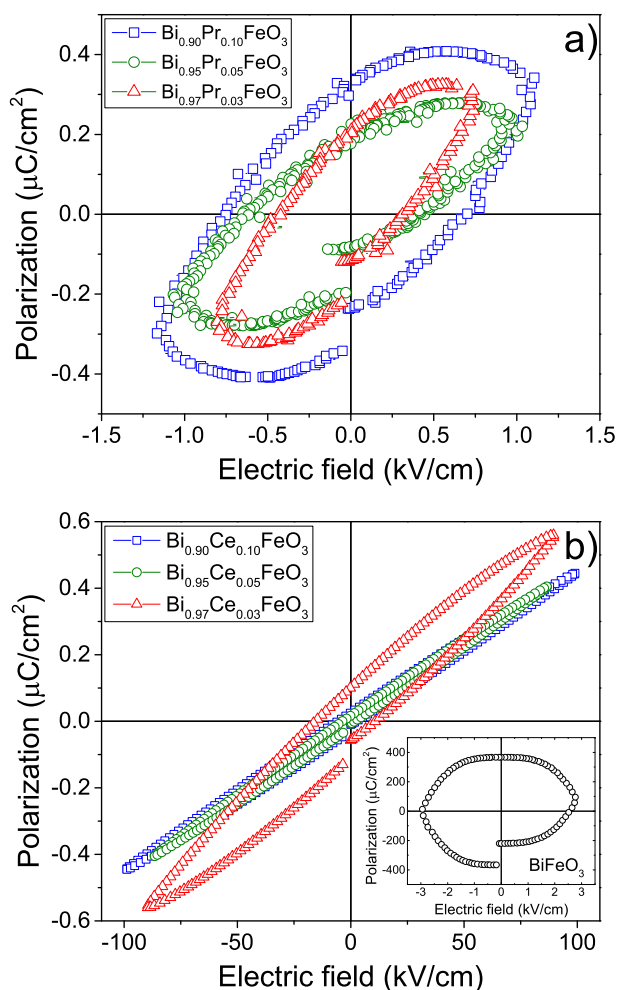
Fig. 5. Room-temperature P–E hysteresis loops for (a) $Bi_{1-x}Pr_xFeO_3$ and (b) $Bi_{1-x}Ce_xFeO_3$ samples ($0.03 \leq x \leq 0.1$). In the inset is presented P–E hysteresis loop for the pristine $BiFeO_3$.

doped with similar content of Pr [24,49]. However, the breakdown electric field for Pr-doped samples is still as low as in the case of the pristine $BiFeO_3$.

Initial Ce doping increases the ability of $BiFeO_3$ to withstand higher electric fields [50], in our case up to 100 kV/cm. This enhancement can be attributed to a decrease of oxygen vacancy concentration, as the substitution of Bi ions with higher valence Ce^{4+} ions would suppress the formation of oxygen vacancies and consequently reduce the leakage current. The polarization has the highest value of about 0.56 $\mu C/cm^2$ in the 3% Ce-doped sample, and the P_R value is about 0.1 $\mu C/cm^2$. With further increase of Ce content, the values of P_M, P_R and coercive field decreased and the samples exhibited a poor P–E loop. This result suggests that the ferroelectric properties were degraded with further increase of Ce content.

Several reasons can be responsible for the lower values of P_R in Pr(Ce)-doped samples. The contraction of $BiFeO_3$ unit cell with Pr(Ce) doping, i.e. the partial phase transition from rhombohedral to orthorhombic (pseudotetragonal) phase can reduce the remnant polarization, as the direction of the spontaneous polarization can be changed [51,29]. Another reason can be found in lowering of the crystal anisotropy and a decrease of Curie temperature with rare earth ion doping [52,53].

Therefore, we can conclude that Pr(Ce) doping causes a

distortion of R3c structure and in 10% Pr(Ce) doped samples, there is an indication that partial structural phase transformation from rhombohedral to orthorhombic (pseudotetragonal) phase started. Pr doping suppresses the formation of oxygen vacancies, decreasing the conductivity of Pr-doped $BiFeO_3$ samples. In the case of Ce-doped samples, improved dielectric and ferroelectric properties exhibited the sample with 3% of Ce. Further increase of Ce content caused the deterioration of ferroelectric properties and in the 10% Ce-doped sample both the dielectric and ferroelectric properties of $BiFeO_3$ ceramics were degraded. The reduction of ferroelectric polarization for $Bi_{0.95}Ce_{0.05}FeO_3$ sample can originate from the presence of impurity $Bi_2Fe_4O_9$ phase which increases the conductivity of $BiFeO_3$. Further, deterioration of dielectric and ferroelectric properties for $Bi_{0.90}Ce_{0.10}FeO_3$ can originate from lower percentage of Ce^{4+} ions in this sample (see Fig. S2 Supplementary material) and increasing content of $Bi_2Fe_4O_9$ phase. On the other hand, the increased Ce content can decrease the stereochemical activity of Bi ions and can lead to the partial transition from ferroelectric to paraelectric phase, like in La-doped $BiFeO_3$ [54].

4. Conclusion

In summary, polycrystalline $Bi_{1-x}Pr(Ce)_xFeO_3$ ceramics ($x = 0$, 0.03, 0.05 and 0.10) were prepared by auto-combustion method. SEM and XRD analysis have shown that the crystallite and grain sizes slightly decreased in Pr(Ce)-doped samples, whereas the compressive strain increased. XRD and Raman spectra of 10% Pr(Ce)-doped samples pointed to probable appearance of orthorhombic (pseudotetragonal) phase. The presence of secondary phase was evident only in Ce-doped samples. The pristine $BiFeO_3$ showed lossy P–E loop, large dispersion of dielectric constant and tan δ at low frequencies, and a broad relaxation peak in tan δ in the intermediate frequency range. The dielectric properties were improved by the Pr substitution, i.e. the dielectric constant had lower values than in the pristine $BiFeO_3$ and exhibited smaller or almost no dispersion in the investigated frequency range, whereas with increasing Pr content the loss tangent decreased and had low values at higher frequencies. Pr-doped samples exhibited better shaped ferroelectric loops with much less pronounced leakage effect. The remnant and maximal polarization increased with increased Pr doping. Such an improvement in dielectric and ferroelectric properties can be attributed to decreased interfacial polarization and reduced conductivity of $BiFeO_3$ ceramic samples. Regarding the Ce-doped samples, the best dielectric and ferroelectric properties were observed in the 3% Ce-doped sample, whereas with further increase of Ce dopant up to 10% these properties were degraded. The reduced polarization and increased dielectric loss may be attributed to the appearance of conducting $Bi_2Fe_4O_9$ phase and decreased stereochemical activity of Bi-sites by Ce doping due to the possible appearance of the pseudotetragonal phase.

Appendix A. Supplementary data

Supplementary data related to this article can be found at http://dx.doi.org/10.1016/j.jallcom.2015.09.235.

References

[1] N.A. Spaldin, Science 309 (2005) 391.
[2] I. Sosnowska, T. Peterlin-Neumaier, E. Steichele, J. Phys. C: Solid State Phys. 15 (1982) 4835–4846.
[3] G. Catalan, J.F. Scott, Adv. Mater. 21 (2009) 2463–2485.
[4] R. Ramesh, N.A. Spaldin, Nat. Mater. 6 (2007) 21–29.
[5] S.-W. Cheong, M. Mostovoy, Nat. Mater. 6 (2007) 13–20.
[6] A.N. Kalinkin, E.M. Kozhbakhteev, A.E. Polyakov, V.M. Skorikov, Inorg. Mater. 49 (2013) 1031–1043.
[7] C. Ederer, N.A. Spaldin, Phys. Rev. Lett. 95 (2005) 257601.
[8] J. Li, J. Wang, M. Wuttig, R. Ramesh, N. Wang, B. Ruette, A.P. Pyatakov, A.K. Zvezdin, D. Viehland, Appl. Phys. Lett. 84 (2004) 5261–5263.
[9] K.Y. Yun, D. Ricinschi, T. Kanashima, M. Noda, M. Okuyama, Jpn. J. Appl. Phys. 43 (2004) L647–L648.
[10] J.F. Scott, Nat. Mater. 6 (2007) 256–257.
[11] S.B. Emery, C.J. Cheng, D. Kan, F.J. Rueckert, S.P. Alpay, V. Nagarajan, I. Takeuchi, B.O. Wells, Appl. Phys. Lett. 97 (2010) 152902.
[12] K.S. Nalwa, A. Garg, A. Upadhyaya, Mater. Lett. 62 (2008) 878–881.
[13] G.L. Yuan, S.W. Or, J.M. Liu, Z.G. Liu, Appl. Phys. Lett. 89 (2006) 052905.
[14] J.H. Lee, H.J. Choi, D. Lee, M.G. Kim, C.W. Bark, S. Ryu, M.A. Oak, H.M. Jang, Phys. Rev. B 82 (2010) 045113.
[15] G.S. Lotey, N.K. Verma, J. Nanopart. Res. 14 (2012) 742.
[16] V.A. Khomchenko, D.A. Kiselev, J.M. Vieira, L. Jian, A.L. Kholkin, A.M.L. Lopes, Y.G. Pogorelov, J.P. Araujo, M. Maglione, J. Appl. Phys. 103 (2008) 024105.
[17] C.H. Yang, D. Kan, I. Takeuchi, V. Nagarajan, J. Seidel, Phys. Chem. Chem. Phys. 14 (2012) 15953–15962.
[18] W. Liu, G. Tan, X. Xue, G. Dong, H. Ren, A. Xia, Ceram. Int. 40 (2014) 12179–12185.
[19] W. Ye, G. Tan, G. Dong, H. Ren, A. Xia, Ceram. Int. 41 (2015) 4668–4674.
[20] Y.J. Kim, J.W. Kim, C.M. Raghavan, J.J. Oak, H.J. Kim, W.J. Kim, M.H. Kim, T.K. Song, S.S. Kim, Ceram. Int. 39 (2013) S195–S199.
[21] C.M. Raghavan, J.W. Kim, S.S. Kim, Ceram. Int. 39 (2013) 3563–3568.
[22] D. Varshney, P. Sharma, S. Satapathy, P.K. Gupta, J. Alloys Compd. 584 (2014) 232–239.
[23] P. Sharma, D. Varshney, S. Satapathy, P.K. Gupta, Mater. Chem. Phys. 143 (2014) 629–636.
[24] N. Kumar, N. Panwar, B. Gahtori, N. Singh, H. Kishan, V.P.S. Awana, J. Alloy. Compd. 501 (2010) L29–L32.
[25] S.K. Pradhan, B.K. Roul, Phys. B 407 (2012) 2527–2532.
[26] M. Arora, M. Kumar, Ceram. Int. 41 (2015) 5705–5712.
[27] B. Yu, M. Li, Z. Hu, L. Pei, D. Guo, X. Zhao, S. Dong, Appl. Phys. Lett. 93 (2008) 182909.
[28] X. Wang, H. Liu, B. Yan, J. Eur. Ceram. Soc. 29 (2009) 1183–1187.
[29] J. Liu, M. Li, L. Pei, J. Wang, B. Yu, X. Wang, X. Zhao, J. Alloy. Compd. 493 (2010) 544–548.
[30] J. Liu, M. Li, L. Pei, B. Yu, D. Guo, X. Zhao, J. Phys. D. Appl. Phys. 42 (2009) 115409.
[31] S. Lorentzou, K. Karadimitra, C. Agrafiotis, A.G. Konstandopoulos, in: Proceedings of the PARTEC 2004, International Conference for Particle Technology, Nuremberg, Germany, March 16–18, 2004.
[32] L. Chen, L. Zheng, Y. He, J. Zhang, Z. Mao, X. Chen, J. Alloys Compd. 633 (2015) 216–219.
[33] P.C. Sati, M. Arora, S. Chauhan, M. Kumar, S. Chhoker, Ceram. Int. 40 (2014) 7805–7816.
[34] V. Singh, S. Sharma, M. Kumar, R.K. Kotnala, R.K. Dwivedi, J. Magn. Magn. Mater. 349 (2014) 264–267.
[35] S.K. Pradhan, B.K. Roul, J. Phys. Chem. Solids 72 (2011) 1180–1187.
[36] N.I. Ilić, A.S. Džunuzović, J.D. Bobić, B.S. Stojadinović, P. Hammer, M.M. Vijatović Petrović, Z.D. Dohčević-Mitrović, B.D. Stojanović, Ceram. Int. 41 (2015) 69–77.
[37] G.K. Williamson, W. Hall, Acta Metall. 1 (1953) 22–31.
[38] X. Xu, T. Guoqiangn, R. Huijun, X. Ao, Ceram. Int. 39 (2013) 6223–6228.
[39] R.K. Mishra, D.K. Pradhan, R.N.P. Choudhary, A. Banerjee, J. Phys. Condens. Matter 20 (2008) 045218.
[40] M.N. Iliev, M.V. Abrashev, D. Mazumdar, V. Shelke, A. Gupta, Phys. Rev. B 82 (2010) 014107.
[41] M.K. Singh, H.M. Jang, S. Ryu, M.H. Jo, Appl. Phys. Lett. 88 (2006) 42907.
[42] P. Hermet, M. Goffinet, J. Kreisel, Ph. Ghosez, Phys. Rev. B 75 (2007) 220102(R).
[43] H. Fukumura, S. Matsui, H. Harima, T. Takahashi, T. Itoh, K. Kisoda, M. Tamada, Y. Noguchi, M. Miyayama, J. Phys. Condens. Matter 19 (2007) 365224.
[44] M.K. Singh, S. Ryu, H.M. Jang, Phys. Rev. B 72 (2005) 132101.
[45] G.L. Yuan, S.W. Or, H.L. Chan, Z.G. Liu, J. Appl. Phys. 101 (2007) 024106.
[46] Y. Yao, W. Liu, Yu Chan, C. Leung, C. Mak, B. Ploss, Int. J. Appl. Ceram. Technol. 8 (2011) 1246–1253.
[47] M.N. Iliev, A.P. Litvinchuk, V.G. Hadjiev, M.M. Gospodinov, V. Skumryev, E. Ressouche, Phys. Rev. B 81 (2010) 024302.
[48] A. Reetu, S. Agarwal, Ashima Sanghi, J. Appl. Phys. 110 (2011) 073909.
[49] V. Kumar, A. Gaur, N. Sharma, J. Shah, R.K. Kotnala, Ceram. Int. 39 (2013) 8113–8121.
[50] Z. Quan, W. Liu, H. Hu, S. Xu, B. Sebo, G. Fang, M. Li, X. Zhao, J. Appl. Phys. 104 (2008) 084106.
[51] X. Li, X. Wang, Y. Li, W. Mao, P. Li, T. Yang, J. Yang, Mater. Lett. 90 (2013) 152–155.
[52] H. Ushida, R. Ueno, H. Funakubo, S. Koda, J. Appl. Phys. 100 (2006) 014106.
[53] P. Pandit, S. Satapathy, P. Sharma, P.K. Gupta, S.M. Yusuf, V.G. Sathe, Bull. Mater. Sci. 34 (2011) 899–905.
[54] G.L. Yuan, S.W. Or, H.L. Chan, J. Phys. D. Appl. Phys. 40 (2007) 1196–1200.

Theoretical and experimental study of octahedral tilting of Ca₁₋ₓGdₓMnO₃ (x = 0.05, 0.1, 0.15, 0.2) nanometric powders

Milena Rosić [a, *], Dejan Zagorac [a], Dušan Milivojević [b], Novica Paunović [c], Jelena Zagorac [a], Zorana Dohčević-Mitrović [c], Branko Matović [a]

[a] *Laboratory for Material Science, Institute of Nuclear Sciences "Vinča", University of Belgrade, P.O. Box 522, 11001 Belgrade, Serbia*
[b] *Laboratory for Radiation Chemistry and Physics, Institute of Nuclear Sciences "Vinča", University of Belgrade, P.O. Box 522, 11001 Belgrade, Serbia*
[c] *Center for Solid State Physics and New Materials, Institute of Physics Belgrade, University of Belgrade, Pregrevica 118, 11080 Belgrade, Serbia*

ARTICLE INFO

ABSTRACT

In order to estimate theoretical stability of the perovskite structure for synthesized Ca₁₋ₓGdₓMnO₃ (x = 0.05, 0.1, 0.15, 0.2) nanopowders, the Goldschmidt tolerance factor G_t and global instability index *GII* were calculated. Furthermore, we have performed structure prediction of Ca₁₋ₓGdₓMnO₃ perovskites and found several possible perovskite-related phases. The influence of gadolinium amount on Mn—O bond angles and distances, tilting of MnO₆ octahedra around all three axes and deformation due to the presence of the Jahn—Teller distortion around Mn³⁺ cation, as well as the influence of the amount of Mn³⁺ cation on Ca₁₋ₓGdₓMnO₃ compound, was examined. Ion Mn valence states were determined by bond valence calculations (BVC). Infrared active phonon modes in Ca₁₋ₓGdₓMnO₃ were studied by infrared reflection spectroscopy and magnetic properties were studied by using EPR (electron paramagnetic resonance) measurements.

© 2016 Elsevier B.V. All rights reserved.

1. Introduction

Manganese oxides with perovskite structure, A₁₋ₓReₓBO₃ (A: alkaline earth element, Re: rare earth element, B: Mn, respectively), have become a matter of great scientific interest, because of their physical, electronic and magnetic properties, and many intriguing phenomena, such as colossal magnetoresistance (CMR) involving potential applications in magnetic memory devices and sensors [1—3]. This series of solid solutions with perovskite type of structure is characterized starting from cubic symmetry, usually as a result of small displacements of the oxygen ions and rare earth element from their positions in the ideal cubic unit cell. The compounds of chemical composition Ca₁₋ₓGdₓMnO₃ crystallize in the orthorhombic space group *Pnma*. Smaller Mn ions occupy octahedral 4b (1/2,0,0), while the larger ions, Ca and Gd, take 4c (x, 1/4, z; x ≅ 0, z ≅ 0) positions and are surrounded by 12 oxygen atoms residing in the two crystallographic unequivalent positions: O1 in 4c (x, 1/4, z; x ≅ 0, z ≅ 1/2) and O2 in 8d (x, y, z; x ≅ 1/4, y ≅ 0, z ≅ 1/4) [4].

In Ca₁₋ₓGdₓMnO₃ compound, valence of Ca, Gd and O ions are +2, +3 and −2, respectively, while Mn ion can be in +3 or +4 valence state. Replacement of Ca²⁺ by Gd³⁺ causes reduction of Mn⁴⁺ to Mn³⁺ in order to maintain $Ca^{2+}_{1-x}Gd^{3+}_xMn^{4+}_{1-x}Mn^{3+}_xO^{2-}_3$ crystal electroneutrality, which has a significant impact on the physical, and especially on the magnetic properties of these materials. An Mn³⁺ ion has 4 electrons in *d* orbital (3*d*⁴), while an Mn⁴⁺ ion has 3 electrons in *d* orbital (3*d*³), and the Mn³⁺/Mn⁴⁺ ratio influences magnetic behavior of the system.

Goldschmidt tolerance factor (G_t) has been used as one of the criteria for the degree of distortion of the perovskite lattice. G_t is defined as $Gt = (r_A + r_o)/\sqrt{2}(r_B + r_o)$ [5], where the r_A and r_B correspond to the averaged radii of cations placed in position A (Ca²⁺ and Gd³⁺) and B (Mn ions), respectively, while r_O represents radius of the oxygen ions. Equation $r_A = (1−x)r_{A'} + xr_d$ gives radius of cation A as the sum of the radius of doped cation $r_{A'}$ and radius of the dopant r_d [6—8]. The relationship between the concentration of dopant x and G_t is $Gt = ((1 − x)r_{A'} + xr_d + r_o)/\sqrt{2}(r_B + r_o)$. Any deviation from ideal value $Gt = 1$, reduces the elementary cubic perovskite cell and leads to formation of a unit cell of lower symmetry. Small difference in the radii of cations placed in positions A leads to a less pronounced rhombohedral distortion, while larger differences give rise to a significant MnO₆ octahedron deformation

which leads to orthorhombic structure. This deformation of the MnO_6 octahedron causes anomaly, also known as the Jahn−Teller effect. Namely, removing the degeneracy of the d level of Mn^{3+} ions will lead to the displacement of ions in octahedral MnO_6, where the octahedron will elongate/shorten in certain direction [9]. Perovskite structure can be stable in the oxides where $0.89 < G_t < 1.02$ [9]. Cation will occupy the position in which G_t is closer to 1.

In the octahedral crystal field, fivefold degenerate $3d$ orbitals of manganese are split into two groups, threefold t_{2g} (of lower energy) and twofold e_g (of higher energy) [9]. In accordance with Hund's rules and with fulfillment of the Pauli exclusion principle, $3d$ electrons in the Mn^{4+} ion have the same spins orientation and filled three t_{2g} orbitals, while the Mn^{3+} ion has one electron more, which fills one of the e_g orbitals and has the same spin orientation as electrons in the t_{2g} orbitals. The Jahn−Teller effect causes additional splitting of d energy levels (e_g and t_{2g}) of the Mn^{3+} ions in order to remove their degeneracy, where the splitting of t_{2g} levels is so small that the Jahn−Teller effect in this case is negligible [9–11]. In an octahedral environment manganese t_{2g} orbitals (d_{xy}, d_{yz}, d_{zx}) are the oxygen $2p$ orbitals weakly overlap with, unlike e_g orbitals ($d_{x^2-y^2}$, $d_{3z^2-r^2}$), which are directed towards the neighboring oxygen $2p$ orbitals and a strong overlapping of these orbitals leads to a high probability of transfer of electrons between manganese and oxygen orbitals [9–11]. This transfer largely determines the magnetic properties of manganites.

Magnetic properties of this mixed valence system are determined by a double exchange between Mn^{3+} and Mn^{4+} ions through the Mn−O−Mn path. The double exchange is ferromagnetic for Mn−O−Mn angle above ~160° [12–17]. When the system is doped with different Gd^{3+} concentrations, it develops ferromagnetic interaction concurrently with antiferromagnetic one and competition of the interactions causes magnetic moments frustration.

In this study we have combined two research methods: structure prediction of $Ca_{1-x}Gd_xMnO_3$ ($x = 0.05, 0.1, 0.15, 0.2$) perovskites by using computational SPuDS software, and characterization of the studied perovskites. We have shown various possible modifications of $Ca_{1-x}Gd_xMnO_3$ ($x = 0.05, 0.1, 0.15, 0.2$) perovskites, unknown so far. Also, we have investigated the influence of Gd doping on octahedral tilting, relation between the crystal structures which have been predicted, and structural and magnetic behavior we have experimentally observed.

2. Material and methods

2.1. Experimental section

2.1.1. Theoretical methods

Our general approach to the crystal structure prediction and determination of structure candidates has been given in detail elsewhere [18–20]. This is usually followed by calculation of material's properties [21,22]. Here, we use restricted structure prediction within the perovskite-related structures. An outline of the main steps of the method and information specific to this study are provided first.

The Structure Prediction Diagnostic Software (SPuDS) [23] has been used to produce new structure candidates of $Ca_{1-x}Gd_xMnO_3$ perovskites. The SPuDS program was developed to predict the crystal structures of perovskites, including those distorted by tilting of symmetric octahedra or caused by the Jahn−Teller distortions [20,24]. Stability of the perovskite structures is determined by comparing the calculated bond-valence sums and ideal formal valences.

The SPuDS program requires minimum amount of input data: the composition and oxidation state of each ion. Afterwards, structure optimization has been performed by restricting the

octahedra to remain rigid during calculation, with six equivalent B-X distances and all X-B-X angles equal to 90°. In this way, a full crystal structure can be generated from the size of the octahedron and magnitude of the octahedral tilting distortion. Furthermore, SPuDS calculates the fractional position of each atom at each tilt angle step over a wide range of octahedral tilt angles [23].

The size of the octahedron and magnitude of the octahedral tilting distortion are calculated by using the bond valence model, s_{ij},

$$S_{ij} = e^{[(R_{ij} - d_{ij})/B]} \tag{1}$$

where d_{ij} is cation−anion distance, B parameter is empirically determined as a universal constant with a value of 0.37, and R_{ij} is empirically determined for each cation−anion pair, based on bond distances measurements. The overall structure stability is determined by comparing the calculated bond valence sums with the ideal formal valences (equal to oxidation state). This quantity is known as the global instability index (GII). It is calculated according to relation [23]:

$$GII = \left\{ \left[\sum_{i=1}^{N} \left(d_i^2 \right) \right] \Big/ N \right\}^{1/2} \tag{2}$$

Variables involved in the GII equation are discrepancy factor d_i, which is a measure of the lattice strains present in the compound, derived as a difference between formal and calculated bond valance, and N is the number of atoms in the asymmetric unit. For the perovskite ABO_3, $N = 5$. Higher values of d_i and N indicate stressed connections which can lead to instability in the crystal structure.

Theoretical determination and identification of the predicted structures was performed by using the KPLOT program [25]. Symmetry of the predicted structures was analyzed by the algorithms SFND („Symmetry FiNDer" [26]) and RGS („Raum Gruppen Sucher" or space group seeker [27]). Duplicate structures are removed by using the CMPZ-algorithm [28] and the CCL algorithm has been used in the investigation of nanosized structures [29]. The investigated structures were visualized by using KPLOT [25] and VESTA [30] software.

2.2. Experimental methods

2.2.1. Materials synthesis

The method of preparation, conditions of synthesis, obtained values for the calcination temperature, and crystal-structural characteristics of the $Ca_{1-x}Gd_xMnO_3$ ($x = 0.05, 0.1, 0.15, 0.2$) samples are described in [31] and [32]. The unit cell parameters of this series of samples were identical to the values obtained in [32].

2.2.2. Materials characterization

XRD patterns of the samples were recorded at room temperature by using X-ray diffractometer Siemens D500 with nickel filtered CuKα radiation, and the step-scan mode (2θ range: 10° - 80° in a continuous scan mode with a step width of 0.02° and exposure of 10 s/step).

The infrared reflectivity measurements were performed at room temperature with a BOMEM DA-8 Fourier-transform IR spectrometer. A Hyper beamsplitter and a deuterated triglycine sulfate (DTGS) pyroelectric detector were used to cover the wavenumber region from 80 to 650 cm^{-1}. Infrared reflectivity spectra were collected with 2 cm^{-1} resolution and with 500 interferometer scans added for each spectrum.

EPR experiments were performed on an X-band Magnettech MS300 spectrometer operating at a nominal frequency of 9.5 GHz. The microwave power was 3.16 mW (microwave attenuation

15 dB), with a modulation amplitude of 0.2 mT. The Magnettech g-factor ZnS:Mn standard was used as the reference sample.

3. Results and discussion

3.1. Crystallographic analysis of XRD the results and investigation of octahedral tilting

Octahedral tilting is most common in the perovskites with space group *Pnma*. Perovskite structure which crystallizes in this space group is of great interest for geologists and materials science [33]. *Pnma* space group belongs to the $a^-b^+a^-$ octahedron tilting system. Octahedra are rotated by the same value of the angle around axes *a* and *c*, whereas the angle of rotation around axis *b* varies. Rotations of two adjacent octahedra along axis *b* are always in the same direction, and along axes *a* and *c* in the opposite direction. There are two types of deformations in the space group *Pnma*, denoted as *Pnma-1* and *Pnma-2*. Both of them have the same symmetry, but *Pnma-1* is much less deformed and only slightly deviates from the cubic structure. *Pnma-2* contains more distorted octahedra due to the Jahn−Teller effect caused by Mn^{3+} ions, which leads to elongation of the MnO_6 octahedron [8]. Our obtained results suggest that investigated samples have the *Pnma-1* structure.

In order to analyze the impact of Gd upon magnitude of the octahedral tilting, we have analyzed values of the Mn−O distances and angles. The characteristic distances and angles between Mn, O1 and O2 atoms are shown in Table 1. Average values of interatomic distances Mn−O vary with the amount of Gd in the structure. The highest value has the $Ca_{0.8}Gd_{0.2}MnO_3$ sample, where the content of Gd is the highest. In our previous work we have published data on the unit cell parameters and volumes depending on Gd concentration [32], and in the following Table 1 we have further investigated interatomic distances and bond angles of $CaMnO_3$ doped with different concentrations of Gd.

Octahedra nets for each of the investigated samples are given in Fig. 1. As one can see from Fig. 1, structural changes related to the change of angle values lead only to a slight octahedral tilting. In an ideal cubic structure the Mn−O1−Mn and Mn−O2−Mn angles are 180°. Because of the octahedral tilting around all three axes in the space group *Pnma* the angle values will be different. Mn−O1−Mn angle represents tilting around axis *b* and for the obtained samples, the closest to 180° is the value for $Ca_{0.8}Gd_{0.2}MnO_3$ sample (Table 1). On the other side, Mn−O2−Mn angle represents octahedral tilting around axes *a* and *c* and the magnitude of octahedral tilting (angle) is in accordance with the $a^-b^+a^-$ tilt system. In the structure, with increasing Gd amount, the deviation from 180° and octahedral tilting magnitude are higher (Table 1). In the cube centers, oxygen ions tend to move toward that center reducing d_{A-O}, because A ions are too small to fill that space. At the same time d_{Mn-O} also changes, and the Mn−O−Mn angle becomes smaller than 180° as a result of the reduced A-site radius [11].

The properties of manganites strongly depend on geometrical quantity G_t [11], which is related to the displacements and deformations in the structure. Difference in the lengths of $A−O$ and $B−O$ bonds has been used as a measure of G_t change: $G_t = (A − O)/\sqrt{2}(B − O)$. In the case when bonds $B−O$ are lengthened and $A−O$ shortened, $G_t < 1$ [8]. Since G_t for all investigated samples is less than 1 and close to 0.93 (calculation based on the bond lengths obtained by Rietveld analysis given in Table 1), we can conclude that in our system occurred elongations of Ca−O and shortenings of Mn−O bonds. The structure alleviates these strains by BO_6 octahedron rotation, which leads to a reduction of symmetry.

We have also analyzed the effects of concentration of gadolinium on octahedral deformations. For $Ca_{1−x}Gd_xMnO_3$ ($x = 0.05, 0.1, 0.15, 0.2$) samples, interatomic Mn−O distances inside octahedra are shown in Fig. 2. In *ac* plane lies the shortest octahedral Mn−O2 bond, which is represented by the first and third bar in Fig. 2. In *b*-axis direction lies the intermediate octahedral Mn−O1 bond, represented by the third bar. The octahedral deformation occurs as a result of the Mn−O distances deviation. The deviation of the Mn−O (dn) distances with respect to the average <Mn−O> ($<d>$) value defines the distortion of the octahedra [34]: $\Delta = (1/6)\sum_{n=1,6}[(d_n − \langle d \rangle)/\langle d \rangle^2]$.

Here, we observe that with an increase of Gd^{3+} content in the structure, difference between the longest and shortest distances increases non-periodically (see Fig. 2). The octahedral deformations indicate the presence of oxygen vacancies caused by reduction of Mn^{4+} to Mn^{3+} due to Gd doping. We note that 10% of the Gd increase in the system has the highest Δ value, which has been used as indication of the Jahn Teller distortion in the structure [34].

The Jahn−Teller effect can be observed by comparing the results obtained for individual Mn−O bond lengths, leading to the conclusion that there has been a change in the valence state of Mn^{4+} i.e. reduction to Mn^{3+}. Rhombohedral and octahedral distortion increases with Gd doping. Increase of Mn^{3+} concentration with Gd doping increases the average Mn−O bond length in the unit cell (for $Mn^{3+}−O$ it is 2.04 Å, and for $Mn^{4+}−O$, 1.88 Å [35]).

Table 1
Interatomic distances and bond angles for investigated samples of $Ca_{1−x}Gd_xMnO_3$ ($x = 0.05, 0.1, 0.15, 0.2$).

Sample	$Ca_{0.95}Gd_{0.05}MnO_3$		$Ca_{0.9}Gd_{0.1}MnO_3$	$Ca_{0.85}Gd_{0.15}MnO_3$	$Ca_{0.8}Gd_{0.2}MnO_3$
$\langle Ca−O \rangle$	2.5759		2.5270	2.5798	2.5304
Ca−O	2×	2.635 (5)	2.6736 (3)	2.6612 (1)	2.7537 (3)
	2×	2.340 (4)	2.3163 (3)	2.36131 (1)	2.3225 (1)
		2.970 (8)	2.9163 (6)	2.9626 (4)	2.9303 (4)
		2.887 (9)	2.3073 (6)	2.9061 (3)	2.3237 (4)
		2.380 (7)	2.4647 (5)	2.3791 (3)	2.4453 (4)
	2×	2.557 (5)	2.5403 (3)	2.5252 (2)	2.4609 (1)
		2.458 (8)		2.4544 (3)	
$\langle Mn−O \rangle$	1.91023		1.91321	1.90885	1.92102
Mn−O	2×	1.8978 (10)	1.84859 (5)	1.90684 (3)	1.88364 (4)
	2×	1.9335 (9)	1.97726 (6)	1.91820 (3)	1.96677 (4)
	2×	1.8994 (7)	1.91378 (5)	1.90151 (2)	1.91264 (3)
O2−Mn−O2	91.32 (9)		91.144 (5)	91.1051 (16)	90.6 (10)
O1−Mn−O1	180.00 (9)		180.000 (6)	179.972 (3)	180.000 (4)
Mn−O1−Mn	159.21 (9)		155.092 (6)	159.294 (3)	162.592 (4)
Mn−O2−Mn	157.16 (11)		156.603 (6)	157.147 (2)	155.6 (5)
Mn(BCV)	3.927		3.931	3.938	3.826
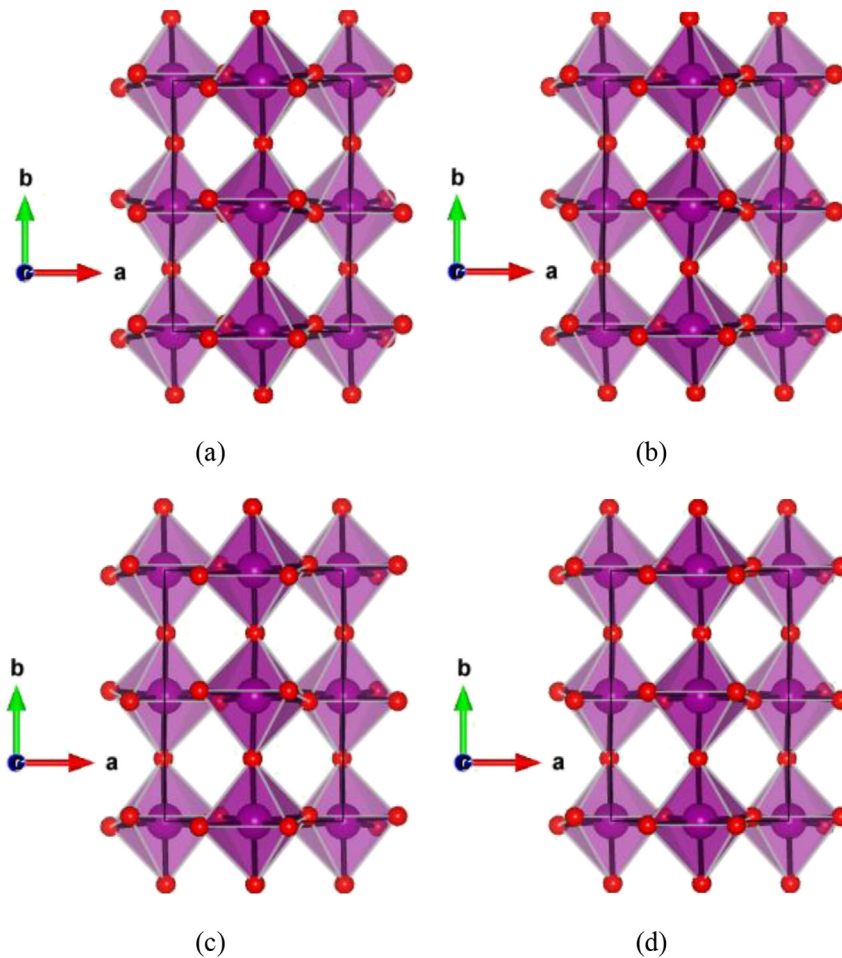
Fig. 1. Octahedral net of perovskite phase in a) $Ca_{0.95}Gd_{0.05}MnO_3$; b) $Ca_{0.9}Gd_{0.1}MnO_3$; c) $Ca_{0.85}Gd_{0.15}MnO_3$; d) $Ca_{0.8}Gd_{0.2}MnO_3$ sample.

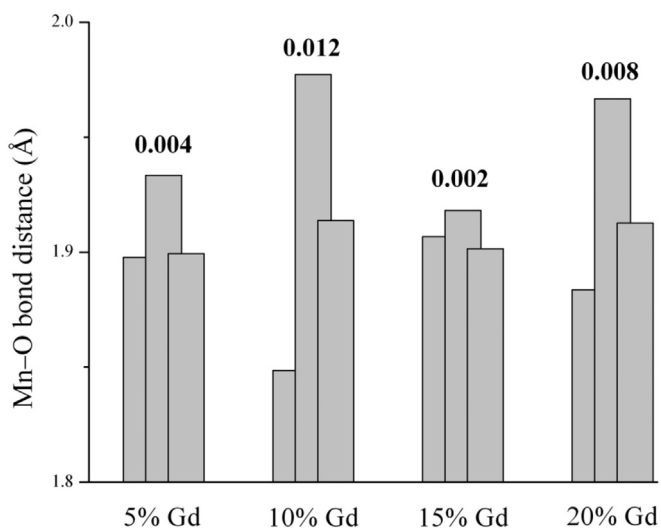**Fig. 2.** Interatomic Mn–O distances of the investigated samples of $Ca_{1-x}Gd_xMnO_3$ (x = 0.05, 0.1, 0.15, 0.2) perovskites. The values of Δ are given above bars.

In addition, for each sample the Mn–O distance systematically increases compared to the average Mn–O distance, clearly indicating that the octahedral expansion is essentially a result of the a-c basal plane increase as a consequence of Gd^{3+} entering Ca^{2+}

position. Of essential importance is the ratio of ionic radii and co-valent nature of the Mn–O bond. There is clearly visible difference between the apical (Mn–O1) and equatorial (Mn–O2) distances in MnO_6 octahedron for all four samples. Difference in the Mn–O bond lengths indicates occurrence of oxygen vacancies. Furthermore, by comparing the apical and equatorial bonds with the results for undoped $CaMnO_3$ [36,37] we can conclude that there is an octahedral tilting in the doped samples. With an increase of the content of Gd in the structure, the deviations are increased pointing at a significant tilting of octahedrons. Based on the previously mentioned, in the $Ca_{1-x}Gd_xMnO_3$ (x = 0.05, 0.1, 0.15, 0.2) samples, MnO_6 octahedrons cannot be described by six nearly equal Mn–O distances. The octahedrons of doped samples are distorted and the expansions are not the same in all three directions. As expected, changes in the bond lengths with increased content of Gd are very similar to the changes in the unit cell parameters [32]. These results clearly show that there is a close connection between the unit cell parameters and presence of the Jahn–Teller distortion due to the presence $Mn^{3+}O_6$ octahedron oriented in ac plane.

3.2. Structure prediction of $Ca_{1-x}Gd_xMnO_3$ perovskites

After performing the structure prediction calculations for $Ca_{1-x}Gd_xMnO_3$ by using SPuDS software, we obtained the equilibrium $Pnma$ structure and ten additional perovskite-related modifications, presented in Tables A.1–A.4 (see the Supporting Information). Each of the calculated $Ca_{1-x}Gd_xMnO_3$ modifications

(marked by 1−10) was sorted by its space group and *GII* values (see Tables 2−5). Here we would like to point out that instability of the CaMnO$_3$ system grows with increase of Gd doping (See Fig. 3). Fig. 3 shows the stability of the most favorable perovskite-related structures with Gd increasing the content of Gd in the CaMnO$_3$ system.

The *Pnma* phase is the most stable form of Ca$_{1-x}$Gd$_x$MnO$_3$, which is in agreement with our experimental findings [32]. Furthermore, we have observed that in the case of a low Gd doping (less than 15%), the $R\overline{3}c$ modification (Ca$_{0.95}$Gd$_{0.05}$MnO$_3$-(2)) is the most stable form next to the equilibrium *Pnma* structure, according to the *GII* values. With an increase of Gd in the system (>20%, see Table 5), we have observed possible orthorhombic (Ca$_{0.8}$Gd$_{0.2}$MnO$_3$-(5), *Pnma*) − tetragonal (Ca$_{0.8}$Gd$_{0.2}$MnO$_3$-(5), *P4$_2$/nmc*), rather than orthorhombic (Ca$_{0.8}$Gd$_{0.2}$MnO$_3$-(5), *Pnma*) − trigonal (Ca$_{0.8}$Gd$_{0.2}$MnO$_3$-(5), $R\overline{3}c$) phase transition. After analyzing the Ca$_{1-x}$Gd$_x$MnO$_3$ predicted structures in Figs. 1 and 4, we observed that Gd was homogeneously distributed over the crystal structure. Also, we noted that in the sample doped with 5% of Gd, the most unstable form was orthorhombic Ca$_{0.95}$Gd$_{0.05}$MnO$_3$-(10) (*I4/mmm*) modification, whereas with a larger amount of doping, the cubic perovskite (Ca$_{0.8}$Gd$_{0.2}$MnO$_3$-(8)) became the most unstable form of Ca$_{1-x}$Gd$_x$MnO$_3$ (see Tables 2−5 and Fig. 4). Similar trends were observed in the previous research with pure CaMnO$_3$ compound by using *ab inito* methods [20]. This change of symmetry is due to distortions away from the ideal perovskite structure that occur at different tilt systems.

Bond valence calculations (BVC) often resulted in a Mn valence state higher than the nominal value and the reason being strong Mn−O bond [38]. For the Ca$_{1-x}$Gd$_x$MnO$_3$ system we have also noticed higher values for BVC than expected, in view of the presence of Mn^{3+} in these perovskites, which could reduce valence state of Mn. In the next step we have compared our calculated and experimentally observed *Pnma* structure in the Ca$_{1-x}$Gd$_x$MnO$_3$ system (see Table 6). Our SPuDS calculations show slight decrease of unit cell volume, whereas in the experiment we observed quite the opposite result, a slight increase of cell volume. This discrepancy originates from the appearance of Mn^{3+} and, as it was pointed out before, these results clearly show that there is a close connection between the unit cell parameters and the presence of the Jahn−Teller distortion due to the presence Mn^{3+}O$_6$ octahedron.

Furthermore, following these results, we have managed to calculate the amount of Mn^{4+} and Mn^{3+} in the doped perovskite compound which, to the best of our knowledge, has never been calculated before, at least not in this way. Due to the fact that cell volume is connected to the presence of Mn^{3+} in the system (see above), at first, we have calculated change of the equilibrium volume as a result of Gd doping. The results showed that total cell volume of the investigated perovskite system has been increased by ~0.01% in the sample doped with 5% of Gd (see Table 6).

Table 3
Calculated values of the global instability index (*GII*) for ten Ca$_{0.9}$Gd$_{0.1}$MnO$_3$ modifications using SPuDS.

Name	Space group	Tilt system	*GII* (a.u.)
Ca$_{0.9}$Gd$_{0.1}$MnO$_3$-(1)	*Pnma*	$a^-b^+a^-$	0.05667
Ca$_{0.9}$Gd$_{0.1}$MnO$_3$-(2)	$R\overline{3}c$	$a^-a^-a^-$	0.09777
Ca$_{0.9}$Gd$_{0.1}$MnO$_3$-(3)	*P4/mbm*	$a^0a^0c^-$	0.10236
Ca$_{0.9}$Gd$_{0.1}$MnO$_3$-(4)	*I4/mcm*	$a^0a^0c^-$	0.10236
Ca$_{0.9}$Gd$_{0.1}$MnO$_3$-(5)	*P4$_2$/nmc*	$a^+a^+c^-$	0.10742
Ca$_{0.9}$Gd$_{0.1}$MnO$_3$-(6)	*Im$\overline{3}$*	$a^+a^+a^+$	0.12980
Ca$_{0.9}$Gd$_{0.1}$MnO$_3$-(7)	*Cmcm*	$a^+b^0c^-$	0.14282
Ca$_{0.9}$Gd$_{0.1}$MnO$_3$-(9)	*Imma*	$a^0b^-b^-$	0.15765
Ca$_{0.9}$Gd$_{0.1}$MnO$_3$-(10)	*I4/mmm*	$a^0b^+b^+$	0.16468
Ca$_{0.9}$Gd$_{0.1}$MnO$_3$-(8)	*Pm$\overline{3}$m*	$a^0a^0a^0$	0.17129

Table 4
Calculated values of the global instability index (*GII*) for ten Ca$_{0.85}$Gd$_{0.15}$MnO$_3$ modifications using SPuDS.

Name	Space group	Tilt system	*GII* (a.u.)
Ca$_{0.85}$Gd$_{0.15}$MnO$_3$-(1)	*Pnma*	$a^-b^+a^-$	0.07013
Ca$_{0.85}$Gd$_{0.15}$MnO$_3$-(2)	$R\overline{3}c$	$a^-a^-a^-$	0.10740
Ca$_{0.85}$Gd$_{0.15}$MnO$_3$-(5)	*P4$_2$/nmc*	$a^+a^+c^-$	0.10742
Ca$_{0.85}$Gd$_{0.15}$MnO$_3$-(3)	*P4/mbm*	$a^0a^0c^-$	0.11204
Ca$_{0.85}$Gd$_{0.15}$MnO$_3$-(4)	*I4/mcm*	$a^0a^0c^-$	0.11204
Ca$_{0.85}$Gd$_{0.15}$MnO$_3$-(6)	*Im$\overline{3}$*	$a^+a^+a^+$	0.12980
Ca$_{0.85}$Gd$_{0.15}$MnO$_3$-(7)	*Cmcm*	$a^+b^0c^-$	0.14282
Ca$_{0.85}$Gd$_{0.15}$MnO$_3$-(9)	*Imma*	$a^0b^-b^-$	0.15304
Ca$_{0.85}$Gd$_{0.15}$MnO$_3$-(10)	*I4/mmm*	$a^0b^+b^+$	0.16468
Ca$_{0.85}$Gd$_{0.15}$MnO$_3$-(8)	*Pm$\overline{3}$m*	$a^0a^0a^0$	0.18620
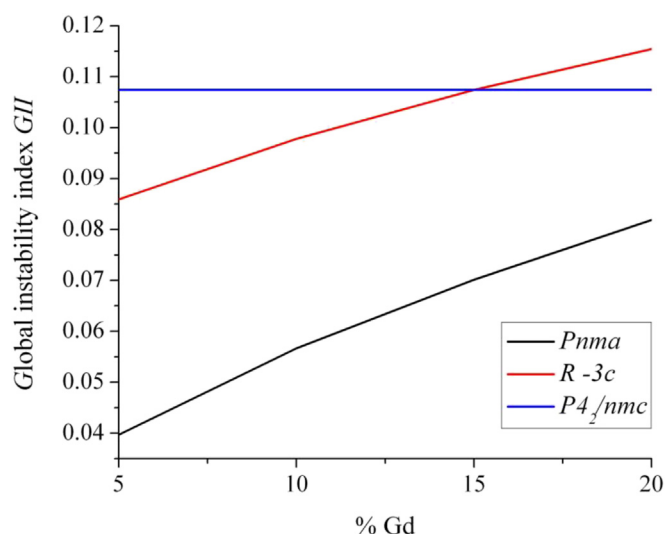
Fig. 3. Phase transition from *Pnma*, $R\overline{3}c$ to *P4$_2$/nmc* with Gd ion increase in CaMnO$_3$ compound.

Next, we have calculated different compositions of Mn^{4+} and Mn^{3+} for the same amount of Gd doping (see Table A.5 in the Supporting Information). We have discovered that the cell volume started to increase, as we obtained by the experiment (see Table 6). In addition, we noted that the best fit for the volume cell increase for 5% of Gd, was obtained for 5% increase of Mn^{3+} in the system, which is ~0.01%, the predicted volume increase and is in very good agreement with our experimental observations. Therefore, we can conclude that with 5% Gd increase in the Ca$_{1-x}$Gd$_x$MnO$_3$ system, we could expect 5% Mn^{3+} increase in the system. Finally, we show the

Table 2
Calculated values of the global instability index (*GII*) for ten Ca$_{0.95}$Gd$_{0.05}$MnO$_3$ modifications using SPuDS software.

| Name	Space group	Tilt system	*GII* (a.u.)
Ca$_{0.95}$Gd$_{0.05}$MnO$_3$-(1)	*Pnma*	$a^-b^+a^-$	0.03969
Ca$_{0.95}$Gd$_{0.05}$MnO$_3$-(2)	$R\overline{3}c$	$a^-a^-a^-$	0.08593
Ca$_{0.95}$Gd$_{0.05}$MnO$_3$-(3)	*P4/mbm*	$a^0a^0c^-$	0.09058
Ca$_{0.95}$Gd$_{0.05}$MnO$_3$-(4)	*I4/mcm*	$a^0a^0c^-$	0.09058
Ca$_{0.95}$Gd$_{0.05}$MnO$_3$-(5)	*P4$_2$/nmc*	$a^+a^+c^-$	0.10742
Ca$_{0.95}$Gd$_{0.05}$MnO$_3$-(6)	*Im$\overline{3}$*	$a^+a^+a^+$	0.12980
Ca$_{0.95}$Gd$_{0.05}$MnO$_3$-(7)	*Cmcm*	$a^+b^0c^-$	0.14282
Ca$_{0.95}$Gd$_{0.05}$MnO$_3$-(8)	*Pm$\overline{3}$m*	$a^0a^0a^0$	0.15494
Ca$_{0.95}$Gd$_{0.05}$MnO$_3$-(9)	*Imma*	$a^0b^-b^-$	0.16295
Ca$_{0.95}$Gd$_{0.05}$MnO$_3$-(10)	*I4/mmm*	$a^0b^+b^+$	0.16468

Table 5
Calculated values of the global instability index (GII) for ten $Ca_{0.8}Gd_{0.2}MnO_3$ modifications using SPuDS.

Name	Space group	Tilt system	GII (a.u.)
$Ca_{0.8}Gd_{0.2}MnO_3$-(1)	$Pnma$	$a^-b^+a^-$	0.08188
$Ca_{0.8}Gd_{0.2}MnO_3$-(5)	$P4_2/nmc$	$a^+a^+c^-$	0.10742
$Ca_{0.8}Gd_{0.2}MnO_3$-(2)	$R\bar{3}c$	$a^-a^-a^-$	0.11544
$Ca_{0.8}Gd_{0.2}MnO_3$-(3)	$P4/mbm$	$a^0a^0c^-$	0.12018
$Ca_{0.8}Gd_{0.2}MnO_3$-(4)	$I4/mcm$	$a^0a^0c^-$	0.12018
$Ca_{0.8}Gd_{0.2}MnO_3$-(6)	$Im\bar{3}$	$a^+a^+a^+$	0.12980
$Ca_{0.8}Gd_{0.2}MnO_3$-(7)	$Cmcm$	$a^+b^0c^-$	0.14282
$Ca_{0.8}Gd_{0.2}MnO_3$-(9)	$Imma$	$a^0b^-b^-$	0.14936
$Ca_{0.8}Gd_{0.2}MnO_3$-(10)	$I4/mmm$	$a^0b^+b^+$	0.16468
$Ca_{0.8}Gd_{0.2}MnO_3$-(8)	$Pm\bar{3}m$	$a^0a^0a^0$	0.20001

phonon features at 286/336 cm^{-1}, 416 cm^{-1} and 556 cm^{-1}, together with a pronounced Drude-like contribution from free charge carriers, which dominates the reflectivity spectra in the range below 200 cm^{-1}, can be seen. The perovskite manganites usually have three strong phonon bands, known as external, bending and stretching modes, located at about 150−180, 350, and 550-600 cm^{-1} respectively [39−42]. For the ideal cubic perovskite structure AMnO$_3$ (space group $Pm\bar{3}m$), the factor group analysis predicts three 3-fold degenerated IR active modes of F$_{1u}$ symmetry. The lowest energy F$_{1u}$ mode (the external mode) originates from vibrations of A cation against MnO$_6$ octahedra, and it is usually found in 150−180 cm^{-1} range. The medium energy F$_{1u}$ mode (the bending mode) originates from bending of Mn−O bonds in the

Fig. 4. Visualization of several calculated perovskite-related structures a) $Ca_{0.8}Gd_{0.2}MnO_3$-(5), $P4_2/nmc$; b) $Ca_{0.8}Gd_{0.2}MnO_3$-(2), $R\bar{3}c$; c) $Ca_{0.95}Gd_{0.05}MnO_3$-(10), ($I4/mmm$); d) cubic perovskite $Ca_{0.8}Gd_{0.2}MnO_3$-(8), ($Pm\bar{3}m$).

Table 6
Unit cell parameters and volumes of the experimentally observed and calculated (SPuDS) equilibrium $Pnma$ structure in $Ca_{1-x}Gd_xMnO_3$ system.

Sample		$Ca_{0.95}Gd_{0.05}MnO_3$		$Ca_{0.9}Gd_{0.1}MnO_3$		$Ca_{0.85}Gd_{0.15}MnO_3$		$Ca_{0.8}Gd_{0.2}MnO_3$	
Method		Experiment	SPuDS	Experiment	SPuDS	Experiment	SPuDS	Experiment	SPuDS
Unit cell parameters (Å)	a	5.2834 (5)	5.3576	5.304 (1)	5.3569	5.3152 (9)	5.3562	5.3186 (5)	5.3555
	b	7.4665 (6)	7.5407	7.475 (1)	7.5385	7.4795 (8)	7.5366	7.4792 (7)	7.5347
	c	5.2994 (4)	5.3073	5.293 (1)	5.3051	5.303 (1)	5.3030	5.3003 (7)	5.3011
Volume (Å^3)	V	209.03 (3)	214.415	209.84 (7)	214.237	210.81 (6)	214.069	210.84 (7)	213.912

calculated structures for $Ca_{1-x}Gd_xMn^{4+}_{1-x}Mn^{3+}_xO_3$ system obtained by using SPuDS software. In Tables A.1−A.4 (see the Supporting Information) we the present unit cell parameters for ten additional perovskite-related modifications.

3.3. Infrared (IR) spectroscopy

IR reflectivity spectra of the $Ca_{1-x}Gd_xMnO_3$ samples in 80−650 cm^{-1} spectral range are shown in Fig. 5. Several broad

MnO$_6$ octahedra, and is usually found around 350 cm^{-1}. The highest energy mode (the stretching mode) originates from Mn−O bond stretching and it is usually positioned in 550−600 cm^{-1} range. In the case of manganites of rhombohedral structure ($R\bar{3}c$), which is of the lower symmetry, 8 IR active modes ($3A_u + 5E_u$) can be expected, among which three A_u and three out of five E_u modes originate from splitting of the degenerated F$_{1u}$ modes [43]. For the orthorhombic structure ($Pnma$) of even lower symmetry, up to 25 IR active modes ($9B_{1u} + 7B_{2u} + 9B_{3u}$) can be expected. There are
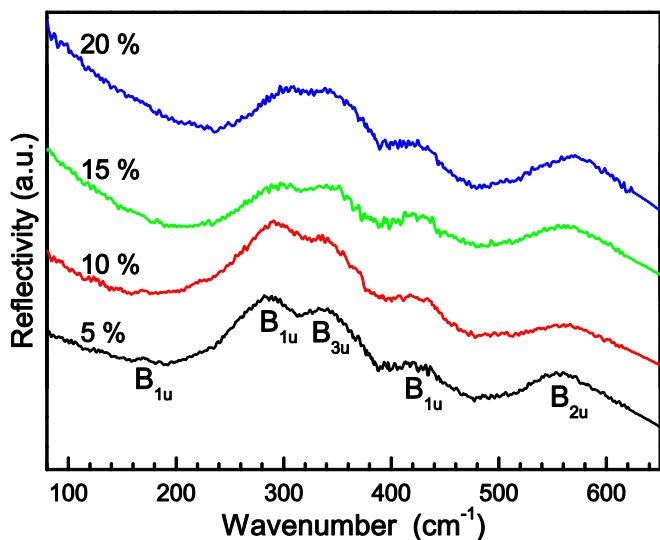
Fig. 5. Infrared reflectivity spectra of the $Ca_{1-x}Gd_xMnO_3$ (x = 0.05, 0.1, 0.15, 0.2) samples. The spectra are offset for clarity.

actually two variations of the orthorhombic structure, denoted as *Pnma-1* and *Pnma-2*. Both of them have the same symmetry, but *Pnma-1* is much less deformed.

Our samples have the *Pnma-1* structure. In this case, due to small deviation from the cubic structure, majority of the IR modes have small strength and cannot be well resolved. In addition to the previous work [44] on isostructural $LaMnO_3$, we have assigned two modes at 286/336 cm^{-1} as B_{1u}/B_{3u}, one mode at 416 cm^{-1} as B_{1u}, and one mode at 556 cm^{-1} as B_{2u}. With Gd doping, modes at 286 and 556 cm^{-1} are shifted to higher energies due to the change in the A-site ion radius with doping, and more importantly due to replacement of Mn^{4+} by Mn^{3+} as a consequence of Ca^{2+} substitution with Gd^{3+}. For higher doping contents, relative intensity of the mode at 336 cm^{-1} with respect to 286 cm^{-1} mode increases. The observed increase of 336 cm^{-1} mode intensity can be a consequence of higher sensitivity of this bending mode to the decrease in the Mn—O—Mn angle [45,46]. The increase of 336 cm^{-1} mode intensity, together with the shift of 286 cm^{-1} to higher energies, for higher doping levels appears as a partial merging of these two modes. The external mode, in manganites often found in 150–180 cm^{-1} range, is strongly screened in our samples by the Drude contribution, and is barely seen only in the 5% doped sample at about 168 cm^{-1} (B_{1u}). Sopracase et al. [46] have theoretically found that in the case of orthorhombic $CaMnO_3$, the low-energy external modes have a small dipole moment, resulting in small strength of the experimentally observed modes, which, together with strong Drude screening, can explain the absence of this mode in most of our samples.

3.4. Electron paramagnetic resonance (EPR) spectroscopy

Replacement of Ca^{2+} with Gd^{3+} causes reduction of Mn^{4+} to Mn^{3+}. Mn^{3+} ($3d^4$ with S = 2) is unlikely to have an observable EPR signal as it exhibits a large zero-field splitting because of the influence of the Jahn–Teller effect on the ^5E_g ground state in the octahedral symmetry.

The observed EPR signal is due to Mn^{4+}, but it cannot be attributed to isolated Mn^{4+} ions. EPR intensity and linewidth can be explained by a model in which a bottlenecked spin relaxation takes place from the constituent Mn^{4+} via the exchange-coupled Mn^{3+} Jahn–Teller ions to the lattice [47].

The measured room-temperature EPR spectra are shown in Fig. 6a. The six sharp lines in the EPR spectra are from the reference sample ZnS:Mn. The spectra shapes are of Lorentzian profile and do not saturate with EPR microwave power ($I(P^{1/2})$ is linear), which is indicated by homogenously broadened line, Fig. 6b.

The EPR linewidth seems to be a physical parameter that closely follows the cell distortion [48]. A weak increase of the line width (Table 7), with increasing Gd content is found, Fig. 7. The observed increase is much lower than the increase of linewidth found in $Ca_{1-x}Y_xMnO_3$ with increasing Y concentration [48]. It is associated with octahedral tilting that weakly depends on the concentration of Gd content (Table 1), compared with larger octahedra tilting increase observed in $Ca_{1-x}Y_xMnO_3$ [48]. The linewidth is inversely proportional to the relaxation time, which depends on interaction between Mn^{4+}—O—Mn^{3+}, which, on the other side, is angle dependent. The Mn—O—Mn angles are given in Table 1. Variation of the angles for our samples is relatively small.

While the line widths show a wide variety of behaviors depending on the temperature and concentration of divalent ions [49], and even on oxygen content [50], the g-factors are nearly constant and close to the free electron value. The g-factor of $Ca_{1-x}Gd_xMnO_3$, presented in Fig. 7. is close to the free electron value. The experimental error is estimated to be about 0.01 (due to high linewidth), which is comparable with the measured variation of g-factor.

Intensities of the lines in Fig. 6 were normalized for easier EPR spectra comparison. The actual intensities reading error was of the order of the expected trend of intensity change for various concentrations due to experimental issues [51], which prevented us from making a conclusion related to intensity.

The magnetization measurements performed on these samples showed that they are paramagnetic at room temperature and obeyed Curie-Weiss law at temperature above ~110 K. The magnetic moments obtained from Curie-Weiss law are in accordance with the theoretical values expected for the Mn^{4+}, Mn^{3+} and Gd^{3+}, and ratio of Mn^{4+}/Mn^{3+} is close to Ca^{2+}/Gd^{3+} ratio. So, there are no clusters of ions at room temperature, the EPR measurement temperature [52]. Clustering and ordering were observed at lower temperatures, T<~110 K. Samples with x = 0.05 or 0.10 show ferromagnetic transition and samples with x = 0.15 or 0.20 show antiferromagnetic transition [52].

The EPR signal, measured at liquid nitrogen temperature is not observed, because intensity of EPR diminishes and linewidth rises rapidly below ordering temperature $T_{C,N}$ [47,53].

4. Conclusion

We have used theoretical and experimental methods to investigate the octahedral tilting and related effects of $Ca_{1-x}Gd_xMnO_3$ (x = 0.05, 0.1, 0.15, 0.2) compound. Both methods have shown that orthorhombic-perovskite structure (space group *Pnma*) is the most stable form and according to Glazer's classification belongs to $a^-b^+a^-$ tilt system. Our bond valence calculations (BVC) have shown ten additional perovskite-related modifications of the equilibrium $Ca_{1-x}Gd_xMnO_3$ structure, and their stability has been investigated as function of Gd doping. We have further studied the influence of gadolinium amount on Mn—O bond angles and distances, tilting of MnO_6 octahedra around all three axes and deformation due to the presence of Jahn–Teller distortion around Mn^{3+} cation, and calculated the amount of Mn^{3+} in the system. Furthermore, our BVC approach is a simple, fast and efficient way of calculating the amount of Mn^{4+} and Mn^{3+} in the doped perovskite compound, which, to the best of our knowledge, has not been done before. The infrared reflection spectra of $Ca_{1-x}Gd_xMnO_3$ samples confirmed XRD results that $Ca_{1-x}Gd_xMnO_3$ nanopowders are of *Pnma-1*
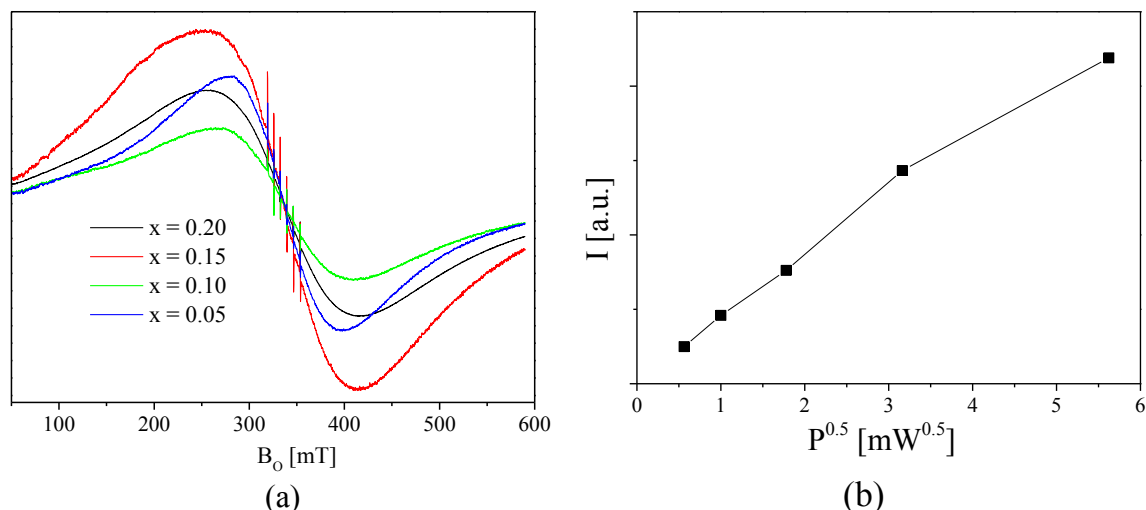
Fig. 6. (a) EPR spectra of $Ca_{1-x}Gd_xMnO_3$ ($x = 0.05, 0.1, 0.15, 0.2$) samples; (b) EPR Intensity vs. square root of the microwave power, for the $Ca_{0.8}Gd_{0.2}MnO_3$ sample.

Table 7
Parameters obtained from the EPR spectra, g-factor, intensity and linewidth (peak-to-peak).

Sample	$Ca_{0.95}Gd_{0.05}MnO_3$	$Ca_{0.9}Gd_{0.1}MnO_3$	$Ca_{0.85}Gd_{0.15}MnO_3$	$Ca_{0.8}Gd_{0.2}MnO_3$
g-factor	2.014	2.005	2.0015	1.992
Int/Mass	6.4	5.7	15.2	9.5
ΔBpp	123.6	149.8	158.6	158.7
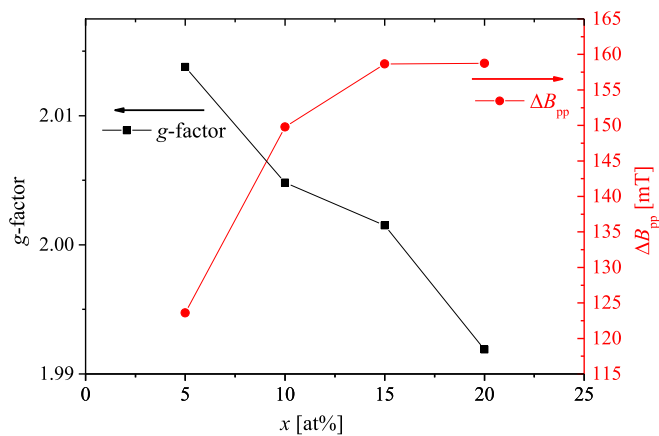
Fig. 7. Line widths and g-factors of observed EPR lines for various concentrations of $Ca_{1-x}Gd_xMnO_3$ samples.

structure and that the tilting of octahedra are increased with Gd doping. Finally, the EPR spectra are in accordance with the assumption that EPR linewidth is Mn−O−Mn angle dependent. The studied samples showed that small octahedra tilting in these samples brought only a small change of the EPR linewidth.

Acknowledgment

Appendix A. Supplementary data

Supplementary data related to this article can be found at http://dx.doi.org/10.1016/j.jallcom.2016.03.173.

References

[1] C.L. Bull, P.F. McMillan, Raman scattering study and electrical properties characterization of elpasolite perovskites Ln2(BB')O6 (Ln = La; Sm…Gd and B; B'=Ni, Co, Mn), J. Solid State Chem. 177 (2004) 2323−2328.
[2] Y.Q. Ma, W.H. Song, J. Yang, R.L. Zhang, B.C. Zhao, Z.G. Sheng, W.J. Lu, J.J. Du, Y.P. Sun, The current-induced effect on the Jahn−Teller distortion in the La0.5Ca0.5MnO3 manganite, Solid State Commun. 133 (2005) 163−167.
[3] Y. Tomioka, Y. Okimoto, J.H. Jung, R. Kumai, Y. Tokura, Phase diagrams of perovskite-type manganese oxides, J. Phys. Chem. Solids 67 (2006) 2214−2221.
[4] P.M. Woodward, Octahedral tilting in perovskites. I. Geometrical consider-ations, Acta Cryst. B 53 (1997) 32−43.
[5] V.M. Goldschmidt, Die Gesetze der Krystallochemie, Naturwissenschaften 14 (1926) 477−485.
[6] D.A. Mota, Y.R. Barcelay, P.B. Tavares, M.R. Chaves, A. Almeida, J. Oliveira, W.S. Ferreira, J.A. Moreira, Competing exchanges and spin−phonon coupling in Eu1−xRxMnO3 (R=Y, Lu), J. Phys. Condens. Mat. 25 (2013) 235602.
[7] E. Bose, S. Karmakar, B.K. Chaudhuri, S. Pal, C. Martin, S. Hébert, A. Maignan, Correlation of structural, magnetic and transport properties with the toler-ance factor in a low-doped La0.875Sr0.125−xCaxMnO3, (0 ≤ x ≤ 0.125) system: cross-over from Mott to Shklovskii−Efros variable range hopping conduction, J. Phys. Condens. Mat. 19 (2007) 266218.
[8] J.B. Goodenough, Electronic and ionic transport properties and other physical aspects of perovskites, Rep. Prog. Phys. 67 (2004) 1915−1993.
[9] J.M.D. Coey, M. Viret, S. Von Molnar, Mixed-valence manganites, Adv. Phys. 48 (1999) 167−293.
[10] R.D. Shannon, Revised effective ionic radii and systematic studies of inter-atomic distances in halides and chalcogenides, Acta Cryst. A32 (1976) 751−767.
[11] E. Dagotto, T. Hotta, A. Moreo, Colossal magnetoresistant materials: the key role of phase separation, Phys. Rep. 344 (2001) 1−153.
[12] R., S.K. Mahendiran, A.K. Tiwary, T.V. Raychaudhuri, R. Ramakrishnan, N. Mahesh, C.N.R. Rangavittal, Rao, Structure, electron-transport properties, and giant magnetoresistance of hole-doped LaMnO3 systems, Phys. Rev. B 53 (1996) 3348−3358.
[13] H.Y. Hwang, S.-W. Cheong, P.G. Radaelli, M. Marezio, B. Batlogg, Lattice effects on the magnetoresistance in doped LaMnO3, Phys. Rev. Lett. 75 (1995)

914—917.

[14] J.L. García-Muñoz, J. Fontcuberta, B. Martínez, A. Seffar, S. Piñol, X. Obradors, Magnetic frustration in mixed valence manganites, Phys. Rev. B 55 (1997) R668—R671.

[15] J.L. García-Muñoz, J. Fontcuberta, M. Suaaidi, X. Obradors, Bandwidth narrowing in bulk $L_{2/3}A_{1/3}MnO_3$ magnetoresistive oxides, J. Phys. Condens. Mat. 8 (1996) L787—L793.

[16] N. Sharma, A.K. Nigam, R. Pinto, N. Venkataramani, S. Prasad, G. Chandra, S.P. Pai, Giant magnetoresistance studies on $La_{(0.8-x)}R_xSr_{0.2}MnO_3$ thin films (R = Pr, Nd, Gd, Ho), J. Magn. Magn. Mater 166 (1997) 65—70.

[17] J.M.D. Coey, M. Viret, S. von Molnar, Mixed-valence manganites, Adv. Phys. 48 (1999) 167—293.

[18] J.C. Schön, M. Jansen, First step towards planning of syntheses in solid-state chemistry: determination of promising structure candidates by global optimization, Angew. Chem. Int. Ed. Eng. 35 (1996) 1286—1304.

[19] D. Zagorac, J.C. Schön, J. Zagorac, M. Jansen, Prediction of structure candidates for zinc oxide as a function of pressure and investigation of their electronic properties, Phys. Rev. B 89 (2014) 075201.

[20] J. Zagorac, D. Zagorac, A. Zarubica, J.C. Schön, K. Djuris, B. Matovic, Prediction of possible $CaMnO_3$ modifications using an ab initio minimization data-mining approach, Acta Cryst. B 70 (2014) 809—819.

[21] D. Zagorac, K. Doll, J.C. Schön, M. Jansen, Sterically active electron pairs in lead sulfide? An investigation of the electronic and vibrational properties of PbS in the transition region between the rock salt and the α-GeTe type modifications, Chem. Eur. J. 18 (2012) 10929—10936.

[22] D. Zagorac, J.C. Schön, M. Jansen, Energy landscape investigations using the prescribed path method in the ZnO system, J. Phys. Chem. C 116 (2012) 16726—16739.

[23] M.W. Lufaso, P.M. Woodward, Prediction of the crystal structures of perovskites using the software program SpuDS, Acta Cryst. B 57 (2001) 725—738.

[24] M.W. Lufaso, P.M. Woodward, Jahn-Teller distortions, cation ordering and octahedral tilting in perovskites, Acta Cryst. B 60 (2004) 10—20.

[25] R. Hundt, KPLOT-program, University of Bonn, Germany, 2012, 1979, Version 9, 6.15, www.crystalimpact.com/download/kplot.htm.

[26] R. Hundt, J.C. Schön, A. Hannemann, M. Jansen, Determination of symmetries and idealized cell parameters for simulated structures, J. Appl. Crystallogr. 32 (1999) 413—416.

[27] A. Hannemann, R. Hundt, J.C. Schön, M. Jansen, A new algorithm for space-group determination, J. Appl. Crystallogr. 31 (1998) 922—928.

[28] R. Hundt, J.C. Schön, M. Jansen, CMPZ — an algorithm for the efficient comparison of periodic structures, J. Appl. Crystallogr. 39 (2006) 6—16.

[29] R. Hundt, J.C. Schön, S. Neelamraju, J. Zagorac, M. Jansen, CCL: an algorithm for the efficient comparison of clusters, J. Appl. Crystallogr. 46 (Pt 3) (2013) 587—593.

[30] K. Momma, F. Izumi, VESTA: a three-dimensional visualization system for electronic and structural analysis, J. Appl. Crystallogr. 41 (2008) 653—658.

[31] M. Rosić, M. Logar, A. Devečerski, M. Prekajski, A. Radosavljević-Mihajlović, V. Kusigerski, V. Spasojević, B. Matović, Synthesis, structural and magnetic properties of nanostructured $Ca_{0.9}Gd_{0.1}MnO_3$ obtained by modified glycine nitrate procedure (MGNP), Ceram. Int. 37 (4) (2011) 1313—1319.

[32] M. Rosić, M. Logar, J. Zagorac, A. Devečerski, A. Egelja, V. Kusigerski, V. Spasojević, B. Matović, Investigation of the structure and the magnetic behaviour of nanostructured $Ca_{1-x}Gd_xMnO_3$ (x=0.05; 01; 0.15; 0.2) obtained by modified glycine nitrate procedure, Ceram. Int. 39 (2) (2013) 1853—1861.

[33] N.W. Thomas, A new global parameterization of perovskite structures, Acta Cryst. B 54 (1998) 585—599.

[34] G.A. Maris, Structural Transition Induced by Charge and Orbital Ordering in

[35] D.M. Sherman, The electronic structures of manganese oxide minerals, Am. Mineral. 69 (1984) 788—799.

[36] C. Silveira, M.E. Lopes, M.R. Nunes, M.E. Melo Jorge, Synthesis and electrical properties of nanocrystalline $Ca_{1-x}Eu_xMnO_{3\pm\delta}$ (0.1≤x≤0.4) powders prepared at low temperature using citrate gel method, Solid State Ionics 180 (2010) 1702—1709.

[37] I. Matos, S. Serio, M.E. Lopes, M.R. Nunes, M.E. Melo Jorge, Effect of the sintering temperature on the properties of nanocrystalline $Ca_{1-x}Sm_xMnO_3$ (0≤x≤0.4) powders, J. Alloys Compd. 509 (2011) 9617—9626.

[38] C.O. Paiva-Santos, R.F.C. Marques, M. Jafelicci Jr., L.C. Varanda, X-ray powder data and bond valence of $La_{0.65}Sr_{0.35}MnO_3$ after Rietveld refinement, Powder Diffr. 17 (2) (2002) 149—152.

[39] F. Mayr, C. Hartinger, M. Paraskevopoulos, A. Pimenov, J. Hemberger, A. Loidl, A.A. Mukhin, A.M. Balbashov, High-frequency conductivity and phonon properties of $La_{7/8}Sr_{1/8}MnO_3$, Phys. Rev. B 62 (2000) 15673—15679.

[40] A.V. Boris, N.N. Kovaleva, A.V. Bazhenov, A.V. Samoilov, N.-C. Yeh, R.P. Vasquez, Infrared optical properties of $La_{0.7}Ca_{0.3}MnO_3$ epitaxial films, J. Appl. Phys. 81 (1997) 5756—5758.

[41] A. Arulraj, C.N.R. Rao, An infrared spectroscopic study of the insulator-metal transition and charge-ordering in rare earth manganates, $Ln_{1-x}A_xMnO_3$ (Ln = rare earth, A = Ca, Sr, Pb), J. Solid State Chem. 145 (1999) 557—563.

[42] A.V. Boris, N.N. Kovaleva, A.W. Bazhenov, P.J.M. Van Bentum, Th Rasing, S.-W. Cheong, A.V. Samoilov, N.-C. Yeh, Infrared studies of a $La_{0.67}Ca_{0.33}MnO_3$ single crystal: optical magnetoconductivity in a half-metallic ferromagnet, Phys. Rev. B 59 (1999) R697—R700.

[43] G. De Marzi, Z.V. Popović, A. Cantarero, Z. Dohčević-Mitrović, N. Paunović, J. Bok, F. Sapiña, Effect of A-site and B-site substitution on the infrared reflectivity spectra of $La_{1-y}A_yMn_{1-x}B_xO_3$ (A=Ba,Sr; B=Cu,Zn,Sc; 0<y<=0.3; 0<=x<=0.1) manganites, Phys. Rev. B 68 (2003) 064302—064307.

[44] I.S. Smirnova, A.V. Bazhenov, T.N. Fursova, A.F. Dubovitskii, L.S. Uspenskaya, M.Y. Maksimuk, IR-active optical phonons in Pnma-1, Pnma-2 and R-3c phases of $LaMnO_{3+\delta}$, Phys. B 403 (2008) 3896—3902.

[45] I.S. Smirnova, Normal modes of the $LaMnO_3$ Pnma phase: comparison with $La2CuO4$ Cmca phase, Phys. B 262 (1999) 247—261.

[46] R. Sopracase, G. Gruener, E. Olive, J.-C. Soret, Infrared study of the phonon modes in $PrMnO_3$ and $CaMnO_3$, Phys. B 405 (2010) 45—52.

[47] A. Shengelaya, G.M. Zhao, H. Keller, K.A. Müller, EPR evidence of Jahn-Teller polaron formation in $La_{1-x}Ca_xMnO_{3+y}$, Phys. Rev. Lett. 77 (26) (1996) 5296—5299.

[48] D.L. Huber, G. Alejandro, A. Caneiro, M.T. Causa, F. Prado, M. Tovar, S.B. Oseroff, EPR linewidths in $La1-xCaxMnO3$: 0<~x<~1, Phys. Rev. B 60 (17) (1999) 12155—12161.

[49] J, Zagorac, S. Bošković, B. Matović, B. Babić-Stojić, structure and magnetic investigations of $Ca_{1-x}Y_xMnO_3$ (x=0, 0.1, 0.2, 0.3) and Mn4+/Mn3+ relation aanalysis, Sci. Sinter. 42 (2010) 221—232.

[50] C. Oliva, L. Forni, EPR and XRD as probes for activity and durability of $LaMnO_3$ perovskite-like catalysts, Catal. Commun. 1 (2000) 5—8.

[51] G.R. Eaton, S.S. Eaton, D.P. Barr, R.T. Weber, Quantitative EPR, A Practitioners Guide, Springer-Verlag Wien, 2010.

[52] M. Rosić, Lj Kljaljević, D. Jordanov, M. Stoiljković, V. Kusigerski, V. Spasojević, B. Matović, Effects of sintering on the structural, microstructural and magnetic properties of nanoparticle manganite $Ca_{1-x}Gd_xMnO_3$ (x = 0.05, 0.1, 0.15, 0.2), Ceram. Int. 41 (2015) 14964—14972.

[53] M.T. Causa, M. Tovar, R.D. Zysler, M. Vallet-Regi, J.M. Gonzales-Calbet, R.D. Sanchez, J. Phys. IV 07 (1997) C1—C355.

Transition Metal Oxides (Ph. D. thesis), University of Groningen, Netherlands, 2004.

Far-infrared spectroscopy of Zn$_{1-x}$Mn$_x$GeAs$_2$ single crystals: Plasma damping influence on plasmon − Phonon interaction

CrossMark

N. Romcevic [a, *], M. Romcevic [a], W.D. Dobrowolski [b], L. Kilanski [b], M. Petrovic [a], J. Trajic [a], B. Hadzic [a], Z. Lazarevic [a], M. Gilic [a], J.L. Ristic-Djurovic [a], N. Paunovic [a], A. Reszka [b], B.J. Kowalski [b], I.V. Fedorchenko [c, d], S.F. Marenkin [c, d]

[a] *Institute of Physics, University of Belgrade, Pregrevica 118, 11080 Belgrade, Serbia*
[b] *Institute of Physics, Polish Academy of Science, 02-668 Warsaw, Poland*
[c] *Kurnakov Institute of General and Inorganic Chemistry RAS, 119991 Moscow, Russia*
[d] *National Institute of Science and Technology, MISiS, Moscow, Russia*

ARTICLE INFO

ABSTRACT

The interest in thorough description of Zn$_{1-x}$Mn$_x$GeAs$_2$ arises from its suitability for application in the field of non-linear optics. The room temperature far-infrared reflectivity spectra of single crystals Zn$_{1-x}$Mn$_x$GeAs$_2$, where $0 \le x \le 0.078$, were measured in the spectral range from 80 cm^{-1} to 500 cm^{-1}. The spectra were analyzed by fitting procedure using a dielectric function which includes interaction between a plasmon and two different phonons. The detected phonons are in excellent agreement with the theoretical predictions. The MnAs cluster phonons are detected, as well.

© 2015 Elsevier B.V. All rights reserved.

1. Introduction

Ternary semiconductors of the form II-IV-V$_2$ are crystal-chemicals that are electrical twins of semiconductors of the form III-V. Ordered replacement of the atom III in a semiconductor by the atoms II and IV in a ternary semiconductor causes doubling of the unit cell size in the direction of the *c*-axis and consequent reduction of symmetry from the cubic to the tetragonal. For example, a representative of this group of materials, ZnGeAs$_2$ with the twin semiconductor GaAs, crystallizes in the chalcopyrite structure.

A diluted magnetic semiconductor whose Curie temperature is as high as 300 K can be obtained by doping ZnGeAs$_2$ with Mn [1,2]. The non-linear optical coefficients of the resulting alloy, i.e., of Zn$_{1-x}$Mn$_x$GeAs$_2$, are large [3], and its direct energy gap corresponding to $T = 300$ K at the Γ point of the Brillouin zone is $E_g = 1.15$ eV [4]. Due to these characteristics, the described material is suitable for application in the non-linear optics; hence the interest for its other attributes.

The plasmons of free carriers and the longitudinal-optical (LO) phonons interact through their macroscopic electric fields, and the

result is appearance of the coupled LO phonon-plasmon modes (CPPMs). The vast majority of published studies are devoted to the *n*-type semiconductors and the interaction of a single phonon with effective plasmons. The studies involving the influence of the plasmon damping on the CPPM followed somewhat later [5]. For example, for low damping rates in the *n*-type GaAs, the coupled modes can be classified in an upper L_+ branch and a lower L_- branch. With the increase in the carrier density, i.e., plasma frequency, the nature of the upper mode changes in energy from the LO phonon-like to a plasmon-like. The change in the lower frequency mode occurs the other way around, reaching the transverse-optical (TO) phonon energy for large plasmon energy. The distinction between the upper and lower mode becomes meaningless for large plasmon dumping. In this case, one mode is more phonon-like with energy ω_{LO} for $\omega_P = 0$ and ω_{TO} for $\omega_P \gg \omega_{LO}$, with nearly pure phonon damping in both cases, whereas the other mode is an overdamped plasmon mode. Further, it is the plasma with high mobilities and low effective masses of the carriers that is often considered, in which case is enabled the detection of low, L_-, and high, L_+, energy branch of the CPPM [6,7].

Despite the early theoretical prediction of the interaction between two phonons and a plasmon [8], experimental confirmations are rare [9–11]. As for the influence of the plasmon damping on the

---

interaction between a plasmon and two different phonons, i.e. on the coupled plasmon-two-phonons modes, CP2PM, to the best of our knowledge it has not been considered so far.

Our intention is to use far-infrared spectroscopy to study the fundamental properties of the coupled plasmon-two-phonons modes in the *p*-type materials, as well as to further investigate these coupled modes under different plasmon damping conditions. The Raman spectra measurements performed on the $Zn_{1-x}Mn_xGeAs_2$ system [12] offer additional justification for the intended course of research.

2. Experimental technique, methods, and groundwork

The studied samples of $Zn_{1-x}Mn_xGeAs_2$ were grown from a stoichiometric ratio of high purity powders of $ZnAs_2$, Ge, and Mn, using the direct fusion method. The chemical composition was within the interval $0 \le x \le 0.078$. The technology of sample preparation is explained in detail in Ref. [13].

The preliminary studies of characteristics of $Zn_{1-x}Mn_xGeAs_2$ samples were undertaken and the results were presented in Refs. [2,14,15]. Using the X-ray diffraction spectra of powdered samples it was found that samples contain two main phases. These are solid solutions of Mn in $ZnGeAs_2$ and in $Zn_2Ge_{11}As_4$ compound, with chalcopyrite and zinc-blade cubic crystal structure, respectively. The magnetic properties of the alloy depend on the presence of Mn in the composition. Low Mn content produces a paramagnetic material, whereas larger amounts of Mn cause a ferromagnetic alignment of the alloy. From the results of the Hall measurements given in Table 1 it can be observed that the samples with relatively high density of the *p*-type free carrier, i.e. samples with $x = 0$, 0.013, and 0.047, have rather low mobility, whereas high mobility is associated with low density of the free carrier in samples with $x = 0.0028$, 0.053, and 0.078.

The presence of MnAs clusters in our $Zn_{1-x}Mn_xGeAs_2$ crystals was done with the use of a scanning electron microscope (SEM) coupled with energy dispersive x-ray spectrometer system (EDX). We used the field emission Hitachi SU-70 Analytical UHR FE-SEM SEM equipped with Thermo Scientific NSS 312 EDX system equipped with silicon drift detector. The samples surface was prepared prior to the SEM measurements including was mechanical polishing and chemical cleaning. The purpose of the sample preparation was to reduce the surface roughness and remove unintentional dirt and impurities. Our equipment allowed simultaneous use of the SEM and EDX techniques which in turn enabled to obtain images of the sample surface and the measurements of the localized elemental information at selected surface spots. A series of SEM maps was obtained for the $Zn_{1-x}Mn_xGeAs_2$ samples with different chemical composition. In agreement with our previous results [2] the SEM data showed no clustering for the samples with x < 0.07. For x = 0.078 the presence of MnAs clusters was observed (see Fig. 1).

The EDX results indicate the presence of MnAs clusters with diameter of about 10 μm. The stoichiometry of the $ZnGeAs_2$ equals 1:1:2 and the chemical content of MnAs inclusions is also close to 1:1.

The study of the CP2PM in *p*-type $Zn_{1-x}Mn_xGeAs_2$ was performed by measuring the far-infrared (FIR) reflection spectra at room temperature in the spectral range of 80 cm^{-1}–500 cm^{-1}, using BOMEM DA 8 spectrometer.

Table 1
Results of Hall measurements for $Zn_{1-x}Mn_xGeAs_2$.

x(Mn)	0	0.0028	0.013	0.047	0.053	0.078
p(10^{19} cm^{-3})	8.1	1.9	10.5	10.2	3.3	5.2
μ(cm^2/Vs)	19.1	67.8	14.9	15.3	44.1	28.7

3. Results and analysis

The far-infrared reflection spectra of single crystal samples of $Zn_{1-x}Mn_xGeAs_2$ are shown in Fig. 2. Each experimentally obtained data point is marked with a circular symbol. Two different spectra types are clearly visible. The samples with low free carrier density, i.e., samples corresponding to $x = 0.0028$, 0.053, and 0.078, show significant phonon structure. For the sample with $x = 0.0028$ the following features are distinguishable: the two dominant structures, clearly separated and located one in section 235 cm^{-1}–245 cm^{-1} and the other in 270 cm^{-1}–290 cm^{-1}, two phonons at about 210 cm^{-1} and 260 cm^{-1}, as well as the weakly expressed structures at approximately 120 cm^{-1} and 190 cm^{-1}. Note that stabilization of tetragonal structures occurred in this sample, according to the results of the X-ray measurements. The described features are visible in the spectra corresponding to $x = 0.053$ and $x = 0.078$, as well, however, in much less pronounced form. In these two cases it would be more appropriate to state that only the two most dominant structures are clearly visible.

When the free carrier density increases, i.e., for the samples corresponding to the remaining three values of *x*, the spectra take a completely different shape. Only the outlines of formerly clear structures can now be distinguished within a single wide shape, which should rather be described as a structure of slightly wavy shape. The most pronounced spectra from this group corresponds to $x = 0.047$. The phonon located at about 210 cm^{-1} and the structure positioned between 235 cm^{-1} and 245 cm^{-1} are broadened, merged, and spread up to 270 cm^{-1}, which is the lower limit of the most pronounced structure in previously described spectra and is now practically hidden by the electrons. The most pronounced became the structures located at about 180 cm^{-1} and 260 cm^{-1}, as well as the phonon positioned at approximately 90 cm^{-1}. The global minimum is shifted to above 320 cm^{-1}. Compared to the samples with low free carrier density, a noticeable reflectivity increase is registered in this area, as well.

A theoretical model of the bulk dielectric function has been discussed by several authors [6,16]. The low-frequency dielectric properties of single crystals are described by classical oscillators corresponding to the TO-modes, to which the Drude part is superimposed to take into account the free carrier contribution:

$$\varepsilon_S(\omega) = \varepsilon_\infty + \sum_{k=1}^{l} \frac{\varepsilon_\infty \left(\omega_{LOk}^2 - \omega_{TOk}^2\right)}{\omega_{TOk}^2 - \omega^2 - i\gamma_{TOk}\omega} - \frac{\varepsilon_\infty \omega_P^2}{\omega(\omega + i\Gamma_P)}, \quad (1)$$

where ε_∞ is the bound charge contribution and it is assumed to be a constant, ω_{LOk} and ω_{TOk} are the longitudinal and transverse optical-phonon frequencies, ω_P the plasma frequency, γ_{LOk} and γ_{TOk} indicate the damping of uncoupled modes of the host crystal, and Γ_P is the plasmon mode damping coefficient.

Our previous works [17–19] support the opinion that the structures located in the regions 235 cm^{-1}–245 cm^{-1} and 270 cm^{-1}–290 cm^{-1}, are a consequence of the combined plasmon-LO phonon modes, ω_{lj}. Therefore, we consider these two structures as good candidates for verification of CP2PM. The outcomes of the coupling between a single phonon and a plasmon, CPPM, for the various values of plasma damping Γ, are given in Fig. 3. The phonon is taken to be the E^2 phonon in $Zn_{1-x}Mn_xGeAs_2$, which in Eq. (1) corresponds to $l = 1$, $\omega_{TO} = 268$ cm^{-1}, and $\omega_{LO} = 273$ cm^{-1}, whereas ω_P defines the plasmon. The positions of the coupled mode were obtained from the real part of Eq. (1) as the solution of the equation Re$\{\varepsilon_S\} = 0$ for $l = 1$. The obtained result is in excellent agreement with the GaAs case described in Ref. [5]. Further, each of the two structures taken as an example can be explained using the approach illustrated in Fig. 3, i.e., for the both cases the appropriate
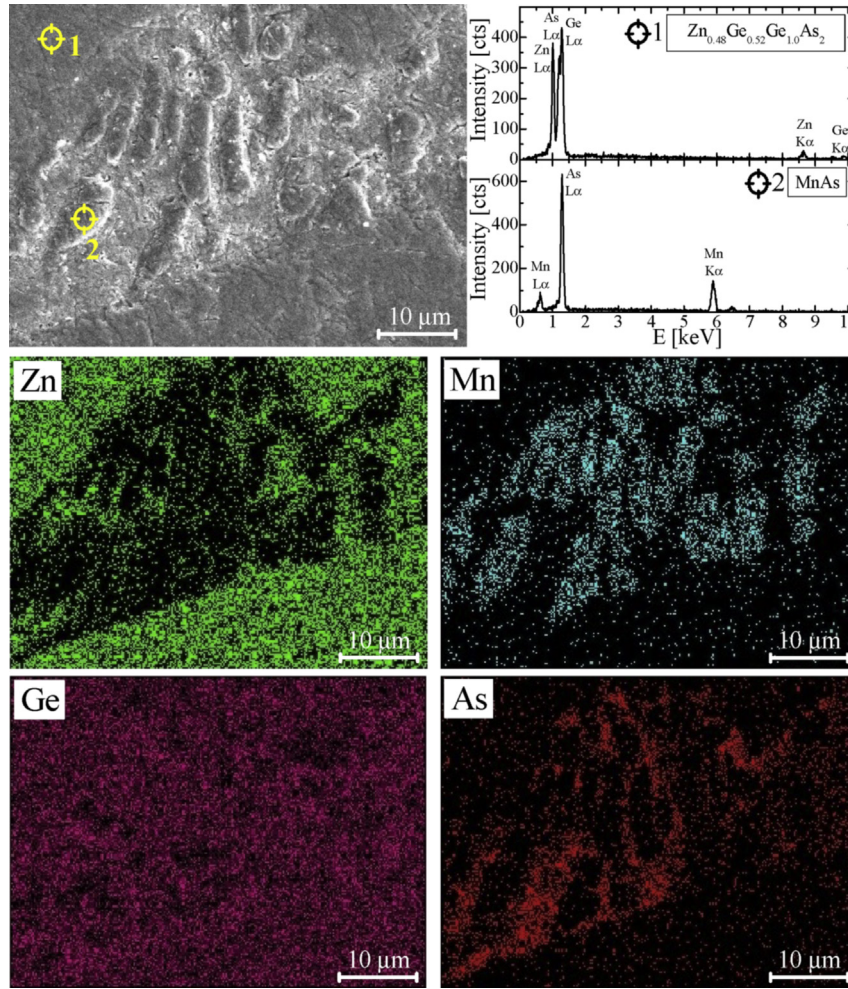
Fig. 1. Exemplary SEM image (top left) and EDX microprobe results including the detailed chemical content measurement (top right) and the maps of the distribution of the alloying elements obtained for the $Zn_{1-x}Mn_xGeAs_2$ sample with $x = 0.078$.

values of plasma frequency and damping can be determined to provide full description of the given structure. However, the dielectric function formed in such a way to account for the interaction of each individual phonon with the plasma, would lead to difficulties in understanding the nature of the multicomponent plasma. Several studies are dedicated to this issue [7–11].

With the intention to avoid the discussed difficulties and to establish better model of reflectivity spectra of $Zn_{1-x}Mn_xGeAs_2$, we used the dielectric function that includes in its initial form the interaction between two different LO phonons and a plasmon, i.e., the plasmon-two-phonons interaction [8,11], namely:

$$\varepsilon(\omega) = \varepsilon_\infty \frac{\prod\limits_{j=1}^{3}\left(\omega^2 + i\gamma_{lj}\omega - \omega_{lj}^2\right)}{\omega(\omega + i\Gamma_P)\prod\limits_{i=1}^{2}\left(\omega^2 + i\gamma_{ti}\omega - \omega_{ti}^2\right)} \times \prod\limits_{k=1}^{s}\frac{\omega^2 + i\gamma_{LOk}\omega - \omega_{LOk}^2}{\omega^2 + i\gamma_{TOk}\omega - \omega_{TOk}^2}.$$

(2)

The first term in Eq. (2) represents coupling of a plasmon and two phonons, whereas the second term accounts for all s uncoupled modes of the crystal. The parameters ω_{lj} and γ_{lj} in the numerator of the first part are eigenfrequencies and damping coefficients of the longitudinal (LO) component of the plasmon-two-phonons waves,

respectively. The parameters ω_{tj} and γ_{tj} in the denominator of the first part correspond to the corresponding characteristics of the transverse (TO) vibrations. The second factor represents uncoupled crystal modes, where ω_{LOk} and ω_{TOk} are the longitudinal and transverse frequencies, while γ_{LOk} and γ_{TOk} are the damping coefficients of the k-th crystal mode.

The dielectric function given with Eq. (2) was used to obtain the theoretical prediction of the experimental spectra shown in Fig. 2. The agreement between the experimental data shown as circles and the theoretical spectra given as solid lines is excellent.

The number of uncoupled phonons, s, depends on the manganese concentration, x, and will be discussed latter. In order to better understand the obtained results, the influence of the plasma damping on the positions of coupled plasmon-two-phonons modes is shown in Fig. 4. As explained earlier, the coupled mode positions are defined as the solutions of the real part of Eq. (1), i.e., $\mathrm{Re}\{\varepsilon_S\} = 0$; however, now under the condition $l = 2$.

The values of frequencies ω_{TO1} and ω_{TO2}, obtained as the best fit to experimental data, are 236 cm^{-1} and 268 cm^{-1} for E^3 and E^2, respectively. Ten values of the parameter Γ were considered, namely $\Gamma = 0$, 40, 60, 80, 100, 120, 140, 160, 180, and 250 cm^{-1}. The obtained dependence of the coupled modes positions depicted in Fig. 4 is qualitatively different from the one given in Fig. 3, which is expected since the number of coupled modes is different. For $\Gamma = 0$,
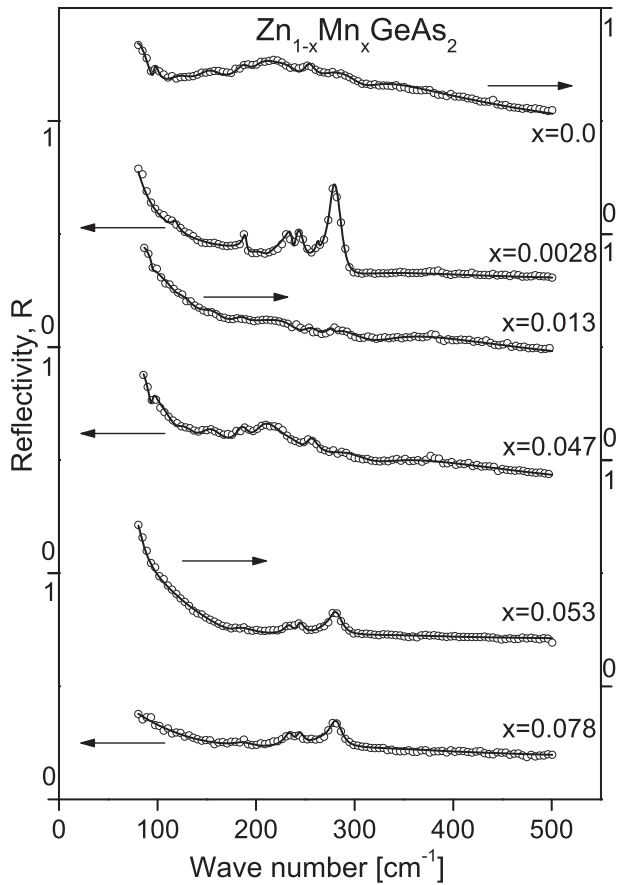
Fig. 2. Far-infrared reflection spectra of $Zn_{1-x}Mn_xGeAs_2$ single crystals. The experimentally obtained data points are depicted by circles. The theoretical spectra obtained with the model defined by Eq. (2) and fitting procedure are given as solid lines. Six different samples were considered with six values of manganese concentration $x = 0$, 0.0028, 0.013, 0.047, 0.053, and 0.078.

here as well as in Fig. 3, the lower branch starts as a plasmon and ends in TO1 phonons, whereas the upper branch begins as a phonon and ends in plasmon tail. The new branch, absent in Fig. 3, begins as LO1 phonon and approaches TO2 phonon at high values
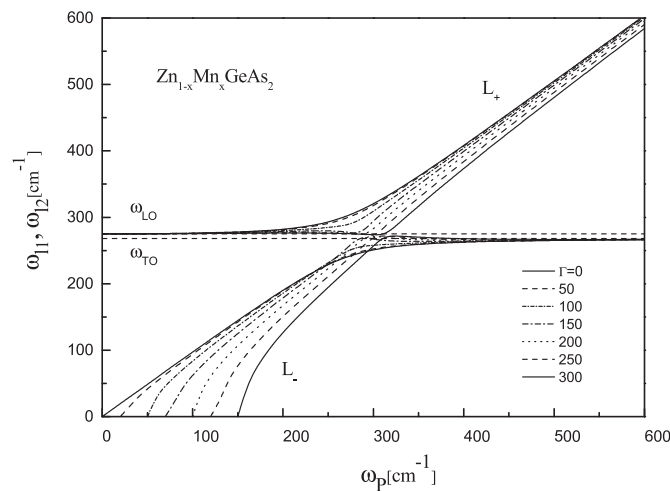
Fig. 3. Eigenfrequencies of plasmon−phonon modes for single crystal $Zn_{1-x}Mn_xGeAs_2$. The solid lines are spectra calculated from $Re\{\varepsilon_S\} = 0$, where ε_S is given by Eq. (1) whose parameter l is set to 1. Seven different values of plasma damping were considered, i.e., $\Gamma = 0$, 50, 100, 150, 200, 250, and 300 cm^{-1}.
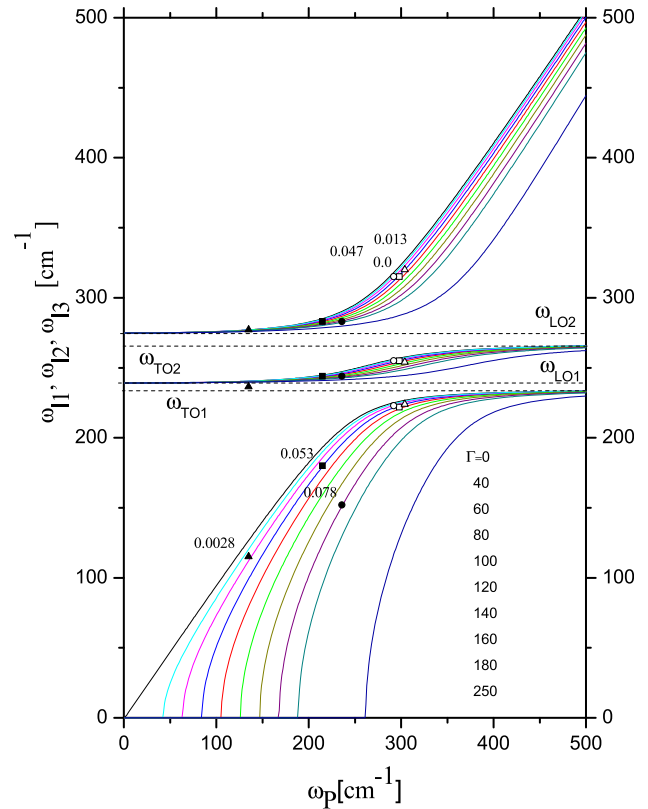
Fig. 4. Eigenfrequencies of plasmon-two-phonon modes for single crystal $Zn_{1-x}Mn_xGeAs_2$. The solid lines are spectra calculated from $Re\{\varepsilon_S\} = 0$, where ε_S is given by Eq. (1) whose parameter l is set to 2. Ten different values of plasma damping were considered, i.e., $\Gamma = 0$, 40, 60, 80, 100, 120, 140, 160, 180, and 250 cm^{-1}. Values obtained with Eq. (2) as the best fit to the experimental data in Fig. 1 are represented by solid symbols for samples with low free carrier density and open symbols for high free carrier density.

of plasma frequency. The values of LO phonon frequencies are obtained from Fig. 4 as a results of best fit. The nature of the branches does not change with the increase of plasma damping up to relatively large value of $\Gamma = 250$ cm^{-1}; instead, each branch is shifted within its range. The regions between TO1 and LO1, as well as between TO2 and LO2 are branch-free, as was the case with the TO−LO region in Fig. 3 for the LO phonon-plasmon interaction.

Results obtained as the best fit to the experimental data are in Fig. 4 denoted by different symbols for different values of x. The obtained values of plasma frequencies follow the change in free carrier density, N, which was expected since ω_P^2 is proportional to N. The most pronounced spectrum from each of the two groups, i.e., the one with $x = 0.0028$ and $x = 0.047$, correspond to the smallest value of plasma damping within its group.

There are three groups of uncoupled phonons. The first group contains the phonons that originated from $ZnGeAs_2$ and were detected in all spectra. These are the phonons located at around 101 cm^{-1}, 117 cm^{-1}, 161 cm^{-1}, and 210 cm^{-1}, with the B_1^3, E^5, E^4, and A_1 symmetry, respectively, as well as the group of phonons in the vicinity of 275 cm^{-1} whose symmetry is of the E^1 and B_2^1 type. These phonons are described in detail in Ref. [20].

The weak phonons around 180 cm^{-1} for $x = 0.053$ and 0.078, and above 320 cm^{-1} for $x = 0.013$ and 0.047, probably correspond to another detected phase, i.e., to $Zn_2Ge_{11}As_4$, or to the surface modes.

The most interesting is the third group of phonons at about 170 cm^{-1} which correspond to $x = 0.013$ and 0.047. Although their presence was noticeable in these two spectra, we did not observe
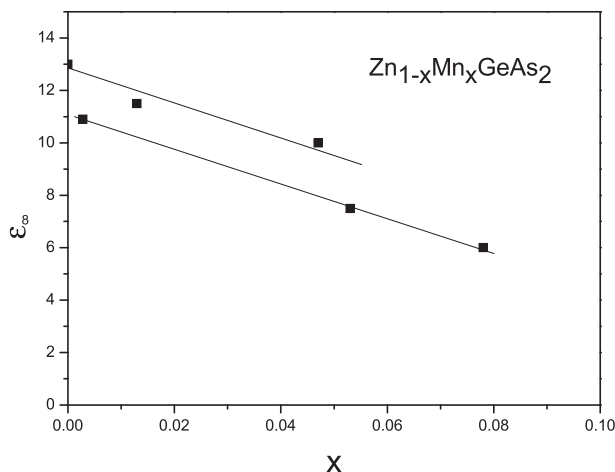
Fig. 5. Dependence of ε_∞ on manganese concentration.

these phonons in the spectra of the basic material. The calculated values of the MnAs clusters are positioned at these frequencies, as well [19]. Note that the Raman spectra measurements offer much more distinguished results. On the other hand, given the number of clusters and high free carrier density, for IR spectra it can be concluded with certainty only that it would not be possible to completely reproduce the spectra if these phonons were not taken into account.

The dependence of ε_∞ on the concentration of Mn is given quantitatively in Fig. 5. It was clear from Fig. 1 that ε_∞ decreases with the increase in Mn concentration. In addition to confirming this conclusion numerically, Fig. 5 shows that the dependence is linear within each of the two groups of samples that were established with respect to the free carrier density, i.e. for the group of samples with high as well as with low carrier density. The carrier density does not influence the shape of the dependence, i.e., the linearity; however, the group of samples with high carrier density has larger ε_∞ compared to the group with low carrier density.

4. Conclusion

We used far-infrared reflectivity measurements to investigate the influence of plasma damping on the interaction between a plasmon and two different phonons in $Zn_{1-x}Mn_xGeAs_2$. The specific nature of the behavior of the coupled phonons frequency is determined. At high plasma damping values entrance of phonons into the region between TO and LO frequencies is not observed for the plasmon-two-phonons interaction, unlike was the case with the plasmon-phonon interaction. Existence of MnAs clusters is confirmed and relation between free carrier concentration and optical parameters is determined.

References

[1] S. Choi, G.B. Cha, S.C. Hong, S. Cho, Y. Kim, J.B. Ketterson, S.Y. Jeong, G.C. Yi, Solid State Commun. 122 (2002) 165.
[2] L. Kilanski, M. Gorska, W. Dobrowolski, E. Dynowska, M. Wojcik, B.J. Kowalski, J.R. Anderson, C.R. Rotundu, D.K. Maude, S.S. Varnavskiy, I.V. Fedorchenko, S.F. Marenkin, J. Appl. Phys. 108 (2010) 073925.
[3] W. Dobrowolski, J. Kossut, T. Story, Handbook of Magnetic Materials, Elsevier, Amsterdam, 2002.
[4] S. Picozzi, Nat. Mater 3 (2004) 349.
[5] G. Irmer, M. Wenzel, J. Monecke, Phys. Rev. B 56 (15) (1997) 9524.
[6] G. Abstreiter, M. Cardona, A. Pinczuk, in: M. Cardona, G. Guntherodt (Eds.), Light Scattering in Solids, IV, Springer-Verlag, Berlin, 1984.
[7] R.T. Holm, J.W. Gibson, E.D. Palik, J. Appl. Phys. 48 (1977) 212.
[8] A.A. Kukharski, Solid State Commun. 8 (1970) 1275.
[9] J. Trajić, N. Romčević, M. Romčević, V.N. Nikiforov, Mater. Res. Bull. 42 (2007) 2192–2201.
[10] J. Trajić, N. Romčević, M. Romčević, D. Stojanović, R. Rudolf, T.A. Kuznetsova, D.R. Khokhlov, J. Alloys Compd. 493 (2010) 41–46.
[11] M. Petrovic, N. Romcevic, J. Trajic, W.D. Dobrowolski, M. Romcevic, B. Hadzic, M. Gilic, A. Mycelski, Infrared Phys. Technol. 87 (2014) 323–326.
[12] M. Romčević, N. Romčević, W. Dobrowolski, L. Kalinski, J. Trajić, D.V. Timotijević, E. Dynowska, I.V. Fedorchenko, S.F. Marenkin, J. Alloys Compd. 548 (2013) 33–37.
[13] V.M. Novotortsev, V.T. Kalinnikov, L.I. Koroleva, R.V. Demin, S.F. Marenkin, T.G. Aminov, G.G. Shabunina, S.V. Boichuk, V.A. Ivanov, Russ. J. Inorg. Chem. 50 (2005) 429.
[14] V.M. Novovotortsev, S.F. Marenkin, S.A. Varnavskii, L.I. Koroleva, T.A. Kupriyanova, R. Szymcak, L. Kilanski, B. Krzmanska, Russi. J. Inorg. Chem. 53 (2008) 22.
[15] L.I. Koroleva, V.Yu Pavlov, D.M. Zashhchirinskii, S.F. Marenkin, S.A. Varnavskii, R. Szimcak, W. Dobrowolski, L. Kilanski, Phys. Solid Sate 49 (2007) 2121.
[16] E. Burstein, A. Pinczuk, R.F. Wallis, in: D.L. Carter, R.T. Bate (Eds.), The Phys. Of Semimetals and Narrow-Gap Semicon, 1971. Pergamon, New York.
[17] M. Romcevic, L. Kilanski, N. Romcevic, B. Hadzic, W. Dobrowolski, I.V. Fedorchenko, S.F. Marenkin, Mater. Res. Bull. 59 (2014) 300–304.
[18] J. Trajić, N. Romčević, M. Romčević, D. Stojanović, L.I. Ryabova, D.R. Khokhlov, J. Alloys Compd. 602 (2014) 300–305.
[19] N. Romčević, J. Trajić, T.A. Kuznetsova, M. Romčević, B. Hadžić, D.R. Khokhlov, J. Alloys Compd. 442 (2007) 324–327.
[20] F.W. Ohrendorf, H. Haeuseler, Cryst. Res. Technol. 34 (1999) 339–349.
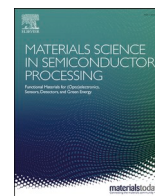
Revealing plasmon-phonon interaction in nanocrystalline MgFe$_2$O$_4$ spinels by far-infrared reflection spectroscopy

Novica Paunović [a,*], Zorana Dohčević-Mitrović [a,**], Dejan M. Djokić [a], Sonja Aškrabić [a], Saša Lazović [a], Ann Rose Abraham [b], Balakrishnan Raneesh [c], Nandakumar Kalarikkal [d,e], Sabu Thomas [e,f]

[a] Institute of Physics Belgrade, University of Belgrade, Pregrevica 118, 11080, Belgrade, Serbia
[b] Department of Physics, Sacred Heart College, Kochi, Kerala, 682013, India
[c] Department of Physics, Catholicate College, Pathanamthitta, Kerala, 689645, India
[d] School of Pure and Applied Physics, Mahatma Gandhi University, Kottayam, Kerala, 686560, India
[e] International & Inter University Centre for Nanoscience and Nanotechnology, Mahatma Gandhi University, Kottayam, Kerala, 686560, India
[f] School of Energy Materials, Mahatma Gandhi University, Kottayam, Kerala, 686560, India

A R T I C L E   I N F O

A B S T R A C T

Room-temperature far-infrared reflectivity spectra of nanocrystalline, partially inverse MgFe$_2$O$_4$ were investigated. MgFe$_2$O$_4$ samples were prepared by sol-gel method and sintered at three different temperatures (400, 600 and 800 °C). Raman spectroscopy was employed to estimate the degree of inversion in the sintered samples. The degree of inversion was found to increase from 0.52 to 0.74 as the sintering temperature increased from 400 °C to 800 °C. The reflectivity spectra, besides the four infrared modes characteristic for spinels (ν_1, ν_2, ν_3, ν_4), revealed the presence of free carriers. Plasmon-longitudinal optical (LO) phonon interaction was analyzed using factorized coupled and decoupled plasmon-phonon models, combined with the Bruggeman effective medium approximation. From these models it was obtained that the ν_1 and ν_3 phonon modes are more strongly coupled with plasmons than the ν_2 mode. A potential mechanism of plasmon-phonon interaction in inverse MgFe$_2$O$_4$ spinel has been discussed.

1. Introduction

Magnesium ferrite (MgFe$_2$O$_4$) belongs to the family of spinel ferrites, a very important group of magnetic spinel oxides with a wide range of applications. It is a soft magnetic n-type semiconducting material which received strong attention due its vast uses such as magnetic applications [1,2], catalyst [3,4], metal ion removal [5], water purification [6], water and CO$_2$ splitting [7,8] or sensors [9]. It is considered as promising candidate for biomedical applications such as hyperthermia and cancer treatment [10–12], targeted drug delivery [13] or magnetic resonance imaging [14]. In recent years MgFe$_2$O$_4$ has been considered as an anode material for lithium-ion batteries [15–17]. Many properties of MgFe$_2$O$_4$ depend on the microstructure, grain size and porosity, or preparative methods. Preparation of MgFe$_2$O$_4$ in nanocrystalline form offers a way to change and tune its optical, electronic, magnetic and other properties [18–20].

Spinel oxides have a general formula AB$_2$O$_4$ and belong to the *Fd$\bar{3}$m* (O_h^7, No. 227) space group. In normal spinels, A cations occupy only the tetrahedral sites, whereas B cations occupy only the octahedral sites (Fig. 1). In inverse spinels, A cations and half of B cations occupy the octahedral sites while the tetrahedral sites are occupied by the other half of the B cations, which can be represented as B[AB]O$_4$. The intermediate configurations are partially inverse spinels and the structural formula can be written as $(A_{1-\delta} B_\delta)_{tetra}[A_\delta B_{2-\delta}]_{octa}O_4$, where δ represents the degree of inversion, which in extreme cases of normal and completely inverse spinels has values $\delta = 0$ and $\delta = 1$, respectively. MgFe$_2$O$_4$ is a partially inverse spinel for which the degree of inversion δ depends on the synthesis method and thermal treatment. The crystallite size also presents an important factor for adjusting the degree of inversion and fine-tuning of MgFe$_2$O$_4$ properties.

Far infrared (IR) reflection spectroscopy is a powerful technique

---

which is often used for investigation of crystal structure, phonon and dielectric properties, phase composition, plasmon-fonon interaction, etc., in various types of materials such as oxides, semiconductors, ceramics and many others (e.g., Refs. [21–26]). IR spectroscopy is also commonly used to study normal and inverse spinels. Group theory analysis predicts four active IR modes for spinel structures. Experimental spectra of spinels show at least two strong modes, which, after works of Waldron [27], Hafner [28], and White and DeAngelis [29], are mostly accepted to originate from stretching vibrations of the tetrahedral (octahedral) groups, although it has been argued by Preudhomme and Tarte [30–33] that the actual behavior might be more complex than this. In many spinels, a third, and sometimes a weak forth mode is present at lower frequencies [28,29,32,34–36]. The exact nature of these two modes is not completely clarified yet, but is generally considered that these modes originate from complex vibrations involving both tetrahedral and octahedral groups [27,32,33,35–37]. In most reports, the IR spectra of spinels are presented as transmission or absorption spectra and the IR modes are simply analyzed by the peaks positions (e.g., Refs. [27–30,32,33,35,38–44]). On the other hand, the IR reflectivity spectra of spinels are significantly less often represented in literature (e.g., Refs. [34,36,39,45–49]). To the best of our knowledge, no infrared reflectivity spectra of $MgFe_2O_4$ has been reported. The reflectivity spectra can be more quantitatively analyzed by using an appropriate model for obtaining the values of phonon TO/LO frequencies and dampings. Furthermore, the advantages of reflectivity spectra over the transmittance ones lies in the fact that not only phonon modes but also plasmons and mutual interaction between phonons and plasmons can be analyzed. The knowledge of plasmon-phonon interaction can be important in characterizing transport and optical properties of spinels. Up to date, no infrared reflectivity study of plasmon-LO phonon interaction in $MgFe_2O_4$ has been carried out.

In the present study we have focused on the analysis of far-IR reflectivity spectra of nanocrystalline $MgFe_2O_4$ samples sintered at different temperatures and of varying degrees of inversion. The reflectivity spectra of the samples showed a clear presence of free carriers contribution. The influence of free carriers on the phonon spectra was analyzed employing two different factorized dielectric-function models, from which the coupled (decoupled) LO-phonon modes frequencies and dampings were obtained. Such analysis of reflectivity spectra paves the way for better understanding of the carrier-lattice coupling in inverse nanocrystalline $MgFe_2O_4$.

2. Experimental

Magnesium ferrite ($MgFe_2O_4$) nanocrystalline samples were prepared by sol-gel method and by sintering in air at different temperatures: 400, 600 and 800 °C. The corresponding samples will be further denoted as MFO400, MFO600 and MFO800. Details of the synthesis procedure, structural analysis, as well as various other methods of characterization of these samples have already been published elsewhere [51]. The schematic diagram of the synthesis procedure is given in the Supplementary Information.

The IR reflectivity measurements of the $MgFe_2O_4$ samples in the form of pressed disk-like pellets were carried out at room temperature with a BOMEM DA8 Fourier-transform IR spectrometer. A Hyper beamsplitter and a deuterated triglycine sulfate (DTGS) pyroelectric detector were used to cover the wavenumber region from 90 to 680 cm^{-1}. Micro-Raman spectroscopy was used to estimate the degree of inversion of nanocrystalline $MgFe_2O_4$. Micro-Raman spectra were acquired in the back-scattering configuration using the triple-monochromator Raman system Princeton TriVista 557. Nd:YAG laser line of 532 nm was used as an excitation and the beam was focused onto the samples using 50x objective magnification. Laser power on the sample was 0.08 mW. Raman spectra were deconvoluted using Lorentzian function. More detailed description of infrared and Raman experimental setups is presented in the Supplementary Information.

3. Results and discussion

$MgFe_2O_4$ crystalizes in a cubic spinel structure belonging to the $Fd\overline{3}m$ space group. The full unit cell contains 56 atoms ($Z = 8$), however the smallest Bravais cell, i.e., the primitive cell, has only 14 atoms ($Z = 2$). The factor group analysis for the primitive cell predicts 42 normal modes, three of which are acoustic modes with T_{1u} symmetry, and the remaining 39 Γ-point optical modes are:

$$\Gamma = A_{1g}(R) + E_g(R) + T_{1g} + 3T_{2g}(R) + 2A_{2u} + 2E_u + 4T_{1u}(IR) + 2T_{2u}. \quad (1)$$

Among these modes, four are triply degenerate infrared (IR) modes of T_{1u} symmetry, five are Raman (R) modes, and the remaining modes are silent. Inverse spinels like $NiFe_2O_4$ or $CoFe_2O_4$ show more Raman-active modes than those predicted by factor-group analysis because of inversion of the cations between the tetrahedral and octahedral sites. These spinel structures are characterized by an additional mode in the frequency region where one A_{1g} mode is expected to appear [52,53]. In
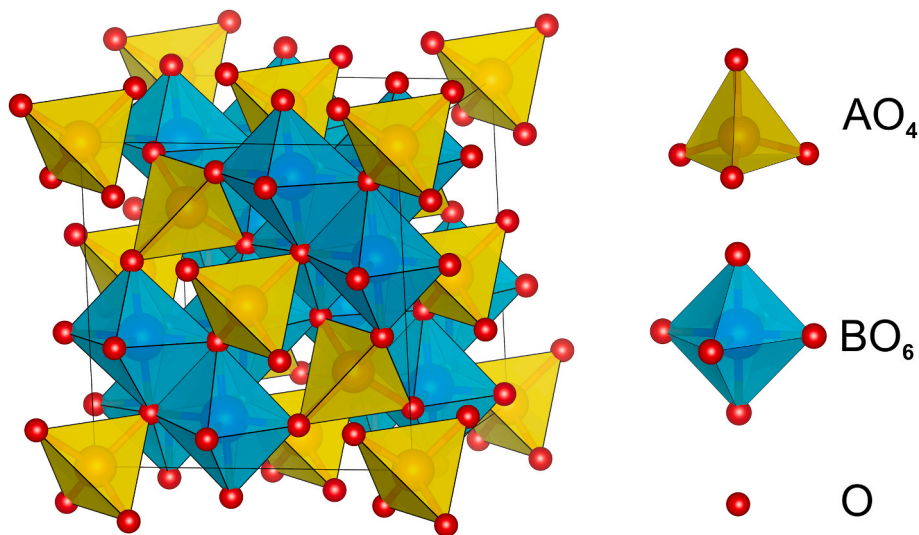

Fig. 1. (Color online) Schematic illustration of normal AB_2O_4 spinel structure with the tetrahedral (AO_4) and octahedral (BO_6) units. The crystal structure visualized by VESTA 3 [50].

the Raman spectra of $MgFe_2O_4$ nanopowders, the A_{1g} mode splits into two modes due to the large difference in mass between Fe^{3+} and Mg^{2+} cations [54–56]. The higher frequency A_{1g} mode corresponds to the vibrations of oxygen anions around Fe^{3+} cations on the tetrahedral sites, whereas the lower frequency mode corresponds to the vibrations of oxygen anions around Mg^{2+} cations on the tetrahedral sites [54,56]. In Fig. 2 are shown deconvoluted room-temperature Raman spectra of MFO400, MFO600 and MFO800 samples, using Lorentzian function. The Raman spectra are presented in the region characteristic for the A_{1g} modes.

Nakagomi et al. [56] have shown that, using corresponding integrated intensities of the two A_{1g} modes, it is possible to quantitatively determine the Mg and Fe content on the tetrahedral sites. Therefore, knowing that the integrated intensities of the two A_{1g} modes are proportional to the concentrations of Mg^{2+} and Fe^{3+} cations on the tetrahedral sites [56], the inversion parameter δ can be calculated from the equation

$$\frac{I\left(A_{1g}^{low}\right)}{I\left(A_{1g}^{high}\right)} = \frac{1-\delta}{\delta} \qquad (2)$$

The calculated inversion parameters are 0.52, 0.62 and 0.74 for the MFO400, MFO600 and MFO800 samples, respectively. These data imply that the sample sintered at 400 °C is closer to the normal spinel structure than the sample sintered at 800 °C, which is in complete accordance with the results of positron annihilation analysis of these samples [51]. The inversion parameters obtained from the Raman spectra are also in good agreement with Bloesser et al., who analyzed $MgFe_2O_4$ samples calcined at 400, 600 and 800 °C, and for the sample calcined at 800 °C obtained the inversion degree of 0.72 [18].

The IR reflectivity spectra of $MgFe_2O_4$ nanocrystalline samples are shown in Fig. 3. In the spectra of all samples were found four T_{1u} modes predicted by group theory. Following the seminal work of Waldron [27], most authors label the four T_{1u} modes as ν_1, ν_2, ν_3 and ν_4, indexing them from the highest to the lowest energies. According to Waldron, the highest energy mode ν_1 was attributed to the vibrations of tetrahedra, and the ν_2 mode to the vibrations of octahedra, considering the vibrations of these groups as mostly isolated molecular vibrations [27]. Such conclusions were later also adopted by Hafner [28], and White and DeAngelis [29]. On the other hand, these conclusions were criticized by

Fig. 2. (Color online) Room-temperature Raman spectra (data in black) of $MgFe_2O_4$ samples sintered at different temperatures, in the region (625–775) cm^{-1}. Experimental curves were deconvoluted with Lorentzian function (blue curves) and cumulative fits are represented by the green curves. The high-frequency A_{1g} mode is shaded for clarity.

Preudhomme and Tarte [30–33] as oversimplified. They argued that, in some cases at least, the observed frequencies cannot be assigned to the vibrations of definite coordinated groups (either tetrahedral or octahedral), but instead are related to complex vibrations of the whole spinel lattice. Nevertheless, many authors still rely mostly on the original Waldron's interpretation of these modes [35,38,42–44,57,58]. It is mostly accepted that the two low frequency modes ν_3 and ν_4 originate from complex vibrations involving both tetrahedral and octahedral groups [27,32,33,35–37].

The MFO400 sample shows two modes ν_1 and ν_2, centered at around 570 and 405 cm^{-1} respectively. These two modes are present in all spinels. For the MFO600 and MFO800 samples, the third mode ν_3 centered at around 330 cm^{-1} is clearly visible. This mode is present in the MFO400 sample too and appears as an asymmetry of the ν_2 mode. In the IR spectra of some spinels a weak forth mode ν_4 appears around 200 cm^{-1} [28,29,32–36,40,49]. This mode can be observed as a small hump centered at around 210 cm^{-1} in the MFO800 sample spectra, and to a lesser extent also in the MFO600 and MFO400 spectra.

In the low frequency region of the IR spectra in Fig. 3, Drude tail appeared and became more pronounced for the MFO600 and MFO800 samples. Its occurrence in the IR spectra is a clear sign of a presence of free carriers. The presence of free carriers in nanocrystalline $MgFe_2O_4$ comes from the presence of vacancies, which introduce electrons as the majority free carriers, making $MgFe_2O_4$ an n-type semiconductor [59]. When free carriers are present in the material, they can interact with phonons. Since plasmons are longitudinal oscillations, they interact with longitudinal-optical (LO) modes, shifting them towards higher frequencies, whereas the transverse-optical (TO) modes remain unaffected. In the analysis of the reflectivity spectra of $MgFe_2O_4$ nanocrystalline samples, two models, both of which include contribution from free carriers, have been applied to investigate the dielectric response. In both models, the factorized form of dielectric function was used. Compared to the classical oscillator model, this factorized form much better describes phonons in strongly polar ionic crystals, where largely split TO/LO modes can have significantly different dampings [60].

The first model, known in literature as the coupled plasmon-phonon model (CPP) [61,62], presents a direct way to characterize plasmon-phonon coupled modes. In this model, the dielectric function has a form:

$$\varepsilon(\omega) = \varepsilon_\infty \frac{\prod_{j=1}^{m+n} \omega^2 + i\gamma_{LOj}\omega - \omega_{LOj}^2}{\omega^m \prod_{j=1}^{m}(\omega + i\gamma_{Pj}) \prod_{j=1}^{n} \omega^2 + i\gamma_{TOj}\omega - \omega_{TOj}^2}, \qquad (3)$$

where ε_∞ is the high frequency dielectric constant, $\omega_{TOj}(\omega_{LOj})$ and $\gamma_{TOj}(\gamma_{LOj})$ are the TO(LO) frequencies and dampings of n phonons ($n = 4$ in our case), which can be coupled with m plasmons with dampings γ_{Pj} ($m = 1$ in our case). From this model, the plasma frequency can be obtained indirectly as [61,62]:

$$\omega_P = \frac{\prod_{j=1}^{n+1} \omega_{LOj}^2}{\prod_{j=1}^{n} \omega_{TOj}^2}, \qquad (4)$$

and the frequency of the coupled plasmon-phonon mode is given by [61, 62]:

$$\Omega_{LOj} = \sqrt{\omega_{LOj}^2 - \frac{1}{4}\gamma_{LOj}^2}. \qquad (5)$$

The second model, named as the decoupled plasmon-phonon (DPP) model, is a conventional additive form for dielectric function of pure phonon and plasmon contributions. This model enables to determine the decoupled phonon and plasma frequencies and dampings using
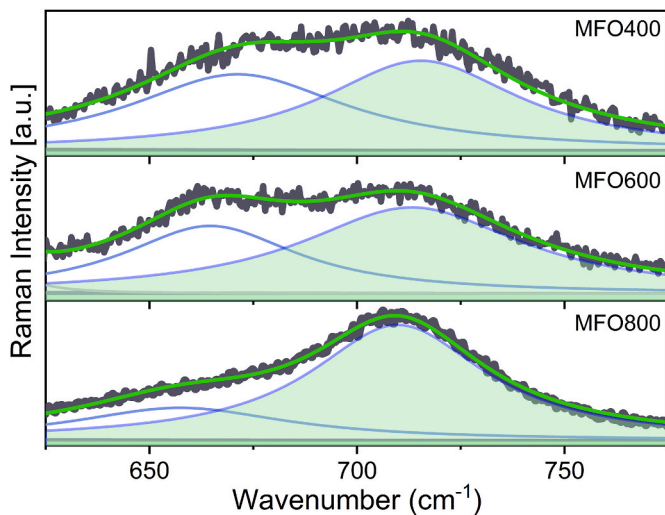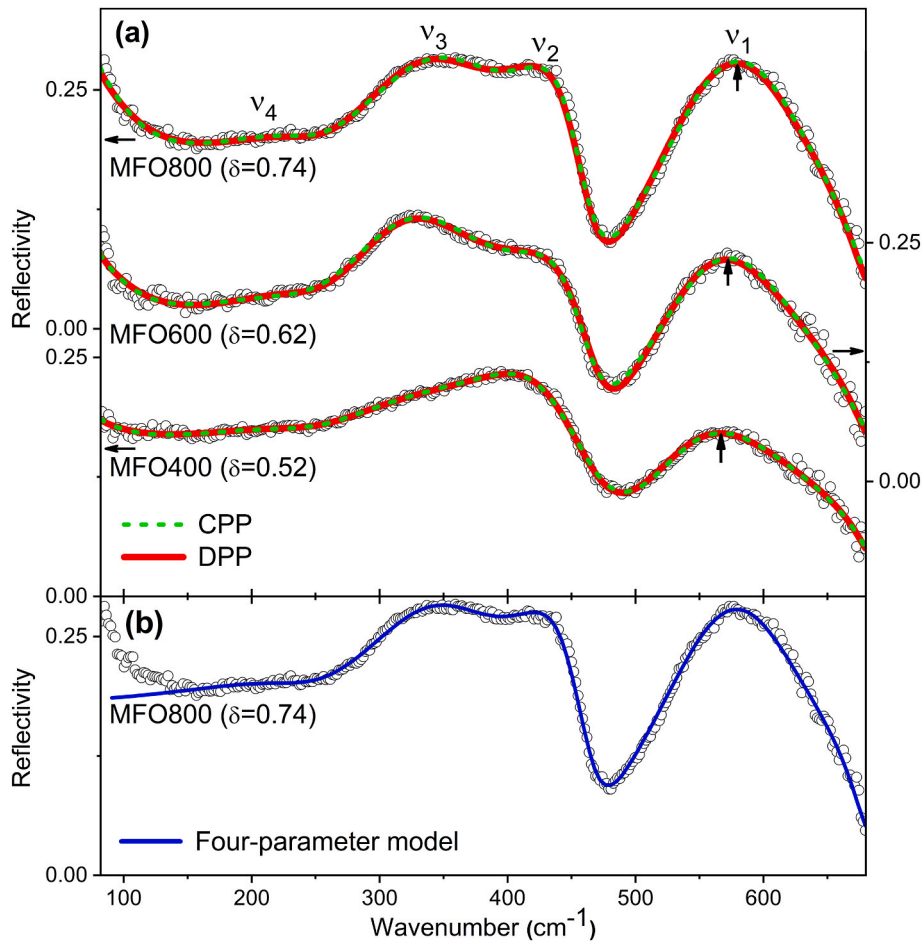
Fig. 3. (Color online) (a) IR reflectivity spectra of MgFe$_2$O$_4$ nanocrystalline samples sintered at different temperatures together with theoretical fits obtained using the coupled plasmon-phonon (CPP) and decoupled plasmon-phonon (DPP) models. The degree of inversion δ is given in parenthesis. Vertical arrows mark the ν_1 peak (explained in the text). (b) The best fit obtained using the four-parameter model for dielectric function, is also given for the MFO800 sample as an example.

dielectric function in the form [60,63]:

$$\varepsilon\left(\omega\right)=\varepsilon_\infty\left(\prod_{j=1}^{n}\frac{\omega_{LOj}^2-\omega^2-i\gamma_{LOj}\omega}{\omega_{TOj}^2-\omega^2-i\gamma_{TOj}\omega}-\frac{\omega_P^2}{\omega(\omega+i\gamma_P)}\right). \quad (6)$$

The first term in this model represents the phonons contribution, where $\omega_{TOj}(\omega_{LOj})$ and $\gamma_{TOj}(\gamma_{LOj})$ are the TO(LO) frequencies and dampings of phonons. The second term is the Drude term which describes the plasmon mode, where ω_P and γ_P are the frequency and damping of the plasmon mode. In the DPP model, the LO frequencies are actually the frequencies of bare phonons decoupled from plasmon, whereas in the CPP models the LO frequencies are for the coupled plasmon-LO phonon modes. In both models, the TO mode frequencies have the same meaning and are unaffected by free carriers. Without the Drude term, Eq. (6) reduces to the so-called four-parameter model for the dielectric function of phonon spectra [60,63].

In order to properly analyze the IR reflectivity spectra of MgFe$_2$O$_4$ nanocrystalline samples, the effect of porosity on the IR spectra must be taken into account. In that sense, the Bruggeman effective medium approximation [64,65] is very often used to describe the optical properties of porous nanomaterials. For a homogenous mixture of a material (ε_M) with volume fraction f_M, and air ($\varepsilon = 1$) with fraction (1-f_M), the effective dielectric function ε_{eff} can be obtained from the equation

$$\left(\frac{\varepsilon_M-\varepsilon_{eff}}{\varepsilon_M+2\varepsilon_{eff}}\right)f_M+\left(\frac{1-\varepsilon_{eff}}{1+2\varepsilon_{eff}}\right)(1-f_M)=0, \quad (7)$$

in which ε_M is described by an appropriate model, in our case by

equation (3) or (6). The calculated reflectivity R_{calc} can be obtained using the Fresnel formula

$$R_{calc}=\left|\frac{\sqrt{\varepsilon_{eff}}-1}{\sqrt{\varepsilon_{eff}}+1}\right|^2. \quad (8)$$

In the IR spectra fitting procedure, the parameters were automatically tuned until the difference between the experimental (R_{exp}) and calculated (R_{calc}) reflectivity, given by the chi-squared value

$$\chi^2=\frac{1}{N}\sum_{i=1}^{N}\left(R_{i,exp}-R_{i,calc}\right)^2, \quad (9)$$

where N is the number of points in spectra, became minimized within the experimental error.

The obtained best fits for both models are shown in Fig. 3(a) (red full and green dashed lines), whereas the best fit parameters are given in Table 1 (CPP model) and Table 2 (DPP model). It can be seen that both models provide satisfactory fits of the experimental spectra. For comparison, the best fit obtained using the four-parameter model for dielectric function, which does not include the free carriers contribution, is also shown in Fig. 3(b) for the MFO800 sample as an example. It is obvious that such a model fails to reproduce experimental spectra at lower frequencies.

Fig. 4 shows the variation of plasma frequency ω_P and damping γ_P for MgFe$_2$O$_4$ samples sintered at different temperatures, for the both used models. As can be seen, similar behavior of ω_P and γ_P was obtained from the both models. The plasma frequency slightly decreases with sintering

Table 1
Fitting parameters obtained by using the Coupled Plasmon-Phonon (CPP) model, for $MgFe_2O_4$ nanocrystalline samples sintered at different temperatures. Plasma/phonon frequencies and damping values are given in cm^{-1}. The estimated errors are also presented.

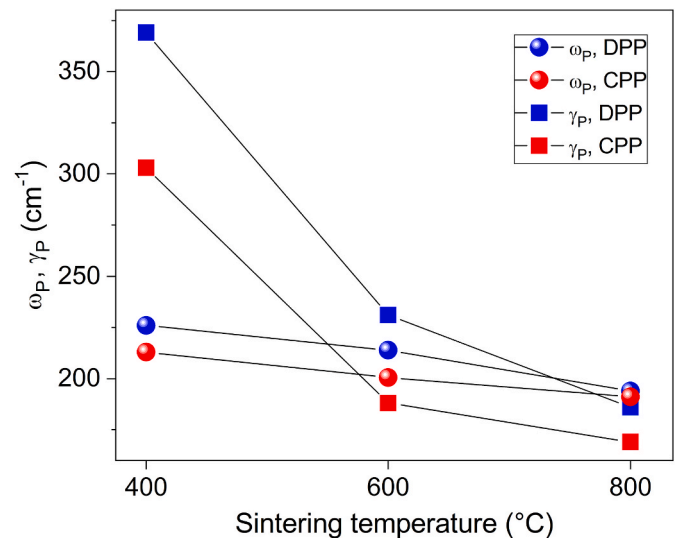| Parameters	MFO400	MFO600	MFO800	Est. err.
f_M	0.63	0.7	0.82	±0.02
ω_P	213	200.6	191.1	±5
γ_P	303	188	169	±5
ω_{TO1} (γ_{TO1})	541 (114)	543 (108)	546 (100)	±3 (±5)
ω_{LO1} (γ_{LO1})	684 (48)	679 (45)	677 (50)	±3 (±5)
ω_{TO2} (γ_{TO2})	422 (122)	445 (89)	436 (81)	±5 (±5)
ω_{LO2} (γ_{LO2})	472 (79)	468 (46)	465 (43)	±5 (±5)
ω_{TO3} (γ_{TO3})	321 (192)	317 (123)	338 (131)	±5 (±5)
ω_{LO3} (γ_{LO3})	412 (262)	398 (181)	399 (144)	±5 (±5)
ω_{TO4} (γ_{TO4})	254 (225)	255 (128)	255 (125)	±12 (±12)
ω_{LO4} (γ_{LO4})	266 (166)	256 (98)	258 (99)	±12 (±12)
ω_{LO5} (γ_{LO5})	112 (237)	121 (194)	121 (168)	±5 (±5)

Table 2
Fitting parameters obtained by using the Decoupled Plasmon-Phonon (DPP) model, for $MgFe_2O_4$ nanocrystalline samples sintered at different temperatures. Plasma/phonon frequencies and damping values are given in cm^{-1}. The estimated errors are also presented.

Parameters	MFO400	MFO600	MFO800	Est. err.
f_M	0.62	0.72	0.82	±0.02
ω_P	226	214	194	±5
γ_P	369	231	186	±5
ω_{TO1} (γ_{TO1})	537 (118)	538 (110)	542 (102)	±3 (±5)
ω_{LO1} (γ_{LO1})	663 (36)	663 (47)	662 (47)	±3 (±5)
ω_{TO2} (γ_{TO2})	423 (135)	448 (111)	436 (97)	±5 (±5)
ω_{LO2} (γ_{LO2})	470 (67)	468 (45)	463 (41)	±5 (±5)
ω_{TO3} (γ_{TO3})	323 (204)	315 (111)	332 (122)	±5 (±5)
ω_{LO3} (γ_{LO3})	378 (251)	373 (175)	380 (147)	±5 (±5)
ω_{TO4} (γ_{TO4})	250 (146)	253 (122)	257 (120)	±12 (±12)
ω_{LO4} (γ_{LO4})	252 (125)	256 (99)	258 (98)	±12 (±12)

Fig. 4. (Color online) Variation of plasma frequency (ω_P) and damping (γ_P) of $MgFe_2O_4$ nanocrystalline samples sintered at different temperatures, obtained by using the CPP and DPP models.

similar behavior of this mode is found in most other spinels for which this mode is either weak or absent. Other modes exhibit large TO-LO splitting, as common for ionic crystals. The TO frequencies, obtained from both CPP and DPP models, are rather similar for each $MgFe_2O_4$ sample. Such a behavior is expected, as the TO frequencies are not affected by the plasmon-phonon interaction.

In Fig. 5(a) are presented the frequencies of the coupled plasmon-LO phonon modes Ω_{LOj} (obtained from the CPP model, Eq. (3) and Eq. (5)), and the decoupled LO phonon modes ω_{LOj} (from the DPP model, Eq. (6)). It can be seen that for the ν_1 and ν_3 modes, the coupled LO frequencies have higher values than the decoupled ones. The difference between these frequencies is approximately the same for all samples. On the other hand, the coupled/decoupled LO frequencies are quite similar for the ν_2 mode. In the case of ν_4 mode, these frequencies also appear to be similar. However, the ν_4 mode is too weak and broad, whereas the fitting errors are too high, for a definitive conclusion to be drawn. As mentioned before, the LO frequencies obtained from the DPP model are actually the frequencies of bare phonons decoupled from plasmon, whereas the LO frequencies obtained from the CPP model are for the combined plasmon–LO phonon modes. The fact that in the case of ν_1 and ν_3 modes, the LO values obtained by the CPP model are higher than those obtained by the DPP model, implies that these modes are more strongly coupled with free carriers than the ν_2 mode.

The TO frequency behavior for all four IR modes, obtained from the CPP and DPP models (Tables 1 and 2), is presented in Fig. 5(b). In Fig. 3(a), one can notice that the ν_1 peak (marked with vertical arrows), is slightly shifted towards higher frequencies as the sintering temperature and degree of inversion increases, which is also corroborated by the slight increase of ω_{TO1} frequencies obtained from the CPP and DPP models. In the case of $MgFe_2O_4$, the tetrahedral cation-oxygen bonds are of higher force constants and lower bond length than the cation-oxygen octahedral bonds, and the corresponding vibrations of the tetrahedra are of higher frequency [27]. The bonding force between the cation and oxygen also depends on the nature of the cation and its valency [30]. Waldron [27] calculated force constants for some ferrites, and showed for $MgFe_2O_4$ that the force constants of the tetrahedral Fe–O vibrations are higher than the tetrahedral Mg–O vibrations [27]. Therefore, the observed increase of the frequency of the ν_1 mode with the increased degree of inversion is consistent with the tetrahedral origin of this mode, because more Mg^{2+} are replaced with Fe^{3+}. On the other hand, the TO frequency of the ν_2 mode, which mainly originates from the octahedral Fe–O vibrations, shows no consistent shift with the increased sintering

temperature. On the other hand, the plasma damping decreases significantly for the MFO600 sample, and then further decreases to a lesser extent for the MFO800 sample, resulting in more pronounced Drude tail in the IR spectra of the MFO600 and MFO800 samples. The material volume fraction f_M has increased with increasing sintering temperature (see Tables 1 and 2), indicating that the MFO600 and MFO800 samples became less porous. This is in accordance with previous research on these samples where it was shown that increased sintering temperature leads to larger crystallite sizes and more agglomeration [51]. In samples with larger and more fussed crystallites, with better agglomeration and less pores, the influence of grain boundaries is smaller, having as a consequence the higher electron mobility and longer scattering relaxation time τ. This, in turn, explains the observed significant decrease of plasma dampings, since $\gamma_P = 1/\tau$.

From Tables 1 and 2, it can be seen that in the case of ν_4 mode, the splitting between the TO and LO frequencies is small, meaning that the oscillator strength, being proportional to ($\omega_{LO}^2 - \omega_{TO}^2$), is also small. The

Fig. 5. (Color online) (a) Coupled (Ω_{LOj}) and decoupled (ω_{LOj}) LO phonon frequencies, and (b) the TO phonon frequencies, obtained from the CPP and DPP models, for MgFe$_2$O$_4$ nanocrystalline samples sintered at different temperatures.

temperature and degree of inversion. It slightly increases for the MFO600 sample, and then slightly decreases for the MFO800 sample. The increase of the TO frequency in the MFO600 sample can be explained by an increasing contribution of the Fe–O tetrahedral vibrations to the ν_2 mode, because with the increasing degree of inversion

more Fe^{3+} cations are situated at the tetrahedral sites. With further increase of the degree of inversion (MFO800), one can presume even more complex behavior of the ν_2 mode, where, besides the Fe–O tetrahedral vibrations, the Mg–O octahedral vibrations can participate too. The behavior of the ν_3 mode becomes also more complex with increased
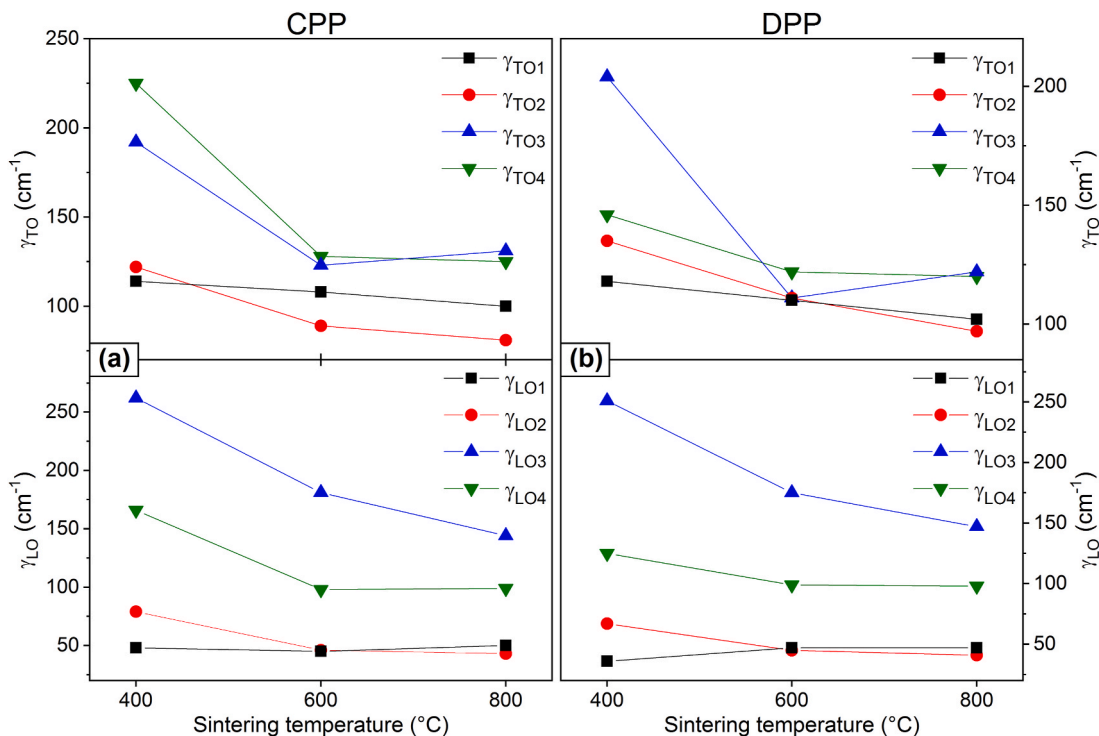
Fig. 6. (Color online) Variation of the TO and LO phonon dampings for MgFe$_2$O$_4$ nanocrystalline samples sintered at different temperatures, obtained from (a) CPP and (b) DPP models.

degree of inversion. It was already pointed out by Preudhomme and Tarte [31,32] that with higher degree of inversion, coupling between different tetrahedra and octahedra can make infrared vibrations of more complex nature. Consequently, it is no longer realistic to ascribe such vibrations and its frequencies to the localized vibrations of definite co-ordinated group (tetrahedral or octahedral), but to the vibrations which involve simultaneous participation of different cations (Mg or Fe) and coordinated groups.

The TO and LO phonon dampings obtained from the CPP and DPP models, are shown in Fig. 6. It can be seen that the TO/LO dampings tend to decrease with the increasing sintering temperature. Such a behavior is a consequence of the fact that the increase of sintering temperature produced samples with larger and more fussed crystallites with less pores and smaller influence of grain boundaries. All this in turn can lead to the smaller scattering rates for phonons, which means longer phonon lifetimes and decreased phonon dampings.

From the analysis of the IR spectra based on the CPP and DPP models (Fig. 5(a)), it was obtained that the ν_1 and ν_3 modes are more strongly coupled with free carriers than the ν_2 mode. We propose that this finding may be related to the presence of antisite defects, which are formed in inverse spinels. Namely, when in inverse spinels the trivalent cation replaces the divalent one in tetrahedra, it introduces excess positive charge at this site. Conversely, the octahedral site becomes a site with excess negative charge by introduction of the divalent cation instead of the trivalent one. In inverse $MgFe_2O_4$, positively charged $[Fe^{3+}_{tetra}]^+$ and negatively charged $[Mg^{2+}_{octa}]^-$ antisite defect centers can be formed in tetrahedra and octahedra (presented in Fig. 7), which behave as electron and hole trap centers, respectively [66–68].

If a particular mode has a significant contribution of the Fe–O tetrahedral vibrations, as it is the case for the ν_1 and ν_3 modes, it is quite reasonable to assume that such an infrared mode would be more strongly coupled with free carriers, due to the existence of positively charged $[Fe^{3+}_{tetra}]^+$ antisite defects. In the case of the ν_2 mode, which is mostly of the octahedral origin, the presence of negatively charged $[Mg^{2+}_{octa}]^-$ antisite defects is expected to weaken the plasmon-phonon interaction. With increased degree of inversion, one might expect a stronger plasmon-phonon coupling of the ν_1 and ν_3 modes as more $[Fe^{3+}_{tetra}]^+$ antisite defects should be formed. However, our analysis has shown that the plasmon-phonon coupling strength did not increase with the increased degree of inversion. We suppose that with the increased degree of inversion, when ν_1 and ν_3 vibrations become more complex, a subtle interplay between the tetrahedral Fe–O and octahedral Mg–O vibrations influences the plasmon-phonon coupling, leading to different strength of coupling between particular phonon modes and free carriers. As the exact mechanism of plasmon-phonon coupling in nanosized $MgFe_2O_4$ is not completely clear at the moment, it presents strong motivation for our future research.

4. Conclusions

In summary, we have investigated room-temperature far-IR reflectivity spectra of partially inverse nanocrystalline $MgFe_2O_4$ samples prepared by sol-gel method and sintered at different temperatures (400, 600 and 800 °C). The degree of inversion of $MgFe_2O_4$ samples was estimated from Raman spectra, and was found to increase with the increase of the sintering temperature. The IR spectra exhibited the presence of free carriers (the so-called Drude tail). The plasmon–LO phonon interaction was investigated by using the factorized coupled and decoupled plasmon-phonon models, combined with the Bruggeman effective medium approximation. From the analysis of the IR spectra, the coupled and decoupled phonon frequencies and dampings, as well as plasma frequencies and corresponding dampings of the plasmon mode were obtained. It was shown that with the increased sintering temperature, the phonon and plasmon dampings significantly decreased due to crystallite size increase, smaller porosity, and better connectivity
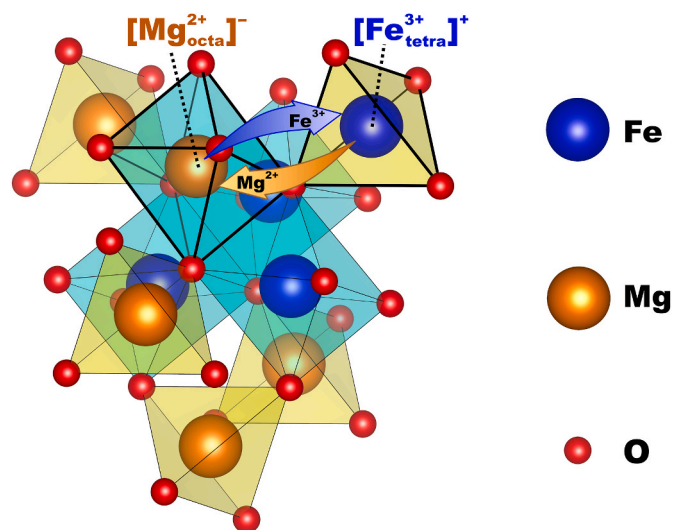
Fig. 7. (Color online) Schematic representation of inversion of trivalent Fe^{3+} and divalent Mg^{2+} cations between octahedra and tetrahedra, and the formation of the $[Fe^{3+}_{tetra}]^+$ and $[Mg^{2+}_{octa}]^-$ antisite defect centers in partially inverse $MgFe_2O_4$. The crystal structure visualized by VESTA 3 [50].

between crystallites. Of particular importance is the finding that the ν_1 and ν_3 modes are more strongly coupled with free carriers than the ν_2 mode. We proposed that in inverse $MgFe_2O_4$ samples, the presence of positively charged $[Fe^{3+}_{tetra}]^+$ and negatively charged $[Mg^{2+}_{octa}]^-$ antisite defects influences the plasmon-phonon interaction. The stronger plasmon-phonon coupling is expected for infrared modes where the contribution of Fe–O tetrahedral vibrations becomes substantial. With the increased degree of inversion, a subtle interplay between the tetrahedral Fe–O and octahedral Mg–O vibrations can lead to different strength of coupling between particular phonon modes and free carriers. Our findings provide a basis for better understanding of plasmon-phonon coupling mechanism in disordered inverse spinels like $MgFe_2O_4$.

CRediT authorship contribution statement

Novica Paunović: Writing – review & editing, Writing – original draft, Visualization, Software, Methodology, Investigation, Formal analysis, Data curation, Conceptualization. **Zorana Dohčević-Mitrović:** Writing – review & editing, Supervision, Project administration, Methodology, Investigation, Formal analysis, Conceptualization. **Dejan M. Djokić:** Writing – review & editing, Visualization, Project administration, Formal analysis. **Sonja Aškrabić:** Writing – review & editing, Visualization, Investigation, Formal analysis. **Saša Lazović:** Writing – review & editing, Visualization, Investigation. **Ann Rose Abraham:** Writing – review & editing, Resources. **Balakrishnan Raneesh:** Writing – review & editing, Resources. **Nandakumar Kalarikkal:** Writing – review & editing, Project administration, Funding acquisition. **Sabu Thomas:** Writing – review & editing, Supervision.

Appendix A. Supplementary data

Supplementary data to this article can be found online at https://doi.org/10.1016/j.mssp.2022.106889.

References

[1] Y.M.Z. Ahmed, E.M.M. Ewais, Z.I. Zaki, In situ synthesis of high density magnetic ferrite spinel ($MgFe_2O_4$) compacts using a mixture of conventional raw materials and waste iron oxide, J. Alloys Compd. 489 (2010) 269–274.

[2] N.M. Deraz, A. Alarifi, Novel preparation and properties of magnesioferrite nanoparticles, J. Anal. Appl. Pyrol. 97 (2012) 55–61.

[3] S.-S. Hong, Catalytic removal of carbon particulates over $MgFe_2O_4$ catalysts, React. Kinet. Catal. Lett. 84 (2005) 311–317.

[4] N. Ma, Y. Yue, W. Hua, Z. Gao, Selective oxidation of styrene over nanosized spinel-type $Mg_xFe_{3-x}O_4$ complex oxide catalysts, Appl. Catal. Gen. 251 (2003) 39–47.

[5] V. Srivastava, Y.C. Sharma, M. Sillanpää, Application of nano-magnesso ferrite (n-$MgFe_2O_4$) for the removal of Co^{2+} ions from synthetic wastewater: kinetic, equilibrium and thermodynamic studies, Appl. Surf. Sci. 338 (2015) 42–54.

[6] D.H.K. Reddy, Y.-S. Yun, Spinel ferrite magnetic adsorbents: alternative future materials for water purification? Coord. Chem. Rev. 315 (2016) 90–111.

[7] R. Dillert, D.H. Taffa, M. Wark, T. Bredow, D.W. Bahnemann, Research Update: photoelectrochemical water splitting and photocatalytic hydrogen production using ferrites (MFe_2O_4) under visible light irradiation, Apl. Mater. 3 (2015), 104001.

[8] G. Takalkar, R.R. Bhosale, F. AlMomani, S. Rashid, R.A. Shakoor, Ni incorporation in $MgFe_2O_4$ for improved CO_2-splitting activity during solar fuel production, J. Mater. Sci. 55 (2020) 11086–11094.

[9] Y. Shimizu, H. Arai, T. Seiyama, Theoretical studies on the impedance-humidity characteristics of ceramic humidity sensors, Sensor. Actuator. 7 (1985) 11–22.

[10] T. Maehara, K. Konishi, T. Kamimori, H. Aono, T. Naohara, H. Kikkawa, Y. Watanabe, K. Kawachi, Heating of ferrite powder by an AC magnetic field for local hyperthermia, Jpn. J. Appl. Phys. 41 (2002) 1620–1621.

[11] K. Konishi, T. Maehara, T. Kamimori, H. Aono, T. Naohara, H. Kikkawa, Y. Watanabe, K. Kawachi, Heating ferrite powder with AC magnetic field for thermal coagulation therapy, J. Magn. Magn Mater. 272–276 (2004) 2428–2429.

[12] S. Kanagesan, M. Hashim, S. Tamilselvan, N.B. Alitheen, I. Ismail, G. Bahmanrokh, Cytotoxic effect of nanocrystalline $MgFe_2O_4$ particles for cancer cure, J. Nanomater. (2013), 865024, 2013.

[13] F. Foroughi, S.A. Hassanzadeh-Tabrizi, A. Bigham, In situ microemulsion synthesis of hydroxyapatite-$MgFe_2O_4$ nanocomposite as a magnetic drug delivery system, Mater. Sci. Eng. C 68 (2016) 774–779.

[14] Q. Chen, Z.J. Zhang, Size-dependent superparamagnetic properties of $MgFe_2O_4$ spinel ferrite nanocrystallites, Appl. Phys. Lett. 73 (1998) 3156–3158.

[15] N. Sivakumar, S.R.P. Gnanakan, K. Karthikeyan, S. Amaresh, W.S. Yoon, G.J. Park, Y.S. Lee, Nanostructured $MgFe_2O_4$ as anode materials for lithium-ion batteries, J. Alloys Compd. 509 (2011) 7038–7041.

[16] Y. Yin, N. Huo, W. Liu, Z. Shi, Q. Wang, Y. Ding, J. Zhang, S. Yang, Hollow spheres of $MgFe_2O_4$ as anode material for lithium-ion batteries, Scripta Mater. 110 (2016) 92–95.

[17] Y. Pan, Y. Zhang, X. Wei, C. Yuan, J. Yin, D. Cao, G. Wang, $MgFe_2O_4$ nanoparticles as anode materials for lithium-ion batteries, Electrochim. Acta 109 (2013) 89–94.

[18] A. Bloesser, H. Kurz, J. Timm, F. Wittkamp, C. Simon, S. Hayama, B. Weber, U.-P. Apfel, R. Marschall, Tailoring the size, inversion parameter, and absorption of phase-pure magnetic $MgFe_2O_4$ nanoparticles for photocatalytic degradations, ACS Appl. Nano Mater. 3 (2020) 11587–11599.

[19] L. Zheng, K. Fang, M. Zhang, Z. Nan, L. Zhao, D. Zhou, M. Zhu, W. Li, Tuning of spinel magnesium ferrite nanoparticles with enhanced magnetic properties, RSC Adv. 8 (2018) 39177–39181.

[20] N. Sivakumar, A. Narayanasamy, J.M. Greneche, R. Murugaraj, Y.S. Lee, Electrical and magnetic behaviour of nanostructured $MgFe_2O_4$ spinel ferrite, J. Alloys Compd. 504 (2010) 395–402.

[21] M. Radović, Z. Dohčević-Mitrović, N. Paunović, S. Bošković, N. Tomić, N. Tadić, I. Belča, Infrared study of plasmon–phonon coupling in pure and Nd-doped CeO_{2-y} nanocrystals, J. Phys. Appl. Phys. 48 (2015), 065301.

[22] Z.V. Popović, M. Grujić-Brojčin, N. Paunović, M.M. Radonjić, V.D. Araújo, M.I. B. Bernardi, M.M. de Lima, A. Cantarero, Far-infrared spectroscopic study of CeO_2 nanocrystals, J. Nanoparticle Res. 17 (2015) 23.

[23] J. Mitric, N. Paunovic, M. Mitric, B. Vasic, U. Ralevic, J. Trajic, M. Romcevic, W. D. Dobrowolski, I.S. Yahia, N. Romcevic, Surface optical phonon – plasmon interaction in nanodimensional CdTe thin films, Phys. E Low-dimens. Syst. Nanostruct. 104 (2018) 64–70.

[24] X. Zhou, L. Liu, J. Sun, N. Zhang, H. Sun, H. Wu, W. Tao, Effects of $(Mg_{1/3}Sb_{2/3})^{4+}$ substitution on the structure and microwave dielectric properties of $Ce_2Zr_3(MoO_4)_9$ ceramics, Journal of Advanced Ceramics 10 (2021) 778–789.

[25] H. Tian, J. Zheng, L. Liu, H. Wu, H. Kimura, Y. Lu, Z. Yue, Structure characteristics and microwave dielectric properties of $Pr_2(Zr_{1-x}Ti_x)_3(MoO_4)_9$ solid solution ceramic with a stable temperature coefficient, J. Mater. Sci. Technol. 116 (2022) 121–129.

[26] L. Huang, Z.F. Li, P.P. Chen, Y.H. Zhang, W. Lu, Far infrared reflection spectra of $InAs_xSb_{1-x}$ (x = 0-0.4) thin films, J. Appl. Phys. 113 (2013), 213112.

[27] R.D. Waldron, Infrared spectra of ferrites, Phys. Rev. 99 (1955) 1727–1735.

[28] S. Hafner, Ordnung/Unordnung und Ultrarotabsorption IV. Die Absorption einiger Metalloxyde mit Spinellstruktur, Z. für Kristallogr. - Cryst. Mater. 115 (1961) 331–358.

[29] W.B. White, B.A. DeAngelis, Interpretation of the vibrational spectra of spinels, Spectrochim. Acta Mol. Spectros 23 (1967) 985–995.

[30] J. Preudhomme, P. Tarte, Infrared studies of spinels–I: a critical discussion of the actual interpretations, Spectrochim. Acta Mol. Spectros 27 (1971) 961–968.

[31] J. Preudhomme, P. Tarte, Infrared studies of spinels–II: the experimental bases for solving the assignment problem, Spectrochim. Acta Mol. Spectros 27 (1971) 845–851.

[32] J. Preudhomme, P. Tarte, Infrared studies of spinels–III: the normal II–III spinels, Spectrochim. Acta Mol. Spectros 27 (1971) 1817–1835.

[33] J. Preudhomme, P. Tarte, Infrared studies of spinels–IV: normal spinels with a high-valency tetrahedral cation, Spectrochim. Acta Mol. Spectros 28 (1972) 69–79.

[34] P. Thibaudeau, F. Gervais, Ab initioinvestigation of phonon modes in the $MgAl_2O_4$ spinel, J. Phys. Condens. Matter 14 (2002) 3543–3552.

[35] O.S. Josyulu, J. Sobhanadri, The far-infrared spectra of some mixed cobalt zinc and magnesium zinc ferrites, Phys. Status Solidi 65 (1981) 479–483.

[36] Z.V. Marinković Stanojević, N. Romčević, B. Stojanović, Spectroscopic study of spinel $ZnCr_2O_4$ obtained from mechanically activated $ZnO–Cr_2O_3$ mixtures, J. Eur. Ceram. Soc. 27 (2007) 903–907.

[37] M. Lenglet, F. Hochu, Correlation between ionic-covalent parameters and infrared spectroscopic data in II-III transition metal spinel-type oxides, Mater. Res. Bull. 32 (1997) 863–872.

[38] A. Pradeep, P. Priyadharsini, G. Chandrasekaran, Sol–gel route of synthesis of nanoparticles of $MgFe_2O_4$ and XRD, FTIR and VSM study, J. Magn. Magn Mater. 320 (2008) 2774–2779.

[39] N.W. Grimes, A.J. Collett, Correlation of infra-red spectra with structural distortions in the spinel series $Mg(Cr_xAl_{2-x})O_4$, Phys. Status Solidi 43 (1971) 591–599.

[40] V.A.M. Brabers, Ionic ordering and infrared spectra of some II-IV spinels, Phys. Status Solidi 12 (1972) 629–636.

[41] M.E. Striefler, G.R. Barsch, S.-I. Akimoto, Infrared absorption spectra of the spinels Fe_2SiO_4 and Co_2SiO_4, Spectrochim. Acta Mol. Spectros 36 (1980) 275–278.

[42] K.A. Mohammed, A.D. Al-Rawas, A.M. Gismelseed, A. Sellai, H.M. Widatallah, A. Yousif, M.E. Elzain, M. Shongwe, Infrared and structural studies of Mg1–xZnxFe2O4 ferrites, Phys. B Condens. Matter 407 (2012) 795–804.

[43] H. Dawoud, L.S.A. Ouda, S. Shaat, FT-IR studies of nickel substituted polycrystalline zinc spinel ferrites for structural and vibrational investigations, Chemical Science Transactions 8 (2017) 179–188.

[44] A. Pradeep, G. Chandrasekaran, FTIR study of Ni, Cu and Zn substituted nano-particles of $MgFe_2O_4$, Mater. Lett. 60 (2006) 371–374.

[45] Z.V. Popović, G. De Marzi, M.J. Konstantinović, A. Cantarero, Z. Dohčević-Mitrović, M. Isobe, Y. Ueda, Phonon properties of the spinel oxide $MgTi_2O_4$ with the S=1/2 pyrochlore lattice, Phys. Rev. B 68 (2003), 224302.

[46] Z.Ž. Lazarević, Č. Jovalekić, A. Rečnik, V.N. Ivanovski, A. Milutinović, M. Romčević, M.B. Pavlović, B. Cekić, N.Ž. Romčević, Preparation and characterization of spinel nickel ferrite obtained by the soft mechanochemically assisted synthesis, Mater. Res. Bull. 48 (2013) 404–415.

[47] Z.V. Marinković Stanojević, N. Romčević, B. Stojanović, Spectroscopic study of spinel ZnCr2O4 obtained from mechanically activated ZnO–Cr2O3 mixtures, J. Eur. Ceram. Soc. 27 (2007) 903–907.

[48] E.Z. Katsnelson, A.G. Karoza, L.A. Meleshchenko, L.A. Bashkirov, IR reflection spectra of manganese-zinc ferrites, Phys. Status Solidi 152 (1989) 657–666.

[49] H.D. Lutz, B. Müller, H.J. Steiner, Lattice vibration spectra. LIX. Single crystal infrared and Raman studies of spinel type oxides, J. Solid State Chem. 90 (1991) 54–60.

[50] K. Momma, F. Izumi, VESTA 3 for three-dimensional visualization of crystal, volumetric and morphology data, J. Appl. Crystallogr. 44 (2011) 1272–1276.

[51] A.R. Abraham, B. Raneesh, P.M.G. Nambissan, D. Sanyal, S. Thomas, N. Kalarikkal, Defects characterisation and studies of structural properties of sol–gel synthesised $MgFe_2O_4$ nanocrystals through positron annihilation and supportive spectroscopic methods, Phil. Mag. 100 (2020) 32–61.

[52] V.G. Ivanov, M.V. Abrashev, M.N. Iliev, M.M. Gospodinov, J. Meen, M.I. Aroyo, Short-range B-site ordering in the inverse spinel ferrite NiFe2O4, Phys. Rev. B 82 (2010), 024104.

[53] P. Chandramohan, M.P. Srinivasan, S. Velmurugan, S.V. Narasimhan, Cation distribution and particle size effect on Raman spectrum of CoFe2O4, J. Solid State Chem. 184 (2011) 89–96.

[54] V. D'Ippolito, G.B. Andreozzi, D. Bersani, P.P. Lottici, Raman fingerprint of chromate, aluminate and ferrite spinels, J. Raman Spectrosc. 46 (2015) 1255–1264.

[55] B.D. Hosterman, Raman Spectroscopic Study of Solid Solution Spinel Oxides, University of Nevada, Las Vegas, 2011.

[56] F. Nakagomi, S.W. da Silva, V.K. Garg, A.C. Oliveira, P.C. Morais, A. Franco, Influence of the Mg-content on the cation distribution in cubic $Mg_xFe_{3-x}O_4$ nanoparticles, J. Solid State Chem. 182 (2009) 2423–2429.

[57] A. Sankaramahalingam, J.B. Lawrence, Structural, optical, and magnetic properties of $MgFe_2O_4$ synthesized with addition of copper, synthesis and reactivity in inorganic, metal-organic, Nano-Metal Chemistry 42 (2012) 121–127.

[58] Z.Ž. Lazarević, Č. Jovalekić, V.N. Ivanovski, A. Rečnik, A. Milutinović, B. Cekić, N.Ž. Romčević, Characterization of partially inverse spinel $ZnFe_2O_4$ with high saturation magnetization synthesized via soft mechanochemically assisted route, J. Phys. Chem. Solid. 75 (2014) 869–877.

[59] J. Guo, L. Shi, L. Wu, S. Pan, X. Yuan, J. Zhao, Spin-polarized electron transport in highly reduced $MgFe_2O_{4-\delta}$, Mater. Res. Express 5 (2018), 126301.

[60] F. Gervais, High-temperature infrared reflectivity spectroscopy by scanning interferometry, in: K.J. Button (Ed.), Infrared and Millimeter Waves, Academic Press, New York, 1983, pp. 279–339.

[61] A.A. Kukharskii, Plasmon-phonon coupling in GaAs, Solid State Commun. 13 (1973) 1761–1765.

[62] O.K. Kim, W.G. Spitzer, Study of plasmon–LO-phonon coupling in Te-doped $Ga_{1-x}Al_xAs$, Phys. Rev. B 20 (1979) 3258–3266.

[63] F. Gervais, Optical conductivity of oxides, Mater. Sci. Eng. R Rep. 39 (2002) 29–92.

[64] D.A.G. Bruggeman, Berechnung verschiedener physikalischer Konstanten von heterogenen Substanzen. I. Dielektrizitätskonstanten und Leitfähigkeiten der Mischkörper aus isotropen Substanzen, Ann. Phys. 416 (1935) 636–664.

[65] J.E. Spanier, I.P. Herman, Use of hybrid phenomenological and statistical effective-medium theories of dielectric functions to model the infrared reflectance of porous SiC films, Phys. Rev. B 61 (2000) 10437–10450.

[66] T.A. Bazilevskaya, V.T. Gritsyna, D.V. Orlinski, L.V. Udalova, A.V. Voitsenya, The effect of composition, processing conditions, and irradiation, on lattice defects in spinel ceramics, J. Nucl. Mater. 253 (1998) 133–140.

[67] N. Pathak, B. Sanyal, S.K. Gupta, R.M. Kadam, $MgAl_2O_4$ both as short and long persistent phosphor material: role of antisite defect centers in determining the decay kinetics, Solid State Sci. 88 (2019) 13–19.

[68] N. Matsubara, T. Masese, E. Suard, O.K. Forslund, E. Nocerino, R. Palm, Z. Guguchia, D. Andreica, A. Hardut, M. Ishikado, K. Papadopoulos, Y. Sassa, M. Månsson, Cation distributions and magnetic properties of ferrispinel $MgFeMnO_4$, Inorg. Chem. 59 (2020) 17970–17980.

Unvailing the spin–phonon coupling in nanocrystalline BiFeO$_3$ by resonant two-phonon Raman active modes

Bojan Stojadinović [a,*], Dejan M. Djokić [a], Novica Paunović [a], Ivica Živković [b], Luka Ćirić [c], Vladan Kusigerski [d], Zorana Dohčević-Mitrović [a,*]

[a] *Institute of Physics Belgrade, University of Belgrade, Pregrevica 118, 11080 Belgrade, Serbia*
[b] *Laboratory for Quantum Magnetism, Institute of Physics, Ecole Polytechnique Féderale de Lausanne, CH-1015 Lausanne, Switzerland*
[c] *Laboratory of Nanostructures and Novel Electronic Materials, Ecole Polytechnique Féderale de Lausanne, CH-1015 Lausanne, Switzerland*
[d] *"Vinča" Institute of Nuclear Sciences, University of Belgrade, P.O. Box 522, Belgrade 11001, Serbia*

ARTICLE INFO

ABSTRACT

We report on temperature dependence of two-phonon Raman spectra in BiFeO$_3$ nanocrystals, above and below the Néel temperature T_N using a resonant laser excitation line (λ = 532 nm). Two-phonon modes exhibited anomalous frequency hardening and deviation from the anharmonic decay below T_N. Such behavior strongly supported the existence of spin-two-phonon interaction, because these modes are known to be very sensitive to the antiferromagnetic ordering. Within the mean-field theory for the nearest-neighbor interaction, the linear relationship between spin–spin correlation function and observed two-phonon frequency shift below T_N was obtained. This approach enabled to quantify the spin–phonon interaction by spin–phonon coupling strength for both two-phonon modes and justified the application of mean-field approach. Magnetic measurements revealed the coexistence of antiferromagnetic and weak ferromagnetic phases below T_N, which were found non competitive, additionally supporting the mean-field approach from which we deduced that the two-phonon modes in BiFeO$_3$ are correlated with antiferromagnetic ordering below T_N.

1. Introduction

Multiferroic materials attract a lot of attention because of their multifunctional properties and interesting fundamental physics [1,2]. Among all the single-phase multiferroic materials studied so far, BiFeO$_3$ takes a prominent place because both ferroelectric (Curie temperature, $T_C \approx 1150$ K) and magnetic (Néel temperature, $T_N \approx 640$ K) transition temperatures are well above room temperature (RT). In bulk phase BiFeO$_3$ has G-type antiferromagnetic ordering (AFM), with a long period cycloidal modulation (62 nm) superimposed below T_N. Above T_N, BiFeO$_3$ becomes paramagnetic (PM) [3]. In nanophased BiFeO$_3$ spin spiral structure can be suppressed [4] and Dzyaloshinskii–Moriya (DM) interaction becomes important. DM interaction induces non-collinear spin states which compete with the exchange interaction that favors anti-parallel spin alignment providing a coexistence of ferromagnetic (FM) and antiferromagnetic ordering [2,5]. Furthermore, the appearance of strong magnetoelectric effect in epitaxial BiFeO$_3$ thin films [6] and nanoparticles [4], positions nanophased BiFeO$_3$ as a leading candidate material for spintronics, magnetic field sensor devices and ferroelectric non-volatile memories [1,5,7–9]. However, the coupling between magnetic and ferroelectric degrees of freedom

in BiFeO$_3$ nanostructures still remains an open issue. Therefore, it is of great importance to study the interplay between lattice vibrations and magnetic excitations, because lattice distortion influences the ferroelectric polarization and accordingly affects its coupling to magnetic order. Furthermore, spin–phonon interaction is fundamental for driving relaxation in magnetic materials.

Among the optical spectroscopy methods, Raman spectroscopy proves to be a powerful experimental tool to elucidate spin–phonon (s-ph) interactions, since Raman mode can be sensitive to the spin correlations. In magnetic nanomaterials, such as BiFeO$_3$, optical phonon modes can be influenced by the exchange coupling between magnetic ions at and below the temperatures of magnetic phase transitions. The spin–phonon interaction usually manifests as atypical temperature dependence of Raman phonon frequency, linewidth or integrated intensity. From the deviation of the Raman mode frequency from the anharmonicity at and below the magnetic phase transition, it is possible to estimate the spin–phonon coupling strength in the antiferromagnets or ferromagnets. Being rather phenomenological, the approach developed by Lockwood and Cottam [10] treats the strength of the spin–phonon coupling through the emergence of the AFM order

---

parameter, that is the sublattice magnetization, but not the net one. Moreover, it turns out that a thorough microscopic treatment due to Djokic et al. [11] further corroborates this fact whereby the majority of the AFM ordering contribution to the phonon spectra is observed through the magnitude of the sublattice magnetization. The influence of any weak FM ordering (canted or so) in the system upon spin–phonon strength is thus greatly overwhelmed by the AFM ordering. Phonon anomalies around and below T_N were observed in the first-order Raman spectra of $BiFeO_3$ single crystal [12,13], ceramics [14] and thin films [15,16] and were ascribed to the influence of spin correlations on the phonon energies. The pioneering works of Cazayous [17] and Ramirez [18] pointed at possible strong spin-two-phonon interaction in $BiFeO_3$ single crystals and thin films, but all above mentioned works were restricted to qualitative description of the effects of spin correlations on the Raman active first and second-order phonons without any deeper analysis of spin–phonon coupling mechanism.

In the light of these facts, to examine more thoroughly the coupling between lattice and spin degrees of freedom in nanocrystalline $BiFeO_3$, we investigated temperature-dependent second-order Raman spectra of $BiFeO_3$ nanocrystals in a wide temperature range below, at and above the Néel temperature using a resonant excitation line. The anomalous phonon hardening and obvious deviation from the anharmonicity of two-phonon Raman modes below Néel temperature was elaborated within a mean-field approach in order to correlate the spin–spin correlation function with observed frequency shift and to estimate the nearest-neighbor spin–phonon coupling constant. Magnetic measurements have shed more light on the nature of spin–phonon coupling mechanism in $BiFeO_3$ nanocrystals.

2. Experimental details

$BiFeO_3$ nanocrystals were synthesized by a sol–gel method and detailed sample preparation and characterization of the crystal structure and phase composition was given in Ref. [19]. $BiFeO_3$ nanoparticles were of spherical shape with average particle size of 64 nm deduced from SEM measurements [19,20]. Raman spectra of $BiFeO_3$ nanocrystals were collected in a backscattering geometry using TriVista 557 triple spectrometer with the spectral resolution of 2 cm^{-1}. Second-order Raman spectra of $BiFeO_3$ nanocrystals pressed into pellets were recorded between 80 and 723 K in the 1000–1500 cm^{-1} frequency range using a Linkam THMSG600 microscope heating stage. The resonant 532 nm line of a solid-state Nd:YAG laser was used as an excitation source, with output laser power low enough (less than 2 mW) to avoid the heating effects and/or sample thermal degradation. The Raman spectra were corrected by thermal occupation factor for the second-order scattering $S(\omega) = S_0(\omega)/(n + 1)^2$, where $S_0(\omega)$ is measured intensity and $n = (e^{\hbar\omega/k_B T} - 1)^{-1}$ is the Bose–Einstein thermal occupation factor [21]. Magnetic measurements at and below 300 K were performed on a SQUID-based Quantum Design magnetometers MPMS-5T and MPMS XL-5.

3. Results and discussions

The room-temperature Raman spectrum of $BiFeO_3$ nanocrystalline sample in the range 40–1500 cm^{-1} is shown in Fig. 1.

Factor group analysis for the rhombohedral $R3c$ structure of $BiFeO_3$ predicts 13 Raman active modes ($4A_1 + 9E$), but the assignment of the Raman modes from the literature is somewhat controversial even in the case of $BiFeO_3$ single crystal Raman spectra measured or calculated in different polarizations [22–26]. As shown in Fig. 1, among the first order Γ-point phonons, modes around 79, 146, 175, 219, 261, 282, 332, 367, 435, 480 and 550 cm^{-1} are clearly seen. According to the polarized Raman spectra of $BiFeO_3$ single crystals [23,25], ceramics [27] and thin films [28] we assigned modes around 146, 175 and 219 cm^{-1} to A_1 modes and modes around 79, 261, 282, 332, 367, 435, 480 and 550 cm^{-1} to E modes. Beside these modes, weaker Raman

modes at around 575 and 656 cm^{-1} and a stronger mode at $\approx$630 cm^{-1} are also observed. The 575 and 656 cm^{-1} modes (marked with * in Fig. 1) can be ascribed to the mullite-type ($Bi_2Fe_4O_9$) secondary phase [29], the presence of which has been confirmed from the X-ray diffraction analysis of $BiFeO_3$ nanocrystalline sample [19]. The Raman mode at $\approx$630 cm^{-1} is not a zone center mode [27,30]. According to Bielecki et al. [30] this mode can be assigned to the Raman inactive A_2 LO phonon mode which appears in $BiFeO_3$ thin films, ceramics and nanoparticles [18,30–33]. As can be seen in Fig. 1, the intense second-order Raman modes were observed above 1000 cm^{-1} and from now on we will focus our attention on the temperature behavior of these Raman modes.

The high-order Raman modes of the ferroelectric materials are usually very weak, but in the spectrum of $BiFeO_3$ from Fig. 1 an intense multiphonon band around 1000–1500 cm^{-1} is observed. This prominent band is already reported in $BiFeO_3$ thin films and single crystals [17,18,25], as well as in $BiFeO_3$ nanoparticles [31,32]. The broad band at 300 K from Fig. 1 was deconvoluted with Lorentzian type profile into four modes: mode at 1090 cm^{-1}, a strong mode at 1252 cm^{-1} and two low-intensity phonon modes at 1150 and 1330 cm^{-1}. The second-order modes at 1090 and 1252 cm^{-1}, labeled as S_1 and S_2 in Fig. 1, are, within the error limits, at the double frequency of the first-order Raman E mode at around 550 cm^{-1} and inactive A_2 mode at around 630 cm^{-1} [22,30]. These modes were ascribed to two-phonon modes in accordance with literature data [13,17,18,30], whereas the remaining two modes can be assigned to $2A_g$ modes of $Bi_2Fe_4O_9$ secondary phase [29]. Yang et al. [34] have investigated the behavior of two-phonon modes in $BiFeO_3$ powders using different excitation lines and reported that the intensity of two-phonon S_1 and S_2 modes are significantly enhanced under the 532 nm excitation. The intensity enhancement of S_1 and S_2 modes was attributed to the resonant enhancement when the excitation energy (532 nm $\approx$2.34 eV) is close to the absorption edge of $BiFeO_3$. The resonant behavior of these modes was explained by exchange mechanism between Fe^{3+} ions. Weber et al. [35] also reported resonant enhancement of second-order Raman modes in $BiFeO_3$ single crystals using 532 nm excitation, but suggested that in-gap electronic states like defect states from oxygen vacancies can be involved in the resonance process. Accordingly, we used 532 nm laser line in order to track the temperature evolution of S_1 and S_2 Raman modes. Two-phonon S_1 and S_2 modes are related to the Fe–O vibrations, i.e. octahedral rotations [17,18,32] which are very sensitive to the change of magnetic ordering. Moreover, it is well known that any perturbation of spiral spin structure in antiferromagnetic $BiFeO_3$ and distortion of FeO_6 octahedra due to the change of Fe–O–Fe bond angle can lead to the appearance of ferromagnetism [2,4,5]. Therefore, we have analyzed the behavior of S_1 and S_2 modes at temperatures below and above the magnetic phase transition.

In Fig. 2a are presented second-order Raman spectra in the 80–723 K temperature range. With increased temperature S_1 and S_2 modes gradually shift to lower wavenumbers and approaching the 600 K, the wavenumber shift is followed by a pronounced decrease of intensity (Fig. 2a). Similar behavior of S_2 mode was first observed by Ramirez [18] and Cazayous [17] and was ascribed to the coupling of S_2 mode with the magnetic sublattice. The accurate wavenumber change of S_1 and S_2 modes with temperature was obtained by deconvoluting the spectra from Fig. 2a with Lorentzian line shape function and Raman spectra at several representative temperatures together with cumulative fits are presented in Fig. 2b.

In magnetic materials, the change of phonon mode frequency with temperature can be expressed as [36,37]:

$$\omega(T) - \omega_0 \equiv \Delta\omega(T) = \Delta\omega_{\text{lat}}(T) + \Delta\omega_{\text{anh}}(T) + \Delta\omega_{\text{e-ph}}(T) + \Delta\omega_{\text{s-ph}}(T), \quad (1)$$

where $\omega(T)$ is measured frequency at temperature T and ω_0 is the harmonic mode frequency at $T = 0$ K. The first term on the right-hand side of the Eq. (1) is the frequency-independent pure-volume contribution due to the lattice expansion/contraction. The second term
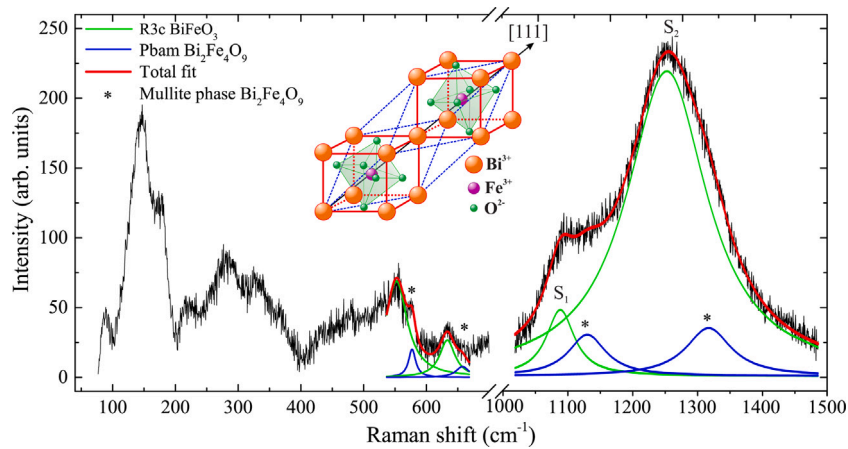
Fig. 1. Room-temperature Raman spectrum of nanocrystalline $BiFeO_3$ with Lorentzian fit (red line) of the first- and second-order phonon regions. The modes of mullite-type secondary phase $Bi_2Fe_4O_9$ are marked with (*). Inset represents the schematic of a pseudocubic unit cell including one formula unit with principle axis of polarization [111].
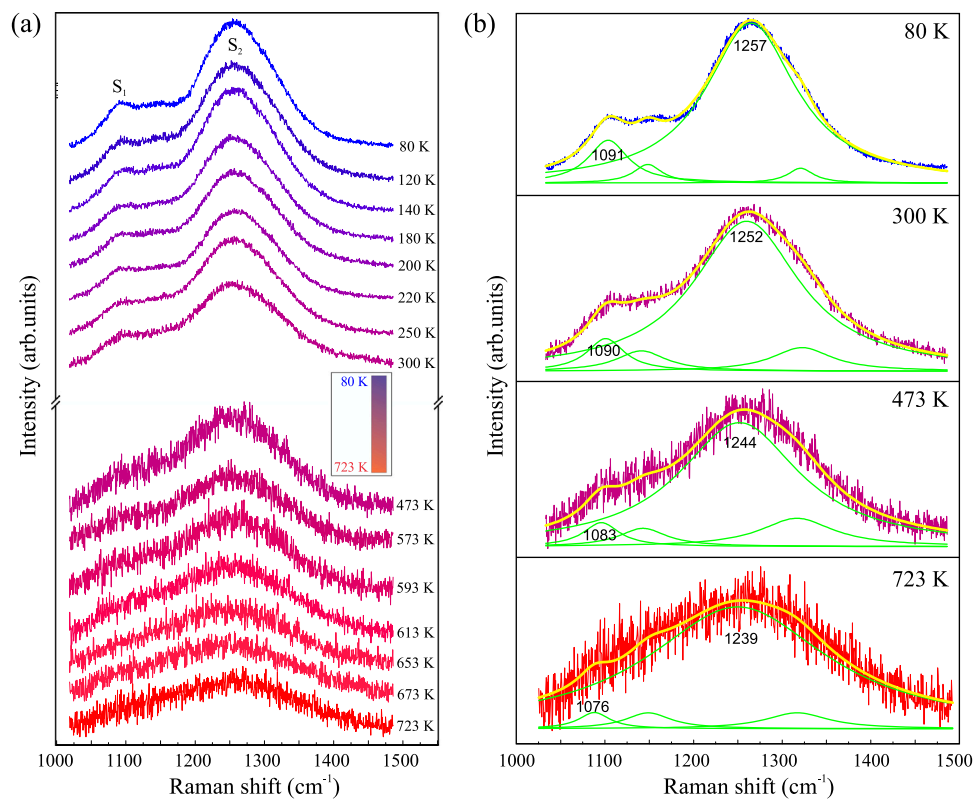
Fig. 2. Second-order Raman spectra of nanocrystalline $BiFeO_3$ (a) in the 80–723 K temperature range and (b) at selected temperatures. The solid lines represent Lorentzian fits of the experimental spectra.

is the anharmonic contribution due to phonon–phonon interactions. The last two terms account for the effects of renormalization of the phonon frequency due to electron–phonon and spin–phonon coupling.

In general, the change of phonon frequency due to pure-volume contribution is much smaller than the intrinsic anharmonic contribution, especially at low temperatures. $BiFeO_3$ in the form of powders or thin films is structurally stable up to 500 °C (773 K) [38] and any phonon frequency change due to lattice distortion is expected to be minimal, hence the first term can be neglected. The anharmonic interactions, significant at elevated temperatures, imply the phonon decay into two or three phonons, with a higher probability of the former. The phonon frequency change due to the decay of the phonon into two lower-energy

phonons (three-phonon processes) can be expressed as [39,40]:

$$\Delta\omega_{anh}(T) = A\left(1 + \frac{2}{e^{\frac{\hbar\omega(T)}{2k_B T}} - 1}\right),$$ (2)

where A is the anharmonic constant. In semiconductor materials like $BiFeO_3$, when the carrier concentration is low the third term can be ignored. Finally, the last term in Eq. (1) is the spin–phonon contribution, $\Delta\omega_{s-ph}(T)$, caused by the modulation of the exchange integral by lattice vibration [36]. In magnetic materials such as $BiFeO_3$, the phonon frequencies can be very sensitive to the spin correlations and in a case of Heisenberg model, Baltensberger and Helman [41] derived the relation for the shift of the phonon frequency due to the spin–phonon
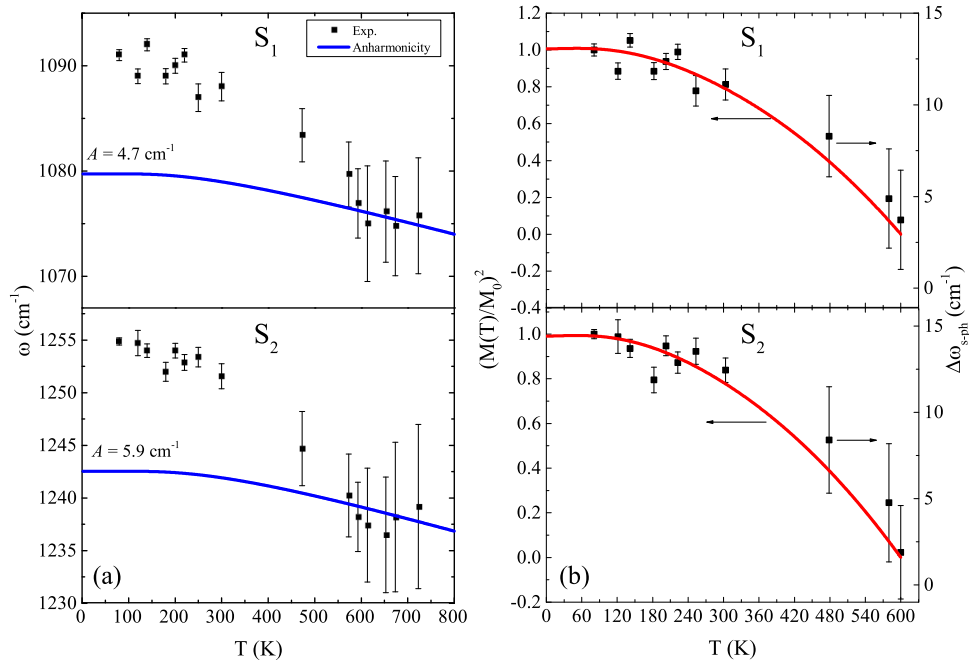
Fig. 3. (a) Temperature dependence of frequencies of the S_1 and S_2 two-phonon modes. The theoretically predicted anharmonic trend is presented by blue line together with the best fit anharmonic parameter (A). (b) Comparison of $(M(T)/M_0)^2$ (left) and $\Delta\omega_{s-ph}(T)$ (right) temperature dependences.

interaction,

$$\Delta\omega_{s-ph}(T) = -\lambda\langle S_i \cdot S_{i+1}\rangle, \qquad (3)$$

where λ stands for the spin–phonon coupling constant and $\langle S_i \cdot S_{i+1}\rangle$ is the spin–spin correlation function between adjacent spins.

The temperature dependence of S_1 and S_2 mode frequencies (squares) is shown in Fig. 3a. As can be seen, at lower temperatures (T < 300 K) frequencies of S_1 and S_2 modes exhibit a slower change and at temperature around 600 K display step like anomaly. This temperature should coincide with Néel temperature, since there is no any known structural transition in BiFeO$_3$ at this temperature.

In order to determine the strength of spin–phonon coupling, it is necessary to separate spin–phonon and anharmonic contributions from the change of the phonon frequency with temperature. Knowing that phonon frequencies can be affected by AFM ordering below T_N and that the anharmonic processes should dominate over the spin–phonon coupling at high temperatures ($T > T_N$) for which the BiFeO$_3$ is in the PM state, the data for T > 593 K from Fig. 3a were fitted by Eq. (2) (blue line on Fig. 3a extrapolated to $T = 0$ K) in order to determine the anharmonic contribution to the phonon frequencies change. It is obvious that frequency change of both S_1 and S_2 modes below T_N show distinct deviation away from the expected anharmonic behavior. Similar frequency behavior has been observed in the Raman spectra of other antiferomagnetic [10,36,42–45] and ferromagnetic materials [46,47]. Thus, anomalous frequency hardening of S_1 and S_2 modes below T_N points out at the presence of spin-two-phonon coupling in nanocrystalline BiFeO$_3$. The difference between measured two-phonon frequencies from Fig. 3a and the calculated and extrapolated anharmonic behavior gives us the temperature dependent frequency shift due to spin–phonon interaction, $\Delta\omega_{s-ph}(T) = \omega(T) - \omega_{anh}(T)$. The $\Delta\omega_{s-ph}$ vs T dependence (squares) for S_1 and S_2 two-phonon modes is presented in Fig. 3b.

Within the mean-field approximation introduced by Weiss [48], spin–spin correlation function $\langle S_i \cdot S_{i+1}\rangle$ for adjacent spins at the ith and $(i+1)$th sites is proportional to the square of normalized magnetization, $(M(T)/M_0)^2$, and can be expressed as [49]

$$\frac{\langle S_i \cdot S_{i+1}\rangle}{S^2} = \left(\frac{M(T)}{M_0}\right)^2, \qquad (4)$$

where $M(T)$ is in our case sublattice magnetization at temperature T and M_0 is the maximal value of sublattice magnetization. Having a look at Eqs. (3) and (4) it is obvious that $\Delta\omega_{s-ph}(T)$ should scale with $(M(T)/M_0)^2$ curve. The $(M(T)/M_0)^2$ curve was obtained using a numerical solution for Weiss equation in a case of Fe^{3+} ions having spin $S = 5/2$ [50] and then compared with experimentally obtained $\Delta\omega_{s-ph}(T)$ for both two-phonon modes, as presented in Fig. 3b. Obviously, for temperatures $T \leq T_N$, $\Delta\omega_{s-ph}(T)$ scales very good with $(M(T)/M_0)^2$ curve confirming that the significant deviation of S_1 and S_2 phonon frequencies from anharmonic behavior below T_N, i.e. the anomalous hardening, is actually due to spin–phonon interaction.

According to Eq. (3), from the plot $\Delta\omega_{s-ph}(T)$ vs $\langle S_i \cdot S_{i+1}\rangle(T)$ shown in Fig. 4 , the spin–phonon coupling constant λ can be determined for both two-phonon modes S_1 and S_2.

The red solid lines on Fig. 4 present the linear fit of the data from which the spin–phonon coupling constants $\lambda_{S_1}=(2.54 \pm 0.10)$ cm^{-1} and $\lambda_{S_2}=(2.51 \pm 0.10)$ cm^{-1} were determined. The linear behavior of $\Delta\omega_{s-ph}(T)$ vs $\langle S_i \cdot S_{i+1}\rangle(T)$ for the $T \leq T_N$ justifies the application of Eq. (3), implying that in the AFM phase spin–phonon coupling dominates over the anharmonicity and terminates in the paramagnetic phase. Furthermore, the fact that both two-phonon modes exhibit anomalous frequency hardening below magnetic ordering temperature and that the values for λ are very similar, indicates that there is a universal influence of the AFM magnetic ordering upon the two-phonon spectra.

Up to now it is well established that in antiferromagnetic BiFeO$_3$ nanoparticles with particle size close to or less than the period of spin cycloid appear ferromagnetic phase at room temperature [4,51–53]. BiFeO$_3$ nanoparticles can be considered to be composed of AFM core and FM shell giving rise to changes in the magnetic characteristics [53] or to the appearance of exchange bias and training effects [[52], and references within]. Since our BiFeO$_3$ nanoparticles are of the average size close to the spin cycloid period, we performed magnetic measurements in order to get better insight into the two-phonon Raman modes coupling with magnetic ordering below T_N.

Fig. 5a presents room-temperature magnetization (M) vs magnetic field (H) dependence for BiFeO$_3$ nanoparticles. From the M–H loop it can be seen that the magnetization curve (black circles) displays
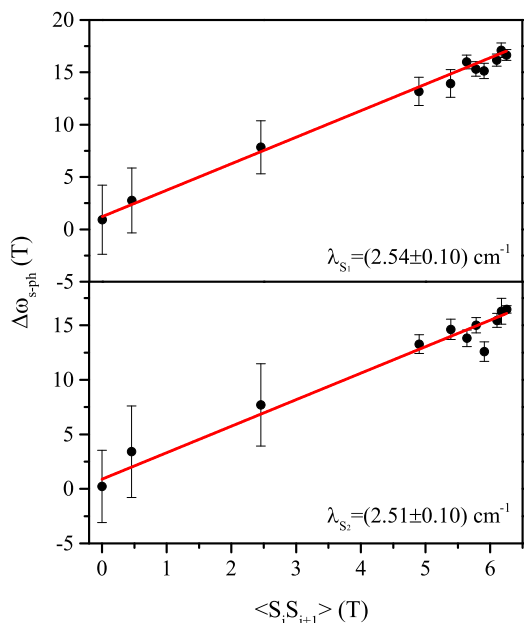
Fig. 4. The plot $\Delta\omega_{s-ph}(T)$ vs $\langle S_i \cdot S_{i+1}\rangle(T)$ for both two-phonon modes S_1 and S_2. The λ values for both modes were determined from the linear fit (red solid line) of the data. (For interpretation of the references to color in this figure legend, the reader is referred to the web version of this article.)

a hysteresis in the low-field region, indicating a presence of weak ferromagnetism. The FM component is superimposed over a linear background from antiferromagnetic BiFeO$_3$ phase and paramagnetic mullite phase. After subtracting the linear background, the ferromagnetic hysteresis curve (red squares) with the saturation magnetization value $M_S = 0.094$ emu/g was obtained. The inset in Fig. 5a displays the magnification of the hysteresis loop in the low-field region. The FM ordering can be considered as genuine one and does not originate from mullite or iron oxide impurity phases. Namely, mullite (Bi$_2$Fe$_4$O$_9$) phase is paramagnetic at room temperature and undergoes a transition to an antiferromagnetic state at $T_N \approx 264$ K [54]. Besides, the presence of iron oxides, leads to significantly enhanced ferromagnetism with large values of saturation magnetization [55]. The origin of FM ordering in otherwise antiferromagnetic BiFeO$_3$ is usually ascribed to the suppression of the spiral spin structure in particles with diameter less than the period of spin cycloid (62 nm) and higher distortion of FeO$_6$ octahedra or to the uncompensated spins on the nanoparticle surface. All of these effects lead to enhanced Dzyaloshinskii–Moriya interaction and appearance of ferromagnetism in nanocrystalline BiFeO$_3$ [2, 4,52,56]. In that case BiFeO$_3$ nanoparticles can be considered to be constituted of core/shell structure, i.e. antiferromagnetic core and ferromagnetic shell. As our nanocrystalline BiFeO$_3$ powders are composed of nanoparticles with average particle size of 64 nm [19,20] it can be supposed that the interruption of long-range AFM ordering takes place primarily on the nanoparticle surface. This assumption is supported by a report of Huang et al. [4] who have shown that BiFeO$_3$ nanoparticles of core–shell structure, with size close to the period of spin cycloid, exhibit increased ferromagnetism. It was further argued that FM ordering originates not only from the surface uncompensated spins, but from enhanced distortion of FeO$_6$ octahedra around the [111] direction. Such enhanced structural distortion can cause suppression of spiral spin structure and strengthening of DM interaction responsible for the appearance of FM. Accordingly, both effects, the suppression of spin cycloid and uncompensated surface spins, can lead to the occurrence of weak ferromagnetism in our sample.

Fig. 5b displays zero field cooled (ZFC) and field cooled (FC) magnetization curves, measured at 1000 Oe. The ZFC and FC curves started

to split below 250 K and the divergence became more pronounced with decreasing temperature. The ZFC curve showed a peak around the temperature of spin reorientation transition (200 K) [17,57] at which the Fe^{3+} magnetic moments are canted out of cycloidal plane. Besides, ZFC curve does not tend to $M = 0$ with approaching $T = 0$, as one would expect in a case of the presence of iron oxide impurity phases [58]. The ZFC/FC magnetization curves of our sample are very different from the ZFC/FC magnetization behavior of BiFeO$_3$ single crystal which was ascribed to the spin-glass ordering [59]. Recent ZFC/FC measurements on BiFeO$_3$ nanoparticles with sizes close to or less than the period of spin cycloid [4,7,56] have shown similar pronounced splitting of the ZFC/FC curves when antiferromagnetic and ferromagnetic orderings co-exist. Unlike the BiFeO$_3$ single crystal with antiferromagnetic ordering, those BiFeO$_3$ nanostructures can be considered as core–shell structures composed of antiferromagnetic core and ferromagnetic shell [4,52,56] in which more pronounced ZFC/FC splitting than in bulk BiFeO$_3$ suggests some irreversible effect on magnetic properties like breaking of AFM order and appearance of ferromagnetism [4,7,51,52]. Furthermore, more detailed analysis of ZFC/FC magnetization measurements on nanocrystalline BiFeO$_3$ [53] has shown that pronounced ZFC/FC splitting more likely originates from the changes in the domain structure at low temperatures and eventual antiferromagnetic domain pinning effect [4] than from spin-glass ordering.

In order to justify the use of mean-field theory approximation which does not include magnetic frustrations nor quantum fluctuations apart from the temperature ones [49], we refer to the study of Rao et al. on polycrystalline BiFeO$_3$ [60], where one can infer from that the Curie–Weiss temperature (θ_{CW}) tends to a very large value. Knowing that in bulk BiFeO$_3$ $T_N = 640$ K [1,2] and in nanostructured BiFeO$_3$ T_N slightly decreases with decreasing crystallite size [61], the BiFeO$_3$ is only seemingly frustrated system, since the frustration factor, $f = |\theta_{CW}|/T_N$ can exceed low frustration values [62]. However, we find magnetic frustration inconsequential because of the two noncompeting magnetic interactions: antiferromagnetic and ferromagnetic. These interactions are known to be cooperative in forming the stable Néel phase like in MnSe$_2$ [11]. Therefore, even at low temperatures, the average value of the relevant spin component per site is nearly 5/2, implying the stability of the AFM phase in BiFeO$_3$. Otherwise, spin–phonon coupling would be more complex, the $\Delta\omega_{s-ph}(T)$ would substantially deviate from the mean-field approximation model which we applied [44, 47] and a different treatment of the spin–phonon coupling mechanism would be required. The presented magnetic measurements are in favor of the picture in which nothing else, but the AFM magnetic ordering, without the presence of magnetic frustrations, influences the anomalous hardening of two-phonon Raman modes below T_N in nanocrystalline BiFeO$_3$.

4. Concluding remarks

In conclusion, we have investigated the temperature evolution of the resonant Raman two-phonon modes in BiFeO$_3$ nanocrystals, which are known to be very sensitive to magnetic ordering. Temperature studies have shown anomalous hardening and significant deviation of two-phonon frequencies from the anharmonicity below Néel temperature. The anomalous phonon hardening was ascribed to spin-two-phonon coupling. Within the mean-field approach, the spin–spin correlation function was correlated to the two-phonon frequency shift and the spin–phonon coupling strength for two-phonon modes was derived. The linear relation between spin–spin correlation function and frequency shift below Néel temperature confirmed no presence of fluctuations or magnetic frustrations and justified the application of mean-field approach. Magnetic measurements revealed the presence of weak FM phase below T_N. The coexistence of AFM and FM ordering were found not competitive, justifying the conclusion derived from mean-field approach that two-phonon Raman modes below T_N are strongly coupled to AFM ordering.
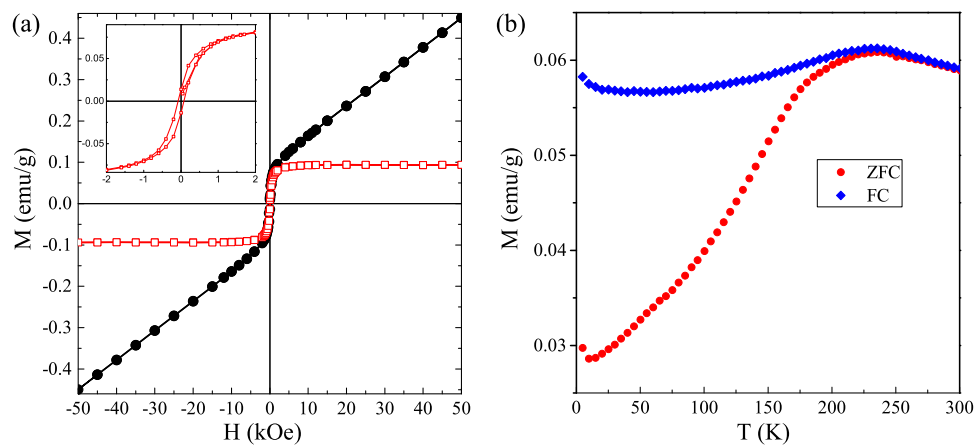
Fig. 5. (a) Room-temperature magnetization (M) vs magnetic field (H) dependence for BiFeO$_3$ nanoparticles, before (circles) and after subtraction (squares) of the linear background component. Inset shows zoom in view of M–H curve. (b) ZFC and FC magnetization curves measured at $H = 1000$ Oe.

Declaration of competing interest

The authors declare that they have no known competing financial interests or personal relationships that could have appeared to influence the work reported in this paper.

Acknowledgments

References

[1] N.A. Spaldin, Multiferroics: Past, present, and future, Phys. Today 63 (2010) 38–43, http://dx.doi.org/10.1063/1.3502547.

[2] G. Catalan, J.F. Scott, Physics and applications of Bismuth ferrite, Adv. Mater. 21 (2009) 2463–2485, http://dx.doi.org/10.1002/adma.200802849.

[3] I. Sosnowska, T.P. Neumaier, E. Steichele, Spiral magnetic ordering in bismuth ferrite, J. Phys. C: Solid State 15 (1982) 4835–4846, http://dx.doi.org/10.1088/0022-3719/15/23/020.

[4] F. Huang, Z. Wang, J. Zhang, K. Min, W. Lin, R. Ti, T. Xu, J. He, C. Yue, J. Zhu, Peculiar magnetism of BiFeO$_3$ nanoparticles with size approaching the period of the spiral spin structure, Sci. Rep. 3 (2013) 2907–2913, http://dx.doi.org/10.1038/srep02907.

[5] C.-H. Yang, D. Kan, I. Takeuchi, V. Nagarajan, J. Seidel, Doping BiFeO$_3$: approaches and enhanced functionality, Phys. Chem. Chem. Phys. 14 (2012) 15953–15962, http://dx.doi.org/10.1039/C2CP43082G.

[6] J. Wang, J.B. Neaton, H. Zheng, V. Nagarajan, S.B. Ogale, B. Liu, D. Viehland, V. Vaithyanathan, D.G. Schlom, U.V. Waghmare, N.A. Spaldin, K.M. Rabe, M. Wuttig, R. Ramesh, Epitaxial BiFeO$_3$ multiferroic thin film heterostructures, Science 299 (2003) 1719–1722, http://dx.doi.org/10.1126/science.1080615.

[7] J. Wu, S. Mao, Z.-G. Ye, Z. Xie, L. Zheng, Room-temperature ferromagnetic/ferroelectric BiFeO$_3$ synthesized by a self-catalyzed fast reaction process, J. Mater. Chem. 20 (2010) 6512–6516, http://dx.doi.org/10.1039/c0jm00729c.

[8] J. Ma, J. Hu, Z. Li, C.-W. Nan, Recent progress in multiferroic magnetoelectric composites: from bulk to thin films, Adv. Mater. 23 (2011) 1062–1087, http://dx.doi.org/10.1002/adma.201003636.

[9] R. Ramesh, N.A. Spaldin, Multiferroics: progress and prospects in thin films, Nature Mater. 6 (2007) 21–29, http://dx.doi.org/10.1038/nmat1805.

[10] D.J. Lockwood, M.G. Cottam, The spin-phonon interaction in FeF$_2$ and MnF$_2$ studied by Raman spectroscopy, J. Appl. Phys. 64 (1988) 5876–5878, http://dx.doi.org/10.1063/1.342186.

[11] D.M. Djokić, Z.V. Popović, F.R. Vukajlović, Influence of antiferromagnetic spin ordering on the far-infrared active optical phonon modes of αMnSe, Phys. Rev. B 77 (2008) 014305, http://dx.doi.org/10.1103/PhysRevB.77.014305.

[12] C.-S. Chen, C.-S. Tu, P.-Y. Chen, V.H. Schmidt, Z.-R. Xu, Y. Ting, Spin-lattice coupling phase transition and phonon anomalies in bismuth ferrite BiFeO$_3$, J. Alloy. Compd. 687 (2016) 442–450, http://dx.doi.org/10.1016/j.jallcom.2016.06.193.

[13] T.M.H. Nguyen, X.N. Nguyen, X.-B. Chen, X.T. To, S. Lee, T.H. Nguyen, I.-S. Yang, Study of spin-phonon coupling in multiferroic BiFeO$_3$ through Raman spectroscopy, J. Mol. Struct. 1222 (2020) 128884, http://dx.doi.org/10.1016/j.molstruc.2020.128884.

[14] J. Wei, C. Wu, Y. Liu, Y. Guo, T. Yang, D. Wang, Z. Xu, R. Haumont, Structural distortion, spin-phonon coupling, interband electronic transition, and enhanced magnetization in rare-earth-substituted bismuth ferrite, Inorg. Chem. 56 (2017) 8964–8974, http://dx.doi.org/10.1021/acs.inorgchem.7b00914.

[15] M.K. Singh, W. Prellier, H.M. Jang, R.S. Katiyar, Anomalous magnetic ordering induced spin-phonon coupling in BiFeO$_3$ thin films, Solid State Commun. 149 (2009) 1971–1973, http://dx.doi.org/10.1016/j.ssc.2009.07.036.

[16] A. Ahlawat, S. Satapathy, S. Maan, V.G. Sathe, P.K. Gupta, Correlation of structure and spin-phonon coupling in (La, Nd) doped BiFeO$_3$ films, J. Raman Spectrosc. 45 (2014) 958–962, http://dx.doi.org/10.1002/jrs.4573.

[17] M. Cazayous, A. Sacuto, D. Lebeugle, D. Colson, Possible interplay between a two phonon mode and high energy magnetic excitations in BiFeO$_3$, Eur. Phys. J. B 67 (2009) 209–212, http://dx.doi.org/10.1140/epjb/e2009-00033-7.

[18] M.O. Ramirez, M. Krishnamurthi, S. Denev, A. Kumar, S.-Y. Yang, Y.-H. Chu, E. Saiz, J. Seidel, A.P. Pyatakov, A. Bush, D. Viehland, J. Orenstein, R. Ramesh, V. Gopalan, Two-phonon coupling to the antiferromagnetic phase transition in multiferroic BiFeO$_3$, Appl. Phys. Lett. 92 (2008) 022511, http://dx.doi.org/10.1063/1.2829681.

[19] B. Stojadinović, Z. Dohčević-Mitrović, D. Stepanenko, M. Rosić, I. Petronijević, N. Tasić, N. Ilić, B. Matović, B. Stojanović, Dielectric and ferroelectric properties of Ho-doped BiFeO$_3$ nanopowders across the structural phase transition, Ceram. Int. 43 (2017) 16531–16538, http://dx.doi.org/10.1016/j.ceramint.2017.09.038.

[20] D.M. Djokić, B. Stojadinović, D. Stepanenko, Z. Dohčević-Mitrović, Probing charge carrier transport regimes in BiFeO$_3$ nanoparticles by Raman spectroscopy, Scr. Mater. 181 (2020) 6–9, http://dx.doi.org/10.1016/j.scriptamat.2020.02.008.

[21] S.S. Mitra, Infrared and Raman spectra due to lattice vibrations, Springer US, Boston, MA, 1969, pp. 398–400, http://dx.doi.org/10.1007/978-1-4757-1123-3-14.

[22] R. Palai, R.S. Katiyar, H. Schmid, P. Tissot, S.J. Clark, J. Robertson, S.A.T. Redfern, G. Catalan, J.F. Scott, β Phase and γ-β metal-insulator transition in multiferroic BiFeO$_3$, Phys. Rev. B 77 (2008) 014110, http://dx.doi.org/10.1103/PhysRevB.77.014110.

[23] M. Cazayous, D. Malka, D. Lebeugle, D. Colson, Electric field effect on BiFeO$_3$ single crystal investigated by Raman spectroscopy, Appl. Phys. Lett. 91 (2007) 071910, http://dx.doi.org/10.1063/1.2771380.

[24] C. Beekman, A.A. Reijnders, Y.S. Oh, S.W. Cheong, K.S. Burch, Raman study of the phonon symmetries in BiFeO$_3$ single crystals, Phys. Rev. B 86 (2012) 020403, http://dx.doi.org/10.1103/PhysRevB.86.020403.

[25] H. Fukumura, S. Matsui, H. Harima, T. Takahashi, T. Itoh, K. Kisoda, M. Tamada, Y. Noguchi, M. Miyayama, Observation of phonons in multiferroic BiFeO$_3$ single crystals by Raman scattering, J. Phys. Condens. Mat. 19 (2007) 365224, http://dx.doi.org/10.1088/0953-8984/19/36/365224.

[26] P. Hermet, M. Goffinet, J. Kreisel, P. Ghosez, Raman and infrared spectra of multiferroic bismuth ferrite from first principles, Phys. Rev. B 75 (2007) 220102, http://dx.doi.org/10.1103/PhysRevB.75.220102.

[27] J. Hlinka, J. Pokorny, S. Karimi, I.M. Reaney, Angular dispersion of oblique phonon modes in BiFeO$_3$ from micro-Raman scattering, Phys. Rev. B 83 (2011) 020101, http://dx.doi.org/10.1103/PhysRevB.83.020101.

[28] M.K. Singh, H.M. Jang, S. Ryu, M.-H. Jo, Polarized Raman scattering of multiferroic BiFeO$_3$ epitaxial films with rhombohedral $R3c$ symmetry, Appl. Phys. Lett. 88 (2006) 042907, http://dx.doi.org/10.1063/1.2168038.

[29] M.N. Iliev, A.P. Litvinchuk, V.G. Hadjiev, M.M. Gospodinov, V. Skumryev, E. Ressouche, Phonon and magnon scattering of antiferromagnetic Bi$_2$Fe$_4$O$_9$, Phys. Rev. B 81 (2010) 024302, http://dx.doi.org/10.1103/PhysRevB.81.024302.

[30] J. Bielecki, P. Svedlindh, D.T. Tibebu, S. Cai, S.-G. Eriksson, L. Börjesson, C.S. Knee, Structural and magnetic properties of isovalently substituted multiferroic BiFeO$_3$: Insights from Raman spectroscopy, Phys. Rev. B 86 (2012) 184422, http://dx.doi.org/10.1103/PhysRevB.86.184422.

[31] S. Chauhan, M. Kumar, P. Pal, Substitution driven structural and magnetic properties and evidence of spin phonon coupling in Sr-doped BiFeO$_3$ nanoparticles, RSC Adv. 6 (2016) 68028–68040, http://dx.doi.org/10.1039/C6RA11021E.

[32] M. Kumar, M. Arora, S. Chauhan, S. Joshi, Raman spectroscopy probed spin-two phonon coupling and improved magnetic and optical properties in Dy and Zr substituted BiFeO$_3$ nanoparticles, J. Alloy. Compd. 692 (2017) 236–242, http://dx.doi.org/10.1016/j.jallcom.2016.09.031.

[33] B. Stojadinović, Z. Dohčević-Mitrović, N. Paunović, N. Ilić, N. Tasić, I. Petronijević, D. Popović, B. Stojanović, Comparative study of structural and electrical properties of Pr and Ce doped BiFeO$_3$ ceramics synthesized by auto-combustion method, J. Alloy. Compd. 657 (2016) 866–872, http://dx.doi.org/10.1016/j.jallcom.2015.09.235.

[34] Y. Yang, J.Y. Sun, K. Zhu, Y.L. Liu, J. Chen, X.R. Xing, Raman study of BiFeO$_3$ with different excitation wavelengths, Physica B 404 (2009) 171–174, http://dx.doi.org/10.1016/j.physb.2008.10.029.

[35] M.C. Weber, M. Guennou, C. Toulouse, M. Cazayous, Y. Gillet, X. Gonze, J. Kreisel, Temperature evolution of the band gap in BiFeO$_3$ traced by resonant Raman scattering, Phys. Rev. B 93 (2016) 125204, http://dx.doi.org/10.1103/PhysRevB.93.125204.

[36] E. Granado, A. Garcí a, J.A. Sanjurjo, C. Rettori, I. Torriani, F. Prado, R.D. Sánchez, A. Caneiro, S.B. Oseroff, Magnetic ordering effects in the Raman spectra of La$_{1-x}$Mn$_{1-x}$O$_3$, Phys. Rev. B 60 (1999) 11879–11882, http://dx.doi.org/10.1103/PhysRevB.60.11879.

[37] X.-B. Chen, N.T. Minh Hien, K. Han, J. Chul Sur, N.H. Sung, B.K. Cho, I.-S. Yang, Raman studies of spin-phonon coupling in hexagonal BaFe$_{12}$O$_{19}$, J. Appl. Phys. 114 (2013) 013912, http://dx.doi.org/10.1063/1.4812575.

[38] J. Ryu, C.-W. Baek, D.-S. Park, D.-Y. Jeong, Multiferroic BiFeO$_3$ thick film fabrication by aerosol deposition, Met. Mater. Int. 16 (2010) 639–642, http://dx.doi.org/10.1007/s12540-010-0818-9.

[39] P.G. Klemens, Anharmonic decay of optical phonons, Phys. Rev. 148 (1966) 845–848, http://dx.doi.org/10.1103/PhysRev.148.845.

[40] M. Balkanski, R.F. Wallis, E. Haro, Anharmonic effects in light scattering due to optical phonons in silicon, Phys. Rev. B 28 (1983) 1928–1934, http://dx.doi.org/10.1103/PhysRevB.28.1928.

[41] W. Baltensperger, J.S. Helman, Influence of magnetic order in insulators on the optical phonon frequency, Helv. Phys. Acta 41 (1968) 668–673, http://dx.doi.org/10.5169/seals-113910.

[42] E. Aytan, B. Debnath, F. Kargar, Y. Barlas, M.M. Lacerda, J. Li, R. Lake, J. Shi, A.A. Balandin, Spin-phonon coupling in antiferromagnetic nickel oxide, Appl. Phys. Lett. 111 (2017) 252402, http://dx.doi.org/10.1063/1.5009598.

[43] P.-H. Shih, C.-L. Cheng, S.Y. Wu, Short-range spin-phonon coupling in in-plane CuO nanowires: a low-temperature Raman investigation, Nanoscale Res. Lett. 8 (2013) 1–6, http://dx.doi.org/10.1186/1556-276X-8-398.

[44] C. Kant, J. Deisenhofer, T. Rudolf, F. Mayr, F. Schrettle, A. Loidl, V. Gnezdilov, D. Wulferding, P. Lemmens, V. Tsurkan, Optical phonons, spin correlations, and spin-phonon coupling in the frustrated pyrochlore magnets CdCr$_2$O$_4$ and ZnCr$_2$O$_4$, Phys. Rev. B 80 (2009) 214417–214426, http://dx.doi.org/10.1103/PhysRevB.80.214417.

[45] J. Zhang, Q. Lian, Z. Pan, W. Bai, J. Yang, Y. Zhang, X. Tang, J. Chu, Spin-phonon coupling and two-magnons scattering behaviors in hexagonal NiAs-type antiferromagnetic MnTe epitaxial films, J. Raman Spectrosc. 51 (2020) 1383–1389, http://dx.doi.org/10.1002/jrs.5928.

[46] M.N. Iliev, M.V. Abrashev, A.P. Litvinchuk, V.G. Hadjiev, H. Guo, A. Gupta, Raman spectroscopy of ordered double perovskite La$_2$CoMnO$_6$ thin films, Phys. Rev. B 75 (2007) 104118, http://dx.doi.org/10.1103/PhysRevB.75.104118.

[47] R.X. Silva, M.C.C. Júnior, S. Yáñez-Vilar, M.S. Andújar, J. Mira, M.A. Señarís-Rodríguez, C.W.A. Paschoal, Spin-phonon coupling in multiferroic Y$_2$CoMnO$_6$, J. Alloy. Compd. 690 (2017) 909–915, http://dx.doi.org/10.1016/j.jallcom.2016.07.010.

[48] B.D. Cullity, C.D. Graham, Introduction to magnetic materials, Second Edition, Wiley-IEEE Press, New Jersey, 2008, pp. 91–99, http://dx.doi.org/10.1002/9780470386323.

[49] K. Yosida, Theory of magnetism, Springer-Verlag Berlin Heidelberg, 1996, pp. 72–74.

[50] V. Barsan, V. Kuncser, Exact and approximate analytical solutions of Weiss equation of ferromagnetism and their experimental relevance, Phil. Mag. Lett. 97 (2017) 359–371, http://dx.doi.org/10.1080/09500839.2017.1366081.

[51] K.P. Remya, D. Prabhu, R.J. Josephus, A.C. Bose, C. Viswanathan, N. Ponpandian, Tailoring the morphology and size of perovskite BiFeO$_3$ nanostructures for enhanced magnetic and electrical properties, Mater. Des. 192 (2020) 108694, http://dx.doi.org/10.1016/j.matdes.2020.108694.

[52] F. Huang, X. Xu, X. Lu, M. Zhou, H. Sang, J. Zhu, The exchange bias behavior of BiFeO$_3$ nanoparticles with natural core-shell structure, Sci. Rep.-UK 8 (2018) 2311, http://dx.doi.org/10.1038/s41598-018-19676-5.

[53] S. Vijayanand, M.B. Mahajan, H.S. Potdar, P.A. Joy, Magnetic characteristics of nanocrystalline multiferroic BiFeO$_3$ at low temperatures, Phys. Rev. B 80 (2009) 064423, http://dx.doi.org/10.1103/PhysRevB.80.064423.

[54] N. Shamir, E. Gurewitz, H. Shaked, The magnetic structure of Bi$_2$Fe$_4$O$_9$ analysis of neutron diffraction measurements, Acta Crystallogr. A 34 (1978) 662–666, http://dx.doi.org/10.1107/S0567739478001412.

[55] H. Béa, M. Bibes, A. Barthélémy, K. Bouzehouane, E. Jacquet, A. Khodan, J.-P. Contour, S. Fusil, F. Wyczisk, A. Forget, D. Lebeugle, D. Colson, M. Viret, Influence of parasitic phases on the properties of BiFeO$_3$ epitaxial thin films, Appl. Phys. Lett. 87 (2005) 072508, http://dx.doi.org/10.1063/1.2009808.

[56] M. Sakar, S. Balakumar, P. Saravanan, S. Bharathkumar, Particulates Vs. fibers: Dimension featured magnetic and visible light driven photocatalytic properties of Sc modified multiferroic bismuth ferrite nanostructures, Nanoscale 8 (2016) 1147–1160, http://dx.doi.org/10.1039/C5NR06655G.

[57] J.F. Scott, M.K. Singh, R.S. Katiyar, Critical phenomena at the 140 and 200 K magnetic phase transitions in BiFeO$_3$, J. Phys. Condens. Matter 20 (2008) 322203, http://dx.doi.org/10.1088/0953-8984/20/32/322203.

[58] D. Parker, V. Dupuis, F. Ladieu, J.-P. Bouchaud, E. Dubois, R. Perzynski, E. Vincent, Spin-glass behavior in an interacting γ-Fe$_2$O$_3$ nanoparticle system, Phys. Rev. B 77 (2008) 104428, http://dx.doi.org/10.1103/PhysRevB.77.104428.

[59] M.K. Singh, W. Prellier, M.P. Singh, R.S. Katiyar, J.F. Scott, Spin-glass transition in single-crystal BiFeO$_3$, Phys. Rev. B 77 (2008) 144403, http://dx.doi.org/10.1103/PhysRevB.77.144403.

[60] T.D. Rao, S. Asthana, Evidence of improved ferroelectric phase stabilization in Nd and Sc co-substituted BiFeO$_3$, J. Appl. Phys. 116 (2014) 164102–164109, http://dx.doi.org/10.1063/1.4898805.

[61] S.M. Selbach, T. Tybell, M.-A. Einarsrud, T. Grande, Size-dependent properties of multiferroic BiFeO$_3$ nanoparticles, Chem. Mater. 19 (2007) 6478–6484, http://dx.doi.org/10.1021/cm071827w.

[62] A.P. Ramirez, Strongly geometrically frustrated magnets, Annu. Rev. Mater. Sci. 24 (1994) 453–480, http://dx.doi.org/10.1146/annurev.ms.24.080194.002321.

RESEARCH ARTICLE

Journal of RAMAN SPECTROSCOPY WILEY

Phonons investigation of ZnO@ZnS core-shell nanostructures with active layer

Branka Hadzic[1] [ORCID] | Branko Matovic[2] | Marjan Randjelovic[3] |
Radmila Kostic[1] | Maja Romcevic[1] [ORCID] | Jelena Trajic[1] | Novica Paunovic[1] |
Nebojsa Romcevic[1]

[1]Institute of Physics, University of Belgrade, Belgrade, Serbia

[2]Institute Vinca, University of Belgrade, Belgrade, Serbia

[3]Faculty of Sciences and Mathematics, University of Nis, Nis, Serbia

Correspondence

Maja Romcevic, Institute of Physics, University of Belgrade, 11080 Belgrade, Serbia.
Email: romcevic@ipb.ac.rs

Abstract

In the present work experimental study of the ZnO@ZnS core-shell nanostructure with an active layer obtained by conversion of zinc oxide powders with H_2S is reported. The prepared structures were characterized by scanning electron microscopy, X-ray diffraction, Raman spectroscopy, and far-infrared spectroscopy. Top surface optical phonon (TSO) in ZnO, characteristic for the cylindrical nano-objects, the surface optical phonon (SOP) mode of ZnS, and SOP modes in ZnO@ZnS core-shell nanostructure are registered. Local mode of oxygen in ZnS and gap mode of sulfur in ZnO are also registered. This result is due to the existence of an active layer in the space between ZnO core and ZnS shell, which is very important for the application of these materials as thermoelectrics.

KEYWORDS

active layer, core-shell nanostructures, local mode, surface phonons, thermoelectric

1 | INTRODUCTION

ZnO and ZnS are two well-known and widely used wide-band gap semiconductors that are still in the focus of scientific research. Different combinations and changeable structures of ZnO and ZnS intrigue researchers all over the world due to the large possibility of their application as optoelectronic devices, sensors, lasers, and other novel devices. Both materials, ZnO and ZnS, are abundant, highly stable, non-toxic, environmentally friendly and intensively studied II-VI materials.[1–3] They can exist in the form of three crystallographic phases: cubic sphalerite, hexagonal wurtzite, or, in the rarest form, cubic rock salt. ZnO at the room temperature preferentially crystallizes in the hexagonal phase, while the ZnS structure depends on the temperature. At the room temperature ZnS crystallizes in the cubic phase but at temperatures above 1020°C ZnS is most stable in the hexagonal phase

form. However, there are also other differences between these two materials besides the difference in existing phases at room temperature. Although both of these materials are characterized by the wide direct band gaps, ZnS shows wider direct band gaps for both of its crystallographic phases. Nevertheless, ZnO is characterized by higher exciton binding energy. Band gaps for the ZnO hexagonal phase are reported to be 3.34, 3.37, and 3.4 eV with the binding energy of 60 mW, for the ZnS cubic phase band gaps are 3.54 and 3.68 eV, while for the ZnS hexagonal phase are 3.80 and 3.91 eV with the binding energy of 40 mW.[4–8]

Excellent features of ZnO and ZnS as individual components contribute to the favorable properties of the materials obtained combining these two components and make them good candidates for a wide range of applications, such are the thermoelectric components.[9,10] The most important parameter in the field of

thermoelectricity is the so-called figure of merit. It provides a connection between the material parameters and the maximum efficiency that will be achieved when this material is used as a thermoelectric generator. The goal of designing new materials or structures is to keep the phonon part of thermal conductivity in the material as small as possible, without changing the electrical parameters (electric conductivity, Seebeck coefficient, and electronic part of thermal conductivity). One possible way to achieve this is to use a ZnO/ZnS superlattice.[11] Another possibility is to use $ZnO_{1-x}S_x$ alloys. In the latter case, impurities act as local scatters that can alter the phonon transport.[12]

The general conclusion of all of the previously mentioned studies is summarized in the work of Bachmann et al.[13] where it is underlined that incorporation of sulfur in ZnO and incorporation of oxygen in ZnS can substantially reduce the thermal lattice conductivity and increase the figure of merit. However, a possible breakthrough in this field can be achieved with the usage of ZnO@ZnS core-shell system.

Core-shell nanostructures are a special class of the biphasic materials whose properties depend not only on the combination of the core and shell materials but also on their geometry, design, and core-shell volume ratio.[14–18] In previous studies of the ZnO@ZnS core-shell structures, this phenomenon was disregarded.[19–24] So far, the research focus was on the methods of synthesis and the quality of the spatial homogeneity of the obtained structures, such are the attempts to eliminate the existence of impurity throughout the system.

In addition, the focus has been on the application of these structures in solar cells,[23] as new materials for luminescence, and for magnetic applications.[24] Characterization methods were also selected for this purpose. Spectroscopic methods were used only to confirm X-ray measurements. Thus, in Sundararajan et al.[19] it was said that the Fourier-transform infrared spectroscopy (FT-IR) spectra confirmed starching vibrations of ZnO and ZnS, respectively. In Flores et al.[20] the same conclusion was reached using Raman spectroscopy. No attention was paid to the possibility of the formation of any layer between the ZnO core and the ZnS shell, which is the topic of our research.

While scanning electron microscopy, X-ray diffraction (XRD) and far-infrared spectroscopy give us information about the global structure, Raman spectroscopy is focused on the local environment, which is crucial for this type of research. The present work aims to determine the existence of the active layer doping phases in the space between the core and the shell by registering the surface, local, and gap modes, as well as by analyzing other structural and optical characteristics of the ZnO@ZnS core-shell system.

2 | EXPERIMENT

For the synthesis of ZnO/ZnS core-shell nanostructures, gas-phase sulfidation of ZnO (Merck) at elevated temperatures was exploited using flow reactor which is schematically presented in Figure S1 (Supporting Information). Hydrogen sulfide was initially obtained from iron (II) sulfide and hydrochloric acid and without further processing was introduced in the round-bottom flask containing 3 g of ZnO powder. Iron sulfide was added into a three neck round bottom flask (B) with mounted dropping funnel with Polytetrafluoroethylene (PTFE) key (A) containing 3 M HCl. Flow of HCl was adjusted to achieve required H_2S flow of 6.5 ml/min during 6 h. Evolved gas was passed into round-bottom flask with ZnS (C) which was heated at 340–400°C. Vinyl laboratory tubings were used to introduce gas into flow reactor.

Unreacted H_2S was collected and retained in two stages. First, the vessel containing $FeCl_3$ solution (D) was used to chemically convert H_2S gas into iron sulfides and small amount of remaining gas was caught in the next stage using solution of NaOH (E).

Morphology of the obtained powders and their evolution during calcination were studied by the field emission scanning electron microscope (FE-SEM) model FE-SEM JEOL-5200F (Japan).

The composition of investigated samples was investigated utilizing a Rigaku IV XRD diffractometer with Cu Kα radiation at room temperature. The present phases were identified by applying the PDXL2 software (version 2.0.3.0),[25] with the reference to the diffraction patterns present in the International Centre for Diffraction Data (ICDD).[26]

The far-infrared reflection spectra were measured at room temperature at the spectral range from 70 to 630 cm^{-1} with a BOMEM DA 8 spectrometer.

The micro-Raman spectra were taken in the backscattering configuration and analyzed by the TriVista 557 system equipped with a nitrogen-cooled charge-coupled-device detector. As an excitation source the Verdi G optically pumped semiconductor laser with the 532 nm line was used. Excitation energy is in the off-resonance regime for all the considered materials.

3 | RESULTS

SEM images of the two starting materials (ZnO and ZnS nanoparticles) and the obtained core-shell structure

(ZnO@ZnS) are given in Figure 1. In Figure 1a large ZnO particles are shown, in Figure 1b long narrow ZnS particles can be observed, while in Figure 1c large particles of the formed core-shell ZnO@ZnS structure are evident. This is confirmation that the core-shell structure usually shows the same morphology as a core. ZnO particles are cylindrical with the diameter ranging from 200 to 500 nm and length in the 300 to 500 nm range. ZnS particles are spiral wire-shaped structures with the diameter in the 20 to 30 nm range and length in the 300 to 500 nm range. The final structure contains mostly ZnO cylinders that originate from the starting ZnO material. ZnS is probably located at the surface of ZnO cylinders as a shell.

The formation of ZnS layer around ZnO particle surface is well known from sulfidation reaction: $ZnO(s) + H_2S(g) = ZnS(s) + H_2O(g)$, where ZnS growth an outward development during ZnO sulfidation. Such a process leads to a core-shell structure, which has been clearly demonstrated in many studies.[27–29]

The X-ray diffractograms of ZnO, ZnS nanoparticles, and ZnO@ZnS core-shell nanostructure are shown in Figure 2. The detailed phase composition investigations revealed the presence of crystalline phases of the hexagonal ZnO and cubic ZnS compounds in the starting materials, while in ZnO@ZnS the cubic ZnS transformed into hexagonal polymorph. Cubic-to-hexagonal phase transition of ZnS has been observed at very low temperatures at 250°C.[30] Since the experiment is conducted in range of 340–400°C, it is normal that a phase transformation takes place.

The plane identification (indexing) is done. The diffraction peaks correspond to the (1 1 1), (2 2 0), and (3 1 1) planes of the cubic phase of ZnS, matching with JCPDS 05-0566, and wurtzite (hexagonal phase) was found in JCPDS 36-1450. The XRD peaks are broadened because of nanocrystalline nature of the synthesized samples. On the other side, ZnO phase is hexagonal wurtzite phase, (JCPDS 01-089-0510). Obtained the core-shell structure consists of 88% ZnO (in core) and 12% ZnS

(shell). Williamson-Hall plots were used to separate the effect of the size and strain in the nanocrystals.[31] The results are shown in Table 1.

By means of the PDXL2 software (version 2.0.3.0),[25] it was calculated that the mean crystalline size $\tilde{a}$ of ZnO is determined as 57 nm, in the case of ZnS is 2.1 nm, while obtained the core-shell structure consists of 88% ZnO (core) with mean crystalline size of about 67 nm
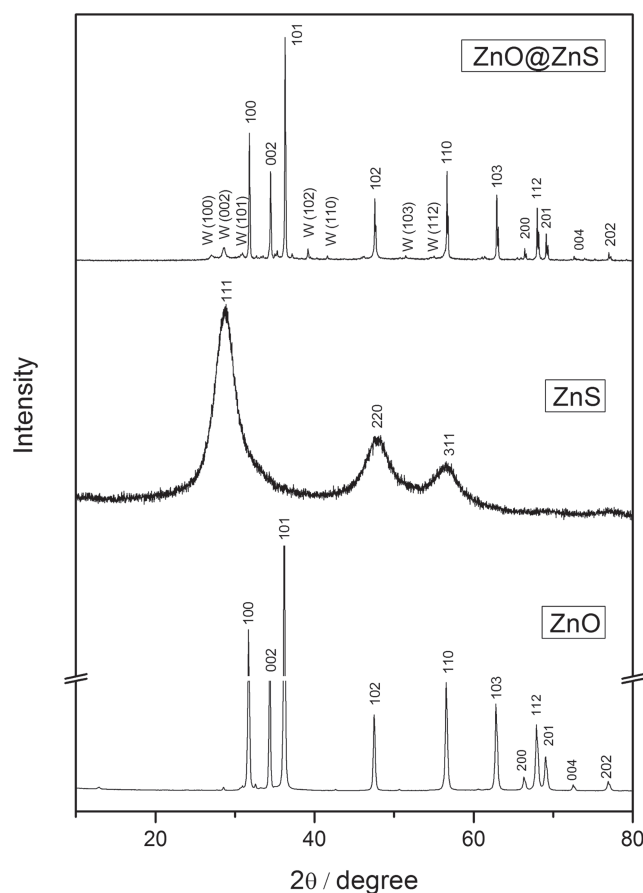
FIGURE 2 XRD spectra for all investigated samples. W = wurtzite (hexagonal) ZnS
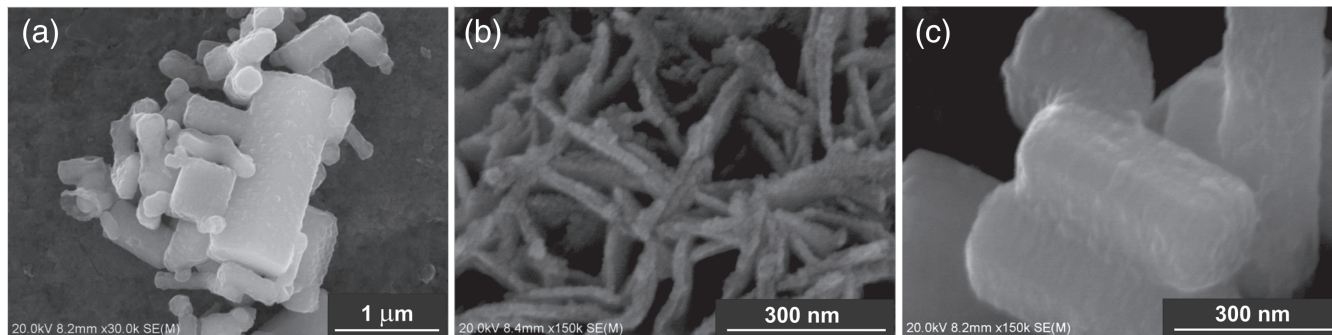
FIGURE 1 SEM images for (a) ZnO, (b) ZnS, and (c) ZnO@ZnS

TABLE 1 Unit cell parameters, crystallite size, and lattice strain of samples

Sample	Lattice parameter (nm)	Crystallite size (nm)	Strain (%)
starting material			
ZnS	$a = 0.53805(3)$	2.1	0.0075
ZnO	$a = b = 0.32521(4)$ $c = 0.52101\,(8)$	57	0.145
ZnO@ZnS core-shell			
ZnS	$a = b = 0.3848$ $c = 0.6317$ $\alpha = 90$ $\beta = 90$ $\gamma = 120$	11	0.001884
ZnO	$a = b = 0.32481(4)$ $c = 0.520044(7)$	69	0.00072

and 12% ZnS (shell) with mean crystalline size of about 11 nm.

The lattice strain of phases in core-shell structure is 0.001884 for ZnS and 0.00072 for ZnO. The value for stress in case of ZnS phase is lower than the stress for ZnO. It can be considered to be the consequence of an ordering of atomic arrangement during sulfidation, that is, the formation of zinc sulfide. The less ordering lead to an increasing strain due to the significant amount of strain that is localized at the surface of crystallites as a result of a high concentration of broken bonds.

The hexagonal phase of ZnO, the cubic, and hexagonal phase of ZnS were previously registered by the XRD analysis. Since the understanding of the bulk material vibrational properties is crucial for the analysis of the vibration properties of the core-shell structure, the vibrational properties analysis was initiated with a brief report of the literature data for the registered phases. The bulk modes are expected to be shifted and broadened as a consequence of the miniaturization.

The hexagonal structure of ZnO belongs to the space group C_{6v}^4, with the unit cell that contains four atoms, where all atoms occupy C_{3v} sites. From the factor group theory analysis existence of nine optical modes, that are classified by the following symmetries $\Gamma_{opt} = A_1 + 2B_1 + E_1 + 2E_2$, is evident.[32] Modes of symmetry A_1, E_1, and E_2 are Raman active, A_1 and E_1 are infrared active, while B_1 is inactive (silent) mode. Both A_1 and E_1 are polar modes and split into transverse (TO) and longitudinal (LO) phonons with different wavenumbers due to the macroscopic crystal field. Anisotropy of the ZnO crystal causes A_1 and E_1 modes to have different wavenumbers.

The cubic ZnS structure belongs to $F-43m$ (T_d^2) space group with a trigonal primitive unit cell containing one formula unit with two atoms. Thus, it has 6 degrees of freedom, three acoustic, and three optical phonons. The Brillouin zone center phonons, both acoustic and optical, are triply degenerate for this cubic structure and have symmetry species $\Gamma_{15}(F_2)$. A macroscopic electric field in polar crystals, such as ZnS, is associated with LO vibrations and makes LO mode energy greater than the TO mode energy. This effect removes the degeneracy of the optical mode yielding a doubly degenerate TO mode and a LO mode. Both, the TO and LO modes are Raman active, while the TO mode is also infrared active.[33,34]

Wurtzite ZnS belongs to the space group P63mc (C46r) and all atoms occupy C3r sites. The nine possible optic modes of the four-atom primitive cell have the following symmetries: $1A_1 + 2B_1 + 1E_1 + 2E_2$. The A_1 and E_1 branches are both Raman and IR active, the E_2's are only Raman active, and the B_1's are neither IR nor Raman active.

3.1 | Far-infrared spectroscopy

The experimental data of two starting materials and the obtained core-shell structure are presented by circles in Figure 3. To analyze the far-infrared spectra the standard analysis, which applies the correlation between the reflection coefficient and dielectric function, was used. A theoretical model of the bulk dielectric function was discussed by several authors.[35,36]

The low-frequency dielectric properties of the single crystals are described by classical oscillators corresponding to the TO-modes, to which the Drude part is superimposed to take into the account the free carrier contribution:

$$\varepsilon_S(\omega) = \varepsilon_\infty + \sum_{k=1}^{l} \frac{\varepsilon_\infty S_k}{\omega_{TOk}^2 - \omega^2 - i\gamma_{TOk}\omega} - \frac{\varepsilon_\infty \omega_P^2}{\omega(\omega + i\Gamma_P)} \quad (1)$$

where ε_∞ is the bound charge contribution and it is assumed to be a constant, $\omega_{TOk}\omega_{TOk}$ is the transverse optical-phonon wavenumber, $\omega_P\omega_P$ the plasma
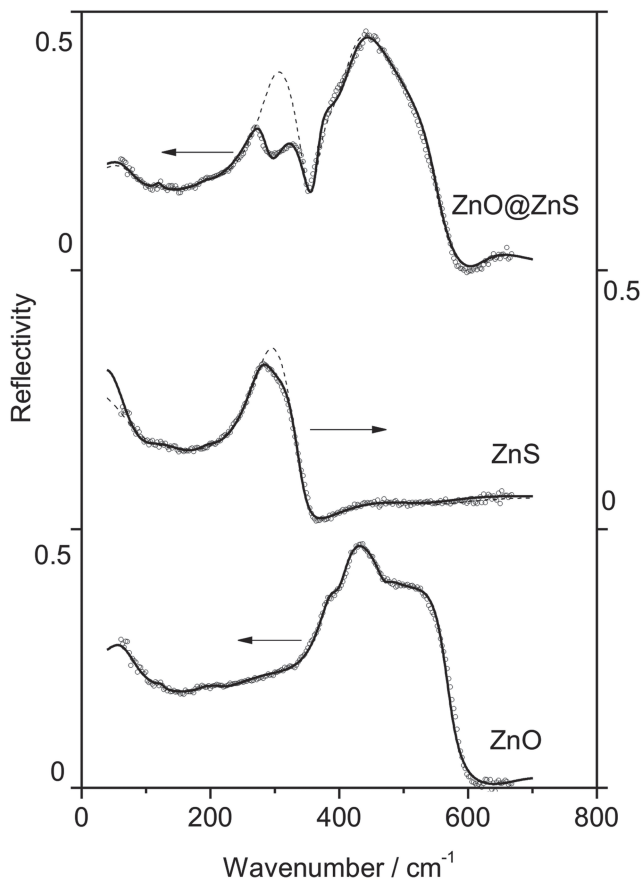
FIGURE 3 Far-infrared reflection spectra for all investigated samples. The experimentally obtained data points are depicted by circles. The theoretical spectra given as the solid lines are obtained with the model defined by Equations (1) and (2) and the fitting procedure

wavenumber, γ_{TOk} is damping, Γ_P is the plasmon mode damping coefficient, and S_k is an oscillator strength.

In general, the optical properties of an inhomogeneous material are described by the complex dielectric function that depends on the 3-D distribution of constituents. The investigated mixture consists of two dielectric components. One is treated as a host, and the other as the inclusion. The characterization of the inhomogeneous material by the two dielectric functions is not useful since the exact geometrical arrangement of the constituents of the material is needed. However, if the wavelength of the electromagnetic radiation is much larger than the size of inclusions, classical theories of inhomogeneous material presume that the material can be treated as a homogeneous substance with an effective dielectric function. In the literature, many mixing models can be found for the effective permittivity of such a mixture.[37] The optical properties of such materials depend

upon the properties of constituents, as well as their volume fraction.

The simplest model that describes an inhomogeneous material by an effective dielectric function can be written as $\varepsilon_{eff} = (1 - f)\, \varepsilon_1 + f\, \varepsilon_2$. This model is applicable in the case of bulk materials of dielectric constant ε_1 in which the second phase or the material of the dielectric constant ε_2, which occupies volume fractions f, is randomly distributed. In the case where nanoparticles are distributed in the air, or in an optically similar medium, the Maxwell–Garnett or Bruggeman formula is usually used.[37]

In general terms, the Maxwell–Garnett Effective Medium Approximation is expected to be valid at relatively low volume fractions f, since it is assumed that the domains are spatially separated and electrostatic interaction between the chosen inclusions and all other neighboring inclusions is neglected.

Since samples used in the present study are well defined with separated nanosized grains (as demonstrated on SEM images presented in Figure 1), the Maxwell–Garnet model was used for the present case. Effective permittivity of mixture, ε_{eff}, according to the Maxwell–Garnet mixing rule is as follows[38]:

$$\varepsilon_{eff} = \varepsilon_1 + 3f\varepsilon_1 \frac{\varepsilon_2 - \varepsilon_1}{\varepsilon_2 + 2\varepsilon_1 - f(\varepsilon_1 - \varepsilon_2)} \tag{2}$$

In this case, nanoparticles of permittivity ε_2 are located randomly in the homogeneous environment ε_1 (air) and occupy a volume fraction f.

Solid lines presented in Figure 3 are calculated spectra obtained by a fitting procedure based on the previously presented model. The parameter adjustment was carried out automatically, using the least squares fitting of the theoretical (R_t) and experimental (R_e) reflectivity at q arbitrarily taken points:

$$\delta = \sqrt{\frac{1}{q}\sum_{j=1}^{q} \left(R_{ej} - R_{tj}\right)^2} \tag{3}$$

The value of δ was minimized until it complied with the commonly accepted experimental error (less than 3%). For all the samples the determination errors of wavenumber and damping coefficients were in the range 3%–6% and 10%–15%, respectively. The agreement of the theoretical model obtained in this manner with the experimental results is excellent. In Table 2, the best fitting parameters are presented. In this case, the wavenumber indicated by ω_{TOk} in Equation 1 is perceived as the characteristic wavenumber for a given material.

TABLE 2 Calculated fit parameters obtained from the Raman and far-infrared spectra

	ZnS		ZnO		ZnO@ZnS		Description
	Raman (cm^{-1})	IR (cm^{-1})	Raman (cm^{-1})	IR (cm^{-1})	Raman (cm^{-1})	IR (cm^{-1})	
ω_P	-	82	-	94	-	91	
ω_1	132	119					[TO$_1$–LA]$_\Sigma$ or 2TA$_2$
ω_2	145				152		[TO$_u$–LA]$_\Sigma$
ω_3	157						[LO–LA]$_\Sigma$
ω_4	174						2TAX
ω_5			203	210	203	190	2TA or E$_2$(low)
ω_6	206	197			219		LA
ω_7					**246**		**Gap-mode S in ZnO**
ω_8	263	281				269	TO
ω_9	**310**	**309**			**305**	**301**	**SOP**
ω_{10}			330	338	334		E$_2$(high)–E$_2$(low)
ω_{11}	**346**	**350**			**349**	**357**	**LO and LO+Plasma (IR)**
ω_{12}			379	379	380	386	A$_1$(TO)
ω_{13}			411	395	409	410	E$_1$(TO)
ω_{14}	415	420					(LO$_\Gamma$ + TA$_L$) or (TO$_\Gamma$ + LA$_L$)
ω_{15}			436	436	436	438	E$_2$(high)
ω_{16}					**472**		**Local-mode O in ZnS**
ω_{17}			**484**	**469**			**TSO**
ω_{18}			**540**		**537**		**SOP**
ω_{19}			578	557	584	557	A$_1$(LO)

The parameters important for discussion are bold.

In Figure 3, the some phonon influence is evident at approximately 310 cm^{-1}. The experimental spectra are in complete agreement with the theoretical ones (please notice the solid lines in Figure 3) when the existence of this phonon is included, while inconsistency between the experimental and theoretical spectra (see the dashed lines in Figure 4) is clear when this phonon is omitted.

3.2 | Raman spectroscopy

The Raman spectra of the ZnO, ZnS, and zno@zns core-shell nanostructure, measured in the spectral range of 100–600 cm^{-1} at room temperature, are presented in Figure 4. Experimental Raman scattering spectra are analyzed by the deconvolution of the Lorentzian curve.[39] The thick red line presents a resulting spectral curve. Positions of Lorentzians are given in Table 2.

The Raman spectrum of the ZnO nanoparticle is presented in Figure 4a. Intense modes at 203, 330, 379, 411, 436, 484, 540, and 578 cm^{-1} were detected. The obtained results are in good agreement with the values given in the literature,[40] as it should be for the commercially supplied materials.

When ZnS is concerned the circumstances are more complex. In our previous research[41] the ZnS nanoparticles obtained by the mechanochemical synthesis dissolved in polymethyl methacrylate (PMMA) were studied. The experimental spectrum of the ZnS nanoparticle is characterized by several broader structures, broad multimodal features in 130–200 cm^{-1} region, along with the broad structures centered at 263, 346, and 425 cm^{-1}. Like in the far-infrared spectra analysis, the phonon influence at 310 cm^{-1} was observed. Congruence of the fitted spectrum with the experimental one is better when it is performed with this phonon.

Figure 4c shows the Raman spectra of the zno@zns core-shell nanostructure. Beside the phonons which originate from the initial constituents, there are two new structures evident at 246 and 472 cm^{-1}. In addition, the structure at approximately 310 cm^{-1} is shifted to the lower wavenumbers, while phonon observed at 346 cm^{-1} originating from ZnS is shifted at 349 cm^{-1}.
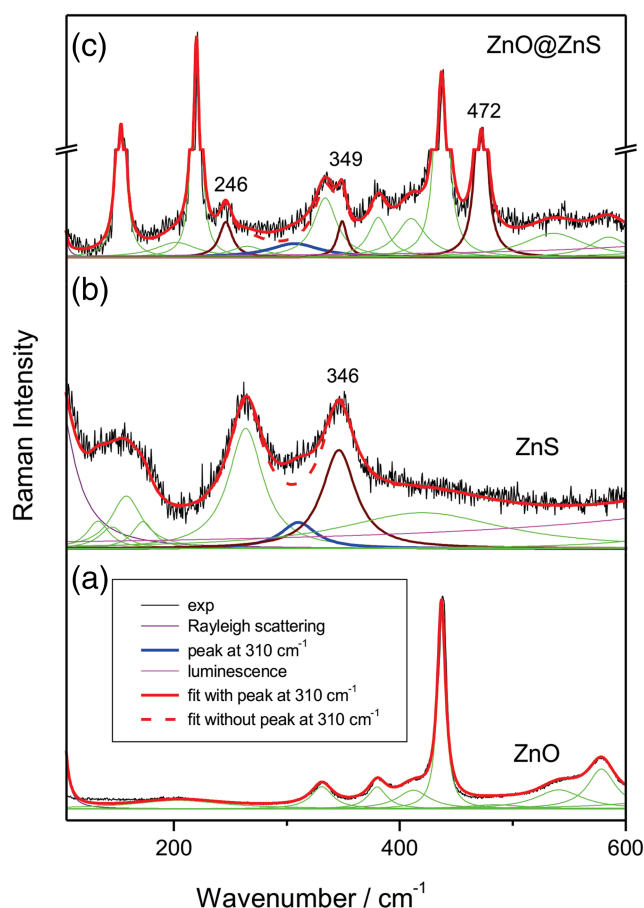
FIGURE 4 (a–c) Raman spectra for all investigated samples. The measured spectra are represented by dark line; theoretical spectra are convolution of Lorentzian curves [Colour figure can be viewed at wileyonlinelibrary.com]

4 | DISCUSSION

In the examined samples the ZnO particles are observed as big cylinders, few hundreds of nm in size. But even for the nanoparticles of few nanometers, as a consequence of the rather flat ZnO dispersion in the Brillouin zone, the effect of the optical phonons confinement is negligible, and the experimental spectra are almost the same as in the case of the bulk samples. This can also be applied to the ω_{LO} phonon of ZnS at about 350 cm^{-1}. Its shift toward the lower wavenumbers is expected and consistent with the corresponding nano dimension.[34]

Surface modes are difficult to be observed experimentally. But we roughly analyzed investigated nanoparticles (particle material, geometry, and dielectric permittivity if surrounding material), and we find that some feature in experimental spectra can be fairly good identified as surface modes. We used typical values of ZnO and ZnS dielectric parameters that are in our earlier papers: ZnO ($\varepsilon_0 = 10.24$, $\varepsilon_{\text{besk}} = 4.47$); ZnS($\varepsilon_0 = 8.1$; $\varepsilon_{\text{besk}} = 5$).

In principle, if nano-objects are present, then the surface of the whole particle is in contact with the matrix. Surface optical phonons (SOP) are characteristic when these nano-objects embedded in the matrix are concerned, and their activity becomes significant since they appear in the experimental spectra. Surface phonons are the most prominent in the spectra of the objects a few nanometers in size. The ZnO nanoparticles in the present study are cylindrical with axial symmetry. To find the wavenumbers of surface phonons the classic electrostatic equation for the appropriate geometry must be solved taking into account the interface conditions, that is, the object geometry must be treated properly.[42,43] Results of the study showed that for the cylinder-like nano-objects two types of surface phonons are characteristic: side surface optical phonons (SSO) and top surface optical phonons (TSO). SSO modes are related to the cylindrical interface (like in the cylindrical wire), and TSO modes are related to the planar interface (base of the cylinder).[42–44] There are two types of TSO mode: anti-symmetric and symmetric. Besides the geometry of the objects, surface optical frequencies are sensitive to the surface environment, that is, dielectric permittivity of the outer medium. All surface mode wavenumbers are in region $\omega_{TO} < \omega_{SOP} < \omega_{LO}$, that is, $\omega_{\text{IITO}} < \omega_{SOP} < \omega_{\text{mixedLO}} \approx 572$ cm^{-1}. In real samples spectra, surface optical wavenumbers depend on the surface quality, that is, surface roughness and arrangement and density of the nano-objects, resulting in the effective surrounding medium permittivity.

In the experimental ZnO spectra a wide feature of very low intensity is centered at ∼484 cm^{-1}. This mode can be assigned as the surface optical mode,[42,43] or even more precise as TSO.[44] In the experimental spectra, a wide feature of middle low intensity centered at about 540 cm^{-1} can also be observed. This mode can be assigned as the surface optical mode.[45]

Surface mode wavenumbers for the ZnS particles are the solution of the same equation [43] but in the spherical case. If the non-polar matrix surrounds spherical QD (case of radial, i.e., central symmetry), there is one surface mode for each quantum number l. The wavenumber of these modes does not depend on the sphere radius. In the case of ZnS QD without matrix, that is, in a vacuum ($\varepsilon_{\text{matrix}} = 1$), wavenumbers of $l = 1$ and $l = 2$ surface phonons are ∼330 and ∼334 cm^{-1}, respectively. When the matrix is concerned, it must be noted that when the dielectric permittivity is increasing to the value higher than 1, then the surface modes wavenumbers are decreasing. The calculated surface mode wavenumber ($l = 1$, $\varepsilon_{\text{matrix}} = 2$) is 310 cm^{-1}. Mode in the spectral region from 300 to 330 cm^{-1} can be assigned as the ZnS nanoparticle surface mode.[34]

In the case of ZnO@ZnS, the surface optical ZnO mode at 484 cm^{-1} (TSO) is completely screened by the impurity mode. Surface optical ZnO mode at 540 cm^{-1} is at the same position and with the almost unchanged intensity as in the ZnO nanoparticles spectra. The surface optical ZnS mode of low intensity is at position 305 cm^{-1}. It is not clear if the ZnS shell is complete and uniform over the entire ZnO cylinder, but this decrease of the surface optical mode wavenumber is a sign that ZnS is effectively in $\varepsilon_{\text{matrix}} < 2$.

Surface optical modes are treated rudimentary, and this is not the main contribution in this paper. It is a possible explanation for these low-intensity features that appear in the experimental spectra. Position of these modes gives fairly good identification.

Raman active modes registered at 246 and 472 cm^{-1} for ZnO@ZnS core-shell nanostructure (Figure 3) were not observed in starting components. It can be assumed that in this case impurity modes are in question. Considering previous observation, it seems that in this case, during the formation of the ZnO@ZnS core-shell nanostructure the phenomenon indicated in Figure 3 occurred. To be precise, in the thin layer between ZnS and ZnO migration of oxygen and sulfur took place. This indicates that oxygen originated from ZnO migrated into the ZnS lattice where it substituted sulfur, while sulfur, in the same way, migrated into the ZnO lattice. New vibrational modes, separated from the host lattice modes, can appear when the supplementary atoms are integrated into the host lattice. When the amount of the impurity atoms is minor in comparison to the amount of the host lattice atoms, the generated mode is "localized." Namely, its eigenvector doesn't have a sinusoidal or wavelike dependence on space, but is strongly peaked at the impurity atom, and wanes rapidly on one or two lattice sites away.[46]

More precisely, when the lighter element (sulfur in this case) in the binary mixture ZnS ($m_S < m_{Zn}$) is replaced by the even lighter impurity (oxygen, $m_O < m_S$), a local mode is formed above the top of the optical band of ZnS. On the other hand, when the heavier impurity (sulfur) replaces the lighter element (oxygen) within the binary mixture (ZnO) a gap-mode is formed below the bottom of the optical band of the binary mixture.

Calculation of the local-mode and gap-mode wavenumbers [47] involves a comprehension of the eigenfrequencies and eigenvectors of the host-crystal vibrational modes, as well as changes in the mass and force constant caused by the impurity atom. The mass-defect parameter $\varepsilon_j = 1 - M/M_j$ plays an important role, where M is the mass of the impurity atom and M_j is the mass of the host/crystal atom. For the limited number of the polar diatomic crystals, the three-dimensional

mass-defect calculation was performed. Using the full lattice dynamics, the additional calculations were made for particular types of impurities in some host crystals.[48–50]

Lucovsky et al.[51] established a simple model for the calculation of local modes in three-dimensional crystals. In the present case, when sulfur in ZnS is substituted with oxygen the obtained position of the local mode is 471 cm^{-1}, which is in excellent agreement with the experimentally obtained result.

In the opposite case, when the gap mode is formed as a consequence of the replacement of oxygen with sulfur in ZnO, the situation is more complex and the mass-defect parameter is $\varepsilon_j = -1$. Consequently, for this parameter value, used models show singularity and that makes them inappropriate. Because of that, the simplest way to calculate gap mode position using only isotope effect was chosen[48]; that is, only mass variation is taken into account, while the gap mode is obtained by the separation from the TO phonons of the starting crystal. Applying this method enabled the obtainment of the position of the sulfur gap-mode in ZnO at approximately 268 cm^{-1}. That is in a good agreement (difference is 9%) with the experimentally obtained position at 246 cm^{-1}.

Few crystallographic planes of crystal material must be present in the crystallite to register particular crystallographic structure of crystallite by XRD. This is not the case in the ZnO-ZnS interface region. We did not observe any peak in the XRD that originates from ZnO-ZnS mixing region. This region seems to be very narrow. But characteristics of this interface region are clearly seen from very intensive new Raman modes of ZnO-ZnS, that is, appearance of local and gap modes. Raman spectroscopy is known as sensitive to the close surrounding.

The registered phonon properties are directly related to the existence of the active layer isolated impurities in the binary system, that is, sulfur in ZnO and oxygen in ZnS. Matching of the experimentally and theoretically obtained values indicates the complete incorporation of the impurities into the binary system with all the properties that this phenomenon brings. Obtained results will be a starting point for the continuation of the research in this field toward the application of these materials as thermoelectrics.

5 | CONCLUSION

The ZnO@ZnS core-shell nanostructure with an active layer is obtained by conversion of zinc oxide powders with H$_2$S. SEM images and XRD patterns shown the existence of a cylindrical nanostructure confirming at the

same time that core-shell structure is usually characterized by the same morphology as a core, in this case ZnO. Using Raman and Far-infrared spectroscopy the phonons characteristics of the starting components were registered. TSO in ZnO, characteristic for the cylindrical nano-objects, the surface optical phonon (SOP) mode of ZnS as well as SOP modes in ZnO@ZnS core-shell nanostructure are registered. Local-mode of oxygen in ZnS and gap-mode of sulfur in ZnO are also registered. These results are due to the existence of an active layer in the space between the ZnO core and the ZnS shell. These findings are very important for the potential application of these materials as thermoelectrics.

ORCID

Branka Hadzic https://orcid.org/0000-0001-5459-7461
Maja Romcevic https://orcid.org/0000-0002-5064-175X

REFERENCES

[1] S. S. Kumar, P. Ventakeswarlu, V. R. Rao, *Int. Nano Lett.* **2007**, *61*, 2054.

[2] A. Kushwaha, M. Aslam, *Electrochim. Acta* **2014**, *130*, 222.

[3] K. J. Klabude, *Nanoscale Materials in Chemistry*, Wiley Intercience, New York **2001**.

[4] N. Romcevic, R. Kostic, B. Hadzic, M. Romcevic, I. Kuryliszyn-Kudelska, W. D. Dobrowolski, U. Narkiewicz, D. Sibera, J. Alloys, *Compd.* **2010**, *507*, 386.

[5] J. M. Azpiroz, E. Mosconi, F. De Angelis, J. Phys. Chem. C **2011**, *115 (51)*, 25219.

[6] P. V. Raleaooa, A. Roodt, G. G. Mhlongo, D. E. Motaung, R. E. Kroon, O. M. Ntwaeaborw, *Physica B Condens. Matter* **2017**, *507*, 13.

[7] C. W. Raubach, Y. V. De Santana, M. M. Ferrer, P. G. Buzolin, J. R. Sambrano, E. Longo, *Dalton Trans.* **2013**, *42*, 11111.

[8] M. Sookhakian, Y. M. Amin, W. J. Basirun, M. Tajabadi, N. Kamarulzaman, *J. Lumin.* **2014**, *145*, 244.

[9] G. Homm, M. Piechotka, A. Kronenberger, A. Laufet, F. Gather, D. Hartung, C. Heiliger, B. Mayer, P. Klar, S. Steinmller, J. Janek, *J. Electron. Mater.* **2010**, *39*, 1504.

[10] G. Homm, J. Teubert, T. Henning, P. J. Klar, B. Szyszka, *Phys. Status Solidi C* **2010**, *7(6)*, 1602.

[11] M. Bachmann, M. Czerner, S. Edalati-Boostan, C. Heiliger, *Eur. Phys. J. B* **2012**, *85*, 146.

[12] J. Huso, J. R. Ritter, L. Bergman, M. D. McCluskey, *Phys. Status Solidi B* **2019**, *256*, 1800607.

[13] M. Bachmann, M. Czerner, C. Heeliger, *Phys. Status Solidi A* **2013**, *210(1)*, 125.

[14] K. L. Pisane, S. K. Singh, M. S. Seehra, *J. Appl. Phys.* **2015**, *117 (17)*, 17D708.

[15] A. V. Nomoev, S. P. Bardakhanov, M. Schreiber, D. G. Bazarova, N. A. Romanov, B. B. Baldanov, B. R. Radnaev, V. V. Syzrantsev, *Beilstein J. Nanotechnol.* **2015**, *6*, 874.

[16] A. M. El-Toni, M. A. Habila, J. P. Labis, Z. A. Althman, M. Alhoshan, A. A. Elzatahry, F. Zhangg, *Nanoscale* **2016**, *8*, 2510.

[17] S. Hou, Y. Chi, Z. Zhao, *IOP Conf. Ser. Mater. Sci. Eng.* **2017**, *182*, 012026.

[18] Y. F. Zhu, D. Fan, W. Shen, *J. Phys. Chem. C* **2008**, *112*, 10402.

[19] M. Sundararajan, P. Sakthivel, A. C. Fernandez, J. Alloys, *Compd.* **2018**, *768*, 553.

[20] E. M. Flores, C. W. Raubach, R. Gouvea, E. Longo, S. Cava, M. L. Moreira, *Mater. Chem. Phys.* **2016**, *173*, 347.

[21] K. T. Lee, B. H. Choi, J. U. Woo, J. S. Kang, J. H. Paik, B. U. Chu, S. Nahm, *J. Europ. Ceramic Soc.* **2018**, *38*, 4237.

[22] B. S. Rema Devi, R. Raveendrana, V. Vaidyan, *Pramana – J. Phys.* **2007**, *68(4)*, 679.

[23] E. Zheng, Y. Wang, J. Song, X. F. Wang, W. Tian, G. Chen, T. Miyasaka, *J. Energy Chem.* **2018**, *27(5)*, 1461.

[24] P. V. Raleaooa, A. Roodt, G. G. Mhlongo, D. E. Motaung, R. E. Kroon, O. M. Ntwaeaborwa, *Phys. B* **2017**, *507*, 13.

[25] Powder Diffraction File, PDF-2 Database, announcement of new data base release **2012**, International Centre for Diffraction Data (ICDD).

[26] C. Suryanarayana, M. Grant Norton, *X-ray Diffraction: A Practical Approach*, Springer, New York **1998** Version 2012.

[27] T. Ghrib, M. A. Al-Messiere, A. L. Al-Otaibi, *J. Nanomater.* **2014**, *2014*, 989632.

[28] J. Han, W. Liu, T. Zhang, K. Xue, W. Li, F. Jiao, W. Qin, *Sci. Rep.* **2017**, *7*, 42536.

[29] P. Banerjee, P. K. Jain, *RSC Adv.* **2018**, *8*, 34476.

[30] A. K. Kole, P. Kumbhakar, *Results Phys.* **2012**, *2*, 150.

[31] T. Ungar, *J. Mater. Sci.* **2007**, *42*, 1584.

[32] B. Hadzic, N. Romcevic, M. Romcevic, I. Kuryliszyn-Kudelska, W. Dobrowolski, J. Trajic, D. Timotijevic, U. Narkiewicz, D. Sibera, J. Alloys, *Compd.* **2012**, *540*, 49.

[33] P. Bruesch, *Phonons: Theory and experiments II* **1986**, 2. United States: Springer-Verlag New York Inc.

[34] J. Trajic, R. Kostic, N. Romcevic, M. Romcevic, M. Mitric, V. Lazovic, P. Balaz, D. Stojanovic, J. Alloys, *Compd.* **2015**, *637*, 401.

[35] G. Abstreiter, M. Cardona, A. Pinczuk, in *Light Scattering in Solids, IV*, Ed. By M. Cardona and G. Guntherodt (Springer-Verlag, Berlin, **1984**).

[36] E. Burstein, A. Pinczuk, R. F. Wallis, in *The Phys. of Semimetals and Narrow-Gap Semicon*, (Eds: D. L. Carter, R. T. Bate), Pergamon, New York **1971**.

[37] A. Sihvola, *IEE Electromagnetic Waves Series* **1999**, *47*.

[38] J. C. Maxwell Garnett, *Phil. Trans. R. Soc. A.* **1904**, *203*, 385.

[39] B. H. Henry, J. R. During (Eds), *Raman spectroscopy: Sixty Years On*, Vol. 10, Elsevier, Amsterdam **1990**.

[40] B. Hadzic, N. Romcevic, M. Romcevic, I. Kuryliszyn-Kudelska, W. Dobrowolski, R. Wróbel, U. Narkiewicz, D. Sibera, J. Alloys, *Compd.* **2014**, *585*, 214.

[41] M. Curcic, B. Hadzic, M. Gilic, V. Radojevic, A. Bjelajac, I. Radovic, D. Timotijevic, M. Romcevic, J. Trajic, N. Romcevic, *Physica E Low Dimens. Syst. Nanostruct.* **2020**, *115*, 113708.

[42] P. M. Chassaing, F. Demangeot, V. Paillard, A. Zwick, N. Combe, *Appl. Phys. Lett.* **2007**, *91 (5)*, 053108.

[43] P. M Chassaing, F. Demangeot, V. Paillard, A. Zwick, N. Combe, C. Pagès, M. L. Kahn, A. Maisonnat, B. Chaudret, *J Phys Conf Ser.* **2007**, *92*, 012165.

[44] P. M. Chassaing, F. Demangeot, V. Paillard, A. Zwick, N. Combe, C. Pages, M. L. Kahn, A. Maisonnat, B. Chaudret, *Phys. Rev. B* **2008**, *77*, 153306.

[45] A. Pescaglini, E. Secco, A. Martin, D. Cammi, C. Ronning, A. Cantarero, N. Garrob, D. Iacopino, *J. Mater. Chem. C* **2016**, *4*, 1651.

[46] A. S. Baker, A. J. Sievers, *Rev. Mod. Phys.* **1975**, *47*, S1.

[47] P. G. Dawber, R. J. Elliott, *Proc. Roy. Soc. (London)* **1963**, *A273*, 222.

[48] J. Mitric, U. Ralevic, M. Mitric, J. Cirkovic, G. Krizan, M. Romcevic, M. Gilic, N. Romcevic, *J. Raman Spectrosc.* **2019**, *50* (6), 802.

[49] R. Kostic, M. Petrovic-Damjanovic, N. Romcevic, M. Romcevic, D. Stojanovic, M. Comor, J. Alloys, *Compd.* **2012**, *521*, 134.

[50] I. F. Chang, S. S. Mitra, *Phys. Rev.* **1968**, *172*(3), 924.

[51] G. Lucovsky, M. H. Brodsky, E. Burstein, *Phys. Rev. B* **1970**, *2*, 3295.

SUPPORTING INFORMATION

Additional supporting information may be found online in the Supporting Information section at the end of this article.

How to cite this article: Hadzic B, Matovic B, Randjelovic M, et al. Phonons investigation of ZnO@ZnS core-shell nanostructures with active layer. *J Raman Spectrosc.* 2021;52:616–625. https://doi.org/10.1002/jrs.6058

Structural and optical properties of ZnO–Al$_2$O$_3$ nanopowders prepared by chemical methods

N. Romcevic [a], B. Hadzic [a,*], M. Romcevic [a], N. Paunovic [a], D. Sibera [b], U. Narkiewicz [b],
I. Kuryliszyn-Kudelska [c], J.L. Ristic-Djurovic [a], W.D. Dobrowolski [c]

[a] Institute of Physics, University of Belgrade, Pregrevica 118, 11080, Belgrade, Serbia
[b] West Pomeranian University of Technology, Institute of Chemical and Environment Engineering, Pulaskiego 10, 70-322, Szczecin, Poland
[c] Institute of Physics, Polish Academy of Science, Aleja Lotnikow 32/46, PL-02668, Warszawa, Poland

ARTICLE INFO

ABSTRACT

The nanopowders of $(ZnO)_{1-x}(Al2O3)_x$, where x ranges from 0 to 0.7, were obtained by two chemical methods: the co-precipitation/calcination and hydrothermal synthesis. The first assessment of structural and optical properties of the obtained nanopowders was undertaken by the SEM, XRD, Raman and far-infrared spectroscopy, which was followed by the photoluminescence spectroscopy at room temperature. The obtained far-infrared reflectivity spectra were analyzed using the fitting procedure. The dielectric function of ZnO–Al$_2$O$_3$ nanopowders was modeled by the Maxwell-Garnet formula under the assumption that the nanopowders are a mixture of homogenous spherical inclusions in air. The combined plasmon-LO phonon modes (CPPM) were observed in the far-infrared reflection spectra. The photoluminescence spectra contain emissions related to the presence of ZnO, ZnAl$_2$O$_4$, and AlOOH phases in the nanomaterial, which is in agreement with the results obtained by other experiments.

1. Introduction

In the field of material science, there are two materials that have held a special position and have attracted significant attention due to a variety of their physical properties and a prospect of numerous applications. These are the wide bandgap semiconductor – zinc oxide (ZnO) and the ceramic material – aluminum oxide (Al$_2$O$_3$).

Most often, ZnO crystallizes as a hexagonal wurtzite structure with the direct band gap of 3.4 eV and the crystal-growth direction along the *c* axis. These properties qualify ZnO as a material suitable for application in the optoelectronic devices. In addition, a unique optical, acoustic and electric properties of ZnO, such as the high binding energy of 60 meV, high radiation, as well as chemical and thermal resistance, can be useful in the light-emitting UV and laser diodes, solar cells, gas sensors, biosensors, varistors, and surface acoustic wave devices [1,2].

Due to different positions of aluminum ions in the oxygen sublattice, aluminum oxide can exist in a variety of metastable structures as well as in its stable α-Al$_2$O$_3$ phase, which makes it suitable for many different uses and consequently results in the high production of aluminum oxide worldwide. For example, it is applied in the chemical industry as an adsorbent, abrasive, filler, ceramics, refractory, and catalyst; it is used as the protective barrier against corrosion, alternative surgical material for implants, as well as in the fabrication of the cutting tools and electronic devices [3,4].

In addtion to the important features of ZnO and Al$_2$O$_3$ themselves, materials that combine the two have been proven to have properties of good candidates for a wide range of applications. For example, spinel ZnAl$_2$O$_4$ may be applied in photoelectronic devices, optical coatings, stress imaging devices, and electroluminesence displays due to its wide energy bandgap, high values of fluorescence efficiency, photocatalytic activity, mechanical resistance, chemical and thermal stability, as well as low surface acidity [5–7]. In a number of studies it has been shown that the optical properties of spinel ZnAl$_2$O$_4$ depend strongly on the method used to prepare the material and the achieved morphology of the material [8–12]; namely, nanodimensional structures introduced enhanced optical and fluorescence properties that were not present in the bulk material. Further, the optical and fluorescence properties depend on the particle size that was achieved, as well. This is expected since larger specific surface area of smaller particles and consequent more present dangling and unsaturated bonds on the particle surface

* Corresponding author.
  E-mail address: branka@ipb.ac.rs (B. Hadzic).

affect defect levels and material properties [13]. Methods of spinal $ZnAl_2O_4$ synthesis vary from the hydrothermal [11], solvothermal [14], microwave-hydrothermal [15], co-precipitation [10], sol-gel [16], combustion synthesis [17], citrate precursor [8], polymeric precursor [18], solid-state reaction method [19,20] to self-generated template [19]. The main disadvantage of the co-precipitation, solid-state reaction, and other common synthesis methods is the large obtained particle size.

With the aim to obtain small diameter nanoparticles of $ZnAl_2O_4$ surrounded by ZnO we used the calcination and hydrothermal method.

The luminescence was used as the principal method of investigation, whereas the XRD, Raman spectroscopy, and IR spectroscopy in the MID range [1–20] where used to characterize the samples. The elipsometric spectroscopy was employed as an aid in the analysis [21]. In addition to the standard methods of characterization of this group of materials, we used the IR spectroscopy in the far-infrared region to detect electron-phonon interaction, which further led to the explanation of the luminescence spectra.

The infrared (IR) spectroscopy is a well-known, simple, and reliable technique that is widely used in studying inorganic and organic materials. It is the absorbing type of spectroscopy, namely, different components of investigated materials absorb infrared light in a different wavelength domain. Consequently, the IR spectroscopy is very sensitive in detecting the presence of functional groups as well as of a single molecule type within a sample, since they each have a different characteristic spectrum that is often referred to as the fingerprint. The main advantages of the IR spectroscopy are the high scan speed, high resolution, high sensitivity, and wide range of application; it does not destroy the sample, and it provides a large amount of information. These advantages of the IR spectroscopy are followed by its use not only as a method for material analysis in science but in the industry as well. For example, it is used in the quality control, dynamic measurements, forensic analysis, identification and analysis of art pieces in general as well as of pigments in paintings, polymer manufacture, semiconductor microelectronics, food industry, gas leak detection devices, etc. [22–27]. In our study, it was the method of choice because it provides insight into the plasmon – phonon interaction. Recorded phonons participate in electron transfers and they must be included in the photoluminescence spectra analysis.

The interaction of electrons with crystal lattice vibrations denoted as phonons plays a significant role in shaping various properties of materials, for example, electrical characteristics of semiconductor-based devices, superconductivity, and the existence of the charge-density waves. Coupling of the longitudinal optical (LO) phonons with the surrounding free charge carrier plasmons result in the formation of the combined LO phonon – plasmon modes (CPPM). The published research most often investigate the interaction between a single phonon and effective plasmons in the n-type semiconductors, as well as the consecutive influence of the plasmon damping on the CPPM [28].

We intend to combine the Raman, far-infrared and photoluminescence spectroscopy to study the fundamental properties of combined plasmon – phonon modes in the ZnO–Al_2O_3 nanoparticles as well as the influence of sample preparation method and dopant concentration on the characteristics of obtained materials.

2. Samples preparation and characterization

The nanocrystalline samples of ZnO doped with Al_2O_3 were obtained by two methods. In the first method, the co-precipitation/calcination method, a mixture of aluminum and zinc hydroxides was obtained by adding an ammonia solution to a 20% solution of a proper amount of Zn $(NO_3)_2 \cdot 6H_2O$ and $Al(NO_3)_3 \cdot 4H_2O$ in water. The obtained hydroxides were filtered, dried, and calcinated at 300 °C for 1 h. The co-precipitation/calcination method is further referred to as the calcination method.

In the second method, namely, in the hydrothermal synthesis, a

similar procedure was applied. Instead of the ammonia solution, now the 2 M solution of KOH was used. The obtained hydroxides were then put in a reactor with the microwave emission. The microwave assisted synthesis was conducted under the pressure of 3.8 MPa that was applied for 30 min. The synthesized product was filtered and dried. The hydrothermal synthesis is further denoted as the hydrothermal method. Each of the described two methods were used to obtain series of nano-sized $(ZnO)_{1-x}(Al2O3)_x$ samples with the nominal concentration of Al_2O_3 ranging from $x = 0$ to 0.7.

Powders obtained by chemical methods were pressed under very small preassure into tablets with 1 cm in diameter. The tablets were used in the vibrational measurements.

2.1. X-ray spectroscopy

The powder diffraction technique (XRD), was applied to determine the phase composition of the samples, using the X'Pert Philips device with the CoK_α radiation, in the 2θ mode. The detail phase composition study revealed the presence of crystalline phases of the hexagonal ZnO and spinel structured $ZnAl_2O_4$ in the samples synthesized by both methods, namely, by the co-precipitation/calcination as well as by the hydrothermal method (Fig. 1).

The XRD data was combined with the Scherrer's formula to determine the mean crystallite size in the studied samples [29]. To determine the mean crystallite size of ZnO phase, the diffraction peak corresponding to (102) reflection (at about 2θ = 47°) was taken, and to determine the mean crystallite size of the spinel $ZnAl_2O_4$ phase - a diffraction peak corresponding to the (400) reflection (located at about 2θ = 44°) was taken, respectively. It was found that the mean crystallite size, d, varies between 12 and 81 nm for the ZnO phases and is of the order of 5 nm for the $ZnAl_2O_4$ phases in the samples obtained by the calcination method, whereas for the samples that were obtained by the hydrothermal method the mean crystallite sizes were determined to be between 22 and 100 nm for the ZnO phases and from 5 to 13 nm for the $ZnAl_2O_4$ phases. The results of the XRD measurements, i.e., the phase compositions, as well as the mean crystallite size, are summarized in Table 1.

The results given in Table 1 indicate that, regardless of the method used to prepare the samples, the crystallite size of ZnO does not change monotonously with the increase of Al_2O_3 concentration. An increase of the ZnO crystallinity above the Al_2O_3 concentration of 20 wt% can be explained by faster transformation of smaller ZnO particles into spinel phase. As smaller particles of ZnO are more prone to react with Al_2O_3 to form a spinel, then the larger ZnO particles remain in the system as non-reacted, giving in the result an increased mean particle size of ZnO phase.

The crystallite size of the phase $ZnAl_2O_4$ in the samples obtained by the calcination method is constant, whereas, for the samples obtained hydrothermally, it becomes constant after the initial decrease with the increase of Al_2O_3 concentration. Consequently, the change of crystallite size of $ZnAl_2O_4$ with the nominal content of Al_2O_3 is smaller than for the ZnO phase. For both methods the obtained data didn't allow to obtain the size of ZnO crystallites above 50% of nominal content of Al_2O_3 although their presence has been registered in Fig. 1.

Similarly, for the samples with low Al_2O_3 concentration (up to 30% of Al_2O_3 for calcination method, and up to 10% of Al_2O_3 for hydrothermal method) the presence of the $ZnAl_2O_4$ phase has been registered; however the data didn't allow to calculate the size of nanocrystallites. Note that the crystallite size of the $ZnAl_2O_4$ phase in the samples obtained by both methods is constant for dopant concentrations higher than 50% (a stoichiometric concentration of Al_2O_3 in the spinel as about 55 wt%). For the highest dopant concentration of 70%, the XRD spectrum corresponding to the hydrothermally prepared sample reveals existence of the AlOOH phase (Fig. 1), as there is an excess of aluminum in the system, and not enough ZnO to form the spinel. The size of ZnO crystallites in the samples obtained by the hydrothermal method is
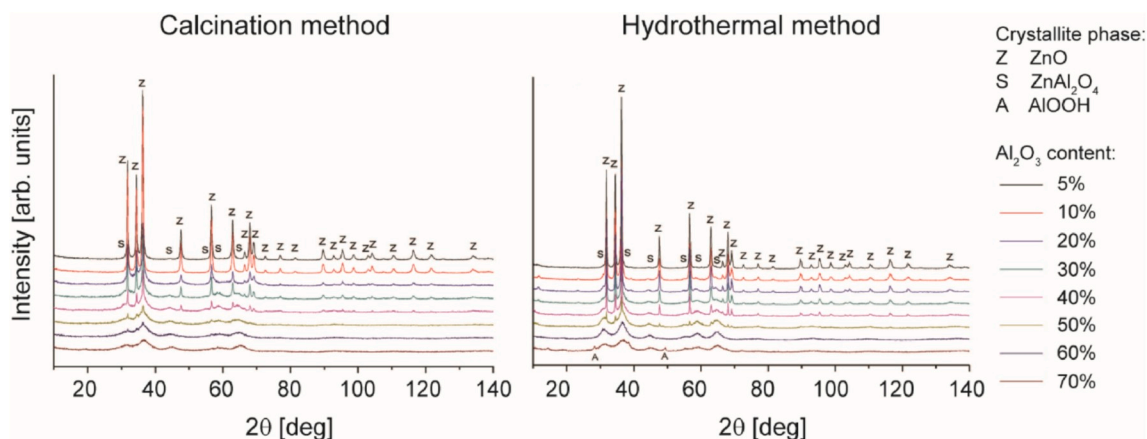
Fig. 1. XRD spectra of $(ZnO)_{1-x}(Al2O3)_x$ nanoparticles. The spectra are grouped into graphs according to the method used to prepare the samples, namely the calcination and hydrothermal method. The spectra given for the eight values of the dopant content, x, are differentiated by the line color. Three different crystallite phases were detected, Z, S, and A, which correspond to the ZnO, $ZnAl_2O_4$, and AlOOH, respectively.

Table 1
Mean crystallite size. The Scherrer's formula and XRD measurements were used to identify crystalline phases and calculate the mean crystallite size, d. The obtained results illustrate the dependence of mean crystallite size on the Al_2O_3 presence as well as on the method used to prepare the samples (calcination and hydrothermal method).

Al_2O_3 wt.%	d [nm] ZnO phase calcination	d [nm] ZnO phase hydrothermal	d [nm] $ZnAl_2O_4$ phase calcination	d [nm] $ZnAl_2O_4$ phase hydrothermal
5	25	41	–	–
10	26	22	–	–
20	12	50	–	13
30	31	34	–	7
40	81	100	5	5
50	–	–	5	5
60	–	–	5	5
70	–	–	5	5

larger than in the samples obtained by the calcination method. A reverse relationship was observed in our previous studies of the nanosized ZnO samples doped with other metal oxides [30–32]. The observed dependence is probably caused by the extension of the hydrothermal synthesis time to 30 min compared to the 15 min long synthesis that was used in our previous studies. Longer synthesis time caused ZnO crystallites to undergo significant agglomeration. Note that no other crystal phases besides the reported ones were observed in all the examined samples.

2.2. Scanning electron microscope (SEM)

The morphology of samples was investigated using the scanning electron microscope LEO 1530. The SEM images of the four representative samples for the calcination as well as hydrothermal method of sample preparation are given in Fig. 2.

The SEM characterization revealed a broad diversity in the morphology of samples. The images of samples with 10%, 30%, 50%, and 70% of Al_2O_3 are shown in Fig. 2. For the calcinated samples two types of agglomerates were observed: the plate-like agglomerates bigger than 100 nm and the smaller, spherical ones. It can be assumed that the larger and smaller ones correspond to the ZnO and $ZnAl_2O_4$ phase, respectively. In the calcinated samples with 50% of Al_2O_3 the particles that belong to the ZnO phase are covered with the smaller $ZnAl_2O_4$ particles, whereas for the Al_2O_3 concentration of 70%, the small particles that belong to the $ZnAl_2O_4$ phase dominate.

In the SEM images of the samples obtained by the hydrothermal method, the hexagonal agglomerates are observed for the sample with 30% of Al_2O_3 in addition to the previously discussed morphologies. In

the sample with the Al_2O_3 concentration of 70% the homogeneous agglomerates that can be related to the $ZnAl_2O_4$ phase are visible.

For both methods of synthesis, the smallest agglomeration is observed in the samples with a high nominal content of the aluminum oxide. Note that these results agree well with those that were obtained by the XRD measurements.

3. Vibrational spectroscopy

The phases of ZnO and $ZnAl_2O_4$ were previously registered by the XRD measurements. Since the understanding of vibrational properties of the bulk material is crucial for the analysis of the vibration properties of nanoparticles, we begin the analysis of vibrational properties with a brief report of the literature data of the registered phases. The bulk modes are expected to be shifted and broadened as a consequence of the miniaturization.

The zinc oxide crystallizes in the wurtzite type hexagonal structure, and the growth of its crystals occurs along the c-axis [33]. Since the unit cell of zinc oxide contains four atoms, its spectrum is characterized by twelve vibrational modes: the three acoustic modes (one longitudinal and two transverse) and nine optical modes. The dispersion of optical phonons at the Γ point of the Brillouin zone is represented by the optical modes $2E_2 + 2E_1 + 2A_1 + 2B_1$. The modes E_1, E_2, and A_1 are active in the Raman scattering. The modes E_1 and A_1 are active in the infrared spectroscopy, and the modes B_1 are the "silent modes". The optical modes E_1 and A_1 are split at the Γ point into the transverse and longitudinal modes by the macroscopic crystal field. The splitting of the E_1 and A_1 modes is caused by the anisotropy of the ZnO crystal. In particular, the A_1 vibrations are parallel to the crystallographic c-axis, whereas the E_1 vibrations are perpendicular to it. Two sets of parameters are required to describe the dielectric function of a phonon, i.e., $\varepsilon_{xx} = \varepsilon_{yy} \equiv \varepsilon_\perp$ and $\varepsilon_{zz} \equiv \varepsilon_{||}$, along the electric field vector (E), perpendicular ($E \perp c$), and parallel ($E \parallel c$) to the crystal c-axis, respectively [34].

The Zn-aluminate, $ZnAl_2O_4$, crystallizes in the space group Fd3m with two formula units in the primitive rhombohedral unit cell [35]. The Zn and Al occupy the tetrahedral and the octahedral positions, respectively, in the close cubic oxygen packing. The group-theory analysis shows that 39 zone-center optical phonons are classified by the following symmetries [36]: the $\Gamma = A_{1g} + 2A_{2u} + E_g + 2E_u + T_{1g} + 4T_{1u} + 2T_{2u} + 3T_{2g}$. All the E modes are double degenerate, and all the T modes are ternary degenerate. The A_{1g}, E_g, and all the T_{2g} modes are Raman active, while all the T_{1u} modes are infrared active.
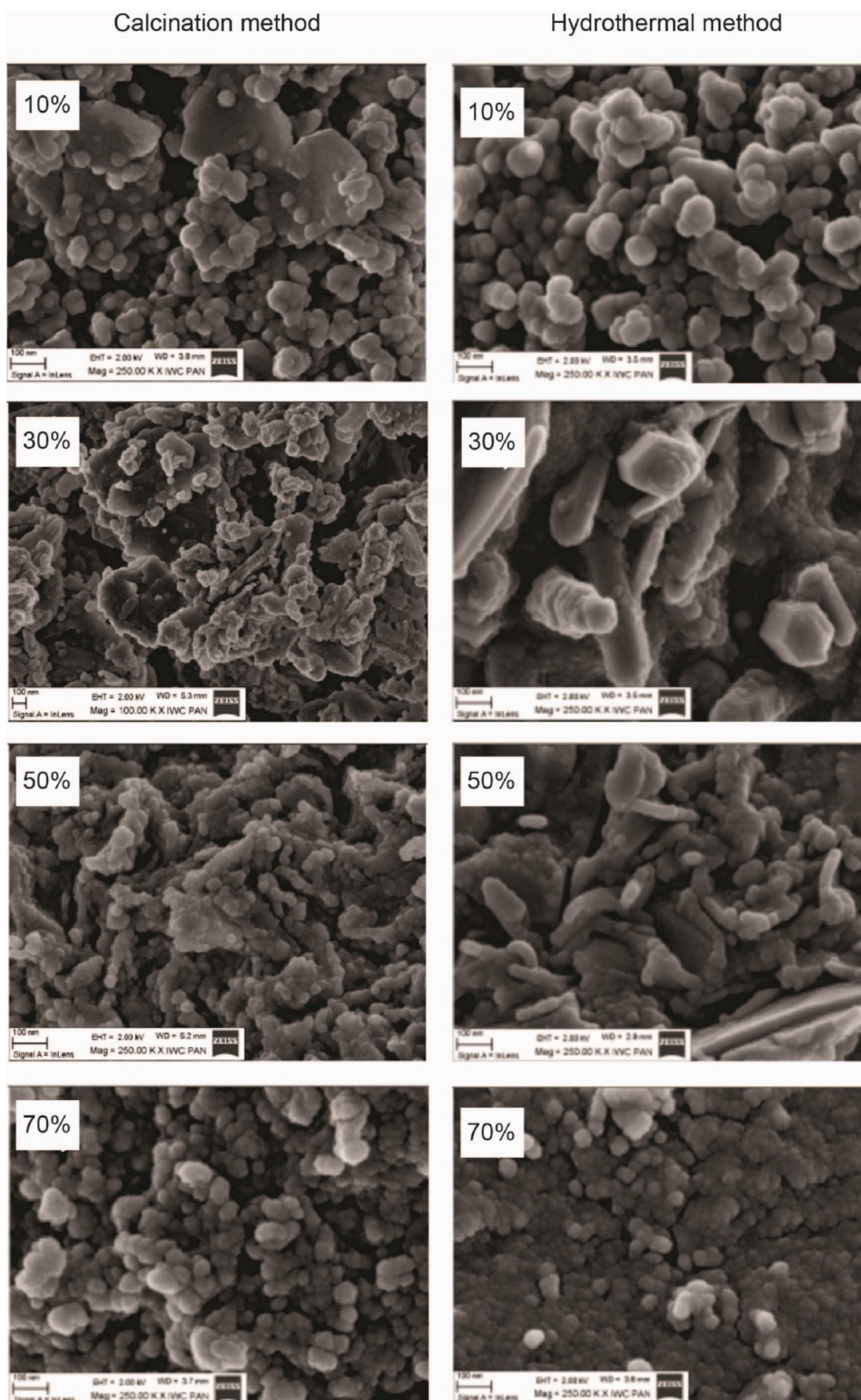
Fig. 2. SEM images of $(ZnO)_{1-x}(Al2O3)_x$ nanoparticles. The images of the samples with the Al_2O_3 content, *x*, of 10, 30, 50, and 70% that were prepared by the calcination as well as by the hydrothermal method, are given.

3.1. Raman spectroscopy

The micro-Raman spectra were taken in the backscattering config-uration and analyzed using Jobin Yvon T64000 spectrometer, equipped with nitrogen cooled charge-coupled-device detector. As an excitation source we used the Verdi G optically pumped semiconductor laser with the 532 nm line. The measurements were performed at 60 mW laser power, which is the same power density as was the case for the photo-luminescence measurements.

In Fig. 3 four representative spectra for samples prepared by the both
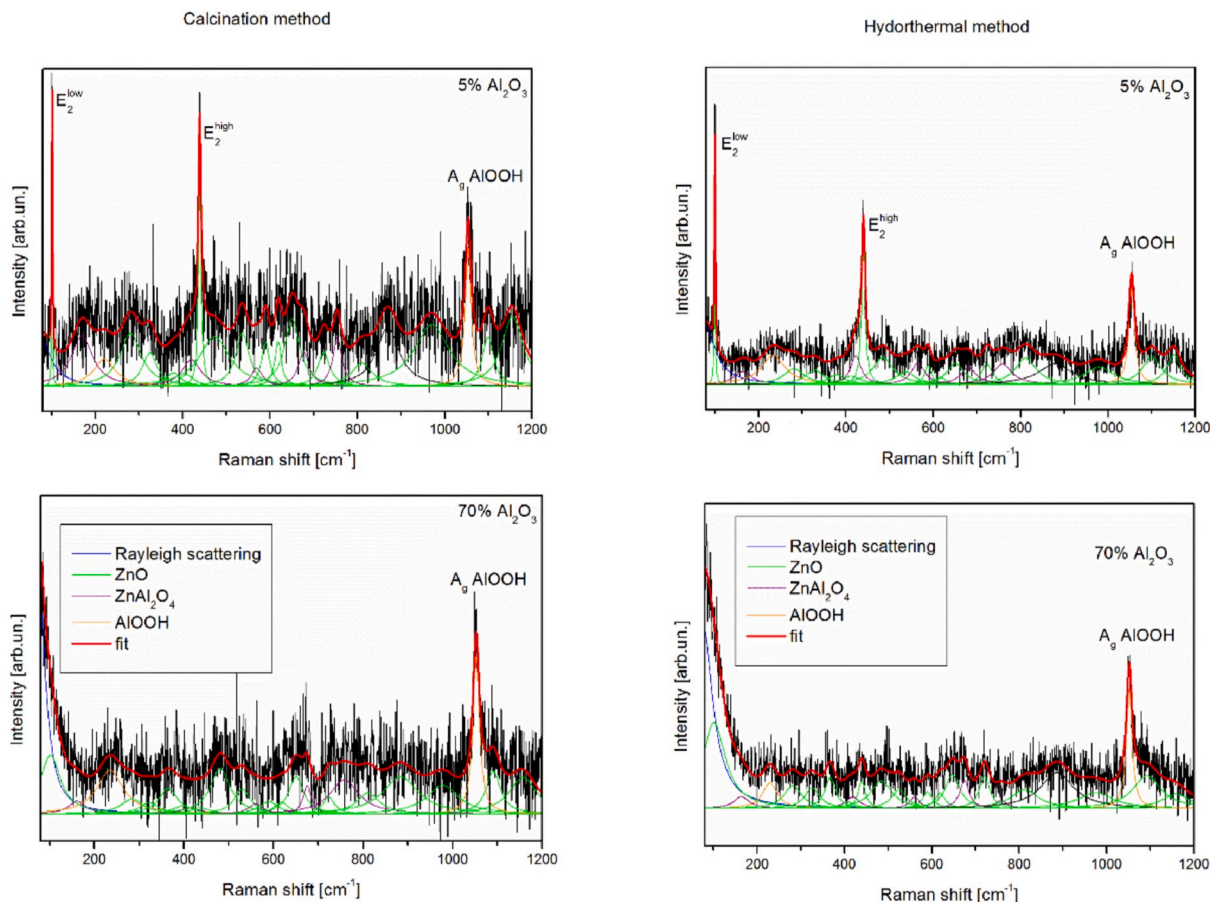
Fig. 3. Raman spectra of $(ZnO)_{1-x}(Al2O3)_x$ nanoparticles. The spectra are given for the reprezentative samples prepared by the calcination as well as by the hydrothermal method. The measured spectra are represented by dark line, theoretical spectra is depicted by a thick line, and the components that comprise the approximated curve are given as thin lines Eq. (1). The parameter defining different curves is the percentage of Al_2O_3.

methods and with nominal dopant concentration of 5% and 70% Al_2O_3 are shown. The Raman spectra are often analyzed using the convolution of the Lorentzian functions, each of which has line intensity, I, given with

$$I(\omega) = \frac{2A}{\pi} \frac{W}{4(\omega - \omega_c)^2 + W^2}, \qquad (1)$$

where ω_c, W, and A are the position of the maximum, the half-width of the peak, and peak intensity, respectively. The measured data depicted with lines in Fig. 3 are approximated with the calculated thick curve, which represents the sum of the components each defined with Eq. (1).

By using all Raman active peaks that correspond to $ZnAl_2O_4$, such as 169, 417, 566, 682 and 758 cm^{-1} [36], and most of the peaks related to ZnO, such as 101, 284, 333, 378, 410, 437, 483, 536, 590, 618, 657, 723, 812, 980, 1105 and 1158 cm^{-1} [30], it was possible to reproduce the obtained experimental spectra. For the smaller dopant concentration, for both types of samples the most dominant peaks in the spectra are the two well-known ZnO peaks at 101 (E_2^{low}) and 437 cm^{-1} (E_2^{high}). All four representative spectra characterize one more peak towering above others. The peak at 1053 cm^{-1} belongs to the AlOOH phase. ZnO has multi phonon peak at 1054 cm^{-1}; however, due to the shape and FWHM (full width at half maximum) of the obtained peak in all four experimental Raman spectra it can assumed that this peak belongs to AlOOH phase. The existence of this phase is also confirmed by another peak at 232 cm^{-1} that is present in all the obtained spectra [37]. Consequently, it can be concluded that when ZnO is doped with Al_2O_3 three phases are formed, namely, ZnO, $ZnAl_2O_4$, and AlOOH. Low visibility of the AlOOH phase in the XRD measurements lead to the conclusion that the

concentration of AlOOH is low but it increases with the increase of the dopant (Al_2O_3) concentration, which once more confirms high sensitivity of the Raman spectroscopy.

Taking into account the results obtained with XRD as well as Raman measurements we get a clear picture of phases present in the investigated ZnO–Al_2O_3 nano-system.

3.2. Far-infrared spectroscopy

The far-infrared measurements were carried out with a BOMEM DA – 8 FIR spectrometer. A DTGS pyroelectric detector was used to cover the wavenumber range from 80 to 680 cm^{-1}. The far-infrared spectra at room temperature of ZnO–Al_2O_3 nanopowders obtained by the calcination and hydrothermal methods are presented in Fig. 4. The experimental data are presented by circles, whereas the solid lines are used to show the calculated spectra.

Let us consider the interaction between a visible light of wavelength λ and semiconducting nanoparticles that are defined by their characteristic size, d, and dielectric function, ε_2, and are distributed in a medium with the dielectric constant ε_1. If a heterogeneous composite can be treated as a homogeneous medium with the effective dielectric permittivity, ε_{eff}, and the condition that relates the light and the nanoparticles, $\lambda \gg d$, is satisfied than the effective medium theory can be applied in a study of the interaction. There are many mixing models of the effective dielectric permittivity that correspond to such a mixture [38]. Since our samples are well defined and separated nanosized grains (Fig. 2), we used the Maxwell-Garnet model. For the spherical inclusions, spheres of permittivity ε_2 are located randomly in a homogeneous environment with permittivity ε_1 and occupy a volume fraction f.
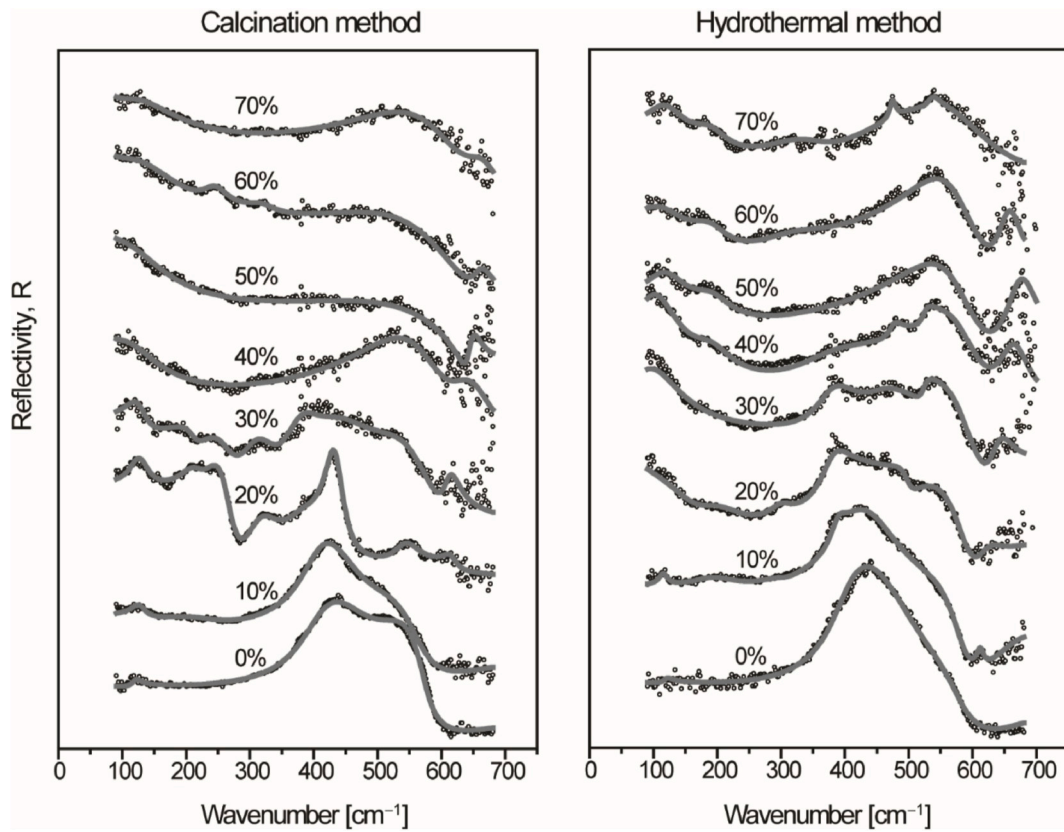
Fig. 4. Far-infrared reflection spectra of $(ZnO)_{1-x}(Al_2O_3)_x$ nanoparticles prepared by calcination and hydrothermal methods. The experimentally obtained data points are depicted by circles. The theoretical spectra given as the solid lines are obtained with the model defined by Eqs. (2) and (4) and the fitting procedure. The curve parameter is the dopant content, x, in percentages.

According to the Maxwell-Garnet mixing rule, the prediction of the effective permittivity of such a mixture is [39,40].

$$\varepsilon_{eff} = \varepsilon_1 + 3f\varepsilon_1 \frac{\varepsilon_2 - \varepsilon_1}{\varepsilon_2 + 2\varepsilon_1 - f(\varepsilon_2 - \varepsilon_1)}, \quad (2)$$

The ZnO–Al$_2$O$_3$ nanoparticles are situated in the air, therefore $\varepsilon_1 = 1$. Defining ε_2, the dielectric function of ZnO–Al$_2$O$_3$ nanoparticles is not so straight forward. The low-frequency dielectric properties of single crystals are described with the classical oscillators corresponding to the TO-modes, to which the Drude part is superimposed in order to take into account the free carrier contribution [41]. Consequently, the dielectric function of a single crystal takes the form

$$\varepsilon_s(\omega) = \varepsilon_\infty + \sum_{k=1}^{l} \frac{\varepsilon_\infty(\omega_{LOk}^2 - \omega_{TOk}^2)}{\omega_{TOk}^2 - \omega^2 - i\gamma_{TOk}\omega} - \frac{\varepsilon_\infty\omega_P^2}{\omega(\omega + i\Gamma_P)}, \quad (3)$$

where ε_∞ is the high frequency dielectric constant, ω_{LOk} and ω_{TOk} are the longitudinal and transverse optical phonon frequencies, ω_{LO} is the plasma frequency, γ_{TOk} is the damping of host crystal modes, and Γ_P is the plasmon mode damping coefficient.

For the ZnO–Al$_2$O$_3$ nanoparticles, the pure LO modes of the lattice are strongly influenced by the plasmon mode, ω_P, which causes the appearance of a combined plasmon – LO phonon mode (CPPM) [41,42]. Consequently, if the LO mode is to be determined, the influence of free carriers must be eliminated. Hence, in the analysis of far-infrared reflection spectra of our samples, we used the dielectric function that includes the interaction between the LO phonon and a plasmon, i.e., the plasmon – phonon interaction [41,43].

$$\varepsilon_2(\omega) = \varepsilon_\infty \frac{\prod_{j=1}^{2}\left(\omega^2 + i\gamma_{lj}\omega - \omega_{lj}^2\right)}{\omega(\omega + i\Gamma_P)\left(\omega^2 + ig\omega - \omega_t^2\right)} \prod_{k=1}^{s} \frac{\omega^2 + i\gamma_{kLO} - \omega_{kLO}^2}{\omega^2 + i\gamma_{kTO} - \omega_{kTO}^2}. \quad (4)$$

The ω_{lj} and γ_{lj} ($j = 1, 2$) parameters of the first numerator are the eigenfrequencies and damping coefficients of the longitudinal plasmon – phonon (LP + LO) waves, that arise from the interaction of the initial modes (ω_{LO} corresponding to ZnO or ω_{LO} corresponding to Al$_2$O$_3$ (actually ZnAl$_2$O$_4$), and ω_P). The parameters of the first denominator correspond to the transverse (TO) vibrations. The second term represents the uncoupled modes of a crystal, where s is the number of uncoupled modes, ω_{LO} and ω_{TO} are the longitudinal and transverse frequencies, and γ_{LO} and γ_{TO} are the damping coefficients of the k-th crystal mode.

Therefore, the TO mode frequencies were obtained directly from the fit, whereas the LO modes were determined by the maximum of the dielectric loss function. As a result, the combined plasmon – LO phonon modes (ω_{l1}, ω_{l2}) were observed. In the experimental spectra, only the coupled-mode positions are observable. Therefore, detection of the LO-modes is closely related to the decoupling procedure [41]. The described procedure, i.e., the dielectric function from Eq. (2) and ε_2 from Eq. (4) is used to obtain the curves depicted with solid lines in Fig. 4.

The parameter adjustment was carried out automatically, using the least-square fitting of the theoretical (R_t) and experimental (R_e) reflectivity at q arbitrarily taken points:

$$\delta = \sqrt{\frac{1}{q}\sum_{j=1}^{q}\left(R_{ej} - R_{tj}\right)^2} \quad (5)$$

The value of δ was minimized until it complied with the commonly

accepted experimental error (less than 3%). For all the samples the determination errors of frequencies and damping coefficients were in the range 3–6 and 10–15%, respectively. The exact values of all determined phonon parameters are given in Tables S1 and S2 of the Supplementary material.

The dependence of the plasma frequency, ω_P, high-frequency dielectric constant, ε_∞, and filling factor, f, on the dopant content is given in Fig. 5. The plasma frequency is given as $\omega_P = \omega_{l1}\omega_{l2}/\omega_t$, $(\omega_P^2 \sim N$, where N is the free carriers concentration) [41]. Note that the dopant content of 20% acts as the limiting value that separates two sets of
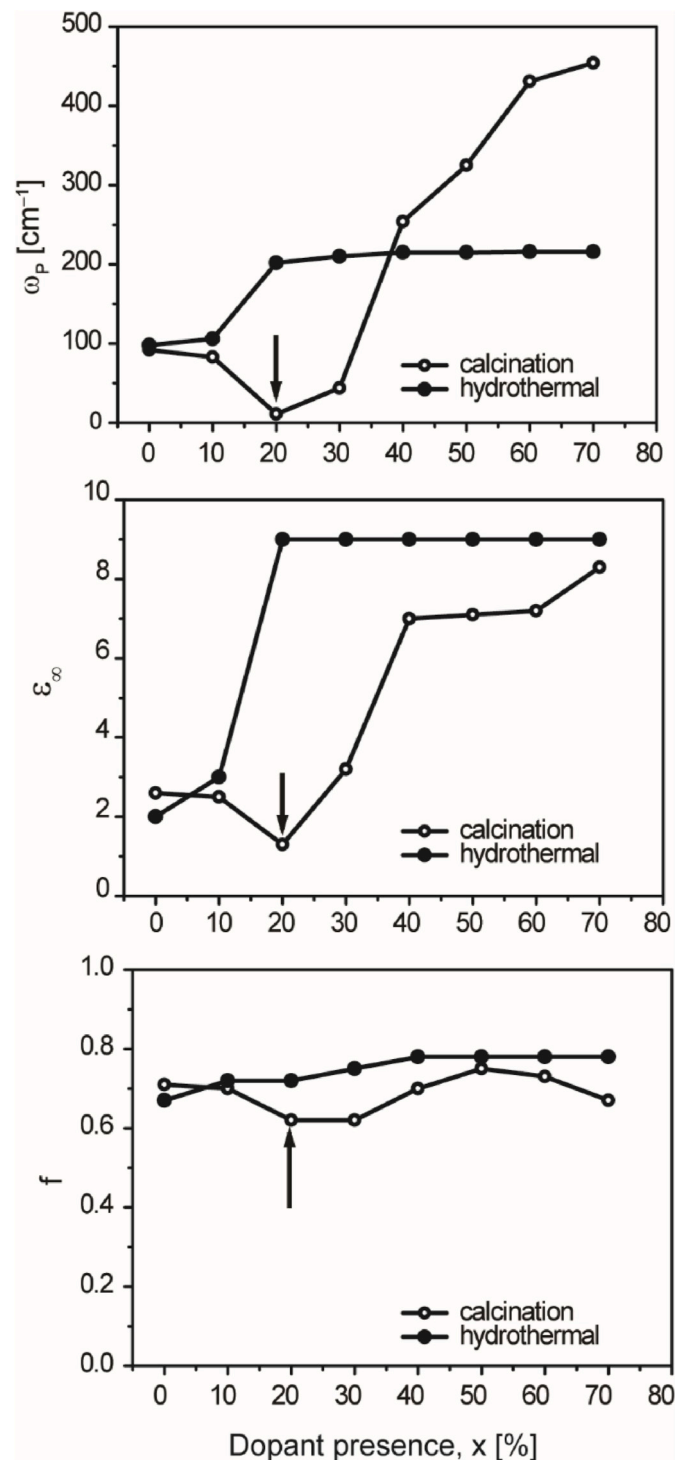

Fig. 5. Dependence of plasma frequency, ω_P, high frequency dielectric constant, ε_∞, and filling factor, f, on dopant content, x.

spectra shown in Fig. 4. It is the same dopant content value of 20% that corresponds to the minimal value of ω_P, and, consequently, the lowest concentration of free carriers, N, in the samples prepared by the calcination method, as shown in Fig. 5. This causes the plasmon – phonon interaction to be the weakest and, therefore, the detection of the primal phonons to be the most accurate for this particular composite. In the samples prepared by the hydrothermal method, ω_P monotonically increases with the increase of dopant concentration. In the samples with dopant concentration below the 20%, an interaction between the plasma and the ZnO phonon ($\omega_{TO} = 370$ cm^{-1}) occurs, whereas for the composites on the other side of the limiting value of 20% the interaction of plasma and ZnAl$_2$O$_4$ phonon ($\omega_{TO} = 543$ cm^{-1} T$_{1u}$(2) symmetry) is registered. This argumentation is supported by the dependence of ε_∞ on the sample composition. Note that it is the effective value of ε_∞ that is being considered here. For the samples obtained by the calcination method ε_∞ has the value of 2.6 for the pure ZnO, it decreases to the value of 1.3 for the samples with 20% of Al$_2$O$_3$, and then increases to reach the value of 8.3 for the Al$_2$O$_3$ content of 70% (Fig. 5).

For the samples prepared by the hydrothermal method the ε_∞ dependence is different, namely, it increases monotonically with the dopant concentration increase. For all our samples the error in determining ε_∞ was 3%. The reflectivity measurements in the mid-infrared region that were used in this process are given in the Supplementary materials as Fig. S1Fig. S1. The filing factor, f, has a similar behavior, which is shown in Fig. 5 as well.

Characteristic spectra for the plasmon – LO phonon interaction are presented in Fig. 6. The frequencies of coupled modes (ω_{l1} and ω_{l2}) and the transverse mode frequencies marked by circles were obtained as the best fits. The lines labeled as ω_+ and ω_- are the solutions of the real part of Eq. (3), namely of Re{ε_S} = 0. The values of the LO and TO frequencies that correspond to the ZnO and ZnAl$_2$O$_4$ are emphasized with the horizontal solid and dashed lines, respectively, for better visualization. As stated earlier, for the composites with 0% and 10% of Al$_2$O$_3$, a plasmon interacts with the ZnO phonon, whereas for the composites with the Al$_2$O$_3$ content larger than 20%, the interaction of a plasmon with the T$_{1u}$(2) ZnAl$_2$O$_4$ phonon occurs. From the results given in Fig. 6 it is evident that the plasmon – phonon interaction exists in the entire range of the studied composites. Note that the experimental and the theoretical spectra match perfectly well.

To obtain a good match between the experimental and the theoretical spectra are given in Fig. 4, several phonons that were not predicted by the selection rules, had to be taken into account in the analysis of certain composites. The TO-LO splitting registered in some phonons is a result of the plasmon-phonon interaction, as can be seen in Tables S1 and S2. The phonon at approximately 110 cm^{-1}, that is most commonly attributed to a defect mode [44] was included in the spectral interpretation of all studied samples. As was the case in the Raman spectra, the phonons at 320, 378, 426, 483, 536, 600, and 670 cm^{-1} correspond to ZnO, whereas those around 200, 410, and 510 cm^{-1} are due to ZnAl$_2$O$_4$. Their appearance is caused by the attenuation of selection rules due to miniaturization. This effect might be the main reason for the difference between the phonons resulting from the fitting procedure illustrated in Fig. 4 and those discussed in Ref. [45]. On the other hand, a similar effect can be caused by the surface-optical phonons [30]; however, they are a consequence of nanoparticles formation, as well. Besides, in the spectra of the some samples the existence of weak modes at approximately 240 and 440 cm^{-1} that can be associated with the AlOOH phase, is evident. This is consistent with the results obtained by the XRD and Raman measurements that detected the AlOOH phase.

4. Photoluminescence spectroscopy

Optical properties of the samples were investigated with the photoluminescence (PL) spectroscopy. The spectro-fluometer SOLAR CM 2203 with the excitation wavelength of 300 nm (4.13 eV) was used and the obtained PL spectra are shown in Fig. 7. The measured spectra are
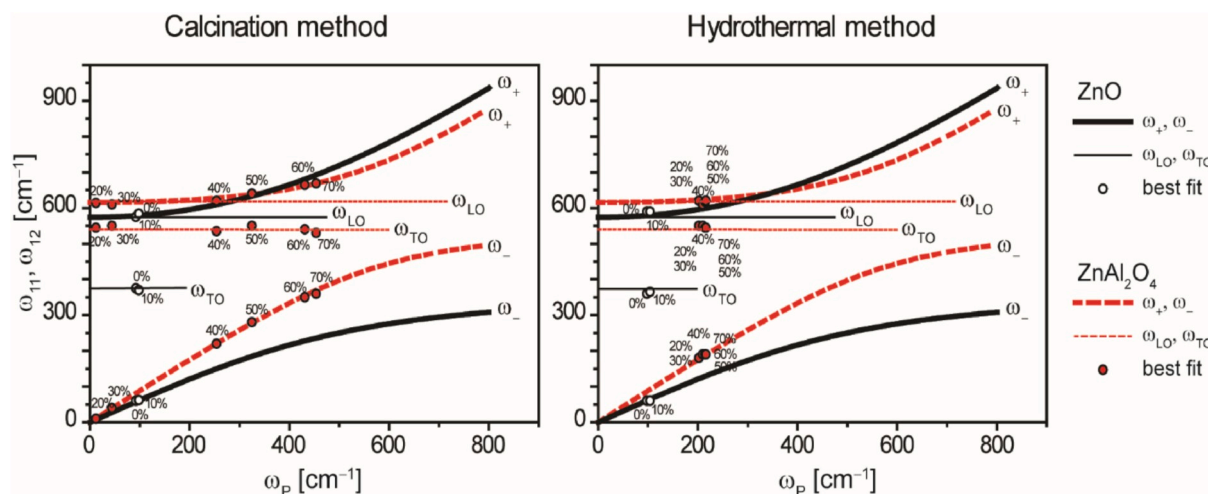
Fig. 6. Eigenfrequencies of plasmon-phonon modes of $(ZnO)_{1-x}(Al2O3)_x$ nanoparticles. The solid and dashed lines are the spectra calculated from $Re\{\varepsilon_s\} = 0$, where ε_s is given by Eq. (3), whereas the open and solid circles represent ω_{l1} and ω_{l2}. The black solid lines and open circles denote the coupling with the ZnO phonon, whereas the red, dashed lines and solid circles correspond to the coupling with the $ZnAl_2O_4$ phonon.

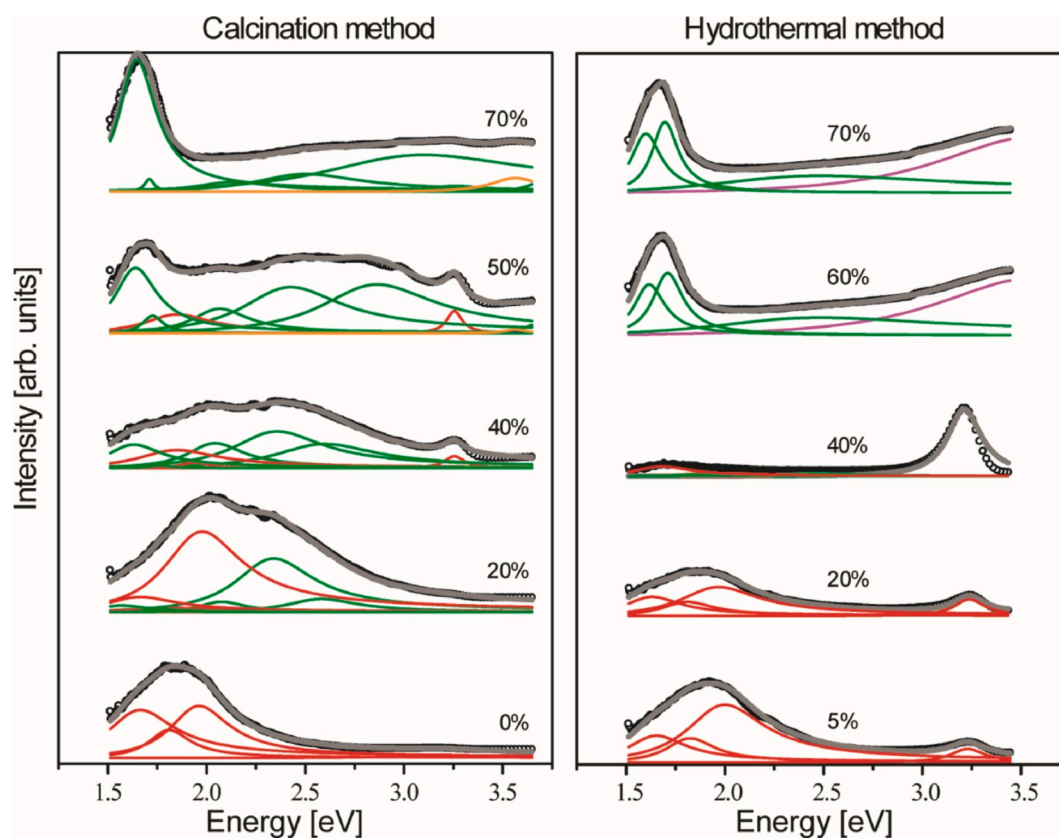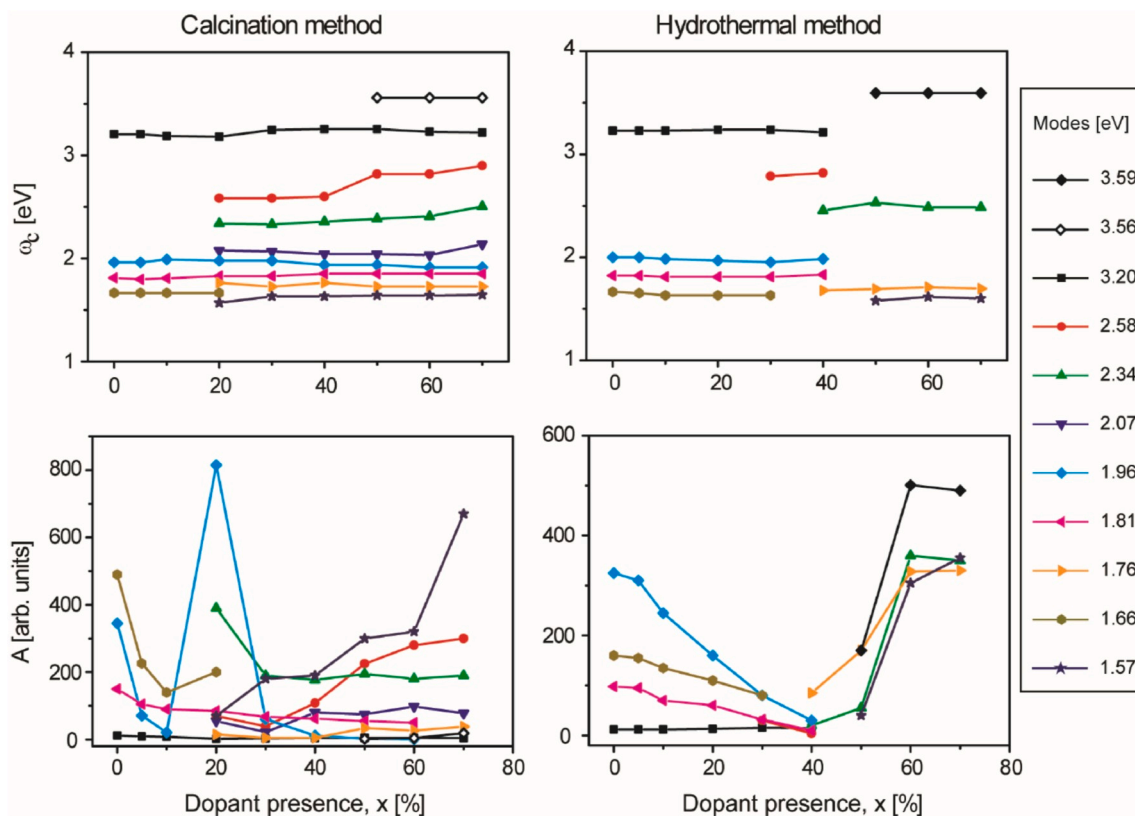**Fig. 7.** Photoluminescence spectra of $(ZnO)_{1-x}(Al2O3)_x$ nanoparticles. The spectra are given for the samples prepared by the calcination as well as by the hydrothermal method. The measured spectra are represented by circles, theoretical spctra is depicted by a thick line, and the components that comprise the approximated curve are given as thin lines. The parameter defining different curves is the percentage of Al_2O_3.

represented by circles, and theoretical spectra is depicted by a thick line, and the components that comprise the approximated curve are given as thin lines (eq. (1)). The values of the positions, ω_c, and intensities, A, of the Lorentzian peaks that provide the best match between the experimental and theoretical spectra are given in Fig. 8.

The spectra in Fig. 7 that correspond to the samples obtained by the hydrothermal method can be divided: the spectra of samples with Al_2O_3 concentration below and above 40%. If the dopant concentration is

lower and equal 40% the PL spectra contain two emission bands, namely the band at 3.20 eV and the broad structure centered at approximately 1.9 eV. For the composites with the dopant concentration higher than 40%, the emission band at 3.20 eV becomes wider and a new band appears at approximately 3.59 eV (purple).

The PL spectra of the samples prepared by the calcination method are qualitatively different from those corresponding to the hydrothermal method. If the samples were prepared by the calcination method,

Fig. 8. Dependence of position and intensity of photoluminescence peaks on dopant concentration. For the nanoparticle compositions of $(ZnO)_{1-x}(Al2O3)_x$ prepared by the calcination as well as by the hydrothermal method, the dependence of the position, ω_c, and intensity, A, of the photoluminescence peaks on the dopant, Al_2O_3, presence, x, is given.

interweaving of all the bands occurs for almost all values of the dopant concentration in the composite. In this case, very weak emission was recorded around 3.56 eV for the samples with more than 40% of Al_2O_3 (orange).

For the hydrothermal method, the intensity of the peaks at 3.20, 2.58, 1.96, 1.81, and 1.66 eV decreases with the increase of the Al_2O_3 concentration in ZnO from 0 to 40% (Fig. 8). This indicates that these bands originate from ZnO; in Fig. 7 these Lorentzians are represented with the thin red lines. On the other hand, the bands at 2.34, 1.76, and 1.57 eV appear for the dopant content of 40% and more, and their intensity increases with the increase of dopant content; these $ZnAl_2O_4$ bands are represented in Fig. 7 with the thin green lines. Besade that, the peak located around 3.59 eV must be considered in the spectra corresponding to the samples with Al_2O_3 concentration larger than 40%. Taking into account the results obtained by the XRD, Raman, and IR measurements, it can be concluded that the emission in question is related to AlOOH, which is detected in our samples. Namely, the results presented in Ref. [46] indicate possible exsisance of a very broad emission in the range between 3 eV and 4 eV in AlOOH. In our case, this emission is supported by the presence of a metal Zn, which is used in disigning biosensors with this base [47]. Such wide emission masks the emission at 3.2 eV related to ZnO as can be seen in Fig. 7.

The structure of PL spectra that corresponds to the samples obtained by the calcination method is more complex. The peak positions are very close to those registered for the samples synthesized by the hydrothermal method. However, the bands that originate from the ZnO phase were registered independently only for the samples with the Al_2O_3 content of 10% or less. In all spectra with dopant content larger than 10% the bands corresponding to the $ZnAl_2O_4$ phase are present. The PL spectrum of the sample, with 20% of Al_2O_3 has several exciting features. The intensity of peaks at 2.34, 1.96, and 1.66 eV significantly deviates from the monotonous change, namely these peaks are much stronger for

this particular value than for any other value of the dopant presence. Consequently, in addition to the enhanced intensity of these bands, the spectrum itself is more intense. Note that this peculiarity was discovered in various ways in the analysis of the infrared spectra as well. The UV band centered at about 3.20 eV originates from the near-band-edge exciton and bound exciton emission of ZnO crystallite. For the samples with more than 40% of Al_2O_3 a very weak, relatively narrow emission is noticed at 3.56 eV. Its intensity very slowly increases with the increase of Al_2O_3 presence in the sample. However, for samples obtained by the hydrothermal method, intensity of emission in that region is 20 times larger than was the case for the samples obtained by the calcination method. The emission is positioned above the E_g of ZnO. In this case, the quantum confinement influence cannot be as strong as to move near-band-edge emission in ZnO to 3.6 eV, since nanoparticles smaller than 1 nm would be required. On the other hand, the value of E_g corresponding to $ZnAl_2O_4$ is arround 3.8 eV. In $ZnAl_2O_4$ narrow phonon supported emissions related to transfers from this level were reported [48]. Probably, one of the phonons of $T_{2g}(3)$, $T_{1u}(4)$, or $T_{2u}(2)$ symmetry in $ZnAl_2O_4$ that were detected in our Raman and IR measurements, participates in this emission, since their energies are appropriate. A detailed analysis is given in Ref. [48]. On the other hand, this emission can be related to the doping level formation in the range between the energy gaps of ZnO and $ZnAl_2O_4$ as suggested in Ref. [49].

On the other hand, for both methods, the bands at 2.58, 1.96, 1.81, and 1.66 eV are correlated with the radiative recombination of a photo-generated hole with an electron occupying the oxygen vacancy in ZnO [50–53], surface states [52,54], and interstitial oxygen defects, impurities as well as defects related to excess oxygen [55,56]. The bands at 2.34, 1.76, and 1.57 eV, which are related to the $ZnAl_2O_4$ phase, originate from the intra band gap defects, for example, oxygen vacancies, as suggested by Ragupathi et al. [57], Wang et al. [58] and Sun et al. [59].

5. Conclusions

The phase composition of nanocrystalline samples of ZnO–Al_2O_3 prepared by the co-precipitation/calcination method and by the hydrothermal synthesis was determined by the X-ray diffraction. The morphology was studied using SEM measurements. In all the studied samples, prepared by use of two different wet chemical methods, the crystalline phases of ZnO, $ZnAl_2O_4$ and AlOOH were identified. In our previous papers, we showed that physical properties (e.g., structural, magnetic) strongly depend on the synthesis method and conditions [60, 61].

The crystallite size of ZnO does not have a monotonous dependence on the nominal Al_2O_3 content. The crystallite size of the $ZnAl_2O_4$ phase is constant in the samples obtained by the calcination method, and it decreases with the increase of the Al_2O_3 content in the samples that were obtained by the hydrothermal method. The analysis of photoluminescence and far-infrared spectra of the samples prepared by the hydrothermal method indicated that the observed features as well as the electronic structure of the nanocomposites monotonically depend on nominal content of Al_2O_3. On the other hand, for the samples obtained by the calcination method with nominal Al_2O_3 content between 20 and 40% PL measurements revealed very complex spectra. In the analysis of the obtained far-infrared spectra, we treated our nanoparticles as homogenous spherical inclusions in air and modeled them by the Maxwell-Garnet formula. Besides the modes that are characteristic for the ZnO and $ZnAl_2O_4$ phases, the far-infrared spectroscopy detected the combined plasmon – LO phonon modes (CPPM). Taking the sample preparation method and dopant concentration as parameters, the relationship between the free carrier concentration and optical parameters was observed. The photoluminescence spectra contain emissions related to the presence of ZnO, $ZnAl_2O_4$, and AlOOH in the nanomaterials, which is in agreement with the results of other experiments.

Declaration of competing interest

The author(s) declared no potential conflicts of interest with respect to the research, authorship, and/or publication of this article.

Acknowledgments

Appendix A. Supplementary data

Supplementary data to this article can be found online at https://doi.org/10.1016/j.jlumin.2020.117273.

References

[1] P. Ooi, S. Lee, S. Ng, Z. Hassan, H. Abu Hassan, Far infrared optical properties of bulk wurtzite zinc oxide semiconductor, J. Mater. Sci. Technol. 27 (2011) 465.

[2] P.A. Rodnyi, I.V. Khodyuk, Optical and luminescence properties of zinc oxide, Optic Spectrosc. 111 (2011) 776.

[3] A. Boumaza, L. Favaro, J. Ledion, G. Sattonnay, J.B. Brubach, P. Berthet, A. M. Huntz, P. Roy, R. Tetot, Transition alumina phases induced by heat treatment of boehmite: an X-ray diffraction and infrared spectroscopy study, J. Solid State Chem. 182 (2009) 1171.

[4] R. Rinaldi, U. Schuchardt, On the paradox of transition metal-free alumina-catalyzed epoxidation with aqueous hydrogen peroxide, J. Catal. 236 (2005) 335.

[5] X.L. Duan, D.R. Yuan, F.P. Yu, Cation distribution in Co-doped ZnAl2O4 nanoparticles studied by X-ray photoelectron spectroscopy and 27Al solid-state NMR spectroscopy, Inorg. Chem. 50 (2011) 5460–5467.

[6] R. Ianos, S. Borcănescu, R. Lazaău, Large surface area ZnAl2O4 powders prepared by a modified combustion technique, Chem. Eng. J. 240 (2014) 260–263.

[7] E.L. Foletto, et al., Synthesis of ZnAl2O4 nanoparticles by different routes and the effect of its pore size on the photocatalytic process, Microporous Mesoporous Mater. 163 (2012) 29–33.

[8] X.Y. Li, Z.R. Zhu, Q.D. Zhao, L.Z. Wang, Photocatalytic degradation of gaseous toluene over ZnAl2O4 prepared by different methods: a comparative study, J. Hazard Mater. 186 (2011) 208–2096.

[9] C. Peng, et al., Fabrication and luminescence properties of one-dimensional ZnAl2O4 and ZnAl2O4: a³⁺ (A = Cr, Eu, Tb) microfibers by electrospinning method, Mater. Res. Bull. 47 (2012) 3592–3599.

[10] B.C. Cheng, Z.Y. Ouyang, B.X. Tian, Y.H. Xiao, S.J. Lei, Porous ZnAl2O4 spinel nanorods: high sensitivity humidity sensors, Ceram. Int. 39 (2013) 7379–7386.

[11] Z.R. Zhu, et al., Photocatalytic performances and activities of ZnAl2O4 nanorods loaded with Ag towards toluene, Chem. Eng. J. 203 (2012) 43–51.

[12] Y. Yang, et al., Hierarchical three-dimensional ZnO and their shape-preserving transformation into hollow ZnAl2O4 nanostructures, Chem. Mater. 20 (2008) 3487–3494.

[13] Z.Q. Yu, C. Li, N. Zhang, Size dependence of the luminescence spectra of nanocrystal alumina, J. Lumin. 99 (2002) 29–34.

[14] G.L. Fan, J. Wang, F. Li, Synthesis of high-surface-area micro/mesoporous ZnAl2O4 catalyst support and application in selective hydrogenation of o-chloronitrobenzene, Catal. Commun. 15 (2011) 113–117.

[15] M. Zawadzki, W. Staszak, F.E. López-Suárez, M.J. Illán-Gómez, A. Bueno-López, Preparation, characterisation and catalytic performance for soot oxidation of copper-containing ZnAl2O4 spinels, Appl. Catal. Gen. 371 (2009) 92–98.

[16] X. Wei, D. Chen, Synthesis and characterization of nanosized zinc aluminate spinel by sol–gel technique, Mater. Lett. 60 (2006) 823–827.

[17] R. Ianos, R. Lazău, I. Lazău, C. Păcurariu, Chemical oxidation of residual carbon from ZnAl2O4 powders prepared by combustion synthesis, J. Eur. Ceram. Soc. 32 (2012) 1605–1611.

[18] L. Gama, et al., Synthesis and characterization of the NiAl2O4, CoAl2O4 and ZnAl2O4 spinels by the polymeric precursors method, J. Alloys Compd. 483 (2009) 453–455.

[19] L. Zou, F. Li, X. Xiang, D.G. Evans, X. Duan, Self-generated template pathway to high-surface-area zinc aluminate spinel with mesopore network from a single-source inorganic precursor, Chem. Mater. 18 (2006), 5852–5856.

[20] N.J. Van der Laag, M.D. Snel, P.C.M.M. Magusin, G. De With, Structural, elastic, thermophysical and dielectric properties of zinc aluminate (ZnAl2O4), J. Eur. Ceram. Soc. 24 (2004) 2417–2424.

[21] Elipsometar.

[22] D.A. Skoog, F.J. Holler, S.R. Crouch, Principles of Instrumental Analysis, sixth ed., Thomson Higher Education, Belmont, CA, 2007.

[23] D.C. Harris, M.D. Bertolucci, Symmetry and Spectroscopy: an Introduction to Vibrational and Electronic Spectroscopy, Dover Publications, New York, 1989.

[24] P. Ricciardi, Unlocking the Secrets of Illuminated Manuscripts, Laboratory News, 2012. Retrieved. (Accessed 11 December 2015).

[25] W.S. Lau, Infrared Characterization for Microelectronics, World Scientific, 1999, ISBN 981-02-2352-8.

[26] A. Villar, E. Gorritxategi, E. Aranzabe, S. Fernandez, D. Otaduy, L.A. Fernandez, Low-cost visible–near infrared sensor for on-line monitoring of fat and fatty acids content during the manufacturing process of the milk, Food Chem. 135 (2012) 2756.

[27] J. Coates, A review of new small-scale technologies for near infrared measurements, June 18 (2014). www.americanpharmaceuticalreview.com.

[28] N. Romcevic, M. Romcevic, W.D. Dobrowolski, L. Kilanski, M. Petrovic, J. Trajic, B. Hadzic, Z. Lazarevic, M. Gilic, J.L. Ristic-Djurovic, N. Paunovic, A. Reszka, B. J. Kowalski, I.V. Fedorchenko, S.F. Marekin, Far-infrared spectroscopy of Zn1-xMnxGeAs2 single crystals: plasma damping influence on plasmon-phonon interaction, J. Alloys Compd. 649 (2015) 375.

[29] A.L. Patterson, The scherrer formula for X-ray particle size determination, Phys. Rev. 56 (1939) 978.

[30] B. Hadžić, N. Romčević, M. Romčević, I. Kuryliszyn-Kudelska, W. Dobrowolski, J. Trajić, D. Timotijević, U. Narkiewicz, D. Sibera, Surface optical phonons in ZnO (Co) nanoparticles: Raman study, J. Alloys Compd. 540 (2012) 49.

[31] B. Hadžić, N. Romčević, M. Romčević, I. Kuryliszyn-Kudelska, W. Dobrowolski, R. Wrobel, U. Narkiewicz, D. Sibera, Raman study of surface optical phonons in ZnO(Mn) nanoparticles, J. Alloys Compd. 585 (2014) 214.

[32] B. Hadžić, N. Romčević, M. Romčević, I. Kuryliszyn-Kudelska, W. Dobrowolski, U. Narkiewicz, D. Sibera, Influence of SOP modes on Raman spectra of ZnO(Fe) nanoparticles, Opt. Mater. 42 (2015) 118.

[33] V.S. Vinogradov, V.N. Dzhagan, T.N. Zavaritskaya, I.V. Kucherenko, N.N. Melnik, N.N. Novikova, E. Janik, T. Wojtowicz, O.S. Plyashechnik, D.R.T. Zahn, Optical phonons in the bulk and on the surface of ZnO and ZnTe/ZnO nanowires in Raman spectra, Phys. Solid State 54 (2012) 2083.

[34] G. Mirjalili, T.J. Parker, S.F. Shayesteh, M.M. Bulbul, S.R.P. Smith, T.S. Cheng, C. T. Foxon, Far-infrared and Raman analysis of phonons and phonon interface modes in GaN epilayers on GaAs and GaP substrates, Phys. Rev. B 57 (1998) 4656.

[35] N.W. Wyckoff, Crystal Structures, vol. 2, Intersciences, New York, 1962.

[36] M.M. Sinha, J.S. Kim, Analysis of vibrational modes and phonon density of states of aluminate spinels, J. Kor. Phys. Soc. 43 (2003) 237.

[37] A.B. Kiss, G. Keresztury, L. Farkas, Raman and i.r. spectra and structure of boehmite (γ-AlOOH). Evidence for the recently discarded D2h¹⁷ space group, Spectrochim. Acta 36 (1980) 653.

[38] K. Karkkainen, A. Saviola, K. Nikoskinen, Analysis of a three-dimensional dielectric mixture with finite difference method, IEEE Trans. Geosci. Rem. Sens. 39 (2001) 1013.

[39] J.C.M. Garnett, Colours in metal glasses and in metallic films, Trans. R. Soc. CCIII (1904) 385.

[40] A. Saviola, I. Lindell, Polarizability modeling of heterogeneous media, in: A. Priou (Ed.), Dielectric Properties of Heterogeneous Materials, PIER 6 Progres in Electromagnetic Research, Elsevier, Amsterdam, The Netherlands, 1992, p. 101.

[41] J. Trajic, N. Romcevic, M. Romcevic, V.N. Nikiforov, Plasmon-phonon and plasmon-two different phonon interaction in Pb1-xMnxTe mixed crystals, Mater. Res. Bull. 42 (2007) 2192.

[42] T. Hamaguchi S. Shimomura Takaoka, K. Murase, Observation of the coupled plasmon- lo phonon mode energy in photo-excited Pb1-xSnxTe doped with indium impurities, Solid State Commun. 54 (1985) 99.

[43] A.A. Kukharskii, Plasmon – phonon coupling in GaAs, Solid State Commun. 8 (1970) 1275.

[44] H. Kepa, T. Giebultowicz, B. Buras, B. Lebech, K. Clausen, A neutron scattering study of lattice dynamics of HgTe and HgSe, Phys. Scripta 25 (1982) 807.

[45] P. Ooi, S. Lee, S. Ng, Z. Hassan, H.A. Hassan, Far infrared optical properties of bulk wurtzite zinc oxide semiconductor, J. Mater. Sci. Technol. 27 (2011) 465.

[46] J. Garcia-Guinea, J. Rubio, V. Correcher, F.J. Valle-Fuenter, Luninescence of α-Al2O3 and α-AlOOH natural mixtures, Radiat. Meas. 33 (2001) 653–658.

[47] B. Rezaei, Z. Hassani, Z. Shshshanaipour, A.A. Ensafi, G. Mohammadnezhad, Applictions of modified mesoporous boehmite (γ-AlOOH) with green synthesis carbon quantum dots for a fabrication biosensor to determine trace amounts of docorucin, Luminescence 33 (8) (2018) 1377–1386.

[48] S.-F. Wang, G.-Z. Sun, L.-M. Fang, L. Lei, X. Xiang, X.-T. Zu, A comparative study of ZnAl2O4 nanoparticles synthesized from different aluminium salt for use as fluorescence material, Sci. Rep. 5 (2015) 12894.

[49] S.V. Motloung, P. Kumari, L.F. Koao, T.E. Motaung, T.T. Hlastshwayo, M. J. Mochane, Effects of anneling time on the structure and optical properties of ZnAl2O4/ZnO prepared via citrate sol/gel process, Mater. Today Commun. 14 (2018) 294–301.

[50] G. Shan, M. Zhong, S. Wang, Y. Li, Y. Liu, The synthesis and optical properties of the heterostructured ZnO/Au nanocomposites, J. Colloid Interface Sci. 326 (2008) 392.

[51] P. Chand, A. Gaur, A. Kumar, Structural and optical properties of ZnO nanoparticles synthesized at different pH values, J. Alloys Compd. 539 (2012) 174.

[52] P.B. Taunk, R. Das, D.P. Bisen, R.k. Tamrakar, Structural characterization and photoluminescence properties of zinc oxide nano particles synthesized by chemical route method, J. Radiat. Res. Appl. Sci. 8 (2015) 433.

[53] Q. Hou, F. Meng, J. Sun, Electrical and optical properties of Al-doped ZnO and ZnAl2O4 films prepared by atomic layer deposition, Nanoscale Res. Lett. 8 (2013) 144.

[54] S.A. Studenikin, N. Golego, M. Cocivera, Fabrication of green and orange photoluminescent, undoped ZnO films using spray pyrolysis, J. Appl. Phys. 84 (1998) 2287.

[55] K.H. Tam, C.K. Cheung, Y.H. Leung, A.B. Djurisic, C.C. Ling, C.D. Beling, S. Fung, W.M. Kwok, W.K. Chan, D.L. Phillips, L. Ding, W.K. Ge, Defects in ZnO nanorods prepared by a hydrothermal method, J. Phys. Chem. B 110 (2006) 20865.

[56] L.E. Greene, M. Law, J. Goldberger, F. Kim, J.C. Johnson, Y. Zhang, R.J. Saykally, P. Yang, Low-temperature wafer-scale production of ZnO nanowire arrays, Angew. Chem. Int. Ed. 42 (2003) 3031.

[57] C. Ragupathi, J.J. Vijaya, A. Manikandan, L.J. Kennedy, Phytosynthesis of nanoscale ZnAl2O4 by using sesamum (Sesamum indicum L.) optical and catlytic properties, J. Nanosci. Nanotechnol. 13 (2013) 8298.

[58] S.-F. Wang, G.-Z. Sun, L.-M. Fang, L. Lei, X. Xiang, X.-T. Zu, A comparative study of ZnAl2O4 nanoparticles synthesized from different aluminum salts for use as fluorescence materials, Sci. Rep. 5 (2015) 12849.

[59] G. Sun, G. Sun, M. Zhong, S. Wang, X. Zu, X. Xiang, Coordination mechanism, characterization and photoluminescence properties of spinel ZnAl2O4 nanoparticles prepared by a modified polyacrylamide gel route, Russ. J. Phys. Chem. A 90 (2016) 691.

[60] I. Kuryliszyn-Kudelska, B. Hadžić, D. Sibera, M. Romčević, N. Romčević, U. Narkiewicz, W. Dobrowolski, Dynamic magnetic properties of ZnO nanocrystals incorporating Fe, J. Alloys Compd. 509 (2011) 3756.

[61] I. Kuryliszyn-Kudelska, W. Dobrowolski, M. Arciszewska, A. Małolepszy, L. Stobiński, R. Minikayev, „Adjusting the magnetic properties of ZrO2:Mn nanocrystals by changing hydrothermal synthesis conditions", Magnetochemistry 4 (2018) 28.

Contents lists available at ScienceDirect

Materials Research Bulletin

Comprehensive studies of structural, electronic and magnetic properties of $Zn_{0.95}Co_{0.05}O$ nanopowders

Ivana Radisavljević[a,*], Nikola Novaković[a], Branko Matović[a], Novica Paunović[b], Mirjana Medić[a], Nenad Bundaleski[a,c], Velibor Andrić[a], Orlando M.N.D. Teodoro[c]

[a] University of Belgrade—Vinča Institute of Nuclear Sciences, P.O. Box 522, 11001 Belgrade, Serbia
[b] University of Belgrade—Institute of Physics, Pregrevica 118, 11000 Belgrade, Serbia
[c] Universidade Nova de Lisboa—Faculdade de Ciências e Tecnologia, Quinta da Torre 2829-516 Caparica, Portugal

ARTICLE INFO

ABSTRACT

X-ray absorption (XANES, EXAFS, XMCD) and photoelectron (XPS) spectroscopic techniques were employed to study local structural, electronic and magnetic properties of $Zn_{0.95}Co_{0.05}O$ nanopowders. The substitutional Co^{2+} ions are incorporated in ZnO lattice at regular Zn sites and the sample is characterized by high structural order. There was no sign of ferromagnetic ordering of Co magnetic moments and the sample is in paramagnetic state at all temperatures down to 5 K. The possible connection of the structural defects with the absence of ferromagnetism is discussed on the basis of theoretical calculations of the O K-edge absorption spectra.

1. Introduction

Diluted magnetic semiconductors (DMS) continue to attract scientific attention both from theoretical and experimental point of view due to their unique properties that will eventually enable to simultaneously manipulate both spin and charge of the electrons. Typical DMS materials of the type II–VI and III–V (e.g., transition metal (TM)-doped InAs, GaAs, ZnTe and CdTe) even if magnetically ordered, have the Curie temperatures (T_C) below room temperature, which makes them less attractive for practical applications. ZnO is a promising host DMS material envisaged to exhibit room temperature ferromagnetism (RTFM) when doped with most of the TM elements [1]. However, there exists a great deal of controversy regarding the origins and nature of the observed magnetic response, even for the most extensively studied Co-doped ZnO. Although many experimental reports ascertain its intrinsic ferromagnetism (FM) [2–8], some found that Co 3d-electrons are not directly at the origin of the FM response [9]. To account for the observed RTFM in $Zn_{1-x}Co_xO$ with a paramagnetic Co sublattice, the research attention focused on resolving the role played by structural defects in inducing and mediating magnetism, which would soon become another highly controversial issue,

especially upon discovery that the host ZnO material itself can be magnetic even without transition-metal doping [10–14]. Many authors believe that stabilization of the FM interaction relies on the presence of oxygen vacancies (O_v) [15,16]. Others claim that an oxygen vacancy by itself would not cause ferromagnetism [17] and that actually zinc interstitials (Zn_i) play a crucial role in mediating FM interaction [18]. According to [3] intrinsic defects suppress magnetism, while according to [19,20] appreciable FM response requires Co interstitials (Co_i) which would directly interact with substitutional Co atoms. The latter is in disagreement with presumable connection between the uniformity of Co ions distribution and inherent FM of $Zn_{1-x}Co_xO$ [3,21]. The existence of Co-enriched zones in the ZnO matrix is expected to favour antiferromagnetic (AFM) interaction between Co ions due to their small separation distance [19,22–25]. To mediate the FM coupling between unpaired Co electrons, co-doping with impurities such as H [26,27], Ga [28], Cu [29,30], Gd [31] and Li [32] is proposed. Recently an increasing number of experimental reports provide evidence for intrinsic paramagnetism (PM) of Co-doped ZnO [19,33–39]. These findings are supported by theoretical calculations which predict the PM ground state of Co-doped ZnO at RT as a result of weak Co–Co coupling [40,41].

Inconsistencies in the experimental findings on Co-doped ZnO magnetic properties and their correlation with the local and electronic structure urge for even more comprehensive investigations. This paper presents detailed analysis of the structural,

* Corresponding author. Fax: +381 11 3440 100.
  E-mail address: iva@vin.bg.ac.rs (I. Radisavljević).

electronic and magnetic properties of the $Zn_{0.95}Co_{0.05}O$ nano-powders. X-ray absorption near edge structure (XANES), x-ray absorption fine structure (EXAFS), x-ray photoelectron spectros-copy (XPS) and x-ray magnetic circular dichroism (XMCD) were employed to study the local electronic and magnetic structure of Co and O. Compositional, structural and magnetic properties were studied by inductively-coupled plasma optical emission spectrom-etry (ICP-OES), x-ray diffraction (XRD), x-ray fluorescence (XRF) and vibrating sample magnetometry (VSM). To examine the presence of intrinsic defects (vacancies and interstitials) in the investigated sample and their possible connection to magnetism, theoretical calculations of the O K-edge absorption spectra were performed.

2. Experiment and theoretical calculation

Glycine–nitrate method was applied to synthesize ZnO solid solutions doped with nominal concentration of 5 at.% Co. Zn–nitrate hexahydrate, Co–nitrate hexahydrate and aminoacteic acid-glycine (Alfa Aesar GmbH, Germany) were dissolved with small amount of distilled water according to desired composition of the final solid solution powder. Stainless steel beaker was used as a reactor. The solution was heated in a muffle furnace until the burn-up process terminated (about 450 °C). The obtained ash powder was afterward calcined at 600 °C for 4 h. X-ray diffraction (XRD) measurements were performed on Siemens D5000 diffractometer with Ni filtered Cu-K$\alpha_{1,2}$ radiation in Bragg–Brentano geometry, in the range of angles $10° < 2\theta < 90°$ using a step width 0.02° and acquisition time 2 s/step. Angular correction by high quality Si standard is done prior to the measurements. Composition of the sample is checked using inductively-coupled plasma optical emission spectrometry. Sample was digested using microwave assisted technique with Milestone Ethos-1 instrument according to Digestion application note DG-ME-32. Specific amount of the sample (0.25 g) was transferred in a teflon vessel and mixed with

HNO_3 (7 ml) and HF (1 ml). Closed sample vessel is then treated with microwaves for 30 min at the temperature 220 °C. Solution with digested sample was transferred in volumetric flask and analyzed on ICP-OES PerkinElmer 5000 apparatus.

Energy dispersive X-ray fluorescence (EDXRF) spectroscopy was performed using EDXRF Camberra spectrometer with Rh excitation source (800 µA, 40 kV, exposure time 180 s).

Magnetic properties were measured with a vibrating sample magnetometer VSM 2000 in the temperature range between 5 K and room temperature (RT). Zero-field cooled/field cooled (ZFC/FC) measurements were performed in the following manner. First at zero field ($B = 0$) the sample was cooled down from RT to 5 K, then the field ($B = 5$, 15 and 50 mT) was applied and the measurements were performed while warming up from 5 K to RT in the field. FC measurements were performed immediately after ZFC measure-ment while cooling down the sample from RT to 5 K under the applied field ($B = 5$, 15, 50 mT).

EXAFS/XANES measurements on Co K-edge were performed in the fluorescence mode at 8 K and RT on the HASYLAB C1 Beamline at Deutsches Elektronen-Synchrotron DESY (Hamburg, Germany). Data processing and analysis were performed using IFEFFIT [42] as implemented in ATHENA and ARTEMIS software packages [43]. XANES/XMCD measurements on Co $L_{2,3}$- and O K-edge were performed in the total-electron yield (TEY) mode at 4 K and RT on the Circular Polarization Beamline at Elettra Synchrotron Radiation Facility (Trieste, Italy). To measure circularly polarized absorption spectra, external magnetic field $B = 0.3$ T was applied perpendicular to the sample surface and photon helicity ρ^+ (right-handed) and ρ^- (left-handed) was reversed at each photon energy. The degree of circular polarization was 80% and the energy resolution 0.6 eV.

XPS measurements were performed on a VSW XPS system and the Class 100 energy analyzer being a part of an experimental setup assembled for surface investigation [44]. The powdered sample was pressed onto an indium foil in order to provide mechanical support and electrical contact. The spectra were taken on as-
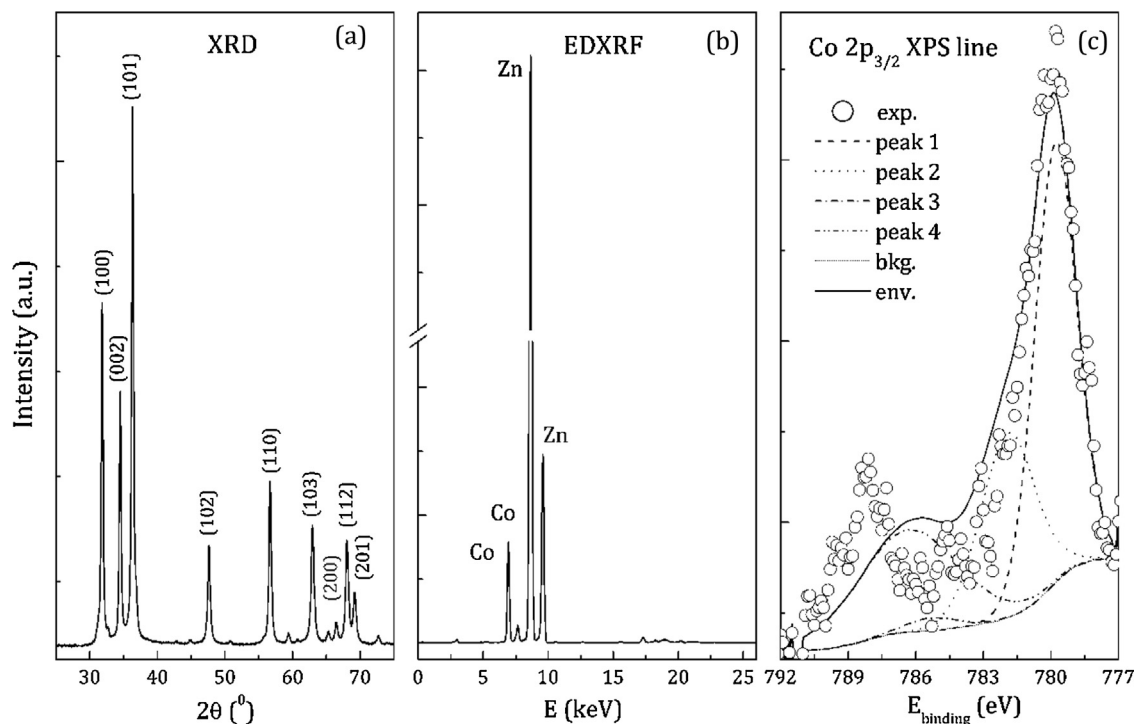
Fig. 1. (a) XRD spectrum and (b) EDXRF spectrum of $Zn_{0.95}Co_{0.05}O$; (c) Experimental Co $2p_{3/2}$ XPS spectrum (open circles) and the fit. The fine multiplet structure of the main Co $2p_{3/2}$ XPS line (at ≈780 eV) and its satellite (at ≈788 eV) can be resolved into four components represented with broken lines (see text for more details). Background (bkg) and envelope (env) functions are represented with full lines.

received sample using non-monochromatic Mg–Kα line (1256.3 eV). The energy axis was calibrated using the Ag-3d$_{5/2}$ XPS line position (368.22 eV) of sputter-cleaned Ag (110) monocrystal and the Au-4f$_{7/2}$ XPS line position (83.96 eV) of sputter-cleaned polycrystalline Au sample. The effect of charging had negligible influence on the energy spectra.

Theoretical modelling of the O K-edge XANES spectra were performed using real space full multiple scattering FEFF 9.03 code [45] on a cluster containing 259 atoms. Self consistent field approach (SCF) with Hedin–Lundqvist exchange-correlation is used to calculate scattering potentials. To reduce effects of potential discontinuities at the muffin–tin spheres automatic overlapping (AFOLP) is included. The effects of screening of the x-ray field and the photoelectron-core hole interaction were neglected. Program ATOMS [46] is used to generate input files containing different point defects (vacancies/interstitials) around the central O. To account for the finite core–hole life-time and the experimental resolution theoretical XANES spectra were convo-luted with 0.1 eV Lorentzian and 0.4 eV Gaussian broadening, respectively.

3. Results and discussion

The XRD pattern of $Zn_{0.95}Co_{0.05}O$ shown in Fig. 1a reveals that the investigated sample has pure wurtzite-type structure (space group P6$_3$mc). The peaks are indexed with their diffraction planes. The obtained lattice parameters $a = b = 3.248$ Å and $c = 5.203$ Å are very close to that of pure ZnO ($a = 3.249$ Å, $c = 5.206$ Å [47]). There was no indication of the presence of impurities and/or secondary impurity phases, within detection limit of XRD and EDXRF measurements (see Fig. 1b). The mass fraction of constitutive elements obtained by ICP-OES compositional analysis (74.97 wt.% Zn, 2.95 wt.% Co and 22.08 wt.% O), within experimental

uncertainty ($\approx$10%), corresponds to the nominal composition of the sample (76.63 wt.% Zn, 3.64 wt.% Co and 19.74 wt.% O).

Experimental Co 2p$_{3/2}$ XPS spectrum and its fit are presented in Fig. 1c. The broad (non-symmetrical) peak shape of the Co 2p$_{3/2}$ XPS spectrum results from the multiplet splitting (i.e., a number of final states created via coupling between the unpaired Co d-electrons in the core with the unpaired outer shell electrons) [48]. The main Co 2p$_{3/2}$ XPS line is positioned at $\approx$780 eV, which corresponds to Co^{2+} oxidation state. Intensive satellite peak at $\approx$788 eV which accompanies the main XPS line, is characteristic for transition metal monoxides [49]. To account for the fine multiplet structure of the Co 2p$_{3/2}$ XPS spectrum, the CoO model [48] is applied, using the same constraints for the number of components (peaks 1–4, see Fig. 2b) and the fitting parameters (intensities and widths of the peaks). The CoO model fairly well describes the experimental spectrum, which implies that Co ions in investigated sample are surrounded by oxygen atoms. The discrepancy between experiment and fit in the region of the satellite peak (785–792 eV) probably originates from the relatively intensive Auger O$_{KLL}$ line [50] superimposed to the main Co 2p$_{3/2}$ XPS line. The fit using the constraints for Co$_3$O$_4$ and Co(OH)$_2$ yields significantly larger discrepancy from the experiment.

Data collection of the integral magnetic properties is presented in Fig. 2. After subtraction of the linear PM background, magnetization curve M(B) taken at RT (Fig. 2a) reveals a weak FM response. The order of magnitude of the saturation magneti-zation ($M_{sat} = 0.0015$ emu/g) is comparable to defect induced magnetization (DIM) in pure ZnO [10]. The M(B) curves taken in the temperature range 5–15 K (Fig. 2b) all have closed hysteresis loops with negligible coercivity and low saturation magnetization ($M_{sat} \approx 4$ emu/g). Magnetization curves measured in zero field cooled (ZFC) and field cooled (FC) regimes (Fig. 3c) show no bifurcation characteristic for superparamagnetic (SPM) ordering.
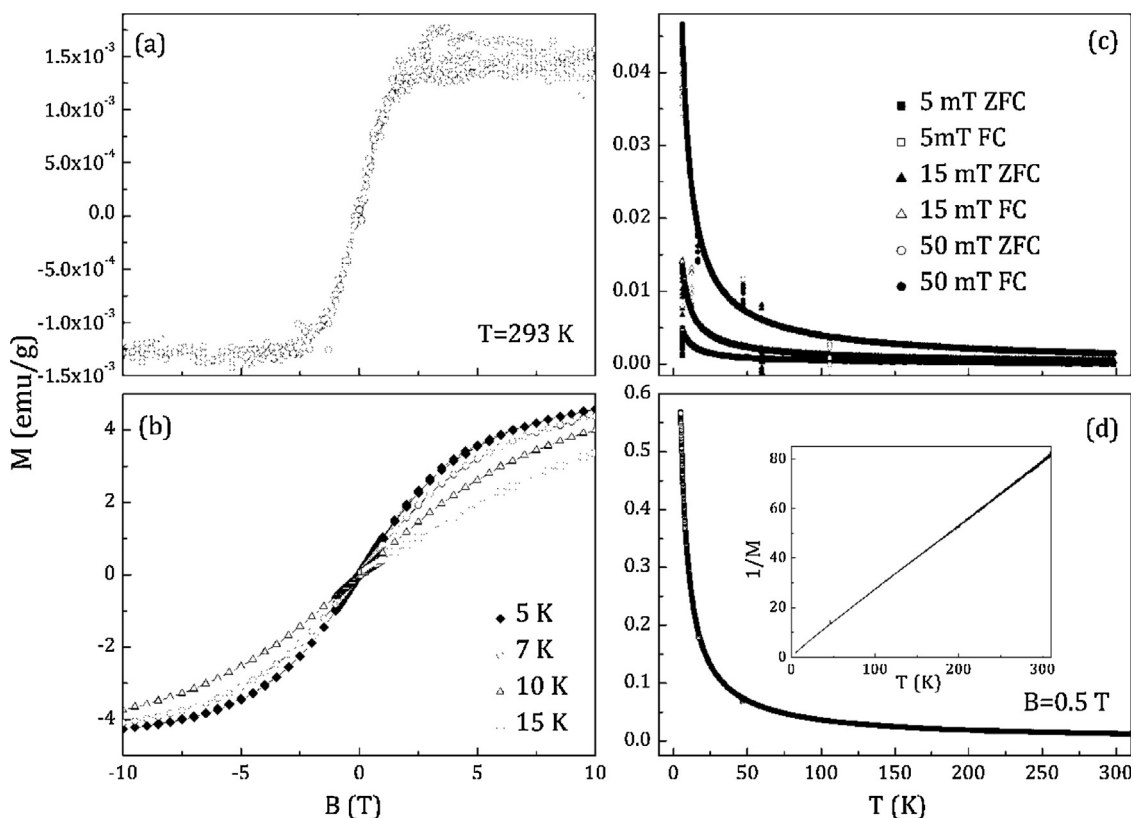
Fig. 2. (a) M(B) curves taken at RT and (b) in the temperature range 5–15 K; (c) ZFC/FC curves measured in the field $B = 5$, 15 and 50 mT; (d) M(T) curve taken at $B = 0.5$ T. Inverse magnetization (1/M) as a function of temperature is shown in inset.
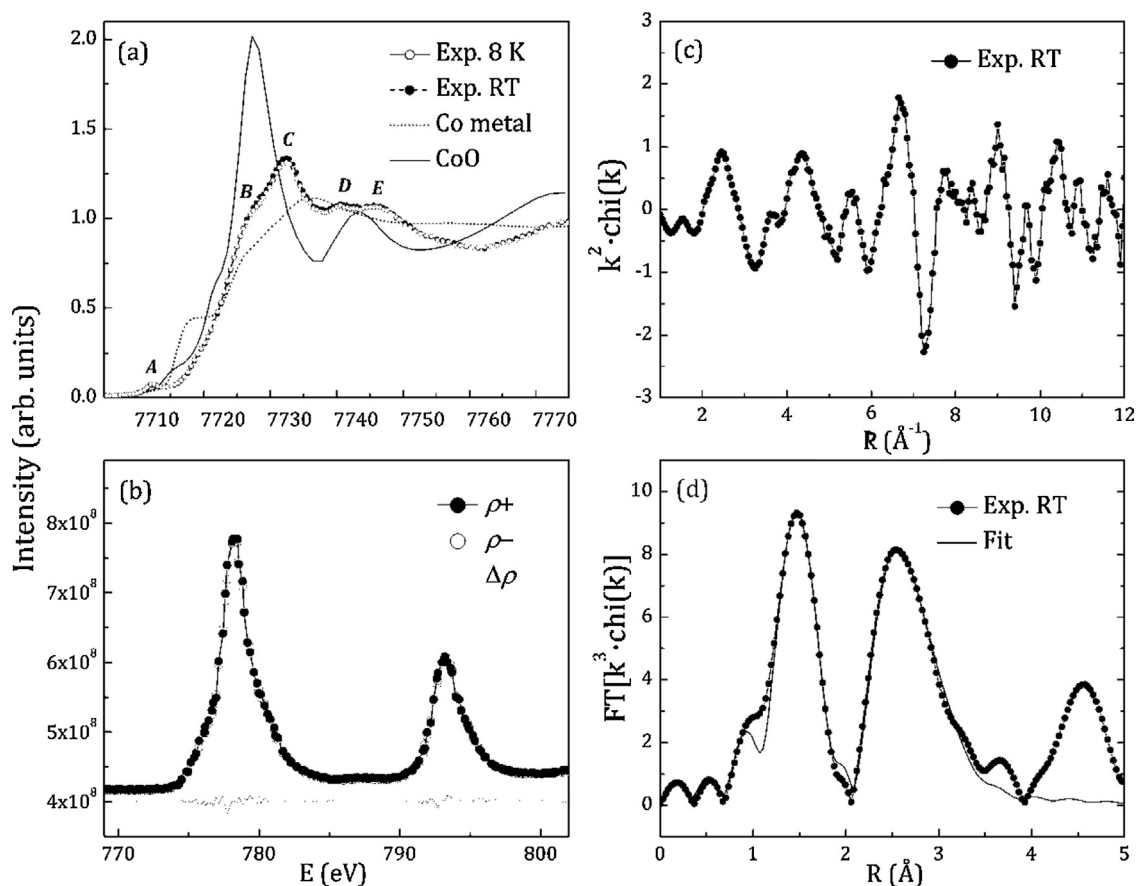
Fig. 3. (a) Experimental Co K-edge XANES spectra taken at 8 K (open circles) and RT (full circles) compared to theoretical spectra of metallic Co (dash–dot line) and CoO (full line); (b) Co $L_{2,3}$-edge XANES spectra taken at RT with right (ρ^+) and left (ρ^-) circularly polarized light and their difference $\Delta\rho = \rho^+ - \rho^-$ (XMCD); (c) Co K-edge EXAFS function taken at RT and (d) its Fourier transform (full circles) with theoretical fit (full line).

The behavior of the magnetization M(T) shown in Fig. 2d is typical for a paramagnet and obeys the Curie–Weiss law. Linear temperature dependence of the inverse magnetization (1/M) (see inset of Fig. 2d) confirms dominating paramagnetic contribution to the magnetic order. At low temperatures, the FM signal is completely overwhelmed by much stronger paramagnetic signal.

Fig. 3a shows experimental Co K-edge XANES spectra taken at 8 K and RT compared to theoretical spectra of metallic Co (dash–dot line) and CoO (full line). Markedly different shapes between the experimental and the model XANES spectra imply that neither Co clusters nor secondary CoO phase can be detected in the investigated sample. Characteristic features of the two experimental spectra (A–E) appear almost exactly alike. The only exception is slightly lower intensity of the main peak C (white line) at 8 K.

The Co K-edge XANES spectrum is determined by dipole transitions from 1 s to empty *p*-like states above the Fermi level and it is dominated by multiple-scattering (MS) events. PM $Zn_{1-x}Co_xO$ systems all share similar spectral shapes [33–37]. The pre-edge peak A results mainly from the 1s transitions to mixed Co 3d-O 2p and Co 4p-Co 3d states, feature B originates from the transitions to mixed sp-states, while the white line C and features D and E are predominantly due to 1 s → 4p transition [51]. The pre-edge in the XANES spectra of the investigated sample is indicative of Co^{2+} in local tetrahedral CoO_4 geometry [35]. Characteristic knee-like shape of the feature B was in [15] related to the presence of Co–O_v complexes aligned along *c*-axis and identified as a possible origin of the RTFM. Decrease in the white line (C) intensity at 8 K implies that there are less available empty Co p-states at low

temperatures, which could be due the self diffusion of intrinsic defects [52], whose presence in the vicinity of Co could lead to larger charge transfer to Co. Feature D originates from MS contributions of the photoelectron backscattered from the nearest anion neighbors [51]. The feature D disappears when an O atom is missing from the second shell around the Co [51], which implies that the presence of the O_v in the second shell in the investigated sample most probably can be excluded.

Fig. 3b shows the RT Co $L_{2,3}$-edge XANES spectra taken with right (ρ^+) and left (ρ^-) circularly polarized light and their difference $\Delta\rho = \rho^+ - \rho^-$ (XMCD). The Co $L_{2,3}$ XANES spectrum results from 2p → 3d dipole transition and the L_3 and L_2 absorption lines are separated by approximately 15 eV due to spin-orbit splitting of the 2p core-hole. Negligible XMCD effect suggests that Co 3d-sublatice does not carry any significant magnetic moment, and that majority of Co ions are in paramagnetic state [2].

The Co K-edge EXAFS spectrum taken at RT is presented in Fig. 3c and its Fourier transform (FT) in Fig. 3d. The spectrum taken at 8 K is similar in appearance and therefore it was not shown. The EXAFS spectra are dominated by single-scattering events and the first FT peak (see Fig. 3d) arises from the photoelectrons backscattered from the first coordination oxygen shell. The mean distance between Co and O atoms (2.03(1) Å) derived from the EXAFS data analysis agrees well with the results reported for the samples with similar Co-doping level (1.977(5) [5]; 1.99(1) [22]; 2.00(1) Å [34]). However, the disorder parameter $\sigma^2 = 0.0013(7)$ $Å^2$ at 8 K and 0.0014(7) $Å^2$ at RT, is much smaller than previously reported ($\sigma^2 = 0.003(1)$ $Å^2$ [5]; $\sigma^2 = 0.0034(2)$ $Å^2$ [34]). These results imply that substitutional Co atoms are incorporated in ZnO
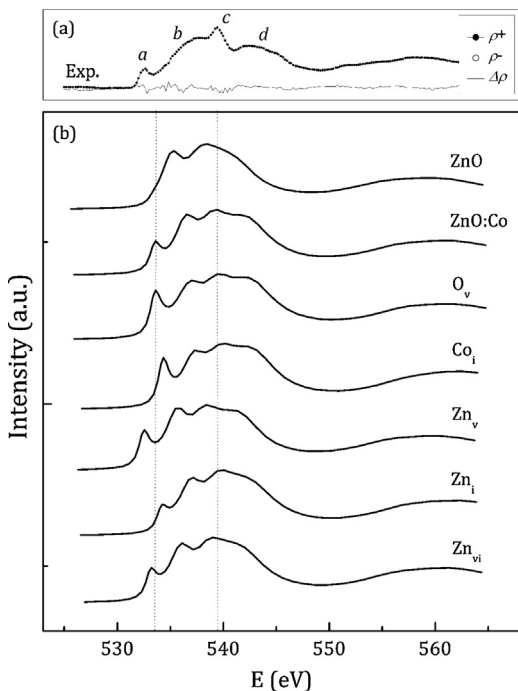
lattice at regular Zn atoms sites. Relatively small disorder induced by the Co-doping (which has been observed also by XRD) implies that Co^{2+} ions are in a high spin state with the tetrahedral covalent radius $R_C^{IV}(Co^{2+}) = 0.60$ Å comparable to $R_C^{IV}(Zn^{2+}) = 0.60$ Å [8]. The second peak in the FT spectrum (see Fig. 3d) is due to the photoelectrons backscattered from the second shell made of cations (Zn and Co). Metallic Co would result in a peak between the two ZnO peaks [35], which confirms that there has been no detectable Co-clustering in the investigated sample. However, from the Co K-edge EXAFS spectrum it is not possible to determine the exact composition of the second coordination shell [22], since Co and Zn have close atomic numbers and similar scattering amplitudes. Thus we cannot ascertain whether the distribution of Co ions is uniform.

Fig. 4a shows the O K-edge XANES spectra taken at 8 K with right (ρ^+) and left (ρ^-) circularly polarized light and their difference $\Delta\rho = \rho^+ - \rho^-$ (XMCD). Negligible XMCD signal indicates that in the investigated sample the O 2p-states are not magnetically polarized. Characteristic features (a–d) appearing in the experimental O K-edge XANES spectrum (see Fig. 4a) are very similar to those reported for FM $Zn_{1-x}Co_xO$ thin films [7], where the appearance of FM is related to formation of Co–O–Co chains. To examine possible connection of the structural defects with the absence of magnetism in the investigated sample, we performed theoretical calculations of the O K-edge absorption spectra of pure and Co-doped ZnO (Fig. 4b). Each particular defect (vacancy-O_v, Zn_v and interstitial-Co_i, Zn_i) is introduced in ZnO:Co constructed by replacing one of the first coordination Zn atoms by Co. In comparison to pure ZnO (see Fig. 4b) the O K-edge XANES spectrum of ZnO:Co exhibits richer structure and the whole spectrum is broader due to more dispersive O 2p-states [3,22]. Defects alter the O 1s binding energy and position of the

conduction band bottom, which is manifested in shift of the XANES onset relative to the ZnO:Co. The pre-edge feature a ($\approx$532 eV), absent in ZnO spectrum due to completely filled d-shell, has previously been ascribed to O 1s transitions to Co 3d-O 2p hybridized states [22], feature b ($\approx$537 eV) to O $1s \rightarrow$ O 2p transitions (with some contribution of mixed O 2p-Zn 4s states) [22,53], feature c ($\approx$539 eV) to O $1s \rightarrow$ O 2p-Zn 4p and feature d ($\approx$543 eV) to O $1s \rightarrow$ O 2p-Co 4p transition [22].

All spectral features (a–d) are reproduced in the ZnO:Co model spectra, but their intensities and energy position vary. It should be stressed that the pre-edge feature a appears only when the substitutional Co atom is in c-axis direction, which could be related to previously observed tendency of Co ions to cluster via O atoms along c-axis [22]. The feature a gains intensity from Co_i due to increased transition probability to Co 3d-O 2p hybridized states [3], but also in the presence of O_v and Zn_v. This implies that the pre-edge region of the XANES spectra also includes MS contribution from higher coordination shells. However, the presence of Co_i and O_v results in highly overestimated pre-edge intensity, which indicates that the tendency for Co–Co clustering and Co–O_v complexes formation in the investigated sample most likely can be excluded. The feature b is very much alike the pure ZnO spectrum and rises notably only in the presence of Zn_v, as a result of more available empty O 2p-states (lesser degree of O 2p-Zn 4s hybridization). The feature c is underestimated in all model spectra. The rise of c-intensity with Co doping [22], suggests that this region of the XANES spectrum involves MS contribution from Co-states from as high as third coordination shell around O. Model with Zn_i is much narrower with the features c and d merged together, and preserves the spectral shape also in the presence of Zn_v (model Zn_{vi}). Despite noticeable impact of each single point defect on the spectral shape (especially in the pre-edge region), none of them can be unambitiously associated with the absence of appreciable FM in the investigated sample. Even if the Co atoms are aligned along the c-axis as our results indicate, their clustering via O atoms would still be unlikely to stabilize the FM state due to AFM Co–O–Co coupling [20,54]. Weak FM response observed at room temperature could have originated from Zn vacancies, which are thought to be at the origin of FM in pure ZnO [12–14], but their amount obviously is not enough to induce substantial magnetic polarization of the O 2p-states, given the high structural perfection of the investigated sample. The later is in line with theoretical predictions of intrinsic PM in $Zn_{1-x}Co_xO$ with low density of defects [40,41].

4. Conclusion

In conclusion, detailed investigations of $Zn_{0.95}Co_{0.05}O$ were carried out in order to better understand the magnetic properties and their correlation with the local and electronic structure. Obtained results reveal that the substitutional Co atoms are incorporated in ZnO lattice at regular Zn atomic sites and that the sample is characterized by high structural order. The Co^{2+} ions show no notable tendency for Co–Co clustering and Co–O_v complexes formation. Possible clustering of Co atoms via O atoms along the c-axis has not lead to stabilization of ferromagnetic order. There was no sign of magnetic polarization of O 2p-and Co 3d-states and the sample is paramagnetic at temperatures down to 5 K.

Fig. 4. (a) The O K-edge XANES spectra taken at 8 K with right (ρ^+) and left (ρ^-) circularly polarized light and their difference $\Delta\rho = \rho^+ - \rho^-$ (XMCD); (b) Theoretical O K-edge XANES spectra of ZnO and ZnO:Co system with a single point defect as indicated on the right (v–vacancy, i–interstitial). Vertical lines denote position of the most pronounced features a (pre-edge) and c (white line).

References

[1] J.M.D. Coey, M. Venkatesan, C.B. Fitzgerald, Donor impurity band exchange in dilute ferromagnetic oxides, Nat. Mater. 4 (2005) 173–179.

[2] M. Kobayashi, Y. Ishida, J.L. Hwang, T. Mizokawa, A. Fujimori, K. Mamiya, J. Okamoto, Y. Takeda, T. Okane, Y. Saitoh, Y. Muramatsu, A. Tanaka, H. Saeki, H. Tabata, T. Kawai, Characterization of magnetic components in the diluted magnetic semiconductor $Zn_{1-x}Co_xO$ by x-ray magnetic circular dichroism, Phys. Rev. B 72 (2005) 201201–201204.

[3] A.P. Singh, R. Kumar, P. Thakur, N.B. Brookes, K.H. Chae, W.K. Choi, NEXAFS and XMCD studies of single-phase Co doped ZnO thin films, J. Phys.: Condens. Matter 21 (2009) 185005–185007.

[4] Z.H. Zhang, X. Wang, J.B. Xu, S. Muller, C. Ronning, Q. Li, Evidence of intrinsic ferromagnetism in individual dilute magnetic semiconducting nanostructures, Nat. Nanotechnol. 4 (2009) 523–527.

[5] S.-Y. Seo, E.-S. Jeong, C.-H. Kwak, C.-I. Park, Z. Jin, S.-H. Kim, S.-W. Han, X-ray absorption fine structure study of cobalt ion distribution in ferromagnetic $Zn_{1-x}Co_xO$ films, J. Phys.: Condens. Matter 25 (2013) 256005–256011.

[6] S. Francis, R. Saravanan, L.J. Berchmans, Effect of Co doping on the properties of ZnO bulk samples, J. Electron. Mater. 42 (2013) 701–710.

[7] S. Gautam, P. Thakur, P. Bazylewski, R. Bauer, A.P. Singh, J.Y. Kim, M. Subramanian, R. Jayavel, K. Asokan, K.H. Chae, G.S. Chang, Spectroscopic study of $Zn_{1-x}Co_xO$ thin films showing intrinsic ferromagnetism, Mater. Chem. Phys. 140 (2013) 130–134.

[8] S. Karamat, R.S. Rawat, P. Lee, T.L. Tan, S.V. Springham, R.V. Ramanujan, Synthesis and characterization of bulk cobalt-doped ZnO and their thin films, J. Supercond. Nov. Magn. 26 (2013) 3115–3123.

[9] A. Barla, G. Schmerber, E. Beaurepaire, A. Dinia, H. Bieber, S. Colis, F. Scheurer, J.-P. Kappler, P. Imperia, F. Nolting, F. Wilhelm, A. Rogalev, D. Müller, J.J. Grob, Paramagnetism of the Co sublattice in ferromagnetic $Zn_{1-x}Co_xO$ films, Phys. Rev. B 76 (2007) 125201–125205.

[10] Q. Wang, Q. Sun, G. Chen, Y. Kawazoe, P. Jena, Vacancy-induced magnetism in ZnO thin films and nanowires, Phys. Rev. B 77 (2008) 205411–205417.

[11] D. Gao, Z. Zhang, J. Fu, Y. Xu, J. Qi, D. Xue, Room temperature ferromagnetism of pure ZnO nanoparticles, J. Appl. Phys. 105 (2009) 113928–113934.

[12] X. Zuo, S.D. Yoon, A. Yang, W.-H. Duan, C. Vittoria, V.G. Harris, Ferromagnetism in pure wurtzite zinc oxide, J. Appl. Phys. 105 (2009) 07C508–3.

[13] X. Xu, C. Xu, J. Dai, J. Hu, F. Li, S. Zhang, Size dependence of defect-induced room temperature ferromagnetism in undoped ZnO nanoparticles, J. Phys. Chem. C 116 (2012) 8813–8818.

[14] C. Guglieri, E. Céspedes, A. Espinosa, M. Ángeles Laguna-Marco, N. Carmona, Y. Takeda, T. Okane, T. Nakamura, M. García—Hernandez, M.Á. García, J. Chaboy, Evidence of oxygen ferromagnetism in ZnO based materials, Adv. Funct. Mater. 24 (2014) 2094–2100.

[15] G. Ciatto, A. Di Trolio, E. Fonda, P. Alippi, A.M. Testa, A. Amore Bonapast, Evidence of cobalt-vacancy Complexes in $Zn_{1-x}Co_xO$ dilute magnetic semiconductors, Phys. Rev. Lett. 107 (2011) 127206–127215.

[16] T. Tietze, M. Gacic, G. Schütz, G. Jakob, S. Brück, E. Goering, XMCD studies on Co and Li doped ZnO magnetic semiconductors, New J. Phys. 10 (2008) 055009–055018.

[17] A. Pham, Y.B. Zhang, M.H.N. Assadi, A.B. Yu, S. Li, Ferromagnetism in ZnO:Co originating from a hydrogenated Co–O–Co complex, J. Phys.: Condens. Matter 25 (2013) 116002–116009.

[18] N. Khare, M.J. Kappers, M. Wei, M.G. Blamire, J.L. MacManus-Driscoll, Defect induced ferromagnetism in Co-doped ZnO, Adv. Mater. 18 (2006) 1449–1452.

[19] G.S. Chang, E.Z. Kurmaev, D.W. Boukhvalov, L.D. Finkelstein, S. Colis, T.M. Pedersen, A. Moewes, A. Dinia, Effect of Co and O defects on the magnetism in Co-doped ZnO: experiment and theory, Phys. Rev. B 75 (2007) 195215–195217.

[20] E.-C. Lee, K.J. Chang, Ferromagnetic versus antiferromagnetic interaction in Co-doped ZnO, Phys. Rev. B 69 (2004) 085205.

[21] B. Martínez, F. Sandiumenge, L. Balcells, J. Arbiol, F. Sibieude, C. Monty, Structure and magnetic properties of Co-doped ZnO nanoparticles, Phys. Rev. B 72 (2005) 165202–165208.

[22] Z. Sun, W. Yan, G. Zhang, H. Oyanagi, Z. Wu, Q. Liu, W. Wu, T. Shi, Z. Pan, P. Xu, S. Wei, Evidence of substitutional Co ion clusters in $Zn_{1-x}Co_xO$ dilute magnetic semiconductors, Phys. Rev. B 77 (2008) 245208–245216.

[23] S.-J. Hu, S.-S. Yan, M.-W. Zhao, L.-M. Mei, First–principles LDA + U calculations of the Co-doped ZnO magnetic semiconductor, Phys. Rev. B 73 (2006) 245205–245207.

[24] T. Dietl, T. Andrearczyk, A. Lipińska, M. Kiecana, M. Tay, Y. Wu, Origin of ferromagnetism in $Zn_{1-x}Co_xO$ from magnetization and spin-dependent magnetoresistance measurements, Phys. Rev. B 76 (2007) 155312–155315.

[25] J.M.D. Coey, J.T. Mlack, M. Venkatesan, P. Stamenov, Magnetization process in dilute magnetic oxides, IEEE T. Magn. 46 (2010) 2501–2503.

[26] Z.H. Wang, D.Y. Geng, S. Guo, W.J. Hu, Z.D. Zhang, Ferromagnetism and superparamagnetism of ZnCoO:H nanocrystals, Appl. Phys. Lett. 92 (2008) 242505–242603.

[27] M.P.F. de Godoy, A. Mesquita, W. Avansi, P.P. Neves, V.A. Chitta, W.B. Ferraz, M.A. Boselli, A.C.S. Sabioni, H.B. de Carvalho, Evidence of defect-mediated magnetic coupling on hydrogenated Co-doped ZnO, J. Alloy. Compd. 555 (2013) 315–319.

[28] Y. He, P. Sharma, K. Biswas, E.Z. Liu, N. Ohtsu, A. Inoue, Y. Inada, M. Nomura, J.S. Tse, S. Yin, J.Z. Jiang, Origin of ferromagnetism in ZnO codoped with Ga and Co: Experiment and theory, Phys. Rev. B 78 (2008) 155202–155207.

[29] M. Xu, H. Zhao, K. Ostrikov, M.Y. Duan, L.X. Xu, Effect of doping with Co and/or Cu on electronic structure and optical properties of ZnO, J. Appl. Phys. 105 (2009) 043708–043806.

[30] A.N. Andriotis, R.M. Sheetz, M. Menon, Defect-induced defect–mediated magnetism in ZnO and carbon-based materials, J. Phys.: Condens. Matter 22 (2010) 334210–334215.

[31] T. Thangeeswari, M. Priya, J. Velmurugan, Enhancement in the optical and magnetic properties of ZnO:Co implanted by Gd^{3+} nanoparticles, J. Mater. Sci.: Mater. Electron. 26 (2015) 2436–2444.

[32] I. Lorite, B. Straube, H. Ohldag, P. Kumar, M. Villafuerte, P. Esquinazi, C.E. Rodríguez Torres, S. Perez de Heluani, V.N. Antonov, L.V. Bekenov, A. Ernst, M. Hoffmann, S.K. Nayak, W.A. Adeagbo, G. Fischer, W. Hergert, Advances in methods to obtain and characterise room temperature magnetic ZnO, Appl. Phys. Lett. 106 (2015) 082406–082505.

[33] S. Yin, M.X. Xu, L. Yang, J.F. Liu, H. Rösner, H. Hahn, H. Gleiter, D. Schild, S. Doyle, T. Liu, T.D. Hu, E. Takayama-Muromachi, J.Z. Jiang, Absence of ferromagnetism in bulk polycrystalline $Zn_{0.9}Co_{0.1}O$, Phys. Rev. B 73 (2006) 224408–224415.

[34] T. Shi, S. Zhu, Z. Sun, S. Wei, W. Liu, Structures and magnetic properties of wurtzite $Zn_{1-x}Co_xO$ dilute magnetic semiconductor nanocomposites, Appl. Phys. Lett. 90 (2007) 102108–102113.

[35] T.C. Kaspar, T. Droubay, S.M. Heald, P. Nachimuthu, C.M. Wang, V. Shutthanandan, C.A. Johnson, D.R. Gamelin, S.A. Chambers, Lack of ferromagnetism in n-type cobalt-doped ZnO epitaxial thin films, New J. Phys. 10 (2008) 055010–055018.

[36] A. Ney, K. Ollefs, S. Ye, T. Kammermeier, V. Ney, T.C. Kaspar, S.A. Chambers, F. Wilhelm, A. Rogalev, Absence of intrinsic ferromagnetic interactions of isolated and paired Co dopant atoms in $Zn_{1-x}Co_xO$ with high structural perfection, Appl. Phys. Lett. 100 (2008) 157201–157204.

[37] H.B. de Carvalho, M.P.F. de Godoy, R.W.D. Paes, M. Mir, A. Ortiz de Zevallos, F. Iikawa, M.J.S.P. Brasil, V.A. Chitta, W.B. Ferraz, M.A. Boselli, A.C.S. Sabioni, Absence of ferromagnetic order in high quality bulk Co-doped ZnO samples, J. Appl. Phys. 108 (2010) 033914–033915.

[38] R. Bhargava, P.K. Sharma, S. Singh, M. Sahni, A.C. Pandey, N. Kumar, Switching in structural, optical, and magnetic properties of self-assembled Co-doped ZnO: effect of Co-concentration, J. Mater. Sci.: Mater. Electron. 25 (2014) 552–559.

[39] J. El Ghoul, M. Kraini, O.M. Lemine, L. El Mir, Sol–gel synthesis, structural, optical and magnetic properties of Co-doped ZnO nanoparticles, J. Mater. Sci.: Mater. Electron. 26 (2015) 2614–2621.

[40] G. Gu, G. Xiang, J. Luo, H. Ren, M. Lan, D. He, X. Zhang, Magnetism in transition-metal-doped ZnO: a first–principles study, J. Appl. Phys. 112 (2012) 023913–023915.

[41] S. Lardjane, G. Merad, N. Fenineche, A. Billard, H.I. Faraoun, Ab initio study of ZnCoO diluted magnetic semiconductor and its magnetic properties, J. Alloys Compd. 551 (2013) 306–311.

[42] M. Newville, IFEFFIT: Interactive XAFS analysis and FEFF fitting, J. Synchrotron Radiat. 8 (2001) 322–324.

[43] B. Ravel, M. Newville, ATHENA, ARTEMIS, HEPHAESTUS. Data analysis for X-ray absorption spectroscopy using IFEFFIT, J. Synchrotron Radiat. 12 (2005) 537–541.

[44] O.M.N.D. Teodoro, J.M.A.C. Silva, A.M.C. Moutinho, Multitechnique surface analysis system: apparatus description, Vacuum 46 (1995) 1205–1209.

[45] A.L. Ankudinov, B. Ravel, J.J. Rehr, S.D. Conradson, Real-space multiple-scattering calculation and interpretation of x-ray-absorption near-edge structure, Phys. Rev. B 58 (1998) 7565–7576.

[46] B. Ravel, ATOMS: crystallography for the X-ray absorption spectroscopist, J. Synchrotron Radiat. 8 (2001) 314–316.

[47] CRC Handbook of Tables for Applied Engineering Science, in: R.E. Bolz, G.L. Tuve (Eds.), CRC, Press, Boca Raton, Florida, 1973.

[48] M.C. Biesinger, B.P. Payne, A.P. Grosvenor, L.W.M. Lau, A.R. Gerson, R. St.C. Smart, Resolving surface chemical states in XPS analysis of first row transition metals, oxides and hydroxides: Cr, Mn, Fe, Co and Ni, Appl. Surf. Sci. 257 (2011) 2717–2730.

[49] G.A. Carson, M.H. Nassir, M.A. Langell, Epitaxial growth of Co_3O_3 on CoO (1 0 0), J. Vac. Sci. Technol. A 14 (1996) 1637–1642.

[50] C.D. Wagner, W.M. Riggs, L.E. Davis, J.F. Moulder, Handbook of X-ray Photoelectron Spectroscopy, PerkinElmer Corp., USA, 1979.

[51] S. Zhang, L. Zhang, H. Li, J. Li, Z. Jiang, W. Chu, Y. Huang, J. Wang, Z. Wu, Investigation of annealing-induced oxygen vacancies in the Co-doped ZnO system by Co K-edge XANES spectroscopy, J. Synchrotron Radiat. 17 (2010) 600–605.

[52] P. Erhart, K. Albe, Diffusion of zinc vacancies and interstitials in zinc oxide, Appl. Phys, Lett. 88 (2006) 201918–202013.

[53] J.-H. Guo, L. Vayssieres, C. Persson, R. Ahuja, B. Johansson, J. Nordgren, Polarization-dependent soft-x-ray absorption of highly oriented ZnO microrod arrays, J. Phys.: Condens. Matter 14 (2002) 6969–6974.

[54] Y. Zhang, M.H.N. Assadi, S. Li, Giant stability of substituent Co chains in ZnO:Co dilute magnetic oxides, AIP Adv. 2 (2012) 042155–042156.

WO₃/TiO₂ composite coatings: Structural, optical and photocatalytic properties

Zorana Dohčević-Mitrović[a,*], Stevan Stojadinović[c], Luca Lozzi[d], Sonja Aškrabić[a],
Milena Rosić[e], Nataša Tomić[a], Novica Paunović[a], Saša Lazović[b], Marko G. Nikolić[b],
Sandro Santucci[d]

[a] Center for Solid State Physics and New Materials, Institute of Physics Belgrade, University of Belgrade, Pregrevica 118, 11080 Belgrade, Serbia
[b] Institute of Physics Belgrade, University of Belgrade, Pregrevica 118, 11080 Belgrade, Serbia
[c] Faculty of Physics, University of Belgrade, Studentski Trg 12-16, 11000 Belgrade, Serbia
[d] Department of Physical and Chemical Sciences, University of L'Aquila, Via Vetoio 67100, L'Aquila, Italy
[e] Laboratory for Material Science, Institute of Nuclear Sciences, Vinča, University of Belgrade, P.O. Box 522, 11001 Belgrade, Serbia

ARTICLE INFO

ABSTRACT

WO₃/TiO₂ and TiO₂ coatings were prepared on titania substrates using facile and cost-effective plasma electrolytic oxidation process. The coatings were characterized by X-ray diffraction, scanning electron microscopy, Raman, UV–vis diffuse reflectance spectroscopy, and X-ray photoelectron spectroscopy. With increasing duration of PEO process, the monoclinic WO₃ phase became dominant and new monoclinic $WO_{2.96}$ phase appeared. The optical absorption edge in the WO₃/TiO₂ samples, enriched with WO₃/$WO_{2.96}$ phase, was shifted to the visible region. The photocatalytic efficiency of WO₃/TiO₂ and pure TiO₂ samples was evaluated by performing the photodegradation experiments in an aqueous solution of Rhodamine 6G and Mordant Blue 9 under the visible and UV light. The WO₃/TiO₂ catalysts are much more efficient than pure TiO₂ under visible light and slightly better under UV light. The improvement of photocatalytic activity in the visible region is attributed to better light absorption, higher adsorption affinity and increased charge separation efficiency.

© 2016 Elsevier Ltd. All rights reserved.

1. Introduction

Among semiconductor materials, titanium dioxide (TiO₂) in anatase phase has been shown as excellent and widely used photocatalyst for the degradation of different organic contaminants, because of its physical and chemical stability, high oxidative power, high catalytic activity, long-term photostability, low cost and ease of production. Many organic compounds can be decomposed in an aqueous solution in the presence of TiO₂, illuminated by photons with energies greater than or equal to the band gap energy of titanium dioxide (3.2 eV for anatase TiO₂) [1–6]. The major drawback for TiO₂ commercial use lies in its wide band gap, and relatively high recombination rate of photoinduced electron-hole pairs. The modification of TiO₂ by doping with metals and non-metals [7–12] or by Ti³⁺ self-doping [13,14] have been extensively performed in order to improve its photocatalytic activity under the visible irradiation.

Another very promising approach is the combination of TiO₂ with metal oxides like V₂O₅, ZnS, InVO₄, WO₃ [15–19] or graphene [20]. Among the metal oxides, WO₃ has smaller band gap (2.8 eV) than TiO₂ and better absorbs visible light. Moreover, WO₃ has a suitable conduction band potential and acts as a trapping site for photoexcited electrons from TiO₂. The photogenerated holes from the valence band of WO₃ move towards and accumulate in the valence band of TiO₂. In such a way the efficiency of charge separation is increased, enhancing at the same time the photocatalytic acivity of TiO₂ [21]. Additionally, the formation of WO₃ monolayer on TiO₂ increases the acidity of the WO₃/TiO₂ surface enabling the adsorption of greater amount of hydroxyl groups and organic reactants on the surface [21,22]. In recent years, WO₃/TiO₂ composites were synthesized using different methods such as sol-gel, ultrasonic spray pyrolysis, ball milling, hydrothermal, sol-precipitation, and impregnation to improve photocatalytic activity of TiO₂ under the visible light [23–28]. Thin films of TiO₂/WO₃ have also been prepared by dip and spin coating [29,30] or by one-step oxidation method [31]. In most of these reports it was demonstrated that WO₃/TiO₂ composites were found to have much

higher photocatalytic activity under the visible light than pure TiO_2 [24,26,28,31]. Therefore, the combination of these two materials can lead to increased charge carrier lifetime and improved photocatalytic activity under the visible irradiation. Among different synthesis routs, plasma electrolytic oxidation (PEO) process is very facile, cost-effective and environmentally benign process for producing of well-adhered and crystalline oxide films, but the studies on structural and photocatlytic properties of WO_3/TiO_2 films (coatings), produced by PEO process, are limited [32–34].

In this study WO_3/TiO_2 coatings were synthetized on titanium substrate by using PEO process. Structural and optical properties of the coatings were fully characterized by XRD, SEM, Raman, XPS, and diffuse reflectance spectroscopy. The aim of this work was to tailor the band gap energy of WO_3/TiO_2 coatings towards the visible spectral region, varying the time of PEO process and to explore the photocatalytic properties of the coatings. The photocatalytic efficiency of WO_3/TiO_2 coatings was tested under the visible and UV light irradiation using Rhodamine 6G and Mordant Blue 9 as model pollutants. We demonstrated that this approach provides an efficient route for the formation of cost-effective and improved visible-light-driven photocatalysts.

2. Experimental

2.1. Preparation of WO_3/TiO_2 coatings

WO_3/TiO_2 coatings were prepared on titanium substrate using plasma electrolytic oxidation (PEO) process. PEO process is an anodizing process of lightweight metals (aluminum, magnesium, zirconium, titanium, etc.) or metal alloys above the dielectric breakdown voltage, when thick, highly crystalline oxide coating with high corrosion and wear resistance, and other desirable properties are produced. During the PEO process, numerous small sized and short-lived discharges are generated continuously over the coating's surface, accompanied by gas evolution. Due to increased local temperature, plasma-chemical reactions are induced at the discharge sites modifying the structure, composition, and morphology of such oxide coatings. The oxide coatings formed by PEO process usually contain crystalline and amorphous phases with constituent species originating both from metal and electrolyte. WO_3/TiO_2 coatings were formed on the rectangular titanium samples (99.5% purity, Alfa Aesar) of dimensions 25 mm $\times$ 10 mm $\times$ 0.25 mm, which were used as working electrodes in the experiment. The working electrodes were sealed with insulation resin leaving only an area of 1.5 cm^2 as an active surface. Before starting the PEO process, titanium samples were degreased in acetone, ethanol, and distilled water, using ultrasonic cleaner and dried in a warm air stream. The anodic oxidation process was conducted in an aqueous solution of 10^{-3} M 12-tungstosilicic acid ($H_4SiW_{12}O_{40}$), at constant current density (150 mA/cm^2). During PEO process, the electrolyte circulated through the chamber–reservoir system. The temperature of the electrolyte was kept fixed at $(20 \pm 1)\,^\circ$C. Detailed description of PEO process is given in the ref. [33].

After plasma electrolytic oxidation, the samples were rinsed in distilled water to prevent additional deposition of electrolyte components during drying. The WO_3/TiO_2 samples were obtained by varying the time of PEO process from 90 s up to 300 s. The pure TiO_2 sample was obtained after 300 s of PEO process.

2.2. Characterization of WO_3/TiO_2 coatings

The crystal structure of WO_3/TiO_2 samples was analyzed by X-ray diffraction (XRD), using a Rigaku Ultima IV diffractometer in Bragg-Brentano geometry, with Ni-filtered CuKα radiation

(λ = 1.54178 Å). Diffraction data were acquired over the scattering angle 2θ from 15° to 75° with a step of 0.02° and acquisition rate of 2°/min. The XRD spectra refinement was performed with the software package Powder Cell. The TCH pseudo-Voigt profile function gave the best fit to the experimental data.

Scanning electron microscope (SEM) JEOL 840A equipped with an EDS detector was used to characterize the morphology and chemical composition of formed oxide coatings.

Micro-Raman scattering measurements were performed at room temperature in a backscattering geometry, using a Jobin-Yvon T64000 triple spectrometer system and Nd:YAG laser line of 532 nm as an excitation source. The incident laser power was kept less than 10 mW in order to prevent the heating effects.

UV-vis diffuse reflectance spectra were acquired using the Specord M40 Carl Zeiss spectrometer.

X-ray photoelectron spectroscopy (XPS) was used for the surface composition analysis of WO_3/TiO_2 coatings. XPS was carried out on a VG ESCALAB II electron spectrometer with a base pressure in the analysis chamber of 10^{-8} Pa. The X-ray source was monochromatized AlKα radiation (1486.6 eV) and the instrumental resolution was 1 eV. The spectra were calibrated using the C 1 s line (284.8 eV) of the adventitious carbon and corrected by subtracting a Shirley-type background.

2.3. Photocatalytic experiments

The photocatalytic activity of WO_3/TiO_2 samples was evaluated by monitoring the decomposition of Rhodamine 6G (R6G) and Mordant Blue 9 (MB9) under the irradiation of two different light sources: fluorescent and UV lamps. The photocatalytic measurements on R6G solution (initial concentration in water: 10 mg/L) have been performed using a 36 W visible fluorescent lamp (Hyundai eagle), whose emission spectrum, compared to sunlight spectrum, is given in Ref. [9]. The cuvette (3 mL) was placed at about 5 cm from the lamp. The evolution of the rhodamine concentration was followed by measuring the variation of the intensity of main absorption peak at ~525 nm. UV–vis absorption measurements as a function of the light exposure time were performed by using USB2000 spectrometer by Ocean Optics. The solution was placed in the dark for 60 min to reach the adsorption/desorption equilibrium before visible light exposure.

The photocatalytic activity of WO_3/TiO_2 samples under UV light irradiation was evaluated using aqueous solution of MB9 as a model pollutant. Batch type experiments were performed in an open thermostated cell (at 25 °C). The cell was equipped with a water circulating jacket to maintain the solution at room temperature. A mercury lamp (125 W) was used as a light source and was placed 13 cm above the surface of the dye solution. The initial concentration of MB9 in an aqueous suspension was 50 mg/L and the working volume was 25 mL. Before the lamp was switched on, the cell was kept in dark for 60 min in order to achieve the adsorption-desorption equilibrium. At regular time intervals the aliquots were taken and the concentration of the dye was determined by UV–vis spectrophotometer (Super Scan) at λ_{max} = 516 nm. The photocatalytic experiments were conducted at the natural pH of the dyes (pH = 7 in a case of R6G solution and at pH = 6 in a case of MB9 solution). All photocatalytic measurements were repeated at least twice to check their reproducibility.

In order to detect the formation of free hydroxyl radicals (OH$^\bullet$) on the UV illuminated WO_3/TiO_2 surface, photoluminescence (PL) measurements were performed using terephthalic acid, which is known to react with OH$^\bullet$ radicals and produces highly fluorescent 2-hydroxyterephthalic acid. The experiment was conducted at ambient temperature. The WO_3/TiO_2 photocatalyst (TW300) was placed in open termostated cell filled with 20 mL of the 5×10^{-4} mol L^{-1} terephthalic acid in a diluted NaOH aqueous solution with

a concentration of 2×10^{-3} mol L^{-1}. UV lamp (125 W) was used as a light source. Sampling was performed after 15, 30, 60 and 90 min. PL spectra of reaction solution, using excitation wavelength of 315 nm, were measured on a Spex Fluorolog spectrofluorometer system at wavelength of 425 nm for which the 2-hydroxyterephthalic acid exhibits intense PL peak.

3. Results and discussion

3.1. Crystal structure and morphology

XRD patterns of the WO$_3$/TiO$_2$ samples obtained for 90 (TW90), 120 (TW120), and 300 s (TW300) of PEO process are presented in Fig. 1. The diffraction peaks which appear in TW90 sample at $2\theta = 23.3°$, $33.4°$, $54.2°$ belong to (002), (022) and (042) planes of monoclinic WO$_3$ phase, which crystallizes in $P2_1/c$ (No. 14) space group. Besides these XRD peaks, the XRD pattern also shows peak at $25.3°$ which belongs to TiO$_2$ anatase crystal phase (space group $I4_1/amd$ (No. 141)) and intense peaks of elemental Ti (space group $P6_3$/mmc (No. 194)). This indicates that Ti substrate is not completely oxidized to form TiO$_2$ during the PEO process. With increasing duration of PEO process, for the TW120 and TW300 samples, the XRD peaks of WO$_3$ phase became more intense. The spectra refinement, using Powder Cell program, showed that besides WO$_3$ phase a monoclinic WO$_{2.96}$ phase appeared (space group $P2/c$ (No. 13)). Furthermore, the intensities of XRD peaks which belong to TiO$_2$ phase and elemental Ti decreased implying that the WO$_3$/TiO$_2$ coatings were enriched with WO$_3$/WO$_{2.96}$ phase. According to the JCPDS database for WO$_3$, WO$_{2.96}$, TiO$_2$, and elemental Ti (JCPDS: 43-1035 (WO$_3$), 30-1387 (WO$_{2.96}$), 16-0934 (TiO$_2$) and 44-1294 (elemental Ti)) very good agreement is obtained between experimental and calculated diffraction patterns of the WO$_3$/TiO$_2$ samples. In Fig. 1 are marked main XRD peaks of WO$_3$ and WO$_{2.96}$ phases for clarity. The lattice parameters and the estimated volume fractions (%) of different phases for the WO$_3$/TiO$_2$ samples are given in Table 1.

In Fig. 2 are presented SEM images of WO$_3$/TiO$_2$ samples. In the TW90 sample produced with shorter PEO time, certain number of microdischarge channels together with molten regions was present because of the rapid cooling of the electrolyte. With increasing time of PEO process, when the thickness of the oxide coating was increased, the number of microdischarge channels and
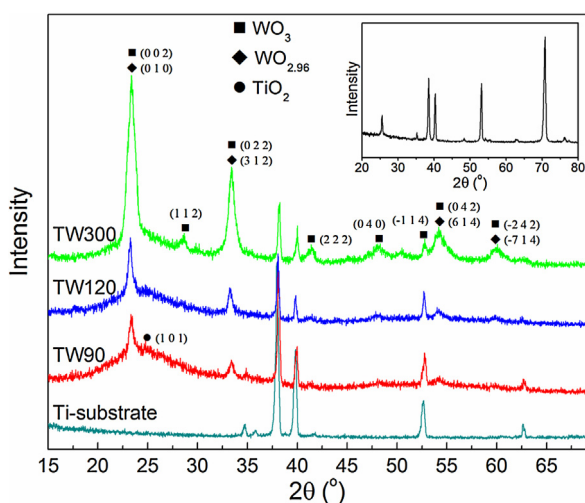
Table 1
Phase fraction (vol%) and cell parameters (Å) of WO$_3$/TiO$_2$ samples.

Phase	TW90	TW120	TW300
WO$_3$	$a = 7.4060$ $b = 7.6400$ $c = 7.6455$ 29.6%	$a = 7.3026$ $b = 7.5398$ $c = 7.6933$ 29.1%	$a = 7.4060$ $b = 7.5177$ $c = 7.5920$ 54.5%
WO$_{2.96}$	/	$a = 11.9006$ $b = 3.8258$ $c = 59.6312$ 36.70%	$a = 11.8000$ $b = 3.8098$ $c = 59.7400$ 20.90%
TiO$_2$	$a = 3.7778$, $c = 9.4440$, 66.0%	$a = 3.7841$, $c = 9.5105$, 32.2%	$a = 3.7790$, $c = 9.4124$ 23.8%
Ti	$a = 2.9481$ $c = 4.7325$ 4.3%	$a = 2.9594$ $c = 4.7254$ 2.0%	$a = 3.0510$ $c = 4.7820$ 0.9%

micropores decreased followed by increased roughness of the coating's surface.

The quantitative elemental analysis confirmed the presence of Ti, O and W and the elemental composition of the samples is shown in Table 2. EDS analysis confirmed the increasing trend of W content with increasing of PEO time.
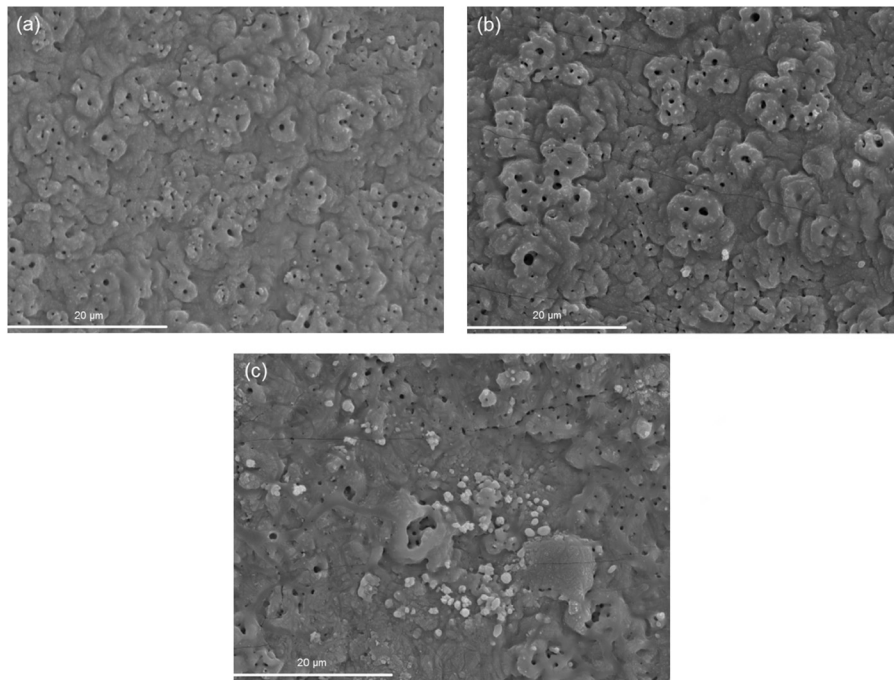
3.2. Raman and diffuse reflectance spectra

The Raman spectra of WO$_3$/TiO$_2$ samples produced for different duration of PEO process are shown in Fig. 3a. Several modes originating from two crystalline oxide phases can be identified (marked on Fig. 3a as T and W).

The Raman modes positions were determined using Lorentzian fit procedure and the deconvoluted spectra of TW90, TW120 and TW300 samples are presented in Fig. 3b. Besides the modes at about 144 cm^{-1} (E$_{g(1)}$), 197 cm^{-1} (E$_{g(2)}$), 393 cm^{-1} (B$_{1g(1)}$), 516 cm^{-1} (A$_{1g}$, B$_{1g(2)}$) and 638 cm^{-1} (E$_{g(3)}$) which belong to anatase phase of TiO$_2$ [35], several modes characteristic for monoclinic WO$_3$ phase are present [22,36,37]. The broad band at ~703 cm^{-1} and strong band at ~793 cm^{-1} are assigned to the stretching (O–W–O) modes of the bridging oxygen of the WO$_6$ octahedra. The bands observed at ~272 cm^{-1} and at ~316 cm^{-1} are assigned to the bending (O—W—O) vibrations of bridging oxygen in monoclinic m-WO$_3$ [22,37]. The band positioned at ~989 cm^{-1} is assigned to the dioxo (W=O)$_2$ symmetric vibration of the isolated surface WO$_4$ structure, whereas its weak shoulder at ~942 cm^{-1} represents asymmetric vibration of the same atomic group [22,37]. The low frequency mode at 58 cm^{-1} belongs to the to lattice modes of monoclinic WO$_3$ phase [38].

Further, from the Lorentzian fit procedure it was obtained that the ratio between the intensity of the peak positioned at 639 cm^{-1} and the sum of the intensities of the 703 cm^{-1} and 793 cm^{-1} peaks decreased with the increase of PEO time. This fact supports the XRD results that WO$_3$ content increases with prolonged duration of PEO process.

In Fig. 4 are presented the Raman spectra of TW90, TW120 and TW300 samples in the C—H and O—H region. The Raman band at around 2885 cm^{-1} originates from the overlapped CH$_3$ and CH$_2$ stretching vibrations [39]. Broad Raman peak in the 3000–3600 cm^{-1} frequency range can be assigned to the O—H stretching vibration of water molecules adsorbed on the surface of the WO$_3$/TiO$_2$ coatings [3,5].

The absorption spectra of TW90, TW120 and TW300 samples are given in Fig. 5a. With increasing content of WO$_3$ phase the absorption edge shifts to higher wavelengths. In the spectra of TW120 a structure around 380–400 nm can be observed, which is

Fig. 1. XRD patterns of TW90, TW120 and TW300 samples formed in various stages of PEO process, together with the XRD spectrum of Ti-substrate. In the inset is given XRD spectrum of anatase TiO$_2$ obtained on Ti-substrate after 300 s of PEO process.

Fig. 2. SEM micrographs of WO_3/TiO_2 samples formed in various stages of PEO process: (a) TW90, (b) TW120 and (c) TW300 sample.

very pronounced in the TW300 sample. The appearance of this absorption structure can be attributed to the electronic population of WO_3 conduction band [40]. From the absorption spectra from Fig. 4a, applying the same procedure as Ghobadi in his work [41], the band gap energies for pure TiO_2 and WO_3/TiO_2 samples were estimated. In Fig. 5b are presented the Tauc plots for indirect transition, as TiO_2 and WO_3 are indirect band gap semiconductors [26]. The band gap (E_g) energies are 3.19 eV for pure TiO_2, and 2.84, 2.77 and 2.6 eV for TW90, TW120 and TW300 samples, respectively. It is obvious that with increasing WO_3 content the band gap decreases compared to pure TiO_2 and shifts to the visible spectral range. Patrocinio et al. [40] have shown that in TiO_2/WO_3 films, the WO_3 conduction band introduces new low lying electronic levels with respect to the conduction band of TiO_2, causing the lowering of the band gap energy of composite samples compared to pure TiO_2. This finding is in accordance with the band gap behavior of our WO_3/TiO_2 samples from Fig. 5b.

3.3. XPS analysis

The XPS study was further used to confirm the chemical binding states of W 4f. The W 4f XPS spectra of the TW90 and TW300 samples and the results of their decomposition into peaks are shown in Fig. 6. The W 4f spectrum of TW90 sample (Fig. 6a) can be deconvoluted into one doublet with binding energies of 35.8 (W $4f_{7/2}$) and 38.1 eV (W $4f_{5/2}$), respectively. The energy position of this doublet corresponds to the W^{6+} oxidation state [42].

In the TW300 sample (Fig. 6c) the contribution of W^{5+} states from nonstoichiometric oxide phase can be seen. The W 4f

spectrum can be deconvoluted with two doublets. The first two characteristic peaks at 36 (W $4f_{7/2}$) and 38.3 eV (W $4f_{5/2}$) correspond to W^{6+} state as in the case of TW90. The binding energies of these peaks are somewhat higher than that for TW90 sample. The up-shift in binding energy can be ascribed to the presence of defects and OH-groups on the surface [43], existence of
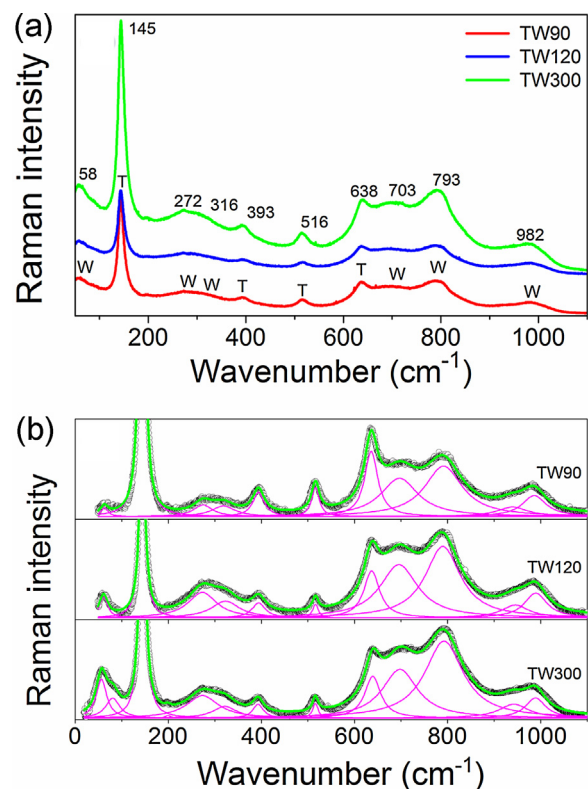
Fig. 3. Room-temperature Raman spectra of WO_3/TiO_2 samples (a). The TiO_2 and WO_3 Raman modes are marked as T and W. Deconvoluted Raman spectra of TW90, TW120 and TW300 samples (b).

Table 2
EDS analysis of the WO_3/TiO_2 composites.

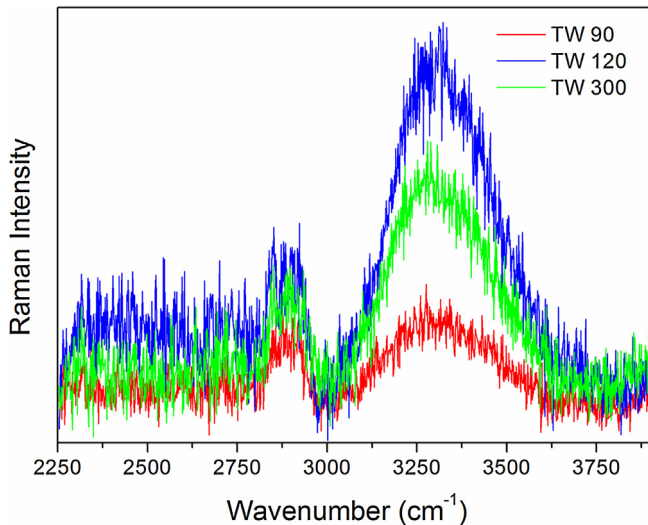| Sample	EDS data			
	Ti (at%)	W (at%)	O (at%)	W/Ti
TW90	6.98	14.17	78.85	2.03
TW120	6.22	16.12	77.66	2.59
TW300	4.09	17.16	78.75	4.1

Fig. 4. Raman spectra of WO$_3$/TiO$_2$ samples in the C–H and O–H spectral region.

which is confirmed by Raman analysis (Fig. 4). The binding energies of the second doublet at 34.5 (W 4f$_{7/2}$) and 36.5 eV (W 4f$_{5/2}$) correspond to W^{5+} state [42]. These results are in accordance with XRD analysis.

The O 1s spectra of TW90 and TW300 samples (Fig. 6b, d) are decomposed into three peaks. The major peak at binding energy of 531.2 eV can be assigned to the oxygen atoms in WO$_3$ and to the OH-groups present on the surface [32,44]. The second peak observed at 530.6 eV has been attributed to oxygen bound to Ti [26], whereas the binding energy of the third peak at 533.1 eV corresponds to the oxygen in water molecules bound in the coating's structure or adsorbed on its surface [45]. The relative intensity of the XPS peaks at 531.2 eV and 533.1 eV was increased in the TW300 sample. The intensity increase of these peaks can be related to the presence of sub-stoichiometric WO$_{3-x}$ phase (WO$_{2.96}$). Similar behavior was reported in the paper of Shpak et al. [44] in which these peaks were more intense in WO$_{3-x}$ oxides than in stoichiometric WO$_3$. This finding is also supported by the Raman spectrum of TW300 sample (Fig. 4), for which the intensity of the Raman mode, corresponding to the water molecules adsorbed on the surface, is higher than in TW90 sample.

3.4. Photocatalytic performances of WO$_3$/TiO$_2$ coatings

Fig. 7a shows the kinetics of degradation of R6G for pure TiO$_2$ and WO$_3$/TiO$_2$ samples under the visible light. No detectable

degradation of R6G was registered without the presence of WO$_3$/TiO$_2$ samples (black circles on Fig. 7a). As can be seen from Fig. 7a, both TiO$_2$ and WO$_3$/TiO$_2$ coatings adsorbed the dye in the equilibrium period of 60 min before the exposure to visible light. It is known from the literature that the zero point charge (pH$_{zpc}$) of TiO$_2$ lies between 6 and 6.8 [46–48], whereas the isoelectric point of WO$_3$ is even lower and lies in the range 1.5–2.5 [49]. At higher pH values than these WO$_3$ and TiO$_2$ surfaces should be negatively charged. Therefore, the adsorption of the R6G as cationic dye at pH = 7, points out that the surfaces of WO$_3$/TiO$_2$ and TiO$_2$ coatings are negative and attract the positively charged R6G. The dye adsorption ability can be crucial for the high catalytic activity of the catalyst, because it can enhance the electron/hole transfer efficiency and contact with photogenerated active species.

When TiO$_2$ and WO$_3$/TiO$_2$ samples were subjected to visible radiation, composite coatings have shown much better photo-efficiency and demonstrated to be far superior than pure TiO$_2$. The highest activity was observed for the TW90 and TW120 samples for which the photodegradation of R6G reached almost 80% after 60 min. With further increase of WO$_3$ content, the photocatalytic efficiency slightly decreased, but is still much higher than for pure TiO$_2$.

Further, the photocatalytic activity of WO$_3$/TiO$_2$ coatings for degradation of MB9 was tested under the UV light. In Fig. 7b is presented the photodegradation of MB9 in the presence of WO$_3$/TiO$_2$ samples. In the dark, WO$_3$/TiO$_2$ coatings showed no adsorption of MB9. The absence of adsorption can be explained by highly anionic character of MB9 and electrostatic repulsion between the dye and negatively charged surface of WO$_3$/TiO$_2$ coatings.

The photocatalytic activity of WO$_3$/TiO$_2$ samples was improved with increased content of WO$_3$ phase, and the TW300 sample exhibited better activity than pure TiO$_2$. As can be seen from Fig. 7b, after 240 min more than 80% of dye was degraded in the presence of WO$_3$/TiO$_2$ coatings.

Photocatalytic degradation of both dyes can be well described by first-order kinetic equation, $ln(C/C_o) = kt$, where C_o is the initial dye concentration and C is the dye concentration at time t. The first order kinetic constant k is obtained from the slope of the $ln(C/C_o)$ versus t for both dyes. In Table 3 are given the first order rate constants for R6G and MB9 (k_{R6G}, k_{MB9}), together with the corresponding linear correlation coefficient (R^2). In a case of R6G degradation under the visible light, the highest k value (k_{R6G}) was obtained for the TW90 sample. In a case of MB9 degradation under UV light, value of k_{MB9} increased with increasing amount of WO$_3$.

The degradation rate constant k of WO$_3$/TiO$_2$ coatings under visible light is almost five times higher than that of TiO$_2$, whereas its value under UV light are comparable with TiO$_2$, suggesting that
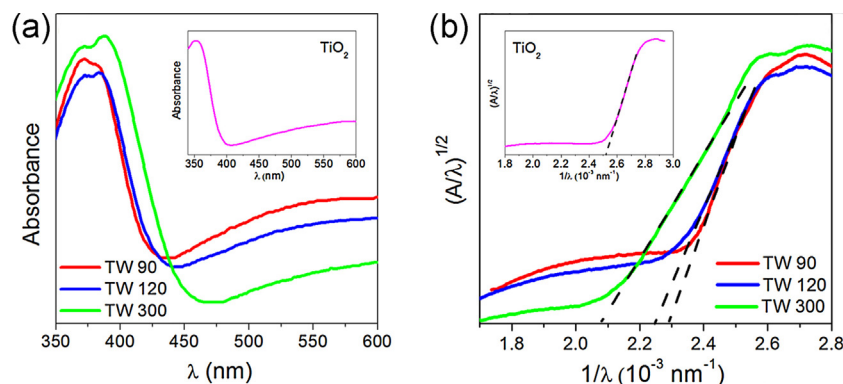

Fig. 5. Absorbance spectra (a) and Tauc plots for indirect band gap for WO$_3$/TiO$_2$ samples (b). In the inset is given Tauc plot for indirect band gap for pure TiO$_2$.

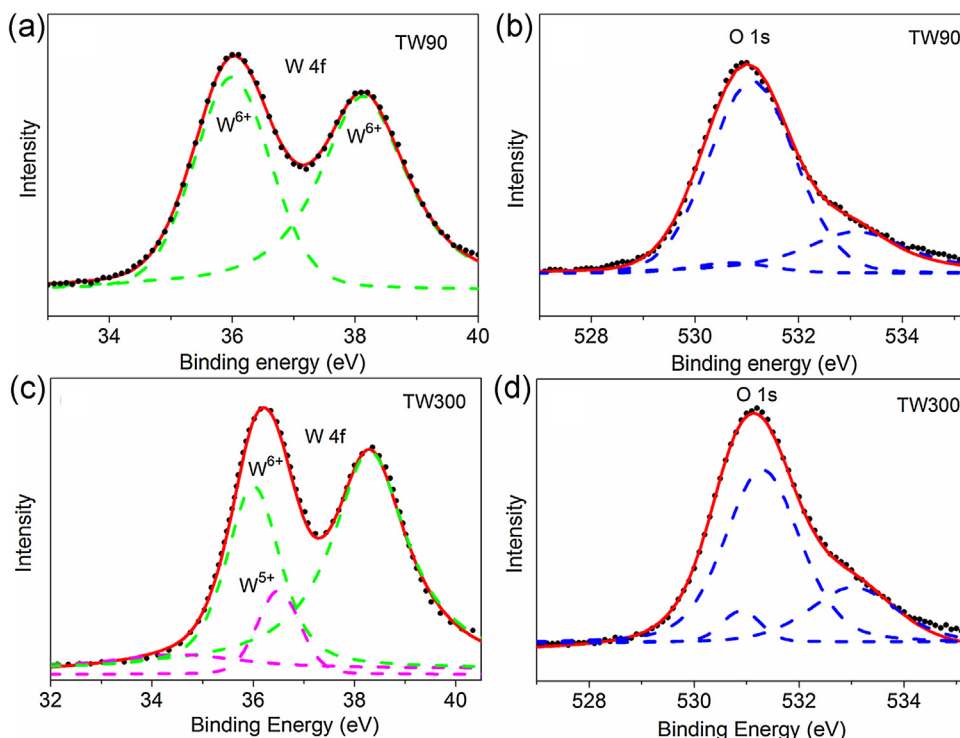**Fig. 6.** XPS spectra of W 4f and O 1s regions for TW90 and TW300 samples.

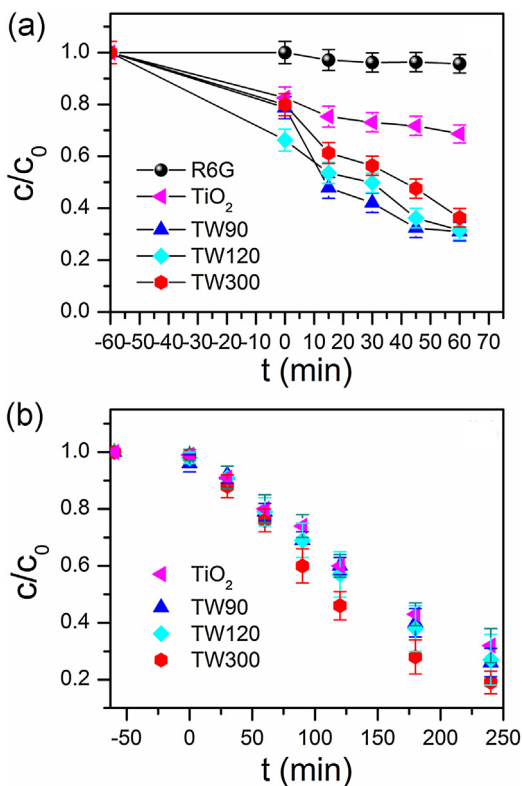composite coatings are very efficient photocatalysts under visible light.

3.5. Hydroxyl radical analysis

The formation of free hydroxyl radicals (OH$^\bullet$) was tested on the surface of TW300 photocatalyst under UV irradiation and detected by PL method. Applying similar procedure as described in the paper of Su et al. [50], TW300 sample was placed in terephthalic acid solution and illuminated by UV light. PL spectra of the reaction solution were measured at room temperature after 15, 30, 60 and 90 min, and these spectra are presented in Fig. 8. The terephthalic acid reacts with OH$^\bullet$ producing 2-hydroxyterephthalic acid, which exhibits PL peak at 425 nm [51]. The intensity of this peak is proportional to the amount of OH$^\bullet$ produced in water [50,51]. As can be seen from Fig. 8, gradual increase of PL intensity at 425 nm with prolonged illumination time points at increasing amount of OH$^\bullet$ radicals produced at the surface of TW300 sample.

3.6. Mechanism of the reaction

The photocatalytic degradation of R6G or MB9 is initiated by the photoexcitation of the WO$_3$/TiO$_2$ coatings when the electron-hole pairs are formed on the catalyst's surface. According to the

Fig. 7. Photocatalytic degradation of R6G under visible light (a) and MB9 under UV light (b) in the presence of WO$_3$/TiO$_2$ and TiO$_2$ coatings.

Table 3
The pseudo-first rate constants for R6G and MB9 together with R^2.

Sample	$k_{R6G} \times 10^{-2}$ (min^{-1})	R^2	$k_{MB9} \times 10^{-2}$ (min^{-1})	R^2
TW90	1.52	0.975	0.44	0.990
TW120	1.24	0.957	0.47	0.982
TW300	1.20	0.963	0.65	0.966
TiO$_2$	0.28	0.888	0.41	0.963
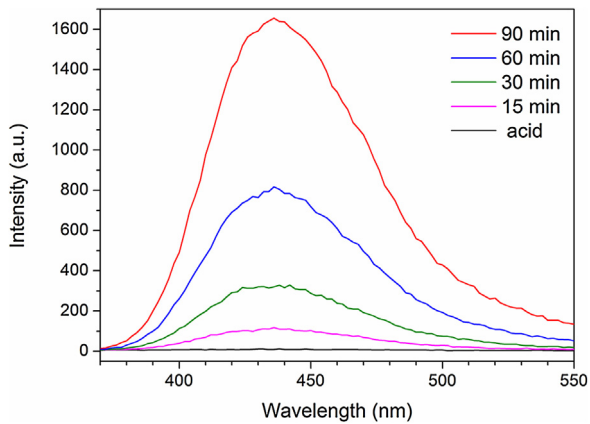
Fig. 8. PL spectral changes observed during UV illumination of TW300 sample in the solution of terephthalic acid after 15, 30, 60 and 90 min. The PL spectra of pure terephthalic acid is also presented.

generally accepted photoexcitation mechanism, electrons from the conduction band of TiO_2 can easily diffuse into the conduction band of WO_3 [40,52]. Since W(VI) can be easily reduced to W(V), WO_3 acts as an acceptor of conduction band electrons from TiO_2, whereas the photogenerated holes migrate in the opposite direction, i.e. from the lower-lying valence WO_3 band to the valence band of TiO_2. In such a way the charge separation efficiency can be increased.

In Fig. 9 is given an illustration of photo-induced electron-hole separation and reacting radicals formation. The presence of holes in the dye solution permits a direct oxidation of the dye, due to high oxidative potential of the holes (h^+):

$$h^+ + dye \rightarrow dye^{\bullet+} \rightarrow oxidation\ of\ the\ dye \qquad (1)$$
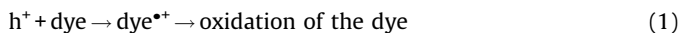
Further, hydroxyl radicals ($OH^\bullet$) are usually formed by the reaction between the holes and OH^- or water molecules present on the surface of the catalyst. The $OH^\bullet$ radicals attack the dye in aqueous solution leading to its degradation:

$$OH^\bullet + dye \rightarrow photodegradation\ of\ the\ dye \qquad (2)$$
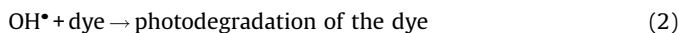
The photo-induced electrons can also react with dissolved oxygen to form superoxide ions ($O_2^{-\bullet}$) which in contact with H_2O molecules form OH^- ions and finally $OH^\bullet$ radicals.

It is known from the literature that WO_3 is almost 15 times more acidic than TiO_2 [21,22,31], so it is expected that the surface of PEO produced WO_3/TiO_2 coatings is more acidic than that of TiO_2, and has a higher affinity for chemical species having unpaired electrons. Because of higher acidity, the surface of WO_3/TiO_2 coatings can absorb more H_2O and OH^- generating more $OH^\bullet$ radicals. The XPS and Raman spectra of WO_3/TiO_2 composite coatings gave an evidence that adsorbed H_2O and hydroxyls are present on the surface of WO_3/TiO_2 coatings, existence of which is important for the formation of $OH^\bullet$ radicals. PL measurements, performed on TW300 sample, (Fig. 8) clearly demonstrated that with increasing illumination time the increasing amount of $OH^\bullet$ radicals is formed on the surface of photocatalysts, which manifests through higher photocatalytic activity of TW300 sample.

The absorption measurements have shown that the band gap energy of TiO_2 is higher than that of WO_3/TiO_2 coatings. Namely, with prolonged time of PEO process, the WO_3 content increases followed by an appearance of $WO_{2.96}$ phase. As the conduction band of nonstoichiometric WO_{3-x} oxides is lower with respect to WO_3 and TiO_2 (Fig. 9) [53], the presence of $WO_{2.96}$ phase will further reduce the band gap of WO_3/TiO_2 samples towards the visible spectral range, as already noticed from the Tauc plots from Fig. 5. As a result, the electron-hole recombination will be more difficult and more reactive radicals can be produced at the WO_3/TiO_2 surface. Therefore, WO_3/TiO_2 coatings should be more efficient as catalysts under the visible light. The photocatalytic degradation of R6G and kinetics of the reaction confirmed that WO_3/TiO_2 coatings are efficient photocatalysts in the visible region. Slight decrease of photocatalytic activity of TW300 sample in a case of R6G photodegaradation (Fig. 7a) can be explained by the occurrence of photochromism [27,40]. Namely, the electron accumulation at the WO_3 conduction band can be more pronounced with increased WO_3 content. The accumulated electrons can react with $OH^\bullet$ radicals forming OH^- ions or can reduce the number of superoxide radicals [27,40] degrading at some extent the photocatalytic activity of WO_3/TiO_2 coatings. The presence of pronounced absorption feature around 380–400 nm in the absorbance spectrum of TW300 sample confirms this assumption. Another reason can be found in the formation of small polarons, appearance of which is characteristic for WO_3 and WO_{3-x} phases. The photoexcited electron-hole pairs can be rapidly quenched by recombination of photoexcited holes with electrons from localized polaron states, whereas photoexcited electrons
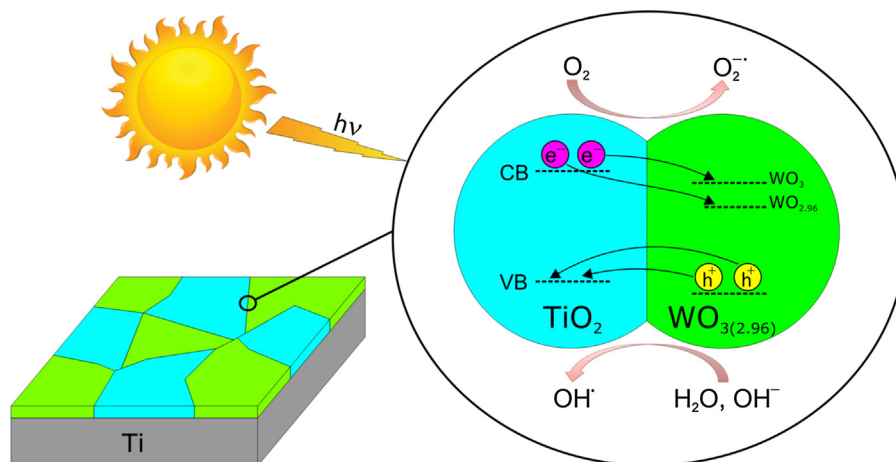
Fig. 9. Schematic diagram of electron-hole pairs separation and proposed mechanism of photodegradation over WO_3/TiO_2 photocatalysts.

populate polaron states [54], reducing on the other side the photocatalytic efficiency of the catalyst.

4. Conclusion

WO_3/TiO_2 composite and pure TiO_2 coatings have been prepared on titania substrates using facile and cost-effective PEO process. The structural, morphological, optical properties and chemical composition of these samples were investigated by different methods such as XRD, SEM, Raman, UV–vis diffuse reflectance spectroscopy and XPS. XRD and Raman analysis revealed that the coatings are mainly composed of monoclinic WO_3 and anatase TiO_2. With increasing duration of PEO process the crystallinity of the samples was improved, the WO_3 phase become dominant and a certain amount of monoclinic $WO_{2.96}$ phase appeared. XPS analysis confirmed the XRD results and revealed the presence of OH-groups and adsorbed H_2O on the surface of WO_3/TiO_2 coatings. The increasing amount of $WO_3/WO_{2.96}$ phase caused a decrease of optical band gap, i.e. shift from near UV to visible spectral region. The photocatalytic activity of WO_3/TiO_2 samples has been measured by monitoring photodecolouration of two model pollutants in aqueous solution, R6G under visible and MB9 under UV light irradiation. The WO_3/TiO_2 samples have shown enhanced photocatalytic activity compared to pure TiO_2 under the visible light irradiation. Slight decrease of photocatalytic activity under the visible light in the sample enriched with $WO_3/WO_{2.9}$ phase can be ascribed to the occurrence of photochromism and/or small polaron formation. Under the UV light, the WO_3/TiO_2 photocatalysts have shown slightly better photocatalytic activity than pure TiO_2. PL mesurements demonstrated the correlation between photoactivity and the formation rate of $OH^\bullet$ radicals under UV light irradiation, i.e. higher amount of $OH^\bullet$ radicals formed, the better photoactivity of WO_3/TiO_2 photocatalysts was achieved. The kinetics of the reaction in the case of both azo dyes followed the pseudo-first order. The degradation rate constant k of WO_3/TiO_2 coatings under the visible light is almost five times higher than that of TiO_2. Much better photocatalytic activity of the WO_3/TiO_2 samples compared to pure TiO_2 in the visible range can be attributed to better light absorption, higher adsorption affinity and increased charge separation efficiency with increasing content of $WO_3/WO_{2.96}$ phase.

Acknowledgements

References

[1] L. Ren, Y. Li, J. Hou, X. Zhao, C. Pan, ACS Appl. Mater. Interfaces 6 (2014) 1608–1615.
[2] F. Ruggieri, A.A. D'Archivio, M. Fanellia, S. Santucci, RSC Adv. 1 (2011) 611–618.
[3] M. Šćepanović, B. Abramović, A. Golubović, S. Kler, M. Grujić-Brojčin, Z. Dohčević-Mitrović, B. Babić, B. Matović, Z.V. Popović, J. Sol-Gel Sci. Technol. 61 (2012) 390–402.
[4] A. Golubović, B. Abramović, M. Šćepanović, M. Grujić-Brojčin, S. Armaković, I. Veljković, B. Babić, Z. Dohčević-Mitrović, Z.V. Popović, Mater. Res. Bull. 48 (2013) 1363–1371.
[5] S. Watson, D. Beydoun, J. Scott, R. Amal, J. Nanoparticle Res. 6 (2004) 193–207.
[6] A.N. Banerjee, Nanotechnol. Sci. Appl. 4 (2011) 35–65.
[7] M. Xing, D. Qi, J. Zhang, F. Chen, Chem. Eur. J. 17 (2011) 11432–11436.
[8] Y. Niu, M. Xing, J. Zhang, B. Tian, Catal. Today 201 (2013) 159–166.
[9] F. Ruggieri, D. Di Camillo, L. Maccarone, S. Santucci, L. Lozzi, J. Nanopart. Res. 15 (2013) 1–11.
[10] W. M. Xing, Y. Li, J. Wu, X. Gong Zhang, J. Phys. Chem. C 115 (2011) 7858–7865.
[11] M. Janus, B. Tryba, E. Kusiak, T. Tsumura, M. Toyoda, M. Inagaki, A.W. Morawski, Catal. Lett. 128 (2009) 36–39.
[12] M. Takeuchi, M. Matsuoka, M. Anpo, Res. Chem. Intermed. 38 (2012) 1261–1277.
[13] X. Chen, L. Liu, P.Y. Yu, S.S. Mao, Science 331 (2011) 746–750.
[14] W. Fang, M. Xing, J. Zhang, Appl. Catal. B: Environ. 160–161 (2014) 240–246.
[15] Y. Wang, J. Zhang, L. Liu, C. Zhu, X. Liu, Q. Su, Mater. Lett. 75 (2012) 95–98.
[16] Y. Xiaodan, W. Qingyin, J. Shicheng, G. Yihang, Mater. Charact. 57 (2006) 333–341.
[17] J. Rashid, M.A. Barakat, S.L. Pettit, J.N. Kuhn, Environ. Technol. 35 (2014) 2153–2159.
[18] B. Gao, Y. Ma, Y. Cao, W. Yang, J. Yao, J. Phys. Chem. B 110 (2006) 14391–14397.
[19] X. Luo, F. Liu, X. Li, H. Gao, G. Liu, Mat. Sci. Semicon. Proc. 16 (2013) 1613–1618.
[20] N.R. Khalid, E. Ahmed, Z. Hong, M. Ahmad, Y. Zhang, S. Khalid, Ceram. Int. 39 (2013) 7107–7113.
[21] Y. Li, P.C. Hsu, S.M. Chen, Sensor. Actuat. B-Chem. 174 (2012) 427–435.
[22] K.K. Akurati, A. Vital, J.P. Dellemann, K. Michalowa, T. Graule, D. Ferri, A. Baiker, Appl. Catal. B: Environ. 79 (2008) 53–62.
[23] D. Ke, H. Liu, T. Peng, X. Liu, K. Dai, Mater. Lett. 62 (2008) 447–450.
[24] H. Song, H. Jiang, X. Liu, G. Meng, J. Photoch. Photobio. A 181 (2006) 421–428.
[25] C. Shifu, C. Lei, G. Shen, C. Gengyu, Powder Technol. 160 (2005) 198–202.
[26] F. Riboni, L.G. Bettini, D.W. Bahnemann, E. Selli, Catal. Today 209 (2013) 28–34.
[27] J. Yang, X. Zhang, H. Liu, C. Wang, S. Liu, P. Sun, L. Wang, Y. Liu Catal, Today 201 (2013) 195–202.
[28] S. Bai, H. Liu, J. Sun, Y. Tian, S. Chen, J. Song, R. Luo, D. Li, A. Chen, C.-C. Liu, Appl. Surf. Sci. 338 (2015) 61–68.
[29] A. Rampaul, I.P. Parkin, S.A. O'Neill, J. DeSouza, A. Mills, N. Elliott, Polyhedron 22 (2003) 35–44.
[30] J.H. Pan, W. In Lee, Chem. Mater. 18 (2006) 847–853.
[31] M. Long, B. Tan, P. Hu, B. Zhou, Y. Zhou, J. Mater. Chem. A 3 (2015) 10195–10198.
[32] J. He, Q. Luo, Q.Z. Cai, X.W. Li, D.Q. Zhang, Mater. Chem. Phys. 129 (2011) 242–248.
[33] S. Stojadinović, N. Radić, R. Vasilić, M. Petković, P. Stefanov, Lj. Zeković, B. Grbić, Appl. Catal. B: Environ. 126 (2012) 334–341.
[34] S. Petrović, S. Stojadinović, Lj. Rožić, N. Radić, B. Grbić, R. Vasilić, Surf. Coat. Technol. 269 (2015) 250–257.
[35] T. Ohsaka, F. Izumi, Y. Fujiki, J. Raman Spectrosc. 7 (1978) 321–324.
[36] Y. Djaoued, S. Balaji, N. Beaudoin, J. Sol-Gel Sci. Technol. 65 (2013) 374–383.
[37] C. Santato, M. Odziemkowski, M. Ulmann, Jan Augustynski, J. Am. Chem. Soc. 123 (2001) 10639–10649.
[38] E. Cazzanelli, C. Vinegoni, G. Mariotto, A.J. Purans, Solid State Ionics 123 (1999) 67–74.
[39] Y. Yu, K. Lin, X. Zhou, H. Wang, S. Liu, X. Ma, J. Phys. Chem. C 111 (2007) 8971–8978.
[40] A.O.T. Patrocinio, L.F. Paula, R.M. Paniago, J. Freitag, D.W. Bahnemann, ACS Appl. Mater. Interfaces 6 (2014) 16859–16866.
[41] N. Ghobadi, Int. Nano Let. 3 (2013) 1–4.
[42] K. Senthil, K. Yong, Nanotechnology 18 (2007) 395604 (1–7).
[43] H. Ling, J. Lu, S. Phua, H. Liu, L. Liu, Y. Huang, D. Mandler, P.S. Lee, X. Lu, J. Mater. Chem. A 2 (2014) 2708–2717.
[44] A.P. Shpak, A.M. Korduban, V.O. Medvedskij, J. Electron. Spectrosc. Relat. Phenom. 156–158 (2007) 172–175.
[45] H.Y. Wong, C.W. Ong, R.W.M. Kwok, K.W. Wong, S.P. Wong, W.Y. Cheung, Thin Solid Films 376 (2000) 131–139.
[46] A.A. Khodja, A. Boulkamh, C. Richard, Appl. Catal. B: Environ. 59 (2005) 147–154.
[47] C.C. Wang, J.Y. Ying, Chem. Mater. 11 (1999) 3113–3120.
[48] M.D. Hernández-Alonso, F. Fresno, S. Suarez, J.M. Coronado, Energy Environ. Sci. 2 (2009) 1231–1257.
[49] M. Anik, T. Cansizoglu, J. Appl. Electrochem. 36 (2006) 603–608.
[50] T.M. Su, Z.L. Liu, Y. Liang, Z.Z. Qin, J. Liu, Y.Q. Huang, Catal. Comm. 18 (2012) 93–97.
[51] K. Ishibashi, A. Fujishima, T. Watanabe, K. Hashimoto, Electrochem. Commun. 2 (2000) 207–210.
[52] H. Park, A. Bak, T.H. Jeon, S. Kim, W. Choi, Appl. Catal. B: Environ. 115–116 (2012) 74–80.
[53] A.K.L. Sajjad, S. Shamaila, B. Tian, F. Chen, J. Zhang, Appl. Catal. B: Environ. 91 (2009) 397–405.
[54] M.B. Johansson, G.A. Niklasson, L. Österlund, J. Mater. Res. 27 (2012) 3130–3140.

Structural dependent room-temperature ferromagnetism in yttrium doped HfO$_2$ nanoparticles

Z. D. Dohčević-Mitrović[a,*], N. Paunović[a], B. Matović[b], P. Osiceanu[c], R. Scurtu[c,d], S. Aškrabić[a], M. Radović[a]

[a]Institute of Physics, University of Belgrade, Pregrevica 118, 11080 Belgrade, Serbia
[b]Institute of Nuclear Sciences 'Vinča', University of Belgrade, 11000, Serbia
[c]Institute of physical chemistry, Romanian academy, Bucharest 060021, Romania
[d]National Institute for Research and Development in Microtechnologies, Bucharest 060021, Romania

Abstract

Y-doped HfO$_2$ nanopowders, produced by metathesis synthesis, exhibit ferromagnetism at room temperature. The X-ray diffraction and Raman measurements have shown that HfO$_2$ nanopowders undergo phase transformation from monoclinic to tetragonal and cubic phase with increasing of Y content. The X-ray photoelectron spectroscopy and Raman analysis gave evidence that Y-doped HfO$_2$ nanopowders are oxygen deficient. The ferromagnetic properties of Y-doped HfO$_2$ nanocrystals are dependent on crystal structure changes. The structural transformation from monoclinic to tetragonal phase with Y doping is followed by increased ferromagnetic ordering because of the increased concentration of oxygen vacancies (V$_O$) in different charge states. Higher Y content favors the formation of cubic phase and the ferromagnetism significantly weakens. In cubic hafnia phase, yttrium can form (V$_O$–Y$_{Hf}$) defect complexes in different charge states. The appearance of these complexes can be responsible for the degradation of ferromagnetic ordering.

1. Introduction

Hafnia (HfO$_2$) is very promising and technologically important material because of potential applications in spintronic devices, high-temperature fuel cells and has attracted much attention as high-*k* dielectric gate material to replace the SiO$_2$ in metal-oxide-semiconductor devices. HfO$_2$ has three polymorphs, i.e. monoclinic (M), tetragonal (T) and cubic (C) phase. Under ambient conditions the monoclinic phase of hafnia is stable phase and undergoes transition to tetragonal or cubic phase at high temperature [1]. These last two phases are far more important in technological applications than the low-temperature monoclinic phase. Stabilization of the tetragonal and cubic hafnia phases at room temperature can be achieved by doping with divalent or

trivalent cation dopants such as Mg^{2+} or Y^{3+} which brings additional oxygen vacancies in the lattice and stabilize one of two high-temperature phases of hafnia [2,3].

HfO$_2$ is an insulating oxide and is expected to be nonmagnetic because Hf^{4+} and O^{2-} are not magnetic ions with full or empty f and d shells of Hf^{4+} ion. The discovery of unexpected room-temperature ferromagnetism (RTFM) in undoped monoclinic HfO$_2$ thin films [4] has opened a path to a new class of ferromagnetic materials which can play important role in new generation of spintronic devices. The magnetic ordering was up to now presumably investigated in monoclinic hafnia thin films and possible mechanism for the observed magnetism is still controversial. Different types of defects like oxygen (V$_O$) or hafnia vacancies (V$_{Hf}$) were claimed responsible for the FM in hafnia. The FM ordering in M-phase of HfO$_2$, proposed by Coey and coworkers [5], can arise from unpaired electrons in bonding molecular orbitals formed by hybridization of hafnium orbitals

*Corresponding author. Tel.: +381 11 3713024; fax: +381 11 3162190.
E-mail address: zordoh@ipb.ac.rs (Z.D. Dohčević-Mitrović).

surrounding a neutral three-coordinated oxygen vacancy. Direct exchange between defect-related molecular orbitals will be ferromagnetic and may be strong if defects are situated in the interface layer [5]. Recent calculations of Glinchuk et al. [6], based on the direct variational method, showed that neutral oxygen vacancies in the vicinity of the film–substrate interface can become magnetic and mediate long range FM order in HfO_2 thin films. Furthermore, theoretical calculations of Muñoz Ramo et al. [7], based on DFT periodic and embedded cluster methods, showed that in monoclinic HfO_2 four-coordinated oxygen vacancies can exist in five different charge states (V^{2+}, V^+, V^0, V^-, and V^{2-}). These defects form localized levels in the hafnia band gap. Some of these states have different electron occupancies and bear different magnetic moments [7]. Contrary to these findings, the first principle calculations [8,9] showed that hafnium vacancies, as cation vacancies, can be responsible for the ferromagnetism in monoclinic HfO_2. The removal of neutral Hf atoms introduces holes in the valence band formed of oxygen 2p levels. This leads to the splitting of the valence band and formation of high-spin defect states, causing the FM order for short V_{Hf}–V_{Hf} distances. On the other hand, the first-principles calculations of Zheng at al. [10], performed on undoped monoclinic HfO_2, showed that there are no stable defects that can carry a magnetic moment and confirmed that it is unlikely that hafnia vacancies are formed since their formation energy is high. From the above cited reports, it can be summarized that the appearance of ferromagnetism in hafnium oxide and its origin, still remains a matter of debate and deserves further investigation.

In the present work, we report room temperature ferromagnetism in Y-doped HfO_2 nanopowders. The ferromagnetic ordering is dependent on the crystal structure changes induced by Y. To the best of our knowledge, magnetic properties of hafnia nanopowders doped with yttrium have not been studied yet. HfO_2-based oxides, as high-k metal-oxide dielectrics, are already under consideration to replace silicon dioxide as gate dielectric for next generation of complementary metal-oxide semiconductors. The combination of ferromagnetic response at room temperature and above with dielectric properties of HfO_2-based oxides should enable the integration of metal-oxide semiconductors with spintronics technology. Therefore, Y-doped HfO_2 can be a promising candidate for the applications in spintronics.

2. Experiment

A highly pure, nanosized yttrium doped HfO_2 powders ($Hf_{1-x}Y_xO_{2-\delta}$, $0.05 \leq x \leq 0.2$) are obtained by metathesis synthesis described in detail elsewhere [11]. Starting chemicals were hafnium chloride ($HfCl_4$), yttrium nitrate hexahydrate ($Y(NO_3)_3 \cdot 6H_2O$) and sodium hydroxide (NaOH) from Alfa Aesar GmbH, Germany. The purity of starting chemicals was 99.9% without any magnetic ion impurity presence (such as Fe, Co etc.). The samples were always handled with Teflon tweezers to avoid any metal contamination. The compositions of the starting reacting mixtures were calculated according to the nominal composition of the final reaction product. Yttrium doped hafnia solid solutions were prepared varying weight fraction of yttrium (Y) in the range 5–20 mol%. All samples

were annealed at 600 °C for 5 min in order to obtain better crystallinity. The obtained $Hf_{1-x}Y_xO_{2-\delta}$ nanopowders were characterized using different methods.

The X-ray diffraction (XRD) spectra of the samples have been measured on a Simens X-ray Diffractometer (Kristaloflex 500) with Ni filtered CuKα radiation. The room temperature measurements were performed in the 2θ range from $20°$ to $80°$ in a continuous scan mode with a step width of $0.02°$ and at a 2θ scanning rate of 1°/min.

Non-contact atomic force microscopy (NC-AFM) measurements were carried out using Omicron B002645 SPM probe VT AFM 25. NC-AFM images were obtained in the constant frequency shift mode (-20 Hz) and with constant vibrating amplitude (0.2 V).

Micro-Raman scattering measurements were performed at room temperature using a Jobin-Yvon T64000 triple spectrometer system and Ar^+/Kr^+ mixed laser line of 488 nm as an excitation source. The incident laser power was kept low (less than 10 mW) in order to prevent heating effects.

X-ray photoelectron spectroscopy (XPS) was used for the oxidation state and atomic ratio analysis. XPS was carried out on a PHI Quantera equipment with a base pressure in the analysis chamber of 10^{-9} Torr. The X-ray source was monochromatized AlKα radiation (1486.6 eV). The spectra were calibrated using the C 1s line (284.8 eV) of the adsorbed hydrocarbon on the sample surface.

The magnetic properties of the $Hf_{1-x}Y_xO_{2-\delta}$ samples were performed on a vibrating sample magnetometer in a high field measuring system (HFMS, Cryogenic Ltd).

3. Results and discussion

X-ray diffraction spectra of pure and Y-doped HfO_2 samples are presented in Fig. 1a. The XRD spectra of pure HfO_2 and $Hf_{1-x}Y_xO_{2-\delta}$ samples up to 10% of Y, show the monoclinic and tetragonal phase coexistence. With further increasing Y content, in 15% and 20% Y-doped samples the cubic phase appears. The main reflections of the monoclinic, tetragonal and cubic phases are marked with M, T and C in Fig. 1a. All diffraction peaks for the M, T and C phases in pure and Y-doped HfO_2 samples are indexed with the P2$_1$/c, P4$_2$/nmc and Fm3m space group, respectively. The lattice parameters of the monoclinic, tetragonal and cubic phases are given in Table 1.

The volume fractions of different hafnia polymorphs in undoped and Y-doped HfO_2 samples were estimated from the integrated intensities of the M (-111), M (111) and T (111) diffraction peaks following the procedure proposed by Toraya et al. [12]. The estimated volume fractions for HfO_2 and Y-doped samples (given in %) are presented in Table 1.

As can be seen from Fig. 1a and Table 1, the monoclinic phase prevails over the tetragonal phase in pure HfO_2 sample. The XRD peaks are broadened which is characteristic of small (about 5 nm), oxygen deficient nanocrystals [11]. The XRD patterns of the Y-doped HfO_2 samples (labeled as HfY5-HfY20 according to the mol% of yttrium in doped samples) indicate the formation of solid solutions in the entire dopant compositional range without a presence of yttrium oxide or hydroxide phases. The yttrium substitution of Hf (Y_{Hf}) introduces oxygen vacancies in hafnia lattice and induces crystal structure changes of the HfO_2 nanopowders. The
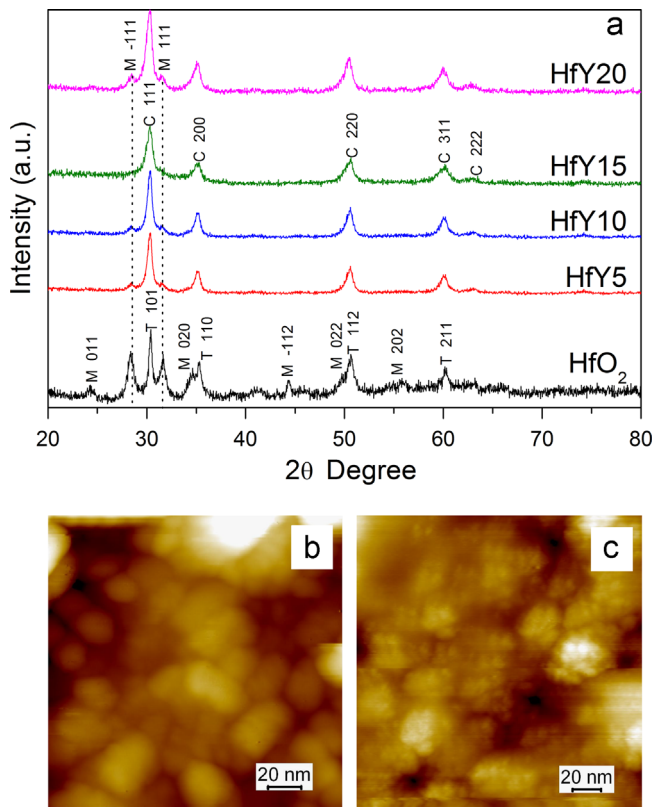
Fig. 1. (a) XRD patterns of Y-doped HfO$_2$ nanopowders at room temperature. The pure HfO$_2$ sample is given as a reference. The symbols stand for: M-monoclinic, T-tetragonal and C-cubic phase. The corresponding AFM images of (b) HfY10 and (c) HfY15 samples are presented.

Table 1
Composition and cell parameters of HfY samples obtained from XRD measurements.

Sample	Monoclinic P2$_1$/c				Tetragonal P4$_2$/nmc			Cubic Fm3m	
	(%)	a	b	c	(%)	a	c	(%)	a
HfY0	58	5.1453	5.1788	5.2919	42	3.5994	5.1191	–	–
HfY5	21	5.1418	5.1613	5.2928	79	3.6103	5.0980	–	–
HfY10	14	5.1265	5.1416	5.2830	86	3.6009	5.1835	–	–
HfY15	3	5.1169	5.1686	5.2967	46	3.6086	5.1800	51	5.1003
HfY20	16	5.1250	5.1797	5.2945	58	3.5737	5.1462	26	5.1166

structural transformation from monoclinic to tetragonal and cubic phase is a consequence of combined effect of doping with a lower valence state dopant and oxygen deficiency [2,3,11]. In the HfY5 sample the intensity of monoclinic reflections decreases implying that the content of monoclinic phase decreases on account of the tetragonal phase. This trend is even more pronounced for the HfY10 sample. In a case of the HfY15 sample, the XRD peaks which belong to M-phase are not visible anymore. The position of main diffraction peaks at 30.35°, 35.20°, 50.63° and 60.17° indicate that the cubic phase is formed [13] as dominant phase in this sample (see Table 1).

The tetragonal-cubic phase transformation is difficult to follow by an XRD method because of very low sensitivity of this method to the structural changes induced by oxygen displacement and

nonstoichiometry. However, disappearance of M-phase, position of diffraction peaks and their significant broadening in a case of the HfY15 sample indicate the tetragonal-cubic phase transformation, as suggested by Fujimori and coauthors [14]. For the HfY20 sample, the content of T and M phases increases on the account of the cubic phase. This fact was somehow surprising because the cubic phase in HfO$_2$ is stabilized around 18 mol% of yttrium [15] or even less [16].

The morphology of the Y-doped nanopowders was analyzed by an AFM method. The AFM images of HfY10 and HfY15 samples, given in Fig. 1b and c, showed that the Hf$_{1-x}$Y$_x$O$_{2-\delta}$ nanopowders are composed of very small and agglomerated particles.

Raman scattering is much more sensitive method than the XRD to the structural changes induced by oxygen displacement and is powerful tool to investigate the tetragonal-cubic phase transformation in Y-doped HfO$_2$. The Raman spectra of Hf$_{1-x}$Y$_x$O$_{2-\delta}$ samples are shown in Fig. 2.

All Raman modes in HfY5 sample can be assigned to the monoclinic phase [17] except the mode at 500 cm^{-1} (marked as M/T1 in Fig. 2), which is also characteristic for the tetragonal phase [14]. The Raman modes are broadened because of the increased oxygen vacancy concentration when hafnia is doped with trivalent ions like Y [15]. With further increase of the Y content in the HfY10 sample, the Raman modes become broader implying that oxygen vacancy concentration further increases. New modes (marked as T2 and T3 in Fig. 2) appear and can be ascribed to the tetragonal phase [18]. The Raman mode denoted with asterisk (*) at ~190 cm^{-1} can originate from a small amount of γ-phase of HfO$_2$. The γ-phase can be identified only by Raman scattering [15]. In the HfY15 sample, the intensity of the Raman peaks which belong to the monoclinic and tetragonal phase decreases and the Raman modes became smeared out. Intensity drop of the mode at ~500 cm^{-1} reflects the tetragonal-cubic phase transition [14]. The F$_{2g}$ mode of C-phase is not seen, because it is usually of very low intensity [17]. In the Raman spectrum of the HfY20 sample, the modes of T-phase became
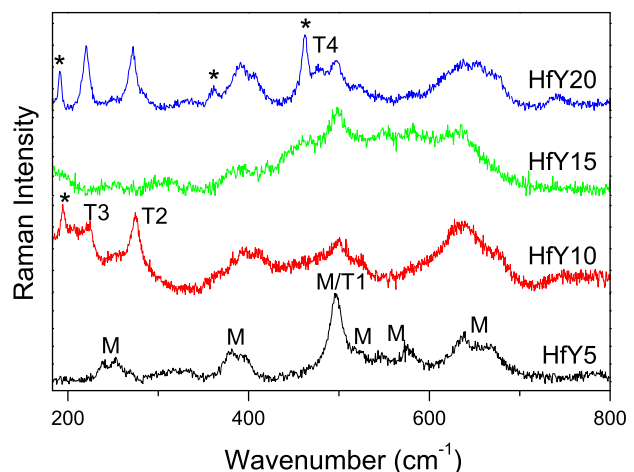

Fig. 2. Raman spectra of Hf$_{1-x}$Y$_x$O$_{2-\delta}$ ($0.05 \leq x \leq 0.2$) samples. The bands of monoclinic and tetragonal phases are designated by M, T1, T2, T3 and T4. Additional modes which can originate from γ-HfO$_2$ and cubic Y$_2$O$_3$ phases are denoted by asterisk (*).

more intensive than the modes of M-phase implying that the T-phase is dominant phase in this sample. This is in accordance with the XRD results. Additional modes at $360 \ cm^{-1}$ and $460 \ cm^{-1}$ can be ascribed to the cubic-Y_2O_3 phase probably formed at the nanoparticle surface [19].

The chemical state and composition of the $Hf_{1-x}Y_xO_{2-\delta}$ nanopowders were studied by XPS analyses. The XPS spectra of Hf 4f, O 1s and Y 3d region for Y-doped samples are given in Fig. 3a–c.

The deconvolution of the Hf 4f, O 1s and Y 3d spectra is performed for Y-doped samples using mixed Gaussian and Lorentzian functions. In Fig. 4a–c are presented deconvoluted XPS spectra of Hf 4f, Y 3d and O 1s region in a case of HfY5 sample for brevity.

The same procedure is applied for the rest of the samples and the binding energies (BE) of the most prominent XPS transitions
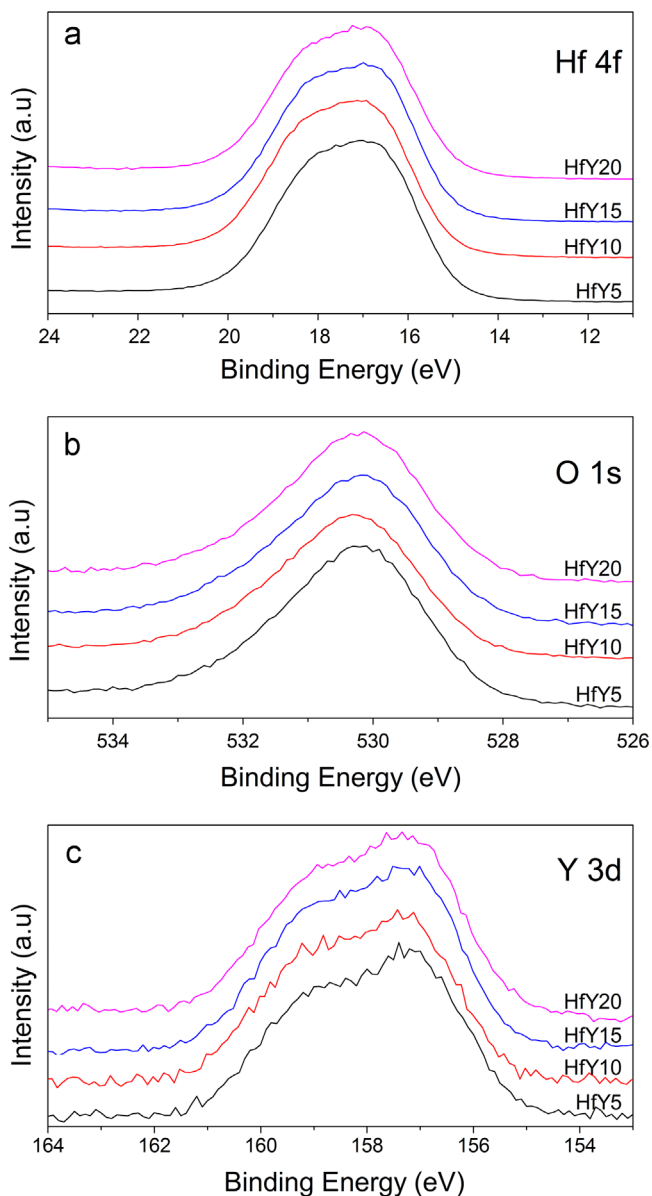
Fig. 3. The XPS spectra of (a) Hf 4f, (b) O 1s and (c) Y 3d region for Y-doped HfO₂ nanopowders.
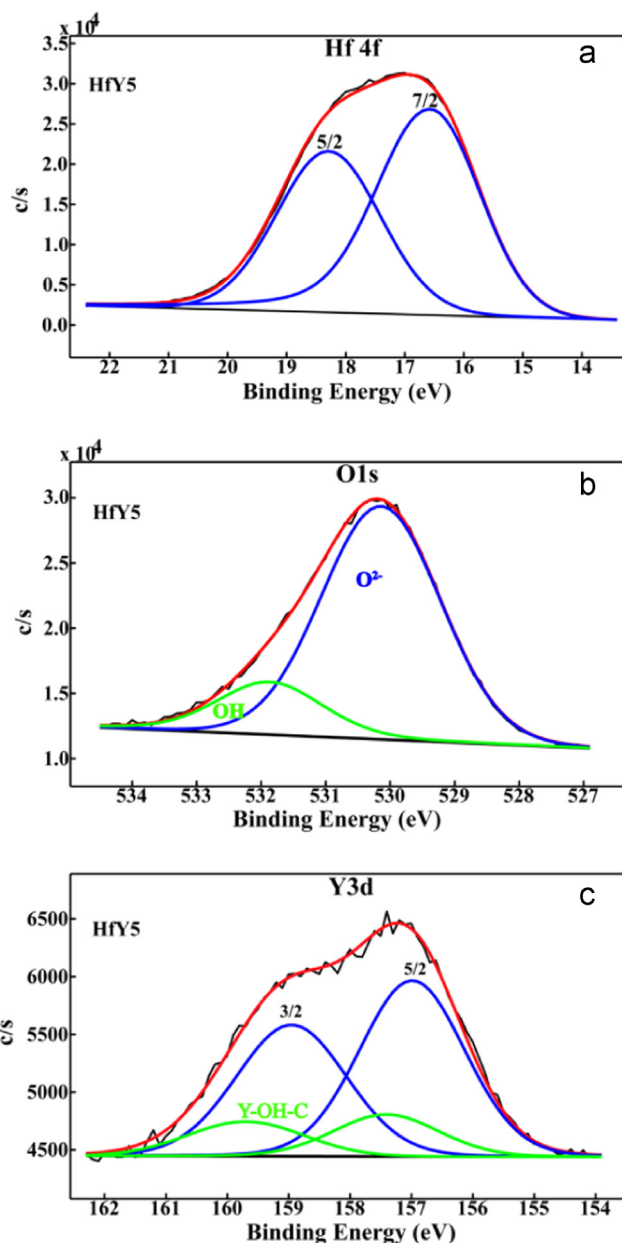
Fig. 4. Deconvoluted XPS spectra of (a) Hf 4f, (b) O 1s and (c) Y 3d region for HfY5 sample.

(Hf 4f, Y 3d, O 1s and C 1s) for $Hf_{1-x}Y_xO_{2-\delta}$ nanopowders are summarized in Table 2. No other contamination except carbon was detected in all investigated samples. XPS analysis of H 4f and O 1s gave evidence that the $Hf_{1-x}Y_xO_{2-\delta}$ samples are nonstoichiometric. From the O/Hf ratio, given in Table 2, it can be seen that the oxygen-deficiency increases with increasing Y content, with the exception of the HfY20 sample. This fact can be explained by the formation of the cubic-Y_2O_3 phase, already seen in the Raman spectrum of this sample.

The cations relative concentration for $Hf_{1-x}Y_xO_{2-\delta}$ samples, presented in Table 3, confirmed very good agreement between the surface and the nominal (bulk) stoichiometry. The errors regarding the quantitative data are found in the range of $\pm 10\%$, whereas the accuracy for BEs assignments is ± 0.2 eV.

Table 2
XPS binding energies (eV) of the individual peaks and composition of the HfY samples.

Sample	C 1s	O 1s		Hf 4f		Y 3d		Y–OH–C		Stoichiometry
		O^{2-}	OH	7/2	5/2	5/2	3/2			O/Hf
HfY5	284.8	530.1	531.8	16.6	18.3	156.9	159.0	157.4	159.6	1.9
HfY10	284.8	530.2	531.9	16.7	18.4	157.0	159.1	157.5	159.8	1.8
HfY15	284.8	530.1	531.9	16.6	18.3	157.0	158.9	157.5	159.8	1.83
HfY20	284.8	530.1	531.8	16.7	18.4	157.0	159.1	157.4	159.7	1.95

Table 3
Composition of HfY samples.

Sample	Y3d at%	Hf4f at%
HfY5	4.9	95.1
HfY10	9.3	90.7
HfY15	14.6	85.4
HfY20	19.1	80.9

The Hf 4f spectrum from Fig. 4a is composed of two spin-orbit doublet peaks (Hf $4f_{5/2}$ and Hf $4f_{7/2}$) which originate from the Hf bound to the oxygen. The Hf $4f_{7/2}$ peak is situated at 16.6 eV with a difference of 1.7 eV in binding energy between doublets. This peak is shifted to higher binding energies compared to the HfO$_2$ standard powdered sample (16.2 eV) [20] in all Y-doped samples (see Table 2). The higher binding energies of Hf $4f_{7/2}$ peak in Y-doped samples suggest that these nanopowders are deficient in oxygen and are non-stoichiometric [21,22]. The primary peak at 530.1 eV in the O 1s spectrum of Y-doped samples (see Fig. 4b and Table 2) is also shifted towards higher BE. This peak is ascribed to the oxygen bonded into the lattice and exhibits the shift probably because of the oxygen deficiency in the samples. Another subpeak in the O 1s spectrum at 531.8 eV (see Table 2) is assigned to adsorbed OH groups in the outermost surface layer [23,24]. The deconvoluted XPS spectrum of the Y 3d doublet ($3d_{5/2}$ and $3d_{3/2}$) is presented in Fig. 4c for the HfY5 sample. The average positions of the Y $3d_{5/2}$ peaks in Hf$_{1-x}$Y$_x$O$_{2-\delta}$ samples are given in Table 2 and are located around 157 eV. These peaks are slightly shifted to higher energy compared to the position of $3d_{5/2}$ peak in Y$_2$O$_3$ standard sample (156.5 eV) [20]. The shift to higher BE is expected if we have the formation of the Hf–Y–O bonds [16]. The fitting of the Y 3d spectra of doped samples requires additional doublet (binding energies are given in Table 2). The second doublet can be attributed to Y–OH–C bonds confined to the surface as a result of the OH and hydrocarbon adsorption from the atmosphere.

In summary, XPS and Raman analysis of the Hf$_{1-x}$Y$_x$O$_{2-\delta}$ samples confirmed that yttrium doping increases the concentration of oxygen vacancies, whereas XRD and Raman results showed that the incorporation of yttrium induces structural phase transformation. These findings are in agreement with Manory et al. [13] who reported that tetragonal and cubic phase of HfO$_2$ are stable at room temperature in nonstoichiometric HfO$_2$. In Fig. 5 we gave an illustration of the phase transformation in HfO$_2$ with Y doping. In Fig. 5a is presented the monoclinic phase of nonstoichiometric

undoped HfO$_2$ with three- and four-coordinated oxygen vacancies. Yttrium as a dopant ion in 3^+ valence state brings additional vacancies in the hafnia lattice in order to keep the charge neutrality (Fig. 5b). With further addition of Y, the concentration of the oxygen vacancies should be increased and the monoclinic phase of HfO$_2$ transforms first into the tetragonal and then into the cubic phase as presented in Fig. 5c and d.

The room temperature magnetization versus magnetic field (M–H) data for pure HfO$_2$ and Y-doped samples is shown in Fig. 6a. It can be seen that all samples show a ferromagnetic signal at room temperature superimposed onto a diamagnetic background. The observed ferromagnetism is characteristic for the nanostructured nature of the investigated samples [25] and is intrinsic as there are no magnetic impurities present in the samples (see experimental part). The susceptibility of the diamagnetic component, i.e. the slope of the high-field parts of the curve, remains constant with yttrium doping because of the closed Y^{3+} shells. After subtracting the diamagnetic component, the corrected magnetization curves are shown in Fig. 6b. The magnetization curves are almost anhysteretic, as it is often the case for ferromagnetic oxides [26]. The saturation magnetization value (M_S) for the undoped sample is about 2.2×10^{-3} emu g^{-1}. The obtained value is comparable with the other reports on ferromagnetism in undoped oxide nanocrystals [25–29], but higher than the reported value on HfO$_2$ powders [5]. The value of M_S increases for the HfY5 sample and reaches its maximum of 2.9×10^{-3} emu g^{-1} for the HfY10 sample. The saturation magnetization significantly drops off in the HfY15 and HfY20 samples to the values of 1.2×10^{-3} emu g^{-1} and 0.7×10^{-3} emu g^{-1} respectively. The change of the M_S for pure HfO$_2$ and Hf$_{1-x}$Y$_x$O$_{2-\delta}$ samples is presented in Fig. 6c.

The experimental reports [30–33] confirmed the existence of RTFM in pure and doped hafnia films and clearly proved that the RTFM originates from the presence of oxygen vacancies. The lack of oxygen vacancies or filling up vacancies can degrade or even completely destroy the FM ordering. Scarce literature data concerning the appearance of the FM in other hafnia nanostructures like nanopowders or nanorods [33–35] have also pointed out that the oxygen vacancies play a major role in the magnetic exchange mechanism. The appearance of RTFM in pure HfO$_2$ can be interpreted in the framework of the impurity band exchange model proposed by Venkatesan et al. [4]. According to this model, the intrinsic oxygen vacancies act as a donor of electrons, leading to the n-type doping of the hafnia. The electrons trapped in oxygen vacancies in HfO$_2$ form extended hydrogen-like orbitals because of the relatively high dielectric constant of hafnia. When the defect
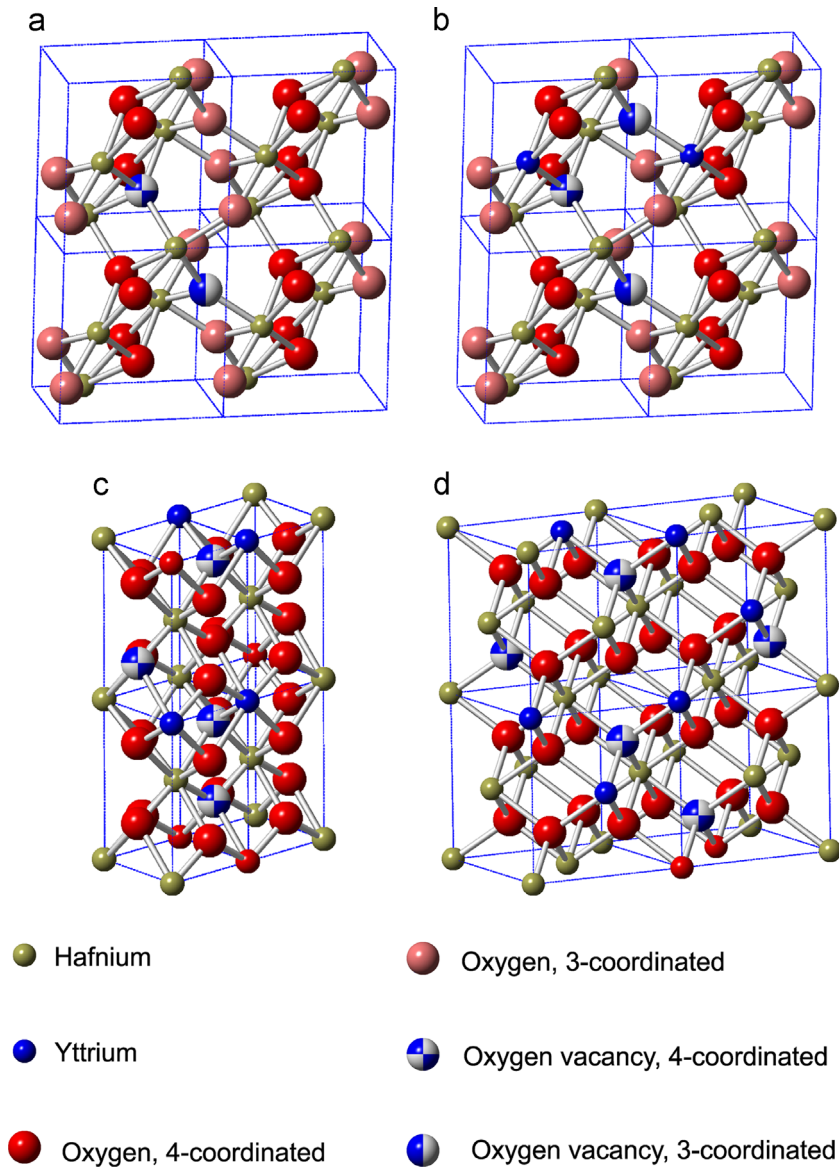
Fig. 5. Structural phase transformation with Y doping (a) pure HfO$_2$ monoclinic phase, (b) monoclinic phase of HfO$_2$ doped with Y, (c) tetragonal phase and (d) cubic phase of HfO$_2$ with increased Y content.

concentration increases, the overlapping of the defect-related orbitals can form an impurity (defect) band. The mixing of the defect band with empty 5d states of hafnia enables the transfer of some of the electrons to the 5d band. The 5d electrons will in turn polarize the defect band establishing the ferromagnetic coupling [4]. The oxygen vacancies in monoclinic hafnia can be in different charge states having different number of trapped electrons and bearing different magnetic moment [7,36]. Some of these defects like negatively (V_O^-) or positively (V_O^+) charged vacancies form levels near the conduction band, as shown in the paper of Xiong et al. [36]. They calculated the energy levels of the oxygen vacancy defects in different charge states for HfO$_2$ and showed that the energy levels of the V_O^- and V_O^+ defects lie very near to the conduction band (approximately at 0.8 and 1.1 eV below the conduction band edge). Consequently, it is reasonable to assume that the defect band, formed from V_O^- and V_O^+ states, will lie near

the conduction band. The fraction of the electrons from defect band can be transferred to the 5d states causing the spin splitting of the defect band. The formation of the spin-split defect band provides necessary condition for the appearance of ferromagnetism [4]. In Fig. 7a is given the schematic representation of the defect levels induced by oxygen vacancies in different charge states according to the calculations performed in Ref. [34]. The mixing of the defect band with the 5d states of hafnia and its spin-splitting is presented in Fig. 7b.

Having in mind theoretical calculations [7,36] and experimental observations [30–33] and knowing from the Raman and XPS results that Hf$_{1-x}$Y$_x$O$_{2-\delta}$ nanopowders are oxygen deficient, we concluded that the oxygen vacancies can be attributed to be the main source of ferromagnetism in undoped and Y-doped HfO$_2$ nanopowders. In the HfY5 sample, with Y doping the concentration of oxygen vacancies should increase (see Fig. 5b) in order to

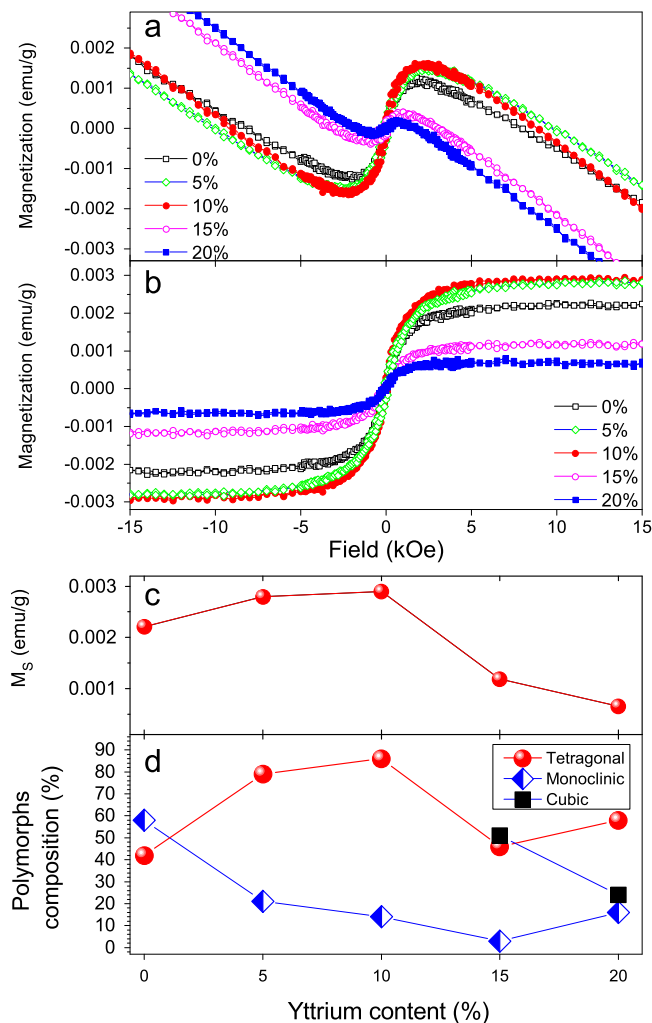Fig. 6. Magnetic properties of $Hf_{1-x}Y_xO_{2-\delta}$ samples. (a) Raw magnetization curves versus magnetic field, $M(H)$, (b) $M(H)$ after subtraction of the linear diamagnetic component, (c) Saturation magnetization (M_S) change and (d) relative polymorph composition change with yttrium content.
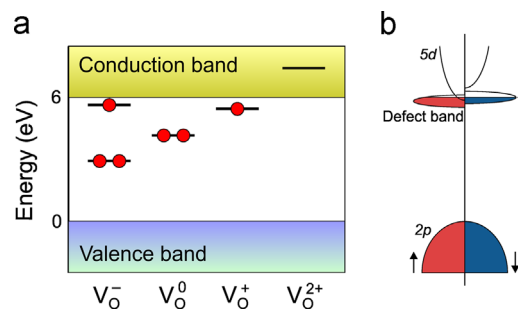

Fig. 7. Schematic representation of the (a) defect levels which originate from point defects and (b) a spin-split defect band.

Y content, oxygen vacancies form complex defects with yttrium (V_O–Y_{Hf}) in different charge states ((V_O–Y_{Hf})$^+$, (V_O–Y_{Hf})$^{++}$ and (V_O–Y_{Hf})^0 complexes). Among these complexes, the single positively charged complexes (V_O–Y_{Hf})$^+$ are the most stable ones. Y as dopant changes the charge state of oxygen vacancies and lowers the highest occupied levels induced by V_O^+ and V_O^{++} vacancies into the valence band. Therefore, the highest occupied levels of (V_O–Y_{Hf})$^+$ and (V_O–Y_{Hf})$^{++}$ complex defects will lie in the vicinity of the valence band. With further increasing of Y content the highest occupied levels of (V_O–Y_{Hf})^0 complexes would also fall into the valence band [37]. Considering the results from Ref. [37], it is reasonable to assume that in HfY15 and HfY20 samples, because of the increased Y content and the presence of cubic phase, certain number of (V_O–Y_{Hf}) defect complexes can be formed. The appearance of (V_O–Y_{Hf}) defect complexes will degrade the ferromagnetic interaction because the defect band formed from (V_O–Y_{Hf}) complex defects states will lie near to the valence band. The mechanism of electron transfer from defect band to 5d empty states which leads to its polarization and establishing of ferromagnetic interaction is not applicable anymore. The formation of cubic-Y_2O_3 phase at nanoparticle surface, seen in the Raman spectrum of HfY20 sample can explain further degradation of ferromagnetism in this sample.

4. Conclusions

In summary, nonstoichiometric $Hf_{1-x}Y_xO_{2-\delta}$ nanosized powders ($0 \le x \le 0.2$) are obtained by metathesis synthesis. The transformation of crystal structure from monoclinic to tetragonal and cubic phase (M→T→C) with increased Y doping was confirmed by XRD and Raman measurements. The XPS and Raman studies testified that the $Hf_{1-x}Y_xO_{2-\delta}$ nanopowders are nonstoichiometric. All samples exhibit room temperature ferromagnetism which increases with increased tetragonal phase content and degrades with the appearance of cubic phase. The FM ordering in $Hf_{1-x}Y_xO_{2-\delta}$ samples can be explained in the framework of impurity band exchange model where oxygen vacancies in different charge state, as n-type dopants, play major role in establishing ferromagnetism. Further increasing of Y content stabilizes the cubic phase in 15% and 20% Y doped samples and the ferromagnetic interaction weakens. In a cubic phase certain number of oxygen vacancy-yttrium complexes (V_O–Y_{Hf}) can be formed. Those complexes form defect states inside the

keep electroneutrality. At the same time the content of tetragonal phase begins to prevail over the monoclinic one. The FM signal is stronger than that in undoped HfO_2. With increasing Y content up to 10%, the saturation magnetization and the strength of FM ordering further increase, when the content of the tetragonal phase in HfY10 sample becomes dominant (Fig. 5c). In the HfY15 sample the cubic phase appears and the strength of FM interaction weakens, reaching the lowest value of M_S (0.7×10^{-3} emu g^{-1}) for HfY20. This value of M_S is almost three times lower than for HfY10 sample. From the change of the polymorphs composition with increasing Y content presented in Fig. 6d, it can be seen that the change of M_S and T-phase content have similar trend. In a case of HfY20 sample, M_S continues to decrease despite the fact that the amount of T-phase is slightly increased.

The theoretical calculations performed by Chen et al. [37] can offer the explanation for the degradation of FM ordering in HfY15 and HfY20 samples. Namely, Chen et al. [37] calculated the formation energies of the oxygen vacancies in different charge states for Y-doped cubic HfO_2. It is found that with higher

bandgap of hafnia. The highest occupied defect states will lie in the vicinity of the valence band. The electron transfer from deep lying defect states to the 5d empty states of hafnia, which enables the establishing of ferromagnetic interaction is not realistic anymore. The presence of cubic-Y_2O_3 phase additionally degrades ferromagnetic ordering in the 20% Y doped sample.

Acknowledgments

References

[1] R. Ruh, V.A. Patel, Proposed phase relations in the HfO_2-rich portion of the system $Hf-HfO_2$, J. Am. Ceram. Soc. 56 (1973) 606–607.

[2] E. Rauwel, C. Dubourdieu, B. Hollander, N. Rochat, F. Ducroquet, M.D. Rossell, G. Van Tendeloo, B. Pelissier, Stabilization of the cubic phase of HfO_2 by Y addition in films grown by metal organic chemical vapor deposition, Appl. Phys. Lett. 89 (2006) 012902.

[3] L. Gao, L. Zhou, J. Feng, L. Bai, C. Li, Z. Liu, J.-L. Soubeyroux, Y. Lu, Stabilization of cubic structure in Mn-doped hafnia, Ceram. Int. 38 (2012) 2305–2311.

[4] M. Venkatesan, C.B. Fitzgerald, J.M.D. Coey, Thin films: unexpected magnetism in a dielectric oxide, Nature 430 (2004) 630.

[5] J.M.D. Coey, M. Venkatesan, P. Stamenov, C.B. Fitzgerald, L.S. Dorneles, Magnetism in hafnium dioxide, Phys. Rev. B 72 (2005) 024450.

[6] M.D. Glinchuk, E.A. Eliseev, V.V. Khist, A.N. Morozovska, Ferromagnetism induced by magnetic vacancies as a size effect in thin films of nonmagnetic oxides, Thin Solid Films 534 (2013) 685–692.

[7] D. Muñoz Ramo, J.L. Gavartin, A.L. Shluger, G. Bersuker, Spectroscopic properties of oxygen vacancies in monoclinic HfO_2 calculated with periodic and embedded cluster density functional theory, Phys. Rev. B 75 (2007) 205336.

[8] C. Das Pemmaraju, S. Sanvito, Ferromagnetism driven by intrinsic point defects in HfO_2, Phys. Rev. Lett. 94 (2005) 217205.

[9] J.I. Beltrán, M.C. Muñoz, J. Hafner, Structural, electronic and magnetic properties of the surfaces of tetragonal and cubic HfO_2, New J. Phys. 10 (2008) 063031.

[10] J.X. Zheng, G. Ceder, T. Maxisch, W.K. Chim, W.K. Choi, First-principles study of native point defects in hafnia and zirconia, Phys. Rev. B 75 (2007) 104112.

[11] B. Matović, D. Bučevac, M. Prekajski, V. Maksimović, D. Gautam, K. Yoshida, T. Yano, Synthesis and characterization of nanometric yttrium-doped hafnia solid solutions, J. Eur. Ceram. Soc. 32 (2012) 1971–1976.

[12] H. Toraya, M. Yoshimura, S. Somiya, Calibration curve for quantitative analysis of the monoclinic-tetragonal ZrO_2 system by X-ray diffraction, J. Am. Ceram. Soc. 67 (1984) C-119–C-121.

[13] R.R. Manory, T. Mori, I. Shimizu, S. Miyake, G. Kimmel, Growth and structure control of HfO_{2-x} films with cubic and tetragonal structures obtained by ion beam assisted deposition, J. Vac. Sci. Technol. A 20 (2002) 549–554.

[14] H. Fujimori, M. Yashima, S. Sasaki, M. Kakihana, T. Mori, M. Tanaka, M. Yoshimura, Cubic–tetragonal phase change of yttria-doped hafnia solid solution: high-resolution X-ray diffraction and Raman scattering, Chem. Phys. Lett. 346 (2001) 217–223.

[15] M. Yashima, H. Takahashi, K. Ohtake, T. Hirose, M. Kakihana, H. Arashi, Y. Ikuma, Y. Suzuki, M. Yoshimura, Formation of metastable forms by

[16] C. Dubourdieu, E. Rauwel, H. Roussel, F. Ducroquet, B. Hollander, M. Rossell, G. Van Tendeloo, S. Lhostis, S. Rushworth, Addition of yttrium into HfO_2 films: microstructure and electrical properties, J. Vac. Sci. Technol. A 27 (2009) 503–514.

[17] X. Zhao, D. Vanderbilt, First-principles study of structural, vibrational, and lattice dielectric properties of hafnium oxide, Phys. Rev. B 65 (2002) 233106.

[18] G.M. Rignanese, X. Gonze, G. Jun, K. Cho, A. Pasquarello, First-principles investigation of high-κ dielectrics: comparison between the silicates and oxides of hafnium and zirconium, Phys. Rev. B 69 (2004) 184301.

[19] A. Ubaldini, M.M. Carnasciali, Raman characterisation of powder of cubic RE_2O_3 ($RE=$Nd, Gd, Dy, Tm, and Lu), Sc_2O_3 and Y_2O_3, J. Alloy. Compd. 454 (2008) 374–378.

[20] J.F. Moulder, W.F. Stickle, P.E. Sobol, K.D. Bomben, Handbook of X-ray Photoelectron Spectroscopy, Perkin-Elmer Corp, Minnesota, 1992.

[21] N. Selvakumar, H.C. Barshilia, K.S. Rajam, A. Biswas, Structure, optical properties and thermal stability of pulsed sputter deposited high temperature HfO_x/Mo/HfO_2 solar selective absorbers, Sol. Energy Mater. Sol. Cells 94 (2010) 1412–1420.

[22] G. He, M. Liu, L.Q. Zhu, M. Chang, Q. Fang, L.D. Zhang, Effect of postdeposition annealing on the thermal stability and structural characteristics of sputtered HfO_2 films on Si(1 0 0), Surf. Sci. 576 (2005) 67–75.

[23] X. Qiu, J.Y. Howe, H.M. Meyer Iii, E. Tuncer, M.P. Paranthaman, Thermal stability of HfO_2 nanotube arrays, Appl. Surf. Sci. 257 (2011) 4075–4081.

[24] J.C. Hackley, T. Gougousi, Properties of atomic layer deposited HfO_2 thin films, Thin Solid Films 517 (2009) 6576–6583.

[25] A. Sundaresan, C.N.R. Rao, Ferromagnetism as a universal feature of inorganic nanoparticles, Nano Today 4 (2009) 96–106.

[26] J.M.D. Coey, Dilute magnetic oxides, Curr. Opin. Solid State. Mater. Sci. 10 (2006) 83–92.

[27] M.Y. Ge, H. Wang, E.Z. Liu, J.F. Liu, J.Z. Jiang, Y.K. Li, Z.A. Xu, H.Y. Li, On the origin of ferromagnetism in CeO_2 nanocubes, Appl. Phys. Lett. 93 (2008) 062505.

[28] Z.D. Dohčević-Mitrović, N. Paunović, M. Radović, Z.V. Popović, B. Matović, B. Cekić, V. Ivanovski, Valence state dependent room-temperature ferromagnetism in Fe-doped ceria nanocrystals, Appl. Phys. Lett. 96 (2010) 203104.

[29] N. Paunović, Z. Dohčević-Mitrović, R. Scurtu, S. Aškrabić, M. Prekajski, B. Matović, Z.V. Popović, Suppression of inherent ferromagnetism in Pr-doped CeO_2 nanocrystals, Nanoscale 4 (2012) 5469–5476.

[30] Y.H. Chang, Y.L. Soo, W.C. Lee, M.L. Huang, Y.J. Lee, S.C. Weng, W.H. Sun, M. Hong, J. Kwo, S.F. Lee, J.M. Ablett, C.C. Kao, Observation of room temperature ferromagnetic behavior in cluster-free, Co doped HfO_2 films, Appl. Phys. Lett. 91 (2007) 082504.

[31] K.K. Bharathi, S. Venkatesh, G. Prathiba, N.H. Kumar, C.V. Ramana, Room temperature ferromagnetism in HfO_2 films, J. Appl. Phys. 109 (2011) 07C318.

[32] N.H. Hong, J. Sakai, N. Poirot, V. Brizé, Room-temperature ferromagnetism observed in undoped semiconducting and insulating oxide thin films, Phys. Rev. B 73 (2006) 132404.

[33] X. Liu, Y. Chen, L. Wang, D.-L. Peng, Transition from paramagnetism to ferromagnetism in HfO_2 nanorods, J. Appl. Phys. 113 (2013) 076102.

[34] M.K. Sharma, D.K. Mishra, S. Ghosh, D. Kanjilal, P. Srivastava, R. Chatterjee, Oxygen vacancy mediated large magnetization in chemically synthesized Ni-doped HfO_2 nanoparticle powder samples, J. Appl. Phys. 110 (2011) 063902.

[35] E. Tirosh, G. Markovich, Control of defects and magnetic properties in colloidal HfO_2 nanorods, Adv. Mater. 19 (2007) 2608–2612.

[36] K. Xiong, J. Robertson, M.C. Gibson, S.J. Clark, Defect energy levels in HfO_2 high-dielectric-constant gate oxide, Appl. Phys. Lett. 87 (2005) 183505.

[37] G.H. Chen, Z.F. Hou, X.G. Gong, Q. Li, Effects of Y doping on the structural stability and defect properties of cubic HfO_2, J. Appl. Phys. 104 (2008) 074101.

RESEARCH PAPER

Far-infrared spectroscopic study of CeO$_2$ nanocrystals

Z. V. Popović · M. Grujić-Brojčin · N. Paunović ·
M. M. Radonjić · V. D. Araújo · M. I. B. Bernardi ·
M. M. de Lima · A. Cantarero

Abstract We present the far-infrared reflectivity spectra of 5 nm-sized pure and copper-doped Ce$_{1-x}$Cu$_x$O$_{2-y}$ ($x = 0$; 0.01 and 0.10) nanocrystals measured at room temperature in the 50–650 cm^{-1} spectral range. Reflectivity spectra were analyzed using the factorized form of the dielectric function, which includes the phonon and the free carriers contribution. Four oscillators with TO energies of approximately 135, 280, 370, and 490 cm^{-1} were included in the fitting procedure. These oscillators represent local maxima of the CeO$_2$ phonon density of states, which is also calculated using the density functional theory. The lowest energy oscillator represents TA(L)/TA(X) phonon states, which become infrared-active E_u modes at the L and X points of the Brillouin zone (BZ). The second oscillator originates from TO(Γ) phonon states. The oscillator at ~ 400 cm^{-1} originates from Raman mode phonon states, which at the L point of BZ also becomes infrared-active E_u mode. The last oscillator describes phonons with dominantly LO(Γ) infrared mode character. The appearance of phonon density of states related oscillators, instead of single F_{2u} infrared-active mode in the far-infrared reflectivity spectra, is a consequence of the nanosized dimension of the CeO$_2$ particles. The best fit spectra are obtained using the generalized Bruggeman model for inhomogeneous media, which takes into account the nanocrystal volume fraction and the pore shape.

Keywords Nano ceria · Far-infrared spectroscopy · Phonon density of states · Bruggeman model · Nanoparticle characterization

Z. V. Popović (✉) · M. Grujić-Brojčin · N. Paunović
Center for Solid State Physics and New Materials,
Institute of Physics, University of Belgrade, Pregrevica
118, 11080 Belgrade, Serbia
e-mail: zoran.popovic@ipb.ac.rs

M. M. Radonjić
Scientific Computing Laboratory, Institute of Physics
Belgrade, University of Belgrade, Pregrevica 118,
11080 Belgrade, Serbia

V. D. Araújo · M. I. B. Bernardi
Instituto de Fisica, Universidade de São Paulo-USP,
São Carlos, SP 13560-970, Brazil

M. M. de Lima · A. Cantarero
Instituto de Ciencia de Los Materiales, Universidad de
Valencia, 46071 Valencia, Spain

Introduction

There are plenty of nanoscopic, microscopic, and other techniques that are used to study nanosized materials and structures (Popović et al. 2011). Among them, the most frequently used spectroscopic techniques are vibrational (phonon) spectroscopy techniques, such as Raman (R) and infrared (IR). The use of these techniques for nanostructure characterization is discussed in Popović et al. (2011), Grujić-Brojčin et al. (2005), and Cantarero (2013).

Ultrafine ceria powders represent an important material for solid oxide fuel cells or catalytic applications, which are attributed to CeO_2 remarkable oxygen-storage capability, i.e., the ability to undergo rapid redox cycles by releasing and storing oxygen (Popović et al. 2012).

In a nanocrystal, the phonons are confined in space, and all the phonons over the entire Brillouin zone (BZ) will contribute to the first-order vibrational spectra. The weight of the off-center phonons increases as the crystal size decreases, and the phonon dispersion causes a mode shape change and the frequency shift. The influence of all these effects on the CeO_2 Raman mode intensity, line shape, and energy were discussed in Popović et al. (2011) and Cantarero (2013).

Infrared spectroscopy is widely used in the 400–4,000 cm^{-1} spectral range to characterize unwished residuals during the synthesis of CeO_2 nanopowders (Orel 1999). To the best of our knowledge there are no study regarding infrared-active lattice vibrations in ceria nanocrystals. In this paper, we have measured room-temperature far-infrared reflectivity spectra of the pure and copper-doped $Ce_{1-x}Cu_xO_{2-y}$ ($x = 0$, 0.01 and 0.10) nanocrystals in the 50–650 cm^{-1} spectral range. In order to assign the obtained features we performed lattice dynamics calculation of CeO_2. Reflectivity spectra were analyzed using the factorized form of the dielectric function, which includes several oscillators and the free carriers contribution to the dielectric function. The oscillators represent the phonon density of states (PDOS)-related IR active modes. The best fit spectra are obtained using the generalized Bruggeman model for inhomogeneous media, which takes into account the volume fraction of nanopowder and the pore shape.

Experiment and numerical method

Ceria samples were prepared in one step by the polymeric precursor method (Araújo et al. 2013). The sizes of nanocrystals obtained by Raman scattering technique are about 5 nm. Specific surface area of the samples (BET-method) were estimated from the N_2-adsorption/desorption isotherms, at liquid nitrogen temperature, using a Micromeritics ASAP 2000 analyzer. The infrared reflectivity measurements were carried out at room temperature with a BOMEM DA-8

Fourier-transform IR spectrometer. A deuterated triglycine sulfate (DTGS) pyroelectric detector was used to cover the wave number region from 50 to 650 cm^{-1}. Spectra were collected with 2 cm^{-1} resolution, with 1,000 interferometer scans added for each spectrum.

In order to interpret the experimental data, we have performed density functional theory calculations implemented within the QUANTUM ESPRESSO package (Giannozzi et al. 2009). We have used the ultrasoft pseudopotentials with PBE exchange–correlation functional with $4f^1$, $5s^2$, $5p^6$, $5d^1$, $6s^2$ valence electrons of cerium and $2s^2$, $2p^4$ valence electrons of oxygen. The energy cutoffs for the wave functions and the electron densities were 60 and 900 Ry, determined to ensure stable convergence. We have sampled the BZ with a $32 \times 32 \times 32$ Monkhorst–Pack **k**-space mesh.

The phonon frequencies are calculated within density functional perturbation theory (Baroni et al. 2001), over the BZ sampled with $8 \times 8 \times 8$ Monkhorst–Pack **q**-point mesh. We have calculated the PDOS using that mesh, and the phonon dispersion curves are obtained from interpolation along the chosen path.

Results and discussion

Cerium dioxide crystallizes in the fluorite-type cubic crystal structure (Fig. 1), space group $Fm\bar{3}m$ (no. 225), in which Ce is located in (4a) (0,0,0), surrounded by eight oxygen atoms located at (8c) (1/4, 1/4, 1/4) Wyckoff positions. This structure has one infrared (F_{2u}) and one Raman (F_{2g}) active mode, each of them being triple degenerated. The normal modes of these vibrations are sketched in Fig. 1. The F_{2u} mode represents vibrations of both the Ce and O atoms in opposite directions, whereas F_{2g} mode originates from the stretching vibrations of only oxygen atoms around Ce. In the CeO_2 single crystals and polycrystalline samples, the infrared and Raman active modes appear at 283/596 cm^{-1} (ω_{TO}/ω_{LO}) (Marabelli and Wachter 1987; Santha et al. 2004) and 465 cm^{-1} (R) (Kourouklis et al. 1988; Weber et al. 1993; Nakajima et al. 1994), respectively. In our less than 5 nm CeO_{2-y} nanocrystals (Popović et al. 2012) the Raman mode is centered at about 456 cm^{-1}.
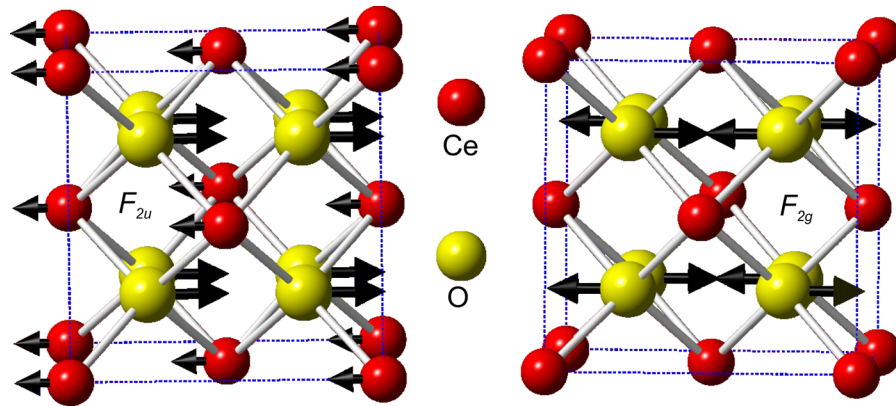
Fig. 1 The normal modes of the infrared (F_{2u}) and Raman (F_{2g}) active lattice vibrations of CeO$_2$ (Color online)

Because our nano CeO$_2$ samples are inhomogeneous (they consist of CeO$_2$ nanoparticles and air pores) we have applied the effective medium approximation (EMA) method to calculate infrared reflectivity of inhomogeneous media, taking into account the macroscopic volume fractions and local microstructural geometry (Grujić-Brojčin et al. 2005; Gonzalez et al. 1997; Spanier and Herman 2000; Bruggeman 1935). Two widely used effective medium theories are the Maxwell–Garnett theory (Maxwell–Garnett 1904) and the Bruggeman theory (Bruggeman 1935). In both theories the effective dielectric constant does not depend explicitly on the size of the grains or inclusions occurring inside the medium. Maxwell–Garnett approximation treats the effective medium as consisting of a matrix in which are embedded inclusions of a specific shape, where the fraction of the inclusions is very small (<0.15), so that the inclusions are spatially separated and can be treated as a perturbation (Spanier and Herman 2000; Saarinen et al. 2003; Gehr et al. 1997). The other widely used approximation is the Bruggeman's, which has no such limitations, and can be used for entire range of fraction values from 0 to 1. That was the reason why we used Bruggeman approach for analysis of infrared reflectivity spectra of inhomogeneous CeO$_2$ nanocrystals.

As nanophase CeO$_2$ is a porous material with a relatively large specific surface (see Table 1), the porosity of the nanopowder is included in modeling its dielectric function. The best agreement between calculated and experimental results is obtained by the generalized Bruggeman EMA (B-EMA), which introduces the effect of pore shape using the adjustable depolarization factor L for ellipsoidal voids ($L = 1/3$

for spherical cavities and $1/3 < L < 1$ for prolate spheroidal cavities).

Similar to the B-EMA, in the generalized Bruggeman model (Grujić-Brojčin et al. 2005, 2006; Spanier and Herman 2000), porous nanopowder with effective dielectric function ε_{eff} is assumed to be an inhomogeneous media composed of nanopowder (ε_{nano}) and air ($\varepsilon_{air} = 1$) with volume fractions f_{nano} and f_{air}, respectively. The basic Bruggeman model is modified to include the influence of porosity:

$$\left(\frac{\varepsilon_{nano} - \varepsilon_{eff}}{\varepsilon_{eff} + L(\varepsilon_{nano} - \varepsilon_{eff})}\right)f_{nano}$$
$$+ \left(\frac{\varepsilon_{air} - \varepsilon_{eff}}{\varepsilon_{eff} + L(\varepsilon_{air} - \varepsilon_{eff})}\right)f_{air} = 0 \qquad (1)$$

Generally, a decrease of nanopowder volume fraction results in a decrease of reflectivity and broadening of the IR features, due to the greater air fraction in the powder. Also, the decrease of depolarization factor L, from prolate spheroidal voids ($L = 1$) to spherical pores ($L = 1/3$), leads to the increase in the reflectivity, with characteristic IR features becoming more pronounced (Grujić-Brojčin et al. 2005).

Since the analysis of the far IR reflectivity spectrum of ceria nanopowders has revealed a presence of a plasmon mode, it was necessary to include both contributions of the phonon and the plasmon (free carrier contribution) to the dielectric function. Therefore, the factorized form of dielectric function has been decomposed into a sum of two independent terms (Gonzalez et al. 1997; Grujić-Brojčin et al. 2006; Gervais 1983):

Table 1 The characteristic TO and LO phonon frequencies (ω) and damping factors (γ) (all given in cm^{-1}) of Ce$_{1-x}$Cu$_x$O$_{2-y}$ nano- and poly-crystals, used in the fitting procedure together with the corresponding plasmon parameters for pure, 1, and 10 % Cu-doped CeO$_2$ samples

| Parameters	0 % Cu	1 % Cu	10 % Cu	10 nm nano	Polycrystal
ω_{TO} (γ_{TO})	135 (190)	137 (220)	137 (300)	130 (132)	135 (130)
ω_{LO} (γ_{LO})	155 (95)	147 (180)	147 (180)	160 (188)	161 (187)
ω_{TO} (γ_{TO})	282 (37)	280 (28)	280 (25)	273 (57)	272 (25)
ω_{LO} (γ_{LO})	375 (180)	380 (165)	385 (180)	280 (108)	416 (137)
ω_{TO} (γ_{TO})	370 (100)	360 (95)	370 (140)	448 (159)	–
ω_{LO} (γ_{LO})	407 (100)	407 (150)	407 (120)	468 (105)	–
ω_{TO} (γ_{TO})	490 (180)	480 (140)	485 (180)	493 (113)	428 (157)
ω_{LO} (γ_{LO})	580 (10)	580 (60)	585 (40)	585 (385)	587 (47)
ω_{TO} (γ_{TO})	–	–	–	333 (67)	–
ω_{LO} (γ_{LO})	–	–	–	350 (88)	–
ω_p (γ_p)	390 (400)	385 (580)	320 (550)	100 (50)	–
f_{nano}	0.80	0.83	0.86		
Pore shape L	0.74	0.70	0.70		
Specific surface area S_{BET} (m^2/g)	40	40	44		
Average pore diameter (nm)	10.8	12.4	9.1		

The fitting parameters from Bruggeman model (powder volume fraction f_{nano} and the pore shape L) together with the specific surface area and pore diameter values are listed for each nanopowder sample

$$\varepsilon(\omega) = \varepsilon_\infty \left[\prod_{j=1}^{n} \frac{\omega_{LO,j}^2 - \omega^2 + i\omega\gamma_{LO,j}}{\omega_{TO,j}^2 - \omega^2 + i\omega\gamma_{TO,j}} - \frac{\omega_p^2}{\omega(\omega - i\gamma_p)} \right] \tag{2}$$

where $\omega_{LO,j}$ and $\omega_{TO,j}$ are longitudinal and transverse frequencies of the jth oscillator, $\gamma_{LO,j}$ and $\gamma_{TO,j}$ are their corresponding dampings, ω_p (γ_p) is the plasma frequency (damping), and ε_∞ is the high-frequency dielectric constant.

Figure 2a shows the PDOS of CeO$_2$. This PDOS is in complete agreement with previously published ones (Marabelli and Wachter 1987; Nakajima et al. 1994; Gürel and Eryiğit 2006; Buckeridge et al. 2013).

The CeO$_2$ IR reflectivity spectra of polycrystalline sample (Santha et al. 2004) and 10-nm particle size undoped CeO$_2$ nanocrystal are given in Fig. 2b, c, respectively. These spectra are fitted using dielectric function model, Eq. (2), with parameters given in Table 1. In the case of the polycrystalline sample three oscillators are used to obtain a rather good agreement with experimental data. The lowest energy oscillator with TO energy of 135 cm^{-1} represents phonon states from the X and L point of BZ. Other two oscillators represent F_{2u} mode. Appearance of two instead of one IR active mode in this spectral range is related to the anharmonicity (Santha et al. 2004). In the case of the
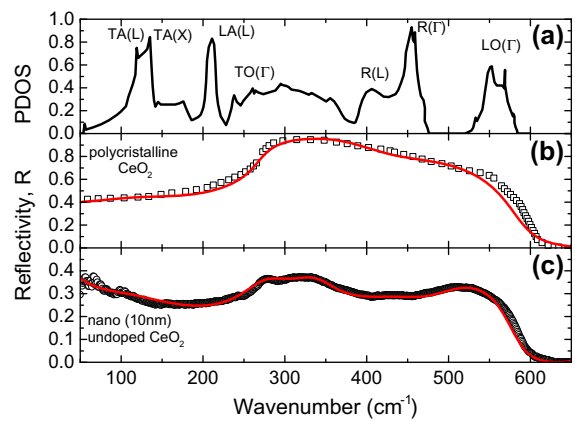
Fig. 2 a The phonon density of states of CeO$_2$. **b** The IR reflectivity spectra of polycrystalline CeO$_2$ sample (Santha et al. 2004); **c** nanocrystalline undoped CeO$_2$ sample (particle size $\sim$10 nm). *Solid lines* represent the calculated reflectivity spectra obtained by the fitting procedure based on Eq. (2), with the parameters given in Table 1 (Color online)

nanosized sample (Fig. 2c) five oscillators are included in the fitting procedure, as well as, plasma term (see Table 1). Origin of these oscillators will be discussed later.
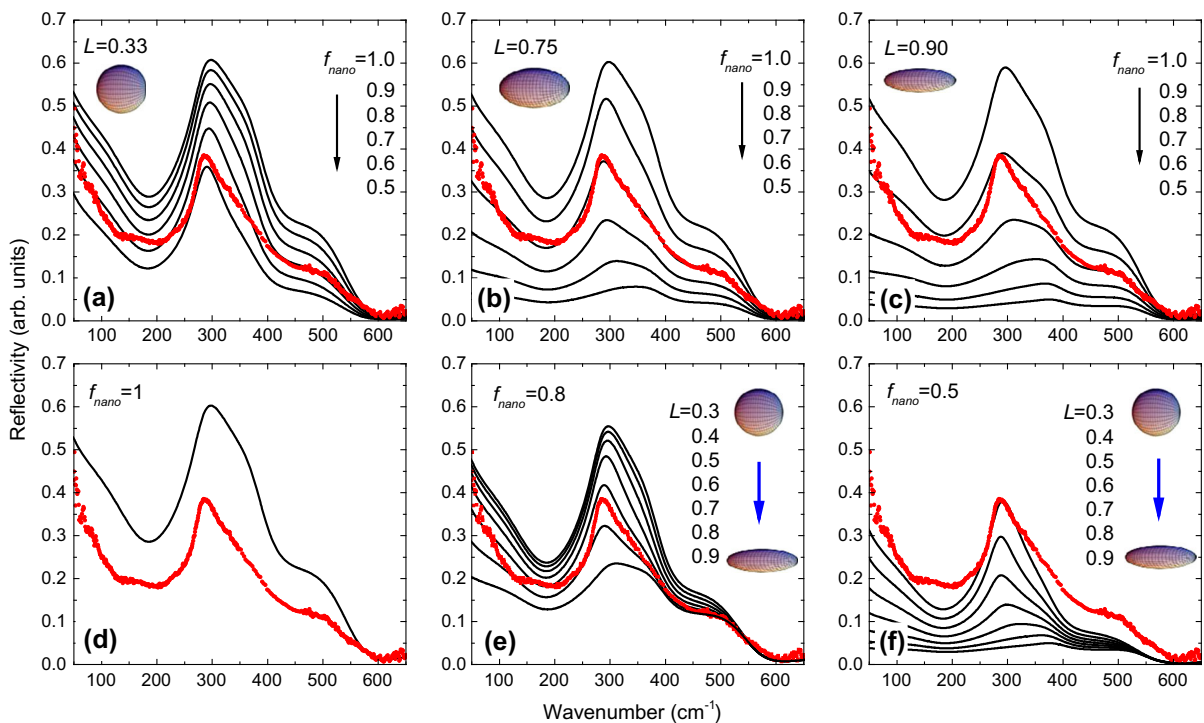
The influence of nanopowder volume fraction and the pore shape on the IR reflectivity spectra is analyzed in Fig. 3a–c, which show the IR reflectivity spectra

calculated with the generalized B-EMA, with the variation of powder volume fraction f_{nano} and fixed value of depolarization factor (pore shape factor) $L = 0.33$, 0.75, and 0.90, respectively. The spectra are calculated with the set of parameters corresponding to the pure CeO_2 sample, listed in the Table 1 (0 % Cu), whereas f_{nano} is varied from 0.5 (50 % of CeO_2 powder in porous sample) to 1 (nonporous powder). The pore shape factor $L = 0.33$ defines ideally spherical pores and for given TO/LO parameters, the best volume fraction fit corresponds to values of f_{nano} between 50 and 60 % of powder content in the sample (Fig. 3a).

The pore shape factor $L = 0.75$ defines pores with elongated structure, as indicated in Fig. 3b. For given TO/LO parameters (Table 1) the best volume fraction fit corresponds to values of f_{nano} around 80 % of powder content in the sample. In Fig. 3c the variation of powder volume fraction f_{nano} with depolarization factor $L = 0.90$ is shown. The pore shape factor $L = 0.90$ corresponds to extremely elongated pores.

For given TO/LO parameters (Table 1) the best volume fraction fit corresponds to values of f_{nano} between 80 and 90 % of powder content in the sample.

The pore shape variation is analyzed in Fig. 3d–f. In Fig. 3d the calculated spectrum for powder volume fraction $f_{nano} = 1$, i.e., nonporous powder is shown together with experimental IR reflectivity of the pure CeO_2 sample. The spectrum is calculated with the set of parameters corresponding to the pure CeO_2 sample, listed in Table 1 (0 % Cu), whereas the pore shape factor (L) variation has no influence in this calculation. Figure 3e, f show the IR reflectivity spectra calculated with the generalized Bruggeman EMA with powder volume fraction of 80 % and 50 %. The pore shape factor varied from $L = 0.3$–0.9. It may be noticed that in both cases, the intensity of the reflectivity is getting lower with the increase in pore shape factor. For given TO/LO parameters (Table 1) the best pore shape fit is obtained for values of L from 0.7 to 0.8 (Fig. 3e), corresponding to the area of elongated pores. These

Fig. 3 The IR reflectivity spectra calculated with the generalized B-EMA. **a** The volume fraction of nanopowder is in the range from 0.5 to 1.0 and the pore shape factor $L = 0.33$ (spherical shape of pores); **b** pore shape factor $L = 0.75$ (elongated pore structure); **c** pore shape factor $L = 0.90$ (extremely elongated pore structure); **d** the IR reflectivity spectra calculated with the generalized B-EMA with the volume

fraction of the nanopowder $f_{nano} = 1$ (nonporous powder); **e** fixed volume fraction of nanopowder ($f_{nano} = 0.8$) with pore shape factor varying from 0.3 to 0.9; **f** fixed volume fraction of nanopowder ($f_{nano} = 0.5$) with pore shape factor varying from 0.3 to 0.9. Experimental IR reflectivity spectrum (*red curve*) of pure CeO_2 sample (0 % Cu) is given for comparison (Color online)

results correspond to those shown in Fig. 3b. Finally, in Fig. 3f the best pore shape fit is obtained for values of L around 0.3, corresponding to ideally spherical pores.

By analyzing the results shown in Fig. 3, we came to the following conclusions:

(i) Bruggeman EMA model can be used to fit the experimental reflectivity spectra of inhomogeneous nanomaterials, in our case CeO_2 nanocrystals.

(ii) The B-EMA model parameters that best describe the experimental CeO_2 reflectivity spectra are close to $f_{nano} = 0.8$ and $L = 0.75$. (see Fig. 3b). Refinement of these parameters for samples under investigation gives values shown in Table 1.

(iii) The very good agreement between the calculated and the experimental spectra illustrated in Fig. 4 suggests that the use of more specific model, which may include the pore shape distribution, instead of the B-EMA general and simple model, is not necessary.

In Fig. 4 experimental IR reflectivity spectra of 5 nm-sized pure, 1, and 10 % Cu-doped CeO_2 samples are shown, together with the corresponding spectra calculated with the generalized B-EMA. Fitting parameters for these spectra are listed in Table 1. As can be seen from Table 1, four oscillators with TO energies of approximately 135, 280, 370, and 490 cm^{-1} were included in the fitting procedure, Eq. (2), for 5 nm-sized CeO_2 samples. These
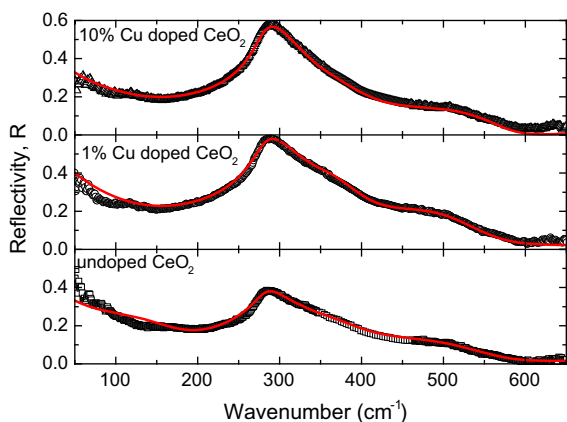
Fig. 4 Experimental IR reflectivity spectra of pure, 1, and 10 % Cu-doped CeO_2 samples, with the corresponding spectra obtained by the fitting procedure based on Eq. (2) and the generalized B-EMA, Eq. (1). Parameters are given in Table 1

oscillators represent local maxima of the PDOS. The lowest energy oscillator represents TA(L)/TA(X) phonon states, which become IR-active E_u modes (Buckeridge et al. 2013) at the L and X points of BZ. The second oscillator originates from TO(Γ) phonon states. The oscillator at ~ 400 cm^{-1} originates from Raman mode phonon states which at the L point of BZ also becomes IR-active E_u mode (Buckeridge et al. 2013). The last oscillator describes phonons with dominantly LO(Γ) IR mode character. The appearance of PDOS-related oscillators, instead of single F_{2u} IR-active mode in the far-infrared reflectivity spectra, is a consequence of the nanosized dimension of the particles, as mentioned earlier. Besides that, the oscillator energies appear at lower energies than the maxima of PDOS. This is also related to the particle size. In fact, in nanoceria the unit cell dimensions abruptly increase by particle size reduction (Tsunekawa et al. 2000; Wu et al. 2004). Consequently, the PDOS softens with the particle size lowering due to an increase in the internal strain, as it was discussed in Buckeridge et al. (2013).

A small variation in the frequencies of TO (LO) modes of the pure and doped samples is noticed, whereas the damping parameters are clearly affected by the variation between pure and doped samples. Plasmon modes are registered in all samples, with significant plasma frequency decrease and damping parameter increase with Cu doping. The values of parameters used in the generalized Bruggeman EMA are varied with doping: similar porosity has been estimated in all studied samples. Namely, the volume fraction parameter is estimated from $f_{nano} = 0.80$ in pure CeO_2 (which means 80 % of CeO_2 fraction in a porous sample) to 0.86 in 10 % Cu-doped CeO_2 sample. The depolarization factor L, defining pore shape is estimated as 0.74 in pure CeO_2 sample and slightly lower (0.70) in doped samples, therefore describing pores filled with the air as very elongated. Comparing these with textural measurement results, we find that in the 10 % Cu-doped sample, the reduction of L and an increase in volume fraction is correlated with a decrease of pore diameter and an increase in specific surface area (see Table 1).

Conclusion

We have measured the unpolarized far-infrared reflectivity spectra of the CeO_2 nanocrystals at room

temperature. Reflectivity spectra were analyzed using the factorized form of the dielectric function, which includes the phonon and plasmon contribution to the dielectric function. The best fit spectra are obtained using the generalized Bruggeman model for inhomogeneous media, which takes into account the volume fraction of CeO_2 nanocrystal and the air pore shape.

References

Araújo VD, de Lima MM Jr, Cantarero M, Bernardi MIB, Bellido JDA, Assaf EM, Balzer R, Probst LFD, Fajardo HV (2013) Catalytic oxidation of n-hexane promoted by $Ce_{1-x}Cu_xO_2$ catalysts prepared by one-step polymeric precursor method. Mater Chem Phys 142:677–681

Baroni S, de Gironcoli S, Dal Corso A, Giannozzi P (2001) Phonons and related crystal properties from density-functional perturbation theory. Rev Mod Phys 73:515–562

Bruggeman DAG (1935) Berechnung verschiedener physikalischer Konstanten von heterogenen Substanzen. I. Dielektrizitätskonstanten und Leitfähigkeiten der Mischkörper aus isotropen Substanzen. Ann Phys 24:636–664

Buckeridge J, Scanlon DO, Walsh A, Catlow CRA, Sokol AA (2013) Dynamical response and instability in ceria under lattice expansion. Phys Rev B 87(21):214304

Cantarero A (2013) Review on Raman scattering in semiconductor nanowires: I. Theory. J Nanophotonics 7(1):071598

Gehr RJ, Fischer GL, Boyd RW (1997) Nonlinear-optical response of porous-glass-based composite materials. J Opt Soc Am B 14(9):2310–2314

Gervais F (1983) High-temperature infrared reflectivity spectroscopy by scanning interferometry. In: Button KJ (ed) Infrared and millimeter waves. Academic Press, New York, pp 279–339

Giannozzi P, Baroni S, Bonini N, Calandra M, Car R, Cavazzoni C, Ceresoli D, Chiarotti GL, Cococcioni M, Dabo I, Corso AD, de Gironcoli S, Fabris S, Fratesi G, Gebauer R, Gerstmann U, Gougoussis C, Kokalj A, Lazzeri M, Martin-Samos L, Marzari N, Mauri F, Mazzarello R, Paolini S, Pasquarello A, Paulatto L, Sbraccia C, Scandolo S, Sclauzero G, Seitsonen AP, Smogunov A, Umari P, Wentzcovitch RM (2009) QUANTUM ESPRESSO: a modular and open-source software project for quantum simulations of materials. J Phys 21(39):395502

Gonzalez RJ, Zallen R, Berger H (1997) Infrared reflectivity and lattice fundamentals in anatase TiO_2. Phys Rev B 55(11):7014–7017

Grujić-Brojčin M, Šćepanović MJ, Dohčević-Mitrović ZD, Hinić I, Matović B, Stanišić G, Popović ZV (2005) Infrared study of laser synthesized anatase TiO_2 nanopowders. J Phys D 38(9):1415–1420

Grujić-Brojčin M, Šćepanović MJ, Dohčević-Mitrović ZD, Popović ZV (2006) Infrared study of nonstoichiometric anatase TiO_2 nanopowders. Sci Sinter 38:183

Gürel T, Eryiğit R (2006) Ab initio pressure-dependent vibrational and dielectric properties of CeO_2. Phys Rev B 74(1):014302

Kourouklis GA, Jayaraman A, Espinosa GP (1988) High-pressure Raman study of CeO_2 to 35 GPa and pressure-induced phase transformation from the fluorite structure. Phys Rev B 37(8):4250–4253

Marabelli F, Wachter P (1987) Covalent insulator 2: optical reflectivity measurements. Phys Rev B 36(2):1234–1238

Maxwell-Garnett JC (1904) Colours in metal glasses and in metallic films. Philos Trans R Soc Lond, Ser.4 203:385–420

Nakajima A, Yoshihara A, Ishigame M (1994) Defect-induced Raman spectra in doped CeO_2. Phys Rev B 50(18):13297–13307

Orel Z (1999) Characterization of cerium dioxide dip-coated films by spectroscopic technique. Internet J Vib Spec Vol 3, Edition 4, Section 6 (www.ijvs.com). Accessed 20 June 2013

Popović ZV, Dohčević-Mitrović Z, Šćepanović M, Grujić-Brojčin M, Aškrabić S (2011) Raman scattering on nanomaterials and nanostructures. Ann Phys 523(1–2):62–74

Popović ZV, Dohčević-Mitrović ZD, Paunović N, Radović M (2012) Evidence of charge delocalization in $Ce_{1-x}Fe_{x}^{2+(3+)}O_{2-y}$ nanocrystals ($x = 0, 0.06, 0.12$). Phys Rev B 85:014302

Saarinen JJ, Vartiainen EM, Peiponen KE (2003) On tailoring of nonlinear spectral properties of nanocomposites having Maxwell Garnett or Bruggeman structure. Opt Rev 10(2):111–115

Santha NI, Sebastian MT, Mohanan P, Alford NM, Sarma K, Pullar RC, Kamba S, Pashkin A, Samukhina P, Petzelt J (2004) Effect of doping on the dielectric properties of cerium oxide in the microwave and far-infrared frequency range. J Am Ceram Soc 87(7):1233–1237

Spanier JE, Herman IP (2000) Use of hybrid phenomenological and statistical effective-medium theories of dielectric functions to model the infrared reflectance of porous SiC films. Phys Rev B 61(15):10437–10450

Tsunekawa S, Ishikawa K, Li ZQ, Kawazoe Y, Kasuya A (2000) Origin of anomalous lattice expansion in oxide nanoparticles. Phys Rev Lett 85(16):3440–3443

Weber WH, Hass KC, McBride JR (1993) Raman study of CeO_2: second-order scattering, lattice dynamics, and particle-size effects. Phys Rev B 48(1):178–185

Wu L, Wiesmann HJ, Moodenbaugh AR, Klie RF, Zhu Y, Welch DO, Suenaga M (2004) Oxidation state and lattice expansion of CeO_{2-x} nanoparticles as a function of particle size. Phys Rev B 69(12):125415

PAPER

Infrared study of plasmon–phonon coupling in pure and Nd-doped CeO_{2-y} nanocrystals

To cite this article: M Radovi et al 2015 *J. Phys. D: Appl. Phys.* **48** 065301

View the article online for updates and enhancements.
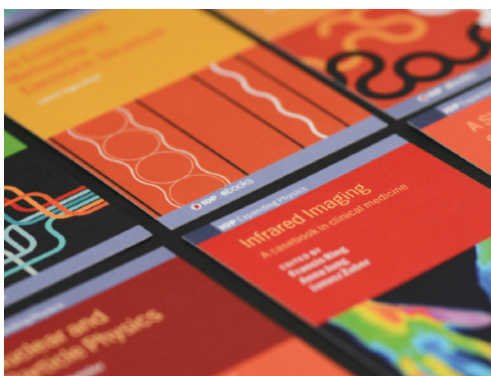
IOP ebooks™

Bringing together innovative digital publishing with leading authors from the global scientific community.

Start exploring the collection−download the first chapter of every title for free.

Infrared study of plasmon–phonon coupling in pure and Nd-doped CeO$_{2-y}$ nanocrystals

M Radović[1]**, Z Dohčević-Mitrović**[1]**, N Paunović**[1]**, S Bošković**[2]**, N Tomić**[1]
N Tadić[3] **and I Belča**[3]

[1] Center for Solid State Physics and New Materials, Institute of Physics, University of Belgrade, 11080 Belgrade, Serbia
[2] Institute for Nuclear sciences 'Vinča', Materials Science Laboratory, University of Belgrade, Belgrade, Serbia
[3] Faculty of Physics, University of Belgrade, 11000 Belgrade, Serbia

E-mail: marrad@ipb.ac.rs

CrossMark

Abstract

Plasmon-longitudinal-optical (LO) phonon interaction in pure and Nd-doped CeO$_{2-y}$ nanocrystals was investigated by measuring far–infrared reflectivity spectra in the 100–700 cm^{-1} spectral range at room temperature. Analysis of the obtained results revealed that the presence of free charge carriers becomes significant with the particle size decrease to nanometer range and increase of lattice defects. The free charge carriers were found to be responsible for a plasmon mode which coupled strongly with two LO phonon modes of ceria. The presence of more pronounced low-frequency Drude tail and the screening of the phonon modes in Nd-doped CeO$_{2-y}$ nanocrystals implied that the Plasmon-LO phonon interaction increased with doping. Factorized and additive dielectric function models were applied to deduce about the coupled and decoupled LO phonon frequencies and the structure of the decoupled plasmon mode in pure and Nd-doped CeO$_{2-y}$ nanocrystals. These models were combined with Bruggeman effective medium approximation in order to properly describe the influence of porosity on the infrared reflectivity spectra. With increasing dopant content, the decoupled plasmon mode exhibited redshift and damping decrease implying that doping induced semiconductor–to–metalic state transition took place.

Keywords: Nd-doped ceria nanocrystals, infrared spectroscopy, plasmon–phonon interaction

(Some figures may appear in colour only in the online journal)

1. Introduction

Cerium dioxide (CeO$_2$, ceria) is a wide band gap semiconductor with ionic and partially covalent bonding nature [1, 2], which has received considerable interest due to the variety of applications in advanced technologies. CeO$_2$-based solid solutions have been acknowledged to be the most promising electrolytes for intermediate temperature solid oxide fuel cells, exhibiting excellent ionic conductivity at intermediate temperatures (500 − 800°C) [3, 4], much better than traditional ionic conductors like yttria-stabilized zirconia [3]. With a reduction of particle size, ceria becomes a mixed ionic–electronic conductor [5], because the presence of defects and unsaturated surface bonds leads to the increase

of the free carrier contribution to the overall conductivity. The electrical conductivity of nanocrystalline ceria based materials can be attributed to the small polaron hopping mechanism [6, 7]. It was shown [8, 9] that the electrical conductivity, measured at different temperatures and oxygen partial pressures, is increased with the decreasing size of nanoparticles and is almost 10^4 times greater than in microcrystalline materials [8, 9]. This property can be utilized for gas sensor applications [10].

The influence of free carrier collective excitations (plasmons) on the optical phonon spectra of nanocrystalline ceria, i.e. plasmon–phonon coupling, has not been studied. The infrared (IR) spectroscopy is a nondestructive and widely applied spectroscopic technique for the investigation of the

mechanism of plasmon–phonon coupling in different materials. From the IR reflection spectra of polar semiconductors, both phonon and plasmon excitations can be registered, enabling the direct investigation of the plasmon − phonon interaction mechanism.

In the present paper, the plasmon − phonon interaction in pure and Nd-doped CeO_{2-y} nanocrystals has been investigated by analyzing the IR reflection spectra of these samples. The application of factorized and additive forms of the dielectric function, together with Bruggeman effective medium approximation, allowed the determination of coupled (decoupled) phonon frequencies, damping parameters and the structure of decoupled plasmon mode with doping. Better insight into the plasmon − phonon coupling mechanism in nanocrystalline ceria can be very important because the plasmon − phonon interaction can influence the ceria electrical conductivity properties.

2. Experimental

Undoped CeO_{2-y} nanopowders were prepared using the self-propagating room temperature synthesis and the detailed preparation procedure is described elsewhere [11, 12]. The as-prepared samples were calcinated at 600 and 800°C for 2 h, in order to induce the growth of crystalite size. The Nd-doped samples were doped with 10, 15, 20 and 25 wt% Nd. X-ray diffraction (XRD) technique was used for the characterization of structural properties and the degree of crystallinity of the synthesized nanopowders. Diffraction patterns were recorded over the 2θ range from 20 to 80° on a Siemens D-5000 diffractometer, using Cu Kα radiation The external standard correction was performed using LaB_6 (NIST) powder. Atomic force microscope (AFM) images were taken using the Omicron B002645 SPM PROBE VT AFM 25 in noncontact mode. The IR reflectivity spectra were measured at room temperature in the far-IR region (100–700 cm^{-1}) on a Bomem DA8 spectrometer using the DTGS detector.

3. Models

In this section, a brief overview of the theoretical models used to analyze the measured IR spectra will be presented.

The IR reflectivity spectra of the ionic crystals where large splitting between transverse-optical (TO) and longitudinal-optical (LO) modes is observed [13, 14], are usually fitted with a dielectric function given by the expression [15]:

$$\varepsilon_M = \varepsilon_\infty \prod_j \frac{\omega_{\text{LO}j}^2 - \omega^2 + i\omega\gamma_{\text{LO}j}}{\omega_{\text{TO}j}^2 - \omega^2 + i\omega\gamma_{\text{TO}j}}, \tag{1}$$

where ε_∞ is the high frequency dielectric constant and $\omega_{\text{TO(LO)}j}$ and $\gamma_{\text{TO(LO)}j}$ are the TO and LO phonon frequencies and damping rates of the corresponding IR mode. This model introduces four adjustable parameters for each TO-LO mode and is used for description of pure phonon properties. In further text it will be named the Lattice Vibrations model (LV). The main disadvantage of this model results from the fact that it does not

take into account the contribution from the electronic excitations i.e. the plasmons and plasmon–phonon coupling.

Most semiconductors have a significant portion of free carriers and a complete description of the far-IR optical properties of semiconductor materials has to take both phonon and plasmon contributions into account. The coexistence of phonons and plasmons usually leads to a strong coupling between plasmons and LO phonons. This effect is most pronounced when the plasma frequency (ω_P) is in the vicinity of the LO phonon frequency. In that case the plasmon–phonon interaction can be described with the factorized form of the dielectric function given by [16, 17]:

$$\varepsilon_M = \varepsilon_\infty \frac{\prod_{j=1}^{m+n} \left(\omega^2 + i\omega\gamma_{\text{LO}j} - \omega_{\text{LO}j}^2 \right)}{\omega^m \prod_{j=1}^{m} \left(\omega + i\gamma_{Pj} \right) \prod_{j=1}^{n} \left(\omega^2 + i\omega\gamma_{\text{TO}j} - \omega_{\text{TO}j}^2 \right)}, \tag{2}$$

where ω_{TOj} and γ_{TOj} are frequencies and damping rates of the TO modes and γ_P is the plasma damping. This expression gives directly the coupled plasmon-LO phonon frequencies ω_{LOj} and damping rates γ_{LOj} and in further text will be named as the Coupled Plasmon − Phonon (CPP) model.

The extension of the Drude model which has been used to fit the IR reflectivity spectra of conducting oxides is known in the literature as the Double-damping extended Drude model [18]. The additive form of the dielectric function in which the plasmon contribution is expressed by Double-damped Drude term, is composed of two terms:

$$\varepsilon_M = \varepsilon_\infty \left(\prod_j \frac{\omega_{\text{LO}j}^2 - \omega^2 + i\omega\gamma_{\text{LO}j}}{\omega_{\text{TO}j}^2 - \omega^2 + i\omega\gamma_{\text{TO}j}} - \frac{\omega_P^2 + i(\gamma_P - \gamma_0)\omega}{\omega(\omega - i\gamma_0)} \right). \tag{3}$$

The first term represents the phonon contribution and the second term is the plasmon contribution. The $\omega_{\text{TO(LO)}j}$ and $\gamma_{\text{TO(LO)}j}$ are TO(LO) frequencies and dampings of decoupled phonon modes, whereas the ω_P, γ_P and γ_0 are the plasma frequency and dampings at $\omega = \omega_P$ and $\omega = 0$. This model allows the decoupling of phonon and plasmon contributions and enables to make a difference between the damping (γ_P) at the plasma frequency and the static damping at zero frequency (γ_0). The second term in equation (3) becomes the classical Drude formula for $\gamma_P = \gamma_0$. The application of this model offers more flexibility in numerical fitting and more precise description of the dielectric function response [18]. In further text this model will be named the Decoupled Plasmon − Phonon (DPP) model.

In order to properly analyze the IR spectra of porous nanomaterials, one of the most commonly used models is the Bruggeman effective medium approximation [19, 20]. For the inhomogeneous, binary material, composed of material (ε_M) and air ($\varepsilon_{\text{air}} = 1$) with the volume fractions f_M and $1 - f_M$ respectively, the empirical relation for the effective dielectric function (ε_{eff}) can be written as [20]:

$$\left(\frac{\varepsilon_M - \varepsilon_{\text{eff}}}{\varepsilon_M + 2\varepsilon_{\text{eff}}} \right) f_M + \left(\frac{1 - \varepsilon_{\text{eff}}}{1 + 2\varepsilon_{\text{eff}}} \right) (1 - f_M) = 0. \tag{4}$$

Therefore, the effective dielectric function (ε_{eff}) from equation (4) of a pure and Nd-doped CeO_{2-y} porous nanocrystalline sample can be expressed in terms of the dielectic function of material (ε_M) given by equations (1), (2) or (3) and volume fractions of material and air.

The theoretical reflectivity is obtained by using the Fresnel formula:

$$R_{calc} = \left| \frac{\sqrt{\varepsilon_{eff}} - 1}{\sqrt{\varepsilon_{eff}} + 1} \right|^2. \tag{5}$$

The least-squares fitting procedure between the theoretical (R_{calc}) and experimental (R_{exp}) reflectivity was carried out until the chi-squared value:

$$\chi^2 = \frac{1}{N} \sum_i^N \left(R_{i,exp} - R_{i,calc} \right)^2 \tag{6}$$

was minimized, where N is the number of measured points.

4. Results and discussion

A detailed analysis of the XRD spectra of undoped and Nd-doped samples has been already given in [11, 12]. The Nd-doped samples crystallized into a fluorite type structure of CeO_2 with Nd^{3+} ions entering substitutionally into a ceria lattice. The presence of amorphous or any other phase was not detected, even for the highest Nd concentration [11, 12]. The synthesized samples were composed of very small particles in the nanometric range (3–4 nm) [11, 12]. Additionally, the undoped CeO_{2-y} sample was calcinated at 600 and 800°C for 2 h in air, in order to compare the structural and vibrational properties of thermally treated and non-treated samples. The XRD spectra of thermally treated samples are given in figure 1(a). Characteristic Miller indices are denoted for main diffraction peaks. The average crystallite size and strain values were calculated using the Williamson–Hall method [21, 22] and the obtained values for each sample are presented in figure 1(a). In the inset of figure 1(a) is presented the Williamson–Hall plot of an as-prepared CeO_{2-y} sample. The calcinated samples exhibited sharper diffraction lines as a consequence of increased crystallite size and much better degree of crystallinity. The XRD pattern of the sample calcinated at 800°C is similar to the XRD spectrum of polycrystalline CeO_2. In figures 1(b) and (c) are presented AFM images of a ceria sample calcinated at 800°C and of an as-prepared CeO_{2-y} sample. The size of nanocrystals was in good agreement with the average crystallite size obtained from the XRD data.

Bearing in mind that ceria phonon properties are very much dependent on the crystallite size, we first investigated the influence of the particle size on the infrared reflectivity spectra of as-prepared and calcinated samples of CeO_{2-y}. In figure 2 are presented the IR reflectivity spectra of a bulk CeO_2 sample (reconstructed according to the literature data [2]) and calcinated ceria samples with different crystallite sizes, determined from XRD spectra from figure 1. Factor-group analysis for a fluorite type CeO_2 structure, predicts only

one triple-degenerate IR active phonon mode of the F_{2u} symmetry, with TO and LO mode frequencies at 218 and 597 cm^{-1}, respectively [2]. In the IR spectrum of the bulk sample, wide reststrahlen band, characteristic for the ionic bond nature, is observed.

With decreasing crystallite size, the reststrahlen band splits into two broad TO-LO modes in the $200 - 550$ cm^{-1} region. The splitting and redshift of both LO modes become more distinct in the sample with the smallest crystallite size (4.2 nm). A similar behavior was previously observed for pure and doped ceria powders [23] and for other nanostructured materials such as porous SiC films [20] and Mn_2O_3 nanocrystals [24]. It is reasonable to expect that the vibrational properties of nanomaterials are changed due to the increased concentration of structural defects (such as oxygen vacancies in ceria) and large number of dangling bonds at the nanoparticles surface, which leads to crystal symmetry breakdown. The lifting of the F_{2u} mode degeneracy in CeO_{2-y} nanocrystals can be ascribed to the long-range Coulomb field which splits the degeneracy of the polar modes in nanocrystals [24]. Another possible explanation for the observed splitting of the restrahlen band was ascribed to the multiphonon (anharmonic) effects [23].

From figure 2, for the CeO_{2-y} sample with the smallest crystallite size, it can be seen that the phonon modes are significantly damped and that the plasmonic background becomes prominent. The presence of lattice defects in the form of oxygen vacancies and consequently free charge carriers, is responsible for the appearance of the plasmonic background. The formation of an oxygen vacancy in the ceria lattice is followed by the localization of two electrons into empty Ce $4f^0$ orbitals [25], causing the change in the valence state of neighboring Ce ions from 4^+ to 3^+. With decreasing particle size, the concentration of oxygen vacancies increases. The electrons tend to be localized not only on the Ce sites, but also on the vacancy sites, giving rise to the formation of the F-center defect states [26, 27]. The electrons localized on vacancy sites behave like free charge carriers, which can significantly contribute to the increasing of ceria electrical conductivity as the crystallite size decreases [10]. Our previous Raman spectroscopy analysis of nonstoichiometric nanosized ceria [28] have demonstrated that anomalous broadening of the Raman F_{2g} mode can be ascribed to the electron-molecular vibrational coupling effect due to the increased concentration of charge carriers at the Fermi surface. It was shown that the delocalization of electrons onto oxygen vacancies causes semiconductor–to–metallic state transition in highly oxygen deficient nanosized ceria. Therefore, the electronic contribution to the dielectric function has to be properly taken into account in the analysis of the IR reflectivity spectra of the nanocrystalline CeO_{2-y} samples.

The IR reflectivity spectrum of CeO_{2-y} nanocrystals, with the smallest crystallite size (4.2 nm in figure 2), was analyzed using two models for plasmon $-$ phonon interaction. The first one was the CPP model, (equation (2)), which enables to directly obtain coupled plasmon $-$ phonon frequencies and dampings. The second one was the DPP model which was used to obtain the LO mode parameters of the decoupled phonons and plasmons, (equation (3)). These two models were
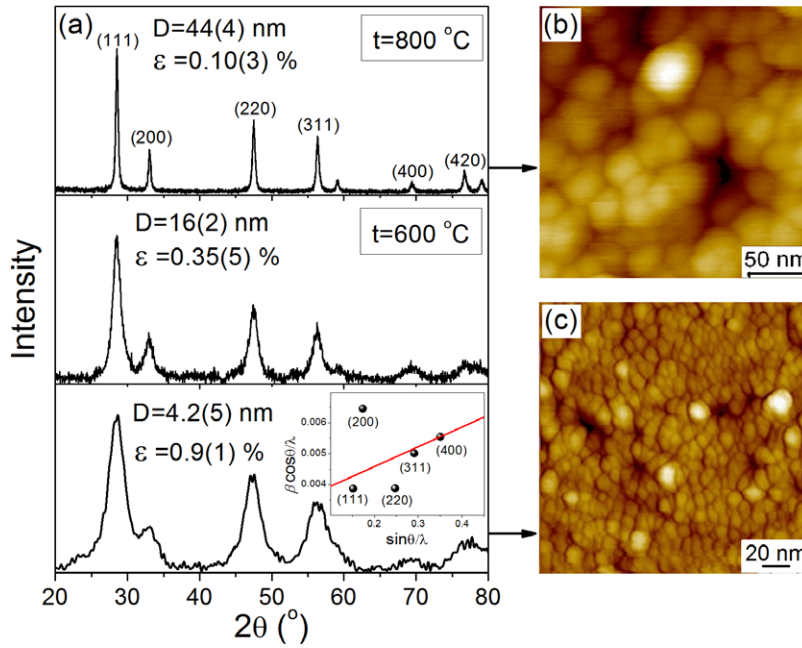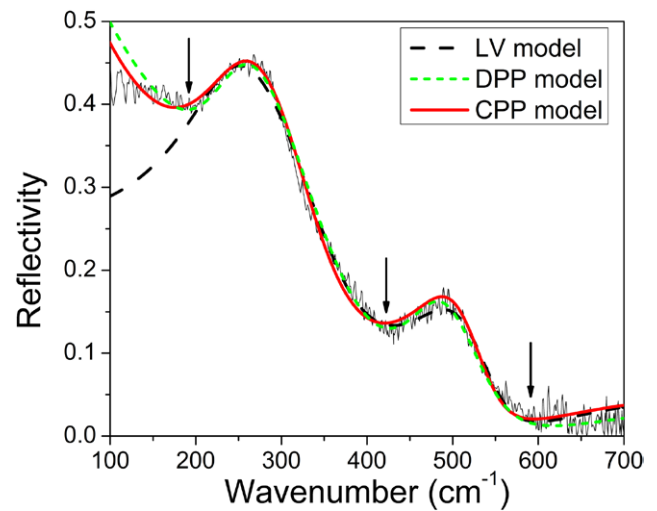
Figure 1. (*a*) XRD patterns of as-prepared and thermally treated CeO_{2-y}, together with the crystallite size (*D*) and strain (*ε*) values. The inset presents the Williamson–Hall plot of as-prepared CeO_{2-y}. AFM images of (*b*) CeO_{2-y} sample calcinated at 800°C and (*c*) as-prepared CeO_{2-y} sample.
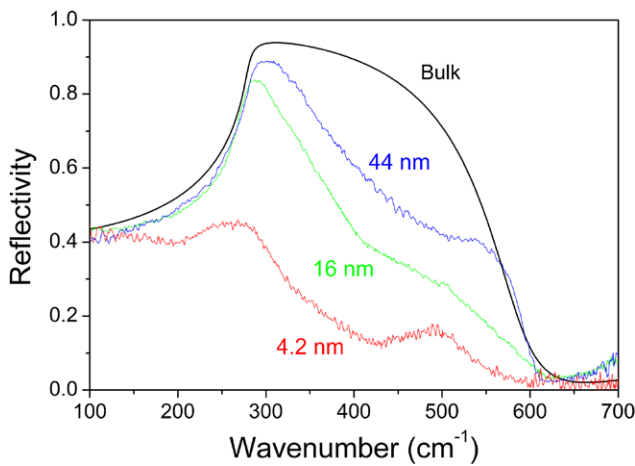
Figure 2. IR reflectivity spectra of CeO_{2-y} nanocrystals with different crystallite sizes and theoretical curve for bulk sample according to the data taken from [2].

Figure 3. IR reflectivity spectrum of a CeO_{2-y} nanocrystalline sample (crystallite size 4.2 nm), together with theoretical fits using the LV, DPP and CPP models. The arrows mark the reflectivity minima.

combined with Bruggeman effective medium approximation (equation (4)) in order to properly include the influence of material porosity f_M on the resulting IR spectra. The dielectric function model which takes into account only the pure lattice vibrations (LV model given by equation (1)) was also applied. A comparison between the theoretical models and the experimental spectrum for a CeO_{2-y} sample is shown in figure 3. In all applied models, the reflectivity spectrum of the CeO_{2-y} sample was fitted with two oscillators (due to the observed splitting of the restsrahlen band).

From figure 3, it can be seen that LV model did not give a good fit of the experimental data in the frequency region bellow 200 cm^{-1}, because of the contribution of free charge carriers. On the contrary, both the CPP and DPP models gave satisfactory fits of the reflectivity data.

The plasmon-LO phonon coupling in the nanocrystalline CeO_{2-y} sample was analyzed by the CPP model, assuming that the plasmon mode is coupled with two LO phonon modes of the nanocrystalline CeO_{2-y} sample. In that case, the equation (2) becomes [17]:

$$\varepsilon_M = \varepsilon_\infty \frac{\left(\omega^2 - \omega_{LO1}^2 + i\omega\gamma_{LO1}\right)\left(\omega^2 - \omega_{LO2}^2 + i\omega\gamma_{LO2}\right)\left(\omega^2 - \omega_{LO3}^2 + i\omega\gamma_{LO3}\right)}{\omega\left(\omega + i\gamma_P\right)\left(\omega^2 - \omega_{TO1}^2 + i\omega\gamma_{TO1}\right)\left(\omega^2 - \omega_{TO2}^2 + i\omega\gamma_{TO2}\right)}.$$

(7)

From this model, the reflection spectrum minima occur for the eigenfrequencies ω_{LOj} (*j* = 1–3) [16], where the coupling between plasmon and two LO phonons manifests as the appearance of an additional longitudinal plasmon − phonon mode.

Table 1. Fitting parameters obtained by using the Coupled Plasmon–Phonon (CPP) model. The estimated errors are given in parenthesis.

Sample	f_M	γ_P	ω_{TO1}	γ_{TO1}	ω_{LO1}	γ_{LO1}	ω_{TO2}	γ_{TO2}	ω_{LO2}	γ_{LO2}	ω_{LO3}	γ_{LO3}	χ^2
	(±0.03)	(±10)	(±5)	(±10)	(±5)	(±15)	(±5)	(±10)	(±5)	(±15)	(±5)	(±15)	
CeO_{2-y}	0.8	210	248	120	370	155	492	105	545	75	210	290	0.0012
10%Nd	0.72	208	248	107	360	180	480	250	549	150	210	290	0.0013
15%Nd	0.61	118	240	176	336	110	477	210	552	190	185	205	0.001
20%Nd	0.56	90	244	95	343	165	480	130	546	110	193	108	0.0023
25%Nd	0.81	130	245	175	332	159	485	180	546	150	173	120	0.0041

Table 2. Fitting parameters obtained by using the Decoupled Plasmon–Phonon (DPP) model. The estimated errors are given in parenthesis.

Sample	f_M	ω_P	γ_P	γ_0	ω_{TO1}	γ_{TO1}	ω_{LO1}	γ_{LO1}	ω_{TO2}	γ_{TO2}	ω_{LO2}	γ_{LO2}	χ^2
	(±0.03)	(±5)	(±15)	(±15)	(±5)	(±10)	(±5)	(±15)	(±5)	(±10)	(±5)	(±15)	
CeO_{2-y}	0.8	450	360	330	245	100	300	45	479	100	505	75	0.0017
10%Nd	0.72	440	360	330	243	98	319	25	477	195	500	145	0.0015
15%Nd	0.61	315	289	151	243	190	273	78	475	190	515	110	0.001
20%Nd	0.56	310	180	83	246	97	299	110	475	110	515	107	0.0021
25%Nd	0.81	238	140	103	249	148	290	145	480	130	509	115	0.0042

In our case, this new mode, ω_{LO3}, corresponds to the reflection minimum at ~200 cm^{-1} in the reflectivity spectrum of the CeO_{2-y} sample. From the CPP model, the plasma frequency can be determined using the following equation [16, 17]:

$$\omega_P = \frac{\omega_{LO1}\omega_{LO2}\omega_{LO3}}{\omega_{TO1}\omega_{LO2}}, \qquad (8)$$

and the frequencies of the coupled plasmon − phonon mode can be obtained by putting $\varepsilon_M = 0$ in the equation (7) [16, 17]:

$$\Omega_{LOj} = \sqrt{\omega_{LOj}^2 + \frac{1}{4}\gamma_{LOj}^2} . \qquad (9)$$

The fitting parameters obtained from the CPP model, which yielded the best fit to the reflectivity spectrum for the CeO_{2-y} sample, are presented in table 1. The best fit parameters obtained from DPP model are presented in table 2. The values of plasma frequency (ω_P) and coupled plasmon–phonon modes (Ω_{LO1}, Ω_{LO2}) obtained from equations (8) and (9) are given in table 3. The value of the high frequency dielectric constant $\varepsilon_\infty = 4$, for nanocrystalline CeO_{2-y}, was used in both applied theoretical models. The reduced chi-squared values are given in the last column of tables 1 and 2.

From the fit parameters for the CeO_{2-y} sample, it can be concluded that the eigenfrequencies of the coupled (ω_{LO1} and ω_{LO2}) plasmon-LO phonon modes are shifted to higher energies with respect to the decoupled LO phonon frequencies (ω_{LO1} and ω_{LO2}). The frequency shift and increased damping of the coupled longitudinal modes can be assigned to the strong plasmon–phonon interaction. The TO frequencies of the corresponding modes are not affected by plasmon − phonon interaction, as expected.

Further, we investigated how Nd doping influences the plasmon–phonon interaction in CeO_{2-y} nanocrystals. In the IR refelctivity spectra of Nd-doped samples, presented in figure 4, the low frequency Drude tail and the screening of the phonon modes became pronounced. Therefore, the IR spectra of doped samples were fitted by using the CPP and
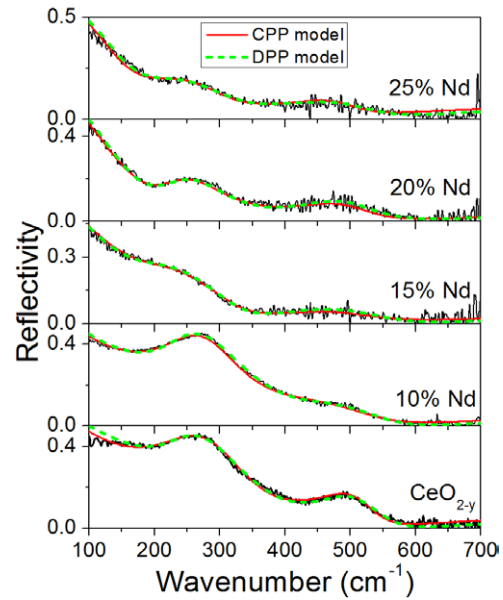
Figure 4. IR reflectivity spectra of pure and Nd-doped samples, together with theoretical fits obtained by CPP and DPP models.

DPP dielectric function models as previously in the case of the undoped CeO_{2-y} sample. In figure 4 are shown the IR reflectivity spectra of undoped and Nd-doped CeO_{2-y} nanocrystals together with theoretical fits obtained by the applied models.

The best fit parameters for Nd-doped samples, obtained from the CPP and DPP models, are given in tables 1 and 2. The materials volume fraction f_M decreased with Nd doping up to 20% of Nd, after which approaches the value for pure CeO_{2-y}. The estimated f_M is in good correlation with specific surface area (S_{BET}) measurements performed earlier on Nd-doped samples. It was found that doping with Nd cations had increased the porosity of ceria nanocrystals except for the sample doped with 25% of Nd for which the porosity decreased [12]. It is worth mentioning that the increased porosity can be also a reason for lower reflectivity of pure and

J. Phys. D: Appl. Phys. **48** (2015) 065301

M Radović *et al*

Sample	ω_P	Ω_{LO1}	Ω_{LO2}
	(±5)	(±5)	(±5)
CeO_{2-y}	347	378	546
10%Nd	349	371	554
15%Nd	300	340	560
20%Nd	308	353	549
25%Nd	264	341	551

doped nanocrystalline ceria samples compared to the reflectivity of the bulk counterpart.

From the reflectivity spectra of Nd-doped samples it can be seen that with an increase of the dopant concentration (more than 10% of Nd) the low frequency Drude tail becomes more prominent and a pronounced screening of the phonon modes takes place. Such a behavior implies that with Nd doping the concentration of the free charge carriers increases. The presence of free charge carriers can be explained by the fact that with increasing Nd content in the ceria lattice, the number of oxygen vacancies increases. According to the paper of Han *et al* [26] in nonstoichiometric ceria, with increasing vacancy concentration the amount of electrons which are localized near the vacancy sites increases too, giving rise to the formation of *F*-center defects in different charge states ([27] and the references within). These electrons are loosely bound and behave more like free charge carriers. Additionally, in the paper of Chen and Wang [29] it was shown that in Nd-doped ZnO nanowires the formation of vacancies near the Nd cations, can induce an increase of concentration of free (delocalized) electrons. In a recent paper of Choudhury *et al* [30], using Hall effect measurements, it was demonstrated that in Nd-doped ceria nanopowders, with increasing Nd content up to 4%, the number of free carriers increased. The increased free carrier concentration caused the widening of the band gap due to Burstein–Moss shift. The above mentioned theoretical and experimatal works support our finding that the plasmon − phonon interaction in Nd-doped ceria samples become stronger.

By analyzing the fitting parameters of the doped samples from tables 1 and 2, we can see that TO frequencies are not much affected by doping, whereas the eigenfrequencies of the plasmon-LO phonon coupled modes (ω_{LO1} and ω_{LO2} from table 1) are notably shifted with respect to decoupled LO modes (ω_{LO1} and ω_{LO2} from table 2). It can be also noticed that the damping parameter γ_{LO1} is significantly increased for doped samples.

In figure 5(*a*) are presented the frequencies of the coupled plasmon–phonon modes (Ω_{LO1}, Ω_{LO2}) and the decoupled LO phonon modes (ω_{LO1} and ω_{LO2} from table 2) as a function of Nd content. From figure 5(*a*) it is obvious that frequencies of the coupled modes are shifted to higher energies. Since the plasma frequency ω_P in doped samples is much closer to the frequency of the Ω_{LO1} mode than to the frequency of the Ω_{LO2} mode (see table 3), it is expected that the plasmon–phonon coupling would be stronger for the Ω_{LO1} mode. The

observed decrease of the Ω_{LO1} frequency with increasing Nd content confirms that this mode is more strongly coupled with plasmon.

In figure 5(*b*) is presented the variation of the plasma frequency ω_P with doping concentration in the case of both applied models. As can be seen from figure 5(*b*), we have obtained similar behavior of the plasma frequency from both models. The plasma frequency shifts towards lower energies as Nd concentration increases. Similar behavior of plasma frequency was found for crystalline and amorphous GaAs [31] when a metal-like phase appeared in these materials.

From the table 2 one can deduce that the plasmon mode is overdamped ($\gamma_P/\omega_P > 1/\sqrt{2}$) for the undoped CeO_{2-y} sample and samples doped up to 15% of Nd. This is a feature of conducting oxides, in particular cuprates [18]. For higher doping content (20 and 25% of Nd), the γ_P/ω_P ratio decreases ($\gamma_P/\omega_P \sim 0.5$). The decreasing trend of the γ_P/ω_P ratio is characteristic for the metallic state [18].

The plasmon dielectric function, according to the Double-damping extended Drude model, can be written in the form [18, 32]:

$$\epsilon_{pl} = \epsilon_\infty \left(1 - \frac{\omega_p^2 + i(\gamma_p - \gamma_0)\,\omega}{\omega\left(\omega - i\gamma_0\right)} \right) \tag{10}$$
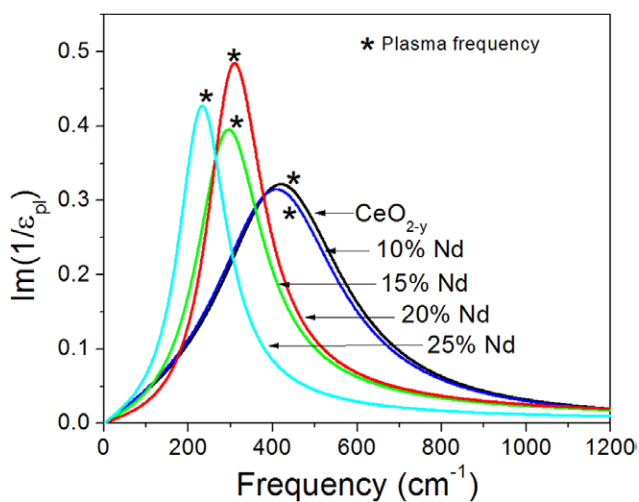
The decoupled plasmon mode structure can be extracted from the imaginary part of the inverse plasmon dielectric function, Im($1/\varepsilon_{pl}$) [32]. The decoupled plasmon mode structure with Nd doping is presented in figure 6, where the positions of the plasma frequencies (table 2) are marked with (*).

As can be seen from figure 6, with increased Nd doping the plasmon mode shifts towards lower energies, as well as the plasma frequency. The shift of the plasma frequency to lower energies is found in perovskite-type oxides like $BaPb_{1-x}Bi_xO_3$ [33] and $Ba_{1-x}K_xO_3$ [34], when these materials undergo semiconductor–to–metal transition. Bearing in mind that the plasma frequency ω_P is proportional to n_e/m^*, where n_e is the free carrier concentration and m^* is the electron effective mass, we can deduce that doping not only influences the free carrier concentration, but also changes the electron effective mass. In fact, our results for plasma frequency (plasmon mode) behavior suggest that the effective mass of free electrons increases with doping. Our conclusion is supported by the results performed on $Ba_{1-x}K_xO_3$ and InN films [34, 35] in which it was found a pronounced increase in the electron effective mass with increasing concentration of free carriers followed by a semiconductor–metal transition [34].

In order to verify how the plasmon–phonon interaction changes in thermally treated Nd-doped samples, the 15% and 25% Nd samples were calcinated in the same manner as it was done for the undoped ceria sample from figure 2. The IR refelctivity spectra of thermally treated 15% (25%) Nd-doped samples together with the corresponding untreated samples are presented in figure 7. As can be seen, the IR spectra of the calcinated samples are very similar to the bulk counterpart (figure 2), as the plasmonic background vanished and TO (LO) frequencies approached the bulk values. The disappearance of the Drude tail is expected, bearing in
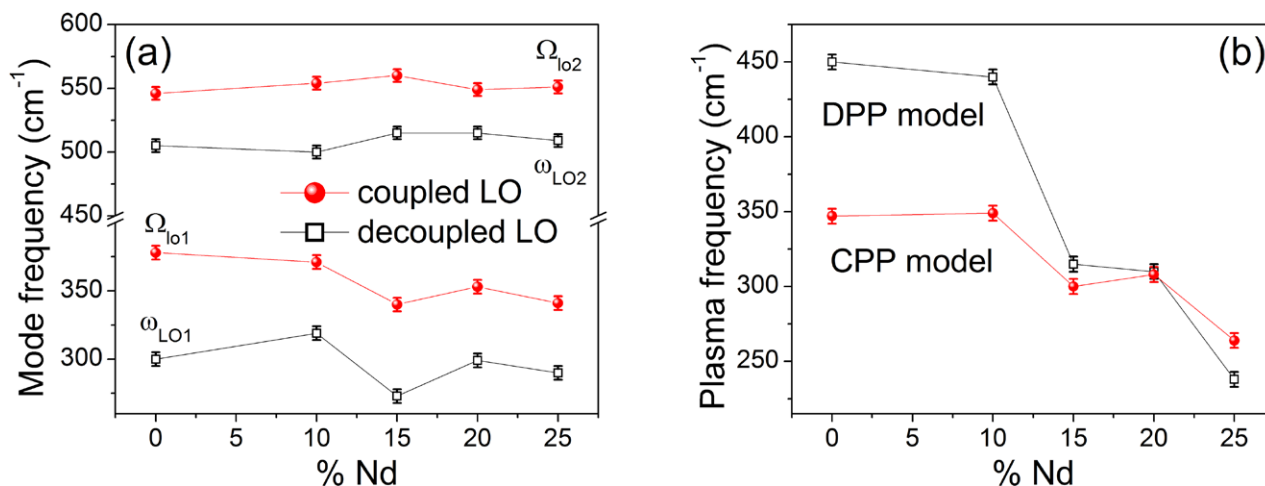
Figure 5. (*a*) Variation of the coupled and decoupled LO mode frequencies and (*b*) plasma frequency variation with Nd dopant concentration, obtained by using the CPP and DPP models.
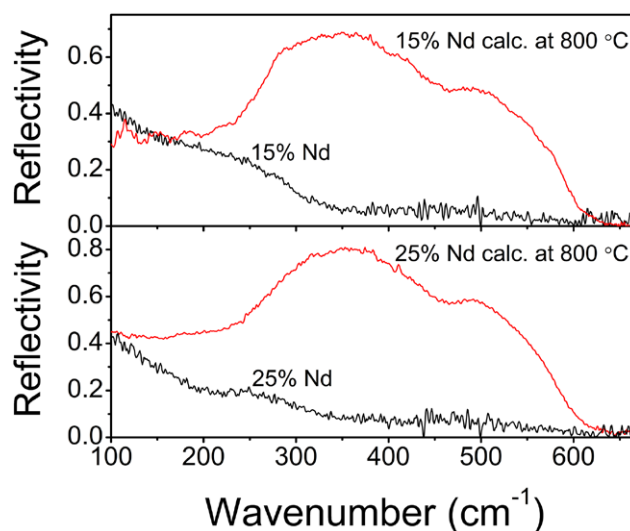

Figure 6. Decoupled plasmon mode structure in undoped and Nd doped samples. The positions of the plasma frequencies are marked with (*).

Figure 7. IR reflectivity spectra of untreated and thermally treated 15% (25%) Nd-doped samples.

mind that with temperature treatment in air, the nanosize effects become less pronounced with increasing crystallite size and that the concentration of the *F*-center defects and free carriers decreases.

Therefore, we can conclude that with increasing Nd content the plasmon–phonon interaction becomes stronger and at higher doping content (≥15% Nd) our samples undergo doping induced semiconductor–to–metallic state transition. With temperature treatment in air, it was demonstrated that the plasmonic background disappeared and the IR reflectivity spectra became similar to the bulk counterpart. The influence of doping on the n/m^* ratio and the estimation of the electron effective mass in pure and doped ceria nanocrystals will be the subject of our further work.

5. Conclusions

The influence of particle size decrease and Nd doping on the plasmon–phonon interaction in CeO_{2-y} nanocrystals

was investigated. Analysis of the infrared reflection spectra of CeO_{2-y} nanocrystalline sample revealed that with decreasing of particle size the contribution of free charge carriers becomes significant, resulting in the appearance of the plasmon mode. The plasmon mode coupled strongly with two LO modes of ceria. The appearance of more pronounced low frequency Drude tail and screening of the phonon modes suggested that doping further increased the plasmon–phonon coupling. The plasmon–phonon interaction in undoped and doped CeO_{2-y} samples was investigated by using factorized and additive models combined with Bruggeman effective medium approximation. The factorized model based on plasmon-two LO phonon interaction has proven to fit the experimental data successfully. From this model, the coupled plasmon-LO phonon frequencies and dampings were derived. The application of the additive form for the dielectric function enabled to obtain decoupled LO phonon frequencies and to deduce about the decoupled plasmon mode structure. The red-shift of the plasmon mode, plasma damping decrease and

pronounced screening of the phonon modes with increasing Nd content in ceria nanocrystalline samples pointed out that doping induced semiconductor–to–metallic state transition took place.

Acknowledgments

References

[1] Nakamatsu H, Mukoyama T and Adachi H 1995 *Chem. Phys. Lett.* **247** 168

[2] Marabelli F and Wachter P 1987 *Phys. Rev.* B **36** 1238

[3] Steele B C H and Heinzel A 2001 *Nature* **414** 345

[4] Suzuki T, Funahashi Y, Yamaguchi T, Fujishiro Y and Awano M 2008 *J. Power Sources* **183** 544

[5] Knauth P 2006 *Solid State Ion.* **177** 2495

[6] Lapplainen J, Tuller H L and Lantto V 2004 *J. Electroceram.* **13** 129

[7] Tschöpe A, Bäuerle C and Birringer R 2004 *J. Appl. Phys.* **95** 1203

[8] Chiang Y-M, Lavik E B, Kosacki I, Tuller H L and Ying J Y 1996 *Appl. Phys. Lett.* **69** 185

[9] Suzuki T, Kosacki I, Anderson H U and Colomban P 2001 *J. Am. Ceram. Soc.* **84** 2007

[10] Jasinski P, Suzuki T and Anderson H U 2003 *Sensors Actuators B-Chem.* **95** 73

[11] Matović B, Dukić J, Devečerski A, Bošković S, Ninić M and Dohčević-Mitrović Z 2008 *Sci. Sintering* **40** 63

[12] Bošković S, Djurović D, Dohčević-Mitrović Z, Popović Z, Zinkevich M, Aldinger F 2005 *J. Power Sources* **145** 237

[13] Gervais F and Servoin J-L 1993 *Phys. Rev.* B **47** 8187

[14] Gonzalez R J, Zallen R and Berger H 1997 *Phys. Rev.* B **55** 7014

[15] Gervais F 1983 *Infrared and Millimeter Waves* vol 8 ed K J Button (New York: Academic) pp 279–339

[16] Kukharskii A A 1973 *Solid State Commun.* **13** 1761

[17] Kim O K and Spitzer G 1979 *Phys. Rev.* B **20** 3258

[18] Gervais F 2002 *Mater. Sci. Eng.* R **39** 29

[19] Webman I, Jortner J and Cohen M H 1977 *Phys. Rev.* B **15** 5712

[20] Spanier J E and Herman I P 2000 *Phys. Rev.* B **61** 10437

[21] Williamson G K and Hall W 1953 *Acta Metall.* **1** 22

[22] Zhou X-D and Huebner W 2001 *Appl. Phys. Lett.* **79** 3512

[23] Santha N I, Sebastian M T, Mohanan P, Alford N McN, Sarma K, Pullar R C, Kamba S, Pashkin A, Samukhina P and Petzelt J 2004 *J. Am. Ceram. Soc.* **87** 1233

[24] Chen Z W, Lai J K L and Shek C H 2006 *J. Non-Cryst. Solids* **352** 3285

[25] Skorodumova N V, Simak S I, Lundqvist B I, Abrikosov I A and Johansson B 2002 *Phys. Rev. Lett.* **89** 166601

[26] Han X, Lee J and Yoo H I 2009 *Phys. Rev.* B **79** 100403(R)

[27] Aškrabić S, Dohčević-Mitrović Z D, Araújo V D, Ionita G Jr, de Lima M M and Cantarero A 2013 *J. Phys. D: Appl. Phys.* **46** 495306

[28] Popović Z V, Dohčević-Mitrović Z D, Paunović N and Radović M 2012 *Phys. Rev.* B **85** 014302

[29] Chen Q and Wang J 2013 *Phys. Chem. Chem. Phys.* **15** 17793

[30] Choudhury B and Choudhury A 2013 *Curr. Appl. Phys.* **13** 217

[31] Callan J P, Kim A M-T, Roeser C A D and Mazur E 2001 *Phys. Rev.* B **64** 073201

[32] Baumard J-F and Gervais F 1977 *Phys. Rev.* B **15** 2316

[33] Tajima S, Uchida S, Masaki A, Takagi H, Kitazawa K and Tanaka S 1985 *Phys. Rev.* B **32** 6302

[34] Goodenough J B and Cooper S L 2001 *Localized to Itinerant Electronic Transition in Perovskite Oxides* vol 98 ed J B Goodenough (Heidelberg: Springer-Verlag) pp 184–5

[35] Wu J, Walukiewicz W, Shan W, Yu K M, Ager J W III, Haller E E, Lu H and Schaff W J 2002 *Phys. Rev.* B **66** 201403

Nanocrystalline CeO$_{2-\delta}$ as Effective Adsorbent of Azo Dyes

Nataša M. Tomić,[†] Zorana D. Dohčević-Mitrović,*,[†] Novica M. Paunović,[†] Dušan Ž. Mijin,[‡] Nenad D. Radić,[§] Boško V. Grbić,[§] Sonja M. Aškrabić,[†] Biljana M. Babić,[‖] and Danica V. Bajuk-Bogdanović[⊥]

[†]Institute of Physics, University of Belgrade, Pregrevica 118, 11080 Belgrade, Serbia

[‡]Faculty of Technology and Metallurgy, University of Belgrade, Karnegijeva 4, 11000 Belgrade, Serbia

[§]IChTM, Department of Catalysis and Chemical Engineering, University of Belgrade, Njegoševa 12, 11000 Belgrade, Serbia

[‖]Institute of Nuclear Sciences "Vinča", University of Belgrade, 11001 Belgrade, Serbia

[⊥]Faculty of Physical Chemistry, University of Belgrade, Studentski Trg 12-16, 11000 Belgrade, Serbia

S *Supporting Information*

ABSTRACT: Ultrafine CeO$_{2-\delta}$ nanopowder, prepared by a simple and cost-effective self-propagating room temperature synthesis method (SPRT), showed high adsorption capability for removal of different azo dyes. Batch type of adsorption experiments with fixed initial pH value were conducted for the removal of Reactive Orange 16 (RO16), Methyl Orange (MO), and Mordant Blue 9 (MB9). The equilibrium adsorption data were evaluated using Freundlich and Langmuir isotherm models. The Langmuir model slightly better describes isotherm data for RO16 and MO, whereas the Freundlich model was found to best fit the isotherm data for MB9 over the whole concentration range. The maximum adsorption capacities, determined from isotherm data for MO, MB9, and RO16 were 113, 101, and 91 mg g^{-1} respectively. The adsorption process follows the pseudo-second-order kinetic model indicating the coexistence of chemisorption and physisorption. The mechanism of azo dye adsorption is also discussed.
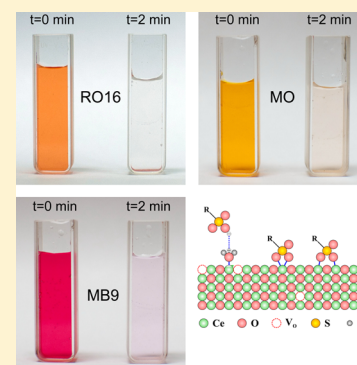
INTRODUCTION

Synthetic dyes are widely used in a number of industries such as textile and leather industries, paper printing, cosmetics, and pharmaceuticals. It is estimated to be more than 10 000 commercially available dyes with over 7×10^5 tons of dyestuff produced annually.[1,2] Azo dyes represent about 60−70% of the dyes used in the textile industry. Some of them show aquatic toxicity or allergenic effects, and under reductive conditions they produce aromatic amines that are carcinogenic.[2,3] Azo dyes represent a class of synthetic, colored, organic compounds, which are characterized by the presence of one or more azo bonds. These dyes belong to the most toxic ones compared to other forms of dyes.[1] Large quantities of these dyes (10−15% of the total world production) are released into the wastewater (typical concentration 10−200 mg L^{-1}), the presence of which poses a major threat to the aquatic organisms as well as animals and humans because of their nonbiodegradability, toxicity, and potential carcinogenic nature.[4−6]

Dye removal from textile effluents is a major environmental problem because of the difficulty to treat such streams by conventional physicochemical and biological treatment methods. The methods such as filtration, coagulation, flocculation, ion exchange, and photocatalytic degradation are unsatisfactory for wastewater treatment because they are expensive and may produce more toxic byproducts. Among the various available water treatment techniques, adsorption is the most reliable and efficient technique for dye removal, despite the fact that usually

the adsorbent needs to be regenerated, which increases the cost of the process and can be a time-consuming procedure. The liquid phase adsorption has been shown to be an efficient way for removing the suspended solids, organic matter, and oil from aqueous solutions. Adsorption appears to offer the best perspective over all the other treatments because it can handle fairly large flow rates, producing a high quality effluent and does not result in the formation of harmful substances, such as ozone and free radicals which are present during the photodegradation process using UV.

Activated carbon is the most widely used adsorbent for this purpose, because it has a high surface area and high capacity for adsorption of organic matter, but its use is limited because of its high production cost and significant problems with the regeneration of the spent activated carbon.[7,8] A great variety of low-cost biomass materials[9−13] have been used to produce activated carbon for the treatment of wastewaters. In recent years, low cost agricultural wastes have been investigated as potential biosorbents,[14] but most of these cheap substitutes have to be subjected to the process of carbonization which increases process costs. Therefore, there is still a high demand for cheaper adsorbent materials with high adsorption capacity.

Nowadays, nanoscience and nanotechnology play important role in environmental protection. There is a strong need to develop simple and economical methods for producing nanomaterials with higher adsorption rates which can efficiently remove various contaminants. Nanomaterials with high surface area are the most promising candidates as adsorbents in organic dye removal.[5,15−19]

Among various metal oxide semiconductors, CeO_2 is widely used in many application areas such as catalysis, fuel cells, sensors, and UV shielding, owing to its outstanding physical and chemical properties. The application of ceria as effective sorbent is not so often studied. There are few reports in which it is demonstrated that ceria is effective sorbent for the removal of high toxic pollutants such as[17] As(V) and Cr(VI) and azo dyes such as Congo Red[18] or Acid Orange[4] from water. The adsorption experiments, performed to remove Reactive Orange 16 and Methyl Orange from wastewaters, mainly used as adsorbent waste biomass,[20] various types of sludge, and biosorbents.[1,13,14,20−26] Although most of these sorbents were relatively cheap and effective in dye removal, they showed modest and rarely high sorption capacities. On the other side, to the best of our knowledge there is almost no study which concerns the adsorption of Mordant Blue 9.

Herein we present the adsorption capability of ceria nanoparticles for removal of different azo dyes such as Reactive Orange 16, Methyl Orange, and Mordant Blue 9. Ceria nanopowder, obtained by a simple and cost-effective method, has shown very high efficiency toward azo dye removal and has been proven to be a promising alternative for wastewater treatment.

■ EXPERIMENTAL SECTION

1. Materials Preparation. The ultrafine $CeO_{2−δ}$ nanopowder was fabricated via a simple and economical self-propagating room temperature synthesis method (SPRT).[27,28] Starting reactants were cerium nitrate hexahydrate ($Ce(NO_3)_3·6H_2O$) (Acros Organics 99.5%) and sodium hydroxide (Carlo Erba). Hand-mixing of nitrate with NaOH was performed in alumina mortar for ∼10 min until the mixture turned light brown. After being exposed to air for 4 h, the mixture was suspended in water. Rinsing of $NaNO_3$ was performed in a centrifuge at 3500 rpm for 10 min. This procedure was performed four times with distilled water and twice with ethanol. The precipitate was dried at 60 °C overnight. The reaction based on the self-propagating room temperature method can be written as follows:

$$2[(Ce(NO_3)_3·6H_2O] + 6NaOH + (1/2 − δ)O_2$$
$$→ 2CeO_{2−δ} + 6NaNO_3 + 15H_2O \qquad (1)$$
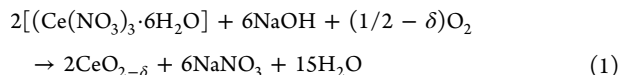
2. Characterization Methods. X-ray powder diffraction (XRD) data of the sample were collected on a Siemens D-5000 diffractometer with Cu Kα radiation over the 2θ range from 20° to 80°. Atomic force microscope (AFM) images were taken using the Omicron B002645 SPM PROBE VT AFM 25 instrument in noncontact mode at room temperature. The powder specific surface area of the sample was calculated following the multipoint BET procedure on the Quantachrome ChemBet-3000 setup. The pore size distribution was derived from nitrogen adsorption-desorption isotherm obtained at 77 K. The infrared (IR) transmission spectra of $CeO_{2−δ}$ pellets before and after dye adsorption were measured on a Thermo Nicolet 6700 Fourier transform infrared spectrophotometer at room temperature. Micro-Raman spectra were collected in the backscattering config-uration using the TriVista 557 Raman system. The 488 nm line of an Ar^+/Kr^+ mixed gas laser was used as an excitation source. In order to avoid sample heating, the incident laser power on the samples was kept below 20 mW. Surface charge (zeta potential) of ceria nanoparticles at different pH was measured using Zetasizer Nano ZS90 (Malvern

Instruments) apparatus. Suspensions were prepared using deionized water as dispersing medium and were ultrasonicated for 15 min prior to the measurements using an ultrasonic bath. The pH values of suspensions were adjusted by adding HCl and NaOH solutions to the starting suspension of $CeO_{2−δ}$ nanopowder.

3. Adsorption Experiments. The adsorption experiments were carried out as batch tests in a magnetically stirred thermostated glass vessel with three different concentrations (50, 100, and 200 mg $L^{−1}$) of Reactive Orange 16 (RO16), Methyl Orange (MO), and Mordant Blue 9 (MB9). All measurements were performed at initial pH values of 6.2, 6, and 4.6 for MO, MB9, and RO16 dye solutions, respectively. The suspensions were stirred for 2 min at room temperature in the dark. The adsorption capacity (for the 200 mg $L^{−1}$ concentration of dyes) of coconut-based powdered activated carbon (PAC), of large specific surface area (1200 m^2/g), was determined for comparison. The working volume (25 mL) and the quantity of ceria nanopowders and PAC (50 mg) were kept fixed in all adsorption experiments. At fixed contact time, the samples were taken, centrifuged, and analyzed on a Shimadzu 1700 UV-vis spectrophotometer within the spectral range where maximum absorption for each dye occurs. In Table S1 (see the Supporting Information) are given the chemical structure and the wavelength of maximal absorption ($λ_{max}$) for each dye.

■ RESULTS AND DISCUSSION

The powder XRD pattern of $CeO_{2−δ}$ nanopowder is presented in Figure 1a. Diffraction peaks corresponding to cubic fluorite structure are clearly observed. All XRD peaks are broadened, indicating that the crystallite size is within the nanometer range. The average size of $CeO_{2−δ}$ nanocrystals, estimated by the Wiliamson-Hall method,[29] is about 6 nm. The noncontact AFM image of $CeO_{2−δ}$ sample (Inset of Figure 1b) shows small and agglomerated nonporous $CeO_{2−δ}$ particles. The pores between agglomerated $CeO_{2−δ}$ nanoparticles are also visible on the AFM image. Particle size distribution obtained from the AFM image of $CeO_{2−δ}$ sample is presented in Figure 1b, and it was modeled by asymmetric double sigmoidal function. The average particle size is 11.4 nm.

To determine the surface area and pore size distribution, nitrogen adsorption−desorption isotherms at 77 K were recorded, and these are given in the inset of Figure 1c. According to the IUPAC classification,[30] the nitrogen adsorption−desorption isotherm is attributed to the Langmuir IV type. The pore size distribution was determined from the desorption branch of the isotherms using the BJH (Barrett−Joyner−Halenda) method and is shown in Figure 1c. It can be observed that the sample has bimodal pore size distribution in the mesoporous area with the first mode peak around 2 nm and the second one in the range 3−4 nm. The value of the BET specific surface area (S_{BET}) is 74 m^2 $g^{−1}$.

Further, we examined the performances of $CeO_{2−δ}$ nano-powder as a potential adsorbent for removal of RO16, MO, and MB9. The adsorption measurements were carried out with three different concentrations of the dye solutions (50, 100, and 200 mg $L^{−1}$), and absorption spectra of the dye solutions were collected after certain time intervals. The UV−vis spectrum of RO16 is given in Figure 2a (blue line) for the concentration of 50 mg $L^{−1}$. The absorption spectrum of RO16 in the presence of $CeO_{2−δ}$ nanoparticles after 2 min is also presented in Figure 2a (red line). As can be seen, the RO16 characteristic bands decreased promptly, indicating that RO16 was removed from the solution. The corresponding photo image (right panel of Figure 2a) shows that the solution is almost colorless. The absorption spectra of the MO and MB9 before (blue line) and after 2 min (red line) in the presence of $CeO_{2−δ}$ nanoparticles are given in Figure 2b,c. Absorption spectra of these two dye
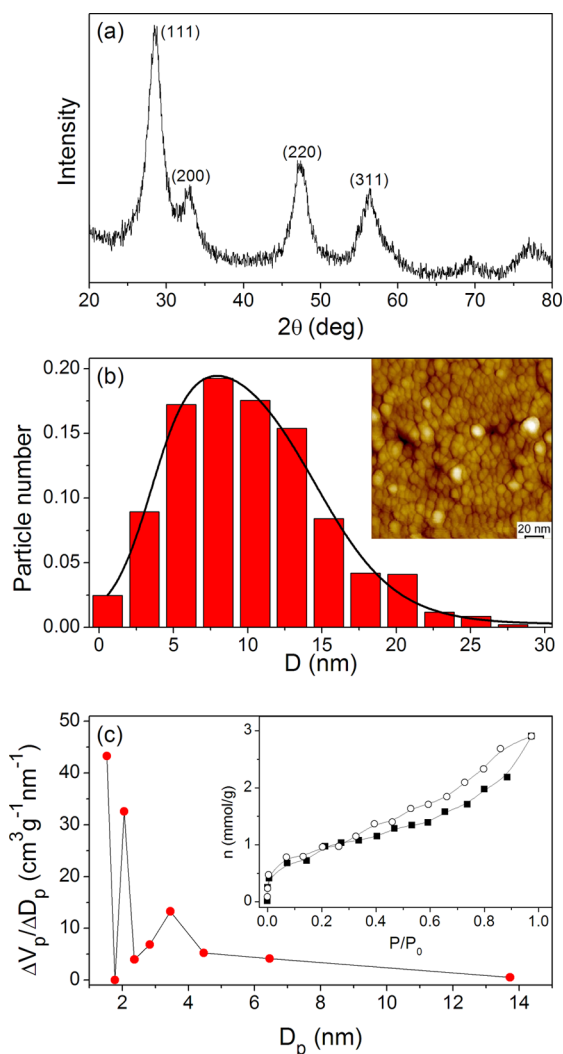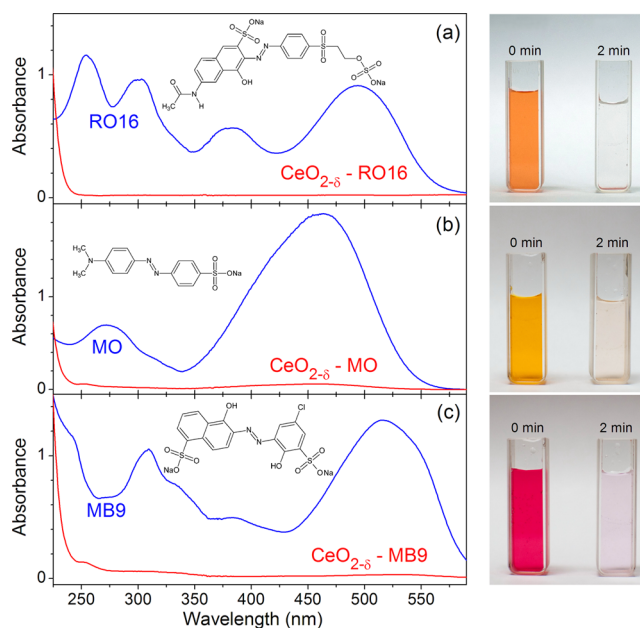
Figure 1. XRD spectrum (a), particle size distribution obtained from AFM (b), and pore size distribution curve obtained from the desorption branch of the isotherm (c) for CeO$_{2-\delta}$ nanopowder. Insets present the AFM image and the nitrogen adsorption—desorption isotherm of CeO$_{2-\delta}$ nanopowder.


Figure 2. Absorption spectra with corresponding photo images of (a) RO16, (b) MO, and (c) MB9 dye solutions (50 mg L^{-1}) before and 2 min after introducing CeO$_{2-\delta}$ nanoparticles (2 g L^{-1}). Mass of adsorbent = 50 mg; solution volume = 25 mL.

solutions after 2 min showed that the dyes were present in a very low concentration. From the photo images (right panel of Figure 2b,c), it can be noticed that the solutions were almost colorless after 2 min. The experiment was repeated with an increased concentration for all three dyes (100 mg L^{-1}), and the obtained results were similar.

The concentration of RO16 in the solution was further increased to 200 mg L^{-1}. The absorption spectra of RO16 dye solution in the presence of CeO$_{2-\delta}$ nanoparticles, presented in Figure S1a (Supporting Information), demonstrate that CeO$_{2-\delta}$ quickly removes the RO16 from the solution. After 40 min, the equilibrium state was reached. The adsorption measurements were also performed on the solutions of MO and MB9 (200 mg L^{-1}) in the presence of CeO$_{2-\delta}$ nanopowder, in order to compare the efficiency of adsorption process onto ceria nanopowder for all three dyes. The adsorption capacity of CeO$_{2-\delta}$ nanopowder was determined from the mass balance relationship:[1,13,15,22]

$$q_e = \frac{(C_0 - C_e)V}{m} \qquad (2)$$

where q_e represents the amount of dye adsorbed per unit mass of adsorbent (mg g^{-1}), C_0 and C_e are the initial and equilibrium liquid phase concentrations (mg L^{-1}), respectively, V is the volume of the solution (L), and m is the mass (g) of CeO$_{2-\delta}$ used.

The adsorption rate and the amount of adsorbed dye with contact time for the solutions of RO16, MO, and MB9 (200 mg L^{-1}) are illustrated in Figure 3a,b. As can be noticed from Figure 3, for all three curves, it is characteristic that the adsorption process is rapid in the initial stage, whereas in the later stage it becomes much slower. The adsorption rate for RO16 was higher at the beginning, but after 60 min much better elimination of MO from the solution was observed, whereas the adsorption rate of MB9 was still lower. The equilibrium was achieved after 40 (60) min for RO16 (MO), whereas for MB9 it was achieved after 180 min. The adsorption capacities of CeO$_{2-\delta}$ nanopowder in the case of MO, MB9, and RO16 were 100, 94, and 91 mg g^{-1}, respectively.

Further, the adsorption capacities of CeO$_{2-\delta}$ nanopowder and activated carbon were compared. The adsorption capacity of commercial activated carbon (50 mg) is presented in Figure 4 for MO (a) , RO16 (b), and MB9 (c) solutions (200 mg L^{-1}). In the case of MO dye solution, it can be noticed that at the beginning of the adsorption process the activated carbon was slightly faster than CeO$_{2-\delta}$ nanopowder and reached the equilibrium state after 20 min. After 60 min, both curves overlapped. In the case of RO16 dye solution, activated carbon was much slower compared to CeO$_{2-\delta}$. After 40 min, CeO$_{2-\delta}$ nanopowder reached equilibrium and eliminated almost 90% of RO16 from the solution, whereas activated carbon needed 2 h to reach the final adsorption capacity of 85 mg g^{-1} which was still lower than that of ceria nanopowder (91 mg g^{-1}). The adsorption capability of CeO$_{2-\delta}$ for MB9 is lower than that for activated carbon, although after 2 h the final adsorption capacities were comparable.
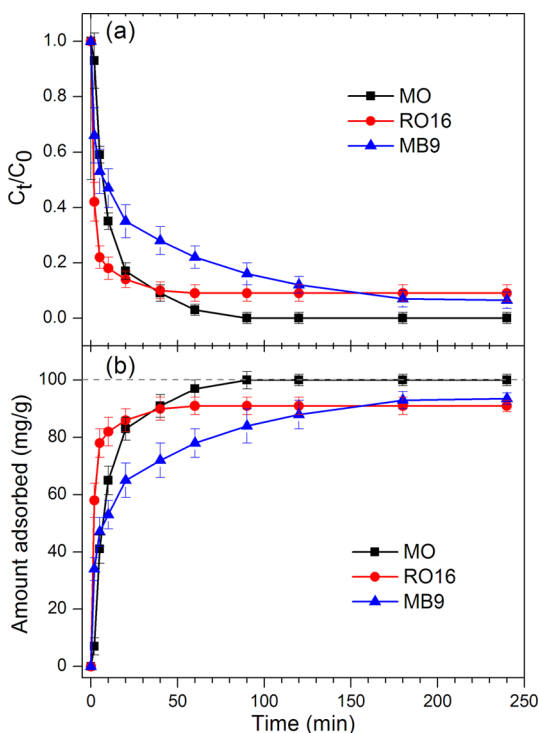
Figure 3. Adsorption rate (a) and amount of adsorbed dyes (b) for the solutions of MO, RO16, and MB9 (200 mg L^{-1}) in the presence of $CeO_{2-\delta}$ nanopowder. Mass of adsorbent = 50 mg; solution volume = 25 mL.

In Figure 5a−c are shown the IR transmission spectra of pure dyes and $CeO_{2-\delta}$ nanopowders after dye adsorption. For comparison, the IR spectrum of pure $CeO_{2-\delta}$ nanopowder is also given in Figure 5a−c.

The IR spectra of pure dyes have some common characteristic bands.[4,6,31−36] The bands at 1040/1120 cm^{-1} in MO, 1054/1139 cm^{-1} in RO16, and 1044/1136 cm^{-1} in MB9 originate from the symmetric stretching vibrations of the SO_3^{-} group ($\nu_s(SO_3^{-})$). The band at 1204 cm^{-1} in MO, 1236 cm^{-1} in RO16, and 1190 cm^{-1} in MB9 represents the asymmetric stretching vibrations of the SO_3^{-} group ($\nu_{as}(SO_3^{-})$). The band at 1368 cm^{-1} in MO and 1372 cm^{-1} in RO16 belongs to the C−N stretching vibrations. The bands at 1422, 1410, and 1409 cm^{-1} in MO, RO16, and MB9, respectively, are assigned to the N=N stretching vibrations. The bands at 1520/1608 cm^{-1} in MO and 1586 cm^{-1} in RO16 are from the aromatic ring stretching vibrations. The band at 1672 cm^{-1} in the spectra of RO16 originates from the stretching vibrations of the carbonyl C=O group.

In the IR spectrum of MO dye adsorbed on $CeO_{2-\delta}$ (shown in Figure 5a), the IR bands of the MO dye are of much lower intensity. The pronounced changes of the IR bands characteristic for sulfonate stretching vibration mode are observed. The $\nu_{as}(SO_3^{-})$ band at 1204 cm^{-1} is much weaker after MO adsorption on $CeO_{2-\delta}$ and shifted to ~1193 cm^{-1} (marked with arrow in Figure 5a). The $\nu_s(SO_3^{-})$ band at 1040 cm^{-1} in MO is slightly shifted to 1034 cm^{-1} (marked with arrow in Figure 5a) in the CeO_2−MO spectrum, the intensity of which is much lower after adsorption. All these changes can indicate that the sulfonate group is strongly involved in the adsorption of MO onto $CeO_{2-\delta}$.[34] In the IR spectrum of RO16 adsorbed onto $CeO_{2-\delta}$ (Figure 5b), a significant intensity decrease of the IR bands at 1054/1139 and 1500 cm^{-1}, characteristic for SO_3^{-}
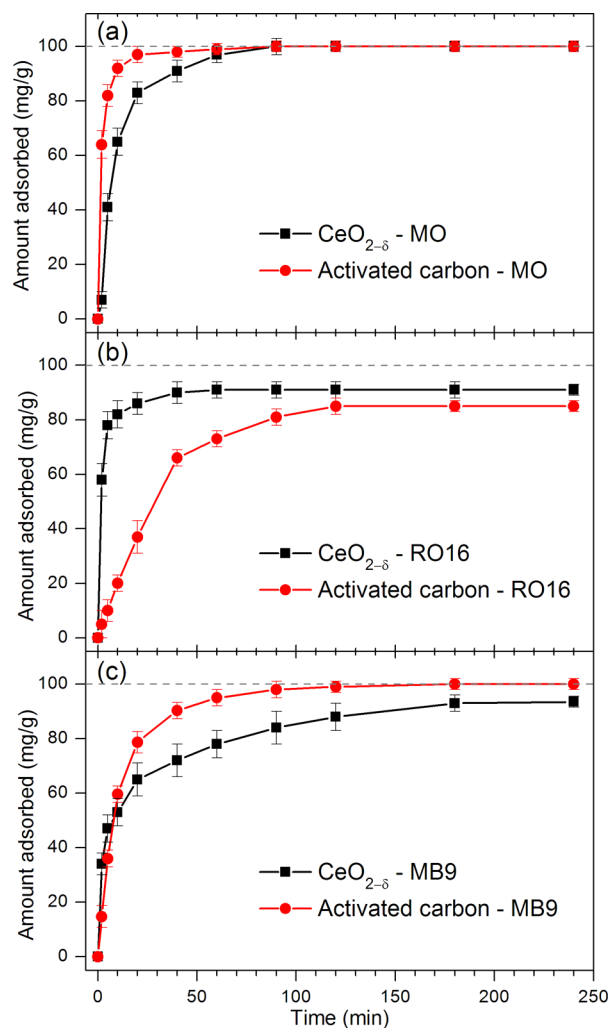

Figure 4. Comparison of adsorption capacities between $CeO_{2-\delta}$ nanopowder and activated carbon in the case of (a) MO, (b) RO16, and (c) MB9 dye solutions (200 mg L^{-1}). Mass of adsorbent = 50 mg; solution volume = 25 mL.

group and N−H bending vibrations,[4,6] is observed too. Many other bands which belong to pure RO16 dye are much weaker or barely visible in the $CeO_{2-\delta}$−RO16 spectrum, as for instance the band at 1410 cm^{-1} for N=N stretching vibrations. The carbonyl C=O peak at 1672 cm^{-1} in the IR spectrum of RO16, is almost absent from the $CeO_{2-\delta}$−RO16 spectrum. The $\nu_s(SO_3^{-})$ band is shifted from 1139 to 1136 cm^{-1} in the $CeO_{2-\delta}$−RO16 spectrum. In the IR spectrum of $CeO_{2-\delta}$−MB9 (Figure 5c), a major decrease of the MB9 band intensity is observed and the slight shift of the asymmetric $\nu_s(SO_3^{-})$ band is barely visible (marked with arrow in Figure 5c). All this indicates that RO16 and MB9 are also strongly adsorbed onto the $CeO_{2-\delta}$ surface. In Figure 5d is presented the IR transmission spectrum of pure $CeO_{2-\delta}$ in the extended spectral range. As can be seen, strong bands near 3400 and 1620 cm^{-1} are attributed to the adsorbed H_2O and hydroxyls.[37,38] The absorption band at 1384 cm^{-1} originates from CO_2 molecule vibrations.

Raman spectra, obtained on $CeO_{2-\delta}$ nanopowder before and after dye adsorption, are presented in Figure 6 and are consistent with the IR measurements. In the Raman spectra of nanocrystalline $CeO_{2-\delta}$ treated with dyes, besides the F_{2g} mode of pure $CeO_{2-\delta}$ positioned at ~456.5 cm^{-1} and the mode at
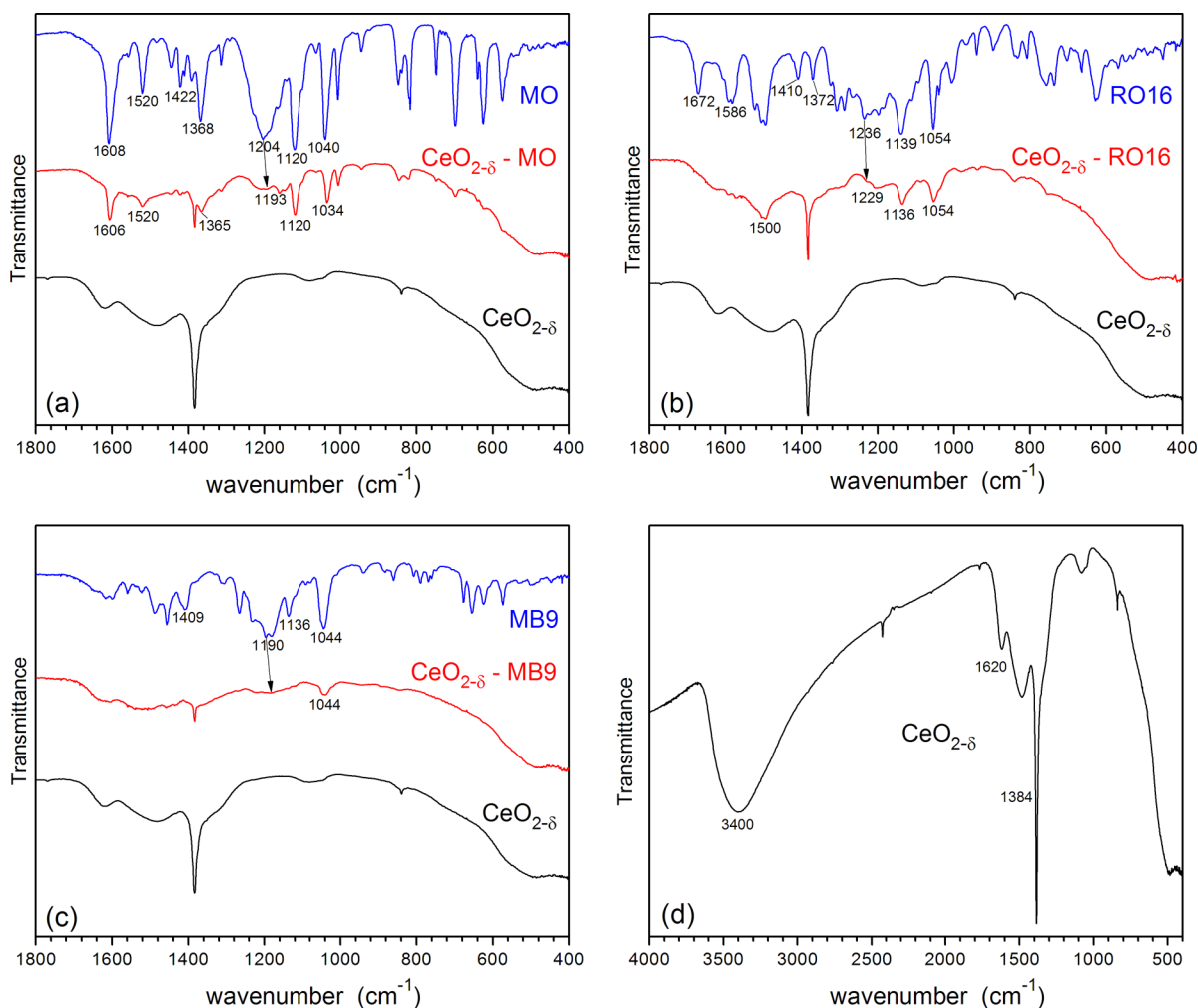
Figure 5. IR transmission spectra of (a) MO, (b) RO16, and (c) MB9 adsorbed on $CeO_{2-\delta}$ together with the transmission spectra of pure dyes and $CeO_{2-\delta}$ nanopowder. (d) IR transmission spectrum of $CeO_{2-\delta}$ nanopowder in the extended range.
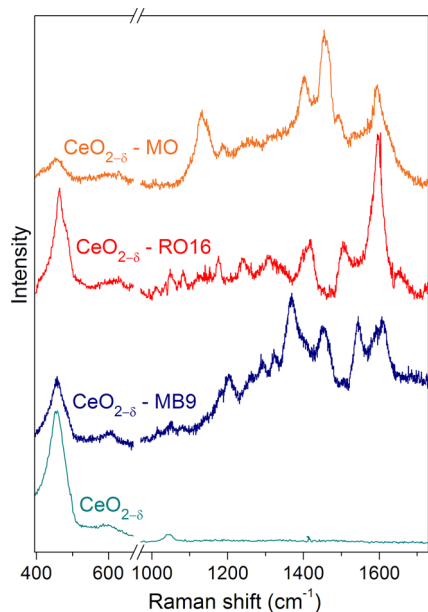
Figure 6. Room temperature Raman spectra of $CeO_{2-\delta}$ nanopowder before and after adsorption of MO, RO16, and MB9 dyes.

$\sim$600 cm^{-1} which belongs to intrinsic oxygen vacancies,[39] additional modes are observed. These new modes correspond to the vibrations of different atomic groups of dye molecules, such as $-N=N-$, $-C=O$, $-S=O$, $-O-H$, and aromatic ring vibrations. The most prominent mode frequencies deduced from the spectra of ceria treated with MO, RO16, and MB9 are summarized in the Table S2 (see the Supporting Information). As the majority of the atomic group vibrations characteristic for the dye molecules in question are observed in the Raman spectra of dyed ceria nanopowder, it can be concluded that in all three cases the adsorption of dye molecules took place.

The IR and Raman spectra unambiguously showed that MO, RO16, and MB9 are adsorbed on $CeO_{2-\delta}$ surface. In addition, from the IR spectra of three azo dyes adsorbed on $CeO_{2-\delta}$ nanopowders, we concluded that ν_{as} and ν_s bands of sulfonate groups are affected considerably. The intensity ratio of these bands ($\nu_{as}(SO_3^-)/\nu_s(SO_3^-) = 0.4$) for adsorbed MO onto ceria is different from the same ratio in the spectrum of isolated MO ($\nu_{as}(SO_3^-)/\nu_s(SO_3^-) = 0.9$). The changes of the ν_{as} and ν_s band intensities of sulfonate groups are also registered in the IR spectra of adsorbed RO16 and MB9 onto ceria. It is further worth mentioning that the frequency difference $\Delta\nu_{as-s}$ ($\nu_{as}(SO_3^-) - \nu_s(SO_3^-)$) in the MO, RO16, and MB9 spectra is higher than that in the corresponding spectra of adsorbed dyes on ceria (see Figure 5). This is characteristic of the

bidentate type coordination according to the Deacon and Phillips[40] empirical rule and the work of Bauer et al.,[41] formed when OH groups situated on the surface metal cations are substituted with oxygen atoms from azo dyes. Ji et al.[4] noticed similar changes to ours in the IR spectra of acid orange adsorbed onto CeO_2 surface and proposed that a bidentate type bridge is formed between sulfonate group and Ce^{4+} cations. According to the observed changes in the IR spectra of MO, RO16, and MB9 adsorbed on $CeO_{2-\delta}$ nanopowder, it is reasonable to assume that all three dyes form a bidentate type bridge on the ceria surface, where two oxygen atoms of the SO_3^- group are bound to one or two Ce^{4+} cations in a process that involves the substitution of surface coordinated OH groups on Ce^{4+} cations with oxygen atoms from azo dyes.

Another very important factor for dye removal concerns the capability of $CeO_{2-\delta}$ nanopowders to easily form oxygen vacancies on the surface which accompany functional groups. The surface functional groups can interact with dye molecules via hydrogen bonds and/or electrostatic forces promoting the adsorption of dye molecules. The first principle density functional theory calculations performed by Yang et al.[42] have shown that, in oxygen deficient ceria, the adsorbed water molecules prefer to decompose near the oxygen vacancy site, forming surface hydroxyls, where H atoms are bonded with surface oxygen atoms. Therefore, they concluded that in reduced ceria both adsorbed H_2O and surface hydroxyls coexist. Their calculations are in good agreement with experimental work of Kundakovic et al.[43] performed on oxidized and reduced CeO_2 thin films, who detected surface hydroxyls only in reduced ceria films.

Having in mind that our ceria is oxygen deficient, it is reasonable to assume that hydroxyl groups, already observed in the IR spectra, are present on the surface of $CeO_{2-\delta}$ nanopowder. The experimental determination of the pH value at zero point charge (pH_{ZPC}) revealed that $CeO_{2-\delta}$ has $pH_{ZPC} = 6.3$ (Figure S2 in the Supporting Information). As pH values of the dye solutions are lower than pH_{ZPC} of $CeO_{2-\delta}$ (see section 3 in Experimental Section), $CeO_{2-\delta}$ as adsorbent acts as a positive surface. The electrostatic attraction between ceria nanoparticles and negatively charged dye ions is an operable mechanism. In that case, the ceria surface hydroxyls are protonated:

$$Ce-OH + H^+ \rightarrow Ce-OH_2^+ \quad (3)$$
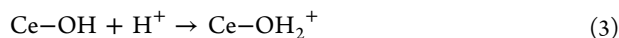
In aqueous solution, the sulfonate groups ($R-SO_3Na$) dissociate and are converted to anionic dye ions. The adsorption process further proceeds due to the electrostatic attraction between these two oppositely charged ions:
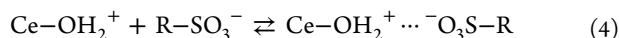
$$Ce-OH_2^+ + R-SO_3^- \rightleftarrows Ce-OH_2^+ \cdots {}^-O_3S-R \quad (4)$$

Illustration of the adsorption mechanisms between dye molecules and $CeO_{2-\delta}$ adsorbent is shown in Figure 7.

As we stated earlier, the adsorption rate at the beginning of the process (presented in Figure 3a) is higher for RO16 than for MO and MB9. The difference in removal efficiency between three dyes can be explained by the fact that the pH value of the RO16 solution is close to the pH value where ceria net positive charge surface has maximum, whereas the pH values of MO and MB9 dye solutions are close to the pH_{ZPC} value of $CeO_{2-\delta}$. Therefore, the electrostatic interaction between RO16 dye molecules and $CeO_{2-\delta}$ at the beginning will be stronger than that for MB9 and MO. It is important to emphasize that
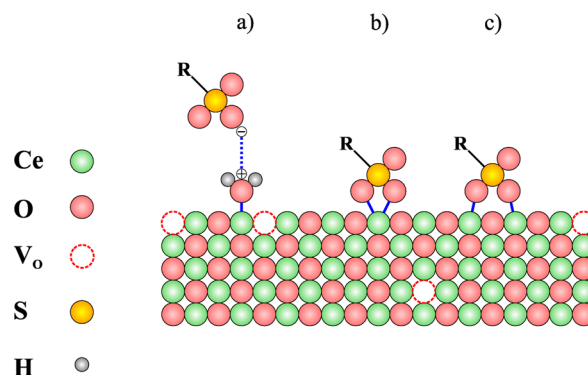

Figure 7. Schematic representation of RO16, MO, and MB9 adsorption on $CeO_{2-\delta}$ surface. (a) Electrostatic interaction between protonated ceria surface and sulfonate group in the dye molecule; (b, c) bidentate type structures between sulfonate group and Ce^{4+} cations.

sulfonic groups, which dissociate in aqueous solution and convert to $R-SO_3^-$ anions, are negatively charged even at higher acidic solutions, because their pK_a values are lower than zero.[44] Finally, the interaction between OH groups on the surface of $CeO_{2-\delta}$ and NH groups of the RO16 is also a possible mechanism for RO16 dye adsorption[19] and can explain the higher adsorption rate in the case of RO16 at the beginning of the process.

The study of the adsorption equilibrium isotherm is helpful in determining the maximum adsorption capacity of adsorbent for given adsorbate. These isotherms relate the dye uptake per unit mass of adsorbent, q_e, to the equilibrium liquid phase concentration C_e. In Figure 8 are presented the adsorption isotherms for RO16 (a), MO (b), and MB9 (c) dye solutions, measured at room temperature. Adsorption isotherms were analyzed according to Langmuir and Freundlich models in order to determine the best-fit model. Langmuir's model predicts the monolayer coverage of the adsorbate, assuming that all adsorption sites are identical and energetically equivalent, whereas the Freundlich's model assumes the adsorption on heterogeneous surface composed of nonidentical adsorption sites with different energy of adsorption. The isotherm equations and isotherm parameters for both models are listed in Supporting Information Table S3.

The adsorption isotherms of RO16 and MO from Figure 8a,b can be fitted by both the Langmuir and Freundlich equations. Both models give reasonable good fit in the case of MO and RO16, although the values of correlation coefficients (Supporting Information Table S3) are slightly higher for the Langmuir isotherm. The sorption data of MB9 are much better represented by the Freundlich model (Figure 8c and Supporting Information Table S3) which expresses adsorption in a multilayer manner on an energetically heterogeneous surface.

The parameter $1/n$ from the Freundlich equation characterizes the heterogeneity of the site energies and the adsorption intensity, that is, the degree of nonlinearity of adsorption isotherm. In their work, Tseng and Wu[45] have defined a favorable level for the adsorption isotherm curves and gave a classification for the values of parameter $1/n$. Despite the fact that the Langmuir model seems more suitable to describe the sorption of MO and RO16 onto ceria, according to Tseng's classification, the parameter $1/n$ (listed in Supporting Information Table S3) lies in the range of strongly favorable (for RO16 and MO) and favorable (for MB9) adsorption.
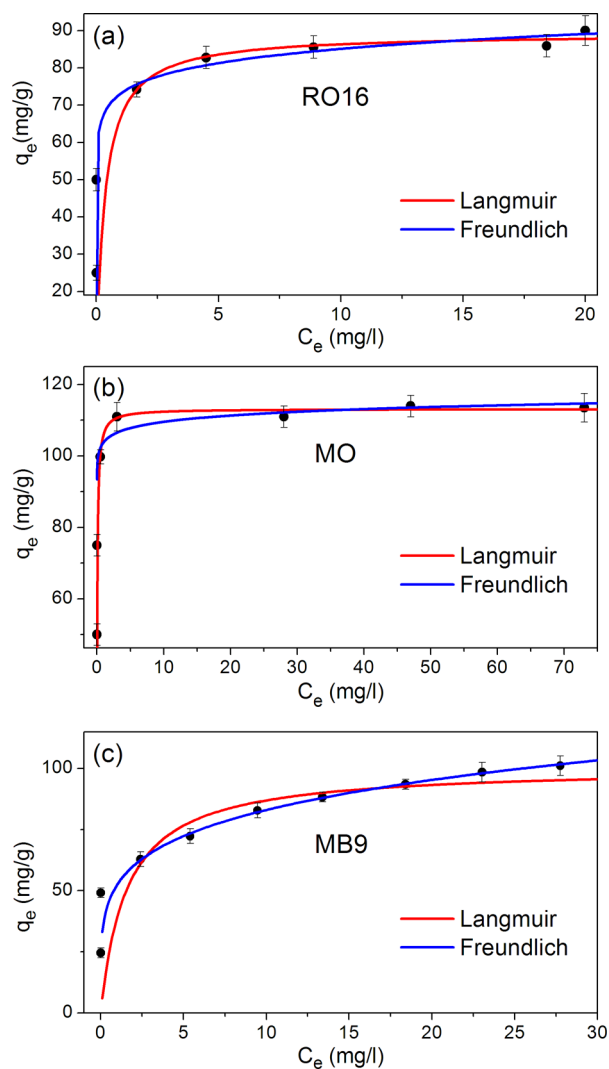
Figure 8. Adsorption isotherms of (a) RO16, (b) MO, and (c) MB9 dye solutions on $CeO_{2-\delta}$ at room temperature. Initial dye concentration = 50−230 mg L^{-1}; mass of adsorbent = 50 mg; solution volume = 25 mL.

Therefore, keeping in mind that oxygen-deficient surface of nanosized ceria is more heterogeneous than homogeneous, it is reasonable to conclude that adsorption of MB9, MO, and RO16 on $CeO_{2-\delta}$ nanopowders reflects the presence of more than one kind of adsorbent−adsorbate surface interaction. The maximal adsorption capacity values of $CeO_{2-\delta}$ nanopowder from isotherm data were found to be 113, 101, and 91 mg g^{-1} in the case of MO, MB9, and RO16 respectively.

To get further insight into the mechanism of adsorption, pseudo-first- and pseudo-second-order models were used to simulate the adsorption data for various contact times from Figure 3b. The pseudo-first-order model didn't give a good fit of the experimental data and will be omitted in further discussion. Kinetic data were further analyzed with the pseudo-second-order kinetic model shown in Figure 9. The linear form of the pseudo-second-order model is expressed as follows:

$$\frac{t}{q_t} = \frac{1}{k_2 q_e^2} + \frac{t}{q_e} \tag{4}$$

where q_e and q_t refer to the amount of adsorbed dye at equilibrium and at time t, respectively, and k_2 is the equilibrium
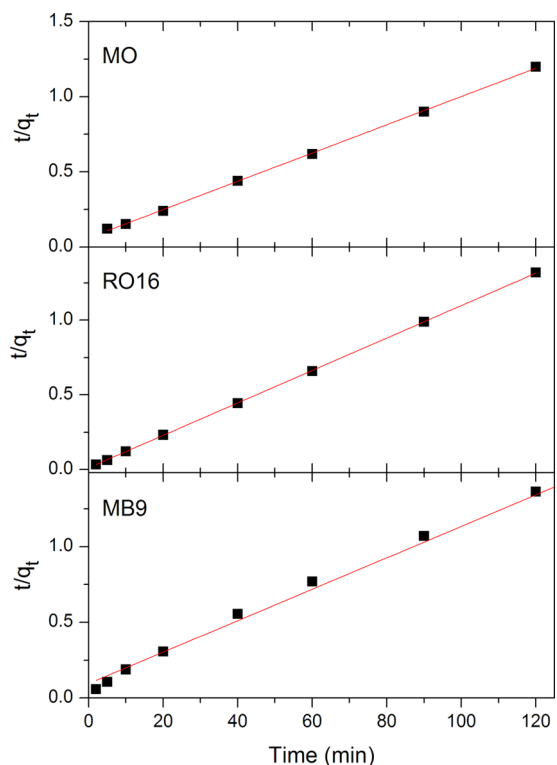
Figure 9. Pseudo-second-order kinetics of MO, RO16, and MB9 onto $CeO_{2-\delta}$ nanopowder. Initial dye concentration = 200 mg L^{-1}; mass of adsorbent = 50 mg; solution volume = 25 mL.

rate constant of the pseudo-second-order kinetic model. The linear plots of t/q_t vs t (Figure 9) show that the experimental data agree well with the pseudo-second-order kinetic model for all three dyes. The values of q_e and k_2 were calculated from the slope and intercept of eq 4, and their values are given in Table 1, together with experimental q_e values and correlation

Table 1. Pseudo-Second-Order Kinetic Model Parameters Together with Experimental q_e Values for Adsorption of Each Dye

	$q_{e,cal}$ (mg g^{-1})	$q_{e,exp}$ (mg g^{-1})	k_2 (g mg^{-1} min^{-1})	R^2
MO	106.3	100	1.44×10^{-3}	0.9994
RO16	100	91	9.09×10^{-3}	0.9999
MB9	96.3	93.6	1.13×10^{-3}	0.9977

coefficients. Calculated q_e values, tabulated in Table 1, are in quite good agreement with experimental ones and the correlation coefficients have large values ($R^2 > 0.99$). It can be concluded that the adsorption of MO, RO16, and MB9 on $CeO_{2-\delta}$ nanopowder follows the pseudo-second-order kinetic model which relies on the assumption that chemisorption and effective electrostatic interactions play a major role in the adsorption process.[46,47] Comparing the adsorption capacities of $CeO_{2-\delta}$ nanopowder with other adsorbents mentioned in the Introduction, we can conclude that $CeO_{2-\delta}$ nanopowder, produced by cost-effective SPRT method, shows efficient adsorption properties and is a promising candidate for environmentally friendly adsorbents in water treatment.

■ CONCLUSIONS

The $CeO_{2-\delta}$ nanopowder, synthesized by a facile and cost-effective SPRT method, appeared to be a very effective sorbent

for the MO, RO16, and MB9 azo dyes. The adsorption process was monitored at fixed initial pH value and varying dye concentration and contact time. Infrared and Raman spectroscopy measurements confirmed that the adsorption of azo dyes on the $CeO_{2-\delta}$ surface took place. The experimental adsorption data for the MO and RO16 were slightly better fitted with the Langmuir isotherm, whereas the Freundlich isotherm was a better fit for MB9 over the whole concentration range. According to the values of the Freundlich constant $(1/n)$, the adsorption of MB9, MO, and RO16 lies in a favorable and strongly favorable zone. The highest adsorption capacity of $CeO_{2-\delta}$ was obtained for MO (113 mg g^{-1}) and then for MB9 (101 mg g^{-1}) and RO16 (91 mg g^{-1}). The formation of a bidentate type bridge between sulfonate group and Ce^{4+} cations and the protonation of ceria surface hydroxyls can be responsible for effective adsorption process. Adsorption of MO, RO16, and MB9 dyes follows the pseudo-second-order equation with good correlation. These results imply that, besides strong electrostatic sorption, chemisorption mechanism may play an important role for the dye adsorption. Based on our results, ceria nanopowder prepared by the SPRT method represents an effective dye adsorbent and can be a promising substitute in wastewater treatment.

■ ASSOCIATED CONTENT

Ⓢ Supporting Information

Figures showing absorption spectra of RO16 (200 mg L^{-1}) and photo image of RO16 solutions in the presence of $CeO_{2-\delta}$ nanopowders, and zeta potential of $CeO_{2-\delta}$ nanoparticles. Tables showing dye structures and their wavelengths of maximal absorption, values of the Raman shifts extracted from the experimental Raman spectra of $CeO_{2-\delta}$ nanopowder after adsorption of MO, RO16, and MB9, and isotherm equations and parameters for azo dyes at room temperature. This material is available free of charge via the Internet at http://pubs.acs.org.

■ AUTHOR INFORMATION

Corresponding Author
*E-mail: zordoh@ipb.ac.rs.

Notes
The authors declare no competing financial interest.

■ ACKNOWLEDGMENTS

■ REFERENCES

(1) Lee, J. W.; Choi, S. P.; Thiruvenkatachari, R.; Shim, W. G.; Moon, H. Evaluation of the performance of adsorption and coagulation processes for the maximum removal of reactive dyes. *Dyes Pigm.* **2006**, *69*, 196−203.

(2) Gomez, V.; Larrechi, M. S.; Callao, M. P. Kinetic and adsorption study of acid dye removal using activated carbon. *Chemosphere* **2007**, *69*, 1151−1158.

(3) Silva, J. P.; Sousa, S.; Rodrigues, J.; Antunes, H.; Porter, J. J.; Goncalves, I.; Ferreira-Dias, S. Adsorption of acid orange 7 dye in aqueous solutions by spent brewery grains. *Sep. Purif. Technol.* **2004**, *40*, 309−315.

(4) Ji, P. F.; Zhang, J. L.; Chen, F.; Anpo, M. Study of adsorption and degradation of acid orange 7 on the surface of CeO_2 under visible light irradiation. *Appl. Catal., B* **2009**, *85*, 148−154.

(5) Venkatesha, T. G.; Viswanatha, R.; Nayaka, Y. A.; Chethana, B. K. Kinetics and thermodynamics of reactive and vat dyes adsorption on MgO nanoparticles. *Chem. Eng. J.* **2012**, *198*, 1−10.

(6) Sahasrabudhe, M.; Pathade, G. Biodegradation of azo dye C.I. Reactive Orange 16 by an actinobacterium Georgenia sp. CC-NMPT-T3. *Int. J. Adv. Res.* **2013**, *1*, 91−99.

(7) Mohan, D.; Pittman, C. U., Jr Activated carbons and low cost adsorbents for remediation of tri- and hexavalent chromium from water. *J. Hazard. Mater.* **2006**, *137*, 762−811.

(8) Pollard, S. J. T.; Fowler, G. D.; Sollars, C. J.; Perry, R. Low-cost adsorbents for waste and wastewater treatment: a review. *Sci. Total Environ.* **1992**, *116*, 31−52.

(9) Amin, N. K. Removal of direct blue-106 dye from aqueous solution using new activated carbons developed from pomegranate peel: Adsorption equilibrium and kinetics. *J. Hazard. Mater.* **2009**, *165*, 52−62.

(10) Sharma, Y. C.; Uma; Upadhyay, S. N. Removal of a cationic dye from wastewaters by adsorption on activated carbon developed from coconut coir. *Energy Fuels* **2009**, *23*, 2983−2988.

(11) Aygün, A.; Yenisoy-Karakaş, S.; Duman, I. Production of granular activated carbon from fruit stones and nutshells and evaluation of their physical, chemical and adsorption properties. *Microporous Mesoporous Mater.* **2003**, *66*, 189−195.

(12) Kannan, N.; Sundaram, M. M. Kinetics and mechanism of removal of methylene blue by adsorption on various carbons—a comparative study. *Dyes Pigm.* **2001**, *51*, 25−40.

(13) Annadurai, G.; Juang, R. S.; Lee, D. J. Use of cellulose-based wastes for adsorption of dyes from aqueous solutions. *J. Hazard. Mater.* **2002**, *92*, 263−274.

(14) Haddadian, Z.; Shavandi, M. A.; Abidin, Z. Z.; Fakhru'l-Razi, A.; Ismail, M. H. S. Removal methyl orange from aqueous solutions using dragon fruit (Hylocereusundatus) foliage. *Chem. Sci. Trans.* **2013**, *2*, 900−910.

(15) Cheung, W. H.; Szeto, Y. S.; Mckay, G. Enhancing the adsorption capacities of acid dyes by chitosan nano particles. *Bioresour. Technol.* **2009**, *100*, 1143−1148.

(16) Wu, C. H. Adsorption of reactive dye onto carbon nanotubes: Equilibrium, kinetics and thermodynamics. *J. Hazard. Mater.* **2007**, *144*, 93−100.

(17) Zhong, L. S.; Hu, J. S.; Cao, A. M.; Liu, Q.; Song, W. G.; Wan, L. J. 3D flowerlike ceria micro/nanocomposite structure and its application for water treatment and CO removal. *Chem. Mater.* **2007**, *19*, 1648−1655.

(18) Ouyang, X. W.; Li, W.; Xie, S. L.; Zhai, T.; Yu, M. H.; Gan, J. Y.; Lu, X. H. Hierarchical CeO_2 nanospheres as highly-efficient adsorbents for dye removal. *New J. Chem.* **2013**, *37*, 585−588.

(19) Zhai, T.; Xie, S. L.; Lu, X. H.; Xiang, L.; Yu, M. H.; Li, W.; Liang, C. L.; Mo, C. H.; Zeng, F.; Luan, T. G.; Tong, Y. X. Porous $Pr(OH)_3$ nanostructures as high-efficiency adsorbents for dye removal. *Langmuir* **2012**, *28*, 11078−11085.

(20) Won, S. W.; Yun, H. J.; Yun, Y.-S. Effect of pH on the binding mechanisms in biosorption of Reactive Orange 16 by Corynebacterium glutamicum. *J. Colloid Interface Sci.* **2009**, *331*, 83−89.

(21) Won, S. W.; Choi, S. B.; Yun, Y.-S. Performance and mechanism in binding of Reactive Orange 16 to various types of sludge. *Biochem. Eng. J.* **2006**, *28*, 208−214.

(22) Janaki, V.; Vijayaraghavan, K.; Ramasamy, A. K.; Lee, K. J.; Oh, B. T.; Kamala-Kannan, S. Competitive adsorption of Reactive Orange 16 and Reactive Brilliant Blue R on polyaniline/bacterial extracellular polysaccharides composite-A novel eco-friendly polymer. *J. Hazard. Mater.* **2012**, *241*, 110−117.

(23) Suteu, D.; Zaharia, C.; Malutan, T. Removal of orange 16 reactive dye from aqueous solutions by waste sunflower seed shells. *J. Serb. Chem. Soc.* **2011**, *76*, 17.

(24) Zhao, D.; Zhang, W.; Chen, C.; Wang, X. Adsorption of Methyl Orange dye onto multiwalled carbon nanotubes. *Procedia Environ. Sci.* **2013**, *18*, 890−895.

(25) Saha, T. K.; Bhoumik, N. C.; Karmaker, S.; Ahmed, M. G.; Ichikawa, H.; Fukumori, Y. Adsorption of Methyl Orange onto Chitosan from Aqueous Solution. *J. Water Resour. Prot.* **2010**, *2*, 8.

(26) Ai, L.; Zhang, C.; Meng, L. Adsorption of Methyl Orange from Aqueous Solution on Hydrothermal Synthesized Mg−Al Layered Double Hydroxide. *J. Chem. Eng. Data* **2011**, *56*, 4217−4225.

(27) Yu, X.; Li, F.; Ye, X.; Xin, X.; Xue, Z. Synthesis of cerium(IV) oxide ultrafine particles by solid-state reactions. *J. Am. Ceram. Soc.* **2000**, *83*, 964−966.

(28) Boskovic, S.; Djurovic, D.; Dohcevic-Mitrovic, Z.; Popovic, Z.; Zinkevich, M.; Aldinger, F. Self-propagating room temperature synthesis of nanopowders for solid oxide fuel cells (SOFC). *J. Power Sources* **2005**, *145*, 237−242.

(29) Zhou, X.-D.; Huebner, W. Size-induced lattice relaxation in CeO_2 nanoparticles. *Appl. Phys. Lett.* **2001**, *79*, 3512−3514.

(30) Lowell, S. *Characterization of Porous Solids and Powders: Surface Area, Pore Size and Density*; Kluwer Academic Publishers: Dordrecht, The Netherlands, 2004.

(31) Jia, T.-J.; Song, G.; Li, P.-W.; He, T.-C.; Mo, Y.-J.; Cui, Y.-T. Vibrational modes study of methyl orange using SERS-measurement and the DFT method. *Mod. Phys. Lett. B* **2008**, *22*, 2869−2879.

(32) Sathiyabama, J.; Rajendran, S.; Selvi, J. A.; Amalraj, A. J. Methyl orange as corrosion inhibitor for carbon steel in well water. *Indian J. Chem. Technol.* **2008**, *15*, 462−466.

(33) Liu, Y.; Sun, D. Z. Development of Fe_2O_3-CeO_2-TiO_2/gamma-Al_2O_3 as catalyst for catalytic wet air oxidation of methyl orange azo dye under room condition. *Appl. Catal., B* **2007**, *72*, 205−211.

(34) Hua, Q.; Shi, F. C.; Chen, K.; Chang, S. J.; Ma, Y. S.; Jiang, Z. Q.; Pan, G. Q.; Huang, W. X. Cu_2O-Au nanocomposites with novel structures and remarkable chemisorption capacity and photocatalytic activity. *Nano Res.* **2011**, *4*, 948−962.

(35) Telke, A. A.; Kalyani, D. C.; Dawkar, V. V.; Govindwar, S. P. Influence of organic and inorganic compounds on oxidoreductive decolorization of sulfonated azo dye CI Reactive Orange 16. *J. Hazard. Mater.* **2009**, *172*, 298−309.

(36) Galindo, C.; Jacques, P.; Kalt, A. Photodegradation of the aminoazobenzene acid orange 52 by three advanced oxidation processes: UV/H_2O_2 UV/TiO_2 and VIS/TiO_2 - Comparative mechanistic and kinetic investigations. *J. Photochem. Photobiol., A* **2000**, *130*, 35−47.

(37) Yue, L.; Zhang, X.-M. Structural characterization and photocatalytic behaviors of doped CeO2 nanoparticles. *J. Alloys Compd.* **2009**, *475*, 702−705.

(38) Danish, M.; Hashim, R.; Ibrahim, M. N. M.; Sulaiman, O. Characterization of physically activated acacia mangium wood-based carbon for the removal of methyl orange dye. *BioResources* **2013**, *8*, 16.

(39) Dohčević-Mitrović, Z. D.; Šćepanović, M. J.; Grujić-Brojčin, M. U.; Popović, Z. V.; Bošković, S. B.; Matović, B. M.; Zinkevich, M. V.; Aldinger, F. The size and strain effects on the Raman spectra of $Ce_{1−x}Nd_xO_{2−d}$ ($0 \leq x \leq 0.25$) nanopowders. *Solid State Commun.* **2006**, *137*, 387−390.

(40) Deacon, G. B.; Phillips, R. J. Relationships between the carbon-oxygen stretching frequencies of carboxylato complexes and the type of carboxylate coordination. *Coord. Chem. Rev.* **1980**, *33*, 227−250.

(41) Bauer, C.; Jacques, P.; Kalt, A. Investigation of the interaction between a sulfonated azo dye (AO7) and a TiO_2 surface. *Chem. Phys. Lett.* **1999**, *307*, 397−406.

(42) Yang, Z.; Wang, Q.; Wei, S.; Ma, D.; Sun, Q. The effect of environment on the reaction of water on the ceria(111) surface: A DFT+U study. *J. Phys. Chem. C* **2010**, *114*, 14891−14899.

(43) Kundakovic, L.; Mullins, D. R.; Overbury, S. H. Adsorption and reaction of H_2O and CO on oxidized and reduced Rh/CeO_x(111) surfaces. *Surf. Sci.* **2000**, *457*, 51−62.

(44) Lima, E. C.; Royer, B.; Vaghetti, J. C. P.; Simon, N. M.; da Cunha, B. M.; Pavan, F. A.; Benvenutti, E. V.; Cataluña-Veses, R.; Airoldi, C. Application of Brazilian pine-fruit shell as a biosorbent to removal of reactive red 194 textile dye from aqueous solution: Kinetics and equilibrium study. *J. Hazard. Mater.* **2008**, *155*, 536−550.

(45) Tseng, R.-L.; Wu, F.-C. Inferring the favorable adsorption level and the concurrent multi-stage process with the Freundlich constant. *J. Hazard. Mater.* **2008**, *155*, 277−287.

(46) Zhu, Y.-P.; Liu, Y.-L.; Ren, T.-Z.; Yuan, Z.-Y. Hollow manganese phosphonate microspheres with hierarchical porosity for efficient adsorption and separation. *Nanoscale* **2014**, *6*, 6627−6636.

(47) Yeddou-Mezenner, N. Kinetics and mechanism of dye biosorption onto an untreated antibiotic waste. *Desalination* **2010**, *262*, 251−259.

Structural and optical characterization of titanium–carbide and polymethyl methacrylate based nanocomposite

Jelena Pešić[1] · **Andrijana Šolajić**[1] · **Jelena Mitrić**[1] · **Martina Gilić**[1] · **Ivan Pešić**[2] · **Novica Paunović**[1] · **Nebojša Romčević**[1]

Abstract

The rich chemistries and unique morphologies of titanium carbide MXenes, made them strong candidates for many applications like sensors and electronic device materials. During the synthesis procedure, chemical etching, oxidation occurs and residual materials, like titanium-dioxide nanocrystals and nanosheets are often present in resulting material. As titanium-carbide MXenes are suggested to be used as additive in organic polymer matrices for production of nanocomposites, it is essential to consider the presence of the oxides and other residuals together with MXene flakes in synthesis results, and consequently in produced nanocomposite. In this study we present structural and optical characterization of such polymer nanocomposite titanium carbide/PMMA (Polymethyl methacrylate) consisting of Ti_3C_2, TiC_2 MXenes and TiC, and TiO_2 residues of synthesis in PMMA matrix, as a multicomponent nanocomposite. Using XRD, infra-red and Raman spectroscopy, followed by comparative study on the vibrational properties using density functional theory calculations, we characterize this nanocomposite. Further, the SEM measurements are performed, demonstrating the produced titanium-carbide-based flakes in nanocomposite are well defined and separated to nanosized grains, allowing us to use Maxwell–Garnet model to analyse infrared spectrum. This enables us to determine the presence of the optical modification of polymer matrices corresponding to a volume fraction of 0.25.

Keywords Titanium-carbide nanoparticles · PMMA composite · Multicomponent nanocompostite

---

Guest edited byJelena Radovanovic, Dragan Indjin, Maja Nesic, Nikola Vukovic andMilena Milosevic.

✉ Jelena Pešić
yelena@ipb.ac.rs

1 Institute of Physics Belgrade, University of Belgrade, Pregrevica 118, Belgrade 11080, Serbia

2 Faculty of Technology and Metallurgy, University of Belgrade, Belgrade 11000, Serbia

1 Introduction

Nanocomposites are the combination of two or more different materials where a minimum of one of the components has dimension less than 100 nm Twardowski (2007). The polymer nanocomposites are made of organic polymer matrix (in this research, polymethyl methacrylate—PMMA) and inorganic components (titanium carbide nanoparticles). The properties of the obtained nanocomposites depend on the individual properties of each component, morphology and the interface characteristics. In an attempt to improve the properties of conventional polymer materials and extend the fields of their applications, functionalization has emerged as important method in improvement of their not satisfactory electronic, thermal and mechanical properties Tamborra et al. (2004); Hussain et al. (2006). In addition to typical advantages of polymers (such are light-weight, low cost, and good processability), the improvement of electrical properties (e.g., electrical conductivity) with the addition of a small amount of conductive fillers into polymer matrices have promoted polymer nanocomposites into versatile multifunctional materials. Many applications like household electronics, memory and microwave devices are potentially available with addition of metal oxide nanoparticles to polymer. This enables the modification of the polymer's physical properties as well as the implementation of new features in the polymer matrix creating new type of materials known as the polymer nanocomposites. PMMA as a thermoplastic polymer, has many extraordinary properties, like great transparency and ultraviolet resistance, high abrasion resistance, hardness and stiffness and making it widely used in many applications ranging from everyday items to high tech devices. Further, PMMA is nondegradable and biocompatible which makes it an excellent candidate in medical applications like tissue engineering with typical applications such as fracture fixation, intraocular lenses and dentures Peppas and Langer (1994).

Multicomponent nanocomposites based of layered and 2D materials have drawn significant attention in past decade with promises of various applications. Reduction of dimensionality of the system to the truly atomic-scale 2D is related to the occurrence of all new amazing properties in low-dimensional material, since the reduction of available phase space and decreased screening lead to enhancement of quantum effects and increased correlations. Low-dimensional materials have been studied intensively both for their fundamental properties and insight in basic principles of matter but as well for their colossal potential for applications. A discovery of true two-dimensional material graphene Novoselov et al. (2004) and its remarkable properties like and experimental observation of Klein tunnelling, quantum Hall effect and superconductivity Novoselov et al. (2004); Katsnelson et al. (2006); Zhang et al. (2005); Durajski et al. (2019); Pešić et al. (2014); Margine et al. (2016); Durajski et al. (2020) paved the way for investigation of a new family of materials in low-dimensional physics. The new field of two-dimensional materials research has arose and investigated not only graphene but many more crystal structures where, just like in graphene, cells are connected in at least one direction by the van der Waals' forces Novoselov et al. (2016).

Transition metal carbides are important group of materials for applications since they possess some desired characteristics such as thermal stability, wear and corrosion resistance, electronic, magnetic as well as catalytic properties. Titanium-carbide powders are generally used for manufacturing cutting tools, used in treatment of metals and as abrasive-resistant materials. In 2011 Naguib et al. (2011), the group of early transition metal carbides and/or carbo-nitrides labeled as MXenes. MXenes are produced by the etching out of the A layers from MAX phases Naguib et al. (2011, 2012, 2013). Name MAX phase

comes from its chemical composition: $M_{n+1}AX_n$, where M is an early transition metal, A is mainly a group IIIA or IVA (i.e., groups 13 or 14) element, X is carbon and/or nitrogen, and n = 1, 2, or 3.

During the synthesis of titanium-carbide MXenes by chemical etching, oxidation can occur which results in presence of TiO_2 consisted of nanosheets and numerous TiO_2 nanocrystals Naguib et al. (2014). There are several studies Zhu et al. (2016); Gao et al. (2015) whose researched is focused in possible applications of TiO_2-MXene structures. It is demonstrated the joint effects of Ti_3C_2 and TiO_2 endowed TiO_2-Ti_3C_2 nanocomposites with excellent properties and improved functionalities Zhu et al. (2016). In this work we investigate the structural and optical properties of polymer nanocomposites prepared by the incorporation of titanium-carbide nanoparticles consisting of Ti_3C_2, TiC_2 TiC and TiO_2 into the matrices of polymer PMMA. The sample of nanocomposite material was prepared, the PMMA matrix with titanium-carbide particles, PMMA/TiC. As for similar materials Shan et al. (2021, 2020, 2021); Tan et al. (2021); Jafari et al. (2020); Tan et al. (2021) proper understanding of composition of materials used in composite is crucial and XRD analysis for the titanium-carbide flakes. The structural and morphology studies of the nanocomposites were carried out by SEM and Raman spectroscopy. Infrared spectroscopy is a very powerful technique in analysis of various nanoparticle and nanocomposite materials prepared in various techiques Dastan (2015); Dastan and Chaure (2014); Dastan et al. (2014); Dastan and Chaure (2017). To further understand properties of our inhomogenious nanocomposite we used infrared spectroscopy with Maxwell–Garnet model. To further support optical characterization, calculations based on density functional theory were performed.

2 Samples preparation and structural characterization

### 2.1 Titan-carbide/PMMA composite synthesis

In this work, titanium-carbide/PMMA nanocomposite sample was made from mixture of MXene based titanium-carbide nanoflakes in PMMA matrix. Production of layered titan-carbide flakes is based on MXene synthesis by selective etching of Al atomic layers from Ti_3AlC_2 MAX phase, we used the so-called 'mild' method with lithium fluoride (LiF) and hydrochloric acid (HCl) Tu et al. (2018). This method was described in Naguib et al. (2011). Procedure of composite preparation is described in Fig. 1.

Commercially available PMMA Acryrex CM205 (Chi Mei Corp. Korea, (Mw $\approx$ 90400 g/mol, $n = 1.49$, $\lambda = 633$ nm) pellets were used as a matrix for sample preparation. Ti_3AlC_2 MAX phase was processed and kindly donated from Layered Solids Group, Drexel University. Titanium-carbide flakes were obtained by sonification in the water and drying the supernatant in a Petri dish in the oven for 30 minutes on 90∘C.

Composite was prepared with 10 wt% PMMA solution in acetone (Carlo Erbe Reagents, Spain) and added dried titanium-carbide flakes. After stirring the solution was poured in Petri dish Cao et al. (2017) and dried in oven 24h on 40 ˚C. Content of titanium-carbide flakes in the sample was 1.7 wt%.

The morphology of the produced composite has been investigated by FESEM using high resolution electron microscope MIRA3 TESCAN. Samples display separated nanosized grains. Fig. 2a presents FESEM image of MXene flakes delaminated in water showing morphology of obtained flakes, b FESEM image of the PMMA/titanium-carbide

Fig. 1 Schematic describing the synthesis process of MXenes from MAX phases and preparation of composite
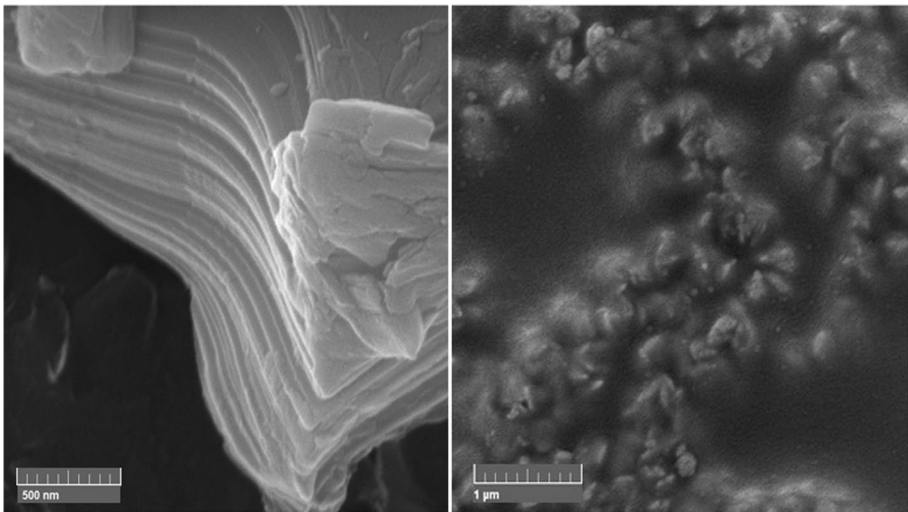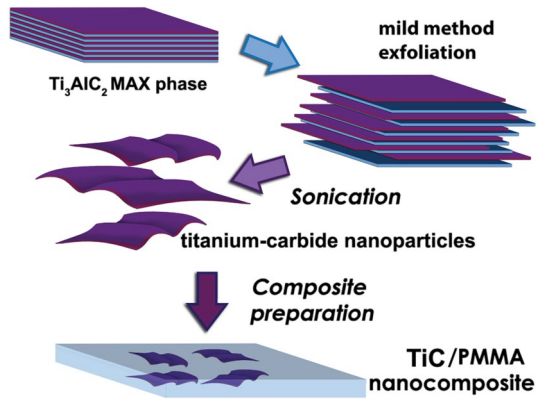
Fig. 2 FESEM photos of **a** Flakes delaminated in water; **b** PMMA composite prepared with titanium-carbide flakes

nanocomposite. Characteristic layered structure of MXenes is visible on FESEM image and confirming success of delamination and exfoliation procedures. Obtained flakes demonstrate multilayered structure with few *μm* in diameter. In Fig. 2b typical accordion like structure can be indicated in nanosize grain-like structures, clustered in PMMA matrix.

2.2 XRD

X–ray diffraction powder (XRD) technique was used to determine structural characteristics of titanium-carbide based flakes to be used in composites. Philips PW 1050 diffractometer equipped with a PW 1730 generator was used. The same conditions were used for all samples, 40 kV×20 mA, using Ni filtered Co Kα radiation of 0.1778897 nm at room temperature. Measurements were carried out in the 2θ range of 20–80° with a scanning step

Fig. 3 XRD pattern for titanium-carbide flakes, starting material for PMMA/TiC composite
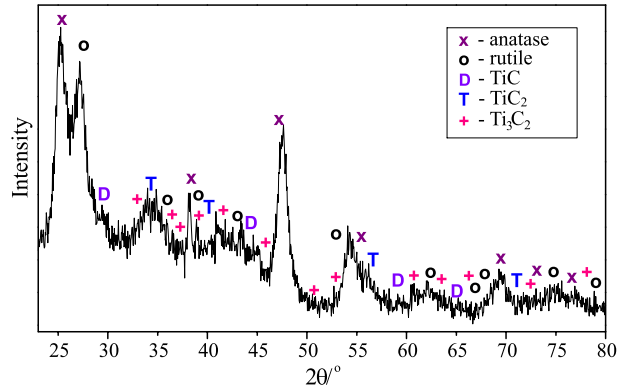
Fig. 4 Schematic representation of Titanum-carbide structures present at composite **a** Ti_3C_2, **b** TiC and **c** TiC_2
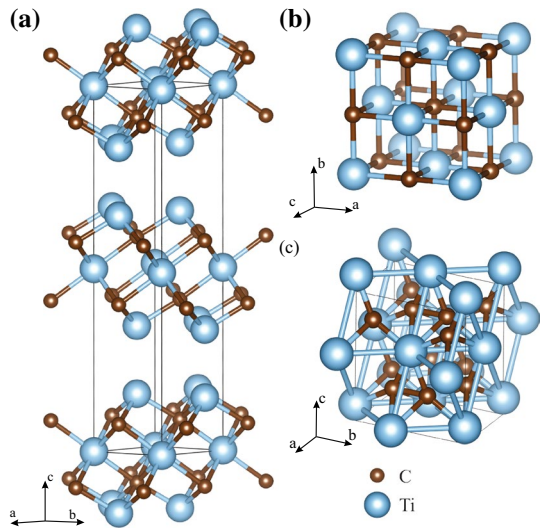
of 0.05° and 10 s scanning time per step. In Fig. 3 is presented XRD pattern for titanium-carbide flakes, starting material for composite. The different phases of titanium carbide can be noticed from diffractogram—Ti_3C_2, TiC and TiC_2 together with TiO_2. TiO_2 is widely present as anatase and rutile. All peaks obtained correspond to the structures of Ti_3C_2, TiC, TiC_2, anatase and rutile and it is confirmed that they belong to space groups $P6_3/mmc$ (194), $Fm3\overline{m}$ (225) Fm2m (42), $I4_1/amd$ (141), $P4_2/mnm$ (136), respectively. The unit cells of MXene structures Ti_3C_2, TiC and TiC_2 are presented in Fig. 4. These structures were further used in DFT analysis of optical spectroscopy results in Sect. 3.3.

3 Results and discussion

3.1 Raman spectroscopy

The micro-Raman spectra were taken in the backscattering configuration and analyzed by the TriVista 557 system equipped with a nitrogen cooled charge-coupled-device

detector. As an excitation source, we used the 532 nm line of Ti:Sapphire laser. Excitation energy is in the off-resonance regime for all the considered materials. The Raman spectra of the PMMA, PMMA/TiC, and titanium-carbide flakes, measured in the spectral range of 100-1100 cm^{-1} at room temperature, are presented in Fig. 5.

The Raman spectrum of PMMA is presented in Fig. 5a. Intense modes at 235, 300, 362, 400, 484, 560, 603, 660, 733, 815, 839, 864, 911, 967, 985, 1063 and 1091 cm^{-1} were detected. The obtained results are in a good agreement with the values given in the literature Willis et al. (1969); Thomas et al. (2008); Ćurčić et al. (2020).
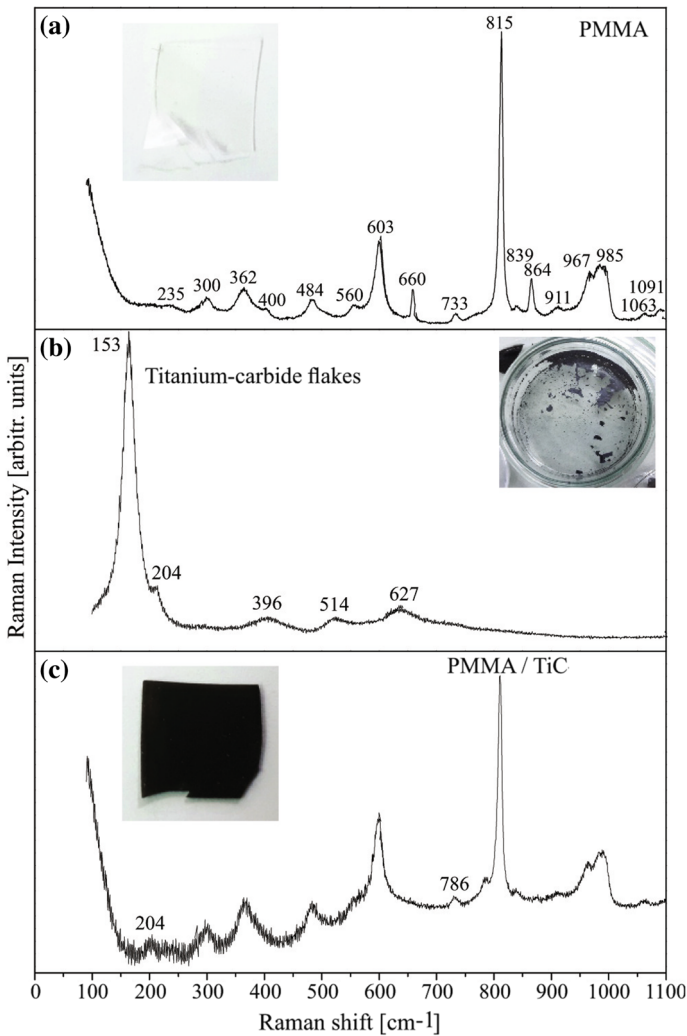
Fig. 5 Raman spectra with photo of the sample of **a** PMMA, **b** Titanium-carbide flakes, **c** PMMA/TiC composite. Only titanium-carbide related peaks are marked in this spectrum. Unassigned peaks correspond to PMMA from **a** spectrum

In Fig. 5b spectrum of titanium-carbide flakes after etching procedure is presented. Several characteristic peaks can be distinguished on 153 cm^{-1}, 204 cm^{-1}, 396 cm^{-1}, 514 cm^{-1} and 627 cm^{-1}. Peaks at 153 cm^{-1} and 627 cm^{-1} correspond to doubly degenerated E$_{2g}$ modes of Ti$_3$C$_2$. The frequency associated with E$_{2g}$ modes is calculated to be at 161 cm^{-1} for the bare Ti$_3$C$_2$. Since their main contribution is from in-plane vibrations of Ti and C atoms, it can be influenced by the vibrations of the terminal atoms (as a residue of synthesis procedure) weaken the in-plane motion of the Ti and C atoms, hence there is shift to lower frequency. The terminal groups play significant roles for the vibrational modes: the terminal atoms weakening the motions in which the surface Ti atoms are involved while strengthening the out-of-plane vibration of the C atoms; the corresponding vibrational frequencies dramatically change with the various terminal atoms Zhao et al. (2016). This is consistent with XRD results suggesting significant amount of TiO$_2$ as a residue of synthesis procedure as described in introduction. This can be also visible in Raman spectrum of titanium-carbide flakes on 204 cm^{-1} and 514 cm^{-1}. The doubly degenerated modes at 621 cm^{-1} correspond to the in-plane vibration of the C atoms Hu et al. (2015). In Fig. 5c spectrum of PMMA/TiC is presented, only titanium-carbide related peaks at 204 and 786 cm^{-1} are marked in this spectrum. Unassigned peaks correspond to PMMA peaks marked on a) panel.

As XRD analysis demonstrated, obtained flakes contain both MXene flakes and titanium-dioxide as the residue of synthesis procedure. To further understand and assign this spectra we performed theoretical analysis of all materials identified in XRD pattern using density functional theory calculations. Calculations provided us a guide for identification of peaks and all results are summarized in Table 1.

3.2 Far-infrared spectroscopy

Far-infrared reflection spectra were measured at room temperature in the spectral range from 40 to 600 cm^{-1}, carried out with a BOMEM DA 8 spectrometer. The experimental data are represented at Fig. 6a and by circles at Fig. 6b–d. As expected, the reflection spectra of nanocomposites are by intensity placed between the starting composites. In order to analyse far-infrared spectra we have used the classical oscillator model with free carrier contribution, as a base for Maxwell–Garnet effective medium approximation Abstreiter (1984); Carter and Bate (1971). The low-frequency dielectric properties of single crystals are described by classical oscillators corresponding to the TO modes, to which the Drude part is superimposed to take into account the free carrier contribution:

$$\epsilon_s(\omega) = \epsilon_\infty + \sum_{k=1}^{l} \frac{\epsilon_\infty S_k}{\omega_{TOk}^2 - \omega^2 - i\gamma_{TOk}\omega} - \frac{\epsilon_\infty \omega_P^2}{\omega(\omega + i\Gamma_P)}, \tag{1}$$

where ϵ_∞ is the bound charge contribution and it is assumed to be a constant, ω_{TOk}^2 is the transverse optical-phonon frequency, ω_P^2 the plasma frequency, γ_{TOk} is damping, Γ_P is the plasmon mode damping coefficient, and S_k is the oscillator strength.

In general, the optical properties of an inhomogeneous material are described by the complex dielectric function that depends on 3D distribution of constituents. The investigated mixture consists of two materials with two different dielectric components. One is treated as a host, and the other as the inclusions. The characterization of the inhomogeneous material by the two dielectric functions is not useful, since one need to know the exact geometrical arrangement of the constituents of the material. However, if the wavelength of
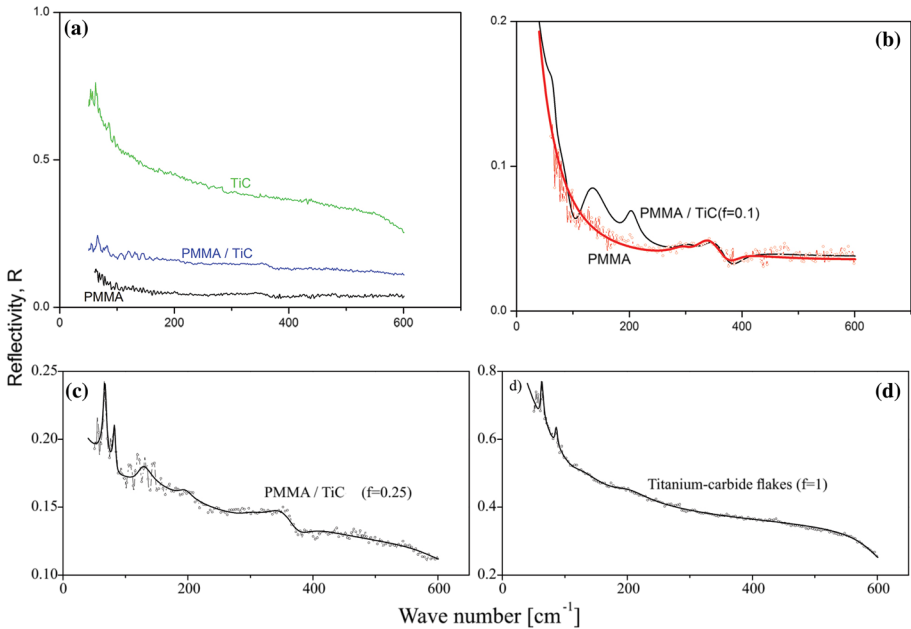
Fig. 6 Infrared analysis: **a** Infrared spectra of Titanium-carbide flakes (green) and composites PMMA/TiC (blue) and pure PMMA (black), **b**, **c**, and **d** circles represent experimental data and solid lines are fit obtained by Maxwell–Garnet model as described in Sect. 3.2

Table 1 Raman and infrared spectrum analysis and modes assignation for synthesized titanium-carbide flakes and PMMA/TiC composite

	Titanium-carbide flakes		PMMA/TiC		Description
	Raman	IR	Raman	IR	
ω_1		62.4		66	E_u, Ti_3C_2
ω_2		85.8		81	B_1, TiO_2 rutile
ω_3		119		127	A_{2u}, Ti_3C_2 and B_1 TiC_2
ω_4	153				E_g, Ti_3C_2
ω_5	204	200	204	195	E, TiO_2 anatase
ω_6	396				A_2, TiC_2; E, TiO_2 anatase
ω_7	514				A_1, TiO_2 anatase
ω_8		620		615	E_u, Ti_3C_2
ω_9	627				E_g, Ti_3C_2
ω_{10}			786		A_g, TiO_2 rutile
ω_P		80		150	
f		1		0.25	

Infrared modes fit is obtained by Maxwell–Garnet model. Modes assignation is performed using values obtained in DFT calculations

the electromagnetic radiation is much larger than the size of inclusions, classical theories of inhomogeneous material presume that the material can be treated as a homogeneous substance with an effective dielectric function. In the literature, many mixing models can

be found for the effective permittivity of such mixture. Some are present in ref Sihvola (1999). Optical properties of such materials depend upon the properties of constituents, as well as their volume fraction. Since our samples are well defined and separated nanosized grains (as demonstrated on FESEM images, Fig. 2), we used Maxwell–Garnet model for present case. For the spherical inclusions case, the prediction of the effective permittivity of mixture, ϵ_{eff}, according to the Maxwell–Garnet mixing rule is Garnett (1904):

$$\epsilon_{eff} = \epsilon_1 + 3f\epsilon_1 \frac{\epsilon_2 - \epsilon_1}{\epsilon_2 + 2\epsilon_1 - f(\epsilon_2 - \epsilon_1)} \tag{2}$$

Here, spheres of permittivity ϵ_2 (Titanium-carbide) are located randomly in homogeneous environment ϵ_1 (PMMA) and occupy a volume fraction f.

Solid lines in Fig. 6 are calculated spectra obtained by a fitting procedure based on the previously presented model. The agreement of the theoretical model obtained in this manner with the experimental results is excellent.

To demonstrate the model, together with the infrared spectrum of PMMA, Fig. 6b is given the theoretical spectrum of PMMA/TiC nanocomposites for f = 0.1. The properties of TiC structures are clearly visible. A larger share of TiC structures leads to the spectrum in Fig 6c, which was obtained for f = 0.25. In Fig. 6d, for f=1 of course there is no effect from PMMA.

3.3 Discussion

In Table 1 are summarized results from spectroscopic measurements of obtained nanocomposites. As stated above, for infrared measurements the agreement of the theoretical model with obtained spectra is excellent and best fit parameters are presented in this table.

To further support our results we performed DFT based calculations and calculated vibrational frequencies in Γ point for all materials present after titanium-carbide flakes exfoliation, which we determined are present using XRD, Fig. 3. Obtained values are compared to experimental Raman and infrared spectrum and modes have been assigned. Results are summarized in Table 1. We presented only modes that can be assigned to peaks from the spectra. In infrared spectra we can notice good agrement with theoretical calculations, specially for low-energy E_u and A_{2u} mode of Ti_3C_2 which is present the composite spectrum (Fig. 6b, c) as in starting titanium-carbide material (Fig. 6d). As shown in XRD we notice peaks originating from TiO_2 and TiC_2 in mid-energy region. High-energy mode E_u on 620 cm^{-1} is present in spectrum of PMMA/TiC. In Table 2 are summarized calculated optical modes for Ti_3C_2 with symmetry 194 group used in analysis.

DFT calculations were performed using the Quantum Espresso software package Giannozzi (2009), based on the plane waves and pseudopotentials. The PBE (Perdew, Burke and Ernzehof) Perdew et al. (1996) exchange-correlation functional was employed and PAW (Projector augmented waves) pseudopotentials were used. Energy cutoff for wavefunctions and charge density were set to 52 Ry and 575 Ry to ensure the convergence. The Brillouin zone was sampled using the Monkhorst-Pack scheme, with 8×8×8 k-points mesh for TiC_2, 8×8×4 for Ti_3C_2, 12×12×12 for TiC, and 8×8×8 for TiO_2 (Rutile and Anatase structures). Phonon frequencies are calculated within the DPFT (Density Functional Perturbation Theory) implemented in Quantum Espresso Baroni et al. (2001). In order to obtain the lattice parameters more accurately, van der Waals forces were treated using the Grimme-D2 correction Grimme (2006)

Table 2 Vibrational modes for Ti$_3$C$_2$ with symmetry group 194, calculated from the measured data

Ti$_3$C$_2$ (P6$_3$/mmc)

cm^{-1}	Symmetry	Raman or IR active
65.0	E$_u$	I
135.2	A$_{2u}$	I
160.6	E$_g$	R
161.4	E$_g$	R
229.9	A$_{1g}$	R
269.3	A$_{1g}$	R
271.1	E$_u$	I
271.7	E$_u$	I
371.4	A$_{2u}$	I
382.4	A$_{2u}$	I
549.1	A$_{2u}$	I
554.4	A$_{2u}$	I
611.2	E$_g$	R
620.4	E$_g$	R
624.1	E$_u$	I
626.4	E$_u$	I
653.2	A$_{1g}$	R
658.3	A$_{1g}$	R

Optical spectroscopy results supported with the DFT numerical calculation confirm that produced composites PMMA/TiC show optical modification comparing to pure PMMA. Our X-ray diffraction investigation of synthesized nanomaterials identified presence of Ti$_3$C$_2$ and TiC$_2$ MXenes and residual TiO$_2$ and TiC from the synthesis procedure, which can be also supported from the optical spectroscopy results.

4 Conclusion

In this paper, we present results of optical and structural investigation of composite based on titanium-carbide nanoflakes (Ti$_3$C$_2$, TiC$_2$ TiC and TiO$_2$)in PMMA matrix. X-ray diffraction (XRD) investigation of synthesized nanomaterials identified presence of Ti$_3$C$_2$ and TiC$_2$ MXenes and residual TiO$_2$ and TiC from the synthesis procedure. The optical properties were studied by Raman and infrared spectroscopy at room temperature. The analysis of the Raman spectra was made by the fitting procedure. For analysis of infrared spectra we used Maxwell–Garnet model. In order to identify and assign vibrational modes, vibrational frequencies of all identified materials were calculated using density functional theory, and compared with experimental results. We confirmed optical modification in composite structure compared to pure PMMA. Further analysis that goes beyond the scope of this publication studies mechanical properties of composite materials, confirming improvements compared to pure PMMA. The obtained composite showed enhanced hardness, elastic modulus and tensile strength compared with pure PMMA Pesic et al. (2019).

Author Contributions Conceptualization, JP and NR; investigation JP, AŠ, JM, MG, IP, NP; validation, JP, NP, NR; formal analysis, JP, AŠ, JM, MG, NP, NR; writing JP and AŠ; writing–review and editing, JP, AŠ, NP, NR; visualization, AŠ; supervision, NR; project administration, NR; funding acquisition, NR. All authors have read and agreed to the published version of the manuscript.

Data availability All additional material is available at authors on request.

Code availability Not applicable.

Declarations

Conflict of interest The Authors declare no conflict of interest.

Ethical approval Not applicable.

Informed consent Not applicable.

Consent for publication All authors consent to publication results presented in manuscript.

References

Abstreiter, G.: Light Scattering in Solids IV. Springer, New York (1984)

Baroni, S., de Gironcoli, S., Dal Corso, A., Giannozzi, P.: Phonons and related crystal properties from density-functional perturbation theory. Rev. Mod. Phys. **73**, 515–562 (2001)

Cao, Y., Deng, Q., Liu, Z., Shen, D., Wang, T., Huang, Q., Du, S., Jiang, N., Lin, C.-T., Yu, J.: Enhanced thermal properties of poly (vinylidene fluoride) composites with ultrathin nanosheets of mxene. RSC Adv. **7**(33), 20494–20501 (2017)

Carter, D.L., Bate, R.T.: The Physics of Semimetals and Narrow-gap Semiconductors: Proceedings, vol. 32. Pergamon, Texas, USA (1971)

Ćurčić, M., Hadžić, B., Gilić, M., Radojević, V., Bjelajac, A., Radović, I., Timotijević, D., Romčević, M., Trajić, J., Romcevic, N.: Surface optical phonon (sop) mode in ZnS/poly (methylmethacrylate) nanocomposites. Physica E **115**, 113708 (2020)

Dastan, D.: Nanostructured anatase titania thin films prepared by sol-gel dip coating technique. J. Atom. Mol. Condens. Matter Nano Phys. **2**, 109–114 (2015)

Dastan, D., Chaure, N.B.: Influence of surfactants on TiO_2 nanoparticles grown by sol-gel technique. Int. J. Mater. Mech. Manuf. **2**, 21 (2014)

Dastan, D., Chaure, N.: Kartha: Surfactants assisted solvothermal derived titania nanoparticles: synthesis and simulation. J. Mater. Sci. **28**, 7784–7796 (2017)

Dastan, D., Londhe, P.U., Chaure, N.B.: Characterization of TiO_2 nanoparticles prepared using different surfactants by sol-gel method. J. Mater. Sci. **25**, 3473–3479 (2014)

Durajski, A.P., Skoczylas, K.M., Szczeaniak, R.: Superconductivity in bilayer graphene intercalated with alkali and alkaline earth metals. Phys. Chem. Chem. Phys. **21**, 5925–5931 (2019). https://doi.org/10.1039/C9CP00176J

Durajski, A.P., Auguscik, A.E., Szczeaniak, R.: Tunable electronic and magnetic properties of substitutionally doped graphene. Physica E **119**, 113985 (2020). https://doi.org/10.1016/j.physe.2020.113985

Gao, Y., Wang, L., Zhou, A., Li, Z., Chen, J., Bala, H., Hu, Q., Cao, X.: Hydrothermal synthesis of TiO_2/Ti_3C_2 nanocomposites with enhanced photocatalytic activity. Mater. Lett. **150**, 62–64 (2015)

Garnett, J.M.: XII. Colours in metal glasses and in metallic films. Philosoph. Trans. R. Soc. Lond. Ser. A **203**, 385–420 (1904)

Giannozzi, P., et al.: QUANTUM ESPRESSO: a modular and open-source software project for quantum simulations of materials. J. Phys. Condens. Matter **21**(39), 395502 (2009)

Grimme, S.: Semiempirical GGA-type density functional constructed with a long-range dispersion correction. J. Comput. Chem. **27**(15), 1787–1799 (2006)

Hu, T., Wang, J., Zhang, H., Li, Z., Hu, M., Wang, X.: Vibrational properties of ti_3c_2 and $ti_3c_2t_2$(t= o, f, oh) monosheets by first-principles calculations: a comparative study. Phys. Chem. Chem. Phys. **17**(15), 9997–10003 (2015)

Hussain, F., Hojjati, M., Okamoto, M., Gorga, R.E.: Review article: polymer-matrix nanocomposites, processing, manufacturing, and application: an overview. J. Compos. Mater. **40**(17), 1511–1575 (2006). https://doi.org/10.1177/0021998306067321

Jafari, A., Tahani, K., Dastan, D., Asgary, S., Shi, Z., Yin, X.-T., Zhou, W.-D., Garmestani, H.: Ştefan Ţălu: Ion implantation of copper oxide thin films; statistical and experimental results. Surf. Interfaces **18**, 100463 (2020)

Katsnelson, M.I., Novoselov, K.S., Geim, A.K.: Chiral tunnelling and the Klein paradox in graphene. Nat. Phys. **2**, 620–625 (2006)

Margine, E.R., Lambert, H., Giustino, F.: Electron-phonon interaction and pairing mechanism in superconducting ca-intercalated bilayer graphene. Sci. Rep. **6**, 21414 (2016)

Naguib, M., Kurtoglu, M., Presser, V., Lu, J., Niu, J., Heon, M., Hultman, L., Gogotsi, Y., Barsoum, M.W.: Two-dimensional nanocrystals produced by exfoliation of ti_3alc_2. Adv. Mater. **23**(37), 4248–4253 (2011). https://doi.org/10.1002/adma.201102306

Naguib, M., Mashtalir, O., Carle, J., Presser, V., Lu, J., Hultman, L., Gogotsi, Y., Barsoum, M.W.: Two-dimensional transition metal carbides. ACS Nano **6**(2), 1322–1331 (2012). https://doi.org/10.1021/nn204153h

Naguib, M., Halim, J., Lu, J., Cook, K.M., Hultman, L., Gogotsi, Y., Barsoum, M.W.: New two-dimensional niobium and vanadium carbides as promising materials for li-ion batteries. J. Am. Chem. Soc. **135**(43), 15966–15969 (2013). https://doi.org/10.1021/ja405735d

Naguib, M., Mashtalir, O., Lukatskaya, M.R., Dyatkin, B., Zhang, C., Presser, V., Gogotsi, Y., Barsoum, M.W.: One-step synthesis of nanocrystalline transition metal oxides on thin sheets of disordered graphitic carbon by oxidation of mxenes. Chem. Commun. **50**, 7420–7423 (2014)

Novoselov, K.S., Geim, A.K., Morozov, S.V., Jiang, D., Zhang, Y., Dubonos, S.V., Grigorieva, I.V., Firsov, A.A.: Electric field effect in atomically thin carbon films. Science **306**(5696), 666–669 (2004). https://doi.org/10.1126/science.1102896

Novoselov, K.S., Mishchenko, A., Carvalho, A., Castro Neto, A.H.: 2d materials and van der Waals heterostructures. Science **353**, 6298 (2016). https://doi.org/10.1126/science.aac9439

Peppas, N., Langer, R.: New challenges in biomaterials. Science **263**(5154), 1715–1720 (1994). https://doi.org/10.1126/science.8134835

Perdew, J.P., Burke, K., Ernzerhof, M.: Generalized gradient approximation made simple. Phys. Rev. Lett. **77**, 3865–3868 (1996)

Pesic, I., Radojevic, V., Barsoum, N. M. Tomic, Romcevic, N.: Preparation, characterization and mechanical properties of mxene/pmma composite. TechConnect World Innovation Conference and Expo, Boston, MA, USA. https://www.techconnectworld.com/World2019/wednesday.htmlW6.26 (2019)

Pešić, J., Gajić, R., Hingerl, K., Belić, M.: Strain-enhanced superconductivity in li-doped graphene. EPL (Europhys. Lett.) **108**(6), 67005 (2014). https://doi.org/10.1209/0295-5075/108/67005

Shan, K., Yi, Z.-Z., Yin, X.-T., Dastan, D., Dadkhah, S., Coates, B.T., Garmestani, H.: Mixed conductivities of a-site deficient Y, Cr-doubly doped srtio3 as novel dense diffusion barrier and temperature-independent limiting current oxygen sensors. Adv. Powder Technol. **31**(12), 4657–4664 (2020)

Shan, K., Yi, Z.-Z., Yin, X.-T., Cui, L., Dastan, D., Garmestani, H., Alamgir, F.M.: Diffusion kinetics mechanism of oxygen ion in dense diffusion barrier limiting current oxygen sensors. J. Alloy. Compd. **855**, 157465 (2021)

Shan, K., Zhai, F., Yi, Z.-Z., Yin, X.-T., Dastan, D., Tajabadi, F., Jafari, A., Abbasi, S.: Mixed conductivity and the conduction mechanism of the orthorhombic CAZRO3 based materials. Surf. Interfaces **23**, 100905 (2021)

Sihvola, A.H.: Electromagnetic Mixing Formulas and Applications, vol. 47. IET, UK (1999)

Tamborra, M., Striccoli, M., Comparelli, R., Curri, M., Petrella, A., Agostiano, A.: Optical properties of hybrid composites based on highly luminescent CDS nanocrystals in polymer. Nanotechnology **15**(4), 240 (2004)

Tan, G.-L., Tang, D., Dastan, D., Jafari, A., Shi, Z., Chu, Q.-Q., Silva, J.P.B., Yin, X.-T.: Structures, morphological control, and antibacterial performance of tungsten oxide thin films. Ceram. Int. **47**(12), 17153–17160 (2021)

Tan, G.-L., Tang, D., Dastan, D., Jafari, A., Silva, J.P.B., Yin, X.-T.: Effect of heat treatment on electrical and surface properties of tungsten oxide thin films grown by HFCVD technique. Mater. Sci. Semicond. Process. **122**, 105506 (2021)

Thomas, K., Sheeba, M., Nampoori, V., Vallabhan, C., Radhakrishnan, P.: Raman spectra of polymethyl methacrylate optical fibres excited by a 532 nm diode pumped solid state laser. J. Opt. A Pure Appl. Opt. **10**(5), 055303 (2008)

Tu, S., Jiang, Q., Zhang, X., Alshareef, H.N.: Large dielectric constant enhancement in mxene percolative polymer composites. ACS Nano **12**(4), 3369–3377 (2018)

Twardowski, T.E.: Introduction to Nanocomposite Materials: Properties, Processing. Characterization, DEStech Publications Inc, Lancaster, USA (2007)

Willis, H., Zichy, V., Hendra, P.: The laser-Raman and infra-red spectra of poly (methyl methacrylate). Polymer **10**, 737–746 (1969)

Zhang, Y., Tan, Y.-W., Stormer, H.L., Kim, P.: Experimental observation of the quantum hall effect and Berry's phase in graphene. Nature **438**, 201–204 (2005)

Zhao, T., Zhang, S., Guo, Y., Wang, Q.: Tic$_2$: a new two-dimensional sheet beyond mxenes. Nanoscale **8**(1), 233–242 (2016)

Zhu, J., Tang, Y., Yang, C., Wang, F., Cao, M.: Composites of tio2 nanoparticles deposited on ti3c2 mxene nanosheets with enhanced electrochemical performance. J. Electrochem. Soc. **163**(5), 785–791 (2016)

Surface optical phonon and multi – phonon transitions in YVO$_4$: Eu^{3+} nanopowders

J. Mitrić [a,*], N. Paunović [a], M. Mitrić [c], J. Ćirković [b], M. Gilić [a], M. Romčević [a], N. Romčević [a]

[a] *Institute of Physics, University of Belgrade, Pregrevica 118, 11080, Belgrade, Serbia*
[b] *Institute for Multidisciplinary Research, University of Belgrade, Kneza Višeslava 1a, 11030, Belgrade, Serbia*
[c] *Institute Vinča, University of Belgrade, P.O. Box 522, 11001, Belgrade, Serbia*

ABSTRACT

In this paper two methods of preparation of yttrium orthovanadate nanopowders were presented: Solid State Reaction (top – down approach) and Solution Combustion Synthesis (bottom – up approach). For starting structural characterization, X – Ray Powder Diffraction (XPRD) and Field Emission Scanning Electron Microscopy (FESEM) were used. We report the change in reflection spectra in europium doped YVO$_4$ nanopowders with comparison to its bulk analog. In UV–Vis reflection spectra we consider the change in values of band gap in these structures, after resizing it from bulk to nanomaterial. In Far – Infrared (FIR) reflection spectra, we registered the existence of Surface Optical Phonon (SOP) and different multi – phonon processes which alter the reflection spectra of bulk YVO$_4$. The influence of Eu ions is reflected through multi – phonon processes that occur and are connected with energy transfer from YVO$_4$ lattice to Eu ions. All IR spectra were modeled using classical oscillator model with Drude part added which takes into account the free carrier contribution. Since our samples are distinctively inhomogeneous materials, we use Effective Medium theory in Maxwell Garnett approximation to model its effective dieletric function.

1. Introduction

Semiconducting nanomaterials, especially nanophosphors have attracted great attention of researchers, due to their wide spectrum of applications in industry, technology as well as in fundamental science. When made in nanorange, phosphor materials exibit enhanced optical properties as against their bulk counterparts, due to quantum size effects and increased surface – to – volume ratio. Yttrium orthovanadate is a widely used red phosphor with many applications in just recent years – in solar cells [1], cancer treatment [2], biotechnology [3], optical imaging [4] etc.

For nanopowders, a valuable tool in the investigation of the structural and optical changes in a material made due to resizing the bulk crystal on nanoscale is the optical spectroscopy – in this case specifically far – infrared and UV – VIS spectroscopy. When excited by UV light, photoluminescence quantum yield of the europium emission in yttrium orthovanadate crystal, goes up to 70% [5]. In YVO$_4$:Eu^{3+} structure UV radiation excites the vanadate group, which has the ability of efficient excitation transfer to the europium ions (Fig. 1).

When irradiated with UV radiation, three major steps occur in the excitation and emission process in YVO$_4$:Eu^{3+} structure. First step is the absorption of UV light by (VO$_4$)$^{3-}$ groups. Then, thermal activated energy, which comes from the UV excitation source, migrates through the vanadate sub – lattice, inducing the transfer of excited energy to europium ions. In the end, strong red (^{5}D$_0$ – ^{7}F$_2$) and orange (^{5}D$_0$ – ^{7}F$_1$) emission due to de – excitation process of excited europium ions occur [6].

One of the important properties of semiconductors is their band gap. Studying the band gap of semiconductors is important for interpreting their structural and optical properties and it is of a great importance examining its expansion in order to understand their properties. Application of semiconductors is in large level determined by their band gap width. Bulk semiconductors are usually very limited in their application due to their small and indirect band gap. Bulk crystal is set up of a large number of atoms and molecules, with a number of adjacent energy levels, which form bulk electronic bands. With the reduction of particle size to a nano level, where every particle is made up out of a small number of atoms or molecules, the number of overlapping orbitals decreases, and the eventually width of the band gap of a nanomaterial gets narrower when compared to bulk crystal (this means that there will be

---

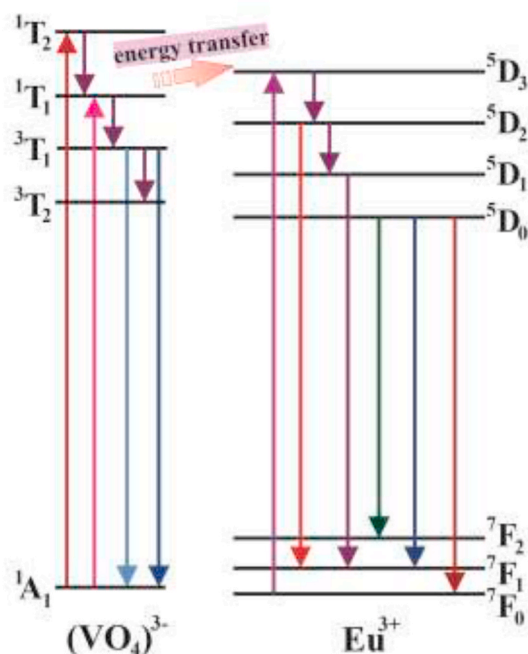**Fig. 1.** Energy levels and energy transfer model of Eu^{3+} ion and $(VO_4)^{3-}$ tetrahedron in YVO4.

an increase of energy between valence and conduction band). This is the reason why nanomaterials have wider band gap compared to their bulk counterparts. The larger the band gap (i.e. forbidden region), the greater the restriction of the electron movement will be. This is well known as the *quantum size effect*. As a consequence of size reduction, there is a shift of absorption spectrum of nanomaterials towards the lower wavelengths, known as a *blue shift*.

In bulk crystals, bulk longitudinal (ω_{LO}) and transversal (ω_{TO}) optical phonon frequency occur. In crystals with relatively small dimensions, a new frequency appears – Surface Optical Phonon (SOP) frequency (ω_{SOP}) which is located between the ω_{LO} and ω_{TO} frequency. That means that due to effects of dimension, in addition to the modes of infinity lattice, surface modes will be manifested. And in the case of crystals with extremely low dimensions, only the surface mode perseveres.

Different types of interactions with electromagnetic radiation takes an important place in semiconductors. On one side, we have investigated electron – phonon interaction in ceramic nanopowders [7]; surface optical phonon – plasmon in thin films [8]. Besides that, we have studied damping influence on interaction appearance [9], plasmon – impurity local phonons [10], as well as plasmon – different phonons interactions [11].

A special attention should be given to the choice of method for nanopowder preparation, because nanostructured samples with good crystallization and homogenous particle size exhibit extraordinary properties different from their bulk analogs. At the same time, a very important thing for their application in industry and technology is finding a fast, cheap and reproducible technique for obtaining fine nanophosphors.

In this paper two types of methods were presented. One, the top – down approach, *Solid State Reaction Method* (SSR), (which implies extensive milling), which is a classical ceramic method and the other, bottom – up approach, *Solution Combustion Synthesis* (SCS). Top down approaches have advantages like large scale production and deposition over a large substrate; also, with these techniques, chemical purifications are not required. Disadvantages of top – down methods are varied particles shapes or geometry, different impurities (stresses, defects and imperfections); also, one must be very careful not to have broad size distribution of particles. Bottom – up approaches, on the other hand,

offer ultra – fine nanoparticles, with controlled deposition and narrow size distribution. Unlike the previous techniques, bottom – up approaches do not offer large scale production so easily, and require chemical purification. Therefore, we have chosen one technique from both approaches so they can be compared. In this paper we offer two simple, fast, cheap and yet reproducible techniques for yttrium orthovanadate nanopowder preparation.

1.1. Bulk crystal of YVO4

Yttrium orthovanadate crystal has a zircon – type of structure, and crystalizes in 141. Space group, $I4_1/amd$ shown in Fig. 2. In this structural type, Y ions occupy **4a** crystallographic (Wyckoff) site with coordinates $[[0, 3/4, 1/8]]$.

V ions occupy **4b** crystallographic site, and coordinates $[[0, 1/4, 3/8]]$; while O ions occupy **16h** crystallographic site, with coordinates $[[0, y, z]]$.

This structure belongs to 4/mmm Laue class, where fourfold axis is a unique symmetry operation and has an expressed anisotropy of physical properties. V ions are in tetrahedral surrounding of O ions, while the surrounding of Y ions is made of oxygen coordination sphere with eight O ions which form a highly distorted cube.

From a group – theory analysis [12] it is known for this type of symmetry with two chemical formulas in the primitive cell ($I4_1/amd$ – D_{4h}^{19}) to have following modes in the center of the Brillouin zone at the Γ point: $\Gamma(k = 0) = 2A_{1g} + 5E_g + 4B_{1g} + 1B_{2g} + 4A_{2u} + 5E_u + 1A_{2g} + 1A_{1u} + 1B_{1u} + 2B_{2u}$. E_u and A_{2u} modes show dipole moments oriented perpendicular and along the c directions, respectively; and four out of five E_u modes are infrared active.

Infrared reflection spectrum of bulk YVO4 can be found in the literature [13]. In the measured reflectivity spectra, two sharp features at the lowest frequency can be found, and they correspond to the unscreened infrared – active optical phonon modes. This spectrum is characterized with four peaks of which three are easily seen, while the fourth is a shoulder of the second reflectivity band, and it is more evident at lower temperatures. Since bulk YVO4 has no metallic contribution (i.e. free carrier contribution), the Lyddane – Sachs Teller (LST) relation (Lorenz oscillator model) can be an optimal model to analyze reflection spectra and to model an appropriate dieletric function of a material.

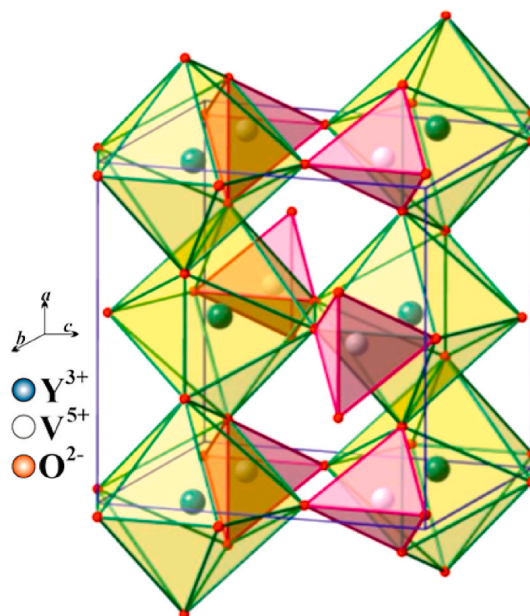In this paper we report the change in reflection spectra of europium

Fig. 2. Crystal structure of YVO4.

doped YVO₄ nanopowders with comparison to its bulk analog. In UV – VIS reflection spectra we consider the change in values of a band gap of europium doped YVO₄ when it is resized from bulk to nanomaterial. In IR reflection spectra we carry out phonon investigation in order to explain the change in optical properties of investigated nanopowders. We show the existence of surface optical phonon (SOP) and different phonon processes which alter the reflection spectra of bulk YVO₄. Full characterization of materials is made with X – Ray Powder Diffraction (XRPD) and Field Emission Scanning Electron Microscopy (FESEM).

2. Sample preparation and characterization methods

Nanopowders prepared by SCS were obtained using stoichiometric quantities of starting chemicals $Y(NO_3)_3 \cdot 6H_2O$, NH_4VO_3, NH_4NO_3 and $Y(NO_3)_3 \cdot 6H_2O$, purchased from ABCR with the purity of 99.99%. Urea was purchased from Sigma – Aldrich. Eu^{3+} concentration was 1%. 4.8 g of NH_4NO_3 and 3.003 g of urea, $(NH_2)_2CO$ which were used as an organic fuels were added to a dry mixture of 0.357 g $Eu(NO_3)_3 \cdot 6H_2O$, 4,676 g of NH_4VO_3 and 15.32 g of $Y(NO_3)_3 \cdot 6H_2O$. Then, mixture was combusted with the flame burner at ~500°C. Then, the solid solution starts to act like cloud – shape mixture which then was annealed in air atmosphere at 1200°C for 2 h. The annealing of material offers full crystallinity. This sample was labeled as **YVS**.

Solid state reaction procedure was performed using stoichiometric quantities of starting chemicals, then powdered and baked on 900°C for 5 h. Starting chemicals, Y_2O_5, Y_2O_3 and Eu_2O_3 with purity of 99.99% were purchased from ABCR. Concentration of Eu ions was 1%. This sample was labeled as **YVC**. Both samples, YVS and YVC, were made in a series of 5 samples, and every measurement is an average of these 5 samples.

These two simple, but yet reproducible and efficient methods provide two morphologically different samples. In this way methods can be compared and analyzed.

Structural characteristics of yttrium orthovanadate nanopowders were obtained using Philips PW 1050 diffractometer equipped with a PW 1703 generator, 40 kV × 20 mA, using Ni filtered Co Kα radiation of 0.1778897 nm, at room temperature. 15–85° range was used during 2 h, with a scanning step of 0.05° and 10s scanning time per step.

Morphologies of prepared samples were examined by Field Emission Scanning Electron Microscopy using FEI Scios 2 with an acceleration voltage between cathode and anode 15 kV.

All UV–Vis reflectance spectra were recorded in the wavelength range of 200–1200 nm on the Shimadzu UV – 2600 spectrophotometer equipped with an integrated sphere. The reflectance spectra were measured relative to a reference sample of BaSO₄.

The infrared reflectivity measurements were performed at room temperature. BOMEM DA – 8 Fourier – transform infrared spectrometer was used. A Hyper beamsplitter and DTGS (deuterated triglycine sulfate) pyroelectric detector were used to cover the wave number region 80–650 cm⁻¹. Spectra were collected with 2 cm⁻¹ resolution with 500 interferometer scans added for each spectrum.

2.1. X – ray powder diffraction

Results for YVC and YVS are shown in Fig. 3. The diffractograms confirm that both samples are monophased and that they crystallized in zircon – type of structure. All reflections are in good agreement with JCPDS card 17–0341. Also, all samples show no other reflections other than ones who originate from YVO₄ structure. Since Eu^{3+} concentration in these samples is 2%, one cannot be identified by XRD. Crystallite sizes are 53 nm and 58 nm for YVC and YVS, respectively. Crystallite sizes were determined using Debye Scherrer formula. This formula gives value of average crystallite size, and from our calculations the deviation is around 5 nm. To reduce this error, series of every sample were made (5 from each) to reduce the influence of chemical modification and other
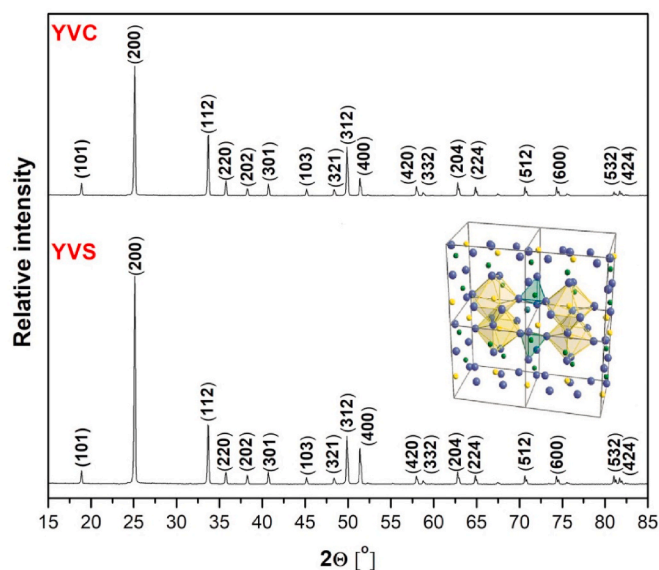

Fig. 3. XRD patterns of europium doped yttrium – orthovanadate nanopowder prepared by Solid State Reaction Method (YVC) and Solution Combustion Synthesis (YVS).

processing conditions). Even though Debye Scherrer is a rough method for determining crystallite size and one could use other methods for determining this value, like Williamson – Hall analysis which could in some way reduce this problem, this would suggest to rely on some other assumptions which could add up to an error. Crystallite size for sample YVC is smaller than one obtained in YVC. This was expected because of method of preparation. YVC was prepared using Solid State Reaction Method, which includes rather aggressive milling, and therefore results in smaller crystallite size than sample YVC, which was obtained with Solution Combustion Synthesis.

2.2. Field emission scanning electron microscopy

FESEM photographs are shown in Figs. 4 and 5, for YVS and YVC respectively; with 10 000 × and 35 000× magnification. Particle sizes are 2 m and 3 μm, for YVC and YVS, respectively. These values are much larger than the ones obtained with XRD. Reason for this is crystallite agglomeration. Regardless of agglomeration, trend in crystallite size between two methods of preparation remains the same as in crystallite sizes determined by XRD. One more thing must be noticed, and that is difference in crystallinity between samples. As can be seen from Figs. 4 and 5, sample YVC is more crystalline than YVS, which has more of a cloud – shape structure. This was marked with yellow rectangles in Figs. 4 and 5. On a larger scale, both samples consist of clearly defined and separated grains which can be seen on right hand side of Figs. 4 and 5.

3. Results and discussion

3.1. UV – VIS spectroscopy

In this section we investigated optical UV–Vis reflection spectra of europium – doped yttrium orthovanadate nanopowders. Special attention was given to obtaining band gap values. Band gap values were obtained using Tauc plot [14]. It is important to have information about band gap values, because band structure is responsible for the wide range of electrical characteristics. Tauc, Davis and Mott [15] have proposed an expression:

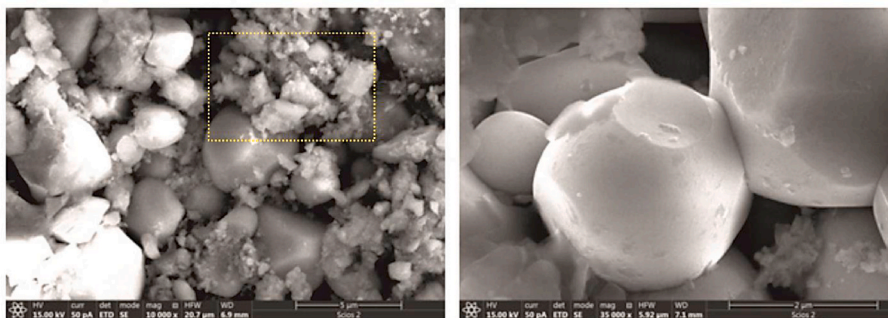$$\alpha h\nu = A\left(h\nu - E_g\right)^{1/n} \qquad (1)$$

Fig. 4. FESEM photographs of europium doped yttrium – orthovanadate nanopowder prepared by Solid State Reaction Method (YVS).
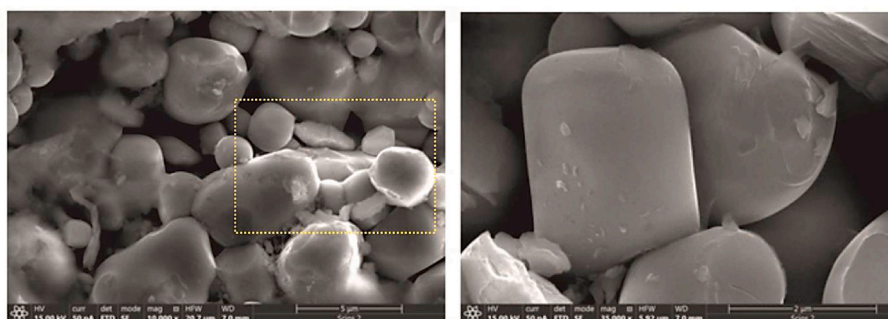

Fig. 5. (a) FESEM photographs of europium doped yttrium – orthovanadate nanopowder prepared by Solid State Reaction Method (YVC).

where α is the absorption coefficient (which is a property of a material; it defines the amount of light absorbed by it); h is the Planck's constant and $h\nu$ is the photon energy. A represents transition probability constant (which depends on the effective mass of the charge carriers in the material) and E_g is the band gap. Number n defines the nature of transition. If transition is direct, n equals 1/2 and 3/2, for the allowed and forbidden transitions, respectively. In the case of indirect transitions, n is 2 for allowed and 3 for forbidden transitions. In our case n is 3/2.

Then, the obtained diffuse reflectance spectra are converted to Kubelka – Munk function [16]:

$$\alpha = \frac{(1-R)^2}{2R} \qquad (2)$$

where R is a reflectance value. Using Eqs. (1) and (2), we obtain $(\alpha h\nu)^{1/n}$ vs. $h\nu$ plot. By extrapolating the linear portion of mentioned dependence to the energy axes at the $(\alpha h\nu)^{1/n} = 0$ value, the band gap value is obtained – the intercept of the plot with x – axe gives the value of band gap. The results obtained with UV – VIS spectroscopy, UV – VIS reflectance and diffuse reflectance Kubelka – Munk spectra for YVS and YVC are presented in Figs. 6 and 7 respectively.

From Table 1 values of calculated band gap for europium doped yttrium orthovanadate nanopowders prepared by two methods, as well as literature data for bulk YVO$_4$ were presented. With regard to section 2 where it was explained how band gap values increases with decreasing grain size, we got matching results. Namely, we got two values of band gap for samples made with two methods, YVC and YVS: 3, 55 eV and 3,17 eV, respectively. Since crystallite size of YVC (53 nm) is smaller than in YVS (58 nm), it is expected that the band gap value will be greater for YVC, due to quantum size effect described earlier. Both E$_g$ values for nanophosphors are greater that the E$_g$ value for bulk crystal YVO$_4$, which is expected. With this we conclude that Solid State Reaction Method provides samples with higher band gap values that samples prepared by Solution Combustion Synthesis.

When under the UV–Vis radiation, three major steps occur in YVO$_4$:

Eu^{3+}: 1. absorbance of radiation by (VO$_4$)$^{3-}$ groups; 2. transfer of the excited energy to Eu^{3+} ions which migrated through vanadate sub-lattice; and 3. red emission induced by de – excitation process of excited Eu^{3+} ions. This was represented in Fig. 1.

Peak at around 272 nm originates from absorption of (VO$_4$)$^{3-}$ groups [17]. According to the literature, this peak is an attribution to charge transfer from oxygen ligands to the central vanadium atom in (VO$_4$)$^{3-}$ group. In that way, UV–Vis spectra from Figs. 6a and 7a prove there is an energy transfer between (VO$_4$)$^{3-}$ and Eu^{3+} ions. Peak at 343 nm originates from (VO$_4$)$^{3-}$ in the lattice [18]. Peak at 272 in YVS is clearly seen. On the other hand, in YVC sample, splitting of 272 mode is obvious. The mode split because reflectance values cannot go below zero values; and increase in intensity of reflectance compared to YVS is caused by multi – phonon processes which seem to be more dominant in YVC rather than in YVS.

In one of our previous papers [19] it is shown how Eu ions exchange with of Y ions, and without any significant disturbance of symmetry take place in YVO$_4$ structure. Clearly, Eu ions have more influence in YVC sample, which has more crystallinity and smaller crystallite size, and are more efficiently distributed throughout the YVC sample. More evidence on multi – phonon processes which are present in YVC will be shown more clearly using Infrared Spectroscopy.

Results like this also confirm that these materials are suitable for many optical devices. Following our previous research [20] these phosphors represent an excellent hosts for optical excitation and emission of europium. Also, since the samples were made using two different techniques on different temperatures (500 and 900 °C), a certain evidence of thermal stability on emission quantum yield and lifetime was shown which is in good agreement with the literature [21].

3.2. Infrared spectroscopy

Subject of this paper are distinctively inhomogeneous materials. They are built out of embedded components in a matrix, and every one of them has its own macroscopic properties. A macroscopic property can
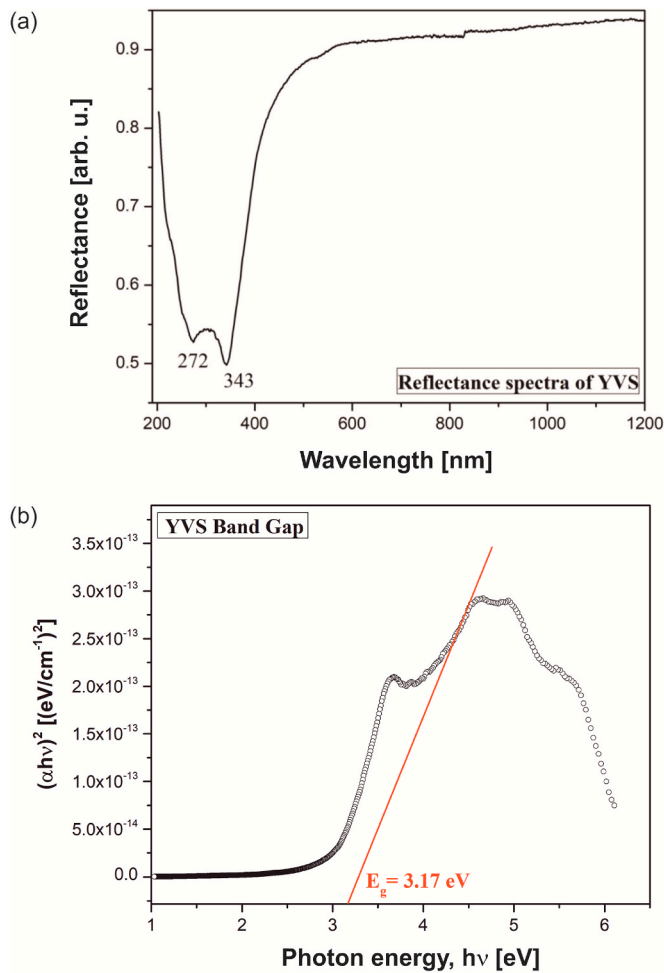
Fig. 6. (a) UV – VIS reflectance spectra of europium doped yttrium – orthovanadate nanopowder prepared by Solid State Reaction (YVC). (b) Kubelka – Munk plot for europium – doped yttrium – orthovanadate nanopowder prepared by Solid State Reaction (YVS).

Fig. 7. (a) UV – VIS reflectance spectra of europium doped yttrium – orthovanadate nanopowder prepared by Solution Combustion Synthesis (YVC). (b) Kubelka – Munk plot for europium – doped yttrium – orthovanadate nanopowder prepared by Solution Combustion Synthesis.

Table 1
Band gap values for YVC, YVS and literature data for bulk YVO_4 bulk crystal.

YVC	YVS	YVO_4 bulk (literature) [22]
3.56 eV	3.16 eV	2.85 eV

be attributed to every component of this material, as well as to a matrix. For example, this can be a dielectric permittivity. A medium where dielectric permittivity of every component and its surrounding (matrix) can be substituted with one value of dielectric permittivity, *an effective dielectric permittivity*, is called an effective medium, and theory which describes this is known as Effective Medium Theory. In other words, within this model, a heterogeneous system can be seen, from a bigger scale, as a homogeneous system, with its own properties which are often called effective properties, with one important fact: on a scale comparable with the dimensions of the system constituents, the system cannot be regarded as a homogeneous medium. Theory of effective medium has several approximations [22], of which two are most common: Maxwell Garnet and Brugemann approximation. The first one implies that constitutive parts of one medium are very well separated out of matrix they've been embedded in, and that there is no electrostatic interactions between them. On the other hand, Brugemann approximation describes systems where constitutive parts cannot be separated out of their surroundings.

When visible light, λ, interacts with a material described above, where its nanoparticles have characteristic size d, and dielectric function ε_2, which are randomly distributed in a matrix with a dielectric constant ε_1, in the limit $\lambda \gg d$, the heterogeneous composite can be treated as a homogenous, and this system can be described with Effective Medium Theory. Since the samples we investigate are well defined, spherical and separated nano grains (as seen in Figs. 4 and 5), we use Maxwell Garnet
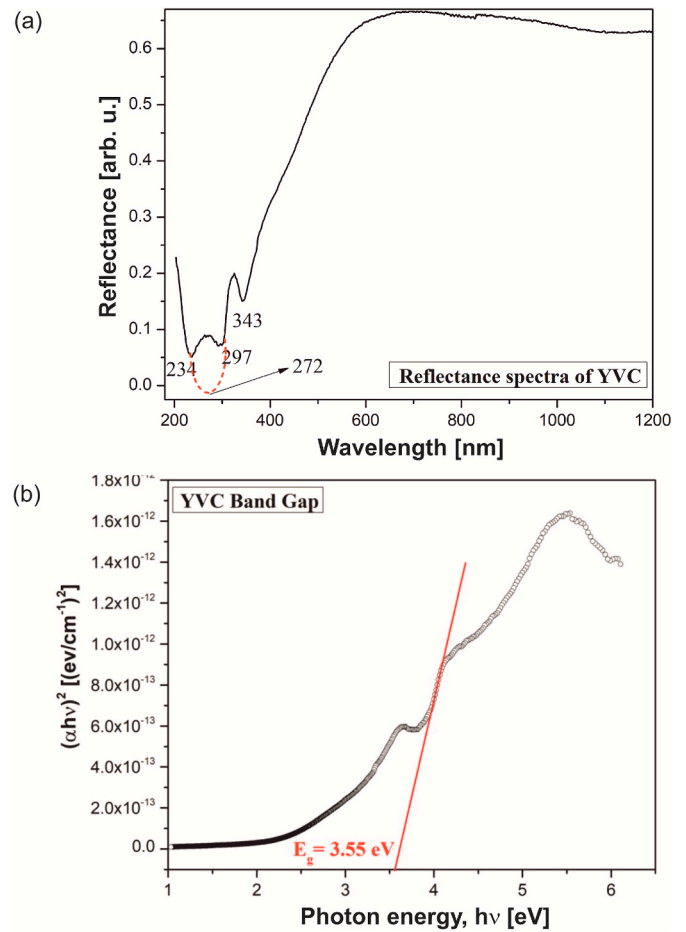
model for the present case. Following postulates of this approximation, for the effective permittivity of so called homogeneous medium we get [23]:

$$\varepsilon_{eff} = \varepsilon_1 + 3f_1 \frac{\varepsilon_1(\varepsilon_2 - \varepsilon_1)}{\varepsilon_2 + 2\varepsilon_1} \tag{3}$$

where ε_2 is a dielectric permittivity of nanoparticles located randomly in a homogeneous environment with dielectric permittivity ε_1, which is, in our case, air; and occupy a volume fraction f (so called filling factor).

For modeling dielectric permittivity of above described nanoparticles, we have used a classical oscillator model with Drude part added (second addition in Eq. (3)) which takes into account the free carrier contribution [24].:

$$\varepsilon_2(\omega) = \varepsilon_\infty \left(\prod_{k=1}^{n} \frac{\omega_{LO}^2 - \omega^2 + i\gamma_{LO}\omega}{\omega_{TO}^2 - \omega^2 + i\gamma_{TO}\omega} - \frac{\omega_P^2}{\omega(\omega - i\tau^{-1})} \right) \tag{4}$$

where ε_∞ is a bound charge contribution (assumed to be constant), transverse and longitudinal frequencies are noted with ω_{TO} and ω_{LO}, γ_{TO} and γ_{LO} are their damping coefficients, ω_P is plasma frequency and free
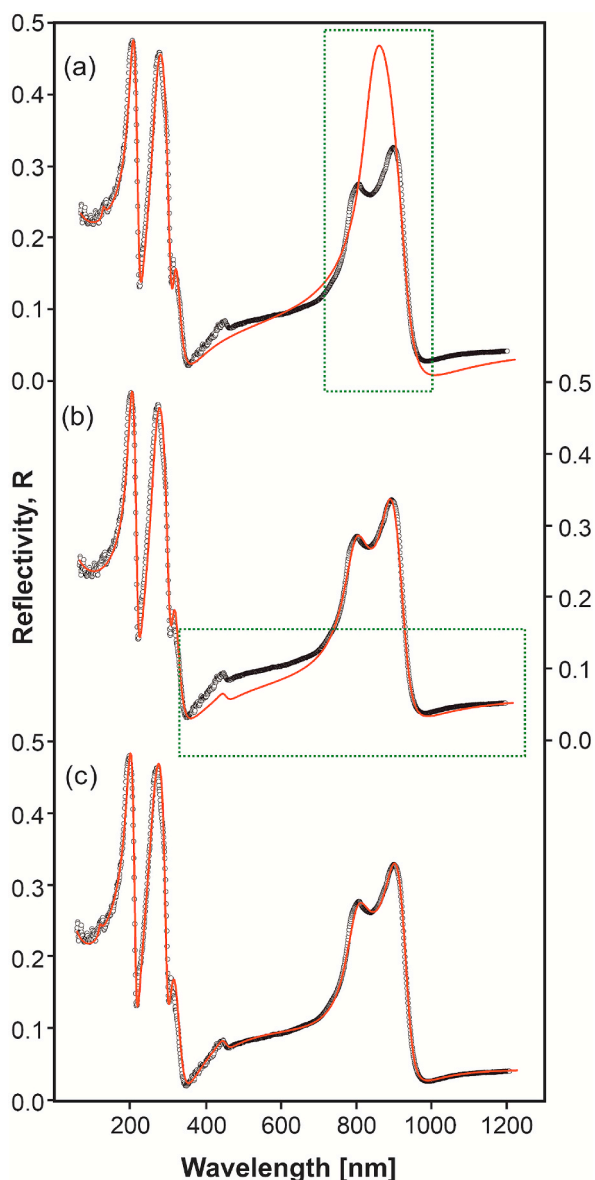
carrier relaxation time is marked by τ.

Calculated spectra were obtained by a fitting procedure using a previously described model which is represented with solid lines in Figs. 8 and 9. Using the least – square fitting procedure of the experimental (R_{exp}) and theoretical (R_{th}) reflectivity, at q arbitrarily taken points, the parameter adjustment was carried out, automatically.
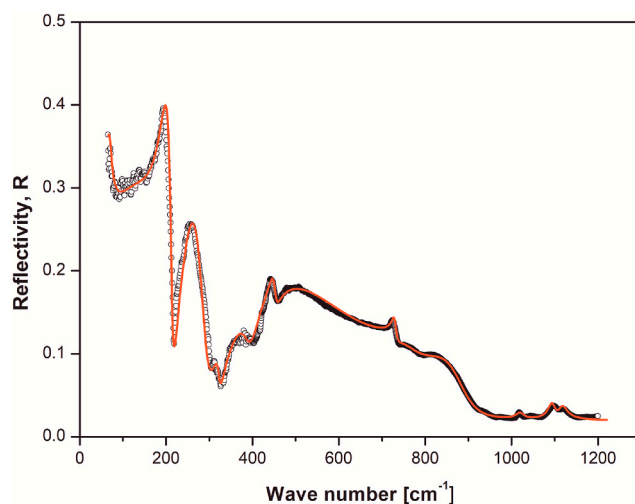
$$\delta = \sqrt{\frac{1}{q} \sum_{j=1}^{q} \left(R_{exp} - R_{th} \right)^2} \tag{5}$$

Minimalization of δ was carried out until it met the conditions of commonly accepted experimental error of less than 3%.

Theoretical model in Figs. 8c and 9, show excellent match with the experimental results, for YVS and YVC samples, respectively. In Table 2, best fitting parameters are presented. In Eq. (4), transversal optical

Fig. 9. Infrared reflection spectra of YVO4 nanopowders prepared by Solid State Reaction (sample YVC). Experimental spectra are presented by open circles, while solid red lines are calculated spectra obtained by a fitting procedure based on the model given by Eqs. (3) and (4).

Table 2
Best fitted parameters of IR reflection spectra for YV, YVC and YVC; bulk literature data and their assignments.

	YVC [cm^{-1}]	YVS [cm^{-1}]	Bulk YVO4 (Literature data) [cm^{-1}] [13]	Assignment
ε_∞	1.8	2.25	4.0	
F	0.79	0.93	1	
Γ_P	85	200		
ω_P	100	89		Plasmon frequency which plays role of ω_-
ω_{TO3}	212	198	195	E_u mode, IR active
ω_{LO3}	214	219	220	
ω_{TO4}	234	259	263	E_u mod, IR active
ω_{LO4}	292	300	309	
ω_{TO5}	321	311	309	E_u mod, IR active
ω_{LO5}	323	337	311	
ω_{TO6}	397	–		Multiphonon processes
ω_{LO6}	393	–		
ω_{TO7}	400	470		
ω_{LO7}	645	650		
ω_{TO8}	450.5	452		
ω_{LO8}	452	454		
ω_{TO9}	730.2	–		
ω_{LO9}	731	–		
ω_{TO10}	759	794	780	SOP formation. E_u mod, IR active
ω_{LOSOP}	863	890		SOP phonon
ω_{LO10}	887	935	930	
ω_{TO11}	1020	–		Multiphonon processes
ω_{LO11}	1021	–		
ω_{TO12}	1093.5	–		
ω_{LO12}	1096	–		
ω_{TO13}	1116	–		
ω_{LO13}	1117.5	–		

Fig. 8. Infrared reflection spectra of YVO$_4$ nanopowders prepared by Solution Combustion Synthesis (sample YVS). Experimental spectra are presented by open circles, while solid red lines are calculated spectra obtained by a fitting procedure based on the model given by Eqs. (3) and (4). Spectrum (a) shows fitting procedure without taking into account SOP phonons, (b) spectrum without taking into account multiphonon processes and (c) IR reflection spectrum of YVS when SOP phonons and multiphonon process were considered.

frequency, ω_{TO}, was precieved as the characteristic frequency for a given material. As regards to spectra from Fig. 8a and 8b, they show the procedure, step by step, in order to get the best fit presented in Fig. 8c. Model used in Fig. 8a did not take into account the existence of SOP. Actually, this model suits the bulk structure of YVO$_4$ the best, when there's no SOP [25]. After we took this into account, we notice that, when bulk YVO$_4$ was resized to nanoscale, wide mode on the highest frequencies in bulk spectrum of YVO$_4$ [13] split into two modes. Since this was modeled with dielectric function which takes into account the existence of SOP, we conclude that the reason for splitting this wide

mode is occurrence of SOP mode in these structures. After including SOP modes into reflection spectra of nanostructures, we still have slight differences between experimental and theoretical results (Fig. 8b) at frequency between two sharp modes at lowest, and one wide mode at highest frequencies.

Reasons for this slight difference presented in Fig. 8b are different multi – phonon processes, with frequencies obtained in Table 2. After we took this into account, we got excellent match of theoretical and experimental results, shown in Fig. 8c.

From this we conclude that influence in reflection IR spectra in majority comes from SOP mode and not from multi – phonons. Still, when we compare two spectra from 8c and 9, we do see differences, which originate from different contributors to reflection IR spectra. In sample made with Solution Combustion Synthesis (YVS), the contribution of SOP is greater than in samples made with Solid State Reaction (YVC). Yet, in sample YVC, influence of multi – phonon contributors is greater than in YVS which is also shown in UV–Vis measurements. We see that from Table 2, for the wavenumbers greater than 1020 cm^{-1}, where we modeled multi – phonon modes for YVC and not for YVS, because of the greater influence of SOP in this sample which completely covered possible multi – phonon processes in YVS. From all of this, we can say that, when we compare to nanopowders prepared with two different methods, one can say that for YVS, influence of SOP mode dominates, and for sample YVC, multi – phonon modes dominate over SOP modes.

Now, let us discuss the results obtained in Table 2. In Eq. (3) we have defined the parameter called filling factor. It is a parameter which describes the volume fraction occupied by the nanoparticle (or nanoparticle aggregates) in the surrounding medium. In Table 2, filling factors of prepared nanopowders, YVC and YVS, together with value for bulk crystal YVO$_4$ are presented. Intensity and shape change of SOP modes presented in Figs. 8 and 9 (described with Eq. (4)) are notably affected by variation of filling factor, f.

In our case, position of SOP modes maxima directly follows the change in filling factor. Position of SOP modes frequencies are obtained from Eq. (6) [26], and the results are presented in Fig. 10.

$$\omega_{SOP} = \max\left(I_m\left(-\frac{1}{\varepsilon_{eff}} \right) \right) \tag{6}$$

In bulk crystal YVO$_4$ [13], at room temperature, four modes in infrared reflection spectra have been detected at 195, 263, 311 and 780 cm^{-1}. These modes are separated into internal (motions of the tetrahedral VO$_4$) and external (translations and rotations of the VO$_4$ tetrahedron). All of these modes, as expected, are shifted after resizing bulk

to nanomaterial to 212, 234, 323 and 759 cm^{-1} for YVC, and to 198, 259, 337 and 794 cm^{-1} for YVS, respectively. Appearance of new phonons is due to break – down of the selection rules, as a consequence of resizing of the bulk crystal to nanostructure. Some modes occur due to appearance of surface optical phonon mode and some due to multi – phonon processes (one is, as we said, more dominant in YVS and other in YVC) in addition to modes which occur owing to Eu ion and its interaction with YVO$_4$ lattice. All of the modes are represented and assigned in Table 2.

Based on these results, it is clear that filling factor of prepared nanopowders depends on method of preparation, but yet it has a linear dependence of occurred surface optical phonon frequency. Also, SOP mode has the role of the LO phonon which we have also showed in our earlier works in different nanostructures [8].

Vibrational spectroscopy of nanostructures for discovering surface optical phonons represents an extremely active and exciting field with many possibilities for scientific and technological development. This arising new phenomena offer not only new perspective for material characterization, but also a fundamental understanding of processes at nanoscale. Better understanding of phonon properties of phosphors shown in this paper leads to wide application of these nanostructured materials for nanophosphor coatings [27], biomedical application [28], luminescence efficiency [29] etc. Also, discovery of surface phonons in these materials offer great use in heteronanostructures [30] to enhance the photoluminescence properties.

On the other side, multiphonon processes have been investigated for the first time in this nanostructured orthovanadate. Understanding multiphonon processes and charge transfers within a phosphor structure leads to its better application in self – assembled quantum dots [31] and different luminescent materials [32].

4. Conclusion

In this paper we showed two methods of preparation of yttrium orthovanadate nanopowders, Solution Combustion Synthesis and Solid State Reaction Method. Samples prepared by Solution Combustion Synthesis offer slightly bigger crystallite size, and therefore smaller width of band gap compared to samples prepared by Solid State Reaction Method, which provides samples with band gap up to 3.56 eV which was obtained using UV–Vis spectroscopy. Splitting of 272 nm mode from UV–Vis spectra for sample made by Solid State Reaction Method gives an indication of more dominant multi – phonon modes in this sample rather than in one made by Solid Combustion Synthesis. This was caused by doping and transfer of excited energy which migrates through vanadate sublattice to Eu ions; and after causes red emission induced by de – excitation process of excited Eu ions. For modeling Infrared Reflection spectra of both samples, Effective Medium Theory in Maxwell Garnett approximation was used and classical oscillator model, with Drude part added which takes into account concentration of free carriers. We showed that in both samples characteristic frequency of Surface Optical Phonon occurs as a consequence of resizing bulk crystal to nano scale. Also, that SOP has greater influence in sample prepared by Solution Combustion Synthesis, while in sample prepared by Solid State Reaction Method multi – phonon modes are more dominant and cover SOP modes. This was a confirmation of previous UV–Vis results. Since change in intensity and shape of SOP modes depends on variation of filling factor, we have considered the values of filling factor and its dependence on SOP mode position and came to a conclusion that SOP frequency has a linear dependence on filling factor, where SOP mode plays a role of LO phonon. All results obtained, show not only occurrence of nanoscale phenomena – surface optical phonon and multiphonon processes in YVO$_4$:Eu^{3+} nanostructures, but its potential use in wide fields of science and technology.
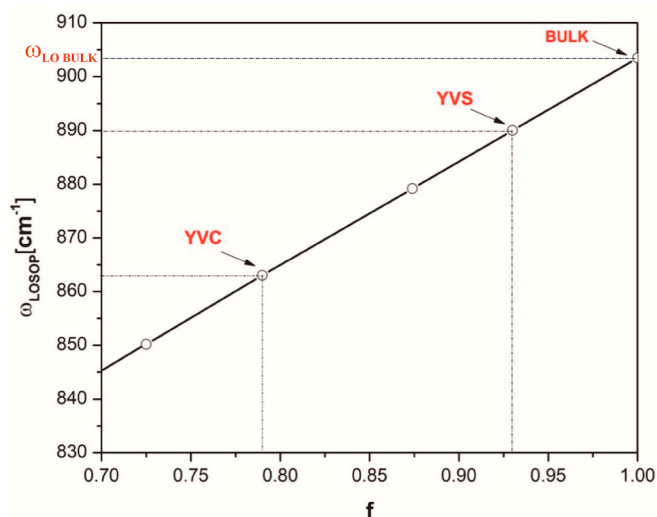

Fig. 10. Surface Optical Phonon mode position vs. filling factor.

Declaration of competing interest

The authors declare that they have no known competing financial interests or personal relationships that could have appeared to influence the work reported in this paper.

Acknowledgments

References

[1] T. Voitenko, S.A. Nedilko, K. Savva, M. Androuulidaki, S.G. Nedilko, E. Stratakis, O. Chukova, A. Papadopoulos, Deposition of luminiscent vanadate nanoparticles on silicon solar cells, in: IEE 40th International Conferece on Electronics and Nanotechnology (ELNANO), Kyiv, Ukraine 251 – 254, 2020.

[2] D. Hu, D. Li, X. Liu, Z. Zhou, J. Tang, Y. Shen, Vanadium – based nanomaterials for cancer diagnosis and treatment, Biomed. Mater. (2020) in press.

[3] D. Dosev, M. Nichkova, I.M. Kennedy, Inorganic lanthanide nanophosphors in biotechnology, J. Nanosci. Nanotechnol. 8 (3) (2008) 1052–1067 (16).

[4] L.P. Singh, N.V. Jadhav, S. Sharma, B.N. Pandey, S.K. Srivastava, R. S. Ningthoujam, Hybrid nanomaterials YVO4:Eu/Fe$_3$O$_4$ for optical imaging and hyperthermia in cancer cells, J. Mater. Chem. C 3 (2015) 1965–1975.

[5] W.L. Wanmaker, A. Bril, J.W. Vrugt, J. Broos, Luminiscent properties of Eu – activated phosphors of the type AIIIBnOn, Philips Res. Rep. 21 (1966) 270.

[6] J. Su, X. Mi, J. Sun, L. Yang, C. Hui, L. Lu, Z. Bai, X. Zhang, Tunable luminescence and energy transfer properties in YVO4:Bi^{3+}, Eu^{3+} phosphors, J. Mater. Sci. 52 (2) (2017) 1–11.

[7] J. Mitrić, J. Križan, J. Trajić, G. Križan, M. Romčević, N. Paunović, B. Vasić, N. Romčević, Structural properties of Eu3+ doped Gd2Zr2O7 nanopowders: far – infrared spectroscopy, Opt. Mater. 75 (2018) 662–665.

[8] J. Mitrić, N. Paunović, M. Mitrić, B. Vasić, U. Ralević, J. Trajić, M. Romčević, W. D. Dobrowolski, I.S. Yahia, N. Romčević, Surface optical phonon – plasmon interaction in nanodimensional CdTe thin films, Physica: Low Dimens. Syst. Nanostruct. 104 (2018) 64–70.

[9] N. Romčević, M. Romčević, W.D. Dobrowolski, L. Kilanski, M. Petrović, J. Trajić, B. Hadžić, Z. Lazarević, M. Gilić, J.L. Ristić – Đurović, N. Paunović, A. Reszka, B. J. Kowalski, I.V. Fedorchenko, S.F. Marenkin, Far – infrared spectrscopy of Zn$_{1-x}$Mn$_x$GeAs$_2$ single crystals: plasma damping influence on plasmon – phonon interaction, J. Alloys Compd. 649 (2015) 375–379.

[10] N. Romčević, J. Trajić, T.A. Kuznetsova, M. Romčević, B. Hadžić, D.R. Khokhlov, Far – infrared study of impurity local modes in Ni – doped PbTe, J. Alloys Compd. 442 (2007) 324–327.

[11] J. Trajić, M. Romčević, M. Romčević, V.N. Nikiforov, Mater. Res. Bull. 42 (2007), 2201–2192.

[12] C. Pecharroman, M. Ocana, P. Tartaj, C.J. Serna, Optical constants of tetragonal and cubic zirconias in the infrared, Mater. Res. Bull. 29 (1994) 417.

[13] C.Z. Bi, J.Y. Ma, J. Yan, X. Fang, D.Z. Yao, B.R. Zhao, X.G. Qiu, Far – infrared optical properties of YVO4 single crystal, Eur. Phys. J. B 51 (2006) 167–171.

[14] P. Makula, M. Pacia, W. Macyk, How to corretly determine the band gap energy of modified semiconductor photocatalysts based on UV – Vis spectra, J. Phys. Chem. Lett. 9 (23) (2018) 6814–6817.

[15] X. Li, H. Zhu, J. Wei, K. Wang, E. Xu, Zh Li, D. Wu, Determination of band gaps of self – assembled carbon nanotube films using Tauc/Davis – Mott model, Appl. Phys. A 97 (2009) 341–344.

[16] P. Kubelka, F. Munk, Ein Beitrag zur Optik der Farbanstriche, Zeits F. Teck. Physik. 12 (1931) 593–601.

[17] H. Wang, O. Odawara, H. Wada, Facile and chemically puyre preparation of YVO4: Eu3+ colloid with novel nanostructures via laser ablation in water, Sci. Rep. 6 (2016) 20507.

[18] J. Su, X. Mi, J. Sun, L. Yang, C. Hui, L. Lu, Z. Bai, X. Zhang, Tunable luminescence and energy transfer properties in YVO4:Bi^{3+}, Eu^{3+} phosphors, J. Mater. Sci. 2 (52) (2017).

[19] J. Mitrić, U. Ralević, M. Mitrić, J. Ćirković, G. Križan, M. Romčević, M. Gilić, N. Romčević, Isotope – like effect in YVO4:Eu3+ nanopowders: Raman spectroscopy, J. Raman Spectrosc. 50 (2019) 802–808.

[20] D. Šević, M.S. Rabasović, J. Križan, S. Savić – Šević, M. Mitrić, M. Gilić, B. Hadžić, N. Romčević, Characterization and luminiscence kinetics of Eu^{3+} doped YVO4 nanopowders, Mater. Res. Bull. 88 (2017) 121–126.

[21] A. Huignard, V. Buissette, A.-C. Franville, T. Gacoin, J.-P. Boilot, Emission processes in YVO4:Eu nanoparticles, J. Phys. Chem. B 107 (2003) 6754–6759.

[22] J. Trajić, M.S. Rabasović, S. Savić – Šević, D. Šević, B. Babić, M. Romčević, J. L. Ristić – Đurović, N. Paunović, J. Križan, N. Romčević, Far – infared spectra of dysprosium doped yttrium aluminum garnet nanopowder, Infrared Phys. Technol. 77 (2016) 226–229.

[23] J.C.M. Garnett, Colours in meta glasses and in metallic films, Philos. Trans. Royal Soc. A 203 (1904) 385–420.

[24] I.J. Uhanov, Opt. Svojstva Poluprovodnikov, Nauka, Moskva, 1977.

[25] C.Z. Bi, J.Y. Ma, J. Yan, X. Fang, D.Z. Yao, B.R. Zhao, X.G. Qiu, Far – infrared optical properties of YVO4 single crystal, Eur. Phys. J. B 51 (2006) 167–171.

[26] B. Hadžić, N. Romčević, M. Romčević, I. Kuryliszyn – Kudelska, W. Dobrowolski, J. Trajić, D.V. Timotijević, U. Narkiewicz, D. Sibera, Surface optical phonons in ZnO(Co) nanoparticles: Raman study, J. Alloys Compd. 540 (2012) 49–56.

[27] R. Kubrin, Nanophosphor coatings: technology and applications, opportunities and challenges, KONA Powder and Particle Journal 31 (22 – 52) (2014).

[28] T. Thu Huong, H. Thi Phuong, L. Thi Vinh, H. Thi Khuyen, T. Kim Anh, L. Quoc Minh, Functionalized YVO4:Eu^{3+} nanophosphors with desirable properties for biomedical applications, J. Sci – Adv. Mater Dev. 1 (3) (2016) 295–300.

[29] T. Minakova, S. Mjakin, V. Bakhmetyev, M. Sychov, I. Zyatikov, I. Ekimova, V. Kozik, Y.-W. Chen, I. Kurzina, High efficient YVPO4 luminescent materials activated by europium, Crystals 9 (2019) 658.

[30] H. Zhu, H. Hu, Z. Wang, D. Zuo, Synthesis of YVO4:Eu3+/YBO3 heteronanostructures with enhanced photoluminescence properties, Nanoscale Res. Lett. 4 (2009) 1009–1014.

[31] L. Magnusdottir, A. Uskov, S. Bischoff, J. Mork, Multiphonon capture processes in self-assembled quantum dots, in: Technical Digest. Summaries of Papers Presented at the Quantum Electronics and Laser Science Conference. Postconference Technical Digest (IEEE Cat. No.01CH37172), 2001, pp. 206–207.

[32] R. Liu, L. Liu, Y. Liang, Energy transfer and color – tunable luminescence properties of YVO4:Re (Re = Eu3+, Sm3+, Dy3+, Tm3+) phosphors via molten salt synthesis, Opt. Mater. Express 8 (6) (2018) 1686.

Plasmon – Phonon interaction in $ZnSnSb_2$ + Mn semiconductors

Maja Romcevic[a,*], Novica Paunovic[a], Uros Ralevic[a], Jelena Pesic[a], Jelena Mitric[a], Jelena Trajic[a], Lukasz Kilanski[b], Witold Dobrowolski[b], Irina Valentinovna Fedorchenko[c,d], Sergey Fedorovich Marenkin[c,d], Nebojsa Romcevic[a]

[a] *Institute of Physics, University of Belgrade, Belgrade, Serbia*
[b] *Institute of Physics, Polish Academy of Sciences, Warsaw, Poland*
[c] *Kurnakov Institute of General and Inorganic Chemistry, Russian Academy of Science, Moscow, Russian Federation*
[d] *College of New Materials and Nanotechnologies, National University of Science and Technology, Moscow, Russian Federation*

ABSTRACT

Semiconductors of II-IV-V₂ type with chalcopyrite structure have been studied for several decades. Due to advances in materials synthesis technologies, and doping with various elements, the possibilities of their application have expanded. In this paper, polycrystalline $ZnSnSb_2$ + Mn was examined with the aim to explain the connection of its high free carrier concentration with the material structure and influence on optical properties. Two samples of $Zn_{1-x}Mn_xSnSb_2$ with different compositions ($x = 0.027$ and $x = 0.076$) and significant difference in carrier concentrations were analyzed. Their structural properties were examined by x-ray diffraction, optical microscopy, and AFM. The existence of several different phases - $ZnSnSb_2$, ZnSb, SnSb, and small amounts of Sn and MnSb, as well as very complex microstructures, were registered. It was found that the high free carrier concentrations are caused by a large number of defects, especially zinc vacancies. Optical properties were analyzed using IR spectroscopy at room temperature. Based on the analysis of IR reflection spectra, the presence of plasmon - phonons interaction was registered. It was determined that three $ZnSnSb_2$ phonons of B_2 symmetry interact with plasma, which then leads to the change of their positions. A detailed analysis of this interaction provides insight into the behavior of some other material parameters. Also, vibration modes of ZnSb and SnSb phases were registered on the spectra. Knowledge of phonon behavior and their interaction with plasma is important for possible applications, especially as a thermoelectric material.

1. Introduction

Semiconductors have been widely used thanks to the ability to adapt to different requirements. The II-IV-V₂ chalcopyrite semiconductors have been intensively studied in recent decades [1]. The fields of their application are considerably expanded by doping with various impurities. A significant breakthrough was achieved by the addition of magnetic impurities, whereby ferromagnetism at room temperature was achieved [2,3]. The synthesis technology of this class of compounds has been developed, but it is still adapting to new requirements [4]. Zn-Sn-Sb based alloys have required thermoelectric properties and find application as low-toxic thermoelectric materials [5,6,7]. The engineering of structural, transport, electrical, optical, magnetic properties as well as other material parameters, goes along with the increasing application of this class of semiconductors.

$ZnSnSb_2$ is II-IV-V₂ type material with the tetragonal chalcopyrite structure, narrow gap of 0.7 eV at room temperature, high

concentration of free carriers (10^{21}–10^{22} cm^{-3}) and inhomogeneous structure [8,9]. In this paper we analyzed ferromagnetic semiconductor $ZnSnSb_2$ + Mn, which has interesting magnetic properties, such as paramagnet-ferromagnet transition with the Curie temperature about 522 K and the cluster-glass behavior with the transition temperature about 465 K, caused by the formation of MnSb clusters in the material [10]. The $Zn_{1-x}Mn_xSnSb_2$ samples were obtained using direct fusion method, and characterization of their structural, magnetic, optical and phonon properties were done [9]. We chose two samples with different chemical contents, x = 0.027 and x = 0.076, which we labeled as samples A and B respectively, with the aim to examine their properties in more detail. Main reason was a ten times difference in their free-carrier concentrations ($p_A = 13 \times 10^{21}$ cm^{-3} and $p_B = 1.2 \times 10^{21}$ cm^{-3}). We wanted to determine what the cause of this difference in concentration is, and whether there is a reaction between the free carriers and the crystal lattice. The question of plasmon-phonon interaction is particularly interesting in the study of thermoelectric

---

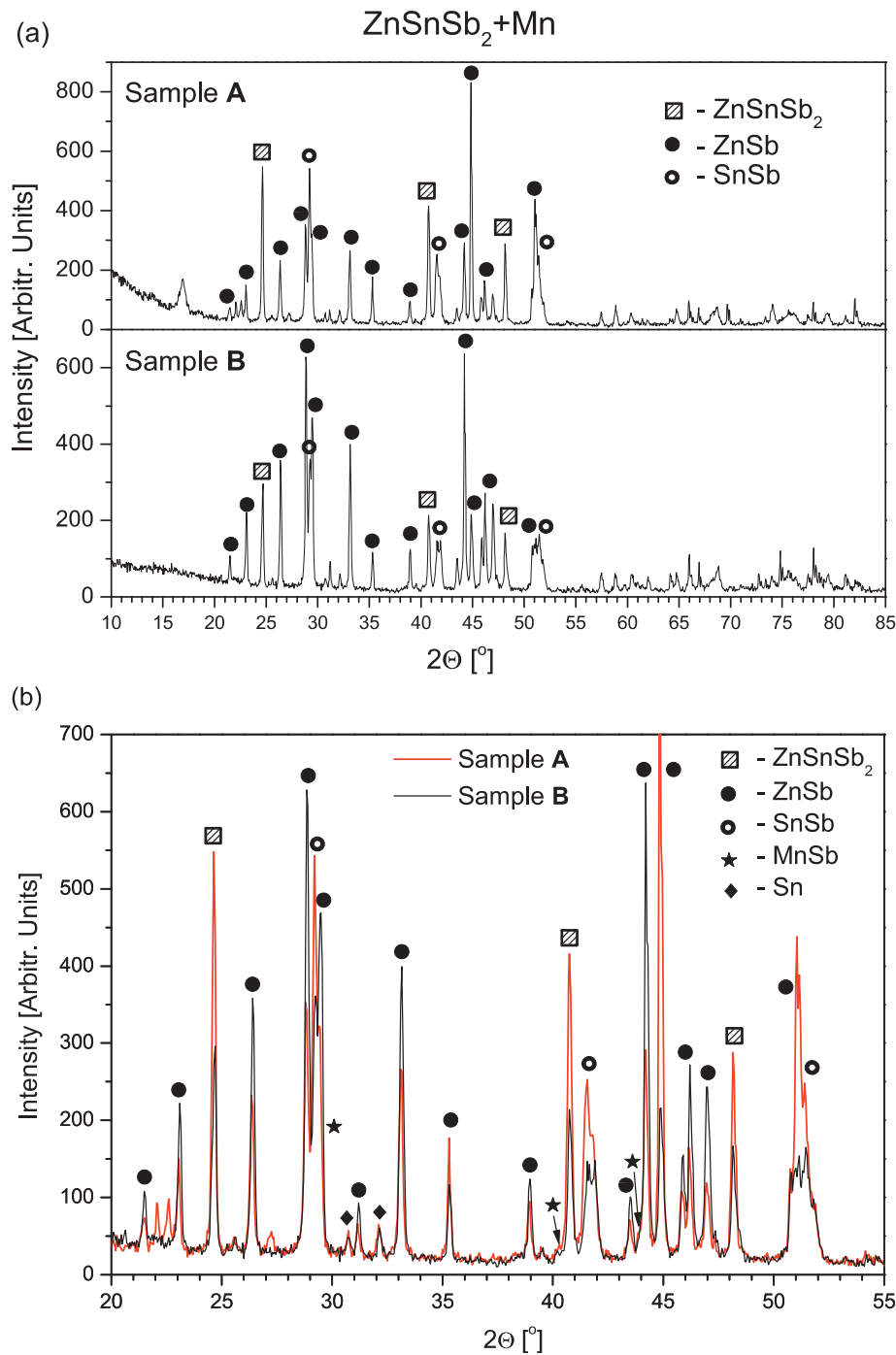**Fig. 1.** (a) X-ray diffraction pattern for ZnSnSb$_2$ + Mn samples which contain different amounts of Mn. The registered crystal phases are marked; (b) The two spectra are overlapped to compare their relative intensities.

materials, as well as their electrical and thermal conductivity, and their interdependence.

ZnSnSb$_2$ is not a homogeneous material, and the consequence is that even two samples from the same crystal can have significantly different properties. This is not surprising given the complicated ZnSnSb$_2$ microstructure. Our goal was to analyze the relationship between microstructures, their phonons and free carriers, their conditionality and interactions. For this purpose we used x-ray diffraction, optical microscopy, AFM and IR spectroscopy measurements. Obtained results were analyzed by applying the model for plasmon-phonon interaction.

2. Samples and characterization

ZnSnSb$_2$ semiconductor has a chalcopyrite structure, spatial group I42d, with lattice parameters $a \approx 6.275$ Å and $c \approx 12.55$ Å and ratio c/a close to 2. ZnSnSb$_2$ melts by a peritectic reaction at $T = 362$ °C with a possible phase transformation of the cubic modification into a tetragonal one at $T = 348$ °C [11,12]. The ZnSnSb$_2$ + Mn ferromagnetic semiconductors were synthesized using the method that makes it possible to obtain single crystals at temperatures below the temperature of the peritectic reaction.

The analyzed samples of Zn$_{1-x}$Mn$_x$SnSb$_2$ were synthesized by the direct fusion method. High purity components were used for the

synthesis: zinc single crystals (99.999%), shots of tin (99.999%), antimony single crystals (99.999%), and manganese powder (99.999%). They were mixed in stoichiometric ratios.

The reaction mixture was put into a quartz glass tube and heated up to 631 °C. After that, ampoules were quenched to 355 °C and then annealed at 355 °C. This is described in more detail in the papers [12,13]. The synthesized crystals were cut into slices of about 1.5 mm thickness.

The chemical composition of the samples (x) was determined using the energy dispersive x-ray fluorescence method (EDXRF) [10]. Obtained results showed that average Mn content (x) in the samples is between 0.027 and 0.138. All the studied crystals had the correct stoichiometry of $Zn_{1-x}Mn_xSnSb_2$ alloy equal to $1-x : x : 1 : 2$, within our measurement accuracy of about 10% of the x value.

Based on the magnetotransport measurements [10] it was found that electrical and magnetotransport parameters, such as resistivity, carrier concentration, and carrier mobility, do not depend linearly on composition, i.e. on the Mn content. Therefore, as mentioned above, two samples with a considerable difference in free-carrier concentrations were selected. The sample with x = 0.027 and $p = 13 \times 10^{21}$ cm^{-3} was labeled as sample A and the one with x = 0.076 and $p = 1.2 \times 10^{21}$ cm^{-3} as sample B. In this way we wanted to determine the connection between the free carriers and the structural and optical properties of the alloy.

The structural properties of these samples were investigated by the XRD powder technique. Measurements were done using a Philips PW 1050 diffractometer equipped with a PW 1730 generator, 40 kV × 20 mA, using Ni filtered Co Kα radiation of 0.1778897 nm at room temperature. The x-ray diffraction patterns were collected during 2 h in the range of $10-100°$ with a scanning step of 0.05° and 10 s scanning time per step. Phase analysis showed that besides the main phase of chalcopyrite $ZnSnSb_2$, the orthorhombic ZnSb, rhombohedral SnSb, and hexagonal MnSb phases are present in the samples. This is consistent with the literature [8,10].

An optical microscope was used to get an insight into the distribution of different phases of the material along the surface. Images were captured using Olympus BH series modular microscope with UIS objective lenses with 50x and 400x enhancement.

The surfaces of $ZnSnSb_2$ + Mn samples were examined in detail using Atomic Force Microscope (AFM), NTEGRA prima from NTMDT. The topography and phase images were acquired simultaneously by operating the AFM in semi-contact mode. NSG01 probes with a typical resonant frequency of 150 kHz and 10 nm tip apex curvature radius were used.

The far-infrared (FIR) reflectivity measurements were done with a BOMEM DA-8 Fourier-transform infrared spectrometer in the spectral range from 40 to 450 cm^{-1} at room temperature. A Hyper beamsplitter and deuterated triglycine sulfate (DTGS) pyroelectric detector were used.

3. Results and discussion

It is known that during the preparation of $ZnSnSb_2$ the polycrystalline material is formed, consisting of the main phase and ZnSb, SnSb and β-Sn inclusions [11].

The structure of the two selected samples was investigated by X-ray diffraction measurements. Obtained results with marked phases are presented in Fig. 1. In Fig. 1(b) the overlap of the results is shown, with the aim to compare their relative intensities. The list of XRD peaks positions and their corresponding Miller indices and phases is given in Table 1 in Supplementary Materials.

Besides the chalcopyrite $ZnSnSb_2$ phase the orthorhombic ZnSb, rhombohedral SnSb, Sn have also been registered, as well as weak lines from hexagonal MnSb inclusions. The idea was to detect differences in the structures of these two samples. It is obvious that diffraction lines corresponding to the $ZnSnSb_2$ phase (squares) are stronger for sample A

Table 1
Expected values of $ZnSnSb_2$ phonons of B_2 and E symmetries, from literature [26].

Phonon	B_2^1	B_2^2	B_2^3	E^1	E^2	E^3	E^4	E^5	E^6
Estimated value [cm^{-1}]	189	199	70	189	185	195	111	88	54

as well as lines of SnSb phase (open circles). Also, it is clear that lines corresponding to ZnSb (black circles) are mostly stronger for sample B. Existence of the Sn phase is evident, but lines corresponding MnSb phase are barely visible.

In order to examine the spatial distribution of the existing different crystal phases, the samples were recorded by an optical microscope with two different magnifications (50 × and 400 ×). Obtained micrographs are presented in Fig. 2.

Existing phases are clearly visible and they form multiphase structures. It should be noted that this is a very non-homogeneous material and that images from different parts of the samples differed, so the characteristic ones are selected and shown in Fig. 2.

In our previous work [9] is determined that gray fields are $ZnSnSb_2$ crystal, white ones correspond SnSb phase and that dark parts consist of ZnSb. Micrometric crystals of MnSb in the shape of dark circles were registered also.

Although microstructures of similar shapes have been formed in both samples, it is apparent that the surfaces significantly differ. Based on previous work [8,9,14], it can be concluded that these spherical and needle like microcrystals are ZnSb, MnSb, Sn, and Sb phases formed during crystallization of the material. As can be seen from Fig. 2. the sample B contains a lot of micron-sizes phases relatively evenly distributed over the surface (volume).

In order to more accurately examine the surface of the samples, we used atomic force microscopy (AFM) measurements. The characteristic results are presented in Fig. 3.

The surfaces of both samples have a granular structure. The sample A has evenly distributed grains over the entire surface with a few larger clusters and an average grain height of around ~100 nm (see Fig. 3(a) and the profile in Fig. 3(c)). The phase contrast in Fig. 3(b) originates exclusively from the abrupt changes in the height, indicating that the material properties of the sample A surface are homogeneous. The grains on the surface of the sample B are exclusively arranged into clusters which are not evenly distributed over the surface. The majority of the clusters reach several tens of nm in height, with a few exceptions having a height of ~100 nm (see Fig. 3(d) and the profile in Fig. 3(f)). The phase contrast of the sample B surface shows that the larger clusters have a distinct phase shift, seen as dark and white regions in Fig. 3(e), so that clusters have different material properties than the remainder of the surface.

This material is known to be difficult to synthesize and beside $ZnSnSb_2$ the ZnSb and SnSb phases are formed [11,15]. The series of $Zn_{1-x}Mn_xSnSb_2$ samples were synthesized under the same conditions with the only difference being the starting amounts of manganese and zinc [10]. Obviously, the small variation in the starting mixture causes rather different structures and properties of the materials.

It was found that a large concentration of lattice defects, especially in the cation sublattice, in $ZnSnSb_2$, as well as in other II-IV-V_2 semiconductors [16,17], causes a high hole concentration. In particular, Zn vacancies are those defects that lead to a very high concentration of holes [18,19,20]. Typical hole concentration in $ZnSnSb_2$ is 10^{20} cm^{-3} [15–20], in two-component p-type ZnSb it is 10^{19} cm^{-3} [18,19], while SnSb is a n-type material with metallic character and electron concentration of about 10^{22} cm^{-3} at 1.8 K [21]. Evidently, the electronic structure is very complex in this material.

It is difficult to say exactly what is the cause of different hole concentrations in the $Zn_{1-x}Mn_xSnSb_2$ samples, but it could be assumed that Zn vacancies are the main reason. Sample A has a higher content of
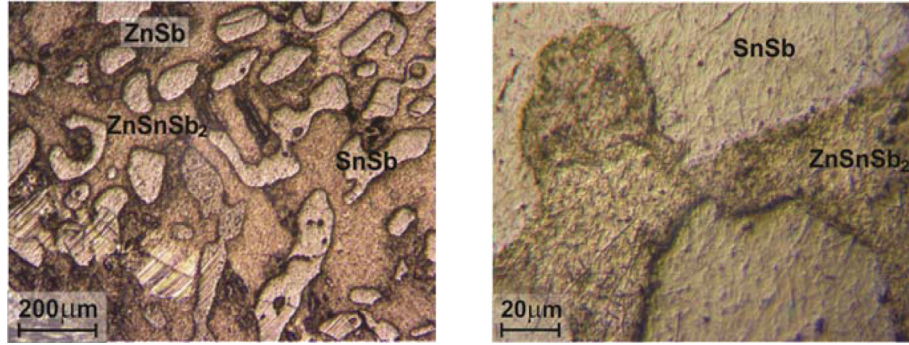
Sample A
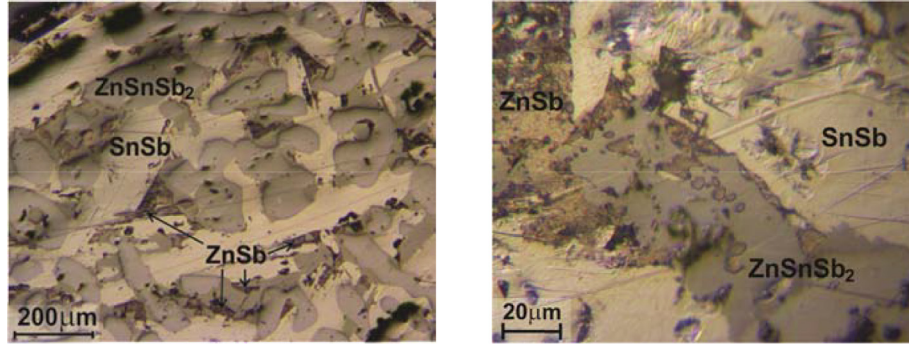
Sample B

Fig. 2. Micrographs of the ZnSnSb$_2$ + Mn samples surfaces with magnifications of 50 $\times$ and 400$\times$.

SnSb, which is related to a higher deficiency of Zn atoms, and therefore higher hole concentration. So, the different concentrations of free carriers in the samples are a consequence of various defects and microstructures which are formed.

In order to examine the interaction of free carriers and a lattice, the far-infrared reflectivity spectra in the range 40–450 cm^{-1} at room temperature have been recorded. Obtained spectra are shown in Fig. 4.

It is obvious that the most distinct difference between the spectra relates to wave numbers above 220 cm^{-1}, where the high carrier concentration has a main influence. Also, in the range from 120 to 180 cm^{-1} the spectrum for sample B (black line) contains some phonon lines which are absent or attenuated in the spectrum for sample A (red line).

A detailed analysis of the obtained results was necessary. For the analysis of the spectra the fitting procedure which includes plasmon - phonon interaction was applied.

4. Plasmon - phonon interaction

In materials with high free carrier concentration a plasmon-phonon interaction should be taken into account, as it significantly affects the properties of the material. Its influence on the dielectric properties of the material is important for the analysis of the reflection spectra.

A theoretical model of the dielectric function in bulk materials [22] has been applied. The dielectric function $\varepsilon(\omega)$ describes dielectric properties of single crystal and includes classical oscillators corresponding to the TO-modes, and Drude part which takes into account the free carrier contribution:

$$\varepsilon(\omega) = \varepsilon_\infty + \sum_{k=1}^{l} \frac{\varepsilon_\infty(\omega_{LOk}^2 - \omega_{TOk}^2)}{\omega_{TOk}^2 - \omega^2 - i\gamma_{TOk}\omega} - \frac{\varepsilon_\infty\omega_P^2}{\omega(\omega + i\Gamma_P)} \quad (1)$$

In this equation ε_∞ is the high-frequency dielectric constant, ω_{TOk} and ω_{LOk} are the transverse and longitudinal optical-phonon frequencies, l is the number of phonons, ω_P is the plasma frequency, γ_{TOk}

and Γ_P are the phonon and plasmon damping. The use of such a dielectric function is valid in multiphase materials, since it is based on a phenomenological approach where the effective values of the material parameters are used, e.g. $\omega_p^2 = \omega_{p1}^2 + \omega_{p2}^2 + \omega_{p3}^2 + \cdots$.

As our ZnSnSb$_2$ + Mn samples have high concentration of free-carriers (p), and therefore high values of ω_P ($\omega_P{}^2 \sim p$), it is expected that plasma interacts with phonons. As a result the phonon frequencies are changed, i.e. their positions are shifted from the expected values. The phonon lines observed at the reflection spectra are these shifted modes i.e. coupled plasmon-phonon modes. So, the situation is much clearer if the dielectric function which takes a plasmon–phonon interaction in advance is used [23,24]. It also allows the possibilities that more than one phonon interact with plasma as well as existence of uncoupled phonons. That dielectric function is:

$$\varepsilon(\omega) = \varepsilon_\infty \frac{\prod_{j=1}^{n+1}(\omega^2 + i\gamma_{lj}\omega - \omega_{lj}^2)}{\omega(\omega + i\Gamma_P)\prod_{i=1}^{n}(\omega^2 + i\gamma_{ti}\omega - \omega_{ti}^2)} \cdot \prod_{k=1}^{s} \frac{\omega^2 + i\gamma_{LOk}\omega - \omega_{LOk}^2}{\omega^2 + i\gamma_{TOk}\omega - \omega_{TOk}^2}$$

$$(2)$$

The first fraction in Eq. (2) describes coupling of a plasmon and n LO phonons, where parameters ω_{lj} and γ_{lj} are eigenfrequencies and damping coefficients of the longitudinal component of the coupled phonons. ω_{ti} and γ_{ti} are frequencies and damping of transverse component of these phonons. Γ_P is the plasma damping. The second factor in Eq. (2) represents s uncoupled phonons of the crystal, wherein ω_{LOk} (ω_{TOk}) and γ_{LOk} (γ_{TOk}) are LO (TO) frequencies and damping coefficients of the k-th uncoupled phonon of the crystal.

The analysis of the obtained reflection spectra was performed by a fitting procedure, by adjusting the parameters of Eq. (2) in order to obtain a match between the experimental and theoretical curves. The values of ω_{lj} and ω_{ti} are directly obtained in this way while the ω_P and ω_{LO} values are calculated [25]. It can be seen that the positions of the ω_{l2} and ω_{l4} are significantly different for samples A and B. The behavior of phonons and interactions with plasma were analyzed based on the data thus obtained.
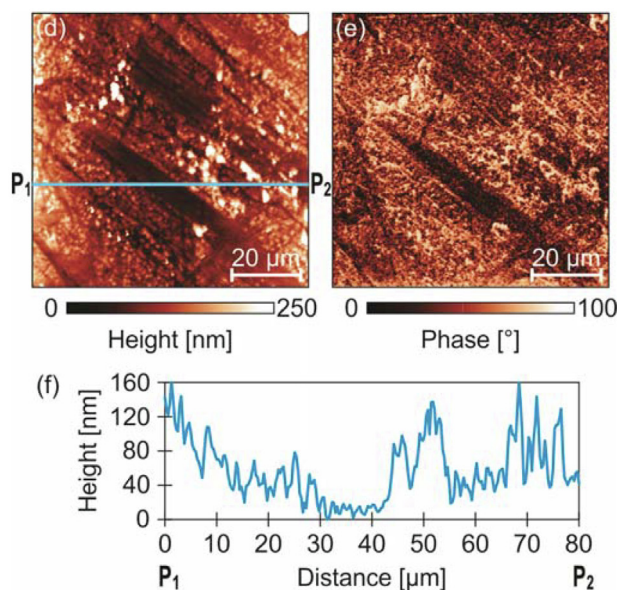
Sample A
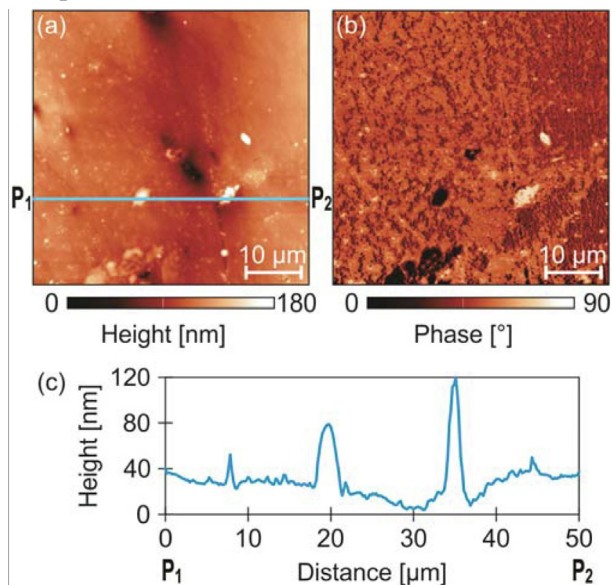
Sample B

Fig. 3. (a) AFM topography and (b) corresponding phase-contrast image of sample A; (c) Height profile taken along the straight solid line in (a) from point P₁ to point P₂; Figures (d), (e), and (f) refer to sample B in the same way.

The phonons of ZnSnSb$_2$ which are IR active are known from literature [26], and they are of B$_2$ and E symmetries. Their estimated values are given in Table 1.

Plasmon - phonon interaction commonly refers to the coupling of the plasma and one phonon [27]. In that case two coupled modes appear ω_{l1} and ω_{l2}, often labeled as ω_+ and ω_-. In the case of ZnSnSb$_2$, based on data obtained by fitting procedure, it was established that the plasma interacts with three phonons of B$_2$ symmetry [28,29,30]. As a result of that their positions are shifted and instead three B$_2$ modes there are four coupled modes ω_{l1}, ω_{l2}, ω_{l3} and ω_{l4}. Obtained values are shown as black points in Fig. 6. Their positions are different for the two samples because of the different influences of the plasma ($\omega_P^2 \sim p$). Because of the high plasma frequency of sample A, the ω_{l4} has high value of 675 cm^{-1} which is outside of the measured range.

For ease of analysis, it is common to draw a dependency diagram of obtained parameters (ω_{lj}, ω_t, ω_{TO}, ω_{LO}) on plasma frequency ω_p, as
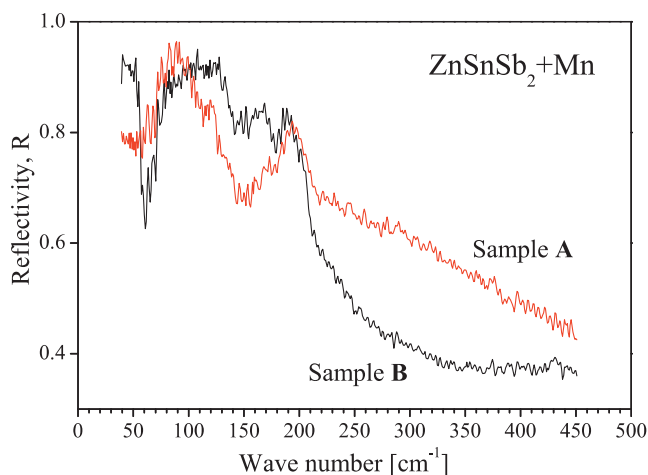

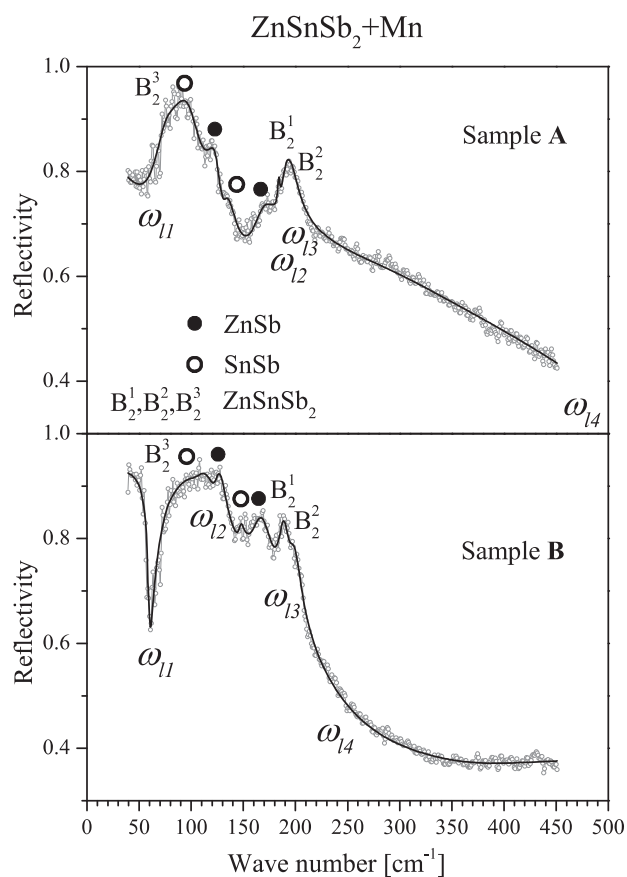**Fig. 4.** Far-infrared reflectivity spectra of ZnSnSb$_2$ + Mn.

Fig. 5. Analyzed reflection spectra; experimental data are represented by circles while black lines are theoretical curves; registered optical phonons are indicated on the spectra.

shown in Fig. 6. The full lines are solutions of Re$\{\varepsilon(\omega)\} = 0$ from Eq. (1). It should be noted that line ω_{l3} between B$_2^1$ and B$_2^2$ phonons is barely visible because they are very close. The lines are calculated for five different values of plasma damping Γ_p (Fig. 6) ($\Gamma_p = 1/\tau$, where τ is a lifetime of plasmon). This was done to determine Γ_p interdependence with plasmon - phonon interaction.

The obtained values of plasma damping and plasma frequency of samples A and B are: $\Gamma_{pA} = 500$ cm^{-1}, $\Gamma_{pB} = 375$ cm^{-1}, $\omega_{pA} = 837$ cm^{-1} and $\omega_{pB} = 405$ cm^{-1}. It should be noted that these parameters represent the effective values that describe the sample as a
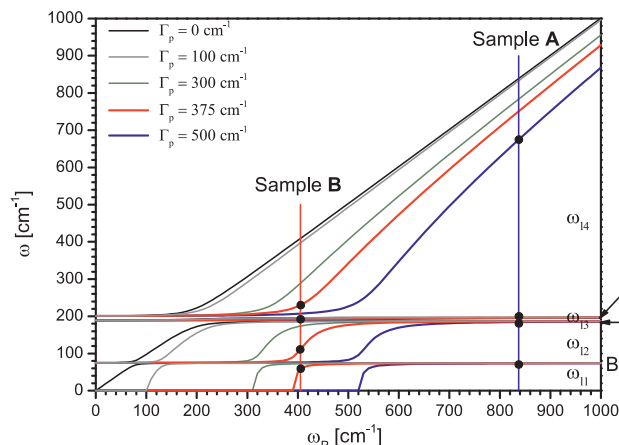
Fig. 6. Analysis of plasmon - three-phonons interaction; Full lines are obtained from Eq.(1), as the solutions of Re$\{\varepsilon(\omega)\} = 0$, for various values of Γ_p; Black points represent experimentally obtained data for ω_{lj} for both samples (Eq. (2)).

whole. It could be expected (based on p_A and p_B values and $\omega_p^2 \sim p$) that ω_{pA} and ω_{pB} differ about three times, which was not established. Plasma frequency is defined as $\omega_p^2 = (n_p e^2)/(\varepsilon_0 \varepsilon_\infty m_h^*)$, i.e. it includes other parameters of the material. Thus, by determining the plasma frequency and plasma damping the other properties of the material can be analyzed.

Besides phonons of B_2 symmetry which interact with plasma, other ZnSnSb$_2$ phonons are not registered on the IR reflectivity spectra. However, characteristic phonons of the other phases can be identified, as can be seen in Fig. 5. It was necessary that these phonons are not covered by the plasmon - phonon interaction. ZnSb modes are noticed at about 125 and 165 cm^{-1}, which is in agreement with results from the literature [31]. Two modes that correspond to SnSb phase are at about 94 and 145 cm^{-1}, which matches the previously obtained data [9,32]. The appearance of these modes is expected due to the significant presence of ZnSb and SnSb phases in the samples. MnSb phonons are not registered, i.e. it was not possible to discern them due to the small amount of that phase.

Based on the performed analyses, it can be seen that different microstructures formed in the investigated samples lead to high concentrations of free carriers, but which are ten times different from each other. Those high values cause plasmon - B_2 phonons interaction. That can be used to analyze optical and electrical properties of the materials, as well as other parameters, such as dielectric constants, effective mass of charge carriers and phonon lifetimes. In this way, the multiphase material with different microstructures was analyzed as a whole.

Investigation of thermoelectric properties of ZnSnSb$_2$ is a current issue [5,15,33]. The analysis of plasmon - phonon interaction performed in this paper can significantly assist in the study and understanding of thermoelectric processes in this as in other semiconducting polycrystalline materials [34].

5. Conclusion

Two samples of ZnSnSb$_2$ + Mn with different amounts of manganese were analyzed in this paper. The small difference in the initial composition of the material led to a difference of ten times in the free carrier concentrations. Their structural properties were examined by x-ray diffraction, optical microscopy, and AFM. Several different phases were registered - ZnSnSb$_2$, ZnSb, SnSb, and small amounts of Sn and MnSb. These phases form different microstructures, which is related to the large irregularities of the lattice. It was found that the high free carrier concentrations are caused by a large number of defects, especially zinc vacancies.

The optical characteristics of these multiphase materials were

examined, whereby the samples were considered as a whole. Based on the analysis of IR reflection spectra the presence of a plasmon - phonons interaction was confirmed. It was determined that three ZnSnSb$_2$ phonons of B_2 symmetry interact with plasma, which led to the change of their positions. It is clear that strong plasmon - phonon interaction modifies optoelectronic properties of the ZnSnSb$_2$ + Mn samples, and that phonon positions depend on a free carrier concentration. A detailed analysis of this interaction also provides insight into the behavior of other material parameters, such as dielectric constants, effective mass of charge carriers and phonon lifetimes. Also, vibration modes of ZnSb and SnSb phases were registered on the spectra. Knowledge of phonon behavior in a material, as well as interaction with plasma, is very important for studying its thermoelectric properties.

Declaration of competing interest

The authors declare that there is no conflict of interest in this paper.

Acknowledgement

Appendix A. Supplementary material

Supplementary data to this article can be found online at https://doi.org/10.1016/j.infrared.2020.103345.

References

[1] J.L. Shay, J.H. Wernick, Ternary Chalcopyrite Semiconductors: Growth, Electronic Properties, and Applications, Chapter 3 - Electronic Structure of II-IV-V$_2$ Compounds, Pergamon Press, New York, 1975, pp. 79–109 https://doi.org/10.1016/B978-0-08-017883-7.50008-1.

[2] W. Dobrowolski , J. Kossut, T. Story. II–VI and IV–VI Diluted Magnetic Semiconductors – New Bulk Materials and Low-Dimensional Quantum Structures. Handbook of Magnetic Materials 15 (2003) pp. 289-377, (Elsevier, Amsterdam, 2003). https://doi.org/10.1016/S1567-2719(03)15003-2.

[3] L. Kilanski, M. Górska, W. Dobrowolski, E. Dynowska, M. Wójcik, B.J. Kowalski, J.R. Anderson, C.R. Rotundu, D.K. Maude, S.A. Varnavskiy, I.V. Fedorchenko, S.F. Marenkin, Magnetism and magnetotransport of strongly disordered Zn$_{1-x}$Mn$_x$GeAs$_2$ semiconductor: The role of nanoscale magnetic clusters, J. Appl. Phys. 108 (2010) 073925, , https://doi.org/10.1063/1.3490231.

[4] S.F. Marenkin, A.D. Izotov, I.V. Fedorchenko, V.M. Novotortsev, Manufacture of magnetic granular structures in semiconductor-ferromagnet systems, Russ. J. Inorg. Chem. 60 (2015) 295300, , https://doi.org/10.1134/S0036023615030146.

[5] M. Ito, Y. Ohishi, H. Muta, K. Kurosaki, S. Yamanaka, Thermoelectric properties of Zn-Sn-Sb based alloys, Mater. Res. Soc. Symp. Proc. 1314 (2011), https://doi.org/10.1557/opl.2011.618.

[6] P. Balasubramanian, M. Battabyal, D. Sivaprahasam, R. Gopalan, On the formation of phases and their influence on the thermal stability and thermoelectric properties of nanostructured zinc antimonide, J. Phys. D: Appl. Phys. 50 015602 (11 (2017) pp), https://doi.org/10.1088/1361-6463/50/1/015602.

[7] G. Coquil, B. Fraisse, S. Biscaglia, D. Ayme-Perrot, M.T. Sougrati, L. Monconduit, ZnSnSb$_2$ anode: A solid solution behavior enabling high rate capability in Li-ion batteries, J. Power Sour. 441 (2019) 227165, , https://doi.org/10.1016/j.jpowsour.2019.227165.

[8] O. Zobac, J. Sopousek, J. Bursik, A. Zemanova, P. Roupcova, Experimental Study of the Sb-Sn-Zn Alloy System, Metall. Mater. Trans. 45A (2014) 1181–1188, https://doi.org/10.1007/s11661-013-2104-1.

[9] M. Romcevic, M. Gilic, L. Kilanski, W. Dobrowolski, I.V. Fedorchenko, S.F. Marenkin, N. Romcevic, Phonon properties of ZnSnSb$_2$ + Mn semiconductors: Raman spectroscopy, J. Raman Spectrosc. 49 (2018) 1678–1685, https://doi.org/10.1002/jrs.5421.

[10] L. Kilanski, M. Gorska, A. Slawska-Waniewska, S. Lewinska, R. Szymczak, E. Dynowska, A. Podgorni, W. Dobrowolski, U. Ralevic, R. Gajic, N. Romcevic, I.V. Fedorchenko, S.F. Marenkin, High temperature magnetic order in Zn$_{1-x}$Mn$_x$SnSb$_2$ + MnSb nanocomposite ferromagnetic semiconductors, J. Phys.:Condens. Matter. 28 (2016) 336004, , https://doi.org/10.1088/0953-8984/28/33/336004.

[11] A. Tenga, F.J. Garcia-Garcia, A.S. Mikhaylushkin, B. Espinosa-Arronte, M. Andersson, U. Haussermann, Sphalerite−Chalcopyrite Polymorphism in Semimetallic ZnSnSb$_2$, Chem. Mater. 17 (2005) 6080–6085, https://doi.org/10.

1021/cm0516053.

[12] A. Tenga, F.J. Garcia-Garcia, Y. Wu, N. Newman, U. Haussermann, Metal-nonmetal transition in the sphalerite-type solid solution $[ZnSnSb_2]_{1-x}[2(InSb)]_x$, J. Solid State Chem. 182 (2009) 1438–1442, https://doi.org/10.1016/j.jssc.2009.03.015.

[13] M. Bostrom, S. Hovmoller, Preparation and Crystal Structure of the Pseudo-Decagonal Approximant Mn_3Ga_5, J. Solid State Chem. 153 (2000) 398–403, https://doi.org/10.1006/jssc.2000.8790.

[14] C. Wang, Y. Xu, S. Yang, H. Jiang, J. Li, J. Zhu, S. Yang, X. Liu, Experimental Determination of Phase Equilibria in the Sn-Zn-Sb System, J. Phase Equil. Diff. 36 (2015) 350–356, https://doi.org/10.1007/s11669-015-0387-1.

[15] A. Nomura, S. Choi, M. Ishimary, A. Kosuga, T. Chasapis, S. Ohno, G.J. Snyder, Y. Ohishi, H. Muta, S. Yamanaka, K. Kurosaki, Chalcopyrite $ZnSnSb_2$: A Promising Thermoelectric Material, ACS Appl. Mater. Interf. 10 (2018) 43682–43690, https://doi.org/10.1021/acsami.8b16717.

[16] V.N. Brudnyi, Electronic properties and pinning of the Fermi level in irradiated II–IV–V_2 semiconductors 43 (2009) 1146–1154, https://doi.org/10.1134/S1063782609090085.

[17] V.G. Voevodin, S.N. Grinyaev, O.V. Voevodina, Nonstoichiometry and point defects in nonlinear optical crystals $A^2B^4C_2^5$, Mater. Sci. Semicond. Proces. 6 (2003) 385–388, https://doi.org/10.1016/j.mssp.2003.07.006.

[18] X. Song, M. Schrade, N. Maso, T.G. Finstad, Zn vacancy formation, Zn evaporation and decomposition of ZnSb at elevated temperatures: Influence on the microstructure and the electrical properties, J. Alloys Comp. 710 (2017) 762–770, https://doi.org/10.1016/j.jallcom.2017.03.339.

[19] L.V. Prokofieva, P.P. Konstantinov, A.A. Shabaldin, On the tin impurity in the thermoelectric compound ZnSb: Charge-carrier generation and compensation, Semicond 50 (2016) 741–750, https://doi.org/10.1134/S1063782616060208.

[20] L. Bjerg, G.K.H. Madsen, B.B. Iversen, Ab initio Calculations of Intrinsic Point Defects in ZnSb, Chem. Mater. 24 (2012) 2111–2116, https://doi.org/10.1021/cm300642t.

[21] B. Liu, J. Wu, Y. Cui, H. Wang, Y. Liu, Z. Wang, Z. Ren, G. Cao, Superconductivity in SnSb with a natural superlattice structure, Supercond. Sci. Technol. 31 (2018) 7, https://doi.org/10.1088/1361-6668/aae6fe 125011.

[22] Abstreiter G., Cardona M., Pinczuk A. Light scattering by free carrier excitations in semiconductors. In: Cardona M., Güntherodt G. (eds) Light Scattering in Solids IV. Topics in Applied Physics, vol 54. Springer, Berlin, Heidelberg. (1984) https://doi.org/10.1007/3-540-11942-6_20.

[23] A.A. Kukharskii, Plasmon-phonon coupling in GaAs, Solid State Commun. 13 (1973) 1761–1765, https://doi.org/10.1016/0038-1098(73)90724-2.

[24] N. Romcevic, M. Romcevic, W.D. Dobrovolski, L. Kilanski, M. Petrovic, J. Trajic, B. Hadzic, Z. Lazarevic, M. Gilic, J.L. Ristic-Djurovic, N. Paunovic, A. Reszka, B.J. Kowalski, I.V. Fedorchenko, S.F. Marenki, Far-infrared spectroscopy of Zn1 − xMnxGeAs2 single crystals: Plasma damping influence on plasmon – Phonon interaction, J. Alloys Comp. 649 (2015) 375–379, https://doi.org/10.1016/j.jallcom.2015.07.087.

[25] J. Trajic, N. Romcevic, M. Gilic, M. Petrovic Damjanovic, M. Romcevic, V.N. Nikiforov, Optical properties of $PbTe_{0.95}S_{0.05}$ single crystal at different temperatures: Far - infrared study, Optoelec. Adv. Mater. Rap. Comm. 6 (2012) 543–546.

[26] F.W. Ohrendorf, H. Haeuseler, Lattice Dynamics of Chalcopyrite Type Compounds. Part I. Vibrational Frequencies, Cryst. Res. Technol. 34 (1999) 339–349, https://doi.org/10.1002/(SICI)1521-4079(199903)34:3<339:: AID-CRAT339>3.0.CO;2-E.

[27] Klein M.V. Electronic Raman Scattering. In: Cardona M. (eds) Light Scattering in Solids. Topics in Applied Physics, vol 8. Springer, Berlin, Heidelberg (1975). https://doi.org/10.1007/978-3-540-37568-5_4.

[28] M. Petrovic, N. Trajic, W.D. Dobrowolski, M. Romcevic, B. Hadzic, M. Gilic, A. Mycielski, Far-infrared spectroscopy of $CdTe_{1−x}Se_x$(In): Phonon properties, Infrared Phys. Tech. 67 (2014) 323–326, https://doi.org/10.1016/j.infrared.2014.08.010.

[29] M. Romcevic, N. Romcevic, W. Dobrowolski, L. Kilanski, J. Trajic, D.V. Timotijevic, E. Dynowska, I.V. Fedorchenko, S.F. Marenkin, Optical properties and plasmon – Two different phonons coupling in ZnGeAs2 + Mn, J. Alloys Comp. 548 (2013) 33–37, https://doi.org/10.1016/j.jallcom.2012.09.017.

[30] I.J. Luxmoore, C.H. Gan, P.Q. Liu, F. Valmorra, P. Li, J. Faist, G.R. Nash, Strong coupling in the far-infrared between graphene plasmons and the surface optical phonons of silicon dioxide, ACS Photonics 1 (2014) 1151, https://doi.org/10.1021/ph500233s.

[31] D.V. Smirnov, D.V. Mashovets, S. Pasquier, J. Leotin, P. Puech, G. Landa, Yu.V. Roznovan, Long-wavelength optical phonons of $Cd_x Zn_{1-x}Sb$ mixed crystals, Semicond. Sci. Technol. 9 (1994) 333–337.

[32] P. Nithyadharseni, M.V. Reddy, B. Nalini, M. Kalpana, B.V.R. Chowdari, Sn-based Intermetallic Alloy Anode Materials for the Application of Lithium Ion Batteries, Electrochim. Acta 161 (2015) 261–268, https://doi.org/10.1016/j.electacta.2015.02.057.

[33] Yu M. Basalaev, Ab Initio Study of the ZnSnSb2 Semiconductor, Semiconductors 52 (2018) 1715–1720, https://doi.org/10.1134/S1063782618130043.

[34] Q. Xu, J. Zhou, T.H. Liu, G. Chen, Effect of electron-phonon interaction on lattice thermal conductivity of SiGe alloys, Appl. Phys. Lett. 115 (2019) 023903, , https://doi.org/10.1063/1.5108836.
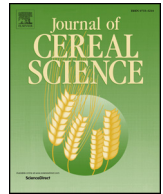
Raman and Fourier transform infrared spectroscopy application to the Puno and Titicaca cvs. of quinoa seed microstructure and perisperm characterization

Borisz Czekus[a], Ilinka Pećinar[b], Ivana Petrović[b], Novica Paunović[c], Slađana Savić[a,*], Zorica Jovanović[b], Radmila Stikić[b]

[a] Faculty of Biofarming, Megatrend University, Bulevar maršala Tolbuhina 8, 11070 Belgrade, Serbia
[b] Faculty of Agriculture, University of Belgrade, Nemanjina 6, 11080 Belgrade, Serbia
[c] Institute of Physics, University of Belgrade, Pregrevica 118, 11080 Belgrade, Serbia

ARTICLE INFO

ABSTRACT

The aim of this study was to investigate the quinoa fruit and seed microstructure, as well as to determine the qualitative composition of quinoa whole seed spatial localisation of food reserves in cultivars Puno and Titicaca using two complementary spectroscopic techniques (Fourier Transform infrared and Raman). The analyses of the seeds also included measurements of the crude proteins and starch contents. The experiment was carried out during the 2016 growing season in rain-fed conditions in the north of Serbia. The analysis of the scores of the principal components based on the Raman spectra revealed two groups in both seed parts (cotyledons and perisperm). The analysis of the loadings highlighted the spectrum region that contributed to the differentiation, e.g. the band at 472 cm^{-1} was related to the amylopectin content in the perisperm region. As for the cotyledons, the spectral range from 1100 to 1650 cm^{-1} was responsible for genotype differences and it included both the most important bands derived from Amide I, II and quinoa protein with globoid crystals composed of phytin. IR analysis, similar to the analyses of the crude proteins and starch contents in the seeds, failed to reveal any differences in biochemical composition between two analyzed genotypes.

1. Introduction

Quinoa (*Chenopodium quinoa* Willd.) is a pseudo-cereal crop belonging to the Amaranthaceae family and originated from South America. It is an annual plant, and currently is in focus due to its high tolerance to various stress factors including frost, drought, salinity (Jacobsen and Muica, 2002), as well as its exceptional nutritional value of seeds and certain vegetative parts of the plants (Gordillo-Bastidas et al., 2016). The storage reserves of proteins, mineral nutrients, and lipids in the seeds are mainly located in the reduced endosperm and the cotyledons (Valencia-Chamorro, 2003), while carbohydrate reserves are found in the perisperm, nominated as seed storage tissues (Prego et al., 1998). The nutritional value is also based on the substantial fiber and protein contents which are higher in comparison to these contents found in corn and rice. On the other hands, these contents are similar those recorded in wheat (Gordillo-Bastidas et al., 2016). The major protein fractions are albumins and globulins. They account for 77% of protein in total, whose biological value is comparable to casein. On the other hand, the specific content of amino acids comes from lysine, histidine and a high level of sulfur containing amino acids (cysteine and methionine) (Gordillo-Bastidas et al., 2016).

Most of the information on the structural features of quinoa fruit and seed to date has been found in studies conducted by Varriano Marston and DeFrancisco (1984), Prego et al. (1998), Sukhorukov and Zhang (2013). Raman microspectroscopy is currently used as a highly powerful and useful tool for the rapid evaluation of seed composition. The advantages of Raman are as follows: this technique is non-destructive, very fast and sensitive; the samples can be analyzed directly without any staining and complicated sample preparation, and at the same time the chemical and structural information can be gained in the native state. Previous studies demonstrated the successful application of Raman spectroscopy in starch analysis in different grains (Kizil et al., 2002; Almeida et al., 2010), as well as proteins in soybean seed (Lee et al., 2013) and phytin in wheat grain (Kolozsvari et al., 2015). However, Raman technique has not yet been used for analyses of quinoa seeds.

Another technique, infrared spectroscopy is a useful tool which provides efficient information of sample composition. It reveals structural components of biological samples based on the specific molecular vibrations and exposes the unique spectral fingerprint of the analyzed object. It is used for analysis of food and other agricultural crops. According to the literature, the quinoa seed was previously analyzed by NIR - near infrared spectroscopy (Encina-Zelada et al., 2017). Similarly, quinoa flour was analyzed by FT-IR and this methodology is recognized as a relevant analytical tool for the determination of flour composition (Rossell, 2013; Garcia-Salcedo et al., 2018). Rossell (2013) showed that a portable FTIR system can be used for detection of quinoa flour authenticity. Out of 45 of different flour samples, quinoa flour was separated by carbohydrate stretching (C—C and C—O bonds) and deformation (C—O—C) spectral signals in the 950-1000 cm^{-1} region. In addition, the amide region at 1560-1665 cm^{-1} was detected as a reliable region for flour differentiation (Rossell, 2013).

The nutritional and health promoting values of the seeds together with stress resistance properties of the quinoa plant make it attractive for numerous countries, especially for those facing the effects of climate change on their food production and food security. United Nations Food and Agriculture Organization (FAO) selected quinoa as one of the crop destined to offer food security in the 21st century and declared 2013 as the International Year of Quinoa (www.fao.org/quinoa-2013/en/). However, although the southern Europe is already faced with climate changes reducing effects on agricultural production, cultivation of quinoa is still limited, except for Italy and Greece (Pulvento et al., 2015; Noulas et al., 2015). In Serbia, as a country with the southeastern European agro-climatic conditions, quinoa has not yet been grown. Preliminary research of Stikic et al. (2012) confirmed good seed nutrient quality, with high protein content and content of mineral and most essential amino acids (especially lysine) when quinoa Danish cultivar Puno (Jacobsen and Muica, 2002) was grown in Serbian rain-fed field conditions.

The aim of the present study was to assess the macro and microstructure of quinoa fruit and to apply Raman and FTIR spectroscopy for determination of seed quantitative composition of two quinoa cultivars Puno and Titicaca. Since the trial was done in Serbian agro-climatological conditions, it is expected that the results would help to introduce the cultivation of quinoa, as an alternative crop, in Serbia.

2. Material and methods

2.1. Source of plant material and measurements

The experiment was carried out during the 2016 growing season in rain-fed conditions using two introduced genotypes of quinoa adapted to the European climate, Puno and Titicaca, selected at the University of Life Sciences in Copenhagen, Denmark (Jacobsen and Muica, 2002). The quinoa was grown on a small Serbian farm near Subotica and in the area between the north latitudes of 46° and east longitudes of 19.68° (about 10 km south from the Serbian and Hungarian border). The soil type was chernozem, medium rich in nitrogen (0.24%) and hummus (3.19%), highly rich in phosphorus (34.68 mg P_2O_5/100 g soil) and rich in potassium (29.42 mg K_2O/100 g soil), slightly alkaline (pH 7.66). The seeds were sowed in the first part of April, when the soil temperature reached 12 °C. The experiment was laid out in a split-split plot system, with four replications. The size of the main plot was 12 m^2. The distance between the rows was 50 cm and between the plants in the row −5 cm (approximately 400 000 seeds per hectare). The seeds were sown at a depth of 2 cm. No fertilizer was applied during the vegetative season. The crops were harvested in the first half of August when quinoa fruits/seeds were ripeness, the moisture content was 12%. During vegetation, there was a 40-day period with the maximum air temperature of over 30 °C, which suited this thermophile plant. The temperature data was obtained from the automatic meteorological station located in the center of Subotica, at a 4-km distance from the

experimental field. The measurements were collected using "Nexus" instruments and "Weather Display" software (http://www.sumeteo.info). The amount of precipitation was measured on site, at the experimental field. Over the five months of vegetation, there were 22 days with precipitation. The overall amount of precipitation before harvest was 317 mm. At physiological maturity, the harvest of Puno and Titicaca seeds was made by hand. The seeds were ground by using a laboratory mill (model Cemotek Sample Mill Foss, Sweden) and then the contents of proteins and starch were analyzed. The content of crude proteins was determined according to Kjeldahl method (Stikic et al., 2012), while for starch measurement the Ewers polarimetric method was used (ISO and 10520: 1997). Two complementary spectroscopic techniques (Fourier Transform infrared and Raman) were carried out for the analyses of Puno and Titicaca seeds and fruits microstructure and composition.

2.2. Light microscopy

Dry fruit materials of *Ch. quinoa* genotypes were studied using light microscopy. The bright field light microscope in reflected light (Stereomicroscope Nikon SMZ18, Tokyo, Japan) was used at a magnification up to 20x. Images were acquired using a Nikon DIGITAL SIGHT DS-Fi1c digital camera. In addition, longitudinal sections of the *Ch. quinoa* seeds were observed by brightfield light microscopy in transmitted light (Leica DM2000, Germany), and documented with a Leica DC320 digital camera, and a Leica IM1000 software was used for sample capture.

2.2.1. Specimen preparation for light microscopy

For microstructure studies, fruit samples were fixed in 50% ethanol. Dehydration of fixed tissue samples was performed in a LEICA TP1020-Automatic Tissue Processor through a gradual series of ethanol (80%, 96% and absolute ethyl alcohol) and the xylene and melted paraffin embedding medium (Histowax, 56–58 °C). Tissues were embedded using an EG1120 Paraffin Dispenser with an integrated hot plate. After cooling and hardening of the paraffin blocks on the Leica EG1130 cold plate, transverse sections (thickness 5–10 μm) were cut on a LEICA SM 2000 R microtome. Paraffin was removed from the sections using a deparaffinisation procedure of passing through a series of ethyl alcohol solutions (absolute, 95%, 70%, 50% and 30%) and the tissue was stained in safranin (overnight) and alcian blue (for a duration of 2s). After staining, the tissue was dehydrated rapidly through absolute alcohol and xylol. Deparaffinisation, staining and dehydratation of microslides were conducted using a LEICA ST4040 Linear stainer. Finally, slides were mounted in Canada balsam for microscopic examination.

2.3. Raman instrumentation

Raman spectroscopy was performed using a XploRA Raman spectrometer from Horiba Jobin Yvon on the longitudinal fruit section samples. The Raman scattering was excited by a frequency-doubled Nd/YAG laser at a wavelength of 785 nm (maximum output power 20–25 mW) equipped with a 600 lines/mm grating. Spectra were accumulated from 5 scans, during 10s and filter 100%. In order to take into account any sample inhomogeneity, at least ten Raman spectra were recorded for each sample and for two parts of seed (cotyledon and perisperm) using single point Raman measurements at 50x objective lens. The spectra were recorded in the range between 200 and 1600 cm^{-1} in the perisperm region and from 250 to 1750 in the cotyledon region. All recorded measurements were with 4 cm^{-1} spectral resolution. The Raman spectra acquisitions were managed by the LabSpec software (Horiba Jobin Yvon).

2.4. FT-IR instrumentation

The IR transmission measurements were performed at room

temperature with the Nicolet Nexus 470 Fourier-transform IR spectrometer. The KBr beamsplitter and the DTGS detector were used to cover the wavenumber range between 600 and 4000 cm^{-1}. The transmission spectra were recorded with the resolution of 2 cm^{-1} and with 256 interferometer scans added for each spectrum. The samples were prepared for the IR spectra measurements by grinding the seeds in liquid nitrogen and mixing it with the KBr powder. The mixture was further pressed into tablets under the conditions outlined above.

The characteristic bands of the specific functional groups were described from the literature records. Raman and FT-IR spectra were analyzed by the OriginPro 8.6 software (OriginLab, Northampton, MA, USA).

2.5. Chemometric analysis of the Raman spectroscopic data

For all PCA analyses, the data were preprocessed, *i.e.* the Raman spectra were smoothed using Savitzky-Golay filters with 4 points and a second-order polynomial function. All Raman scattering intensities were normalized by the highest intensity band. After preprocessing, PCA was performed in the region 200-1700 cm^{-1} for two parts of seed (cotyledons and perisperm) and two quinoa genotypes (Puno and Titicaca). The spectra preprocessing was realized using the Spectragryph software (Menges, 2018) while PCA analysis was performed using the PAST software (Hammer et al., 2001). In general, principal components are composed of scores and loadings. When using PCA analysis, it is possible to make data visualization and to simultaneously reduce data size, allowing segregation between classes. In other words, the scores and loadings reveal the differences between the samples.

3. Results and discussion

3.1. The quinoa fruit

The quinoa fruit, at the anatomical level, comprises pericarp covering seed. The fruit of quinoa in an achene covered by perigonium. The outer layer of the fruit, consisting of one seed, is the pericarp. The perisperm is the storage organ of quinoa seeds (Jacobsen and Stølen, 1993). The quinoa fruit achene (1–2.6 mm in diameter) is round, flattened, and oval-shaped, with its basic colors ranging from yellow to pink (Fig. 1A–D), which most likely depends on the phase of maturity (Valcárcel-Yamani and Lannes, 2012).

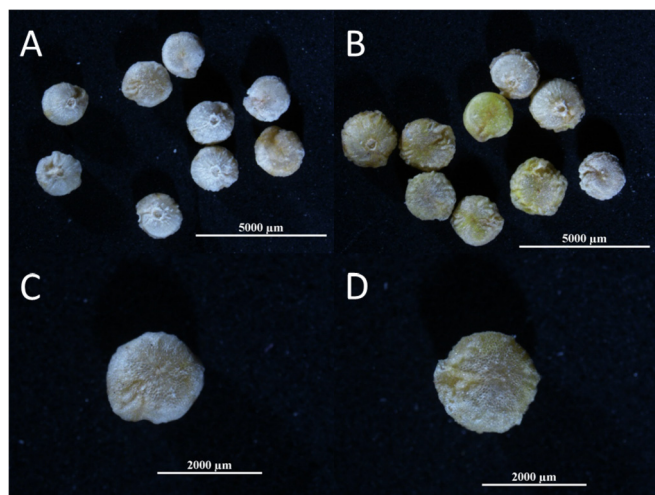As seen in the fruit's longitudinal section (Fig. 2 A, B), the pericarp is
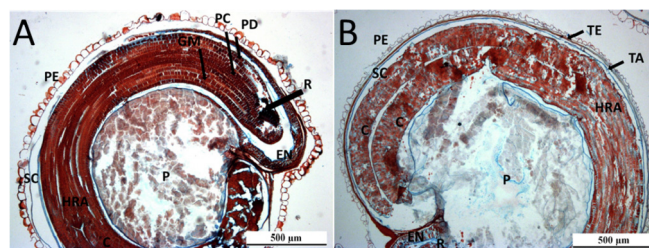
Fig. 2. Light microscopy of a median longitudinal section of the *Chenopodium quinoa* fruit, for Puno (A) and Titicaca (B) genotypes. Pericarp (PE), seed coat (SC), two cotyledons (C), Hypocotyl Radicle Axis (HRA), Endosperm (EN), perisperm (P), radicle or root cup (R), Testa (TE), Tapetum (TA), Protoderm (PD), Ground meristem (GM), Procambium (PC). Sections were stained with safranin and alcian blue and observed at 5 times magnification.

formed from two layers, easily detached from the seed coat. The outer pericarp cells are large and papillose, while a secondary discontinuous layer is composed of a tangentially stretched cell (Prego et al., 1998). The remaining structures below the pericarp represent the seed compartments.

3.2. The quinoa seed

The seed coat is smooth and thin, consisting of two cell layers (Fig. 2A and B): the testa and the integumentary tapetum, both presented by dry cells without cell content (Sukhorukov and Zhang, 2013). In the quinoa seed (Fig. 2 A, B), the embryo or germ is campylotropous, surrounding the starch-rich perisperm like a ring, and together with the seed coat, they represent the bran fraction, which is relatively rich in fat and protein (Valcárcel-Yamani and Caetano da Silva Lannes, 2012). The embryo consists of a hypocotyl-radicle axis (Fig. 2A and B) and two cotyledons (Fig. 2B), though lacking a leaf primordia. In the axis, both the root apical meristem with the root cap and the shoot apical meristem are differentiated. The shoot apical meristem forms a conical structure between the two cotyledons. Protoderm, ground meristem and procambium are visible in the axis and cotyledons. The endosperm of the mature seed consists only of two cell layers around the radicule, enveloping the hypocotyl-radicle axis of the embryo (Fig. 2A). The perisperm consists of large and thin-walled cells, mostly uniform in shape (Fig. 2A and B), completely full of starch grains, morphologically similar to the grass starchy endosperm (López-Fernández and Maldonado, 2013).

3.3. Raman signature of main storage seed reserves

Fig. 3 shows the characterization of the quinoa seed by Raman microspectroscopy. The Raman spectra of quinoa seeds show predominant bands of polysaccharides and proteins arising from vibrations of the C−H, C=O, C−N, N−H. The major Raman scattered bands of polysaccharides in the perisperm were recorded in the range from 200

Fig. 1. Stereomicroscope micrographs of achene apical and basal pole of two quinoa genotypes Puno (A, C) and Titicaca (B, D) after harvesting. Magnification was up to 20x.
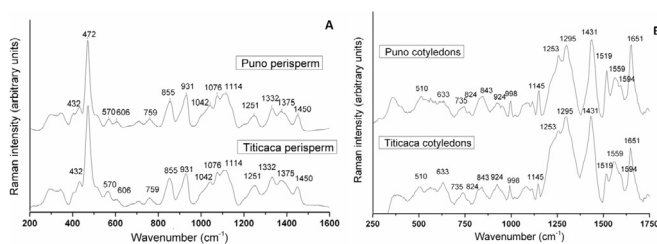

Fig. 3. Raman spectra of the quinoa seed recorded at perisperm (A) and cotyledon position (B). The most intensive peak at 472 cm^{-1} refers to starch (A), 1431 cm^{-1} and 1651 cm^{-1} refers to amino acid tryptophan and Amide I group (B), respectively.

to 1600 cm^{-1} (Fig. 3A), and are in line with previously published results from histochemical analysis of *Ch. quinoa* seeds (Prego et al., 1998) where there was not any indication of protein fraction occurrence in the perisperm. The region between 800 and 1500 cm^{-1} (Fig. 3A) provided a complex of exact band assignments to polysaccharides, because the vibrations of glucose molecules dominate in that spectral region, and consequently starch exhibits characteristic spectral vibrations (Kizil et al., 2002). The region between 1200 and 1500 cm^{-1} mainly shows the bands from basic structural compounds, including several bands originated from carbohydrates. For instance, the band at 1450 cm^{-1} (Fig. 3A) corresponds to CH$_2$ bending modes. The region between 1200 and 1340 cm^{-1} presents the contributions of several vibrational modes (Fig. 3A), such as medium intensity bands at 1332 and 1251 cm^{-1} (assignment to C—O, C—O—H stretching and C—C—H, C—O—H deformations) (Almeida et al., 2010). In the spectral region between 800 and 1200 cm^{-1}, the positions of the C—O, C—C and C—H stretching are assigned to 1114, 1076, 1042, 855 cm^{-1} and C—O—C deformation modes of R-1,4 glycosidic linkages in starches at 931 cm^{-1} (Kizil et al., 2002). That region is also known as the "fingerprint" for carbohydrates, containing the majority of the Raman bands used for unique identification of the sample (Kizil et al., 2002). Vibrations in the 400–800 cm^{-1} spectral region are in general due to C—C—O and C—C—C deformations, which are related to the glycosidic ring skeletal deformations. The most specific and highly intense Raman band at 472 cm^{-1} has been used as a marker to identify the presence of starch in different samples, as well as to characterize the pyranose ring in glucose of amylose and amylopectin, with low intensity bands at 432, 759, and 1375 cm^{-1}, as constituents of starch. In this study, low intensity bands at 570 and 606 cm^{-1} represent starches (Fig. 3A), and can be also attributed to the skeletal modes of the pyranose ring (Almeida et al., 2010). The starch composition of the quinoa perisperm was previously described by Varriano Marston and DeFrancisco (1984). Since the perisperm cells are full of angular-shaped starch grains, Prego et al. (1998) have indicated that quinoa seed starch mainly contains amylopectin.

It was found that the second type of Raman spectra of the *Ch. quinoa* seed corresponded to the protein content located at the embryonic region (Fig. 3B). This is also in agreement with results of the histochemical analysis of this seed region (Prego et al., 1998). The protein components are primarily represented by a spectrum of globulin as the main quinoa protein, with three characteristic signal regions of Amide I, II, and III. The typical Raman spectrum of quinoa seed protein shows C=O stretching vibration and N—H wagging in the peptide bonds coming from Amide I group at 1651 cm^{-1}. The Amide II and III broad bands are centered near 1559 and 1295 cm^{-1} (Fig. 3B), and they are due to N—H bend and C—N stretching vibration, respectively. The line at 924 cm^{-1} can be assigned to amino acid proline as well as low intensity bands at 633 cm^{-1}, with doublets at 824 and 843 cm^{-1} (Schulmerich et al., 2013). According to Stikic et al. (2012), the seed of the Puno cultivar has higher contents of proline and alanine. The band at 1253 cm^{-1} could indicate the presence of tyrosine while the band at 1519 cm^{-1} is consistent with the peak for glutaminic acid as a amino acids present in quinoa globulin (Zhu et al., 2011; Lee et al., 2013). In addition, the broad peak near 1431 cm^{-1} could be due to amino acid tryptophan, namely, the band is assignable to indole aromatic ring stretching (Zhu et al., 2011). A sharp and low intensity band at 998 cm^{-1} position is assigned to aromatic ring vibration (Fig. 3B), which arises from C—C symmetric ring breathing of phenylalanine amino acid residues (Lee et al., 2013). Also, some studies (Kolozsvari et al., 2015) described the presence of phytin globoids by the band at about 1000 cm^{-1}. Konishi et al. (2004) have already described phytin as a major component of protein bodies inside the quinoa embryonic cells.

The Raman spectrum in the 500-540 cm^{-1} spectral region could indicate the presence of quinoa globulin and the Raman band at 510 cm^{-1} correspond to the most preferred conformations of the bonds
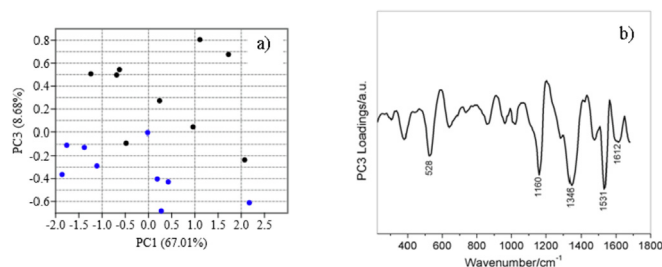

Fig. 4. a) Score plot of the first principal component (PC1) *versus* the third principal component (PC3) of the Puno quinoa cotyledons (blue cycle) and Titicaca quinoa cotyledons (black cycles); b) Loading plot corresponding to PC3.

(gauche-gauche-gauche/trans) in many naturally occurring proteins with disulphide (S—S) bridges (Schulz and Baranska, 2007). A similar observation was reported in the study of rice globulins with Raman spectroscopy, where the results revealed the high amount of sulfur containing amino acids such as cysteine or methionine, as constituents of globulins (Ellepola et al., 2006).

3.4. PCA of the Raman spectra recorded from quinoa cotyledon and perisperm

Multivariate analysis, based on PCA, was applied in order to differentiate between the quinoa genotypes. Fig. 4 presents the scores and loadings plots of the PCA for characteristic spectral region. The PCA analysis was performed using 9 samples of cotyledon and 8 samples of perisperm for each genotype.

The score plot of PC1 *versus* PC3 (Fig. 4a) shows a reasonably good separation between the samples.

The loading plot of the PC3 (Fig. 4b) displays the peaks that separate the Puno quinoa cotyledon from the Titicaca quinoa cotyledons.

As can be seen, the bands such as those in the spectral range 1200-1700 cm^{-1} are primarily assigned to the protein structure (e.g. Amide I and Amide II) and some specific amino acids (e.g. glutaminic acid) according to Zhu et al. (2011). These results indicate that differences between our genotypes are based on protein structural properties. The differences between investigated genotypes may be explained by their chemical composition. However, Aluwi et al. (2017) have compared Puno and Titicaca cultivars and found similar percentages of proteins (14.7 and 14.4%, respectively). Our results also did not show significantly different values in protein content between the seeds of Puno (14.1%) and Titicaca (14.0%). Fig. 5a highlights the relatively good separation of perisperm samples from two genotypes into two different groups, where the first and third principal components described ~78.5% of data variance.

The peaks, which are mainly responsible for this differentiation, can be observed in Fig. 5b. In the spectral range from 460 to about 600 cm^{-1}, the most important peaks for genotypes separation at
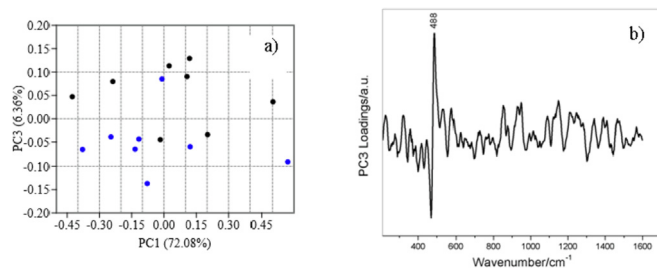

Fig. 5. A ccore plot of the first principal component (PC1) *versus* the third principal component (PC3) of the Puno quinoa perisperm (blue cycle) and Titicaca quinoa perisperm (black cycles); b) A loading plot corresponding to PC3.
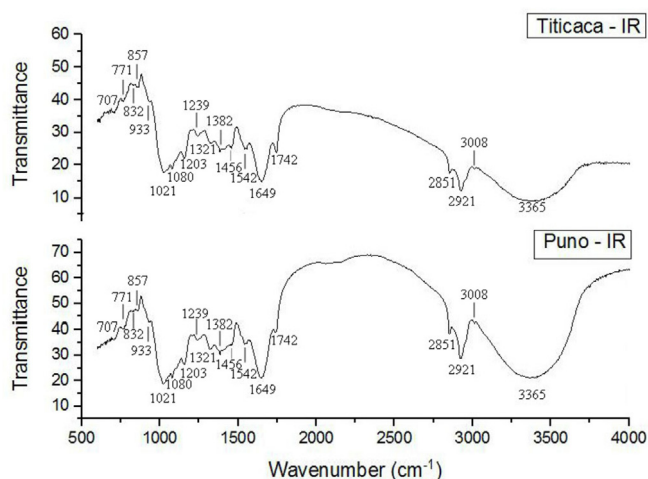
Fig. 6. Infrared spectra of ground quinoa seeds of two genotypes (Titicaca and Puno).

perisperm region can be detected. The peaks are mainly responsible for the differentiation of perisperm of the Titicaca cultivar compared to the perisperm of the Puno cultivar. That spectral region involves the deformation modes of the C–C–O and C–C–C deformations, as a marker for identifying the presence of starch. According to Aluwi et al. (2017), a higher percentage of quinoa seed starches was detected in Puno (62.6%) than in Titicaca (56.4%). In general, as for the Titicaca cultivar, the total carbohydrate represents the main seed component at approximately 54–57%, according to the study of Pulvento et al. (2012). The main carbohydrate component of quinoa is a starch and in our research the seeds of Titicaca and Puno contained similar starch content (54.1 and 55.6%, respectively). The identified peaks in our study peaks may be assigned to the pyranose ring of amylose, or predominantly amylopectin as specific for quinoa (Prego et al., 1998). As previously discussed by Almeida et al. (2010), the bands in the region 430-490 cm^{-1} are related to the evaluation of the amylose and amylopectin concentration present in the starchy samples.

3.5. FT-IR of quinoa seed

There was no distinction in the IR spectra between the two analyzed genotypes and main peaks, as presented in Fig. 6.

The band at 3365 cm^{-1} is assigned to the O–H stretching vibrations. Peaks at 3008 and 2921 cm^{-1} are due to C–H bonds, while the peak at 2851 cm^{-1} is assigned to the CH$_2$ and CH$_3$ groups from aldehydes/ketones (Garcia-Salcedo et al., 2018). The band at 1741 cm^{-1} is a result of C=O carbonyl stretching, while the 1648 cm^{-1} band may be assigned to the amide region of the proteins (Rossell, 2013). The observed alcohol and carbonyl stretching could be assigned to the chemical structure of quinoa saponins (Soliz-Guerrero et al., 2002). Those two peaks and the peak registered at 1542 cm^{-1} are particularly important since they represent protein amino acids and can reveal modifications in the secondary structure of proteins (Garcia-Salcedo et al., 2018). The band at 1080 cm^{-1} can be attributed to the pyranose structure of CH, while the 1021 cm^{-1} band can be assigned to the C–H bending from aromatic structures, which is also recorded in certain previous studies (Abugoch et al., 2011). Different substitutions in aromatic rings can be detected in the fingerprint region, characterized by aromatic C–H out-of-plane bend (857, 831, 771, 706 and 687 cm^{-1}).

4. Conclusions

This study confirmed the successful application of Raman spectroscopy in the detection of proteins and polysaccharides of quinoa seed storage reserves, and in a straightforward and fast manner. The

assessment of the scores of the principal components based on the Raman spectra revealed two groups in both seed parts (cotyledons and perisperm). The analysis of the loadings highlighted the band at 472 cm^{-1}, presumably related to the amylopectin content in perisperm, as compound which contributes to the differences between the genotypes. Regarding the spectra recorded at the cotyledons part, the highest loadings derived from Amide I, II and quinoa protein with globoid crystals were responsible for the genotype separation. These results indicate that Raman spectroscopy is very useful method for localisation, quantification and structural identification of stored reserves inside the seeds of different genotypes of quinoa. IR analysis, similar to the measurements of the crude proteins and starch contents in the seeds, showed no differences in biochemical composition of seeds of two analyzed genotypes.

Conflicts of interest

None.

Acknowledgements

References

Abugoch, L.E., Tapia, C., Villaman, M.C., Yazdani-Pedram, M., Diaz-Dosque, M., 2011. Characterization of quinoa proteinechitosan blend edible films. Food Hidrocolloids 25, 879–886. https://doi.org/10.1016/j.foodhyd.2010.08.008.

Almeida, M.R., Alves, R.S., Nascimbem, L.B., Stephani, R., Poppi, R.J., de Oliveira, L.F., 2010. Determination of amylose content in starch using Raman spectroscopy and multivariate calibration analysis. Anal. Bioanal. Chem. 397 (7), 2693–2701. https://doi.org/10.1007/s00216-010-3566-2.

Aluwi, N.A., Murphy, K.M., Ganjyal, G.M., 2017. Physicochemical characterization of 28 different varieties of Quinoa. Cereal Chem. 94 (5), 847–856. https://doi.org/10.1094/CCHEM-10-16-0251-R.

Ellepola, S.W., Choi, S.M., Phillips, D.L., Ma, C.Y., 2006. Raman spectroscopic study of rice globulin. Cereal Sci. 43, 85–93. https://doi.org/10.1016/j.jcs.2005.06.006.

Encina-Zelada, C., Cadavez, V., Pereda, J., Gomez-Pando, L., Salva-Ruiz, B., Teixeira, J.A., Ibanez, M., Liland, K.H., Gonzales-Barron, U., 2017. Estimation of composition of quinoa (*Chenopodium quinoa* Willd.) grains by Near-Infrared Transmission spectroscopy. LWT- Food, Sci. Technol. 79, 126–134. https://doi.org/10.1016/j.lwt.2017.01.026.

Garcia-Salcedo, A.J., Torres-Vargas, O.L., Ariza-Calderon, H., 2018. Physical-chemical characterization of quinoa (*Chenopodium quinoa* Willd.), amaranth (*Amaranthus caudatus* L.), and chia (*Salvia hispanica* L.) flours and seeds. Acta Agron. 67 (2), 215–222. https://doi.org/10.15446/acag.v67n2.63666.

Gordillo-Bastidas, E., Díaz-Rizzolo, D.A., Roura, E., Massanés, T., 2016. Quinoa (*Chenopodium quinoa* Willd), from nutritional value to potential health benefits: an integrative review. J. Nutr. Food Sci. 6 (3), 1–10. https://doi.org/10.4172/2155-9600.1000497.

Hammer, Ø., Harper, D.A.T., Ryan, P.D., 2001. PAST: paleontological statistics software package for education and data analysis. Palaeontol. Electron. 4 (1), 9pp. http://palaeo-electronica.org/2001_1/past/issue1_01.htm.

ISO (International Organization for Standardization) 10520, 1997. Native Starch - Determination of Starch Content - Ewers Polarimetric Method. (en).

Jacobsen, S.-E., Muica, A., 2002. Genetic resources and breeding of the Andean grain crop quinoa (*Chenopodium quinoa* Willd.). Plant Genet. Resour. Newsl. 130, 54–61.

Jacobsen, S.-E., Stølen, O., 1993. Quinoa-morphology and phenology and prospects for its production as a new crop in. Eur. J. Agron. 2, 19–29.

Kizil, R., Irudayaraj, J., Seetharaman, K., 2002. Characterization of irradiated starches by using FT-Raman and FTIR spectroscopy. J. Agric. Food Chem. 50 (14), 3912–3918. https://doi.org/10.1021/jf011652p.

Kolozsvari, B., Firth, S., Saiardi, A., 2015. Raman spectroscopy detection of phytic acid in plant seeds reveals the absence of inorganic polyphosphate. Mol. Plant 8 (5), 826–828. https://doi.org/10.1016/j.molp.2015.01.015.

Konishi, Y., Hirano, S., Tsuboi, H., Wada, M., 2004. Distribution of minerals in quinoa (*Chenopodium quinoa* Willd.) seeds. Biosc. Biotech. Biochem. 68 (1), 231–234. https://doi.org/10.1271/bbb.68.231.

Lee, H., Cho, B.C., Kim, M.S., Lee, W.H., Tewari, J., Bae, H., Sohn, S.I., Chi, H.Y., 2013. Prediction of crude protein and oil content of soybeans using Raman spectroscopy. Sensor. Actuator. B Chem. 85, 694–700.

López-Fernández, M.P., Maldonado, S., 2013. Programmed cell death during quinoa perisperm development. J. Exp. Bot. 64 (11), 3313–3325. https://doi.org/10.1093/

jxb/ert170.

Menges, F., 2018. Spectragryph - Optical Spectroscopy Software. Version 1.2.8, 2018. http://www.effemm2.de/spectragryph/.

Noulas, C., Karyotis, T., Iliadis, C., 2015. GREECE (Chapter 6).1.6 In: FAO & CIRAD. State of the Art Report of Quinoa in the World in 2013, pp. 492–510 (Rome).

Prego, I., Maldonado, S., Otegui, M., 1998. Seed structure and localization of reserves in *Chenopodium quinoa*. Ann. Bot. 82, 481–488. https://doi.org/10.1006/anbo.1998. 0704.

Pulvento, C., Riccardia, M., Biondib, S., Orsinic, F., Jacobsen, S.E., Ragabe, R., Lavinia, A., 2015. Quinoa in Italy: research and perspectives (Chapter 6).1.3 In: FAO & CIRAD. State of the Art Report of Quinoa in the World in 2013, pp. 454–465 (Rome).

Pulvento, C., Riccardi, M., Lavini, A., Iafelice, G., Marconi, E., d'Andria, R., 2012. Yield and quality characteristics of Quinoa grown in open field under different saline and non-saline irrigation regimes. J. Agron. Crop Sci. 198, 254–263. https://doi.org/10. 1111/j.1439-037X.2012.00509.x.

Rossell, C.A., 2013. Authentication of Andean Flours Using a Benchtop FT-IR System and a Portable FT-IR Spectrometer. Master Thesis. Graduate Program in Food Science and Technology, The Ohio State University, USA.

Schulmerich, M.V., Gelber, M.K., Azam, H.M., Harrison, S.K., McKinney, J., Thompson, D., Owen, B., Kull, L.S., Bhargava, R., 2013. Amino acid quantification in bulk soybeans by transmission Raman spectroscopy. Anal. Chem. 85 (23), 11376–11381. https://doi.org/10.1021/ac402284b.

Schulz, H., Baranska, M., 2007. Identification and quantification of valuable plant substances by IR and Raman spectroscopy. Vib. Spectrosc. 43, 13–25. https://doi.org/10. 1016/j.vibspec.2006.06.001.

Soliz-Guerrero, J.B., Jasso de Rodriguez, D., Rodriguez-Garcia, R., Angulo-Sanches, J.L., Mendez-Padilla, G., 2002. Quinoa saponins: concentration and composition analysis. In: Janick, J., Whipkey, A. (Eds.), Trends in New Crops and New Uses. ASHS Press, Alexandria, VA, pp. 110–114.

Stikic, R., Glamoclija, Dj, Demin, M., Vucelic-Radovic, B., Jovanovic, Z., Milojkovic-Opsenica, D., Jacobsen, S.E., Milovanovic, M., 2012. Agronomical and nutritional evaluation of quinoa seeds (*Chenopodium quinoa* Willd.) as an ingredient in bread formulations. J. Cereal. Sci. 55, 132–138. https://doi.org/10.1016/j.jcs.2011.10.010.

Sukhorukov, A.P., Zhang, M., 2013. Fruit and seed anatomy of *Chenopodium* and related genera (*chenopodioideae, chenopodiaceae/amaranthaceae*): implications for evolution and taxonomy. PLoS One 8 (4), e61906. https://doi.org/10.1371/journal.pone. 0061906.

Valcárcel-Yamani, B., Lannes, S.C.S., 2012. Applications of quinoa (*Chenopodium quinoa* Willd.) and amaranth (*Amaranthus spp.*) and their influence in the nutritional value of cereal based foods. Food Public Health 2 (6), 265–275. https://doi.org/10.5923/j. fph.20120206.12.

Valencia-Chamorro, S.A., 2003. Quinoa. In: Caballero, B. (Ed.), Encyclopedia of Food Science and Nutrition 8. Academic Press, Amsterdam, pp. 4895–4902.

Varriano-Marston, E., DeFrancisco, A., 1984. Ultrastructure of quinoa fruit (*Chenopodium quinoa* Willd.). J. Food Microst. 3 (2), 165–173. http://digitalcommons.usu.edu/ foodmicrostructure/vol3/iss2/9.

Zhu, G., Zhu, X., Fan, Q., Wan, X., 2011. Raman spectra of amino acids and their aqueous solutions. Spectrochim. Spectrochim. Acta Part A: Mol. Biomol. Spectrosc. 78, 1187–1195. https://doi.org/10.1016/j.saa.2010.12.079.
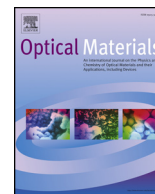
Far infrared spectra of Si doped PbTe single crystals

J. Trajic[a,*], N. Paunovic[a], M. Romcevic[a], V.E. Slynko[b], Jasna L. Ristic-Djurovic[a], W.D. Dobrowolski[c], N. Romcevic[a]

[a] Institute of Physics, University of Belgrade, Pregrevica 118, 11080, Belgrade, Serbia
[b] S.P.Timoshenko Institute of Mechanics, National Academy of Sciences, Kiev, Ukraine Nesterov st., 03680, MSP, Kiev 57, Ukraine
[c] Institute of Physics, Polish Academy of Sciences, Al. Lotnikow 32/46, 02-668, Warsaw, Poland

ABSTRACT

The far-infrared spectroscopy was used to analyze optical properties of PbTe single crystals doped with different amounts of Si. A dielectric function that takes into account the plasmon-phonon interaction was employed in the measured data manipulation. Two frequencies of plasmon-phonon coupled modes were obtained with the best-fit method, whereas the values for LO mode and plasma frequency (ω_p) were calculated. The best-fit to the experimentally obtained spectra agrees very well with the theoretical prediction.

1. Introduction

Specific physical and chemical properties of PbTe draws attention of numerous scientific studies. In particular, small band gap and high carrier mobilities qualify it for application in infrared optoelectronic devices [1] and thermoelectric materials [2]. The PbTe is also a good candidate for topological insulators materials. For instance, there are theoretical predictions that Te antisite defects in nonstoichiometric Te-rich PbTe could induce a band inversion, turning it into a topological crystalline insulator [3].

Thermoelectric materials found use in searches for alternative and complementary energy sources due to their ability to convert heat to electricity and *vice versa* [4–7]. Advantages of thermoelectric systems for direct heat-to-electricity conversion are environmental friendliness, absence of pollutants, small size, reliability, and large operating temperature range. Performance efficiency of a thermoelectric material, ZT, is expressed as ZT = $(S2\sigma/\kappa)T$, where S, T, ρ, and κ are the Seebeck coefficient, temperature, electrical resistivity, and thermal conductivity, respectively. The rocksalt-structured PbTe and related materials of n-as well as of p-type are shown to be good thermoelectric materials that operate in the mid-temperature range. As a matter of fact, PbTe-based materials have the highest recorded ZT among the bulk TE materials [8]. However, the materials based on PbTe have low mechanical strength, which can be improved by using Si as a dopant [9].

In order to absorb electromagnetic radiation, free carriers have to interact with a lattice. Transitions of an individual carrier as well as formation of collective plasma oscillators (plasmons) can contribute to the absorption. Consequently, the free-carrier absorption contains individual-carrier excitations (individual-carrier scattering), as well as collective carrier excitations (plasmon generation). Coupling of elementary excitations in solids has been investigated in a number of studies [10–13]. Studies of photon-plasmon processes usually start with a dielectric function for free carriers in a perfect crystal. Our approach [14,15] is to create a dielectric function that explains registered processes, and to compare it to the parameters obtained with the classical approach [13,16,17]. Comparison of the two yields to the physical explanation of the processes that take place in the doped semiconductors.

Raman spectroscopy is the commonly used technique to analyze optical properties of different materials. But, acquiring information about the coupled plasmon-phonon modes from the Raman spectra of PbTe samples is closely related to the ability to eliminate the influence of the oxide layer that is being formed at the sample surface. For film-samples, an additional problem can be removal of the substrate influence [18]. Further, analysis of the obtained results must be performed with elaborate mechanisms related to the microscopic approach in calculation of the Raman scattering cross-section [11] because the position of plasmon-phonon modes does not always coincide with the spectral maximum. Use of the IR spectroscopy in the analysis of the coupled plasmon-phonon modes takes into account all of these issues. In addition, in IR spectroscopy the position of global minimum remains directly related to the frequency of the coupled plasmon-phonon modes.

In this paper far-infrared spectroscopy (FIR) is used to study optical properties of PbTe single crystals doped with Si. Three values of Si

---

* Corresponding author.
  E-mail address: jelena@ipb.ac.rs (J. Trajic).

concentration in the samples were considered, namely 1, 3, 5.6 at.%. Analysis of the reflection spectra in a wide spectral range was used to detect plasmon-phonon coupling in the studied system.

2. Experiment

Single crystal ingots of PbTe(Si) were grown by the modified Bridgman method. The samples were synthesized using high purity components. The impurity content in the starting mixture was from 3 to 8 at.%. The Si concentration in the crystals used here was 1, 3, and 5.6 at.%. Distribution of silicon along ingots was determined by the XRF (X-ray fluorescence) analysis. Prior to analysis, the ingots were cut into discs of the same thicknesses. The XRF measurements were carried out on both sides of each disc and the spectra are given as the average of the two. Distribution of silicon along these ingots is in accordance with the model given in Ref. [19] according to which impurities always moves back to the end of the ingot.

The infrared reflectivity measurements were carried out at room temperature with a BOMEM DA-8 Fourier-transform IR spectrometer. A deuterated triglycine sulfate (DTGS) pyroelectric detector was used to cover the wave number region from 50 to 450 cm^{-1}.

3. Results and discussion

The low-frequency dielectric properties of single crystals are described by classical oscillators corresponding to the TO-modes and the Drude part which takes into account the free carrier contribution [10,17]:

$$\varepsilon_S(\omega) = \varepsilon_\infty + \sum_{k=1}^{n} \frac{\varepsilon_\infty(\omega_{LOk}^2 - \omega_{TOk}^2)}{\omega_{TOk}^2 - \omega^2 - i\gamma_{TOk}\omega} - \frac{\varepsilon_\infty\omega_P^2}{\omega(\omega + i\gamma_P)} \quad (1)$$

where ε_∞, ω_{LOk}, ω_{TOk}, ω_P, γ_{TOk}, and γ_P are the bound charge contribution taken to be constant, longitudinal and transverse optical-phonon frequencies, plasma frequency, and phonon and plasma damping. Therefore, the TO mode frequency is obtained directly from the fit, whereas the LO modes are determined from the maximum of the dielectric loss function.

In the PbTe doped with Si the pure LO-mode of the lattice is strongly influenced by the plasmon mode of the free carriers, which causes appearance of a combined plasmon-LO phonon mode [12]. Consequently, only coupled mode positions are observable in the experimental spectra and the LO-modes are detectable only if the influence of the free carrier is eliminated [13]. Therefore, in the analysis of far-infrared reflectivity spectra of PbTe doped with Si we used the dielectric function that includes the interaction between LO phonon and a plasmon, i.e. the plasmon-phonon interaction in its initial form [13, 15]. Namely, the expression for dielectric function is

$$\varepsilon_f(\omega) = \varepsilon_\infty \frac{\prod_{j=1}^{2}(\omega^2 + i\gamma_{lj}\omega - \omega_{lj}^2)}{\omega(\omega + i\gamma_P)(\omega^2 + i\gamma_t\omega - \omega_t^2)} \cdot \prod_{p=1}^{l} \frac{\omega^2 + i\gamma_{LOp}\omega - \omega_{LOp}^2}{\omega^2 + i\gamma_{TOp}\omega - \omega_{TOp}^2} \quad (2)$$

The parameters ω_{lj} and γ_{lj} in the first numerator represent the eigenfrequencies and damping coefficients of the coupled plasmon-longitudinal phonon waves. The parameters in the first denominator correspond to the similar characteristics of the transverse (TO) vibrations. The second term in Eq. (2) represents l uncoupled modes of the crystal. Consequently, ω_{LOp} and ω_{TOp} are the longitudinal and transverse frequencies, whereas γ_{LOp} and γ_{TOp} are the corresponding damping parameters. Therefore, the determination of LO-mode and plasma frequency is connected with the decoupled procedure.

The far-infrared reflection spectrum at room temperature of the PbTe single crystal doped with 1 at.% Si is presented in Fig. 1. The experimental data are depicted with circles, whereas the solid line represents the calculated reflectivity spectrum, which is obtained by the fitting procedure that is based on the model for plasmon-phonon coupling given by Eq. (2). In the fitting procedure, the modes characteristic
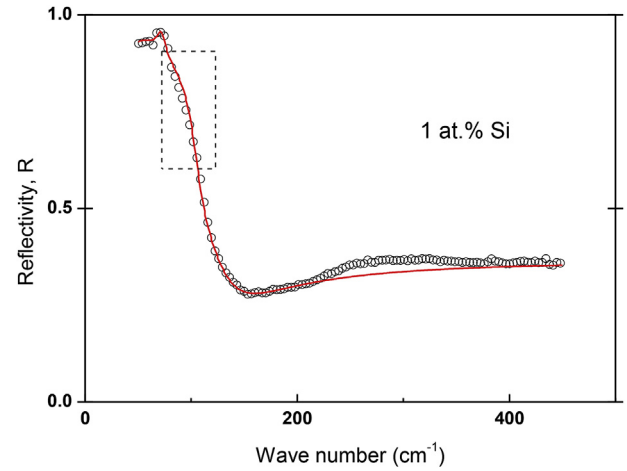

Fig. 1. Far-infrared reflection spectra of PbTe single crystal doped with 1 at.% Si. The spectrum obtained experimentally at room temperature is presented with circles. The solid lines depict the calculated spectrum obtained by the fitting procedure that is based on the model given by Eq. (2) where $p = 1$.

for this type of material are included, namely the pair of PbTe TO/LO modes and the mode at about 73 cm^{-1}, which is the PbTe Brillouin zone edge mode. These modes are considered because the phonon density of PbTe has a maximum at their frequencies [20].

Slight discrepancy between the theoretical spectrum and the experimental results in the frequency range at about 100 cm^{-1} (marked by dashed lines) indicates the existence of the mode that corresponds to the Si impurity. Fig. 2 shows the same spectrum as Fig. 1; however, in addition to the modes considered previously, the fitting procedure contains the Si impurity mode at about 90 cm^{-1}. Note that lead telluride grows with rather high concentration of native defects (vacancies, etc). In the PbTe lattice Si is a substitute for Pb and as such is a substitution impurity ion. Consequently, every ion in PbTe is no longer in the center of inversion symmetry and PbTe vibration modes could be Raman as well as far-infrared active. The impurity mode can arise simply because of the difference between masses and force constants of the impurity ion and the ion of the host material [21]. Their appearance can be caused by more complex mechanism of electron-phonon interaction [22]. When the semiconductor is doped with a substitution impurity [10] (in our case Si), and if the substitution takes place with the atoms of the heavier mass (Pb), lighter impurity leads to two modes: a
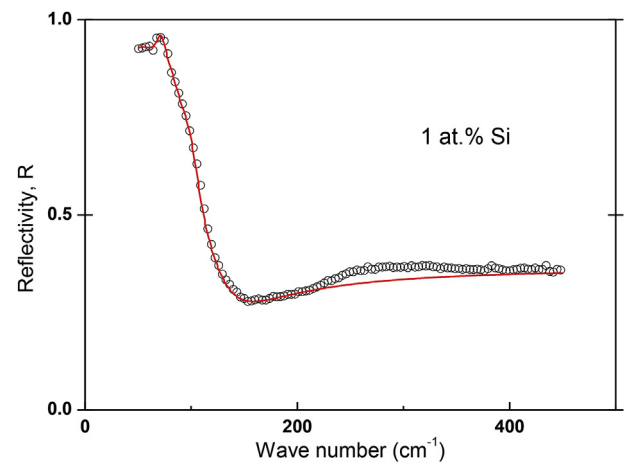

Fig. 2. Far-infrared reflection spectra of PbTe single crystal doped with 1 at.% Si. The experimental spectrum obtained at room temperature is presented with circles. The solid lines are calculated spectrum with additional Si impurity mode, obtained by the fitting procedure that is based on the model given by Eq. (2) where $p = 2$.
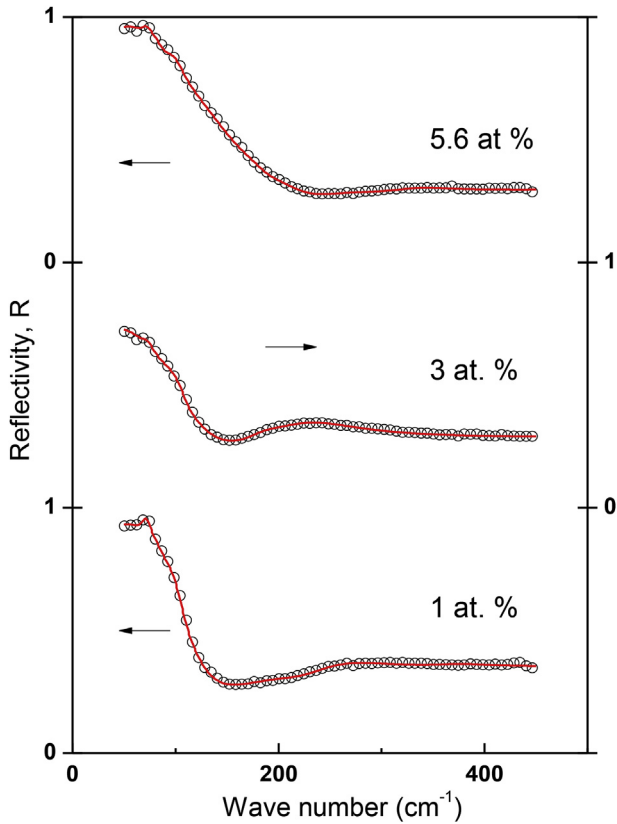
Fig. 3. Far-infrared reflection spectra of PbTe single crystals doped with 1, 3 and 5.6 at.% Si. The experimental spectra obtained at room temperature are depicted with circles. The solid lines are calculated spectra obtained by the fitting procedure that is based on the model given by Eqs. (2) and (4).

local mode situated above the optical band and a gap mode situated above the acoustic band and below the optical band of the host lattice. The position of Si impurity mode in PbTe was estimated in the manner described in detail in Ref. [23], namely with the expression

$$\omega_I(Si) = \omega_{TO}(PbTe)\sqrt{\frac{M_{Pb}}{M_{Si}}} \tag{3}$$

where M_{Pb} and M_{Si} are the masses of the atoms Pb and Si, respectively.

We did not manage to determine the set of parameters that provide good spectrum overlapping in the whole range of frequencies. Registered discrepancy between the experimental and the calculated reflectivity spectra is obvious, and the new structure is observable above $220\,cm^{-1}$ In order to remove this discrepancy, Eqs. (1) and (2) were extended to include the term [24]:

$$\frac{\omega_{loc}^2}{\omega_0^2 - \omega^2 - i\omega G} \tag{4}$$

where ω_0, G, and ω_{loc} are the characteristic frequency, damping, and "strength" of the additional oscillator. According to Ref. [24], $(\omega_{loc})^2$ is proportional to the N_{loc} carrier concentration at the localized level.

In Fig. 3 we compare the experimental results to the theoretical spectrum at room temperature of PbTe single crystals doped with 1, 3 and 5.6 at.% Si, which take into account additional term described with Eq. (4) in Eq. (2).

We obtained the value of $\omega_0 = 235 \pm 8\,cm^{-1}$ as the result of the best fit procedure. In the SiTe electron transition from the excited state E to the ground state X exists in the range above $220\,cm^{-1}$ [25]. It seems that during the process of doping PbTe with Si, localization of electrons occurs in the vicinity of Si impurity atom as a consequence of the appearance of Te−SiTe clusters with cubic symmetry. As one can
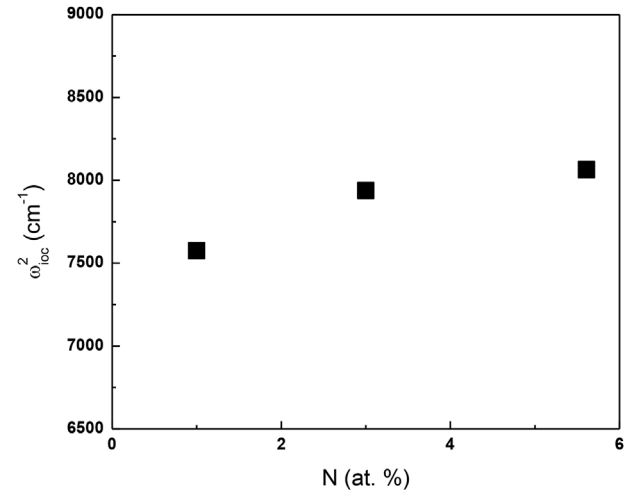

Fig. 4. The "strength" of the oscillator described by Eq. (4) vs silicon concentration.
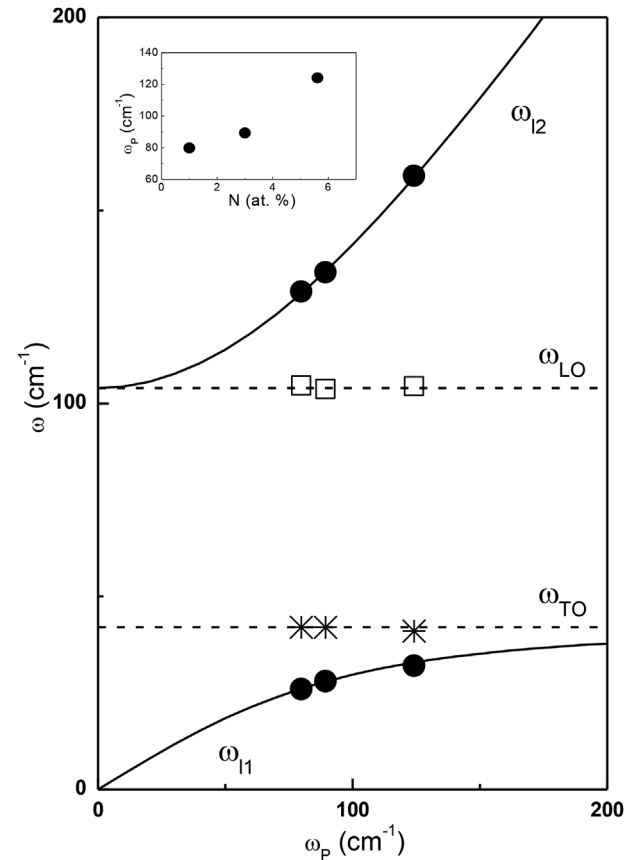

Fig. 5. The eigenfrequencies of the plasmon-LO phonon modes (full lines - Eq. (1)); ● - eigenfrequency spectra ω_{lj} obtained by procedure based on Eq. (2); □ - calculated values for ω_{LO} and * - experimentally determined values for ωTO. Inset: plasma frequencies (ω_P) vs. Si concentration.

see from Fig. 4, the "strength" of the oscillator connected with electron transition increases with the increase of Si concentration.

In Fig. 5 characteristic spectra for plasmon-phonon interaction are presented. Obtained results describe the relationship between the results obtained with Eq. (2) and those resulting from the traditional approach described with Eq. (1). The solid lines represent coupled frequencies, and as it was given in Ref. [13], the positions of the coupled modes were defined as the solutions of Eq. (1) (Re{ε} = 0). Dashed

lines, obtained experimentally as the best fit, correspond to the well-known values for PbTe LO and TO phonon positions [19]. As a result of the best fit, using Eq. (2) with additional term given by Eq. (4), we obtained the frequencies of coupled modes (ω_{l1} and ω_{l2}), and then we calculated the values for ω_{LOPbTe} and ω_P, as is described in Ref. [15]. The value for the ω_{LOPbTe} obtained in this manner is in good agreement with the literature. The characteristic parameters obtained as the best fit are shown in Fig. 5. The plasma frequencies (ω_P) dependence on Si concentration is presented in the inset of Fig. 5.

As we already said, localization of electrons occurs in the vicinity of the impurity, i.e. Si atom. Localization of electrons leads to the decrease of electrical conductivity. Since the thermal and electrical conductivities are proportional (Wiedemann-Franz Law), the decrease of electrical conductivity causes the decrease of thermal conductivity. Also, electrons localized around this impurity cause the localization of phonons. Since phonons are responsible for heat transmission, their localization also leads to the decrease of phonon thermal conductivity. As it is well known, a good thermoelectric material must have low thermal conductivity in order to retain the heat and to reduce the heat transfer losses. This lead us to conclude that localization of electrons in the vicinity of Si atom impurity makes PbTe doped with Si a good thermoelectric material.

These results are very significant since they represent the basis for investigation these effects in nanocrystals [26].

4. Conclusion

The far-infrared spectroscopy was employed to investigate phonon properties of PbTe single crystal doped by 1, 3, and 5.6 at.% Si. The spectra were analyzed using the dielectric function that takes into account the existence of plasmon-phonon interaction in advance. As a result of the best fit procedure the two frequencies corresponding to the coupled modes (ω_{l1} and ω_{l2}) were obtained, whereas the frequency values for LO mode (ω_{LO}) and plasma frequency (ω_P) were calculated. In addition to the modes that are characteristic for this type of material, we registered the Si impurity mode as well as the localization of electrons in the vicinity of Si impurity atom.

Declaration of interests

The authors declare that they have no known competing financial interests or personal relationships that could have appeared to influence the work reported in this paper.

Acknowledgements

References

[1] A.M. Samylov, M.K. Saharov, S.A. Buchnev, A.M. Khoviev, E.A. Dolgopolova, Crystal structure, carrier concentration and IR-sensitivity of PbTe thin films doped with Ga by two different methods, J. Cryst. Growth 240 (3) (2002) 340–346.

[2] M.S. Dresselhaus, G. Dresselhaus, X. Sun, Z. Zhang, S. Cronin, T. Koda, Y.I. Ying, The promise of low-dimensional thermoelectric materials, Microscale Thermophys. Eng. 3 (2) (1999) 89–100.

[3] M. Songsong, G. Chunyu, X. Chengcheng, W. Fan, S. Michael, L. Yunhao, Y. Huiqiu, W. Huizhen, Adv. Funct. Mater. 28 (2018) 1803188.

[4] X. Shi, L. Chen, C. Uher, Recent advances in high-performance bulk thermoelectric materials, Int. Mater. Rev. 61 (6) (2016) 379–415.

[5] G. Tan, L.D. Zhao, M.G. Kanatzidis, Rationally designing high-performance bulk thermoelectric materials, Chem. Rev. 116 (19) (2016) 12123–12149.

[6] J. He, T.M. Tritt, Advances in thermoelectric materials research: looking back and moving forward, Science 357 (2017) 1369.

[7] L. Yang, Z.G. Chen, M.S. Dargusch, High performance thermoelectric materials: progress and their applications, Adv. Energy Mater. 8 (6) (2017) 1701797.

[8] B. Cai, J. Li, H. Sun, L. Zhang, B. Xu, W. Hu, D. Yu, J. He, Z. Zhao, Z. Liu, Y. Tian, Enhanced thermoelectric performance of Na-doped PbTe synthesized under high pressure, Sci. China Mater. 61 (9) (2018) 1218–1224.

[9] Q. Zhang, H. Wang, Q. Zhang, W. Liu, B. Yu, H. Wang, D. Wang, G. Ni, G. Chen, Z. Ren, Effect of silicon and sodium on thermoelectric properties of thallium-doped lead telluride-based materials, Nano Lett. 12 (5) (2012) 2324–2330.

[10] E. Burstein, A. Pinczuk, R.F. Wallis, By D.L. Carter, R.T. Bate (Eds.), The Physics of Semimetals and Narrow-Gap Semiconductors, Pergamon, New York, 1971, p. 251.

[11] M. Cardona, G. Gunterodt (Eds.), Light Scattering in Solids, Top. Appl. Phys. vol. 8, Springer, Berlin, 1975.

[12] S. Takaoka, T. Hamaguchi, S. Shimomura, K. Murase, Observation of the coupled plasmon-lo phonon mode energy in photo-excited Pb1-xSnxTe doped with indium impurities, Solid State Commun. 54 (1) (1985) 99–102.

[13] A.A. Kuharskii, Solid State Commun. 8 (1970) 1275.

[14] J. Trajic, N. Romcevic, M. Romcevic, D. Stojanovic, R. Rudolf, T.A. Kuznetsova, D.R. Khokhlov, Far-infrared study of impurity local modes in Co-doped PbTe, J. Alloy. Comp. 493 (1–2) (2010) 41–46.

[15] J. Trajić, N. Romčević, M. Romčević, V.N. Nikiforov, Plasmon-phonon and plasmon-two different phonon interaction in Pb1-xMnxTe mixed crystals, Mater. Res. Bull. 42 (12) (2007) 2192–2201.

[16] V. Gopal, Analysis of the infrared plasma reflectivity spectra of semiconductors, Infrared Phys. 18 (2) (1978) 121–125.

[17] G. Abstreiter, M. Cardona, A. Pinczuk, M. Cardona, G. Guntherodt (Eds.), Light Scattering in Solids, IV, Springer-Verlag, Berlin, 1984.

[18] H. Wu, C. Cao, J. Si, T. Xu, H. Zhang, H. Wu, J. Chen, W. Shen, N. Dai, Observation of phonon modes in epitaxial PbTe films grown by molecular beam epitaxy, J. Appl. Phys. 101 (10) (2007) 103505.

[19] B.A. Volkov, L.I. Ryabova, D.R. Khokhlov, Mixed-valence impurities in lead telluride-based solid solutions, Uspekhi Fizicheskih Nauk 172 (8) (2002) 875–906 [Phys. Usp. 45 (8) (2002) pp. 819–846].

[20] W. Cochran, R.A. Cowley, G. Dolling, M.M. Elcombe, The crystal dynamics of lead telluride, Proc. R. Soc. A 293 (1966) 433–451.

[21] A.A. Maradudin, F. Seitz, D. Turnball (Eds.), Solid State Physics, vol. 19, Academic, New York, 1966.

[22] D.E. McCumber, One-phonon collision corrections to the high-frequency dielectric function of semiconductors, Phys. Rev. 154 (1967) 790.

[23] S. Venigopalan, A. Petrov, R.R. Galazka, A.K. Ramdas, S. Rodriguez, Raman scattering by phonons and magnons in semimagnetic semiconductors: Cd1−xMnxTe, Phys. Rev. B 25 (1982) 2681.

[24] N. Romcevic, Z.V. Popovic, D. Khokhliv, A.V. Nikorich, V. Konig, Far-infrared study of localized states in In-doped Pb0.75Sn0.25Te single crystals, Phys. Rev. B 43 (8) (1991) 6712–6716.

[25] S. Chattopadhyaya, A. Pramanik, A. Banerjee, K. Kumar Das, Electronic states and spectroscopic properties of SiTe and SiTe+, J. Phys. Chem. A 110 (44) (2006) 12303–12311.

[26] J. Mitric, N. Paunovic, M. Mitric, B. Vasic, U. Ralevic, J. Trajic, M. Romcevic, W.D. Dobrowolski, I.S. Yahia, N. Romcevic, Surface optical phonon – plasmon interaction in nanodimensional CdTe thin films, Phys. E Low-dimens. Syst. Nanostruct. 104 (2018) 64–70.
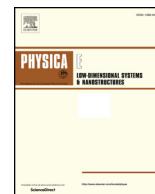
Surface optical phonon – Plasmon interaction in nanodimensional CdTe thin films

J. Mitric[a,*], N. Paunovic[a], M. Mitric[b], B. Vasic[a], U. Ralevic[a], J. Trajic[a], M. Romcevic[a], W.D. Dobrowolski[c], I.S. Yahia[d,e], N. Romcevic[a]

[a] Institute of Physics, University of Belgrade, Pregrevica 118, 11080 Belgrade, Serbia
[b] Institute Vinca, University of Belgrade, P.O. Box 522, 11001 Belgrade, Serbia
[c] Institute of Physics, Polish Academy of Science, al. Lotnikov 32/46, 02-668 Warsaw, Poland
[d] Department of Physics, Faculty of Science, King Khalid University, P.O. Box 9004, Abha, Saudi Arabia
[e] Nano-Science & Semiconductor Labs, Department of Physics, Faculty of Education, Ain Shams University, Roxy, Cairo, Egypt

ARTICLE INFO

ABSTRACT

Structural and optical properties of CdTe thin films were investigated applying atomic force microscopy (AFM), XRD powder technique, Raman spectroscopy and far–infrared spectroscopy. CdTe thin films were prepared by using thermal evaporation technique. In the analysis of the far – infrared reflection spectra, numerical model for calculating the reflectivity coefficient for system which includes films and substrate has been applied. Effective permittivity of film mixture (CdTe and air) was modeled by Maxwell – Garnet approximation. We reveal the existence of surface optical phonon (SOP) mode and coupled plasmon-SOP modes (CPSOPM).

1. Introduction

II – VI semiconductor compounds, especially thin films, have become very popular because of their applications in numerous electronic and optoelectronic devices. Due to low production cost, thin films nowadays enjoy great attention in basic research and solid state technology.

The interest in various properties of photonic CdTe is well justified, as this material plays an important role in expanding variety of applications as in: integrated optics, optoelectronics, or solar energy conversion [1].

Two main properties of CdTe thin film are its high optical absorption coefficient (a thin film of CdTe with thickness of approximately 2 μm will absorb nearly 100% of the incident solar radiation) and its near ideal band gap for photovoltaic conversion efficiency of 1.45eV [2]. Also, its ease of film fabrication and low cost make it a representative material among II – VI semiconductors.

For fabrication of the CdTe films, various techniques have been applied: RF magnetron sputtering [3], molecular beam epitaxy (MBE) [4], pulsed laser deposition (PLD) [5], successive ionic layer adsorption and reaction method (SILAR) [6], metal organic chemical vapor deposition [7], screen printing [8], thermal evaporation method [9] etc. Thermal evaporation method shows some advantages such as: minimalization of impurities proportional to the growing layer, reduced

chances of oxidation and direction of propagation (occurs from the source to the substrate) [9,10]. This makes thermal evaporation technique the most suitable method, thanks to very high deposition rate, low material consumption and low cost of fabrication [11].

In the case of crystal with relatively small dimension, in the frequency range between bulk longitudinal optical phonon frequency (ω_{LO}) and transversal optical phonon frequency (ω_{TO}), a new mode known as a surface phonon mode appears [12,13]. It is known for the case of real crystal, that when its dimension is relatively small, surface modes and effects of dimension will be manifested in addition to the normal modes of infinite lattice. But, when crystal is reduced to extremely small dimensions, only the surface mode will persevere [12–14].

On the other side, electron – phonon interaction takes an important place in semiconducting materials [15]. In our earlier work we have registered plasmon (collective electron excitation) and LO phonons interaction in different systems [16–19]. Besides that, we have studied the impact of damping on interaction appearance [20], interaction between plasmon and different phonons [21,22], as well as interaction between plasmon and impurity local phonons [23–25].

In this work we report experimental studies of CdTe thin films prepared by thermal evaporation technique. Existence of nanodimensional structures in these thin films enabled us to observe effects associated with interactions between surface optical phonon (SOP) and

---

plasmon for the first time.

Samples characterization was performed using atomic force microscopy (AFM). Structural properties were analyzed using XRD powder technique, and optical properties were characterized using Raman and far–infrared spectroscopy.

2. Sample preparation and characterization methods

CdTe single crystal was grown by the Bridgman technique. Different thickness of CdTe thin films were deposited by thermal evaporation from a resistance heating quartz glass crucible onto glass substrates using high vacuum coating unit type Edward 306 A. Films were grown at a pressure of 106 Pa. The mechanical rotation of the substrate holder during deposition produced homogeneous film. The distance between the source heater and substrates holder is 21 cm, in order to avoid any heat flow from the source to the substrates.

The morphology of the four CdTe thin films of different thicknesses was investigated by Atomic force microscopy (AFM). Atomic force microscopy measurements were performed using NT-MDT system NTEGRA Prima. Imaging was done in tapping mode using NSG01 probes. All AFM measurements were done at ambient conditions. For the sake of statistical analysis of sample surface, we calculated histograms and bearing ratios for each topographic image. The histogram represents a height distribution density of all points in a two-dimensional topographic image, or in other words, it is a number of points with height given on x-axis. On the other hand, the bearing ratio curve gives a percent of points in a corresponding two-dimensional topographic image with a height less than the number given on x-axis.

The structural characteristics were obtained by the XRD powder technique. All samples were examined under the same conditions, using a Philips PW 1050 diffractometer equipped with a PW 1730 generator, $40 \, kV \times 20 \, mA$, using Ni filtered Co Kα radiation of 0.1778897 nm at room temperature. Measurements were carried out in the 2 h range of 10–100° with a scanning step of 0.05° and 10 s scanning time per step. Crystallite size was determined by using XFIT computing program which is based on Fundamental Parameter convolution approach [26].

Raman measurements were performed using commercial NTegra Spectra system from NT-MDT. A linearly polarized semiconductor laser operating at a wavelength of 532 nm was used. All the spectra were obtained by setting the laser power to 2 mW within the ~0.5 × 0.5 µm sized focus with exposure time of 600 s.

The far-infrared (FIR) reflectivity measurements were performed at room temperature with a BOMEM DA-8 Fourier-transform infrared spectrometer. A Hyper beamsplitter and deuterated triglycine sulfate (DTGS) pyroelectric detector were used to cover the wave number region from 80 to 650 cm^{-1}.

3. Results and discussion

3.1. Atomic force microscopy

Three dimensional topographic images of all four samples are shown in the left side of Fig. 1. As can be seen, sample surfaces are rather flat, but still they are characterized with bright protrusions and dark holes (which represent air) resulting in a small surface roughness of several nanometers.

In order to characterize fraction of both observed topographic features, the statistical analysis have been performed by calculating histograms and bearing ratios from two dimensional topographic images. The results for all four samples are given in the right side of Fig. 1. They show that the peaks in the histograms are positioned in the middle of bearing ratio curves. Therefore, from these curves we can conclude that the fraction of holes and protrusions are rather similar, around 50%.

In order to estimate thicknesses of studied films, their step edges were measured by AFM. 3D AFM topographic images of the step edges are depicted in Fig. 2(a1-d1). The films are brighter and the substrates

are dark in the images, while the step edges are clearly resolved. Based on the AFM images, height distributions were calculated and presented in Fig. 2 (a2-d2). In all histograms, there are two characteristic peaks: a lower one corresponds to the substrate, while a higher one corresponds to the film. Therefore, the film height can be then approximately calculated as a difference between these two peaks. Estimated film thicknesses are given in Fig. 2 (a2-d2). The best resolved height peaks were found on CdTe 1 in Fig. 2 (a2) due to a smooth sample surface as can be seen in Fig. 2 (a1).

3.2. XRD

Structures of four synthesized CdTe thin films with different thicknesses were identified by XRD pattern as shown in Fig. 3. The diffractograms confirm that all samples are monophased, and that they crystallized in sphalerite type structure in 216. space group, $F\bar{4}3m$. All of the observed diffraction peaks are indexed according to this space group. Therefore, in our thin film samples there is no other structures other than CdTe. In this structural type, Cd ions occupy $4a$ Wyckoff positions, [[0, 0, 0]] with local symmetry $\bar{4}3m$, while Te ions occupy $4c$ Wyckoff positions [[1/4, 1/4, 1/4]] with the same local symmetry. Cd ions are in tetrahedral surrounding of Te ions (and vice versa). The tetrahedrons are regular and share common vertices. Crystallite size (R) is determined and presented in Fig. 2 and Table 1.

3.3. Raman spectroscopy

The cubic face-centered structure of balk crystal CdTe is characterized by the 216. space group $F\bar{4}3m$ and contains four formula units, while the primitive cell is one fourth as many. Optical modes consist of one three fold –degenerated mode F_2 which is active in IR and Raman spectra. The dipole mode F_2 is split into the transverse (TO) and longitudinal (LO) modes in the vibrational spectra. It is very well known that reduction of the particle dimensions to nanoscale results in a breakdown of phonon selection rules and allows phonons with $l \neq 0$ to contribute to Raman scattering [27–31]. Consequently, some new forbidden vibration modes (low frequency region, acoustic modes, and high frequency region, surface optical modes) occur due to imperfections, impurity, valence band mixing and/or nonspherical geometry of the nanostructures [14].

TO (142 cm^{-1}) and LO (170.5 cm^{-1}) modes for the CdTe bulk crystal are both active in the Raman spectra. Also, the modes in band near 120 cm^{-1} correspond to phonons of Te on the CdTe surface and can be seen in the Raman spectra [32].

Raman spectra of CdTe thin films of different thickness at room temperature are presented in Fig. 4.

For analyzing obtained spectra Lorentz profiles were used. Solid lines are their sums. In the top right corner Raman spectra of bulk CdTe crystal for ambient conditions is presented [32]. The observed Raman spectra for all samples among characteristic CdTe TO mode at 142 cm^{-1} and phonon of Te of the CdTe surface (127 cm^{-1}), show the LO phonon like frequency shift from 170.5 cm^{-1} to 164 cm^{-1}. That can be attributed to the surface optical phonon (SOP) mode effect [33–38]. It is clear that SOP phonon is wider compared to LO phonon of bulk crystal, as well as when it's compared to phonon of nanodimensional film. This effect is associated with interaction between SOP and plasmon, which will be mentioned later on.

In order to analyze the surface optical phonon we have to take into account that a part of crystallites are surrounded by air. We will analyze the dependence of the SOP mode position on filling factor (*f*) of the mixed material.

Surface phonon modes can be detected in systems where particle size is much smaller when compared to wavelength of exciting light source [39]. These modes can be obtained for in the case of polar crystals [40], so we consider expression for dielectric function which describes optical properties of polar semi – insulating semiconductor in
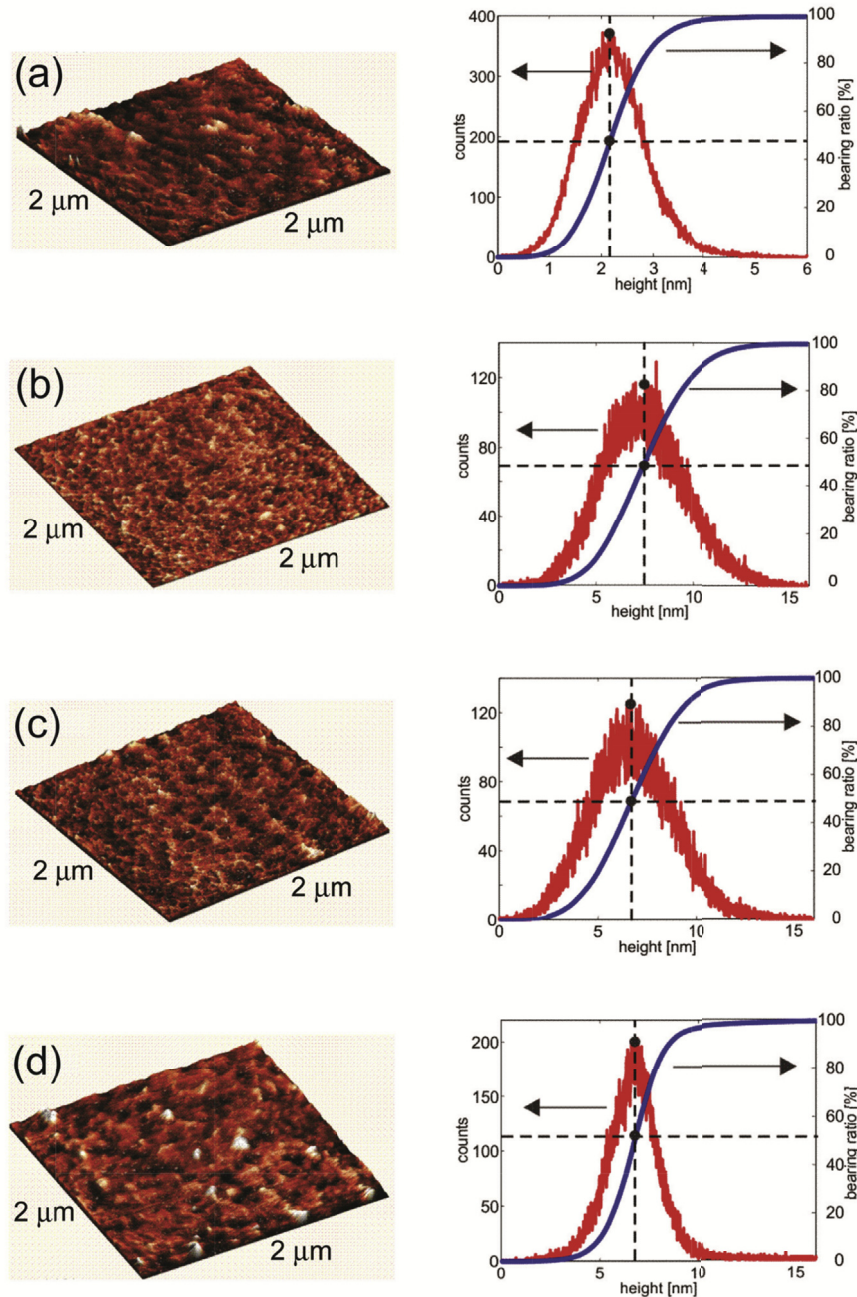
Fig. 1. Three-dimensional topographic image (left) and corresponding histogram and bearing ratio (right) for (a) CdTe 1, (b) CdTe 2, (c) CdTe 3, and (d) CdTe 4. Scan size is 2 μm.

IR region [24]:

$$\varepsilon_2(\omega) = \varepsilon_\infty \left(1 + \sum_{k=1}^{n} \frac{\omega_{LOk}^2 - \omega_{TOk}^2}{\omega_{TOk}^2 - \omega^2 - i\gamma_{TOk}\omega} - \frac{\omega_P^2}{\omega(\omega + i\Gamma)} \right) \tag{1}$$

ωTO and ωLO represent transverse and longitudinal optical bulk phonons, respectively; $\varepsilon\infty$ is the dielectric constant at high frequencies, ωP is plasma frequency and γ and Γ are the damping constants. Surface phonons can be considered similarly to phonons in infinite crystals, but with adapted wave functions to the geometry of the small particle.

Here, we will apply effective medium theory: Because the size of semiconducting nanoparticles, L, (with dielectric function ε_2, and are distributed in a medium with dielectric constant ε_1) is considerably

smaller than the interacting wavelength of visible light, λ ($\lambda \gg L$), we treat the heterogeneous composite as a homogeneous medium.

Even though there are numerous models for the effective dielectric permittivity for these kinds of mixtures [41], we decided to use Maxwell – Garnet model, because all our samples are thin films with well defined and separated nanosized grains. According to the Maxwell – Garnet mixing rule [42,43], effective permittivity of mixture, including spherical geometry of particles is given with:

$$\varepsilon_{eff} = \varepsilon_1 + 3f\varepsilon_1 \frac{\varepsilon_2 - \varepsilon_1}{\varepsilon_2 + 2\varepsilon_1 - f(\varepsilon_1 - \varepsilon_2)} \tag{2}$$

In this case, nanoparticles are spheres with permittivity ε_2 and are randomly distributed in homogeneous environment, with permittivity
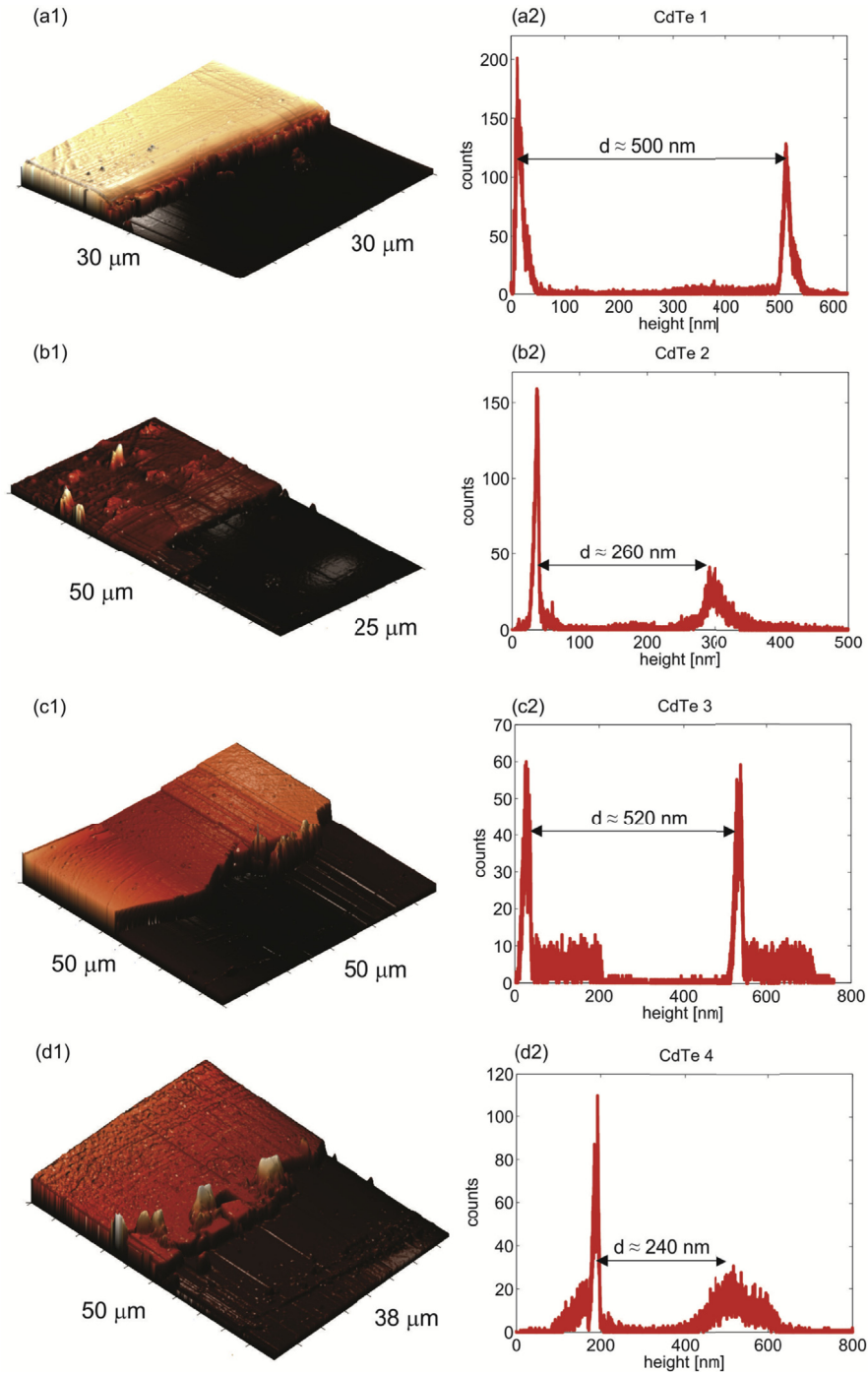
Fig. 2. (a1-d1) 3D AFM topographic images of step edges of studied films, and (a2-d2) corresponding height histograms. Average films thicknesses are denoted in the histograms.

ε_1 and occupy a volume fraction f.

Position surface optical phonon (SOP) mode frequencies are obtained from Ref. [44]:

$$\omega_{SOP} = max\left(I_m\left(-\frac{1}{\varepsilon_{eff}}\right)\right) \tag{3}$$

The result is shown in Fig. 5. The practical liner dependence of the position of the SOP mode on the filing factor f has been obtained. For the frequency of the SOP mode determined in Fig. 4 we have $f = 0.53$. This result is in accordance with the one obtained from the AFM measurements.

3.4. Far-infrared spectroscopy

Thicknesses of our films, as we will see, are in a range from $\sim 0.39\,\mu m$ to $\sim 0.72\,\mu m$, so reflectivity spectra contain information about CdTe films together with information about substrate. Representative scheme of our layered structure can be presented in Fig. 6 [45]. Medium 1 is air, medium 2 is thin bulk CdTe crystal layer and medium 3 is substrate glass, with dielectric functions ε_1 ($\varepsilon_1 = 1$), ε_2 and ε_3, respectively. We can now write [46]:

$$R_A = \frac{A_r}{A_i} = \frac{r_{12}e^{-i\alpha} + r_{23}e^{i\alpha}}{e^{-i\alpha} + r_{12}r_{23}e^{i\alpha}} \tag{4}$$
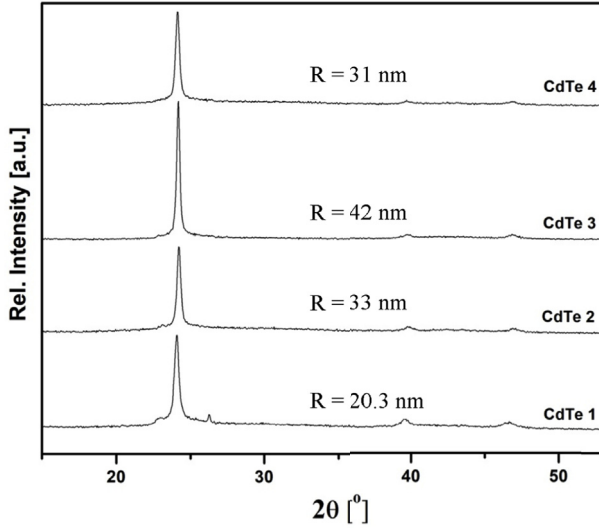
Fig. 3. XRD analysis of CdTe thin films of different thickness. Obtained crystallite sizes (R) are presented too.

Table 1
Parameters obtained from XRD measurements and FIR reflection spectroscopy. Thin films thickness - d, Crystallite size – R.

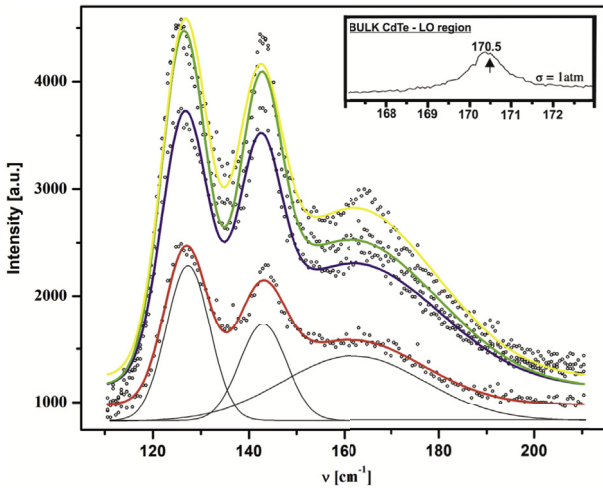| Name	d [µm]	R [nm]	ω_{l1} (ω_+) [cm^{-1}]	ω_{l2} (ω_-) [cm^{-1}]	ω_P [cm^{-1}]	ω_t [cm^{-1}]	f
CdTe 4	0.39	31.0	187	103	137.5	140.0	0.53
CdTe 2	0.43	33.0	174	78	96.6	140.5	0.53
CdTe 3	0.71	42.0	170	65	79.5	139	0.53
CdTe 1	0.72	20.3	165	30	35.2	140.5	0.53

Fig. 4. Raman spectra of CdTe thin films of different thickness. Experimental spectra are shown by open dots. Solid lines are sums of three Lorentz profiles as it shown for spectrum of CdTe 1. In the top right corner LO region of bulk CdTe is presented, taken from the literature [32].

$r_{ij} = (n_i - n_j)/(n_i + n_j) = (\sqrt{\varepsilon_i} - \sqrt{\varepsilon_j})(\sqrt{\varepsilon_i} + \sqrt{\varepsilon_j})$ describe Fresnel coefficients, A_i and A_r represent amplitudes of incident and reflection beams, n is complex index of refraction, ε is the dielectric constant and $\alpha = 2\pi\omega d(\varepsilon_2)^{1/2}$ is the complex phase change related to the absorption in the crystal layer with the thickness d.

Reflectance, R, is given with:

$$R = |R_A|^2 \tag{5}$$

In this case we decided to use dielectric function which takes into

consideration the existence of plasmon – phonon interaction in advance.

The dielectric function of the CdTe crystal layer is:

$$\varepsilon_2(\omega) = \varepsilon_{\infty CdTe} \prod_{j=1}^{2} \frac{\omega^2 + i\gamma_{lj}\omega - \omega_{lj}^2}{\omega(\omega + i\Gamma_p)(\omega^2 + i\gamma_t\omega - \omega_t^2)} \tag{6}$$

The ω_{lj} and γ_{lj} ($j = 1, 2$), parameters of the first numerator are the eigenfrequencies and damping coefficients of the longitudinal plasmon-phonon (LP + LO) waves, that arise as a result of the interaction of the initial phonon ($\omega_{LO,CdTe} = 170.5$ cm^{-1}) and plasmons (ω_P) modes. The parameters of the denominator correspond to the similar characteristics of the transverse vibrations (ω_t, γ_t) and plasmon damping Γ_P. As a result of the best fit, we obtain coupled mode frequencies (ω_{l1} and ω_{l2}).

The dielectric function of the glass substrate is:

$$\varepsilon_s(\omega) = \varepsilon_{\infty sup} \prod_{k=1}^{n} \frac{\omega_{LOk}^2 - \omega^2 + i\gamma_{LOk}\omega}{\omega_{TOk}^2 - \omega^2 + i\gamma_{TOk}\omega} \tag{7}$$

where ω_{TO} and ω_{LO} are the transversal and longitudinal optical vibrations, and γ_{TO} and γ_{LO} are damping parameters, respectively.

In our case, layer 2 consists of a CdTe crystals and air (see Fig. 6). The size of the crystallites (R) is given in Fig. 2 and Table 1. These crystallites are described by a dielectric function given in Eq. (1) or Eq. (6) and located randomly in homogeneous environment ε_1 (air) and occupy a volume fraction f, so we can use effective medium theory and Maxwell - Garnet mixing rule, given with Eq. (2).

The far – infrared reflectivity spectrum of the glass substrate is shown in Fig. 7(e). The calculated spectrum, presented by solid line, was obtained using the dielectric function given by equation (7). As a result of the best fit we obtained three modes, whose characteristic frequency are $\omega_{TO1} = 60$ cm^{-1}, $\omega_{LO1} = 140$ cm^{-1}, $\omega_{TO2} = 441$ cm^{-1}, $\omega_{LO1} = 443$ cm^{-1} and $\omega_{TO3} = 471$ cm^{-1}, $\omega_{LO3} = 522$ cm^{-1}. Frequency values of these modes have remained the same during the fitting procedure for all CdTe thin film samples.

The parameters obtained by the best fit between the experimental results and the models for CdTe film described earlier are also given in Table 1. The far-infrared spectra of CdTe thin films, in the spectral range of 80–600 cm^{-1}, at room temperature, are presented in Fig. 7. Experimental data are presented by circles, while the solid lines are calculated spectra obtained by a fitting procedure based on the previously presented model. Experimental and theoretical spectra show an excellent match.

The thicknesses of our films obtained by Far – infrared spectroscopy are 20% greater, which is within the limits of error for both techniques. When using Far – infrared spectroscopy for calculating thickness of layered structured, we bring errors in absolute measurements, because we calculate effective thickness. The important thing is, the trend is the same, the films does not differ in the relative thickness, i.e. thickness ratios between films are the same.

We note that the thickness (d) of the film changes in the range of ~0.39–~0.7 µm. While the thickness of the film is in the 0.40 µm region, the crystallite size is about 32 nm, and for a film thickness of about 0.72 µm, we have two sizes of crystallites different for a factor of 2. In addition, from Table 1, we have for thicker films CdTe 1 and CdTe 3, that the position of the coupled plasmon-phonon mode ω_{l1} is below the values of $\omega_{LO,CdTe} = 170.5$ cm^{-1}. On the other hand, these values are above $\omega_{LO,CdTe}$ for thin films CdTe 2 and CdTe 4. In both cases plasmon damping (Γ_p) is relatively low. The obtained eigenfrequencies of the plasmon – phonon coupled modes for CdTe thin films are presented in Fig. 8. As a result of the best fit from Fig. 7, we obtained the frequencies of coupled modes (ω_{l1} and ω_{l2}) marked by open circles and transverse mode frequencies which are denoted by - x. Value of ω_P are calculated by Refs. [16–18]:

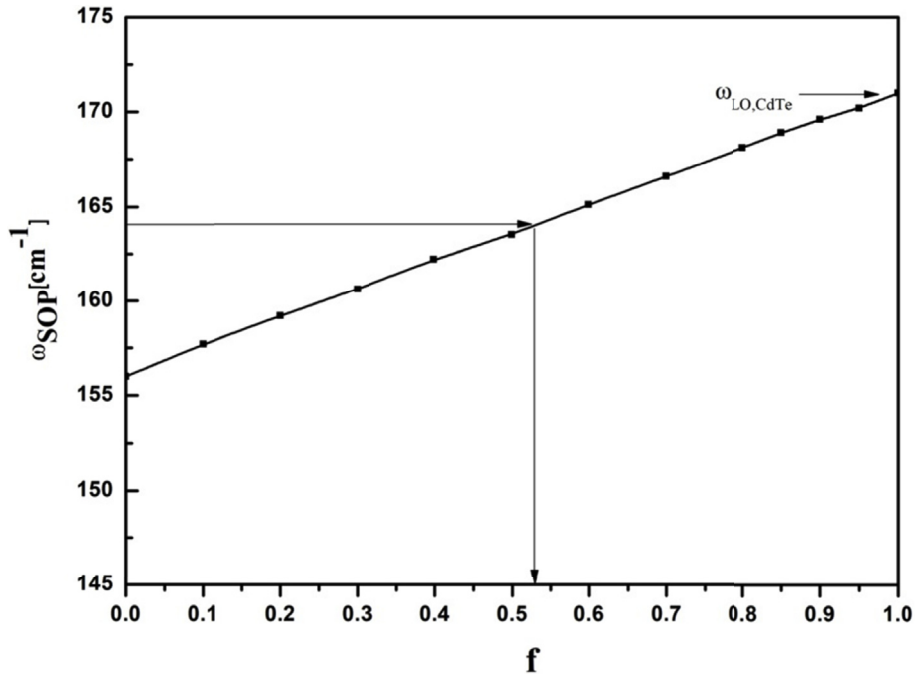$$\omega_P = \frac{\omega_{l1}\omega_{l2}}{\omega_t} \tag{8}$$

Fig. 5. Surface optical phonon (SOP) mode position vs. filing factor.
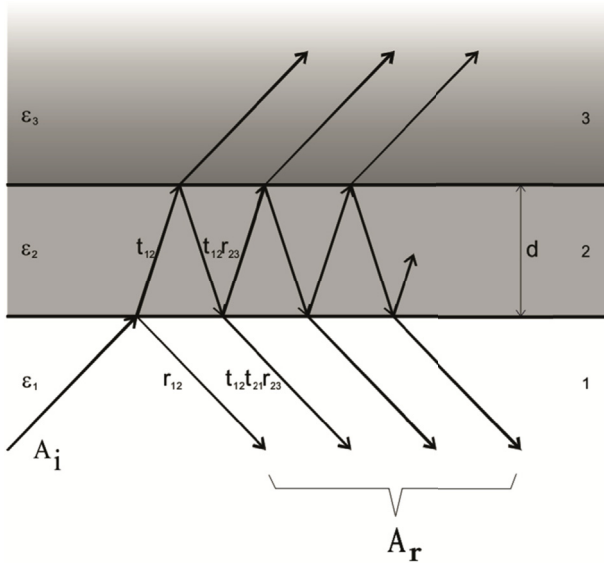

Fig. 6. Schematic presentation of a three layer structure [46].

The calculated lines at Fig. 7 are solution of a real part of uncoupled dielectric function (Eq. (1)). However, for plasma-phonon modes positions are obtained:

$$\omega_{\pm} = \frac{\omega_P^2 + \omega_{LO}^2}{2} \pm \sqrt{\frac{(\omega_P^2 + \omega_{LO}^2)^2 - \omega_P \omega_{TO}}{4}} \qquad (9)$$

The full lines in Fig. 7 were obtained for the case $\omega_{LO,\text{CdTe}} = 170.5\,\text{cm}^{-1}$. It is clear that all values of ω_{l1} and ω_{l2} are out of this theoretical model. Best fit, dashed lines in Fig. 7, was obtained for $\omega_{SOP} = 164\,\text{cm}^{-1}$ which in Eq. (9) plays a role ω_{LO}. Shift of about $7\,\text{cm}^{-1}$ is registered in relation to $\omega_{LO,\text{CdTe}}$, just like in the case of Raman spectra. As we said earlier, the LO phonon shift of CdTe crystal is attributed to the surface optical phonon (SOP) mode effect.

Based on these results, it is clear that in the case of CdTe thin films, prepared by using thermal evaporation technique, the filing factor is constant and does not depend on film thickness, crystallite size and
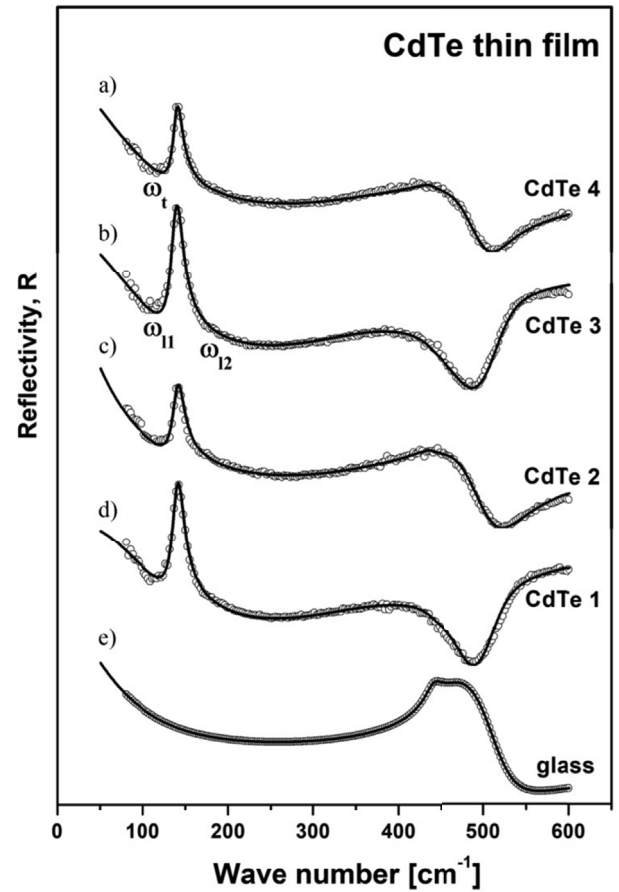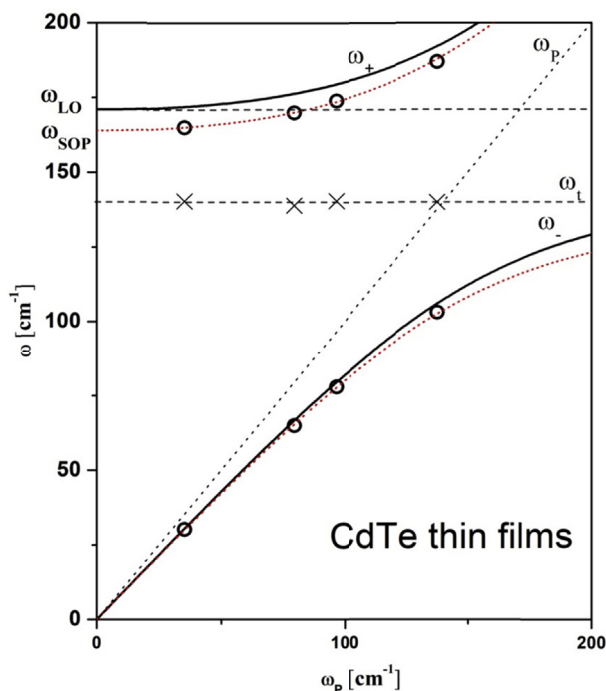

Fig. 7. Far – infrared reflection spectra of: CdTe thin films with thickness of (a) 0.39 μm, (b) 0.71 μm, (c) 0.43 μm, (d) 0.72 μm, and glass substrate (e). Experimental spectra are presented by circles while solid lines are calculated spectra obtained by a fitting procedure based on the model given by Eqs. (2) and (4)–(7).

Fig. 8. The eigenfrequencies of the plasmon–phonon modes for CdTe thin films. The lines are calculated spectra [Re{ε_2} = 0; ε_2 is given by Eq. (1)]: solid line with $\omega_{LO,CdTe} = 170.5\,\text{cm}^{-1}$; dashed line with $\omega_{SOP} = 164\,\text{cm}^{-1}$; ○ - ω_{l1}, ω_{l2}; x – ω_t.

concentration of free carriers. On the other hand, the reflection spectra depend on the thickness of the film and the concentration of free carriers in the film, which is expected. In general, thin films have a higher concentration of free carriers ($\sim \omega_p$) (see Table 1). The linear dependence of the position of the SOP mode on the filing factor causes the existence of a modified plasmon – phonon interaction, where the SOP has the role of the LO phonon.

Of course, there are many models that can describe the registered frequency shift of the LO phonon in CdTe e.g. a continuum model of the optical phonon confinement [47,48] would also give a shift of 7 cm^{-1}, but for spherical nanoparticles of about 5 nm, which is far from our case.

4. Conclusion

In this paper, we present results of investigation of CdTe thin films prepared with thermal evaporation technique, with different thicknesses. Sample's surfaces are rather flat, but still they are characterized with bright protrusions and dark holes (air) resulting in a small surface roughness of several nanometers. We showed that, when using thermal evaporation technique we get high quality thin films, especially for thicker films with greater crystallite size. We conclude that the filling factor of our thin films is constant and does not depend on film thickness, crystallite size or concentration of free carriers, but yet has linear dependence on SOP position. This kind of morphology, with filling factor of ~50% causes existence of surface optical phonon and its interaction with plasmon, because of the free surface around nanoparticles. A numerical model for calculating the reflectivity coefficient for complex system, which includes films and substrate, has been applied, and CdTe thin film were treated as a mixture of homogenous spherical inclusion in air modeled by Maxwell – Garnet formula.

Acknowledgements

References

[1] S. Chandra Ray, K. Mallick, Int. J. Chem. Eng. Appl. 4 (2013) 183–186.
[2] C.S. Ferekides, U. Balasubramanian, R. Mamazza, V. Viswanathan, H. Zhao, D.L. Morel, Sol. Energy 77 (2004) 823–830.
[3] R. Kulkarni, et al., Energy Procedia 110 (2017) 188–195.
[4] A. Arnoult, J. Cibert, Appl. Phys. Lett. 66 (1995) 2397–2399.
[5] P. Bhattacharya, D.N. Bose, Semicond. Sci. Technol. 6 (1991) 384–387.
[6] A.U. Ubale, D.K. Kulkarni, Indian J. Pure Appl. Phys. 44 (2006) 254–259.
[7] T.L. Chu, S.S. Chu, C. Ferekides, J. Britt, C.Q. Wu, J. Appl. Phys. 71 (1992) 3870.
[8] A. Nakano, et al., Sol. Cell. 17 (1986) 233.
[9] K.S. Rahman, F. Haque, 3rd International Conference on the Developments in Renewable Energy Technology (ICDRET), 2014, pp. 29–31.
[10] S. Lalitha, S. Zh Karazhanov, P. Ravindran, S. Senthilarasu, R. Sathyamoorthy, J. Janabergenov, Physica B 387 (2007) 227–238.
[11] S. Singh, et al., Thin Solid Films 519 (2010) 1078–1081.
[12] D.S. Chuu, C.M. Dai, W.F. Hsieh, C.T. Tsai, J. Appl. Phys. 69 (1991) 12.
[13] A. Singha, B. Satpati, P.V. Satyam, A. Roy, J. Phys. Condens. Mater. 17 (2005) 5708–5967.
[14] M. Gilić, J. Trajić, N. Romčević, M. Romčević, D.V. Timotijević, G. Stanišić, I.S. Yahia, Opt. Mater. 35 (2013) 1112–1117.
[15] M. Cardona (Ed.), Top. Appl. Phys, vol. 8, Springer, Berlin, 1975.
[16] N. Romčević, M. Romčević, A. Golubović, Le Van Khoi, A. Mycielski, Đ. Jovanović, D. Stojanović, S. Nikolić, S. Đurić, J. Alloy. Compd. 397 (2005) 52–57.
[17] M. Romčević, N. Romčević, V.N. Nikiforov, Infrared Phys. Technol. 42 (2001) 541–545.
[18] N. Romčević, M. Romčević, A. Milutinović, S. Kostić, J. Alloy. Compd. 478 (2009) 41–44.
[19] J. Trajić, M. Romčević, N. Romčević, B. Babić, B. Matović, P. Balaž, Opt. Mater. 57 (2016) 225–230.
[20] N. Romčević, M. Romčević, W.D. Dobrowolski, L. Kilanski, M. Petrović, J. Trajić, B. Hadžić, Z. Lazarević, M. Gilić, J.L. Ristic-Djurović, N. Paunović, A. Reszka, B.J. Kowalski, I.V. Fedorchenko, S.F. Marenkin, J. Alloy. Compd. 649 (2015) 375–379.
[21] J. Trajić, N. Romčević, M. Romčević, V.N. Nikiforov, Mater. Res. Bull. 42 (2007) 2192–2201.
[22] M. Romčević, N. Romčević, W. Dobrowolski, L. Kalinski, J. Trajić, D.V. Timotijević, E. Dynowska, I.V. Fedorchenko, S.F. Marenkin, J. Alloy. Compd. 548 (2013) 33–37.
[23] N. Romčević, J. Trajić, T.A. Kuznetsova, M. Romčević, B. Hadžić, D.R. Khokhlov, J. Alloy. Compd. 442 (2007) 324–327.
[24] J. Trajić, N. Romčević, M. Romčević, D. Stojanović, R. Rudolf, T.A. Kuznetsova, D.R. Khokhlov, J. Alloy. Compd. 493 (2010) 41–46.
[25] J. Trajić, N. Romčević, M. Romčević, D. Stojanović, L.I. Ryabova, D.R. Khokhlov, J. Alloy. Compd. 602 (2014) 300–305.
[26] R.W. Cheary, A. Coelho, J. Appl. Crystallogr. 25 (1992) 109–121.
[27] R. Triboulet & P. Siffert, first ed., Elsevier, 2010.
[28] H. Zeng, W. Cai, B. Cao, J. Hu, Y. Li, P.S. Liu, Appl. Phys. Lett. 88 (2006) 181905.
[29] A. Ghosh, R.N.P. Chodhary, J. Phys. D Appl. Phys. 42 (2009) 075416.
[30] F. Friedrich, N.H. Nickel, Appl. Phys. Lett. 91 (2007) 111903.
[31] J. Xu, W. Ji, X.B. Wang, H. Shu, Z.X. Shen, S.H. Tang, J. Raman Spectrosc. 29 (1998) 613.
[32] V.C. Stergiou, Y.S. Raptis, E. Anastassakis, N. Pelekaneos, A. Nahmani, J. Cibert, Phys. Status Solidi 223 (2001) 237.
[33] J.F. Scott, T.C. Damem, Optic Commun. 5 (1972) 410.
[34] R. Rossetti, S. Nakahara, L.E. Bru, J. Chem. Phys. 79 (1983) 1086.
[35] B.F. Variano, N.E. Schlotter, D.M. Hwangand, C.J. Sandroff, J. Chem. Phys. 88 (1988) 2848.
[36] A.V. Baranov, Y.S. Bobovich, N.I. Grebenshchikova, V.I. Petrov, M.Y. Tsenter, Optic Spectrosc. 60 (1986) 685.
[37] H. Jerominek, M. Pigeon, S. Patela, Z. Jakubczk, C. Delisle, R.J. Tremblay, Appl. Phys. 63 (1986) 957.
[38] E.F. Hilinski, P.A. Lucas, J. Chem. Phys. 89 (1988) 3435.
[39] J. Trajić, M. Gilić, N. Romčević, M. Romčević, G. Stanišić, B. Hadžić, M. Petrović, Y.S. Yahia, Sci. Sinter. 47 (2015) 145–152.
[40] G. Irmer, J. Raman Spectrosc. 38 (2007) 634.
[41] K. Karkkainen, A. Saviola, K. Nikoskinen, IEEE Trans. Geosci. Rem. Sens. 39 (5) (2001) 1013.
[42] J.C.M. Garnett, Trans. Roy. Soc. Can. CIII (1904) 385420.
[43] A. Saviola, I. Lindell, A. Priou (Ed.), Dielectric Properties of Heterogeneous Materials PIER 6 Progres in Electromagnetic Research, Elsevier, Amsterdam, 1992, pp. 101–115 1.
[44] B. Hadžić, N. Romcević, M. Romcević, I. Kuryliszyn-Kudelska, W. Dobrowolski, J. Trajić, D.V. Timotijević, U. Narkiewicz, D. Sibera, J. Alloy. Compd. 540 (2012) 49–56.
[45] M. Gilić, et al., Infrared Phys. Technol. 76 (2016) 276–284.
[46] J. Trajić, M. Gilić, N. Romčević, M. Romčević, G. Stanišić, Z. Lazarević, D. Joksimović, I.S. Yahia, Phys. Scr., T 162 (2014) 014031.
[47] R. Roca, C. Trallero-Giner, M. Cardona, Phys. Rev. B 49 (1994) 13704.
[48] M.P. Chamberlain, C. Trallero-Giner, M. Cardona, Phys. Rev. B 51 (1995) 1680.

Regular article

Far-infrared study of the mechanochemically synthesized Cu_2FeSnS_4 (stannite) nanocrystals

J. Trajic [a,*], M. Romcevic [a], N. Paunovic [a], M. Curcic [a], P. Balaz [b], N. Romcevic [a]

[a] Institute of Physics, University of Belgrade, 11080 Belgrade, Serbia
[b] Institute of Geotechnics, Slovak Academy of Sciences, 043 53 Kosice, Slovakia

HIGHLIGHTS

- Stannite Cu_2FeSnS_4 nanocrystals were synthesized mechanochemically.
- Optical properties and compositional purity of Cu_2FeSnS_4 nanocrystals were characterized.
- Optical properties were investigated by Far-infrared spectroscopy.
- The influence of the milling time on synthesis of the stannite Cu_2FeSnS_4 was observed.

GRAPHICAL ABSTRACT
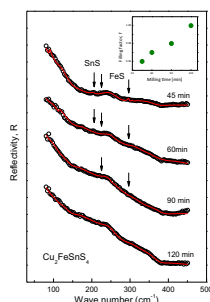
ABSTRACT

The analysis of the optical properties of mechanochemically synthesized stannite Cu_2FeSnS_4 nanocrystals has been performed using far-infrared spectroscopy. The Cu_2FeSnS_4 stannite nanocrystals were synthesized mechanochemically from elemental precursors Cu, Fe, Sn, and S. Milling time was 45, 60, 90 and 120 min. Reflectivity spectra were analyzed using the classical form of the dielectric function, which includes the phonon and the free carrier contribution. The influence of milling time on synthesis of stannite Cu_2FeSnS_4 is observed. Among the modes that are characteristic for the stannite Cu_2FeSnS_4, we registered the modes of binary phases of FeS and SnS. The total disappearance of the binary phases of FeS and SnS and forming pure Cu_2FeSnS_4 is observed when the milling time is 120 min. Effective permittivity of Cu_2FeSnS_4 and binary phases of FeS and SnS were modeled by Maxwell – Garnet approximation.

© 2018 Elsevier B.V. All rights reserved.

1. Introduction

Stannite (Cu_2FeSnS_4) is one of the best-known sulphide minerals, not only because of its economic importance as a tin ore, but also because of its structural and physical characteristics [1] such as adequate direct band gap (1.0–1.5 eV), low toxicity and a relatively high abundance of the elements in the Earth's crust [2]. Its constituents are abundantly available [3].

To deal with the increasingly severe energy crisis, research on high-efficient and low-cost solar cells is of pressing need and of great significance. Various types of semiconductors such as CdTe, $Cu(In,Ga)Se_2$ and TiO_2, have been extensively studied for thin film solar cells. Nevertheless, due to the toxicity of Cd and the limited availability of In and Ga, naturally abundant and non-toxic photo-voltaic materials are of considerable interest [4]. Quaternary semiconductor Cu_2FeSnS_4 is one of promising photovoltaic materials as an alternative absorber layer for the development of low-cost and environment-friendly thin film solar cells due to its analogous crystal structures to $Cu(In,Ga)Se_2$, suitable band gap and high absorption coefficient [5].

Several low-cost, highly efficient, environmental friendly and easy-to operate methods have been developed for preparation of Cu_2FeSnS_4, such as pulse laser and electro deposition [6], hot

---

injection [7], electrospinning [8], dip coating [9], microwave assisted approach [4,10,11] and oxide-nanoparticles-based process [12]. However, these techniques are complex as well as time-consuming, and require high temperature, while in some cases it is necessary to use the toxic organic solvents. Mechanochemical treatment is a powerful technique for synthesis of a wide range of materials where the high energy milling is being applied to induce and speed up chemical reactions [13,14]. This approach is simple, solvent-free, and reproducible, and also the synthesis might be easily scaled up. However, the control of stoichiometry and crystal structure during synthesis of the quaternary nanocrystals remains a challenge.

In this paper, the optical and structural properties of Cu_2FeSnS_4 nanoparticles which are mechanochemically synthesized have been investigated using far-infrared spectroscopy. The reflectivity spectra of the tetragonal Cu_2FeSnS_4 obtained after different milling time have been analyzed using the Maxwell–Garnett approximation. We have determined the influence of the milling time on the purity of the Cu_2FeSnS_4 nanocrystals.

2. Samples preparation and characterisation

The elemental precursors (Cu, Fe, Sn and S) were used to obtain stannite (CFTS) by a solid state one-pot mechanochemical synthesis. The starting materials were elemental Cu (99%), Fe (99%), Sn (99.9%), and S (99%). These materials were weighed and mixed in atomic ratios of 2:1:1:4, according to the stoichiometry Cu_2FeSnS_4. The particularities of synthesis and initial characterization of Cu_2FeSnS_4 nanoparticles were presented previously in Refs. [15,16], and will be briefly discussed here.

The mechanochemical synthesis of Cu_2FeSnS_4 nanoparticles was performed in a Pulverisette 6 planetary mill (Fritsch, Germany). The milling conditions were as follows: milling pot volume-250 ml, material of milling pot – tungsten carbide (WC) with 50 WC balls of 10 mm diameter in it, total weight of reactants – 5 g, ball-to-powder mass ratio – 70, milling speed – 500 min^{-1}. Milling time was 45, 60, 90 and 120 min using an argon protective atmosphere in the mill. Using the described synthesis process, the unique nanostructures and properties are developed. Cu_2FeSnS_4 polymorphs with tetragonally body-centred structure with crystallite sizes of 18–19 nm were obtained.

X-ray diffraction (XRD) is the most commonly used technique to characterize the crystal structure and compositional purity of stannite Cu_2FeSnS_4 nanoparticles. All samples were examined under the same conditions, using a D8 Advance Bruker X-ray diffractometer in the Bragg-Brentano geometry, using the Cu Kα radiation of 0.15418 nm and a scintillation detector at room temperature. The commercial Bruker tools have been used for data processing.

The XRD patterns of the elemental mixture (Cu, Fe, Sn and S powders) obtained after various milling times are shown in the Fig. 1. Diffraction patterns show the reflection of the tetragonal body-centred stannite Cu_2FeSnS_4 according to card JCPDS 44-1476 in the tetragonal space group I-42m. The XRD spectra shows three most intensive peaks at 2θ = 28.5°, 47.5° and 56.0° that can be assigned to the (1 1 2), (2 0 4), and (3 1 2) planes of the tetragonal crystals. Besides mentioned peaks, the peak of the Fe is observed at the Cu_2FeSnS_4 nanocrystal samples obtained after 45 and 60 min milling time. This peak disappears with increasing milling time.

In the attempt to characterize compositional purity of stannite, and observe the influence of the milling time on the mechanochemical synthesis of Cu_2FeSnS_4 nanocrystals we used far-infrared (FIR) spectroscopy. The infrared reflectivity measurements were carried out at room temperature with a BOMEM DA-
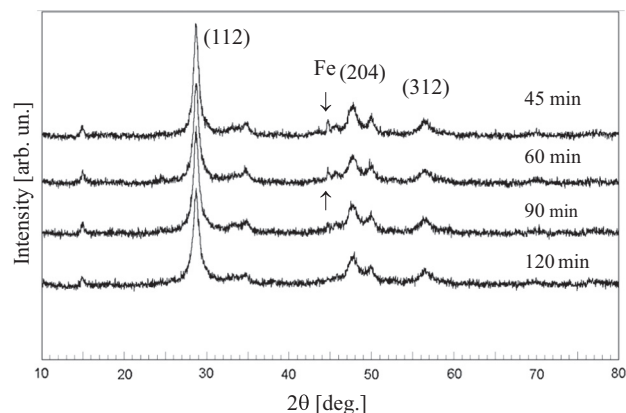

Fig. 1. XRD spectra of Cu_2FeSnS_4 nanocrystals obtained after various milling times.

8 Fourier-transform IR spectrometer. A deuterated triglycine sulfate (DTGS) pyroelectric detector was used to cover the wave number region from 80 to 450 cm^{-1}.

3. Results and discussion

The Cu_2FeSnS_4 is a tetrahedrally coordinated semiconductor in which each sulphur anion is bonded to four cations and each cation is bonded to four sulphur anions [17]. The factor group analysis of the allowed zone-centre vibrations for the I-42m tetragonal crystallographic structures of Cu_2FeSnS_4, indicates that ten infrared (IR) and fourteen Raman active phonon modes of irreducible representations are expected for this compound [18]:

$$\Gamma = 2A_1 + A_2 + 2B_1 + 4B_2 + 6E \tag{1}$$

The B_2 and E modes are IR active and they represent LO-TO splitting due to their polar character. The modes A_1, B_1, B_2 and E are Raman active.

Reflectivity spectra were analyzed using the classical form of the dielectric function, which includes several oscillators and the free carrier contribution to the dielectric function [19]. Whereas the analysis of the far IR reflectivity spectrum of Cu_2FeSnS_4 nanopowders revealed a presence of a plasmon mode, it was necessary to include both contributions of the phonon and the plasmon (free carrier contribution) to the dielectric function:

$$\varepsilon_s(\omega) = \varepsilon_\infty \left(\sum_{j=1}^{l} \frac{\omega_{LOk}^2 - \omega^2 + i\gamma_{LOk}\omega}{\omega_{TOk}^2 - \omega^2 + i\gamma_{TOk}\omega} - \frac{\omega_{P2}}{\omega(\omega + i\Gamma_P)} \right) \tag{2}$$

where ε_∞ is the high-frequency dielectric constant, ω_{LOk}, and ω_{TOk} are longitudinal and transverse frequencies of the k-th oscillator, γ_{LOk} and γ_{TOk} are their corresponding dampings, ω_p and Γ_p are the plasma frequency and damping. The first term in Eq. (2) is the lattice contribution whereas the second term is the Drude expression for the free carrier contribution to the dielectric constant. The far-infrared reflection spectrum of Cu_2FeSnS_4 nanocrystal obtained after 45 min milling time is presented in Fig. 2. The experimental data are presented by circles, while the solid line represents the calculated reflectivity spectra obtained by the fitting procedure based on Eq. (2). In the fitting procedure we included modes at about 93, 120, 144, 250, 315 and 350 cm^{-1} that are in accordance with the reported values for tetragonal Cu_2FeSnS_4 [18,20] as well as, plasma term. We did not succeed to determinate the set of parameters that provide good spectrum overlapping in the whole range of frequencies. Discrepancy between experimental and calculated reflectivity spectra in some regions is obvious,
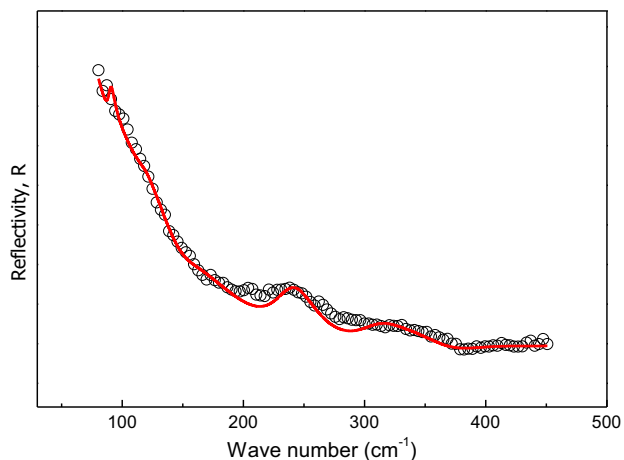
Fig. 2. Far-infrared reflection spectra of stannite Cu$_2$FeSnS$_4$ obtained after 45 min milling time. Experimental spectra are presented by circles. The solid lines are calculated spectra obtained by a fitting procedure based on the model given by Eq. (2).
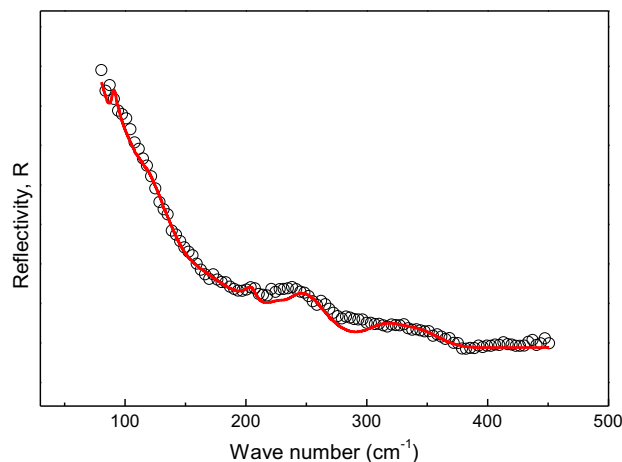
Fig. 3. Far-infrared reflection spectra of stannite Cu$_2$FeSnS$_4$ obtained after 45 min milling time. Experimental spectra are presented by circles. The solid lines are calculated spectra obtained by a fitting procedure based on the model given by Eq. (3).

which indicates that in this system among the nanocrystals of Cu$_2$FeSnS$_4$ exists another mixtures of starting elements and their phases.

Because our sample consists of Cu$_2$FeSnS$_4$ nanoparticles and binary and/or ternary phases of starting elements we have applied the effective medium approximation method to calculate infrared reflectivity spectra. The widely used effective medium theory is the Maxwell–Garnett approximation which treats the effective medium as consisting of a matrix in which are embedded inclusions and where the fraction of the inclusions is very small, so that the inclusions are spatially separated and can be treated as a perturbation [21,22]. For the spherical inclusions case, the prediction of the effective permittivity of mixture ε_{eff} according to the Maxwell-Garnet mixing rule reads [23,24]:

$$\varepsilon_{ff} = \varepsilon_1 + 3f\varepsilon_1 \frac{\varepsilon_2 - \varepsilon_1}{\varepsilon_2 + 2\varepsilon_1 - f(\varepsilon_1 - \varepsilon_2)} \qquad (3)$$

Here, spheres of permittivity ε_2 are located randomly in homogeneous environment ε_1 and occupy a volume fraction f. In the case of mechanochemicaly sintesized Cu$_2$FeSnS$_4$, multicomponent phases of starting elements with dielectrical function ε_2 are randomly located in pure Cu$_2$FeSnS$_4$ with dielectrical function ε_1, where ε_1 and ε_2 are defined by Eq. (2).

In Fig. 3 is presented the far-infrared reflection spectrum of Cu$_2$FeSnS$_4$ nanocrystal obtained after 45 min milling time where the solid line is obtained by applying Maxwell–Garnett approximation. In the fitting procedure, besides modes which originated from tetragonal Cu$_2$FeSnS$_4$ we included mode at about 215 cm^{-1} which is corresponding to infrared frequency of SnS binary component [25]. Occurrence of SnS binary phase is in accordance with the observation of Bernardini et al, where, by thermal synthesis, also, the minor traces of herzenbergite SnS have been detected, besides stannite [1,26].

Taking into account this mode, corresponding to infrared frequency of SnS binary component, we obtained better overlapping, but it is obvious that besides binary phase of SnS the other multicomponent phases are formed. Satisfactory overlapping of experimental and theoretical spectra is achieved when in the fitting procedure the modes at about 225 and 297 cm^{-1} (Fig. 4a) are added. These two modes are originated from impurity FeS binary phases [17,27]. Slight difference in frequencies between available literature data as well as data we gathered probably arises from the differences in the cation-anion bond distances. Also, disordered
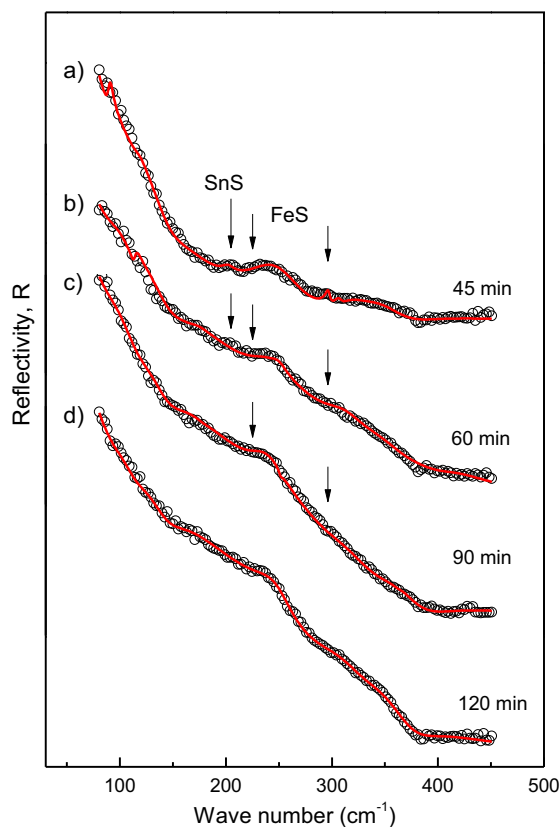
Fig. 4. Far-infrared reflection spectra of stannite Cu$_2$FeSnS$_4$ obtained after different milling times. Experimental spectra are presented by circles. The solid lines are calculated spectra obtained by a fitting procedure based on the model given by Eq. (3).

distribution of Cu and Fe atoms leads to the presence of a high content of Cu$_{Fe}$ and Fe$_{Cu}$ anti-site defects that would degrade the crystalline quality of these regions. The existence of a highly disordered distribution of cations in these domains would lead to a shift of the peak towards lower frequencies [28].

The far-infrared reflection spectra of Cu$_2$FeSnS$_4$ nanocrystals obtained after various milling times, in the spectral range from 80 to 450 cm^{-1}, are presented in Fig. 4. The experimental data

Table 1
Volume fraction of tetragonal Cu_2FeSnS_4 as a function of milling time.

Milling time [min]	Filling factor, f
45	0.96
60	0.97
90	0.98
120	1

are presented by circles, while the solid line represent the calculated reflectivity spectra obtained by the fitting procedure based on Eq. (3).

The spectrum of Cu_2FeSnS_4 nanocrystals obtained after 60 min milling time is presented in Fig. 4b. In the case of this nanocrystal the same modes are registered as in the sample obtained after 45 min milling time. Namely, modes originated from tetragonal Cu_2FeSnS_4, together with modes originated from binary phases FeS and SnS are registered at infrared spectra samples obtained after 45 and 60 min milling time. In infrared spectrum of sample obtained after 90 min milling time (Fig. 4c), the mode that corresponds to SnS was not observed, whereas in the case of the nanocrystal obtained after 120 min milling time (Fig. 4d), only the modes originated from pure tetragonal Cu_2FeSnS_4 are registered. This spectrum, obtained after 120 milling time, is calculated with the set of parameters corresponding to the pure Cu_2FeSnS_4 sample.

The total disappearance of the mode originated from SnS binary phase is observed after 60 min milling time, and FeS modes disappear when the milling time is 120 min (longer than 90 min). Absence of those modes excluded the presence of FeS and SnS binary phases, which indicates that after 90 min milling time pure stannite Cu_2FeSnS_4 is synthesized.

Volume fraction of tetragonal Cu_2FeSnS_4 obtained as estimation of the best fit parameter are presented in Table 1. As milling time increases, the filling factor increase also, which indicates that during miling the contribution of impurity binary phases FeS and SnS decrease, while contribution of pure, tetragonal Cu_2FeSnS_4 increases. Namely, Cu_2FeSnS_4 is synthesized from elemental precursors Cu, Fe, Sn and S by applying the high-energy milling. During synthesis besides tetragonal Cu_2FeSnS_4 nanocrystal the binary phases of starting elements FeS and SnS occur. In our case where the multicomponent phases of starting elements are randomly located in Cu_2FeSnS_4, the filling factor f gives us information about the contribution (volume fraction) of pure Cu_2FeSnS_4.

4. Conclusion

We have measured the far-infrared reflectivity spectra of the mechanochemically synthesized Cu_2FeSnS_4 nanocrystals obtained after different milling time. Reflectivity spectra were analyzed using the classical form of the dielectric function, which includes the phonon and plasmon contribution to the dielectric function. The best fit spectra are obtained using the Maxwell–Garnett approximation. Besides modes which are characteristic for tetragonal Cu_2FeSnS_4 nanocrystals we registered the existence of modes that originates from binary phases of FeS and SnS. The total disappearance of the mode originated from SnS binary phase is observed after 60 min milling time, and FeS modes disappear when the milling time is longer than 90 min. Absence of those modes excluded the presence of FeS and SnS binary phases, which indi-

cates that after 90 min milling time pure stannite Cu_2FeSnS_4 is synthesized. As a best fit parameter we determined volume fraction of tetragonal Cu_2FeSnS_4 as a function of milling time. Analyzing the reflectivity spectra we determine not only which impurity components occur during the synthesis of Cu_2FeSnS_4, and we find out the change in contribution of these impurity components as the miling time is varied.

Conflict of interest

None.

## References:

[1] G.P. Bernardini, D. Borrini, A. Caneschi, F. Di Benedetto, D. Gatteschi, S. Ristori, M. Romanelli, Phys. Chem. Miner. 27 (2000) 453–461.
[2] B. Zhou, X. Yan, P. Li, L. Yang, D. Yu, Eur. J. Inorgan. Chem. 1 (2015) 2690–2694.
[3] H. Guan, H. Shen, B. Jiao, Xu Wang, Mater. Sci. Semicond. Process. 25 (2014) 159–162.
[4] X. Meng, H. Deng, J. He, L. Sun, P. Yang, J. Mater. Lett. 151 (2015) 61–63.
[5] X. Zhang, N. Bao, K. Ramasamy, Y.A. Wang, Y. Wang, B. Lin, A. Gupta, Chem. Commun. 48 (2012) 4956–4958.
[6] Y. Li, T.F. Yuan, L.X. Jiang, Z.H. Su, F.Y. Liu, J. Alloys Comp. 610 (2014) 331–336.
[7] L. Li, B.L. Zhang, M. Cao, Y. Sun, J.C. Jiang, P.F. Hu, Y. Shen, J. Alloys Comp. 551 (2013) 24–29.
[8] F. Ozel, M. Kus, A. Yar, E. Arkan, M. Can, A. Aljabour, N.M. Varal, M. Ersoz, J. Mater. Sci. 50 (2015) 777–783.
[9] G. Rajesh, N. Muthukumarasamy, E.P. Subramaniam, S. Agilan, D. Velauthapillai, J. Sol-Gel Sci. Technol. 66 (2013) 288–292.
[10] M. Sabet, M.S. Niasari, D. Ghanbari, O. Amiri, M. Yousefi, Mater. Sci. Semicond. Process. 16 (2013) 696–704.
[11] S.M.H. Mashkani, F. Mohandes, M.S. Niasari, K.V. Rao, Mater. Res. Bull. 47 (2012) 3148–3159.
[12] G. Chen, J. Li, S. Chen, Z. Huang, M. Wu, Mater. Chem. Phys. 188 (2017) 95–99.
[13] P. Baláž, Mechanochemistry in Nanoscience and Minerals Engineering, Springer, Berlin Heidelberg, 2008, p. 413.
[14] P. Baláž, M. Achimovičová, M. Baláž, P. Billik, Z. Cherkezova-Zheleva, J.M. Criado, F. Delogu, E. Dutková, E. Gaffet, F.J. Gotor, R. Kumar, I. Mitov, T. Rojac, M. Senna, A. Streletskii, K. Wieczorek-Ciurowa, Chem. Soc. Rev. 42 (2013) 7571–7637.
[15] P. Baláž, M. Baláž, M.J. Sayagués, I. Škorvánek, A. Zorkovská, E. Dutková, J. Briančin, J. Kováč, J. Kováč Jr, Y. Shpotyuk, Nanoscale Res. Lett. 12 (2017) 256–266.
[16] P. Baláž, M. Baláž, A. Zorkovská, I. Škorvánek, Z. Bujnáková, J. Trajić, Acta Phys. Polon. 131 (4) (2017) 1153–1155.
[17] C. Yan, C. Huang, J. Yang, F. Liu, J. Liu, Y. Lai, J. Li, Y. Liu, Chem. Commun. 48 (2012) 2603–2605.
[18] T. Gürel, C. Sevik, T. Cagin, Phys. Rev. B 84 (2011) 205201.
[19] R.J. Gonzalez, R. Zallen, H. Berger, Phys. Rev. B 55 (11) (1997) 7014–7017.
[20] M. Himmrich, H. Haeuseler, Spectrochim. Acta 47A (7) (1991) 933–942.
[21] J.E. Spanier, I.P. Herman, Phys. Rev. B 61 (15) (2000) 10437.
[22] J.J. Saarinen, E.M. Vartiainen, K.E. Peiponen, Opt. Rev. 10 (2) (2003) 111.
[23] J.C.M. Garnett, Transaction of the Royal Society CCIII 385420, 1904.
[24] A. Saviola, I. Lindell, Dielectric Properties of Heterogeneous Materials PIER 6 Progres in Electromagnetic Research ed. A. Priou, Amsterdam, Elsevier, 1992, pp. 101–151.
[25] J.M. Chamberlain, P.M. Nikolic, M. Merda, P. Mihailovic, J. Phys. C: Solid State Phys. 9 (1976) L637–L642.
[26] G.P. Bernardini, P. Bonazzi, M. Corazza, F. Corsini, G. Mazzetti, L. Poggi, G. Tanelli, Eur. J. Mineral. 2 (1990) 219–225.
[27] Y. El Mendili, B. Minisini, A. Abdelouas, J.-F. Bardeau, RSC Adv. 4 (2014) 25827–25834.
[28] X. Fontané, V. Izquierdo-Roca, E. Saucedo, S. Schorr, V.O. Yukhymchuk, M.Ya. Valakh, A. Pérez-Rodríguez, J.R. Morante, J. Alloys Comp. 539 (2012) 190–194.
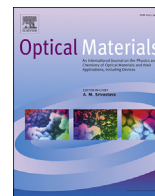
Structural properties of Eu^{3+} doped Gd$_2$Zr$_2$O$_7$ nanopowders: Far-infrared spectroscopy

J. Mitrić [a], [*], J. Križan [b], J. Trajić [c], G. Križan [b], M. Romčević [c], N. Paunović [c], B. Vasić [c], N. Romčević [c]

[a] *School of Computing, University Union, Knez Mihailova 6, Belgrade 11 000, Serbia*
[b] *AMI, d. o. o., Ptuj, Slovenia*
[c] *Institute of Physics, University of Belgrade, Pregrevica 118, 11080 Belgrade, Serbia*

A R T I C L E   I N F O

A B S T R A C T

The Solution Combustion Synthesis (SCS) method was used to prepare nanopowders of europium doped cubic Gd$_2$Zr$_2$O$_7$ nanopowders. The surface of the samples have been investigated using atomic force spectroscopy (AFM) and far-infrared spectroscopy (FIR). Far-infrared reflectivity spectra of Eu^{3+} doped Gd$_2$Zr$_2$O$_7$ nanopowders were measured at room temperature in spectral region between 80 and 650 cm^{-1}. The Maxwell–Garnet formula was used to model dielectric function of Eu^{3+} doped Gd$_2$Zr$_2$O$_7$ nanopowders as mixtures of homogenous spherical inclusions in air.

1. Introduction

A$_2$B$_2$O$_7$ type of pyrochlores are important class of materials because of their diverse scientific and technological applications like in nuclear waste storage [1], electro/photo catalysis [2,3], luminescence [3], CO$_2$ hemisorption [4], photoluminescence hosts [5], topological Mott insulator [6] etc.

Pyrochlore oxides which occur in various crystalline phases, manifest numerous interesting and important physicochemical properties which make them eligible for potential hosts for the chemical substitution [7].

Rare earth based zirconates (Re$_2$Zr$_2$O$_7$) pyrochlores have wide scientific and technological applications as: potential thermal barrier coatings (TBC), high temperature heating devices or luminescence hosts [8].

Among all rare earth based pyrochlores, Gd$_2$Zr$_2$O$_7$ stands out as a material with a distinctively low thermal conductivity and high phase stability [9]. Besides that, Gd$_2$Zr$_2$O$_7$ could be an excellent candidate for potential photoactive materials [10].

As shown through our previous work [4,11], there are two different crystal structures for Gd$_2$Zr$_2$O$_7$, pyrochlore and the fluorite type.

Rare earth ions are widely used as activators for various phosphors and other organic and inorganic luminescent materials, because they offer high color purity, high luminescence lifetime and also a narrow emission profile, thanks to its optically active 4f electrons which are strongly shielded from the rest of ions by the other 5s and 5p shells [12].

Among all lanthanides, Eu^{3+} ion is in advantage as a dopant ion for structural probing, as well as for synthesis of red light emitting phosphor [8]. The reason this ion is a useful spectroscopic probe is because of its main source of luminescence - single level, ^{5}D$_0$ state, which prevents the convolution of overlapping emission peaks from different levels [13]. Also, doping any aliovalent ion in these oxides is not only used for structural probing, but it could also generate significant changes in photophysical behavior of those materials in such way that doping creates various kinds of defects like ion/oxygen vacancies, which can alter the band gap of materials, i.e. photophysical characteristics of one material. Particularly for Gd$_2$Zr$_2$O$_7$, it is proven that efficient doping results in tuning of thermal [14], electrical [15], optical [4] and other properties.

In this paper, we present the results obtained by using far — infrared spectroscopy (FIR) to study optical properties of the Eu^{3+} doped Gd$_2$Zr$_2$O$_7$ nanopowders which were prepared by the Solution Combustion Synthesis (SCS) method. The dielectric function of Eu^{3+} doped Gd$_2$Zr$_2$O$_7$ nanopowder is modeled as a mixture of

* Corresponding author.
  E-mail address: jmitric@ipb.ac.rs (J. Mitrić).

homogenous spherical inclusions in air, by the Maxwell-Garnet formula.

2. Sample and characterization

Europium doped cubic $Gd_2Zr_2O_7$ nanopowders were prepared by Solution Combustion Synthesis (SCS) method. Starting chemicals $Gd(NO_3) \cdot 6H_2O$, $Zr(NO_3)_2 \cdot H_2O$, $Eu(NO_3) \cdot 6H_2O$ with the purity of 99,99% were purchased from ABCR, Gd_2O_2 (99,9%) from the NOAH Technologies and urea $(NH_2)_2CO$ from Sigma-Aldrich.

Due to its simplicity and low cost of the synthesis procedures and possibility of tailoring the size and morphology of particles, the flame combustion process is the most frequently used. After the synthesis, the nanopowder was annealed, in order to achieve the full crystallinity, in air atmosphere at 1200 °C for 2 h. The Eu^{3+} concentration in $Gd_2Zr_2O_7$ was 2 mol%. The morphology analysis of the synthesized materials indicates the irregular crystallite size distribution and existence of agglomerated grains which are in the submicron size.

In our previous work [4,11] we performed X — ray powder diffraction (XRD) and photoluminescence measurements of the same material. XRD analysis confirmed that sample was crystallized in fluorite (F) type structure (space group Fm3m). The photoluminescence spectra showed a number of electronic transitions, among them were those at 705 nm and 713 nm ($^5D_0 - {}^7F_4$), 654 nm ($^5D_0 - {}^7F_3$), 630 and 611 nm ($^5D_0 - {}^7F_2$), 593 nm ($^5D_0 - {}^7F_1$), 584 nm ($^5D_0/^5D_1 - {}^7F_1$) and 578 nm ($^5D_0/^5D_1 - {}^7F_0$).

The Raman spectra of Eu^{3+} doped $Gd_2Zr_2O_7$ nanopowders were measured. We registered three phonons at 177 cm^{-1}, 268 cm^{-1} and 592 cm^{-1}, as well as their overtones at 354 cm^{-1}, 445 cm^{-1}, 708 cm^{-1}, 1062 cm^{-1}, 1184 cm^{-1}, ~1530 cm^{-1} and ~1720 cm^{-1}. The phonon at 592 cm^{-1} was already known to be characteristic for $Gd_2Zr_2O_7$ fluorite — type structure, and we found that other two phonon positions to be characteristic with the observed electron — phonon observed interaction and that the registered multiphonon processes were a consequence of miniaturization that further induces changes in electronic structure of Eu^{3+} doped $Gd_2Zr_2O_7$ nanopowders. All the above mentioned results will be useful in the far — infrared spectroscopy analysis of Eu^{3+} doped $Gd_2Zr_2O_7$ nanopowders.

3. Results and analysis

3.1. AFM

Atomic force microscopy (AFM) measurements were done using NTEGRA Prima system from NT-MDT at room temperature and ambient conditions. Imaging was done in tapping mode using NSG01 probes. Phase lag of AFM cantilever was recorded simultaneously during tapping mode imaging.

Two dimensional and three dimensional topography of the sample surface are shown in Fig. 1(a) and (b), respectively (scan size is $5 \times 5 \ \mu m^2$). As can be seen, the surface is rather flat with characteristic holes represented with dark color. Cross section of one characteristic hole (along dashed line in Fig. 1(a)) is given in the inset of Fig. 1(a). Hole width and depth are around 1 μm and 200 nm, respectively. Apart from this holes, the sample surface consists of small grains. They are better visualized in Fig. 1(c) and (d) showing the topography and phase contrast image of a zoomed part (scan size is $1 \times 1 \ \mu m^2$). Grains are clearly visible, especially
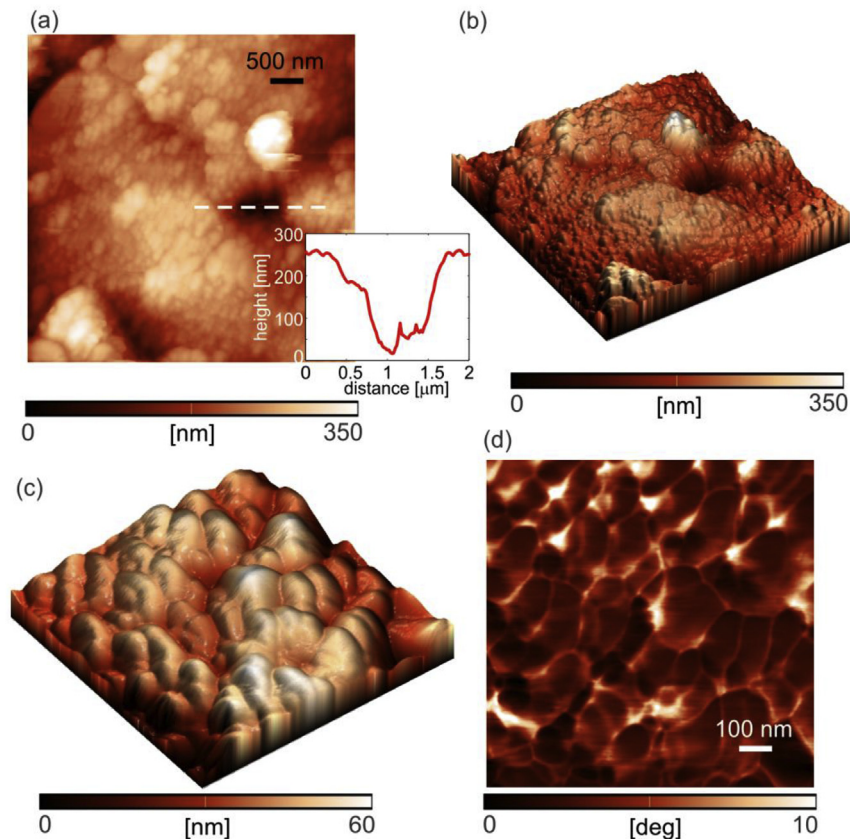
Fig. 1. (a) Two-dimensional and (b) three-dimensional topography of the sample surface. The inset in part (a) shows the cross-section along the corresponding dashed line. (c) Three-dimensional topography and (b) corresponding phase contrast image of a zoomed region from part (a).

grain boundaries in the phase contrast image since the phase is very sensitive to abrupt changes in the topography. Dispersion of grain size is rather wide, but still we can conclude that the characteristic grain size is in the order of 100 nm.

3.2. Far-infrared spectroscopy

The infrared reflectivity measurements were performed at room temperature with a BOMEM DA-8 Fourier-transform infrared spectrometer. A Hyper beamsplitter and deuterated triglycine sulfate (DTGS) pyroelectric detector were used to cover the wave number region from 80 to 650 cm^{-1}. Spectra were collected with 2 cm^{-1} resolution and with 500 interferometer scans added for each spectrum.

When visible light, λ, interacts with semiconducting nanoparticles (characteristic size d, dielectric function ε_2) which are distributed in a medium with the dielectric constant ε_1 in the limit $\lambda \gg$ d, the heterogeneous composite can be treated as a homogeneous medium and effective medium theory is applied. There are many mixing models for the effective dielectric permittivity of such mixture [16]. Since our samples are well defined and separated nanosized grains, we used Maxwell-Garnet model for present case. For the spherical inclusions case, the prediction of the effective permittivity of mixture, ε_{eff}, according to the Maxwell-Garnet mixing rule is [17]:

$$\varepsilon_{eff} = \varepsilon_1 + 3f\varepsilon_1 \frac{\varepsilon_2 - \varepsilon_1}{\varepsilon_2 + 2\varepsilon_1 - f(\varepsilon_1 - \varepsilon_2)} \tag{1}$$

Here, spheres of permittivity ε_2 are located randomly in homogeneous environment ε_1 and occupy a volume fraction f. The observed nanoparticles are situated in air, therefore the ε_1 is 1. For dielectrical function of observing nanoparticles (ε_2) we used the standard model [18]:

$$\varepsilon_2(\omega) = \varepsilon_\infty \left(\prod_{k=1}^{n} \frac{\omega_{LOk}^2 - \omega^2 + i\gamma_{LOk}\omega}{\omega_{TOk}^2 - \omega^2 + i\gamma_{TOk}\omega} - \frac{\omega_P^2}{\omega(\omega - i\tau^{-1})} \right) \tag{2}$$

where ε_∞ is the bound charge contribution and it is assumed to be a constant, ω_{TOk} and ω_{LOk} are transverse and longitudinal frequencies, γ_{TOk}, and γ_{LOk} are their dampings, ω_P is the plasma
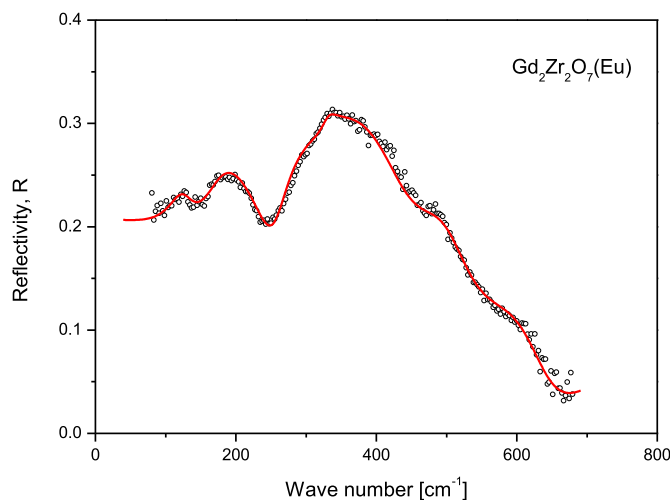
Fig. 2. Far – infrared reflection spectra of Eu^{3+} doped Gd$_2$Zr$_2$O$_7$ nanopowder. The experimental data are represented by circles. The solid lines are the calculated spectra obtained with the parameter values given in Table 1 and the fitting procedure based on the model given by Eqs. (1) and (2).

frequency and τ is the free carrier relaxation time. The first term in (2) is the lattice contribution, whereas the second term is the Drude expression for the free carrier contribution to the dielectric constant. In this case, we will consider ω_{TOk} as a characteristic frequency of material (v_k), and we will link ω_{LOk} with oscillator strength ($S_k \sim \omega_{LOk}^2 - \omega_{TOk}^2$) which does not have big influence on discussion.

The far-infrared spectra of Eu^{3+} doped Gd$_2$Zr$_2$O$_7$ nanopowders, in the spectral range of 80–650 cm^{-1}, at room temperature, are presented in Fig. 2. The experimental data are presented by circles, while the solid lines are calculated spectra obtained by a fitting procedure based on the previously presented model. In Table 1 the best fit parameters are presented. Values for Eu^{3+} doped Gd$_2$Zr$_2$O$_7$ single crystal are taken from literature [11,19–22].

McCauley [23], and Vandenborre [24] came to the result that of the total number of 26 normal modes ($\Gamma = A_{1g} + E_g + 2F_{1g} + 4F_{2g} + 3A_{2u} + 3E_u + \underline{\mathbf{8F_{1u}}} + 4F_{2u}$) only those of F_{1u} vibrations are active in the IR absorption. One of the eight F_{1u} modes is associated with three degrees of translation of the unit cell and refers to the acoustic branch of the crystal vibrations and thus analysis predict 7 IR − active optic modes [22]. Our results confirm all of the seven active vibrations and their assignations are shown in Table 1 and also indicate that anharmonicity factors are not significant. The analysis [23,24] also predicts that six vibrations of the types A_{1g}, E_g and $4F_{2g}$ are Raman − active modes. As per the selection rules, the remaining modes (F_{1g}, A_{2u}, E_u and F_{2u}) are inactive both in the IR and Raman spectra. According to the group-theoretical analysis, all the atoms of the crystal lattice are involved in the seven IR active F_{1u} vibrations (and six Raman − active modes) of the pyrochlore [22–24].

Following other authors' and our previous work [11,25] we started our analysis from the bulk material, considering that understanding bulk properties will lead to better understanding of properties of small particles, and therefore, as a result we expect the bulk modes to be shifted and broadened.

All modes are shifted compared to literature data. We believe that this is not because of the doping with Eu^{3+} and that in relatively small concentrations/amounts, doping did not induce changes in phonon spectra of Gd$_2$Zr$_2$O$_7$ [26]. We confirm our previous work [11] where we used Raman spectroscopy to obtain modes at 177 cm^{-1} and 268 cm^{-1} which noticeably differed from results obtained by many other authors who claimed that these modes occur at ~140 cm^{-1} (O-A-O vibrations) and ~220 cm^{-1} (O-B-O vibrations), respectively. Using FIR spectroscopy we obtained significant modes at 175 cm^{-1} and 255 cm^{-1} which describe O-A-O and O-B-O vibrations, respectively. The reason for this shift, as we believe, is electron − phonon interaction which led to the breakdown of the selection rules and appearance of the new phonons in fluorite structure Gd$_2$Zr$_2$O$_7$:Eu spectrum [11].

Interesting thing is, FIR spectrum shows two modes characteristic for pyrochlore type of structure, at 365 cm^{-1} and 490 cm^{-1}, although they are weak [19]. These two modes correspond to the vibrations of GdO$_8$ and ZrO$_6$ polyhedra, respectively. This confirm some earlier thoughts of P phase and F phase co-existing in the sample [19]. As it was said earlier [4,11], Gd$_2$Zr$_2$O$_7$ has two isometric structures, disordered fluorite (F) and ordered pyrochlore (P). In general, disordered fluorite structure type for this compound is confirmed [4]. But, it is also known that Ln$_2$Zr$_2$O$_7$ (Ln = elements of lanthanide series) have a pyrochlore-type structure stable at low temperature [19]. The Raman activity allowed for the pyrochlore structure results from oxygen vibrations, and only four bands are observed in the Raman spectra of Ln$_2$Zr$_2$O$_7$ pyrochlore-type compounds (Table 1 [21]). In the ordered structure there is no evidence of the significant band at 125 cm^{-1}, like our FIR spectrum shows.

Table 1
Best fit parameters of far − infrared spectra of Eu^{3+} doped $Gd_2Zr_2O_7$.

Exp. results: $Gd_2Zr_2O_7$: Eu^{3+} nanopowder	Literature: $Gd_2Zr_2O_7$: Eu^{3+} single crystal	Assignment
50	−	ν_7: O′-Gd-O′ bending vibrations
126	−	ν_6: Gd-ZrO_6 streching vibrations
175	177 [11]	ν_5: O-Gd-O bending vibrations
255	268 [11]	ν_4: O-Zr-O bending vibrations
330	310 [20], 315 [21]	ν_3: Zr-O + O-Zr-O vibrational mode (O-Zr-O bending)
365	370 [19], 400 [21]	ν_2: vibrations of GdO_8 polyhedra
490	500 [19], 538 [21]	ν_1: Zr-O stretching vibration, vibrations of ZrO_6 polyhedra
610	599 [20], 592 [21]	E_g: Zr-O′ stretching vibration

The thing is, for $Ln_2Zr_2O_7$ compounds, an order − disorder transition pyrochlore ↔ defective fluorite may occur when the temperature is raised [21]. This confirms that in $Gd_2Zr_2O_7$:Eu nanopowder P- and F- phase coexist. At first, this is not in agreement with XRD results for $Gd_2Zr_2O_7$:Eu nanopowder [4], but using FIR spectroscopy in reflectivity mode, we concern mainly the surface of material and coexistence of two phases is characteristic for the surface, but not for the general structure which is generally investigated using XRD.

Modes at 330 cm^{-1} and 610 cm^{-1} are clearly visible in both F phase and P phase spectra [20] and they correspond to Zr-O + O-Zr-O vibrational mode.

The rest of well known IR active vibrations, O-Gd-O and O′-Gd-O′ (O′ represents the 8(a) site oxide ion [27,28]) bending vibrations, are not yet assigned for Gd - zirconates. We assume that these vibrations correspond to 50 cm^{-1}, 126 cm^{-1} modes, respectively. The mode at 50 cm^{-1} clearly could not be obtained with our spectrometer which works in 80–650 cm^{-1} region, but that mode is well-suited to the fitting procedure based on the model given by Eqs. (1) and (2). Value of 50 cm^{-1} for Gd-zirconate is expected, regarding [[22], pg. 78, Table VII] which shows O′-Gd-O′ assignments for lanthanide series from La to Sm, but not for the Gd. We find answer in the isotope effect. The change in spectrum is conditioned with the mass of nuclei, and if the mass of some element is greater, spectral lines will move to lower values of wave number. Therefore, considering the increase in mass from La to Gd, we assume that previously unknown wave number value of O′-Gd-O′ vibration for Gd-zirconates corresponds to our result of 50 cm^{-1} (value of wave numbers from La to Gd are decreasing). We also use isotopic shift to explain the 126 cm^{-1} for which we assume corresponds to O-Gd-O vibration band and it also may suggest the possibility of a lowered local symmetry for some crystallographic sites [24] (that is in agreement with our assumptions with order ↔ disorder transition).

4. Conclusion

In this paper far-infrared reflectivity measurements were used to obtain phonon properties of Eu^{3+} doped $Gd_2Zr_2O_7$ nanopowders. We registered phonons of both isomeric structures characteristic for $Gd_2Zr_2O_7$ nanopowder and concluded coexistence of these two phases on the surface of the material, whereas fluorite structure is typical for the general structure. Low frequency modes were registered and regarding isotope effect they have been assigned.

Acknowledgments

References

[1] C. Fischer, S. Finkeldei, F. Brandt, D. Bosbach, A. Luttge, Direct measurement of surface dissolution rates in potential nuclear waste forms: the example of pyrochlore, ACS Appl. Mater. Interfaces 7 (32) (2015) 17857—17865.

[2] M.C. Hsieh, G.C. Wu, W.G. Liu, W.A. Goddard, C.M. Yang, Nanocomposites of tantalum-based pyrochlore and indium hydroxide showing high and stable photocatalytic activities for overall water splitting and carbon dioxide reduction, Angew. Chem. Int. Ed. 53 (51) (2014) 14216—14220.

[3] J. Parrondo, M. George, C. Capuano, K.E. Ayers, V. Ramani, Pyrochlore electrocatalysts for efficient alkaline water electrolysis, J. Mater. Chem. A 3 (20) (2015) 10819—10828.

[4] M.S. Rabasovic, D. Sevic, J. Krizan, M. Terzic, J. Mozina, B. Marinkovic, N.R.M. Mitric, M.D. Rabasovic, Characterization and luminescent properties of Eu^{3+} doped $Gd_2Zr_2O_7$ nanopowders, J. Alloys Compd. 622 (3) (2014) 292—295.

[5] R.J. Walker, et al., Surface termination and CO2 adsorption onto bismuth pyrochlore oxides, Chem. Mater. 28 (1) (2016) 90—96.

[6] T. Kondo, et al., Quadratic Fermi node in a 3D strongly correlated semimetal, Nat. Commun. 6 (2015) 10042.

[7] S.K. Gupta, P.S. Ghosh, C. Reghukumar, N. Pathak, R.M. Kadam, Experimental and theoretical approach to account for green luminescence from $Gd_2Zr_2O_7$ pyrochlore: exploring the site occupancy and origin of host-dopant energy transfer in $Gd_2Zr_2O_7$, RSC Adv. 6 (50) (2016) 44908—44920.

[8] J. Wu, et al., Thermal-barrier-coating applications, J. Am. Ceram. Soc. 35 (2002) 3031—3035.

[9] L. Wang, J.I. Eldridge, S.M. Guo, Thermal radiation properties of plasma-sprayed $Gd_2Zr_2O_7$ thermal barrier coatings, Scr. Mater. 69 (9) (2013) 674—677.

[10] K.-J. Hu, Z.-G. Liu, J.-Y. Wang, T. Wang, J.-H. Ouyang, Synthesis and photoluminescence properties of Eu^{3+}- doped $Gd_2Zr_2O_7$, Mater. Lett. 89 (2012) 276—278.

[11] G. Križan, M. Gilić, J.L. Ristić - Đurović, J. Trajić, M. Romčević, J. Križan, B. Hadžić, B. Vasić, N. Romčević, Raman Spectroscopy and electron - phonon coupling in Eu^{3+} doped $Gd_2Zr_2O_7$ nanopowders, Opt. Mater. 73 (2017) 541—544.

[12] Y.S. Chang, H.J. Lin, Y.L. Chai, Y.C. Li, Preparation and luminescent properties of europium-activated $YInGe_2O_7$ phosphors, J. Alloys Compd. 460 (1—2) (2008) 421—425.

[13] W. Zheng, P. Huang, D. Tu, E. Ma, H. Zhu, X. Chen, Lanthanide-doped upconversion nano-bioprobes: electronic structures, optical properties, and biodetection, Chem. Soc. Rev. (6) (2015) 1379—1415.

[14] K.S. Lee, K.I. Jung, Y.S. Heo, T.W. Kim, Y.G. Jung, U. Paik, Thermal and mechanical properties of sintered bodies and EB-PVD layers of Y_2O_3 added $Gd_2Zr_2O_7$ ceramics for thermal barrier coatings, J. Alloys Compd. 507 (2) (2010) 448—455.

[15] X.L. Xia, Z.G. Liu, J.H. Ouyang, S. Gao, X.M. Liu, Effect of Ce substitution for Zr on electrical property of fluorite-type $Gd_2Zr_2O_7$, Solid State Sci. 13 (6) (2011) 1328—1333.

[16] J. Trajić, M.S. Rabasović, S. Savić-Šević, D. Šević, B. Babić, M. Romčević, J.L. Ristić-Djurović, N. Paunović, J. Križan, N. Romčević, Far-infrared spectra of dysprosium doped yttrium aluminium garnet nanopowder, Infrared Phys. Technol. 77 (2016) 226—229.

[17] J.C.M. Garnett, Colours in metal glasses and in metallic films i (1904).

[18] I.J. Uhanov, Opt. Svojstva Poluprovodnikov, Nauka, Moskva, 1977.

[19] L. Zhou, et al., Thermal-driven fluorite—pyrochlore—fluorite phase transitions of $Gd_2Zr_2O_7$ ceramics probed in large range of sintering temperature, Metall. Mater. Trans. A Phys. Metall. Mater. Sci. (2015) 1—8.

[20] T. Moriga, S. Emura, A. Yoshiasa, S. Kikkawa, F. Kanamaru, X-ray and Raman study on coordination states of fluorite- and pyrochlore- type compounds in the system ZrO_2-Gd_2O_3 50 (1990) 357—361.

[21] D. Michel, M.P.Y. Jorba, R. Collongues, Study by Raman spectroscopy of order-disorder phenomena occurring in some binary oxides with fluorite-related structures, J. Raman Spectrosc. 5 (2) (1976) 163—180.

[22] M.A. Subramanian, G. Aravamudan, G.V. Subba Rao, Oxide pyrochlores - a review, Prog. Solid State Chem. 15 (2) (1983) 55—143.

[23] R.A. McCauley, Infrared-absorption characteristics of the pyrochlore structure, J. Opt. Soc. Am. 63 (6) (1973) 721.

[24] R.A. McCauley, Infrared-absorption characteristics of the pyrochlore structure, J. Opt. Soc. Am. 63 (6) (1973) 721.

[25] C.S.S.R. Kumar, Raman Spectroscopy for Nanomaterials Characterization, Springer-Verlag, Berlin Heidelberg, 2012.

[26] X.L. Xia, J.H. Ouyang, Z.G. Liu, Electrical properties of gadolinium-europium zirconate ceramics, J. Am. Ceram. Soc. 93 (4) (2010) 1074—1080.

[27] M.T. Vandenborre, E. Husson, J.P. Chatry, D. Michel, Rare-earth titanates and stannates of pyrochlore structure; vibrational spectra and force fields, J. Raman Spectrosc. 14 (2) (1983) 63—71.

[28] M.T. Vandenborre, E. Husson, Comparison of the force field in various pyrochlore families II. Phases presenting structural defects, J. Solid State Chem. 5359 (1984) 253—262.

Low-temperature photoluminescence of CuSe$_2$ nano-objects in selenium thin films

Martina Gilić[1,*], Milica Petrović[1], Jovana Ćirković[2], Novica Paunović[1], Svetlana Savić-Sević[1], Željka Nikitović[1], Maja Romčević[1], Ibrahim Yahia[3], Nebojša Romčević[1]

[1]*Institute of Physics Belgrade, University of Belgrade, Pregrevica 118, Belgrade, Serbia*
[2]*The Institute for Multidisciplinary Research, University of Belgrade, Belgrade, Serbia*
[3]*Nano-Science and Semiconductors Labs., Physics Department, Faculty of Education, Ain Shams University, Roxy, Cairo, Egypt*

Abstract

Thin films of CuSe$_2$ nanoparticles embedded in selenium matrix were prepared by vacuum evaporation method on a glass substrate at room temperature. The optical properties of the films were investigated by photoluminescence spectroscopy (T = 20–300 K) and UV-VIS spectroscopy (T = 300 K). Surface morphology was investigated by scanning electron microscopy. The band gap for direct transition in CuSe$_2$ was found to be in the range of 2.72–2.75 eV and that for indirect transition is in the range of 1.71–1.75 eV determined by UV-VIS spectroscopy. On the other hand, selenium exhibits direct band gap in the range of 2.33–2.36 eV. All estimated band gaps slightly decrease with the increase of the film thickness. Photoluminescence spectra of the thin films clearly show emission bands at about 1.63 and 2.32 eV at room temperature, with no shift observed with decreasing temperature. A model was proposed for explaining such anomaly.

Keywords: chalcogenides, thin films, optical properties, spectroscopy, SEM

I. Introduction

Selenides of copper (Cu-Se) exist in many phases and structural forms: i) stoichiometric forms, such as CuSe (klockmannite), Cu$_2$Se$_x$, CuSe$_2$ (marcasite), α-Cu$_2$Se (bellidoite), Cu$_3$Se$_2$ (umangite), Cu$_5$Se$_4$ (athabaskite), Cu$_7$Se$_4$ etc., as well as ii) non-stoichiometric forms, such as Cu$_{2-x}$Se (berzelianite). All those phases can be classified into several crystallographic forms (monoclinic, cubic, tetragonal, hexagonal, etc.). Copper selenide is a semiconductor with p-type conductivity, and has numerous applications in various devices, such as solar cells [1–3], photo detectors [4], optical filters [5], microwave shielding [6], thermoelectric converters [7], etc. Photovoltaic cells and Shottky diodes are also based on these metal chalcogenide compounds [8,9]. CuSe$_2$ is a superconductor at low temperatures with a transition temperature $T_C \sim 2.4$ K [10], and has a weak ferro-

magnetic response below 31 K [11,12]. CuSe$_2$ is widely used as a precursor material for CuInSe$_2$ (CIS) and Cu(In,Ga)Se$_2$ (CIGS) preparation, suitable for highly efficient photovoltaic elements [13]. Also, CuSe$_2$ is used as a typical anion conductor and significant Cu-Se alloys targets for the preparation of CIGS/CIS thin film solar cells in RF magnetic sputtering [14].

Possible application of Cu-Se strongly depends on its optical properties. Despite the numerous publications of the optical properties of Cu-Se thin films, the estimated value of band gap of Cu-Se is not well defined. Cu-Se has both direct and indirect transitions, so the presence of both band gaps, direct and indirect, can be observed. Literature data are quite controversial: direct allowed transitions are reported to have corresponding band gap in the range of 2 to 3 eV, and indirect band gap between 1.1 and 1.5 eV [15–18]. The indirect band gap being near the optimum value for solar cell applications makes this material capable of potentially offer a high efficiency of conversion. However, Cu-Se nanoparticles

*Corresponding author: tel: +381 11 3713 036, fax: +381 11 3713 052, e-mail: martina@ipb.ac.rs

have been reported to possess a direct band gap of 4 eV and indirect one of 1.87 eV [19]. The reasons of such variation in band gaps could lie in the sharp cut off of the wavelength with the spectral transmittance instead of the slow increase, the presence of large number of dislocations, wide range of stoichiometric deviation and quantum confinement effect.

In our previous report [20], we prepared Cu-Se thin films of three different thicknesses by vacuum evaporation technique using Mo boat onto glass substrate at room temperature, and investigated their structural properties. XRD and far-infrared spectroscopy revealed the presence of $CuSe_2$ nanocrystals in predominant Se films.

The objective of this research was to determine optical properties of Cu-Se thin films, using UV-VIS and low-temperature photoluminescence spectroscopy, and to investigate how the film thickness could influence the band gap value and photoluminescence properties. SEM analysis was also performed in order to get information about the morphology of the obtained Cu-Se thin films.

II. Experimental

Thin films were obtained by evaporating commercially high purity CuSe powder (99.99%) supplied from Aldrich Company. The powder was deposited onto highly pre-cleaned glass substrates with use of Mo boat. The procedure was done in a high-vacuum environment with typical background pressures of 3 mPa. The deposition rate, 10 nm/s, was monitored by quartz crystal thickness monitor - FTM4, Edwards and the final films thicknesses was found to be 56 nm, 79 nm and 172 nm for the films labelled as F-55, F-80 and F-170, respectively [20].

SEM imaging was done using scanning electron microscope equipped with a high brightness Schottky field emission gun (FEGSEM, TESCAN) operating at 4 kV. The samples were coated with gold/palladium to make them conductive.
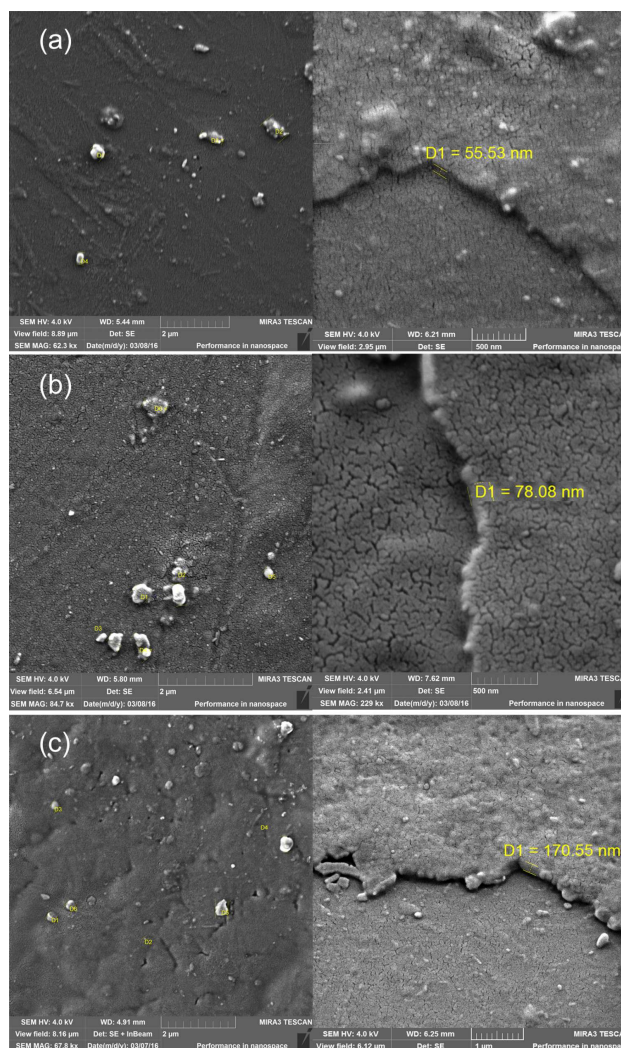
The UV-VIS diffusion reflectance and transmittance spectra were recorded in the wavelength range of 300–1000 nm on a Shimadzu UV-2600 spectrophotometer equipped with an integrated sphere. The diffuse reflectance and transmittance spectra were measured relative to a reference sample of $BaSO_4$.

Photoluminescence measurements on various temperatures ($T = 20–300$ K) were obtained by Jobin-Yvon U1000 spectrometer, equipped with RCA-C31034A photomultiplier with housing cooled by Peltier element, amplifiers and counters. The 488 nm laser line of argon laser was used as excitation source.

III. Results and discussion

3.1. SEM analyses

Scanning electron microscopy (SEM) images were obtained for the Cu-Se thin films deposited on glass substrate in order to study the surface morphology and

Figure 1. Top view and tilted SEM micrographs of films: a) F-55, b) F-80 and c) F-170

agglomeration of the samples.

Top view and tilted micrographs of the thin films are presented in Fig. 1. From the top view micrographs it can be observed that the surface of the samples is relatively uneven and rather rough, with presence of cracks and voids. Formation of the Cu-Se thin films most probably proceed unevenly, in the form of islands which later grew into agglomerates. Agglomerated clusters of few hundreds nanometers in diameter are distributed nonuniformly along the surface and form the structure consisting of $CuSe_2$ nanocrystals in predominant Se matrices. In order to determine the film thicknesses, the samples were tilted at 30°. The thicknesses estimated by SEM are: ~56 nm, ~78 nm and ~171 nm for the films F-55, F-80 and F-170, respectively. The thickness values estimated by SEM analysis match the ones obtained during the preparation of thin films.

3.2. UV-VIS spectroscopy

In Fig. 2 diffuse reflectance R and transmittance T spectra of the thin films samples in the wavelength range 300–1000 nm (4.13–1.24 eV) on room temperature (*T*
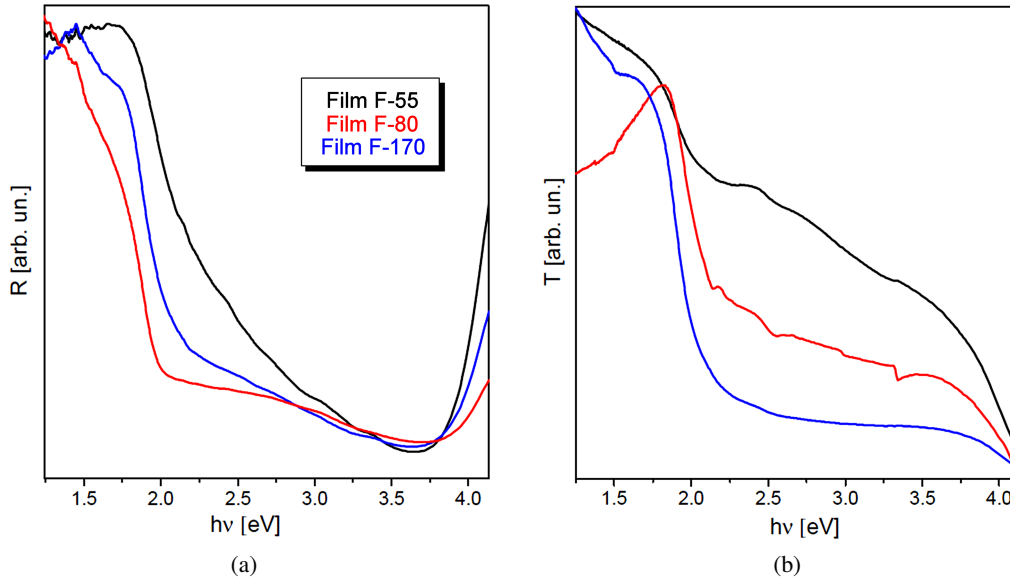
Figure 2. Diffuse reflectance, *R* (a), and transmittance, *T* (b) spectra

= 300 K) are presented. As it can be seen, the transmittance increases with decrease in the film thickness, which is not the case for reflectance. This is typical for films with high electrical conductivity and implies a reflection coefficient nearing 1 for films with metallic conductivity.

In this study we used the Tauc plot for the determination of the optical band gap from diffuse reflectance measurements. The determination of band gap in semiconductors is significant for obtaining the basic solid state physics. The relation expression proposed by Tauc, Davis and Mott [21–23] is the following:

$$\alpha \cdot h \cdot v = A \left(h \cdot v - E_g \right)^{1/n} \tag{1}$$

where h is the Planck's constant, A is the transition probability constant depending on the effective mass of the charge carriers in the material, E_g is the band gap, $h \cdot v$ is the photon energy and α is the absorption coefficient which is defined as the relative rate of decrease in light intensity along its propagation path, i.e. a property of a material that defines the amount of light absorbed by it. The value of n denotes the nature of the transition. In case of direct transitions n equals ½ and ³⁄₂ for allowed and forbidden transitions, respectively. As for indirect transitions, n equals 2 and 3 for allowed and forbidden transitions, respectively. Since CuSe exhibits both direct and indirect allowed transitions, $n = $ ½ and n = 2.

Then, the acquired diffuse reflectance spectra are converted to Kubelka-Munk function [24]:

$$\alpha = \frac{(1 - R)^2}{2R} \tag{2}$$

So using this function, a plot of $(\alpha \cdot h \cdot v)^{1/n}$ against $h \cdot v$ is obtained. The energy band gap is determined by extrapolating the linear portion of $(\alpha \cdot h \cdot v)^{1/n}$ vs. $h \cdot v$
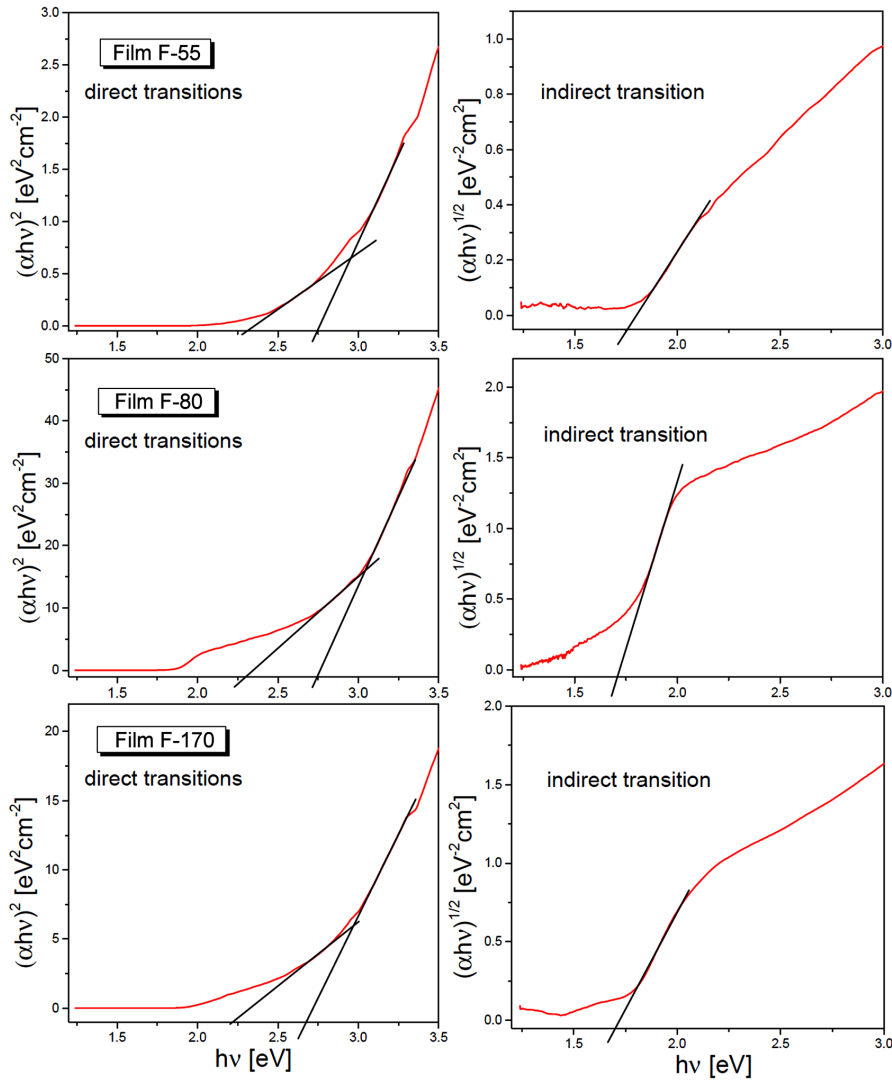
to the energy axis at $(\alpha \cdot h \cdot v)^{1/n} = 0$. The intercept of these plots on the energy axis gives the energy band gap. Such plots are given in Fig. 3. Direct transitions (left part of Fig. 3) reveal band gap for both selenium and CuSe$_2$, while indirect transitions (right part of Fig. 3) reveal band gap for CuSe$_2$ only.

The experimentally determined values of energy gaps for CuSe$_2$ show slight decrease with film thickness and their values range from 2.75 to 2.72 eV for direct transitions, and from 1.75 to 1.71 eV in case of indirect transitions. The estimated band gaps for selenium follow the same trend with film thickness and range between 2.33 and 2.36 eV. The estimated band gap positions for each sample are given in Table 1. The difference in the film thicknesses causes the small difference in band gaps in the second decimal place and they follow the well-established trend, the smaller the thickness, the wider the band gap is. Also, their values are quite wider than the ones that can be found in literature [7,16,25–33].

Table 1. Estimated band gap energies of thin films determined with UV-VIS spectroscopy

	F-55	F-80	F-170
CuSe$_2$ direct transition [eV]	2.75	2.74	2.72
CuSe$_2$ indirect transition [eV]	1.75	1.72	1.71
Se direct transition [eV]	2.36	2.34	2.33

Broad range of energy band gap values for Cu-Se can be found in literature. For direct transitions those values are usually between 2 and 3 eV. Bari *et al.* [25] obtained the value of 2.51 eV for the sample with thickness of 150 nm, and with the increase of film thickness they reported the decrease of band gap width. Grozdanov [26], Garcia *et al.* [16] and Sakr *et al.* [27] obtained the value of 2.33, 2.13–2.38 and 2.74 eV, respectively. The latter is very similar to the results obtained in this paper. Rajesh *et al.* [28] got a diversity of band gaps ranging from

Figure 3. Dependence of $(\alpha \cdot h \cdot \nu)^2$ on photon energy $(h \cdot \nu)$ – left side, and dependence of $(\alpha \cdot h \cdot \nu)^{1/2}$ on photon energy $(h \cdot \nu)$ – right side

1.95 (the thickest film) to 3.70 eV (the thinnest film). However, for indirect transitions they received less attention. Garcia *et al.* [16] obtained values in the range 1.22–1.34 eV, whereas the value obtained by Bhuse *et al.* [7] is about 1.4 eV. Our values (~1.7 eV) are bigger than the reported in literature. According to our opinion, the larger indirect band gap values are due to quantum confinement effect [29,30] whereby the electrons are localized in individual crystallites, and due to specific border conditions between $CuSe_2$ nanoparticles and selenium matrix.

For the pure selenium, the direct band gap was reported to be about 2 eV for the bulk [31,32] and 2.20–2.06 for the thin films of thickness 130–290 nm [33]. Our films are thinner than the ones mentioned in the literature and it is not surprising that we obtained wider band gap values, about 2.3 eV. The film F-170 has the thickness between 130 and 290 nm, but the higher value in band gap is the result of specific border conditions between selenium matrix and $CuSe_2$ nanoparticles. We presume that $CuSe_2$ nanoparticles directly influence the

band gap of predominant selenium, and vice versa.

The Urbach energy is also analysed. Urbach rule states that the optical absorption coefficient α just below the band edge in insulators and semiconductors varies exponentially with the incident photon energy [34]:

$$\alpha = \alpha_0 \exp\left(\frac{h \cdot \nu}{E_U}\right) \qquad (3)$$

where α_0 is a constant and characteristic parameter of the material, $h \cdot \nu$ is incident photon energy, and the term E_U which is the width of the exponential tail is called Urbach energy. The Urbach energy represents the width of defect states in the band gap. Figure 4 shows $\log \alpha$ as a function of incident photon energy for the film F-170, as a representative one. By extrapolating the linear part of the plot and with use of Equation 3, the Urbach energy can be determined as the inverse of the slope and α_0 from the intercept of extrapolated plot. From the slope and inception of extrapolated plot it was determined that E_U is 0.32 eV and α_0 is 3.02 cm^{-1}.
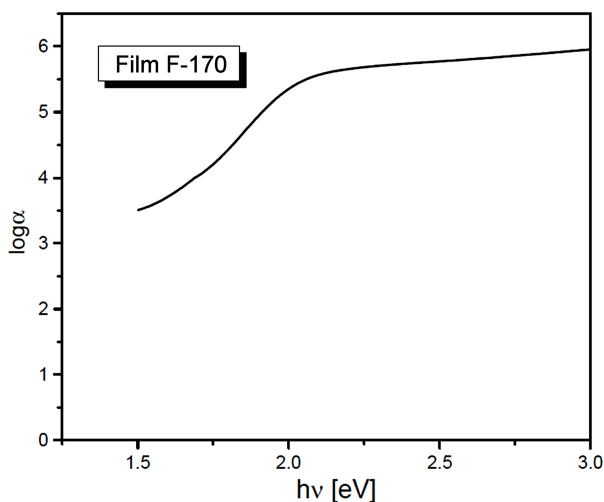
Figure 4. Logarithmic dependence of the absorption coefficient on the photon energy for F-170 film

3.3. Photoluminescence spectroscopy

Photoluminescence (PL) spectra can be used for investigating the possible outcomes of photo-induced electrons and holes in a semiconductor, since photoluminescence emission results from the recombination of free charge carriers. There are two types of photoluminescence phenomenon according to its attributes and formation mechanism: the band-to-band photoluminescence and the excitonic photoluminescence [35–37]. The band-to-band PL spectrum regards the separation situation of photo-generated charge carriers. The excitonic PL spectrum, however, cannot directly reflect the separation situation of photo-induced carriers. If discrete energy levels are present in the band gap, these may dominate the optical spectrum. PL measurements then yield information about the energetic positions of the electronic states in the gap. Such localized states can originate from various types of imperfections like vacancies, interstitial atoms, atoms at surfaces and grain boundaries. However, it is often difficult to determine the exact position and origin of these states.

Photoluminescence spectra of thin films on various temperatures are presented in Fig. 5. The spectra are rather complex, thus for their analysis the deconvolution method had to be employed. Two typical resolved spectra are presented in Fig. 6 (on 20 K and room temperature), and the deconvolution of the others is done in the same manner. Each spectrum is characterized with 5 bands. Band-to-band photoluminescence dominates the room temperature spectra. The band in red area at ~1.6 eV is clearly seen. According to the UV-VIS results (see previous chapter), we can attribute this mode to band-to-band transition for indirect transition in CuSe$_2$. In green area, a broad band is observed at ~2.3 eV which originates from direct transitions in selenium (also see prev. chapter). Due to Stokes shift, the obtained positions are a bit lower than the ones obtained by UV-VIS spectroscopy. Between these two bands there are three defect modes at 2.1 eV, 1.9 eV and
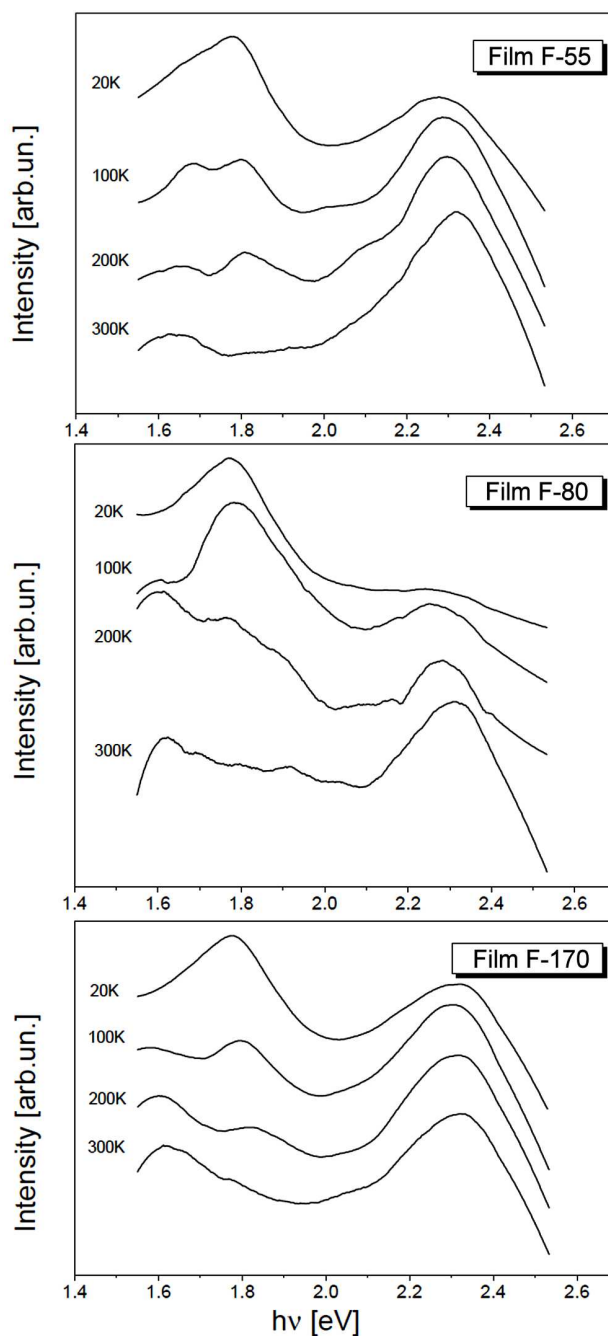

Figure 5. Photoluminescence spectra of thin films at various temperatures: a) F-55, b) F-80 and c) F-170

1.8 eV, which are of small intensity on room temperature. Lowering the temperature, the band at ~1.8 eV increases its intensity, and becomes the dominant one at 20 K. According to literature data [32] this band is attributed to selenium defect mode – negative U-centre. This mode is expected to appear at 0.5 eV from the band edges. Another two defect modes, at 2.1 and 1.9 eV, are attributed to the defect modes of CuSe$_2$, according to the work of Urmila *et al.* [38]. In their work they obtained bands at 2.1, 1.9 and 1.5 eV in PL spectrum of Cu$_7$Se$_4$ thin film. They concluded that there is nonradiative transition from conduction band to defect levels with energies 2.1, 1.9 and 1.5 eV and from these lev-
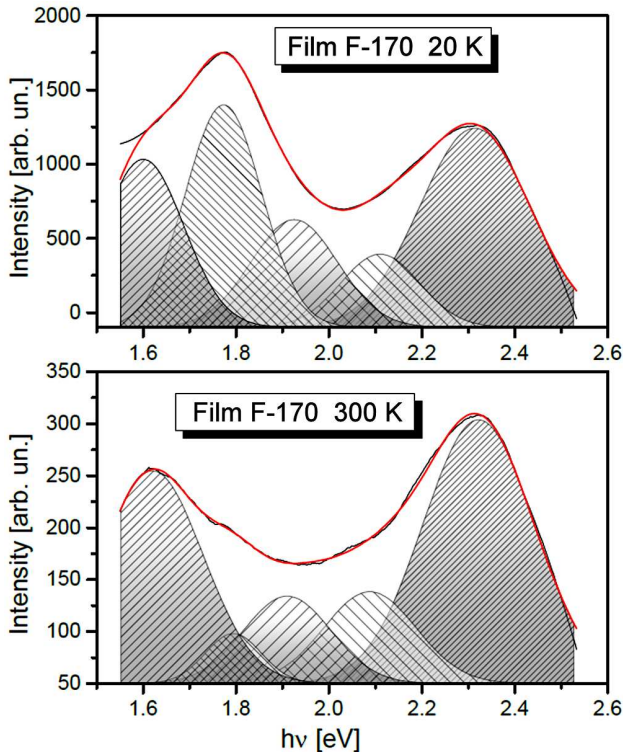
Figure 6. Typical resolved photoluminescence spectra of thin films F-170: a) on 20 K and b) room temperature
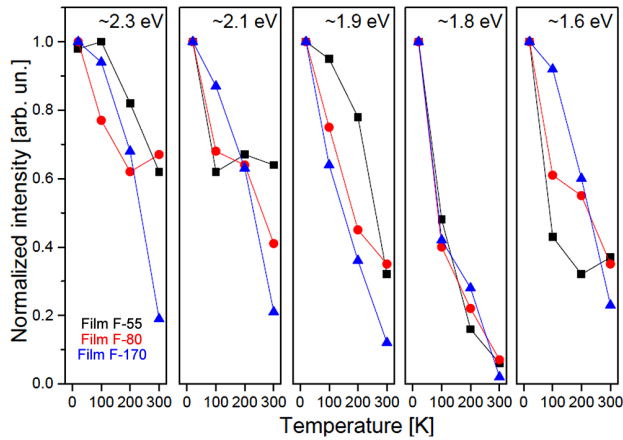

Figure 7. Temperature dependence of PL emission bands intensities, normalized on the most intensive ones (black squares – film F-55, red circles – film F-80, blue triangles – film F-170)

els radiative transitions occurred to valence band. The values 2.1 and 1.9 eV match the band positions we obtained in this work, thus we can assign these bands to defect modes in CuSe$_2$. Due to predominant phase of selenium, these bands are hidden by the bands originated from selenium and cannot be observed without the deconvolution method. Chong [39] in his work also obtained a PL band at ∼2.16 eV without assigning it to any transition. In all spectra, the uprise of peak intensity with lowering temperature is observed, Fig. 7. The intensities have their maximum values at the lowest temperature (20 K) and show decrease with rising temperature. The most radical decrease is observed for the band

at ∼1.8 eV, which intensity drops to ∼40% at 200 K, and only to ∼6% at room temperature.

Temperature dependence of PL emission band positions is shown in Fig. 8. Let us discuss the band position of indirect transitions of CuSe$_2$. At the room temperature, there are differences on the second decimal place for films of different thicknesses, the same as observed when analysing UV-VIS spectra. The same trend is observed on 20 K. If the shift of this band with temperature is analysed for each film, it can be noticed the temperature invariance, i.e. small non-monotonous differences in positions on the second decimal place. This is in contradiction with the expected red shift, characteristic for the semiconductors. The temperature invariance is observed for other bands as well. There is a question that needs to be answered: why the PL measurements show no shift with increasing temperature, instead of the conventional red shift characteristic for the semiconductors? A model proposed by Shen *et al.* [40] explains those discrepancies. It involves surface electron accumulation as a result of severe band bending in nanorods. However, the same trend was observed in thin film samples (including ours), whose curvature-less surface does not support a spatial charge separation such as in 1D nanostructures. Wei *et al.* [41] gave more exact explanation of this phenomenon in their work. They began the analysis by making difference between E_{PL} and E_g:

$$E_{PL}(n, T) = E_g(n, T) + E_{Fn}(n, T) - E_{Fp}(n, T) \quad (4)$$

where E_{Fn} and E_{Fp} are the electron and hole quasi-Fermi levels measured from the bottom of conduction band and the top of valence band, respectively. So the temperature dependence of the band gap shift is the competition between the lattice dilation dE_g/dT on the one hand, and the sum (dE_{Fn}/dT − dE_{Fp}/dT) on the other hand. The former results in the conventional red shift of the band gap with increasing temperature and the latter gets the blue shift. The resulting shift depends
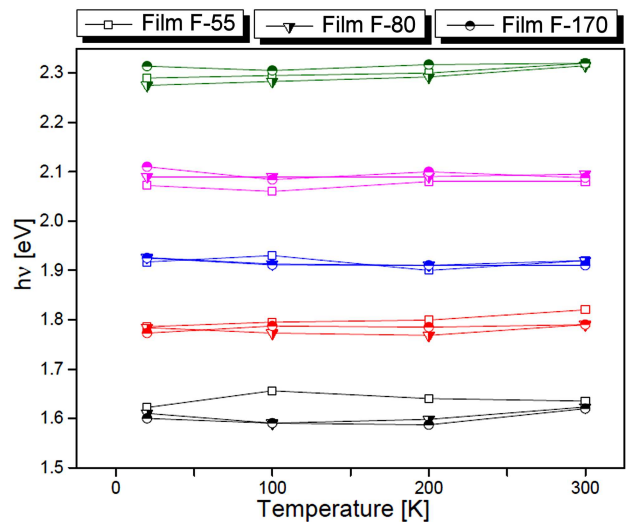

Figure 8. Temperature dependence of photoluminescence emission bands positions

on the magnitude of these two contributions. Usually when the electron density n is high, the thermal response in the material is governed by electronic rather than photonic interactions, the sum $(dE_{Fn}/dT - dE_{Fp}/dT)$ becomes dominant thus the blue shift of E_{PL} is observed. However, if these two contributions are of the same magnitude, it will result in no shift with changing temperature, as in case of our samples.

PL emission bands positions as a function of film thicknesses are presented in Fig. 9. It is common knowledge that as the confining dimension decreases, typically in nanoscale, the energy spectrum turns to discrete so the band gap of a semiconductor becomes size dependent. For one-dimensional confinement (film thickness), the quantization energies increase when the size along the confinement direction decreases [42,43]. In an amorphous or structurally disordered film, the imperfection in the film causes the bands of localized states to get broaden and a band gap reduction may occur due to the Urbach edge [44]. If we observe the shift of the band at ~1.6 eV, which corresponds to indirect transitions in $CuSe_2$, we can see the blue shift with decreasing size, as being expected. On the other hand, the band at ~2.3 eV which corresponds to direct transitions in Se, we can see no size dependence with the band position. The reason of this behaviour lies in specific composition of our films, i.e. $CuSe_2$ nano-objects embedded in selenium matrix. The particles of $CuSe_2$ are small enough to react on the size reduction, but the selenium matrix the amorphous effect becomes dominant.

As it can be seen from the above, the temperature changes do not affect the band gap. The size changes, i.e. the reduction of film thickness affects the band gap only on a second decimal place. Thus, we can state that the low cost technique of vacuum evaporation gives us the opportunity to produce quality, stable thin films
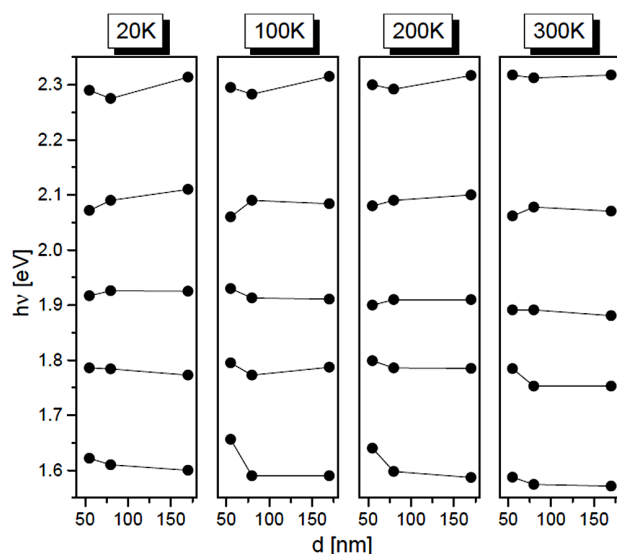
suitable for further applications in heterojunction solar cells and photo detectors.

IV. Conclusions

Cu-Se thin films of three different thicknesses, obtained by vacuum evaporation technique on glass substrate, underwent through photoluminescence investigation along with UV-VIS measurements and SEM analysis. Reflectance measurements revealed values for both direct and indirect band gap: ~2.7 and 1.7 eV, respectively for $CuSe_2$ and ~2.3 eV for Se. The existence of indirect band gap in $CuSe_2$ at this value, little wider than in literature, is confirmed by photoluminescence measurements. A band at ~1.8 eV, registered by PL measurements at low temperatures, is attributed to defect level of selenium – negative U-center. In this paper we proved that simple and low-cost technique as vacuum evaporation is capable of producing high-quality thin films.

References

1. T.P. Hsieh, C.C. Chuang, C.S. Wu, J.C. Chang, J.W. Guo, W.C. Chen, "Effects of residual copper selenide on CuInGaSe$_2$ solar cells", *Solid State Electron.*, **56** (2011) 175–178.
2. M. Singh, J. Jiu, T. Sugahara, K. Suganuma, "Thin-film copper indium gallium selenide solar cell based on low-temperature all-printing process", *ACS Appl. Mater. Interfaces*, **6** (2014) 16297–16303.
3. J.H. Scofield, A. Duda, D. Albin, B.L. Ballard, P.K. Predecki, "Sputtered molybdenum bilayer back contact for copper indium diselenide-based polycrystalline thin-film solar cells", *Thin Solid Films*, **260** (1995) 26–31.
4. S. Lei, A. Sobhani, F. Wen, A. George, Q. Wang, Y. Huang, P. Dong, B. Li, S. Najmaei, J. Bellah, G. Gupta, A.D. Mohite, L. Ge, J. Lou, N.J. Halas, R. Vajtai, P. Ajayan, "Ternary CuIn$_7$Se$_{11}$: Towards ultra-thin layered photodetectors and photovoltaic devices", *Adv. Mater.*, **45** (2014) 7666–7737.
5. G. Juska, V. Gulbinas, A. Jagminas, "Transient absorption of copper selenide nanowires of different stoichiometry", *Lith. J. Phys.*, **50** (2010) 233–239.
6. C. Levy-Clement, M. Neumann-Spallart, S.K. Haram, K.S.V. Santhanam, "Chemical bath deposition of cubic copper (I) selenide and its room temperature transformation to the orthorhombic phase", *Thin Solid Films*, **302** (1997) 12–16.
7. V.M. Bhuse, P.P. Hankare, K.M. Garadkar, A.S. Khomane, "A simple, convenient, low temperature route to grow polycrystalline copper selenide thin films", *Mater. Chem. Phys.*, **80** (2003) 82–88.
8. S.Y. Zhang, C. Fang, Y. Tian, K. Zhu, B. Jin, Y. Shen, J. Yang, "Synthesis and characterization of hexagonal CuSe nanotubes by templating against trigonal Se nanotubes", *Cryst. Growth Des.*, **6** (2006) 2809–2813.
9. H.M. Pathan, C.D. Lokhande, D.P. Amalnerkar, T. Seth, "Modified chemical deposition and physico-chemical

Figure 9. PL emission bands positions dependence of film thicknesses

properties of copper (I) selenide thin films", *Appl. Surf. Sci.*, **211** (2003) 48–56.

10. Y. Takana, N. Uchiyama, S. Ogawa, N. Mori, Y. Kimishima, S. Arisawa, A. Ishii, T. Hatano, K. Togano, "Superconducting properties of $CuS_{2-x}Se_x$ under high pressure", *Physica C: Superconduct.*, **341-348** (2000) 739–740.

11. G. Krill, P. Panissod, M.F. Lapierre, F. Gautier, C. Robert M.N. Eddine, "Magnetic properties and phase transitions of the metallic CuX_2 dichalogenides (X = S, Se, Te) with pyrite structure", *J. Phys. C*, **9** (1976) 1521–1533.

12. M. Kontani, T. Tutui, T. Moriwaka, T. Mizukoshi, "Specific heat and NMR studies on the pyrite-type superconductors CuS_2 and $CuSe_2$", *Physica B*, **284** (2000) 675–676.

13. R.R. Pai, T.T. John, M. Lakshimi, K.P. Vijayakumar, C.S. Kartha, "Observation of phase transitions in chemical bath deposited copper selenide thin films through conductivity studies", *Thin Solid Films*, **473** (2005) 208–212.

14. N.H. Kim, S. Oh, W.S. Lee, "Non-selenization method using sputtering deposition with a $CuSe_2$ target for CIGS thin film", *J. Korean Phys. Soc.*, **61** (2012) 1177–1180.

15. P. Hankare, A. Khomane, P. Chate, K. Rathod, K. Garadkar, "Preparation of copper selenide thin films by simple chemical route at low temperature and their characterization", *J. Alloys Comp.*, **469** (2009) 478–482.

16. V. Garcia, P. Nair, M. Nair, "Copper selenide thin films by chemical bath deposition", *J. Cryst. Growth*, **203** (1999) 113–124.

17. O. Arellano-Tanori, M. Acosta-Enriquez, R. Ochoa-Landin, R. Iniguez-Palomares, T. Mendivil-Reynoso, M. Flores-Acosta, S. Castillo, "Copper-selenide and copper-telluride composites powders sintetized by ionic exchange", *Chalcogenide Lett.*, **11** (2014) 13–19.

18. A. Jagminas, R. Juskenas, I. Gailiute, G. Statkute, R. Tomasinuas, "Electrochemical synthesis and optical characterization of copper selenide nanowire arrays within the alumina pores", *J. Cryst. Growth*, **294** (2006) 343–348.

19. D. Patidar, N.S. Saxena, "Characterization of single phase copper selenide nanoparticles and their growth mechanism", *J. Cryst. Growth*, **343** (2012) 68–72.

20. M. Gilic, M. Petrovic, R. Kostic, D. Stojanovic, T. Barudzija, M. Mitric, N. Romcevic, U. Ralevic, J. Trajic, M. Romcevic, I. Yahia, "Structural and optical properties of $CuSe_2$ nanocrystals formed in thin solid Cu-Se film", *Infrared Phys. Techn.*, **76** (2016) 276–284.

21. J. Tauc, R. Grigorovici, A. Vancu, "Optical properties and electronic structure of amorphous germanium", *Phys. Status Solidi*, **15** (1966) 627–637.

22. J. Tauc, *Optical Properties of Solids*, F. Abeles ed. North Holland, 1972.

23. E. Davis, N. Mott, "Conduction in non-crystalline systems V. Conductivity, optical absorption and photoconductivity in amorphous semiconductors", *Philos. Mag.*, **22** (1970) 903–922.

24. P. Kubelka, F. Munk, "Ein Beitrag zur Optik der Farbanstriche", *Zeits F. Teckn. Physik.*, **12** (1931) 593–601.

25. R. Bari, V. Ganesan, S. Potadar, L. Patil, "Structural, optical and electrical properties of chemically deposited copper selenide films", *Bull. Mater. Sci.*, **32** (2009) 37–42.

26. I. Grozdanov, "Electroconductive copper selenide films on transparent polyester sheets", *Synthetic Metals*, **63** (1994) 213–216.

27. G. Sakr, I. Yahia, M. Fadel, S. Fouad, N. Romcevic, "Optical spectroscopy, optical conductivity, dielectric properties and new methods for determining the gap states of CuSe thin films", *J. Alloys Comp.*, **507** (2010) 557–562.

28. D. Rajesh, R. Chandrakanth, C. Sunandana, "Annealing effects on the properties of copper selenide thin films for thermoelectric applications", *IOSR J. Appl. Phys.*, **4** (2013) 65–71.

29. G. Hodes, A. Albu-Yayor, F. Decker, P. Motisuke, "Three-dimensional quantum-size effect in chemically deposited cadmium selenide films", *Phys. Rev. B*, **36** (1987) 4215–4221.

30. V. García, M. Nair, P. Nair, R. Zingaro, "Chemical deposition of bismuth selenide thin films using N,N-dimethylselenourea", *Semicond. Sci. Technol.*, **12** (1997) 645–653.

31. S. Kasap, J.B. Frey, G. Belev, O. Tousignant, H. Mani, L. Laperriere, A. Reznik, J.A. Rowlands, "Amorphous selenium and its alloys from early xeroradiography to high resolution X-ray image detectors and ultrasensitive imaging tubes", *Phys. Status Solidi*, **246** (2009) 1794–1805.

32. M. Benkhedir, *Defect Levels in Amoprphous Selenium Bandgap*, Katholieke Universiteit Leuven, PhD Thesis 2006.

33. M. Singh, K. Bhahada, Y. Vijay, "Variation of optical band gap in obliquely deposited selenium thin films", *Indian J. Pure Appl. Phys.*, **43** (2005) 129–131.

34. F. Urbach, "The long-wavelength edge of photographic sensitivity and of the electronic absorption of solids", *Phys. Rev.*, **92** (1954) 1324.

35. F.B. Li, H.Z. Li, "Photocatalytic properties of gold/gold ion-modified titanium dioxide for wastewater treatment", *Appl. Catal. A*, **228** (2002) 15–27.

36. P. Kumar, K. Singh, "Wurtzite ZnSe quantum dots: Synthesis, characterization and PL properties", *J. Opto. Biomed. Mater.*, **1** (2009) 59–69.

37. J.G. Yu, Y.R. Su, B. Cheng, "Template-free fabrication and enhanced photocatalytic activity of hierarchical macro-/mesoporous titania", *Adv. Funct. Mater.*, **17** (2007) 1984–1990.

38. K. Urmila, N. Asokan, B. Pradeep, "Photoluminescence study of copper selenide thin films", *AIP Conf. Proc.*, **1391** (2011) 770–772.

39. W.S. Chong, "Synthesis and characterization of copper selenide nanoparticles via emulsion technique". *A project report submitted to the Department of Chemical Science Faculty of Science, Universiti Tunku Abdul Rahman*, In partial fulfilment of requirements for the degree of Bachelor of Science (Hons) Chemistry, May 2011.

40. C.H. Shen, H.Y. Chen, H.-W. Lin, S. Gwo, A.A. Klochikhin, V.Y. Davydov, "Near-infrared photoluminescence from vertical InN nanorod arrays grown on silicon: Effects of surface electron accumulation layer", *Appl. Phys. Lett.*, **88** (2006) 253104.

41. P. Wei, S. Chattopadhyay, F. Lin, C. Hsu, S. Jou, J. Chen, P. Huang, H. Hsu, H. Shih, K. Chen, L. Chen, "Origin of the anomalous temperature evolution of photoluminescence peak energy in degenerate InN nanocolumns", *Opt. Express*, **17** (2009) 11690–11697.

42. S.V. Gaponenko, *Optical Properties of Semiconductor Nanocrystals*, Cambridge University Press, Cambridge, 1998.

43. A. Shik, *Quantum Wells: Physics and Electronics of Two-*

Dimensional Systems, World Scientific, Singapore, 1997.

44. S.G. Tomlin, E. Khawaja, G.M.K. Thutupalli, "The optical properties of amorphous and crystalline germanium", *J. Phys. C*, **9** (1976) 4335–4347.

Low-temperature photoluminescence of CuSe$_2$ nano-objects in selenium thin films

Martina Gilić[1,*], Milica Petrović[1], Jovana Ćirković[2], Novica Paunović[1],
Svetlana Savić-Sević[1], Željka Nikitović[1], Maja Romčević[1], Ibrahim Yahia[3],
Nebojša Romčević[1]

[1]*Institute of Physics Belgrade, University of Belgrade, Pregrevica 118, Belgrade, Serbia*
[2]*The Institute for Multidisciplinary Research, University of Belgrade, Belgrade, Serbia*
[3]*Nano-Science and Semiconductors Labs., Physics Department, Faculty of Education, Ain Shams University, Roxy, Cairo, Egypt*

Abstract

Thin films of CuSe$_2$ nanoparticles embedded in selenium matrix were prepared by vacuum evaporation method on a glass substrate at room temperature. The optical properties of the films were investigated by photoluminescence spectroscopy (T = 20–300 K) and UV-VIS spectroscopy (T = 300 K). Surface morphology was investigated by scanning electron microscopy. The band gap for direct transition in CuSe$_2$ was found to be in the range of 2.72–2.75 eV and that for indirect transition is in the range of 1.71–1.75 eV determined by UV-VIS spectroscopy. On the other hand, selenium exhibits direct band gap in the range of 2.33–2.36 eV. All estimated band gaps slightly decrease with the increase of the film thickness. Photoluminescence spectra of the thin films clearly show emission bands at about 1.63 and 2.32 eV at room temperature, with no shift observed with decreasing temperature. A model was proposed for explaining such anomaly.

Keywords: chalcogenides, thin films, optical properties, spectroscopy, SEM

I. Introduction

Selenides of copper (Cu-Se) exist in many phases and structural forms: i) stoichiometric forms, such as CuSe (klockmannite), Cu$_2$Se$_x$, CuSe$_2$ (marcasite), α-Cu$_2$Se (bellidoite), Cu$_3$Se$_2$ (umangite), Cu$_5$Se$_4$ (athabaskite), Cu$_7$Se$_4$ etc., as well as ii) non-stoichiometric forms, such as Cu$_{2-x}$Se (berzelianite). All those phases can be classified into several crystallographic forms (monoclinic, cubic, tetragonal, hexagonal, etc.). Copper selenide is a semiconductor with p-type conductivity, and has numerous applications in various devices, such as solar cells [1–3], photo detectors [4], optical filters [5], microwave shielding [6], thermoelectric converters [7], etc. Photovoltaic cells and Shottky diodes are also based on these metal chalcogenide compounds [8,9]. CuSe$_2$ is a superconductor at low temperatures with a transition temperature $T_C \sim 2.4$ K [10], and has a weak ferro-

magnetic response below 31 K [11,12]. CuSe$_2$ is widely used as a precursor material for CuInSe$_2$ (CIS) and Cu(In,Ga)Se$_2$ (CIGS) preparation, suitable for highly efficient photovoltaic elements [13]. Also, CuSe$_2$ is used as a typical anion conductor and significant Cu-Se alloys targets for the preparation of CIGS/CIS thin film solar cells in RF magnetic sputtering [14].

Possible application of Cu-Se strongly depends on its optical properties. Despite the numerous publications of the optical properties of Cu-Se thin films, the estimated value of band gap of Cu-Se is not well defined. Cu-Se has both direct and indirect transitions, so the presence of both band gaps, direct and indirect, can be observed. Literature data are quite controversial: direct allowed transitions are reported to have corresponding band gap in the range of 2 to 3 eV, and indirect band gap between 1.1 and 1.5 eV [15–18]. The indirect band gap being near the optimum value for solar cell applications makes this material capable of potentially offer a high efficiency of conversion. However, Cu-Se nanoparticles

*Corresponding author: tel: +381 11 3713 036,
fax: +381 11 3713 052, e-mail: *martina@ipb.ac.rs*

have been reported to possess a direct band gap of 4 eV and indirect one of 1.87 eV [19]. The reasons of such variation in band gaps could lie in the sharp cut off of the wavelength with the spectral transmittance instead of the slow increase, the presence of large number of dislocations, wide range of stoichiometric deviation and quantum confinement effect.

In our previous report [20], we prepared Cu-Se thin films of three different thicknesses by vacuum evaporation technique using Mo boat onto glass substrate at room temperature, and investigated their structural properties. XRD and far-infrared spectroscopy revealed the presence of $CuSe_2$ nanocrystals in predominant Se films.

The objective of this research was to determine optical properties of Cu-Se thin films, using UV-VIS and low-temperature photoluminescence spectroscopy, and to investigate how the film thickness could influence the band gap value and photoluminescence properties. SEM analysis was also performed in order to get information about the morphology of the obtained Cu-Se thin films.

II. Experimental

Thin films were obtained by evaporating commercially high purity CuSe powder (99.99%) supplied from Aldrich Company. The powder was deposited onto highly pre-cleaned glass substrates with use of Mo boat. The procedure was done in a high-vacuum environment with typical background pressures of 3 mPa. The deposition rate, 10 nm/s, was monitored by quartz crystal thickness monitor - FTM4, Edwards and the final films thicknesses was found to be 56 nm, 79 nm and 172 nm for the films labelled as F-55, F-80 and F-170, respectively [20].

SEM imaging was done using scanning electron microscope equipped with a high brightness Schottky field emission gun (FEGSEM, TESCAN) operating at 4 kV. The samples were coated with gold/palladium to make them conductive.
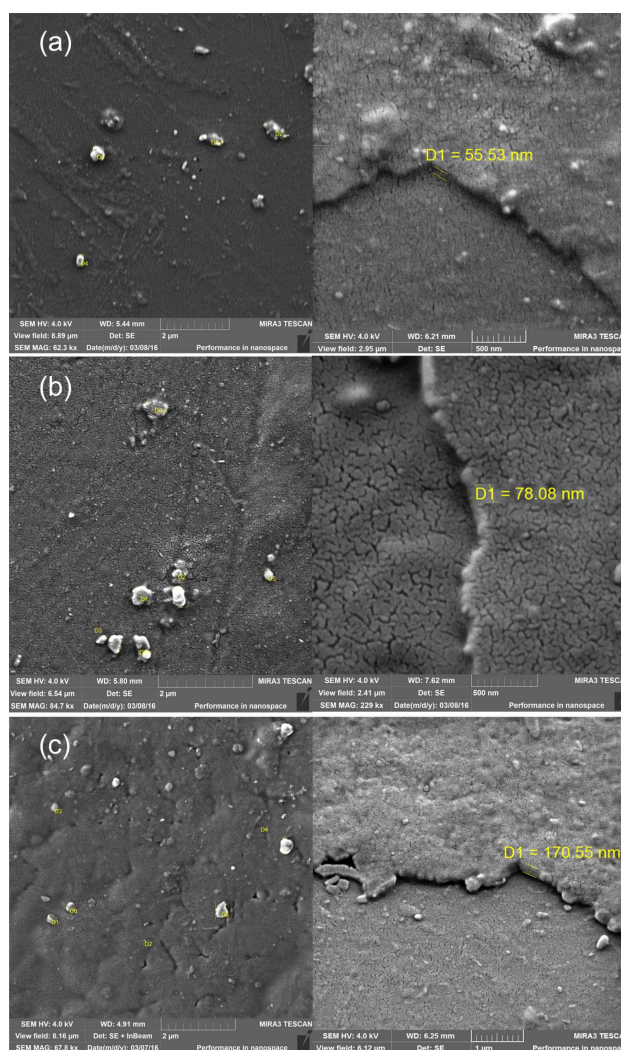
The UV-VIS diffusion reflectance and transmittance spectra were recorded in the wavelength range of 300–1000 nm on a Shimadzu UV-2600 spectrophotometer equipped with an integrated sphere. The diffuse reflectance and transmittance spectra were measured relative to a reference sample of $BaSO_4$.

Photoluminescence measurements on various temperatures (T = 20–300 K) were obtained by Jobin-Yvon U1000 spectrometer, equipped with RCA-C31034A photomultiplier with housing cooled by Peltier element, amplifiers and counters. The 488 nm laser line of argon laser was used as excitation source.

III. Results and discussion

3.1. SEM analyses

Scanning electron microscopy (SEM) images were obtained for the Cu-Se thin films deposited on glass substrate in order to study the surface morphology and

Figure 1. Top view and tilted SEM micrographs of films: a) F-55, b) F-80 and c) F-170

agglomeration of the samples.

Top view and tilted micrographs of the thin films are presented in Fig. 1. From the top view micrographs it can be observed that the surface of the samples is relatively uneven and rather rough, with presence of cracks and voids. Formation of the Cu-Se thin films most probably proceed unevenly, in the form of islands which later grew into agglomerates. Agglomerated clusters of few hundreds nanometers in diameter are distributed nonuniformly along the surface and form the structure consisting of $CuSe_2$ nanocrystals in predominant Se matrices. In order to determine the film thicknesses, the samples were tilted at 30°. The thicknesses estimated by SEM are: ~56 nm, ~78 nm and ~171 nm for the films F-55, F-80 and F-170, respectively. The thickness values estimated by SEM analysis match the ones obtained during the preparation of thin films.

3.2. UV-VIS spectroscopy

In Fig. 2 diffuse reflectance R and transmittance T spectra of the thin films samples in the wavelength range 300–1000 nm (4.13–1.24 eV) on room temperature (*T*
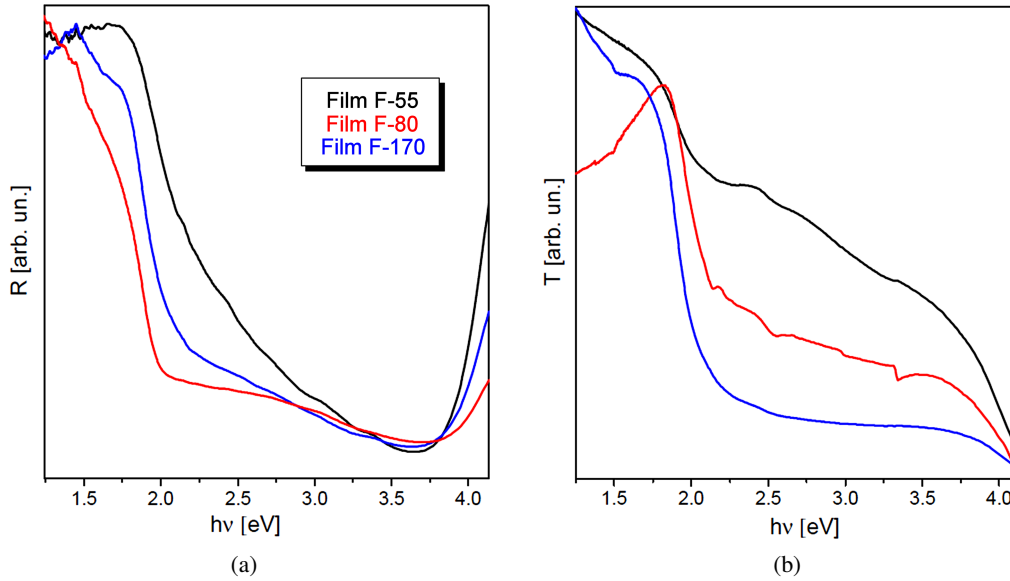
Figure 2. Diffuse reflectance, *R* (a), and transmittance, *T* (b) spectra

= 300 K) are presented. As it can be seen, the transmittance increases with decrease in the film thickness, which is not the case for reflectance. This is typical for films with high electrical conductivity and implies a reflection coefficient nearing 1 for films with metallic conductivity.

In this study we used the Tauc plot for the determination of the optical band gap from diffuse reflectance measurements. The determination of band gap in semiconductors is significant for obtaining the basic solid state physics. The relation expression proposed by Tauc, Davis and Mott [21–23] is the following:

$$\alpha \cdot h \cdot v = A \left(h \cdot v - E_g \right)^{1/n} \quad (1)$$

where *h* is the Planck's constant, *A* is the transition probability constant depending on the effective mass of the charge carriers in the material, E_g is the band gap, $h \cdot v$ is the photon energy and α is the absorption coefficient which is defined as the relative rate of decrease in light intensity along its propagation path, i.e. a property of a material that defines the amount of light absorbed by it. The value of *n* denotes the nature of the transition. In case of direct transitions *n* equals ½ and ³⁄₂ for allowed and forbidden transitions, respectively. As for indirect transitions, *n* equals 2 and 3 for allowed and forbidden transitions, respectively. Since CuSe exhibits both direct and indirect allowed transitions, *n* = ½ and n = 2.

Then, the acquired diffuse reflectance spectra are converted to Kubelka-Munk function [24]:

$$\alpha = \frac{(1-R)^2}{2R} \quad (2)$$

So using this function, a plot of $(\alpha \cdot h \cdot v)^{1/n}$ against $h \cdot v$ is obtained. The energy band gap is determined by extrapolating the linear portion of $(\alpha \cdot h \cdot v)^{1/n}$ vs. $h \cdot v$
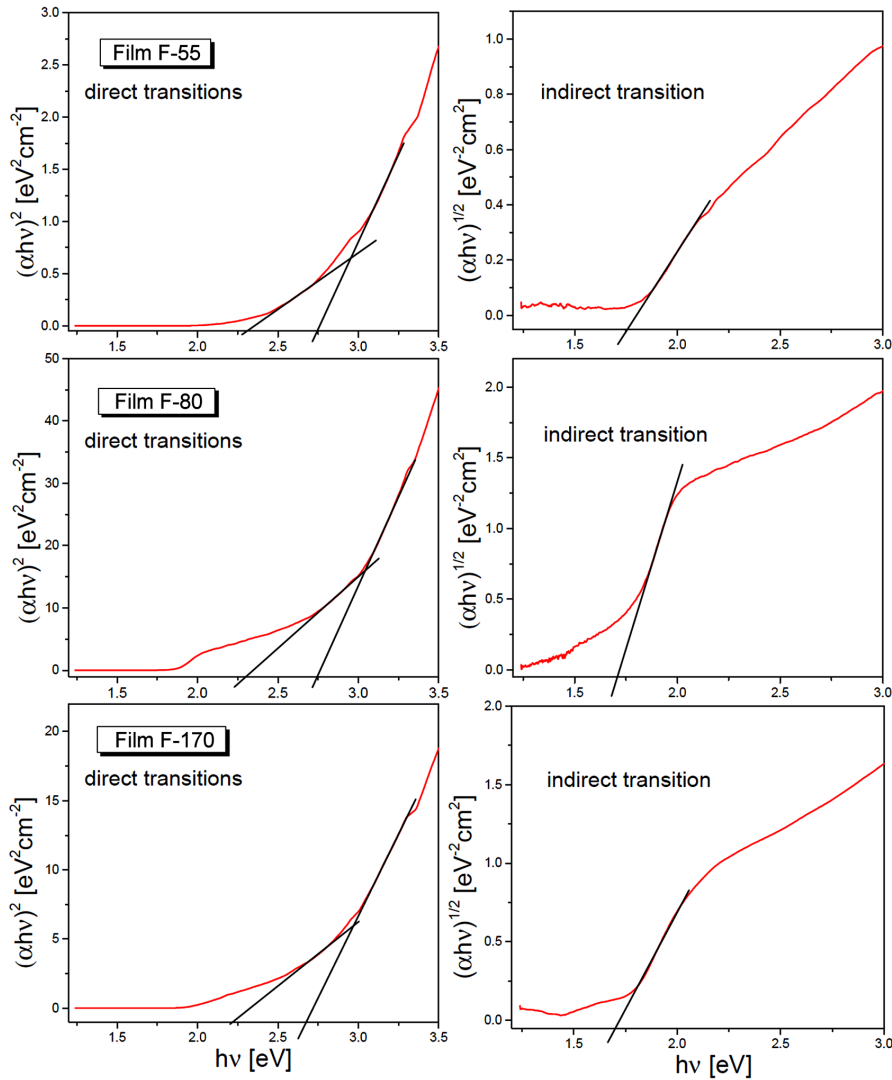
to the energy axis at $(\alpha \cdot h \cdot v)^{1/n} = 0$. The intercept of these plots on the energy axis gives the energy band gap. Such plots are given in Fig. 3. Direct transitions (left part of Fig. 3) reveal band gap for both selenium and CuSe₂, while indirect transitions (right part of Fig. 3) reveal band gap for CuSe₂ only.

The experimentally determined values of energy gaps for CuSe₂ show slight decrease with film thickness and their values range from 2.75 to 2.72 eV for direct transitions, and from 1.75 to 1.71 eV in case of indirect transitions. The estimated band gaps for selenium follow the same trend with film thickness and range between 2.33 and 2.36 eV. The estimated band gap positions for each sample are given in Table 1. The difference in the film thicknesses causes the small difference in band gaps in the second decimal place and they follow the well-established trend, the smaller the thickness, the wider the band gap is. Also, their values are quite wider than the ones that can be found in literature [7,16,25–33].

Table 1. Estimated band gap energies of thin films determined with UV-VIS spectroscopy

	F-55	F-80	F-170
CuSe₂ direct transition [eV]	2.75	2.74	2.72
CuSe₂ indirect transition [eV]	1.75	1.72	1.71
Se direct transition [eV]	2.36	2.34	2.33

Broad range of energy band gap values for Cu-Se can be found in literature. For direct transitions those values are usually between 2 and 3 eV. Bari *et al.* [25] obtained the value of 2.51 eV for the sample with thickness of 150 nm, and with the increase of film thickness they reported the decrease of band gap width. Grozdanov [26], Garcia *et al.* [16] and Sakr *et al.* [27] obtained the value of 2.33, 2.13–2.38 and 2.74 eV, respectively. The latter is very similar to the results obtained in this paper. Rajesh *et al.* [28] got a diversity of band gaps ranging from

Figure 3. Dependence of $(\alpha \cdot h \cdot \nu)^2$ on photon energy $(h \cdot \nu)$ – left side, and dependence of $(\alpha \cdot h \cdot \nu)^{1/2}$ on photon energy $(h \cdot \nu)$ – right side

1.95 (the thickest film) to 3.70 eV (the thinnest film). However, for indirect transitions they received less attention. Garcia *et al.* [16] obtained values in the range 1.22–1.34 eV, whereas the value obtained by Bhuse *et al.* [7] is about 1.4 eV. Our values (~1.7 eV) are bigger than the reported in literature. According to our opinion, the larger indirect band gap values are due to quantum confinement effect [29,30] whereby the electrons are localized in individual crystallites, and due to specific border conditions between $CuSe_2$ nanoparticles and selenium matrix.

For the pure selenium, the direct band gap was reported to be about 2 eV for the bulk [31,32] and 2.20–2.06 for the thin films of thickness 130–290 nm [33]. Our films are thinner than the ones mentioned in the literature and it is not surprising that we obtained wider band gap values, about 2.3 eV. The film F-170 has the thickness between 130 and 290 nm, but the higher value in band gap is the result of specific border conditions between selenium matrix and $CuSe_2$ nanoparticles. We presume that $CuSe_2$ nanoparticles directly influence the band gap of predominant selenium, and vice versa.

The Urbach energy is also analysed. Urbach rule states that the optical absorption coefficient α just below the band edge in insulators and semiconductors varies exponentially with the incident photon energy [34]:

$$\alpha = \alpha_0 \exp\left(\frac{h \cdot \nu}{E_U}\right) \qquad (3)$$

where α_0 is a constant and characteristic parameter of the material, $h \cdot \nu$ is incident photon energy, and the term E_U which is the width of the exponential tail is called Urbach energy. The Urbach energy represents the width of defect states in the band gap. Figure 4 shows $\log \alpha$ as a function of incident photon energy for the film F-170, as a representative one. By extrapolating the linear part of the plot and with use of Equation 3, the Urbach energy can be determined as the inverse of the slope and α_0 from the intercept of extrapolated plot. From the slope and inception of extrapolated plot it was determined that E_U is 0.32 eV and α_0 is 3.02 cm^{-1}.
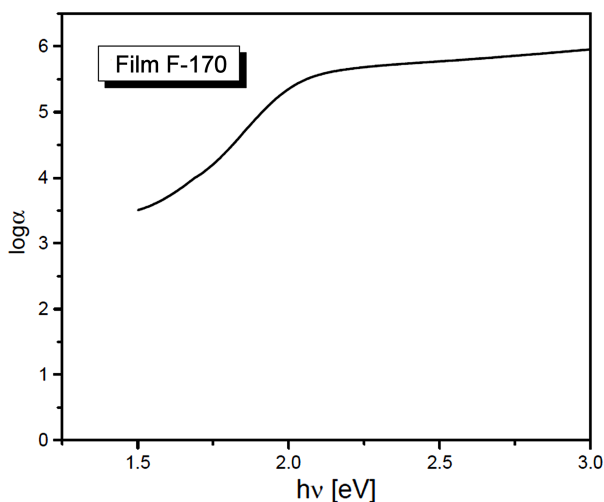
Figure 4. Logarithmic dependence of the absorption coefficient on the photon energy for F-170 film

3.3. Photoluminescence spectroscopy

Photoluminescence (PL) spectra can be used for investigating the possible outcomes of photo-induced electrons and holes in a semiconductor, since photoluminescence emission results from the recombination of free charge carriers. There are two types of photoluminescence phenomenon according to its attributes and formation mechanism: the band-to-band photoluminescence and the excitonic photoluminescence [35–37]. The band-to-band PL spectrum regards the separation situation of photo-generated charge carriers. The excitonic PL spectrum, however, cannot directly reflect the separation situation of photo-induced carriers. If discrete energy levels are present in the band gap, these may dominate the optical spectrum. PL measurements then yield information about the energetic positions of the electronic states in the gap. Such localized states can originate from various types of imperfections like vacancies, interstitial atoms, atoms at surfaces and grain boundaries. However, it is often difficult to determine the exact position and origin of these states.

Photoluminescence spectra of thin films on various temperatures are presented in Fig. 5. The spectra are rather complex, thus for their analysis the deconvolution method had to be employed. Two typical resolved spectra are presented in Fig. 6 (on 20 K and room temperature), and the deconvolution of the others is done in the same manner. Each spectrum is characterized with 5 bands. Band-to-band photoluminescence dominates the room temperature spectra. The band in red area at ~1.6 eV is clearly seen. According to the UV-VIS results (see previous chapter), we can attribute this mode to band-to-band transition for indirect transition in CuSe$_2$. In green area, a broad band is observed at ~2.3 eV which originates from direct transitions in selenium (also see prev. chapter). Due to Stokes shift, the obtained positions are a bit lower than the ones obtained by UV-VIS spectroscopy. Between these two bands there are three defect modes at 2.1 eV, 1.9 eV and
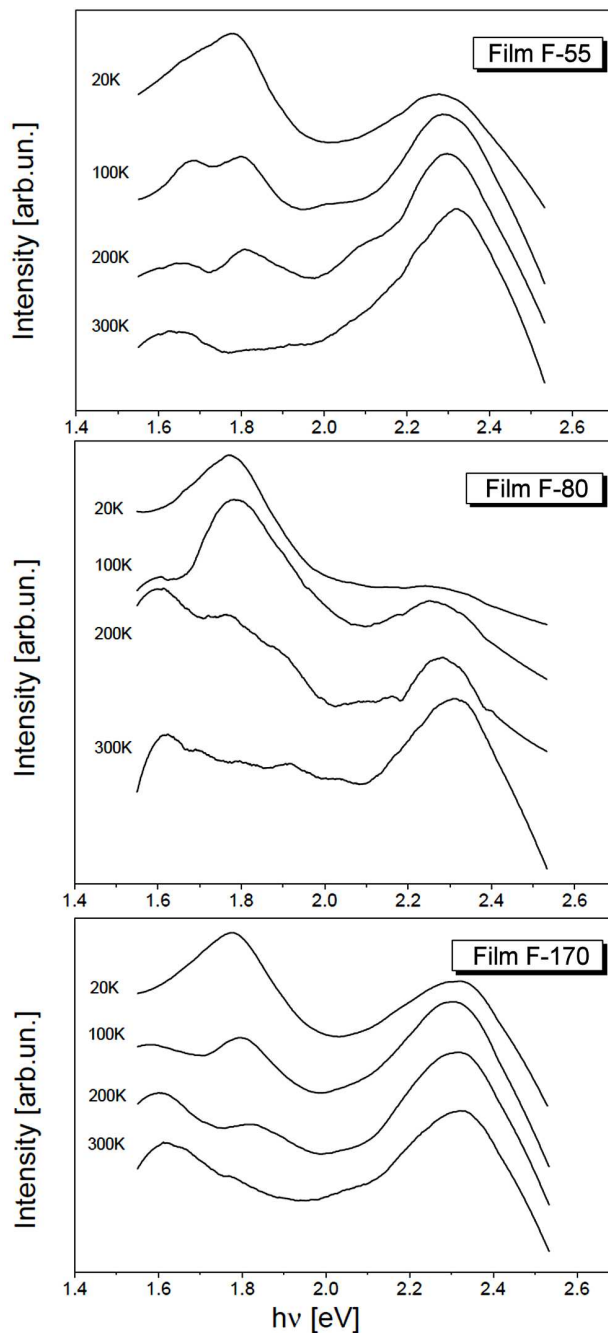

Figure 5. Photoluminescence spectra of thin films at various temperatures: a) F-55, b) F-80 and c) F-170

1.8 eV, which are of small intensity on room temperature. Lowering the temperature, the band at ~1.8 eV increases its intensity, and becomes the dominant one at 20 K. According to literature data [32] this band is attributed to selenium defect mode – negative U-centre. This mode is expected to appear at 0.5 eV from the band edges. Another two defect modes, at 2.1 and 1.9 eV, are attributed to the defect modes of CuSe$_2$, according to the work of Urmila *et al.* [38]. In their work they obtained bands at 2.1, 1.9 and 1.5 eV in PL spectrum of Cu$_7$Se$_4$ thin film. They concluded that there is nonradiative transition from conduction band to defect levels with energies 2.1, 1.9 and 1.5 eV and from these lev-
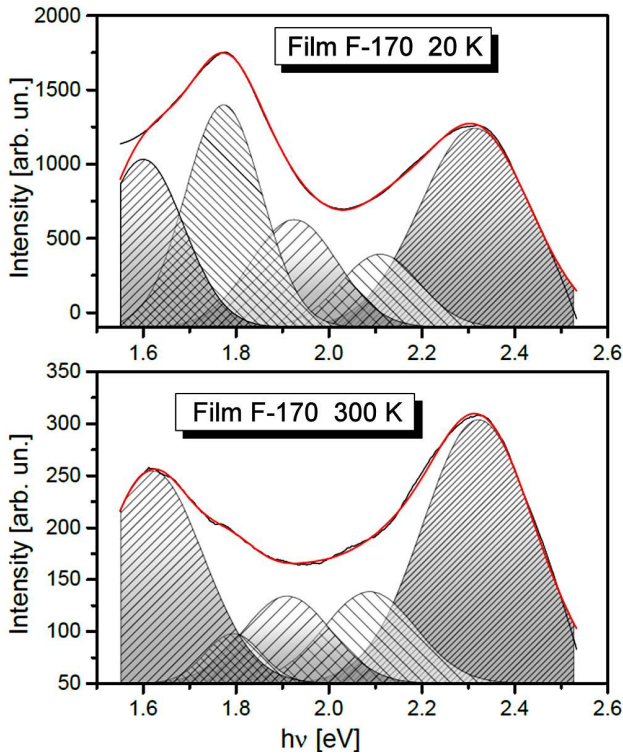
Figure 6. Typical resolved photoluminescence spectra of thin films F-170: a) on 20 K and b) room temperature
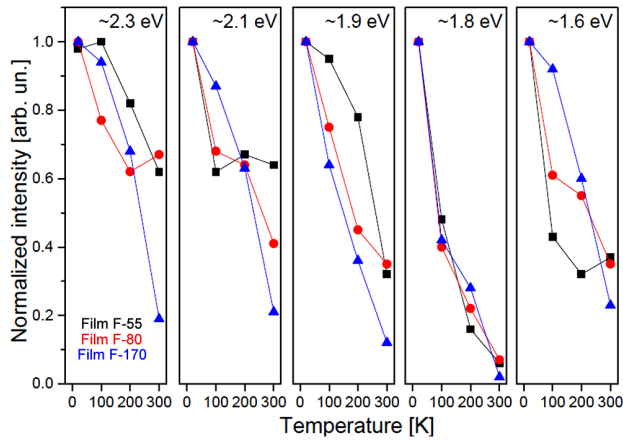

Figure 7. Temperature dependence of PL emission bands intensities, normalized on the most intensive ones (black squares – film F-55, red circles – film F-80, blue triangles – film F-170)

els radiative transitions occurred to valence band. The values 2.1 and 1.9 eV match the band positions we obtained in this work, thus we can assign these bands to defect modes in $CuSe_2$. Due to predominant phase of selenium, these bands are hidden by the bands originated from selenium and cannot be observed without the deconvolution method. Chong [39] in his work also obtained a PL band at ~2.16 eV without assigning it to any transition. In all spectra, the uprise of peak intensity with lowering temperature is observed, Fig. 7. The intensities have their maximum values at the lowest temperature (20 K) and show decrease with rising temperature. The most radical decrease is observed for the band

at ~1.8 eV, which intensity drops to ~40% at 200 K, and only to ~6% at room temperature.

Temperature dependence of PL emission band positions is shown in Fig. 8. Let us discuss the band position of indirect transitions of $CuSe_2$. At the room temperature, there are differences on the second decimal place for films of different thicknesses, the same as observed when analysing UV-VIS spectra. The same trend is observed on 20 K. If the shift of this band with temperature is analysed for each film, it can be noticed the temperature invariance, i.e. small non-monotonous differences in positions on the second decimal place. This is in contradiction with the expected red shift, characteristic for the semiconductors. The temperature invariance is observed for other bands as well. There is a question that needs to be answered: why the PL measurements show no shift with increasing temperature, instead of the conventional red shift characteristic for the semiconductors? A model proposed by Shen *et al.* [40] explains those discrepancies. It involves surface electron accumulation as a result of severe band bending in nanorods. However, the same trend was observed in thin film samples (including ours), whose curvature-less surface does not support a spatial charge separation such as in 1D nanostructures. Wei *et al.* [41] gave more exact explanation of this phenomenon in their work. They began the analysis by making difference between E_{PL} and E_g:

$$E_{PL}(n, T) = E_g(n, T) + E_{Fn}(n, T) - E_{Fp}(n, T) \quad (4)$$

where E_{Fn} and E_{Fp} are the electron and hole quasi-Fermi levels measured from the bottom of conduction band and the top of valence band, respectively. So the temperature dependence of the band gap shift is the competition between the lattice dilation dE_g/dT on the one hand, and the sum $(dE_{Fn}/dT - dE_{Fp}/dT)$ on the other hand. The former results in the conventional red shift of the band gap with increasing temperature and the latter gets the blue shift. The resulting shift depends
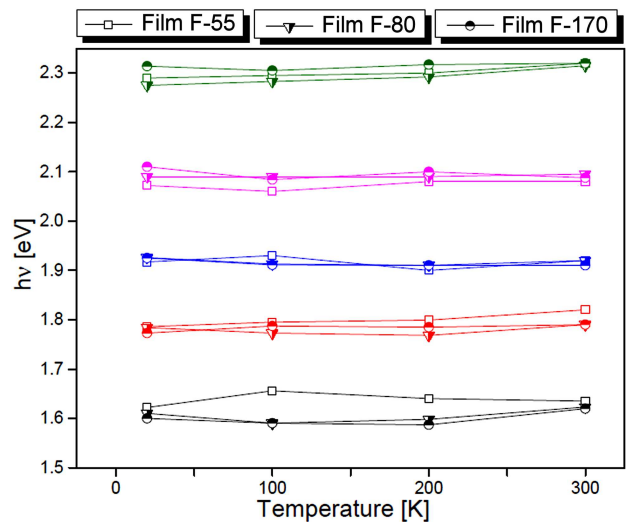

Figure 8. Temperature dependence of photoluminescence emission bands positions

on the magnitude of these two contributions. Usually when the electron density n is high, the thermal response in the material is governed by electronic rather than photonic interactions, the sum $(dE_{Fn}/dT - dE_{Fp}/dT)$ becomes dominant thus the blue shift of E_{PL} is observed. However, if these two contributions are of the same magnitude, it will result in no shift with changing temperature, as in case of our samples.

PL emission bands positions as a function of film thicknesses are presented in Fig. 9. It is common knowledge that as the confining dimension decreases, typically in nanoscale, the energy spectrum turns to discrete so the band gap of a semiconductor becomes size dependent. For one-dimensional confinement (film thickness), the quantization energies increase when the size along the confinement direction decreases [42,43]. In an amorphous or structurally disordered film, the imperfection in the film causes the bands of localized states to get broaden and a band gap reduction may occur due to the Urbach edge [44]. If we observe the shift of the band at ~1.6 eV, which corresponds to indirect transitions in $CuSe_2$, we can see the blue shift with decreasing size, as being expected. On the other hand, the band at ~2.3 eV which corresponds to direct transitions in Se, we can see no size dependence with the band position. The reason of this behaviour lies in specific composition of our films, i.e. $CuSe_2$ nano-objects embedded in selenium matrix. The particles of $CuSe_2$ are small enough to react on the size reduction, but the selenium matrix the amorphous effect becomes dominant.

As it can be seen from the above, the temperature changes do not affect the band gap. The size changes, i.e. the reduction of film thickness affects the band gap only on a second decimal place. Thus, we can state that the low cost technique of vacuum evaporation gives us the opportunity to produce quality, stable thin films
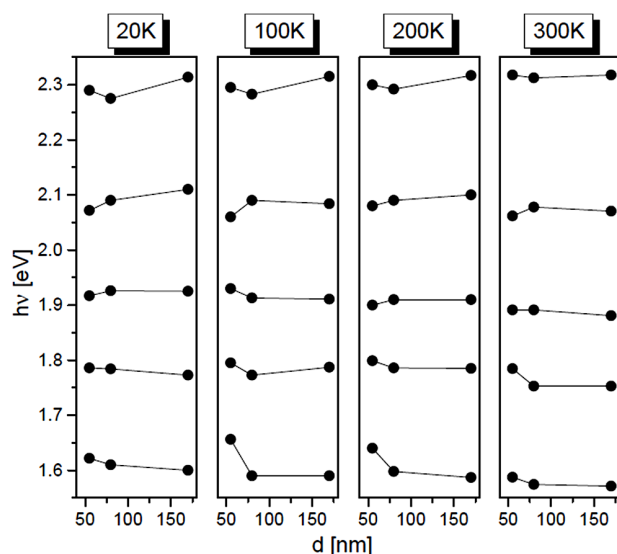
suitable for further applications in heterojunction solar cells and photo detectors.

IV. Conclusions

Cu-Se thin films of three different thicknesses, obtained by vacuum evaporation technique on glass substrate, underwent through photoluminescence investigation along with UV-VIS measurements and SEM analysis. Reflectance measurements revealed values for both direct and indirect band gap: ~2.7 and 1.7 eV, respectively for $CuSe_2$ and ~2.3 eV for Se. The existence of indirect band gap in $CuSe_2$ at this value, little wider than in literature, is confirmed by photoluminescence measurements. A band at ~1.8 eV, registered by PL measurements at low temperatures, is attributed to defect level of selenium – negative U-center. In this paper we proved that simple and low-cost technique as vacuum evaporation is capable of producing high-quality thin films.

References

1. T.P. Hsieh, C.C. Chuang, C.S. Wu, J.C. Chang, J.W. Guo, W.C. Chen, "Effects of residual copper selenide on CuInGaSe$_2$ solar cells", *Solid State Electron.*, **56** (2011) 175–178.
2. M. Singh, J. Jiu, T. Sugahara, K. Suganuma, "Thin-film copper indium gallium selenide solar cell based on low-temperature all-printing process", *ACS Appl. Mater. Interfaces*, **6** (2014) 16297–16303.
3. J.H. Scofield, A. Duda, D. Albin, B.L. Ballard, P.K. Predecki, "Sputtered molybdenum bilayer back contact for copper indium diselenide-based polycrystalline thin-film solar cells", *Thin Solid Films*, **260** (1995) 26–31.
4. S. Lei, A. Sobhani, F. Wen, A. George, Q. Wang, Y. Huang, P. Dong, B. Li, S. Najmaei, J. Bellah, G. Gupta, A.D. Mohite, L. Ge, J. Lou, N.J. Halas, R. Vajtai, P. Ajayan, "Ternary CuIn$_7$Se$_{11}$: Towards ultra-thin layered photodetectors and photovoltaic devices", *Adv. Mater.*, **45** (2014) 7666–7737.
5. G. Juska, V. Gulbinas, A. Jagminas, "Transient absorption of copper selenide nanowires of different stoichiometry", *Lith. J. Phys.*, **50** (2010) 233–239.
6. C. Levy-Clement, M. Neumann-Spallart, S.K. Haram, K.S.V. Santhanam, "Chemical bath deposition of cubic copper (I) selenide and its room temperature transformation to the orthorhombic phase", *Thin Solid Films*, **302** (1997) 12–16.
7. V.M. Bhuse, P.P. Hankare, K.M. Garadkar, A.S. Khomane, "A simple, convenient, low temperature route to grow polycrystalline copper selenide thin films", *Mater. Chem. Phys.*, **80** (2003) 82–88.
8. S.Y. Zhang, C. Fang, Y. Tian, K. Zhu, B. Jin, Y. Shen, J. Yang, "Synthesis and characterization of hexagonal CuSe nanotubes by templating against trigonal Se nanotubes", *Cryst. Growth Des.*, **6** (2006) 2809–2813.
9. H.M. Pathan, C.D. Lokhande, D.P. Amalnerkar, T. Seth, "Modified chemical deposition and physico-chemical

Figure 9. PL emission bands positions dependence of film thicknesses

properties of copper (I) selenide thin films", *Appl. Surf. Sci.*, **211** (2003) 48–56.

10. Y. Takana, N. Uchiyama, S. Ogawa, N. Mori, Y. Kimishima, S. Arisawa, A. Ishii, T. Hatano, K. Togano, "Superconducting properties of $CuS_{2-x}Se_x$ under high pressure", *Physica C: Superconduct.*, **341-348** (2000) 739–740.

11. G. Krill, P. Panissod, M.F. Lapierre, F. Gautier, C. Robert M.N. Eddine, "Magnetic properties and phase transitions of the metallic CuX_2 dichalogenides (X = S, Se, Te) with pyrite structure", *J. Phys. C*, **9** (1976) 1521–1533.

12. M. Kontani, T. Tutui, T. Moriwaka, T. Mizukoshi, "Specific heat and NMR studies on the pyrite-type superconductors CuS_2 and $CuSe_2$", *Physica B*, **284** (2000) 675–676.

13. R.R. Pai, T.T. John, M. Lakshimi, K.P. Vijayakumar, C.S. Kartha, "Observation of phase transitions in chemical bath deposited copper selenide thin films through conductivity studies", *Thin Solid Films*, **473** (2005) 208–212.

14. N.H. Kim, S. Oh, W.S. Lee, "Non-selenization method using sputtering deposition with a $CuSe_2$ target for CIGS thin film", *J. Korean Phys. Soc.*, **61** (2012) 1177–1180.

15. P. Hankare, A. Khomane, P. Chate, K. Rathod, K. Garadkar, "Preparation of copper selenide thin films by simple chemical route at low temperature and their characterization", *J. Alloys Comp.*, **469** (2009) 478–482.

16. V. Garcia, P. Nair, M. Nair, "Copper selenide thin films by chemical bath deposition", *J. Cryst. Growth*, **203** (1999) 113–124.

17. O. Arellano-Tanori, M. Acosta-Enriquez, R. Ochoa-Landin, R. Iniguez-Palomares, T. Mendivil-Reynoso, M. Flores-Acosta, S. Castillo, "Copper-selenide and copper-telluride composites powders sintetized by ionic exchange", *Chalcogenide Lett.*, **11** (2014) 13–19.

18. A. Jagminas, R. Juskenas, I. Gailiute, G. Statkute, R. Tomasinuas, "Electrochemical synthesis and optical characterization of copper selenide nanowire arrays within the alumina pores", *J. Cryst. Growth*, **294** (2006) 343–348.

19. D. Patidar, N.S. Saxena, "Characterization of single phase copper selenide nanoparticles and their growth mechanism", *J. Cryst. Growth*, **343** (2012) 68–72.

20. M. Gilic, M. Petrovic, R. Kostic, D. Stojanovic, T. Barudzija, M. Mitric, N. Romcevic, U. Ralevic, J. Trajic, M. Romcevic, I. Yahia, "Structural and optical properties of $CuSe_2$ nanocrystals formed in thin solid Cu-Se film", *Infrared Phys. Techn.*, **76** (2016) 276–284.

21. J. Tauc, R. Grigorovici, A. Vancu, "Optical properties and electronic structure of amorphous germanium", *Phys. Status Solidi*, **15** (1966) 627–637.

22. J. Tauc, *Optical Properties of Solids*, F. Abeles ed. North Holland, 1972.

23. E. Davis, N. Mott, "Conduction in non-crystalline systems V. Conductivity, optical absorption and photoconductivity in amorphous semiconductors", *Philos. Mag.*, **22** (1970) 903–922.

24. P. Kubelka, F. Munk, "Ein Beitrag zur Optik der Farbanstriche", *Zeits F. Teckn. Physik.*, **12** (1931) 593–601.

25. R. Bari, V. Ganesan, S. Potadar, L. Patil, "Structural, optical and electrical properties of chemically deposited copper selenide films", *Bull. Mater. Sci.*, **32** (2009) 37–42.

26. I. Grozdanov, "Electroconductive copper selenide films on transparent polyester sheets", *Synthetic Metals*, **63** (1994) 213–216.

27. G. Sakr, I. Yahia, M. Fadel, S. Fouad, N. Romcevic, "Optical spectroscopy, optical conductivity, dielectric properties and new methods for determining the gap states of CuSe thin films", *J. Alloys Comp.*, **507** (2010) 557–562.

28. D. Rajesh, R. Chandrakanth, C. Sunandana, "Annealing effects on the properties of copper selenide thin films for thermoelectric applications", *IOSR J. Appl. Phys.*, **4** (2013) 65–71.

29. G. Hodes, A. Albu-Yayor, F. Decker, P. Motisuke, "Three-dimensional quantum-size effect in chemically deposited cadmium selenide films", *Phys. Rev. B*, **36** (1987) 4215–4221.

30. V. García, M. Nair, P. Nair, R. Zingaro, "Chemical deposition of bismuth selenide thin films using N,N-dimethylselenourea", *Semicond. Sci. Technol.*, **12** (1997) 645–653.

31. S. Kasap, J.B. Frey, G. Belev, O. Tousignant, H. Mani, L. Laperriere, A. Reznik, J.A. Rowlands, "Amorphous selenium and its alloys from early xeroradiography to high resolution X-ray image detectors and ultrasensitive imaging tubes", *Phys. Status Solidi*, **246** (2009) 1794–1805.

32. M. Benkhedir, *Defect Levels in Amoprphous Selenium Bandgap*, Katholieke Universiteit Leuven, PhD Thesis 2006.

33. M. Singh, K. Bhahada, Y. Vijay, "Variation of optical band gap in obliquely deposited selenium thin films", *Indian J. Pure Appl. Phys.*, **43** (2005) 129–131.

34. F. Urbach, "The long-wavelength edge of photographic sensitivity and of the electronic absorption of solids", *Phys. Rev.*, **92** (1954) 1324.

35. F.B. Li, H.Z. Li, "Photocatalytic properties of gold/gold ion-modified titanium dioxide for wastewater treatment", *Appl. Catal. A*, **228** (2002) 15–27.

36. P. Kumar, K. Singh, "Wurtzite ZnSe quantum dots: Synthesis, characterization and PL properties", *J. Opto. Biomed. Mater.*, **1** (2009) 59–69.

37. J.G. Yu, Y.R. Su, B. Cheng, "Template-free fabrication and enhanced photocatalytic activity of hierarchical macro-/mesoporous titania", *Adv. Funct. Mater.*, **17** (2007) 1984–1990.

38. K. Urmila, N. Asokan, B. Pradeep, "Photoluminescence study of copper selenide thin films", *AIP Conf. Proc.*, **1391** (2011) 770–772.

39. W.S. Chong, "Synthesis and characterization of copper selenide nanoparticles via emulsion technique". *A project report submitted to the Department of Chemical Science Faculty of Science, Universiti Tunku Abdul Rahman*, In partial fulfilment of requirements for the degree of Bachelor of Science (Hons) Chemistry, May 2011.

40. C.H. Shen, H.Y. Chen, H.-W. Lin, S. Gwo, A.A. Klochikhin, V.Y. Davydov, "Near-infrared photoluminescence from vertical InN nanorod arrays grown on silicon: Effects of surface electron accumulation layer", *Appl. Phys. Lett.*, **88** (2006) 253104.

41. P. Wei, S. Chattopadhyay, F. Lin, C. Hsu, S. Jou, J. Chen, P. Huang, H. Hsu, H. Shih, K. Chen, L. Chen, "Origin of the anomalous temperature evolution of photoluminescence peak energy in degenerate InN nanocolumns", *Opt. Express*, **17** (2009) 11690–11697.

42. S.V. Gaponenko, *Optical Properties of Semiconductor Nanocrystals*, Cambridge University Press, Cambridge, 1998.

43. A. Shik, *Quantum Wells: Physics and Electronics of Two-*

Dimensional Systems, World Scientific, Singapore, 1997.

44. S.G. Tomlin, E. Khawaja, G.M.K. Thutupalli, "The optical properties of amorphous and crystalline germanium", *J. Phys. C*, **9** (1976) 4335–4347.

Far-infrared spectra of dysprosium doped yttrium aluminum garnet nanopowder

CrossMark

J. Trajić [a,*], M.S. Rabasović [a], S. Savić-Šević [a], D. Ševic [a], B. Babić [b], M. Romčević [a], J.L. Ristić-Djurović [a], N. Paunović [a], J. Križan [c], N. Romčević [a]

[a] Institute of Physics, University of Belgrade, Pregrevica 118, 11080 Belgrade, Serbia
[b] Vinca Institute of Nuclear Sciences, University of Belgrade, 11001 Belgrade, Serbia
[c] AMI, d.o.o., Ptuj, Slovenia

HIGHLIGHTS

- YAG:Dy nanopowder was produced by Solution Combustion Synthesis (SCS) method.
- Powders are composed by well-defined and separated nanoparticles.
- Some particles are agglomerated but there are also separated particles.
- The dielectric function was modeled by the Maxwell–Garnet formula.
- Optical phonon confinement is registered.

GRAPHICAL ABSTRACT
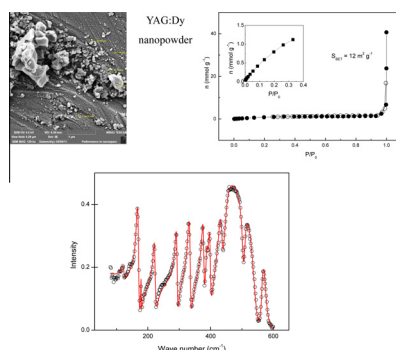
ABSTRACT

The solution combustion synthesis was used to prepare nanopowders of yttrium aluminum garnet (YAG) and YAG doped with dysprosium ions, Dy^{3+}, (YAG:Dy). The morphology, specific surface area, texture, and optical properties of the prepared materials were studied by the means of scanning electron microscopy (SEM), nitrogen adsorption method, and far-infrared spectroscopy at room temperature in the spectral region between 80 and 600 cm^{-1}. It was established that all the examined samples were microporous. The Maxwell–Garnet formula was used to model dielectric function of YAG and YAG:Dy nanopowders as mixtures of homogenous spherical inclusions in air.

© 2016 Elsevier B.V. All rights reserved.

1. Introduction

Importance of yttrium aluminum garnet, $Y_3Al_5O_{12}$, commonly abbreviated as YAG, arises from its high chemical stability as well as excellent optical and high-temperature mechanical properties [1]. It is a ceramic material with a cubic garnet crystallographic structure whose thermal expansion is isotropic, whereas its optical properties are homogeneous, without birefringence effects [2,3]. Over the last five decades the structural properties of YAG were the subject of numerous studies, which proved its technological relevance and led to its use in a broad range of applications. For example, YAG has found its role as a host material in solid-state lasers of different kinds, luminescence materials, and scintillators [4–6].

Two prospective applications particularly draw attention toward trivalent dysprosium-activated optical materials. Namely,

if the phonon energy of host matrix is low, these materials could be an alternative to praseodymium-doped optical amplifiers used in the second telecommunication window [7]. The second promising area of application, the solid-state lasers operating in the visible part of the spectrum [8], is based on the blue and yellow emissions originating from $^4F_{9/2}$ level of Dy^{3+}. These emissions are much more probable than the non-radiative relaxation to the next lower energy level, $^6F_{3/2}$, that corresponds to large energy gap of approximately 7500 cm^{-1}. Consequently, relatively high phonon energy of yttrium aluminum garnet presents YAG crystal as a prospective host material for dysprosium ions [9].

We used solution combustion synthesis (SCS) method to prepare nanopowder samples of YAG and YAG doped with 2 mol% Dy. Optical properties of the samples were analyzed by far-infrared spectroscopy (FIR), whereas nitrogen adsorption method was employed to examine specific surface area and texture. The dielectric function of the nanopowders was modeled using the Maxwell–Garnet formula.

2. Samples preparation and characterization

The SCS method used to prepare the YAG and YAG:Dy nanopowder samples was performed in several steps. Yttrium oxide (Y_2O_3) and aluminum oxide (Al_2O_3) of 99.99 % purity was purchased from the NOAH Technologies. The oxides were dissolved in HNO_3 followed by the addition of carbohydrazide to the solution of aluminum nitrate and yttrium nitrate:

$$3Y(NO_3)_3 + 5Al(NO_3)_3 + 15CH_6N_4O$$
$$\rightarrow YAG + 42N_2 + 15CO_2 + 45H_2O.$$
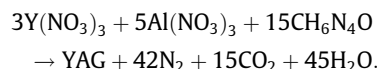
Good reactivity of the raw materials provided absence of the intermediate phases, e.g., YAM ($Y_4Al_2O_9$) or YAP ($YAlO_3$), in the obtained YAG powder. The YAG:Dy samples were produced by doping YAG host with Dy^{3+} ions using the concentration of 2 mol %. Further, YAG:Dy nanopowder was annealed in the air atmosphere at 1300 °C with the aim to obtain full crystallinity [10].

The morphology of the prepared YAG and YAG:Dy nanopowders was examined using a high resolution scanning electron microscope (SEM) equipped with the high brightness Schottky Field Emission gun (FEGSEM, TESCAN) operating at 4 kV. In order to provide conductivity of the samples needed for SEM analysis, the samples were coated with gold/palladium. The SEM images of our YAG and YAG:Dy samples are given in Fig. 1. The powders are composed of well-defined and separated nanoparticles,

clusters, and agglomerated particles. The size of individual spherical particles is in the range of about 30–50 nm. The spherical shape of particles is of great importance because it provides lower light scattering and brighter luminescence performance [11].

3. Results and discussion

3.1. Adsorption isotherms – BET experiments

The analyzer Surfer (Thermo Fisher Scientific, USA) was used to examine YAG and YAG:Dy nanopowders.

The dependences of the adsorbed amount of N_2 on the relative pressure, P/P_0, at the temperature of −196 °C, i.e., the nitrogen adsorption isotherms, for the YAG and YAG:Dy samples are given in Fig. 2. The adsorptions at low relative pressures, given in the graph inserts, indicate that there are micropores on the particle surfaces. According to the IUPAC classification pores are classified as macropores (pore width above 50 nm), mesopores (pore width 2–50 nm) and micropores (pore width below 2 nm) [12]. At the same time, non-limiting adsorption at high P/P_0, was found to correspond to non-rigid aggregates of particles giving rise to slit-shaped pores [13]. Note that these conclusions are in agreement with the SEM images given in Fig. 1, which show that our samples contain agglomerated as well as separated particles. The separated particles are found to be spherical with the diameter of approximately 40 nm. The specific surface areas calculated by the BET equation, S_{BET}, are found to be 5 $m^2 g^{-1}$ and 12 $m^2 g^{-1}$ for the YAG and YAG:Dy samples, respectively. Since the radius of Dy^{3+} ion of 0.1167 nm is larger than the radius of Y^{3+} ion, which is 0.1159 nm, it comes as no surprise that the presence of Dy led to increase of the overall specific surface of particles. Also, dopants introduce defects into the structure of the material which results in different charge on the particle surface when doped and undoped are compared. This charge on the particle surface leads to differences in packaging particles and their greater or lesser agglomeration, which on the other hand have significant role on the porosity and specific surface area. Incorporated dopants have a tendency to concentrate at the surface of nanomaterials. All these have significant role on the increasing of the specific surface area.

3.2. Far-infrared spectroscopy

The far-infrared measurements were carried out with the BOMEM DA – 8 FIR spectrometer. The wave number range between 80 and 600 cm^{-1} was covered with the DTGS pyroelectric detector.
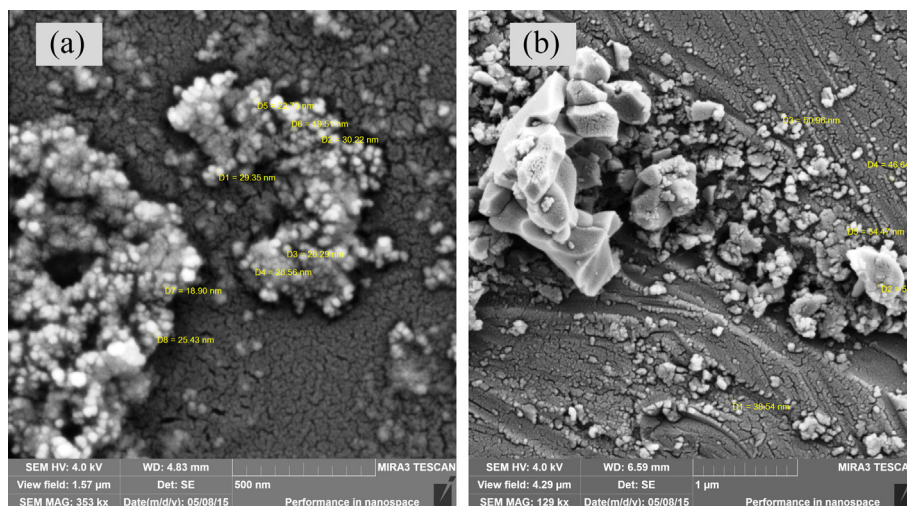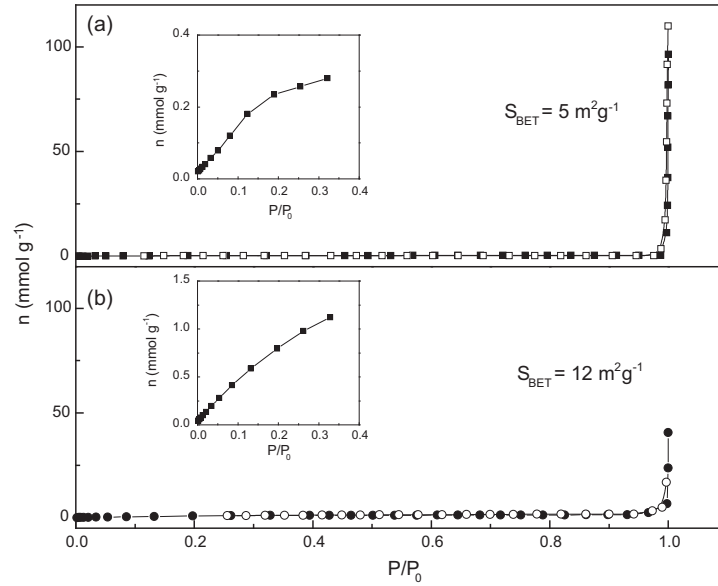

Fig. 1. SEM micrographs. The micrographs of YAG and YAG:Dy nanopowders are given in part (a) and (b), respectively.

Fig. 2. Nitrogen adsorption isotherms. The amount of adsorbed N_2 given as a function of the relative pressure is shown in graphs (a) and (b) for YAG and YAG:Dy nanopowders, respectively. Solid symbols correspond to adsorption, whereas open symbols represent desorption. The shapes of the curves around zero are enlarged in the inserts.

If the visible light wavelength, λ, is much larger than the characteristic size of semiconducting nanoparticles, d, i.e., if $\lambda \gg d$, the heterogeneous composite of nanoparticles with the dielectric function ε_2 distributed in a medium with the dielectric constant ε_1 can be treated as a homogeneous medium and effective medium theory is applicable. The effective dielectric permittivity of such a mixture can be modeled by a number of mixing models [14]. We chose the Maxwell–Garnet model since our samples are well defined and separated nanosized spherical grains. Consequently, the predicted effective permittivity of the mixture becomes [15]:

$$\varepsilon_{eff} = \varepsilon_1 + 3f\varepsilon_1 \frac{\varepsilon_2 - \varepsilon_1}{\varepsilon_2 + 2\varepsilon_1 - f(\varepsilon_1 - \varepsilon_2)}, \tag{1}$$

where spheres of permittivity ε_2 were taken to occupy a volume fraction f as well as to be randomly located in a homogeneous environment characterized with ε_1. In the considered nanopowders, nanoparticles are situated in air, therefore $\varepsilon_1 = 1$. To determine the dielectric function of the nanoparticles, i.e., ε_2, we used the plasmon–phonon interaction model [16]:

$$\varepsilon_2(\omega) = \varepsilon_\infty \left(\prod_{k=1}^n \frac{\omega_{LOk}^2 - \omega^2 + \imath\gamma_{LOk}\omega}{\omega_{TOk}^2 - \omega^2 + \imath\gamma_{TOk}\omega} - \frac{\omega_P^2}{\omega(\omega - \imath\tau^{-1})} \right) \tag{2}$$

where ε_∞ is the bound charge contribution and it is assumed to be a constant, ω_{TOk} and ω_{LOk} are the transverse and longitudinal frequencies, $\gamma_{TOk,}$ and γ_{LOk} are their dampings, ω_P is the plasma frequency and τ is the free carrier relaxation time. The first term in Eq. (2) is the lattice contribution, whereas the second term corresponds to the Drude expression for the free carrier contribution to the dielectric constant.

The measured and calculated far-infrared spectra of YAG and YAG:Dy nanopowders, in the spectral range between 80 and 600 cm^{-1}, at room temperature are shown in Fig. 3. The experimental data are depicted by circles, whereas the solid lines are used to draw the calculated spectra obtained by the fitting procedure based and the model defined by Eqs. (1) and (2). The best fit parameters corresponding to YAG and YAG:Dy nanopowders are given in Table 1. The values corresponding to the YAG single crystal are taken from [17].
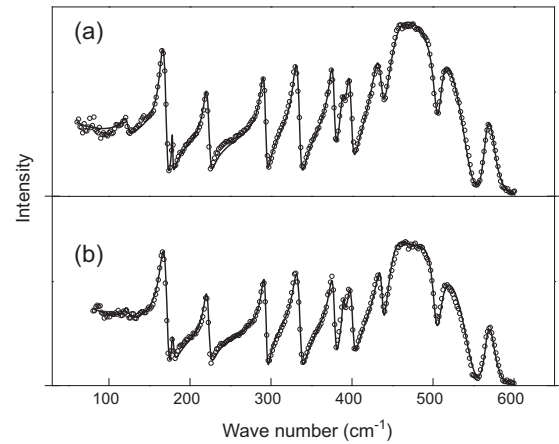
Fig. 3. Far-infrared reflection spectra of YAG nanopowder (a) and YAG:Dy nanopowder (b) at room temperature. The experimental data are represented by circles. The solid lines are the calculated spectra obtained with the parameter values given in Table 1 and the fitting procedure based on the model given by Eqs. (1) and (2).

YAG crystallizes in the cubic structure, it has the symmetry of O_h^{10}–$Ia3d$ space group, and eight molecules of $Y_3Al_5O_{12}$ per primitive unit cell. Out of the ninety-eight theoretically predicted Brillouin zone center modes that correspond to the O_h structure in the YAG group, $3A_{1g} + 5A_{2g} + 8E_g + 14T_{1g} + 14T_{2g} + 5A_{1u} + 5A_{2u} + 10E_u + 18T_{1u} + 16T_{2u}$, only the eighteen T_{1u} modes are IR-active [19]. Further, out of these eighteen theoretically predicted IR-active modes, fourteen are visible in the experimental and modeled far-infrared reflectivity spectra of the YAG and YAG:Dy nanopowders, and in the data corresponding to the YAG single crystal retrieved from literature, see Fig. 3 and Table 1. The bands at around 430, 453, 477, 510 and 566 cm^{-1} represent the characteristic metal–oxygen vibrations, which are in our example Y–O and Al–O. Our data are in agreement with the previous reports regarding single crystals [18,19] as well as with the results on nanocrystals of YAG [20,21]. The peaks located in the vicinity of 477, 510 and 566 cm^{-1} are the asymmetric stretching vibrations, whereas the peak at approximately 453 cm^{-1} is the symmetric vibration

Table 1
Best fit parameters of far-infrared spectra of YAG single crystal, YAG nanopowder and YAG:Dy nanopowder.

	YAG single crystal	YAG nanopowder	YAG:Dy nanopowder	Vibrations
ω_{TO} (cm^{-1})	122	122	122	T (+T$_d$) translations of tetrahedral and dodecahedral cation
	165	165	163	T$_d$ translations of dodecahedral cation
	180	178	178	T$_d$ (+T) translations of tetrahedral and dodecahedral cation
	221	220	219	T$_d$ translations of dodecahedral cation (translations of cations in YO$_3$ and AlO$_4$)
	291	290	289.5	T$_0$
	327	330	328	T translations of tetrahedral cation
	375	375	373	R libration of tetrahedral cation
	390	388.5	389	T$_0$ translations of octahedral cation
	396	399.5	396	R libration of tetrahedral cation
	432	431	431	T$_0$ translations of octahedral (translations + libration) cations in AlO$_6$ and AlO$_4$
	453	447	444	ν_2 symmetric
	477	465	465	ν_4 symmetric
	510	508	507	ν_4
	566	563	564	ν_4 (symmetric and asymmetric stretching of Al–O in octahedrons)
ω_p (cm^{-1})	220	190	220	–
τ (cm^{-1})	0.001	0.002	0.035	–
f	1	0.96	0.80	–

of Al–O bond in the octahedral arrangement of garnet structure. The four lowest energy peaks correspond to the translation and vibration of cations in different coordination – tetrahedral, octahedral and dodecahedral [22]. The peaks around 165, 220, 375 and 396 cm^{-1} have been attributed to the translator motion of Y^{3+} ions within the distorted cube that has eight oxygen ions at its vertices, as well as to the heavy mixing of the translational, rotational, and ν_3 mode of the (AlO$_4$) unit.

Differences in the structure of YAG single crystal and YAG nanopowder cause changes in the phonon frequencies. Namely, decrease in the crystallite size causes optical phonon confinement. The influence of doping of YAG by Dy^{3+} on the spectral properties and lattice vibrations is not significant. Compared to the spectra of YAG single crystal and YAG nanopowder, there are no new phonon modes corresponding to the YAG:Dy nanopowder; however, further decrease of phonon frequencies is registered. Since Dy^{3+} ions are by 0.69%, larger than Y^{3+} ions, substitution of Y^{3+} with Dy^{3+} leads to further distortion of the cubic cell, and consequently to the shift of characteristics frequencies toward lower frequencies, as can be seen in Fig. 3 and Table 1.

The values of filling factors were determined from the analysis of reflection spectra. The main volume fraction, f, obtained as the best fit parameter estimation, is listed in Table 1. These results are consistent with the results obtained by the BET experiment described in Section 3.1. Namely, high values of the filling factor are associated with the existence of micropores.

4. Conclusions

Due to their prospective application in optical amplifiers for the second telecommunication window and solid-state lasers that operate in the visible part of the spectrum, properties of the YAG:Dy nanopowder were investigated and compared to those corresponding to the YAG nanopowder and YAG single crystal. The nanopowders were synthetized by the solution combustion synthesis technique and the samples were analyzed by the scanning electron microscopy, nitrogen adsorption method as well as by the far-infrared spectroscopy. The measured far-infrared spectra were in complete agreement with the modeled spectra obtained with the Maxwell–Garnet formula, plasmon–phonon interaction model, and fitting procedure. It was determined that the Dy doped as well as non-doped YAG nanopowders are microporous. Spherical, well-defined and separated nanoparticles as well as agglomerated particles were detected. The far-infrared measurements revealed that the YAG nanopowder has lower phonon

frequencies than the YAG single crystal as well as that doping of YAG by Dy^{3+} does not have significant influence on the spectral properties and lattice vibrations. However, the doping caused further decrease of phonon frequencies, with respect to the frequencies that correspond to the YAG single crystal and YAG nanopowder.

References

[1] Ji-Guang Li, Takayasu Ikegami, Jong-Heun Lee, Toshiyuki Mori, J. Am. Ceram. Soc. 83 (4) (2000) 961–963.
[2] L. Wen, X. Sun, Z. Xiu, S. Chen, Chi-Tay Tsai, J. Eur. Ceram. Soc. 24 (2004) 2681–2688.
[3] J.W.G.A. Vrolijk, J.W.M.M. Willems, R. Metselaar, J. Eur. Ceram. Soc. 6 (1990) 47–51.
[4] Y. Fujimoto, T. Yanagida, H. Yagi, T. Yanagidani, V. Chani, Opt. Mater. 36 (2014) 1926–1929.
[5] C.R. Varney, D.T. Mackay, S.M. Reda, F.A. Selim, J. Phys. D Appl. Phys. 45 (2012) 015103–015106.
[6] A. Senyshyn, L. Vasylechko, Acta Phys. Pol., A 124 (2013) 329–335.
[7] B. Cole, L.B. Shaw, P.C. Pureza, R. Mossadegh, J.S. Sanghera, I.D. Aggarwal, J. Non-Cryst, Solids 256–257 (1999) 253–259.
[8] A. Kaminskii, U. Hommerich, D. Temple, J.T. Seo, K.-I. Ueda, S. Bagayev, A. Pavlyulk, Jpn. J. Appl. Phys., Part 2: Lett. 39 (3A/B) (2000). L208-11.
[9] M. Klimczak, M. Malinowski, J. Sarnecki, R. Piramidowic, J. Lumin. 129 (2009) 1869–1873.
[10] M.S. Rabasovic, D. Sevic, J. Krizan, M.D. Rabasovic, S. Savic-Sevic, M. Mitric, M. Petrovic, M. Gilic, N. Romcevic, Opt. Mater. 50 (2015) 250–255.
[11] Joo-Yun Chong, Yuelan Zhang, Brent K. Wagner, Zhitao Kang, J. Alloys Compd. 581 (2013) 484–487.
[12] K.S.W. Sing, D.H. Everett, R.A.W. Haul, L. Moscou, R.A. Pierotti, J. Rouquerol, et al., Pure Appl. Chem. 57 (4) (1985) 603–619.
[13] S. Lowell, J.E. Shields, M.A. Thomas, M. Thommes, Charactrization of Porous Solids and Powders: Surface Area, Pore Size and Density, Kluwer Academic Publishers, Dordrecht Netherlands, 2004. 44.
[14] K. Karkkainen, A. Saviola, K. Nikoskinen, IEEE Trans. Geosci. Remote Sensors 39 (5) (2001) 1013–1018.
[15] J.C.M. Garnett, Trans. R. Soc. Vol. CCIII (1904) 385–420.
[16] I.J. Uhanov, Opt. svojstva poluprovodnikov, Nauka, Moskva (1977).
[17] S. Kostić, Z.Ž. Lazarević, V. Radojević, A. Milutinović, M. Romčević, N.Ž. Romčević, A. Valčić, Mater. Res. Bull. 63 (2015) 80–87.
[18] J.P. Hurrel, P.S. Porto, I.F. Chang, S.S. Mitra, R.P. Bauman, Phys. Rev. 173 (1968) 851–856.
[19] G.A. Slack, D.W. Oliver, R.M. Chrenko, S. Roberts, Phys. Rev. 177 (1969) 1308–1314.
[20] Z.H. Chen, Y. Yang, Z.G. Hu, J.-T. Li, S.L. He, J. Alloys Compd. 433 (2007) 328–331.
[21] E. De la Rosa, L.A. Díaz-Torres, P. Salas, A. Arredondo, J.A. Montoya, C. Angeles, R.A. Rodríguez, Opt. Mater. 27 (2005) 1793–1799.
[22] A.M. Hofmeister, K.R. Campbell, J. Appl. Phys. 72 (1992) 638–646.

Far-infrared spectroscopy of laser power modified MnO nanoparticles

B. BABIC[a], B. HADZIC[a], I. KURYLISZYN-KUDELSKA[b], N. PAUNOVIC[a], B. VASIC[a], W. D. DOBROWOLSKI[b], M. ROMCEVIC[a], J. TRAJIC[a,*], N. ROMCEVIC[a]

[a]Institute of Physics, University of Belgrade, Pregrevica 118, 11080 Belgrade, Serbia
[b]Institute of Physics, Polish Academy of Science, al. Lotnikow 32/46, 02-668 Warszawa, Poland

The influence of the locally induced laser heating on MnO nanoparticles were investigated by atomic force microscopy (AFM) and far-infrared spectroscopy (FIR) at room temperature, in the spectral region between 80 and 600 cm^{-1}. The FIR spectra were analyzed by using Maxwell-Garnet formula, where MnO nanoparticles are modeled as a mixture of homogeneous spherical inclusions in air. Laser induced heating leads to the conversion of the part MnO nanoparticles into the MnO$_2$, Mn$_3$O$_4$ and MnOOH, along with possible formation of elemental Mn on the sample surface.

1. Introduction

MnO is transitional metal oxide which crystallizes in the simple rock salt structure. It is well known that this structure has a certain number of defects, usually in the cationic sublattice, what leads to the formation of structure which can be described as an ordered Mn vacancy cubic structure with the formula $Mn_{1-\delta}O$, where $0 \leq \delta \leq 0.15$ [1-3].

Due to this non-stoichiometry, MnO has unique electrical, magnetic, optical and mechanical properties, characteristic for the rock salt structure [1, 2]. Recently, Hiramoto and co-workers proposed a new synthetic route which enables the control of the non-stoichiometric defects in the structure [4]. Bulk MnO acts as a p-type semiconductor and has anti-ferromagnetic properties [5]. But, the presence of impurities can significantly change the magnetic properties of the MnO [6 - 9].

The size of the particles has considerable influence on the properties of MnO. For instance, literature data shows that nanometric MnO has ferromagnetic characteristics [5]. New characteristics on nanometric scale can be explained with significant changes into the surface to volume ratio. The decreasing of the particle size increases the amount of edge atoms and, consequently, the number of unsaturated chemical bonds which, further, changes the physical and chemical properties of the material. Manganese can exists in the several oxidation states among which Mn(II) is the lowest. By different oxidation treatment, manganese can be transverse in to the different, higher, oxidation states.

Recently, we have investigated the influence of the lacer induced heating of ZnO(Co) [10], Bi$_{12}$GeO$_{20}$ [11] and MnO [12] nanoparticles, with different laser powers. It has been shown that laser induced heating leads to creation of new phases, depending on laser power.

In order to further investigate the influence of the locally induced laser heating on MnO nanoparticles, non-irradiated, as well as irradiated MnO sample, were investigated by using far-infrared spectroscopy (FIR) and atomic force microscopy (AFM).

2. Sample characterization

Commercially available polycrystalline MnO powder of the analytical grade (Sigma-Aldrich Co) was pressed into a pellet. Verdi G optically pumped semiconductor laser with wavelenght of 532 nm was used as excitation source. In this paper we analyzed one sample, at first before laser treatment and afterwards after treatment with a laser with a power of 24 mW.

AFM measurements of non-irradiated and irradiated sample with the highest energy were done using NT-MDT system NTEGRA Prima at ambient conditions. AFM images were recorded in tapping mode, using NSG01 probes from NT-MDT.

The far-infrared measurements on non-irradiated and irradiated sample with laser power (24mV) were carried out with a BOMEM DA-8 FIR spectrometer. A DTGS pyroelectric detector was used to cover the wave number range from 80 to 600 cm^{-1}.

3. Results and analysis

3.1. AFM measurements

AFM topographies of non-irradiated (a) and irradiated (b) MnO samples are presented on Fig. 1. Fig. 1 shows a clear difference between the surfaces of the sample before and after irradiation. Prior to irradiation, a granulated structure, with well recognized grain boundaries, is visible.

Grains size is about few tens of nanometers. In our previous investigations X-ray analysis showed that mean crystallite size is about 44 nm [12] which is in good agreement with results obtained with AFM.

After irradiation, the topography of the surface was significantly changed. The grain boundaries are not visible and surface is smooth. Due to the laser induced heating and increasing of the energy, MnO particles on the surface of the samples interact with the elements and compounds from the vicinity (mostly oxygen and water) and create compounds in which manganese is in the higher oxidation state. Process is spontaneous and these different species are inhomogeneously arranged on the surface of the sample and, consequently, clear boundaries between grains are lost.
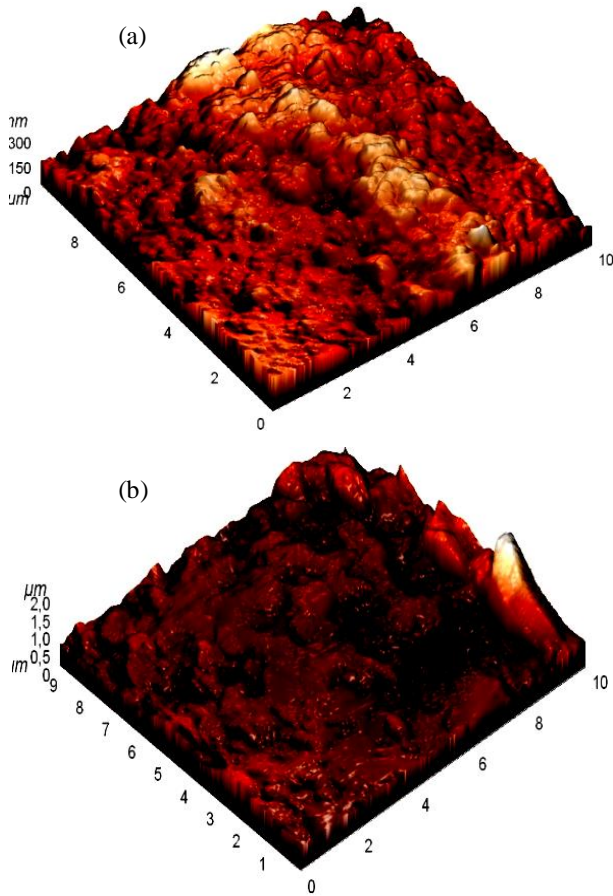

Fig. 1. AFM 3D topography of (a) non-irradiated and (b) irradiated sample of MnO nanoparticles

After irradiation, the topography of the surface was significantly changed. The grain boundaries are not visible and surface is smooth. Due to the laser induced heating and increasing of the energy, MnO particles on the surface of the samples interact with the elements and compounds from the vicinity (mostly oxygen and water) and create compounds in which manganese is in the higher oxidation state. Process is spontaneous and these different species are inhomogeneously arranged on the

surface of the sample and, consequently, clear boundaries between grains are lost.

3.2. Far-infrared spectroscopy

When visible light, of wavelength λ interacts with semiconducting nanoparticles (characteristic size d, dielectric function ε_2) which are distributed in a medium with the dielectric constant ε_1 in the limit $\lambda \gg$ d, the heterogeneous composite can be treated as a homogeneous medium and effective medium theory is applied. There are many mixing models for the effective dielectric permittivity of such a mixture [13]. Since our samples are well defined and separated nanosized grains, we used Maxwell-Garnet model for present case. For the spherical inclusions case, the prediction of the effective permittivity of mixture ε_{eff} according to the Maxwell-Garnet mixing rule is [14]:

$$\varepsilon_{eff} = \varepsilon_1 + 3f\varepsilon_1 \frac{\varepsilon_2 - \varepsilon_1}{\varepsilon_2 + 2\varepsilon_1 - f(\varepsilon_1 - \varepsilon_2)} \quad (1)$$

Here, spheres of permittivity ε_2 are located randomly in homogeneous environment ε_1 and occupy a volume fraction f. The observed nanoparticles are situated in air, therefore the ε_1 is 1. For dielectric function of observing nanoparticles (ε_2) we are using the standard model [15]:

$$\varepsilon_2(\omega) = \varepsilon_\infty + \sum_{k=1}^{l} \frac{\varepsilon_\infty \left(\omega_{LOk}^2 - \omega_{TOk}^2\right)}{\omega_{TOk}^2 - \omega^2 - i\gamma_{TOk}\omega} - \frac{\varepsilon_\infty \omega_P^2}{\omega\left(\omega + i\tau^{-1}\right)} \quad (2)$$

where ε_∞ is dielectric constant at high frequencies, ω_{TOk} and ω_{LOk} are transverse and longitudinal frequencies, γ_{TOk} is the phonon damping, ω_P is the plasma frequency and τ is the free carrier relaxation time. The first term in (2) is the lattice contribution whereas the second term is the Drude expression for the free carrier contribution to the dielectric constant. In this case, ω_{TOk} is considered as characteristic frequency of the material and ω_{LOk} is connected with the oscillator strength ($S_k \sim \omega_{LOk}^2 - \omega_{TOk}^2$).

The far-infrared spectra of non-irradiated and irradiated MnO nanopowders, in the spectral range of 80 to 600 cm^{-1}, at room temperature are presented in Fig. 2. The experimental data are presented by circles, while the solid lines are calculated spectra obtained by a fitting procedure based on the previously presented model. Obviously, a very good correlation between experimental data and calculated spectra is achieved. Parameters, such as: filling factors, *f,* plasma frequencies, ω_P, effective permittivity of mixtures, ε_{eff}, and transversal and longitudinal frequencies ω_{TO}/ω_{LO}, for the non-irradiated and irradiated sample, estimated from the reflection spectra, are presented in Table 1. Induced laser heating leads to the increasing of the filling factor. Result is expected and in agreement with result obtained by AFM. Namely, phase transformation and loss of the grain boundaries leads to the decreasing of the space between particles. In accordance with that, the dielectric constant at high frequencies and plasma frequency decrease. Also, we should keep in mind that surface affected by the laser beam

is significantly smaller (radius 1 mm) in comparison with the overall surface of the pallet (radius 6 mm) which means that, in the case of the irradiation of the whole sample the differences would be more significant.
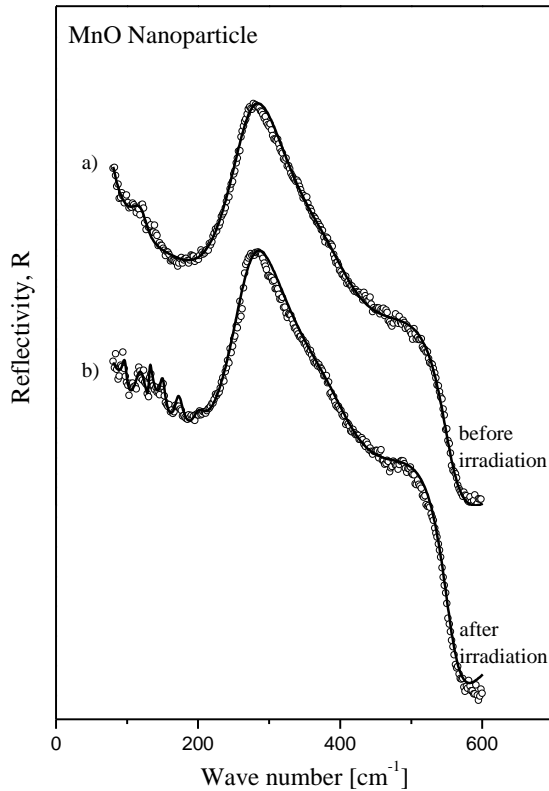

MnO Nanoparticle

Fig. 2. Far – infrared reflection spectra of (a) non-irradiated and (b) irradiated MnO nanoparticles. The experimental data are represented by circles. The solid lines are the calculated spectra obtained by fitting procedure based on the model given by Eqs. (1,2)

Five vibration modes were determined for both non-irradiated and irradiated sample and their values are presented in Table 1. To our knowledge, there are no literature data for the FIR characterization of the MnO and we compared these results with data collected by Raman spectroscopy. By summarizing different literature data [12, 16-24], three characteristics peaks for MnO are obtained in the range 520-545, 559-595 and 645-660 cm^{-1}. First two peaks we registered by using FIR spectroscopy, also. In both cases, non-irradiated and irradiated sample, additional two peaks, in the range of 310-410 cm^{-1} are recorded. According to literature data, these peaks can be attributed to the β-MnO$_2$ (TO/LO pair at 324/330cm^{-1}) [18, 22, 23] and α-MnO$_2$ (395/405cm^{-1}) [20, 21]. Additionally, according to Kim at al. [24] peak at 324 cm^{-1} can be attributed to Mn$_3$O$_4$.

Additional vibration peaks that appear in FIR spectra of irradiated samples can be identified in the following way: peaks at 131, 140, 171 and 199.5 cm^{-1} could be attributed to a α–MnOOH [20, 21] and peak at 171.5 cm^{-1} could be attributed to α–MnO$_2$ [20, 21].

Some authors peak at 171 cm^{-1} attributed to Mn$_5$O$_8$ phase (binary Mn$_2^{2+}$Mn$_3^{4+}$O$_8$ oxide with layer structure) [25]. These peaks are also registered at Raman spectra of the irradiated samples.

Table 1. Calculated fit parameters obtained from the far - infrared spectra of non - irradiated and irradiated MnO nanoparticles

	Before irradiation [cm^{-1}]	After irradiation [cm^{-1}]
f	0.81	0.89
ω_P	301	291
ε_∞	2.8	2.5
ω_{TO}/ω_{LO}	120/123	116.8/117
ω_{TO}/ω_{LO}	140/148	140/140
ω_{TO}/ω_{LO}	324/330	320/330
ω_{TO}/ω_{LO}	395/405	398/407
ω_{TO}/ω_{LO}	520/526	515/558
ω_{TO}/ω_{LO}	575/590	579/584
ω_{TO}/ω_{LO}	-	96.8/97.4
ω_{TO}/ω_{LO}	-	131/131.3
ω_{TO}/ω_{LO}	-	140/141
ω_{TO}/ω_{LO}	-	171.5/172
ω_{TO}/ω_{LO}	-	199.5/200

Mode at about 100 cm^{-1} (TO/LO pair is 116.8/117 cm^{-1} in our case) was registered before for this group of materials [26] as a "defect mode". Mod at 96.8/97.4 cm^{-1}, in the some region, can be describe us „defect mode", also. However, since it occurs only in an irradiated sample, we can assume that we have a case of disorder-enabled phonon (DAP) mode [27]. This is the case registered in a large number of A^{2}B^6 semiconductors [28].

Finally, it was shown that FIR spectroscopy is a useful technique for the characterization of laser power induced phase changes in MnO nanoparticles.

4. Conclusion

MnO nanoparticles modified by laser heating are investigated by using far-infrared spectroscopy. Effective permitivity of MnO nanoparticles (mixture of homogeneous spherical inclusions in air) are modeling by Maxwell-Garnet formula. In consequence of laser irradiation, volume fraction of nanoparticles increase while dielectric constant and plasma frequencies decrease, due to the formation of the different species on the surface of the MnO sample.

Additional vibration modes characteristic for the irradiated samples, were confirmed by using FIR method.

References

[1] M. Jimenez-Melendo, A. Dominguez-Rodriguez, J. Castaing, Acta Metallurgica et Materialia **43**, 3589 (1995).

[2] R. Aragon, Physical Review B **46,** 5328 (1992).

[3] M. J. Radler, J. B. Cohen, G. P. Sykora, T. Mason, D. E. Ellis, J. Faber Jr., Journal of Physics and Chemistry of Solids **53**, 141 (1992).

[4] M. Hiramoto, N. Okinaka, T. Akyimam, Materials Chemistry and Physics **134**, 98 (2012).

[5] I. Djerdj, D. Arcon, Z. Jaglicic, M. Niederberger, Journal of Physical Chemistry C **111**, 3614 (2007).

[6] N. Mironova-Ulmane, A. Kuzmin, M. Grube, Journal of Alloys and Compounds **480**, 97 (2009).

[7] J. Park, E. Kang, C. J. Bae, J. G. Park, H. J. Noh, J. Y. Kim, J. H. Park, H. M. Park, T. Hyeon, Journal of Physical Chemistry B **108**, 13594 (2004).

[8] A. E. Berkowitz, G. F. Rodriguez, J. I. Hong, K. An, T. Hyeon, A. Agarwal, D. J. Smith, E. E. Fullerton, Physical Review B **77**, 024403 (2008).

[9] J. J. Hauser, J. V. Waszczak, Physical Review B **30**, 5167 (1984).

[10] B. Hadžić, N. Romčević, D. Sibera, U. Narkiewicz, I. Kurylisyn-Kudelska, W. Dobrowolski, M. Romčević, Journal of Physics and Chemistry of Solids **91**, 80 (2016).

[11] A. Kovačević, J. Ristić-Djurović, M. Lekić, B. Hadžić, G. Saleh Isa Abudagel, S. Petričević, P. Mihailović, B. Matović, D. Dramlić, Lj. Brajović, N. Romčević, Materials Research Bulletin **83**, 284 (2016).

[12] B. Hadzic, B. Vasic, B. Matovic, I. Kuryliszyn-Kudelska, W. Dobrowolski, M. Romcevic, N. Romcevic, Journal of Raman Spectroscopy (2018) in press.

[13] K. Karkkainen, A. Sihvola, K. Nikoskinen, IEEE Transactions on Geoscience and Remote Sensing **39**, 1013 (2001).

[14] J. C. M. Garnett, Philosophical Transactions of the Royal Society of London, Series A **203** 385 (1904).

[15] J. Trajic, N. Romcevic, M. Romcevic, V. N. Nikiforov, Materials Research Bulletin **42**, 2192 (2007).

[16] F. Buciuman, F. Patcas, R. Cracium, D. R. T. Zahn, Physical Chemistry Chemical Physics **1**, 185 (1999).

[17] C. Julien, M. Massot, R. Baddour-Hadjean, S. Franger, S. Bach, J. P. Pereira-Ramos, Solid State Ionics **159**, 345346 (2003).

[18] C. M. Julien, M. Massot, C. Poinsignon, Spectrochimica Acta Part A **60**, 689 (2004).

[19] B. K. Pandey, A. K. Shahi, R. Gopal, Materials Focus **2**, 221 (2013).

[20] T. Gao, H. Fjellvag, P. Norby, Analytica Chimica Acta **648**, 235 (2009).

[21] S. Cheng, L. Yang, D. Chen, X. Ji, Z.-J. Jiang, D. Ding, M. Liu, Nano Energy **9** 161 (2014).

[22] C. M. Julien, M. Massot, Proceedings of the International Workshop Advanced Techniques for Energy Sources Investigation and Testing, Sofia, Bulgaria, September 2004, pp. 1–17.

[23] S. Kumar, A. K. Ojha, R. K. Singh, Journal of Raman Spectroscopy **45**, 717 (2014).

[24] M. Kim, X. M. Chen, X. Wang, C. S. Nelson, R. Budakian, P. Abbamonte, S. L. Cooper, Physical Review B **84**, 174424 (2011).

[25] J. Gao, M. A. Lowe, H.D. Abruna, Chemistry of Materials **23**, 3223 (2011).

[26] H. Kepa, T. Giebultowicz, B. Buras, B. Lebech, K. Clausen, Physica Scripta **25**(6A), 807 (1982).

[27] V. Dzagan, I. Lokteva, C. Himcinschi, X. Jin, J. Kolny-Olesik, D. R. T. Zahn, Nanoscale Research Letters **6**, 79 (2011).

[28] A. Ingale, K. C. Rustagi, Physical Review B **58**, 7197 (1998).

[*]Corresponding author: jelena@ipb.ac.rs

Synthesis and spectroscopic characterisation of LiFePO$_4$ cathode materials

Z. LAZAREVIĆ[a,*], G. KRIŽAN[b,c], J. KRIŽAN[d], M. MITRIĆ[e], N. PAUNOVIĆ[a], A. MILUTINOVIĆ[a], N. ROMČEVIĆ[a]

[a]*Institute of Physics, University of Belgrade, Pregrevica 118, 11080 Belgrade, Serbia*
[b]*Department of Materials Chemistry, National Institute of Chemistry, Ljubljana, Slovenia*
[c]*Faculty of Chemistry and Chemical Technology, University of Ljubljana, Ljubljana, Slovenia*
[d]*AMI d.o.o., Trstenjakova ulica 5, Ptuj, Slovenia*
[e]*Institute of Nuclear Sciences Vinča, University of Belgrade, Belgrade, Serbia*

Lithium iron phosphate (LiFePO$_4$) are synthesized in complete and incomplete combustion and calcined at 700°C. The obtained samples were characterized by XRD, IR spectroscopy and magnetic measurement. Morphology of samples was controlled by SEM. The aim of this work is to show that it is possible to achieve a desired crystal phase by pulse combustion in a relatively cheap and fast way. The extremely rapid synthesis of almost pure phase material is possible due to the reduction in size of interacting particles and to an enormous number of collisions between them as a result of the strong turbulent flow associated with explosive combustion.

1. Introduction

Many researchers worked in developing the rechargeable lithium battery. Synthesis of new cathode materials for high capacity rechargeable lithium ion batteries is experiencing a great expansion in past few decades [1]. Chemistry, performance, cost and safety characteristics vary across battery types. LiFePO$_4$ crystallizes in the orthorhombic system (No. 62) with *Pnma* space group. It consists of a distorted hexagonal-close-packed (hcp) oxygen network forming 16 octahedral and 32 tetrahedral sites. There are two distinct and differ in size octahedral sites in this material: M1 is occupied by Li$^+$, and M2 is occupied by Fe^{2+}. The M1 sites form linear chains of edge sharing octahedra along the *b*-axis within Li$^+$ can be transferred to the anode in the first charge process, compensating for the oxidation of iron (Fe^{2+} to Fe^{3+}) [2]. The structure may contain one lithium ion per formula unit, which results in the theoretical capacity of 170 mAhg^{-1}. However, these one-dimensional paths are particularly vulnerable to blockage by defects and impurities. The M2 sites form zigzag lines of corner sharing octahedra and there is no continuous network of FeO$_6$ edge-shared octahedra that might contribute to electronic conductivity [3, 4]. Cations, Li (M1) and Fe (M2), are placed in half the octahedral sites and P ions in one-eighth of the tetrahedral sites [5]. The peculiar distribution of Li$^+$ and Fe^{2+} within the octahedral sites generates layers that have a direct impact on both electronic and ionic conductivities. Corner-shared FeO$_6$ octahedra are linked together in the *bc*-plane [6]. The FeO$_6$ octahedra are distorted lowering their local cubic-octahedral O_h to the C_s symmetry. The tetrahedral PO$_4$

polyanions bridge neighbouring layers of FeO$_6$ octahedra by sharing a common edge with one FeO$_6$ octahedron and two edges with LiO$_6$ octahedra. The PO$_4$ bridges provide three-dimensionality to the lattice and structure stability. Low intrinsic electrical conductivity and low Li-ion diffusion can be override by reducing the size of LFP nano-crystallites (and the diffusion path length for electrons and Li$^+$ ions), and by making composites with conductive graphitic materials, what resulting in better electronic contact between the particles.

It is generally known that there are a number of methods for obtaining Li-ion cathode materials. In the case of LiFePO$_4$ these methods can be divided into two groups - solid state syntheses and solution syntheses [7]. Solid state techniques are carried out at high temperatures without the addition of any solvent. On the other hand, solution based methods are based on reactions that take place in the presence of appropriate solvent systems.

There are some excellent reviews on the properties of LiFePO$_4$ that deal with its structural, morphological, electrochemical, and other physical properties targeting its cathode application. In a review paper [2] provides a detailed overview of the synthetic methods with the possible advantages and disadvantages of obtaining LiFePO$_4$ powders. A major difficulty related to the synthesis of orthophosphate LiFePO$_4$ comes from the existence, of two oxidation degrees of iron in nature, namely Fe^{2+} and Fe^{3+}, which makes the preparation of this material difficult.

Solid state synthesis, mechano-chemical activation, carbothermal reduction and microwave heating are based on solid state chemistry and are the most common solid-state methods for preparing LiFePO$_4$ powders [2, 8, 9].

Solid state methods are of importance in terms of obtaining ordered crystal structure in a simple way at elevated temperatures.

Although solid state methods are simple to use, they are typically time and energy consuming techniques and often lead to large particle size, low purity and deliver relatively poor electrochemical performance. Therefore, solution-based methods are of increasing importance as they often result in smaller and more uniform particle sizes, higher purity, more homogeneous carbon coating and higher electrochemical capacity. Hydrothermal synthesis [10], sol-gel synthesis [11], spray pyrolysis [12], co-precipitation [13] and micro emulsion drying [14] are common solution-based methods used for the preparation of LiFePO$_4$ powders.

An interesting technique is also the solution combustion synthesis, utilizing a reaction between metal nitrates an organic fuel, intricately mixed in a solution, after the solvent is evaporated [6, 15]. The method is easy to scale, very energy efficient, can combust stoichiometric fuel and air mixtures and is suitable for the production of powders in nanometric range because of acoustically driven droplet size reduction [16]. Furthermore, this method is very fast as the heat transfer is enhanced in the acoustic field of pulse combustion and solution combustion synthesis proceeds in a fraction of a second once the components reach the decomposition temperature [15]. There is also no waste water since it evaporates and the only by products are flue gases common for burning carbonaceous fuels.

The main goal of our work was to produce LiFePO$_4$ by a pulse combustion reactor method. The obtained olivine LiFePO$_4$ was characterized using XRD, IR spectroscopy and magnetic measurement. The morphology was studied using scanning electron microscopy.

2. Experimental procedure

The investigated samples are produced in reactor with a Helmholtz-type pulse combustor. The reactor, its capabilities and operating conditions, as well as the control of the synthesis processes, are described comprehensively in Ref.-s [7, 17].

The precursor is sprayed with a two fluid nozzle, the spraying gas being 99.9 % nitrogen with a pressure of 1.5 bar and a flow of 45 NL min^{-1}, measured using a thermal mass flow-meter. The precursor composition is 41,3 g of LiNO$_3$, 230,5 g of Fe(NO$_3$)$_3$.9H$_2$O, 69,0 g of NH$_4$H$_2$PO$_4$, 137,1 g of urea, 78,2 g of sucrose and 46,4 g of NH$_4$NO$_3$, dissolved in 700 g of deionized water. The reactor is operating under different conditions with the main difference being the frequency and amplitude of pressure oscillations. The sample was synthesized in reductive reactor conditions with low pressure amplitude (10 mbar).

Obtained material was annealed in the inert atmosphere. Annealing is taking place in an electrical oven under a constant argon flow and in presence of carbon at 700 °C for 6 h. High temperature and inert environment allow a reduction of Fe^{3+} from α-Fe$_2$O$_3$ and formation of additional LiFePO$_4$ according to: 4 Li$_3$Fe$_2$(PO$_4$)$_3$ + 2 Fe$_2$O$_3$ + 3C → 12 LiFePO$_4$ + 3CO$_2$.

Four types of samples were investigated: 1) samples of the *as prepared* material synthesized in complete combustion and resonance mode of reactor (CC); 2) annealed samples of the material synthesized in complete combustion (A-CC); 3) samples of the *as prepared* material synthesized in incomplete combustion and resonance mode of reactor (ICC) and 4) annealed samples of the material synthesized in incomplete combustion (A-ICC).

Characterization of the sample was carried out by several methods:

• X-ray diffraction analysis was performed on X-ray diffractometer (Rigaku Corporation, Japan) at room temperature. CuKα radiation (λ = 0.15418 nm) with a step size of 0.02° in the range of 2θ = 15-60° was used for all samples. The peaks were identified using the Powder Diffraction File (PDF) database created by International Centre for Diffraction Data (ICDD).

• The infrared (IR) measurements were carried out with a BOMMEM DA-8 FIR spectrometer. A DTGS pyroelectric detector was used to cover the wave number range from 50 cm^{-1} to 700 cm^{-1}.

• Magnetic susceptibility measurements were carried out at Cryogenic vibrating sample magnetometer (VSM) with an ultra-sensitive superconducting quantum interference device (SQUID) in the temperature range 4-160 K. *AC* magnetic susceptibility were performed using a mutual inductance method with an alternate excitation field of 5 Oe and frequencies in the range 7-10000 Hz.

• Scanning electron microscopy - SEM (Zeiss Supra 35 VR) was used to make images of the particles.

3. Results and discussion

X-ray diffraction analysis was used to identify the crystalline phases of the investigated samples. Fig. 1 shows the XRD patterns of two as prepared samples (CC and ICC) and two annealed samples (A-CC and A-ICC). Spectra of samples CC and ICC are with subtracted baselines. Original diffraction patterns are shown in inserts.
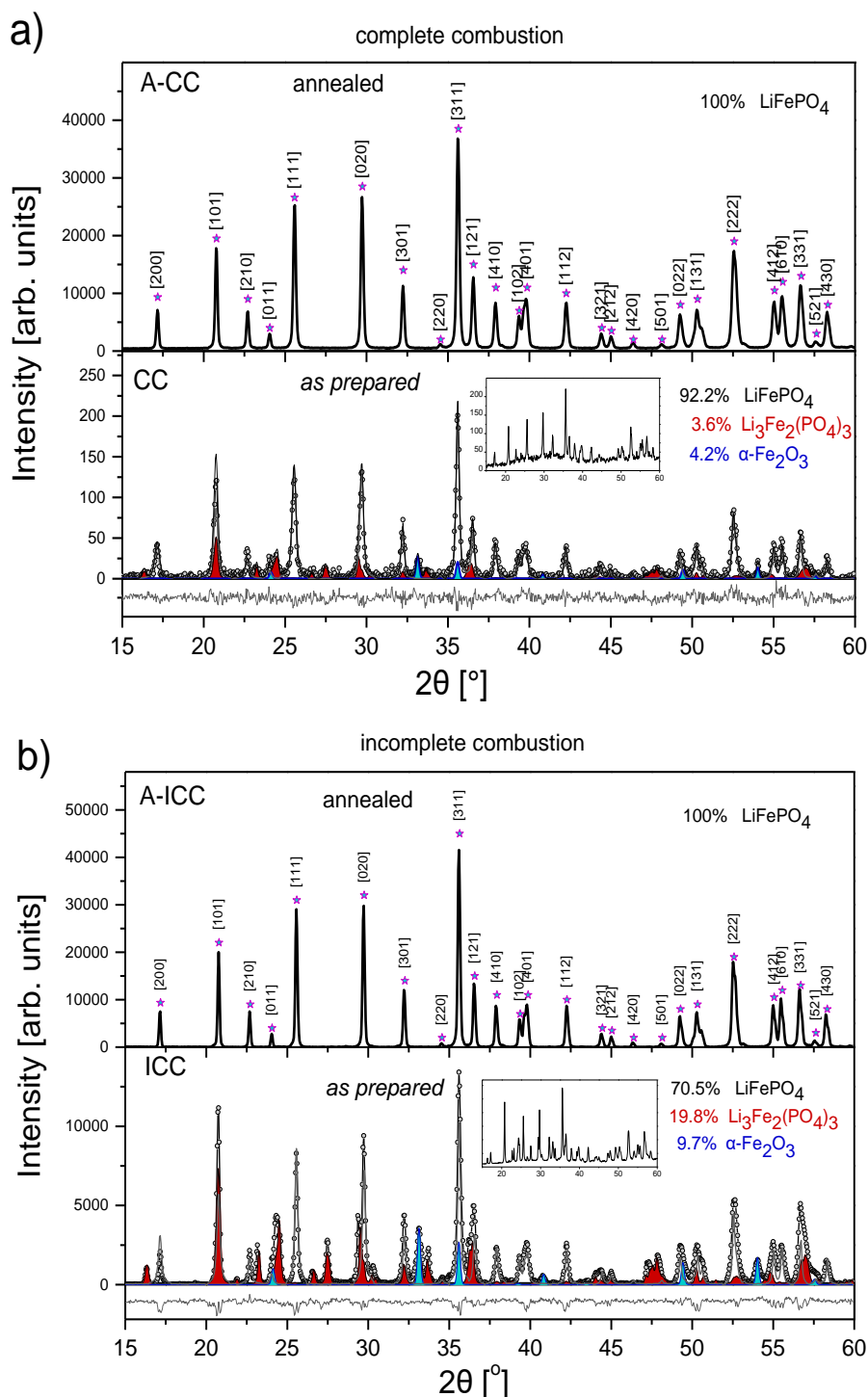
Fig. 1. a) XRD spectra of samples obtained by complete combustion: as prepared CC and annealed A-CC;
b) XRD spectra of samples obtained by incomplete combustion: as prepared ICC and annealed A-ICC

All diffraction patterns were analysed by Rietveld refinement software. Except dominant LiFePO$_4$ phase, *as prepared* samples contain phases with Fe^{3+}: α-Li$_3$Fe$_2$(PO$_4$)$_3$ and α-Fe$_2$O$_3$. Phase content is given in Fig. 1. A sample CC, of the material obtained in complete combustion has over 92% of LiFePO$_4$ phase and sample ICC obtained in incomplete combustion has 70.5%. After annealing at 700 °C for 6 h in reductive atmosphere both materials exhibit pure olivine LiFePO$_4$ phase.

Annealing of *as prepared* material leads to certain enlargement of LiFePO$_4$ crystallographic cell volume. In A-CC sample enlargement is 0.01% related to CC sample (crystal cell constant *a* increases 0.07%; *b* increases 0.03%; *c* decreases 0.01%) and internal strain decreases for 28%. In A-ICC sample enlargement is even 0.3% related to ICC sample (crystal cell constant *a* increases 0.1%; *b* increases 0.2%; *c* slightly decreases 0.02%) but internal strain increases for 5%. The results of Rietveld

refinement are given in Table 1 for the fraction of pure LFP-phase in the investigated samples.

Table 1. Fraction of pure LFP-phase in the investigated samples and the microstructural characteristics: crystal cell constants, crystallite size and strain obtained from the Rietveld analysis

Sample	Crystal cells constants [Å]			Size [nm]	Strain 10^{-4}
	a	*b*	*c*		
A-CC	10.3211	6.0039	4.6908	57.0	13.7
A-ICC	10.3228	6.0084	4.6897	71.3	13.2
CC	10.3140	6.0022	4.6912	30.3	19.08
ICC	10.3129	5.9956	4.6907	46.7	12.56

Similar behaviour is noticed for many nanocrystalline samples. Smaller nanoparticles with greater surfaces and more incomplete bonds have a great deal of Li$_{1-x}$(Fe^{3+}, Fe^{2+})(PO$_4$) phase. LiFePO$_4$ and FePO$_4$ present both the *Pnma* olivine structure. Chemical extraction of Li$^+$ from LiFe^{2+}PO$_4$ results in oxidation of Fe^{2+} into Fe^{3+}. Decrease of ionic radii of Fe cation in crystallographic site M2 (4*c*) leads to changes in lattice parameters in Fe^{3+}PO$_4$.

According to Rousse at al. [18] in FePO$_4$, related to LiFePO$_4$, contractions of lattice along the *a* and *b* axis are -5.6% and -4.3%, respectively, and the *c* lattice parameter being increased by +1.5%. Gibot *at al.* [19] by *in situ* XRD analysis have registered a continuous shift of the diffraction peaks (and unit cell volume) during the charge/discharge of their LiFePO$_4$ cathode. This is equivalent to a continuous change of *x* in Li$_{1-x}$(Fe^{3+}, Fe^{2+})(PO$_4$) material. In full discharged state, according to XRD, cathode material exhibits the smallest cell volume of 273 Å^3, close to those of the fully delithiated FePO$_4$ phase.

Our annealed samples have crystal cell volumes a little lower than LFP cell standard PDF card No. 81-1173 (*a* = 1.0330 nm, *b* = 0.6010 nm, and *c* = 0.4692 nm), or in Ref. [20] (*a* = 10.3131 Å, *b* = 6.0025 Å and *c* = 4.6948 Å). In light of Results in Table 1 all our samples contain a certain amount of delithiated LiFePO$_4$ and the amount of this phase is larger in *as prepared* samples.

The infrared reflectivity of all samples is rather low, only about 0.2. The highest values of 0.3 achieve peaks of annealed samples owing to better crystallinity. Spectra of annealed samples are very similar. General appearance of un-annealed samples spectra is different. Experimental spectra are properly fitted with 18 phonon modes. It is obvious that the concentration of electrons is small enough that there was no need for fitting of plasma frequency in the investigated range of spectra.

Kramers-Krönig (KK) analysis of reflectivity spectra gives $\varepsilon_2(\omega)$ and energy loss function, $\sigma(\omega) = \text{Im}(-1/\varepsilon(\omega))$. Local maximums of $\varepsilon_2(\omega)$ correspond to the values of ω_{TO}, and local maximums of $\sigma(\omega)$ to ω_{LO}. Values of $\omega_{LO(TO)}$ obtained by fitting procedure are in accordance with values calculated by KK analysis (except the beginnings of spectra that were not fitted precisely owing to high level of noise). In Fig. 2 are given $\varepsilon_2(\omega)$ functions obtained from KK analysis for all investigated samples. Dotted "vertical" lines show modes with frequencies shifted in relation to the corresponding modes in the annealed samples. Full vertical lines show modes that stayed unchanged. In near normal incidence measurements TO modes correspond to minimums of transmittance. Only TO modes are IR active.
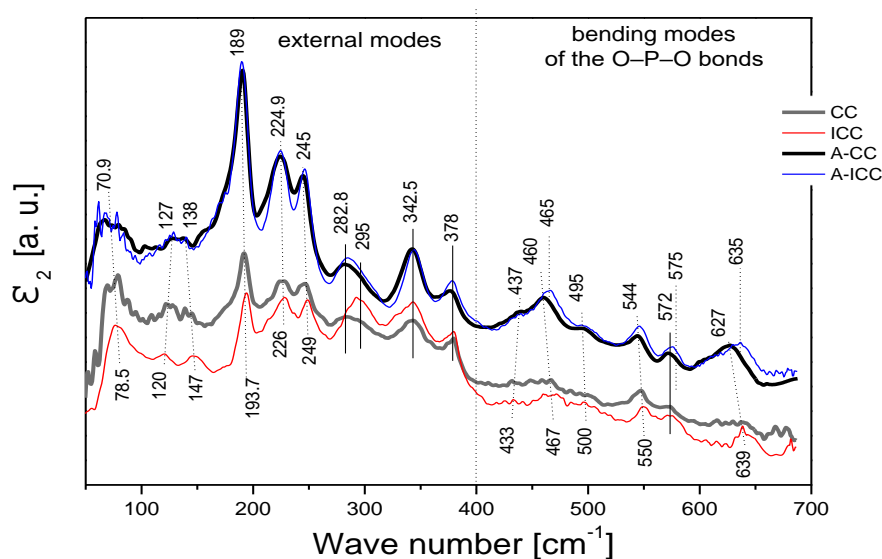

Fig. 2. Kramers-Krönig analysis of reflectivity spectra

Strength of TO modes, i.e. LO modes, can be deduced through fitting of reflectance spectra. Therefore, we can compare our $\varepsilon_2(\omega)$ functions with theoretical predictions of Shi [21] and available transmission/absorption measurements [22-27]. It should be bare in mind that intensity of peaks in $\varepsilon_2(\omega)$ doesn't correspond to real strength of modes obtained by fitting procedure.

The origin of a few coarse features at low wave numbers is not clear. We suppose that it can be a combination of acoustic modes activated by disorder. Further 15 phonons with remarkably reduced damping are attributed to optical modes of the crystal structure. Infrared reflectivity spectra of annealed samples A-CC and A-ICC evidently exhibit modes of LiFePO$_4$. Phonons with frequencies at 189, 224.9, 245 and 282.8 cm^{-1} are connected with vibrations of LiO$_6$ octahedrons. Peak at about 225 cm^{-1} is distinguishing for LiO$_6$ and related to asymmetric stretching vibration of Li - O bonds. Phonons at 324.5 and 378 cm^{-1} are connected with FeO$_6$ octahedrons and all together belong to external modes. From 400 to 647 cm^{-1} is the range of internal PO$_4^{3+}$ anion bending modes. A weak mode at 437 cm^{-1} is probably a $B_{2u}(6)$ mode [26]. Modes of PO$_4$ at 460-495 in A-CC sample, and 465-495 in A-ICC sample, represent "ν_2" modes, i.e. symmetric O-P-O bending modes. ν_2 modes in LFP are a mixture of Li translations and PO$_4$ bending motions of the same symmetry. Burba and Frech [22] suggest that these bands in LiFePO$_4$ are predominantly Li-ion "cage modes", ie. Li-translation. At 572-627 cm^{-1} in A-CC and 575-635 cm^{-1} in A-ICC are ν_4 modes, i.e. anti-symmetric O-P-O bending modes.

By comparing literature data it can be seen that obtained values for certain mode vary a litle. Possible resons are different methods of producing samples, or different size of crystallites. For example, Burba and Frech were registered the doublet ν_2 at 470-506 cm^{-1}, in Ref.[22] at 465-503 cm^{-1}, or in Ref. [26] at 469-499 cm^{-1}. The positions of the other modes vary in similar way.

Since external modes of annealed samples do not differ from each other, the difference in values of internal modes could not be asscribed to the producing of samples. A blue shift of A-ICC internal modes could be explained by superposition of LFP modes and modes of slightly delithiated phase Li$_{1-x}$(Fe^{3+}, Fe^{2+})PO$_4$, or a small amount of FePO$_4$ – phase with olivine structure "invisible" for XRD.

Samples CC and ICC have broader modes with partially changed energies due to superposition of LiFePO$_4$ modes and modes of other phases Fe$_2$O$_3$ and Li$_3$Fe$_2$(PO$_4$)$_3$, registered by XRD analysis. Except modes from the group of FeO$_6$ vibrations (and two weak modes at the beginning of spectra), other modes are shifted toward higher frequencies. That can be explained by contraction of bonds in LiO$_6$ octahedral, as well as in PO$_4$ tetrahedral. Cell volume shrinking was observed by XRD analysis of as prepared samples. IR spectra suggest that for volume shrinking two reasons exists: presence of smaller Fe^{3+} cations in crystal cell and a lack of Li related to pure LFP phase. Contraction in LiO$_6$ suggest that phase without Li (like hematite), or delithiated phase is present together with LFP phase. In the range of 200-400 cm^{-1} a certain increasement of peaks intensity is noticeable especially in the case of ICC sample. This range corresponds to the strongest modes of Li$_3$Fe$_2$(PO$_4$)$_3$ phase [24]. Such behaviour confirms that ICC sample contains much more fraction of Li$_3$Fe$_2$(PO$_4$)$_3$ phase than CC sample.

AC-magnetic susceptibility measurements were shown that the sample of annealed A-CC material has a typical triphylite antiferromagnetic behaviour with a Neel temperature at 53.4 K [25, 27]. The sample A-ICC except the predominant triphylite transition has a visible AFM transition of delithiated FePO$_4$ phase at T$_N$ = 130 K [25]. The results for poly-phase as prepared CC and ICC samples with small crystallites are shown in Fig. 3. Nell temperature of 29 K corresponds to Li$_3$Fe$_2$(PO$_4$)$_3$ phase [27] and about 51 K is a poorly visible antiferromagnetic transition of LiFePO$_4$. It means that as prepared samples are mostly superparamagnetic.

A peak at about 7.6 K in CC-sample (and 8.7 K in ICC) shifts toward higher temperatures with increasing measurement frequency. Such frequency dependence is specific for a spin glass. Therefore, a peak temperature is a spin-glass freezing temperature T$_f$ [28]. The dependence of T$_f$ with frequency is illustrated in the inset of Fig. 3.
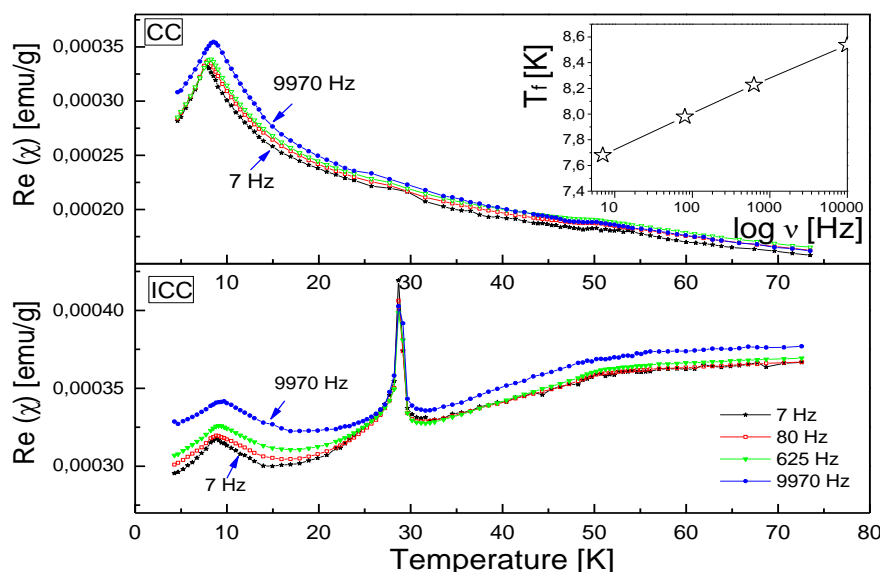

Fig. 3. AC susceptibility measurements at alternating fields with intensity 5 Oe and frequencies of 7, 80, 625 and 9970 Hz

SEM images of samples obtained by complete combustion (as prepared CC and annealed A-CC) and incomplete combustion (as prepared ICC and annealed A-ICC) are presented in Fig. 4. The difference in particle size is evident from images. The agglomerates are of approximately the same size (from 4 to 10μm), shaped like porous balls. In the annealed sample A-ICC are visible much larger structures than in A-CC sample. An average diameter of hollow spheres is about 10 μm. In the SEM image of the as prepared ICC sample (at the bottom, right) except globular form, a disk- like aggregates are seen. It can be seen a number of small shinny nanocrystals with average size about 30 nm. This supports the claim that particle size might affect the cell parameters, as indicating from Ritveld refinement of XRD data.
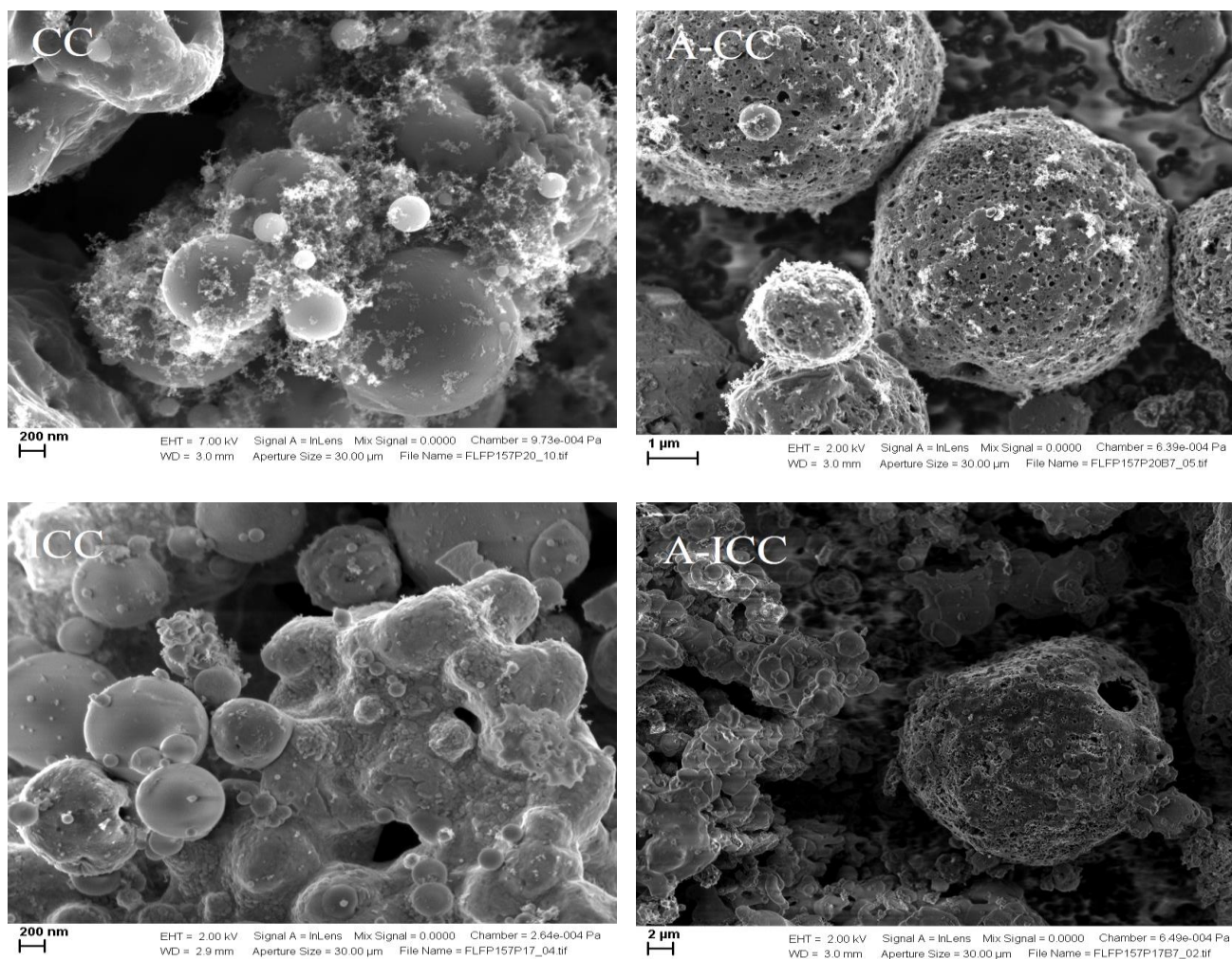

Fig. 4. SEM images of samples obtained by complete combustion (as prepared CC and annealed A-CC) and incomplete combustion (as prepared ICC and annealed A-ICC)

4. Conclusions

In this paper were investigated carbon coated LiFePO$_4$ cathode materials obtained by pulse combustion at the same temperature 700 °C, but in one case - under the conditions that leaded to complete combustion, and in the other case - under the conditions of incomplete combustion. After XRD analysis it seemed that in both cases after annealing we have obtained a good cathode material (samples A-CC and A-ICC). Therefore, further analysis IR and magnetic measurement, were implied that these, at first sight, perfect samples differed from each other. Analysis showed a significant excess of Fe^{3+} ions in the A-ICC sample and the magnetic measurements definitively identified a small quantity of delithiated FePO$_4$ phase in these sample.

In conclusion, performed measurements and analyses proved that (among investigated samples) the sample obtained under the applied conditions of complete combustion and annealed after that (in the presence of carbon under a constant argon flow at 700 °C for 6 hours),

A-CC, has a good structure and morphology that promises good electrochemical properties.

References

[1] T. V. S. L. Satyavani, A. Srinivas Kumar, P. S. V. Subba Rao, Engineering Science and Technology, an International Journal **19**, 178 (2016).

[2] D. Jugović, D. Uskoković, J. Power Sources **190**, 538 (2009).

[3] D. Morgan, A. Van der Ven, G. Ceder, Electrochem. Solid St. **7**(2), A30 (2004).

[4] S. Okada, S. Sawa, M. Egashira, J. Yamaki, M. Tabuchi, H. Kageyama, T. Konishi, A. Yoshino, J. Power Sources **97-98**, 430 (2001).

[5] K. Zaghib, A. Mauger, C. M. Julien, Olivine-Based Cathode Materials, Springer International Publishing Switzerland, 2015.

[6] S. Geller, J. L. Durand, Acta Crystallogr. **13**, 325 (1960).

[7] G. Križan, J. Križan, R. Dominko, M. Gaberšček, J. Power Sources **363**, 218 (2017).

[8] K. Ding, W. Li, Q. Wang, S. Wei, Z. Guo, J. Nanosci. Nanotechnol. **12**, 3812 (2012).

[9] K. S. Smirnov, V. A. Zhorin, N. A. Yashtulov, Russ. J. Appl. Chem. **86**, 603 (2013).

[10] S. Yang, P. Y. Zavalij, M. S. Whittingham, Electrochem. Commun. **3**, 505 (2001).

[11] R. Dominko, M. Bele, M. Gaberscek, M. Remskar, D. Hanzel, J. M. Goupil, S. Pejovnik, J. Jamnik, J. Power Sources **153**, 274 (2006).

[12] J. H. Lee, K. Y. Jung, S. B. Park, J. Mater. Sci. **34**, 4089 (1999).

[13] G. Arnold, J. Garche, R. Hemmer, S. Strobele, C. Vogler, M. Wohlfahrt-Mehrens, J. Power Sources **119-121**, 247 (2003).

[14] T. H. Cho, H. T. Chung, J. Power Sources **133**, 272 (2004).

[15] A. Varma, A. S. Mukasyan, A. S. Rogachev, K. V. Manukyan, Chem. Rev. **116**, 14493 (2016).

[16] X. Meng, W. de Jong, T. Kudra, Renew. Sustain. Energy Rev. **55**, 73 (2016).

[17] G. Križan, J. Križan, I. Bajsić, M. Gaberšček, Instrum. Sci. Technol. **46**, 43 (2018).

[18] G. Rousse, J. Rodriguez-Carvajal, S. Patoux, C. Masquelier, Chem. Mater. **15**, 4082 (2003).

[19] P. Gibot, M. Casas-Cabanas, L. Laffont-Dantras, S. Levasseur, P. Carlach, S. Hamelet, J.-M. Tarascon, C. Masquelier, Nat. Mater. **7**, 741 (2008).

[20] D. Jugović, M. Mitrić, M. Milović, B. Jokić, M. Vukomanović, D. Suvorov, D. Uskoković, Powder Technology **246**, 539 (2013).

[21] S. Shi, H. Zhang, X. Ke, C. Ouyang, M. Lei, L. Chen, Phys. Letters A **373**, 4096 (2009).

[22] C. M. Burba, R. Frech, Spectrochim. Acta A **65**, 44 (2006).

[23] C. M. Julien, K. Zaghib, A. Mauger, H. Groult, Advances in Chemical Engineering and Science **2**, 321 (2012).

[24] A. A. Salah, P. Jozwiak, J. Garbarczyk, K. Benkhouja, K. Zaghib, F. Gendron, C. M. Julien, J. Power Sources **140**, 370 (2005).

[25] A. Ait-Salah, J. Dodd, A. Mauger, R. Yazami, F. Gendron, C. M. Julien, Z. Anorg. Allg. Chem. **632**, 1598 (2006).

[26] W. Kang, C. Zhao, R. Liu, F. Xu, Q. Shen, Cryst. Eng. Comm. **14**, 2245 (2012).

[27] N. Ravet, M. Gauthier, K. Zaghib, J.B. Goodenough, A. Mauger, F. Gendron, C. M. Julien, Chem. Mater. **19**, 2595 (2007).

[28] V. Palomares, A. Goñi, A. Iturrondobeitia, L. Lezama, I. de Meatza, M. Bengoechea, T. Rojo, J. Mater. Chem. **22**, 4735 (2012).

*Corresponding author: lzorica@yahoo.com